Insights into Sanukitoid Formation and Evolution from Novel Stable Isotope Systems

Laura Mary Spencer

School of Earth and Environmental Sciences

Cardiff University

Thesis submitted for the degree of Doctor of Philosophy

March 2025

Summary

Sanukitoid magmatism is a unique feature of the late Archean-early Proterozoic transition (~3.0 – 2.0 billion years ago) that marks a major shift in continental crust composition and is thought to be linked to a geodynamic change. Sanukitoids are distinctively enriched in both mantle-compatible and incompatible elements, showing they formed by interaction between the mantle and a recycled crust-derived component. However, many aspects of sanukitoid parental magma formation, as well as their magmatic differentiation and temporal evolution, are poorly constrained, leading to multiple interpretations of their link to geodynamics. This thesis uses novel stable isotope systems, specifically titanium ($\delta^{49}Ti$) and uranium ($\delta^{238}U$) isotopes, to provide new insights into the formation and evolution of sanukitoids. Primitive sanukitoids have significantly heavier $\delta^{49}Ti$ than the mantle and modern arc basalts which requires a hydrous metabasite melt component. This metabasite melt likely formed via fluid-fluxed eclogite melting, suggesting the sanukitoid mantle source was generated by a subduction-like process in the late Archean. Sanukitoid Ti isotope systematics demonstrate that their parental magmas were as water-rich and oxidised as modern arc magmas, however their U isotope systematics imply that they were oxidised via a different mechanism to them. Sanukitoids display a small $\delta^{49}Ti$ increase during differentiation due to fractional crystallisation of abundant hornblende alongside Fe-Ti oxides. High-Sr "high pressure" TTGs (tonalites-trondhjemites-granodiorites) constitute the evolved end of the sanukitoid $\delta^{49}Ti$ differentiation trend in the Yilgarn Craton, supporting their formation by sanukitoid fractional crystallisation instead of by high pressure (≥ 2 GPa) metabasite melting. High-Sr "high pressure" TTGs are temporally and spatially associated with sanukitoids on many Archean cratons, suggesting this petrogenetic process was widespread in the late Archean. Turning to U isotopes, variations in sanukitoid and TTG $\delta^{238}U$ are primarily driven by apatite fractional crystallisation. While samples not affected by this process are limited in number, they hint at potential variations in sanukitoid, granitoid and oxidised magma U isotope compositions through time.

Table of contents

List of figures

List of tables

Statement on the status of publications

The work in Chapter 3 is published in an international, peer-reviewed journal:

> Spencer, L.M., Albert, C., Williams, H.M., Nebel, O., Parkinson, I.J., Smithies, R.H., Bruno, H., Fowler, M., Moreira, H., Lissenberg, C.J., Millet, M-A., 2024. Tracing hydrous eclogite melts in the source of sanukitoids. *Earth and Planetary Science Letters* 648, 119067. https://doi.org/10.1016/j.epsl.2024.119067

While the text and figures are largely the same as those in the published paper, the content has been re-formatted and edited to be suitable for the thesis chapter and to avoid repetition. The following edits have been made:

- The title has been modified to "Tracing hydrous eclogite melts in the source of sanukitoids with titanium stable isotopes"
- The section "2. Samples and methods" has been removed and incorporated into Chapter 2 of the thesis
- Table 3.1 has been added to present the titanium isotope data analysed
- Supplementary figures 1 and 2 have been added into the main chapter text at appropriate locations
- Supplementary material section "5. The high Ba-Sr granite suites" has been added into the main chapter text at appropriate locations
- Supplementary material sections "3. Rayleigh fractionation modelling of titanium isotopes during sanukitoid differentiation" and "4. Modelling of titanium isotope fractionation during partial melting" are included in Appendices D and E respectively
- Supplementary dataset 2 is included in Appendix F

The titanium stable isotope data presented in Chapter 3 are available through the DIGIS Geochemical Data Repository:

> Spencer, L.M., Albert, C., Williams, H.M., Nebel, O., Parkinson, I.J., Smithies, R.H., Bruno, H., Fowler, M., Moreira, H., Lissenberg, C.J., Millet, M-A., 2024. Titanium stable isotope and major and trace element compositions of Archean and Paleoproterozoic sanukitoids and Paleozoic high Ba-Sr granite suites. *GFZ Data Services*. https://doi.org/10.5880/digis.2024.004

Acknowledgements

I would first like to thank my incredible supervisory team for all their support throughout this PhD. In particular, thank you to my lead supervisor Marc-Alban Millet for his guidance, for encouraging me and helping me build my confidence as a scientist, for always making time for me, and for being patient with my many questions. Similar thanks go to Johan Lissenberg for all his advice and encouragement, and for frequently providing a different perspective on my research. I would also like to thank my co-supervisors Ian Parkinson, Oliver Nebel and Helen Williams for their help over the past three and a half years and for the valuable discussions I have had with them. Additional thanks go to Oliver and everyone at Monash University for being so welcoming when I visited Melbourne.

This PhD was funded by a NERC GW4+ Doctoral Training Partnership studentship (NE/S007504/1). Thank you to the GW4+ DTP team for organising various events, training and conferences that introduced me to a wonderful cohort of fellow PhD students.

A big thank you goes to the Geological Survey of Western Australia (GSWA) for providing additional funding (CASE studentship STU40714) that enabled me to visit them and do fieldwork in Western Australia, and for providing many of the samples that I analysed for this thesis. I would particularly like to thank Hugh Smithies for providing so much wisdom and insight about sanukitoids, and for the valuable discussions we had that helped shape this thesis. Doing fieldwork in the Yilgarn and Pilbara Cratons was such an incredible experience that I will never forget. I would like to thank GSWA geologists Raphael Quentin de Gromard, Klaus Gessner, Hugh Smithies, Yongjun Lu and Jyotindra Sapkota for letting me tag along on their field campaigns and for showing me what Archean rocks really look like. Thank you to field assistants Viv, Ray and Scott, and our local guide Nathan for their expertise and assistance in the field. And thank you to everyone I went on fieldwork with for the wonderful company and excellent cooking! Further thanks go to Alicia Verbeeten and the rest of the GSWA team in Kalgoorlie for being so welcoming and hospitable when

you for all the advice and support over the years, as well as for the meandering lunchtime chats and pub trips.

Finally, a huge thank you to my family (Mum, Dad, Julia, Helen, plus Erin and the dogs) and friends (Emma, Meg, Rowan and Sarah) for all their support and encouragement. And thank you to my partner Gwynfor – I will forever be grateful that this PhD brought us together.

1. Introduction

1.1. The late Archean-early Proterozoic transition

In the late Archean to early Proterozoic, approximately 3.0 to 2.0 billion years ago (Ga), the Earth underwent a transformation. The composition of continental crust-forming granitoids, which are the focus of this thesis, permanently changed from sodic Archean tonalite-trondhjemite-granodiorite (TTG) suites to potassic granites (e.g. Condie, 1993; Moyen and Laurent, 2018; Taylor and McLennan, 1995). Ultramafic komatiite lavas almost completely vanished from the rock record (e.g. Condie, 1993; Nesbitt et al., 1982) and global changes in basalt geochemical compositions are reported (e.g. Condie et al., 2022; Keller and Schoene, 2018, 2012; Zhang et al., 2025). The sedimentary rock record was transformed, with lithologies such as banded iron formations (BIFs) and detrital uraninite and pyrite deposits disappearing (e.g. Cuney, 2010; James, 1983; Pufahl and Hiatt, 2012), while others such as mature sandstones, red beds and phosphorites appeared (e.g. Cosgrove et al., 2024; Pufahl and Hiatt, 2012; Veizer and Mackenzie, 2014). Paired metamorphic belts and low T/P (temperature/pressure gradient) metamorphism began emerging and instances of high T/P metamorphism increased (e.g. Brown and Johnson, 2019; Cerri et al., 2024; Holder et al., 2019), while the appearance of features like major sedimentary basins and regional dyke swarms indicate increasing lithospheric rigidity at this time (e.g. Cawood et al., 2018; Hawkesworth et al., 2024). Numerous chemical proxies record rising atmospheric O_2 levels in the early Paleoproterozoic (~2.45 – 2.05 Ga) (e.g. Bekker et al., 2004; Gumsley et al., 2017; Luo et al., 2016; Poulton et al., 2021) and eukaryotic life is thought to have emerged during this time (e.g. Butterfield, 2015; Westall and Xiao, 2024). Figure 1.1 summarises the approximate timings of these key changes. Overall, the late Archean-early Proterozoic transition significantly evolved the Earth towards its present state.
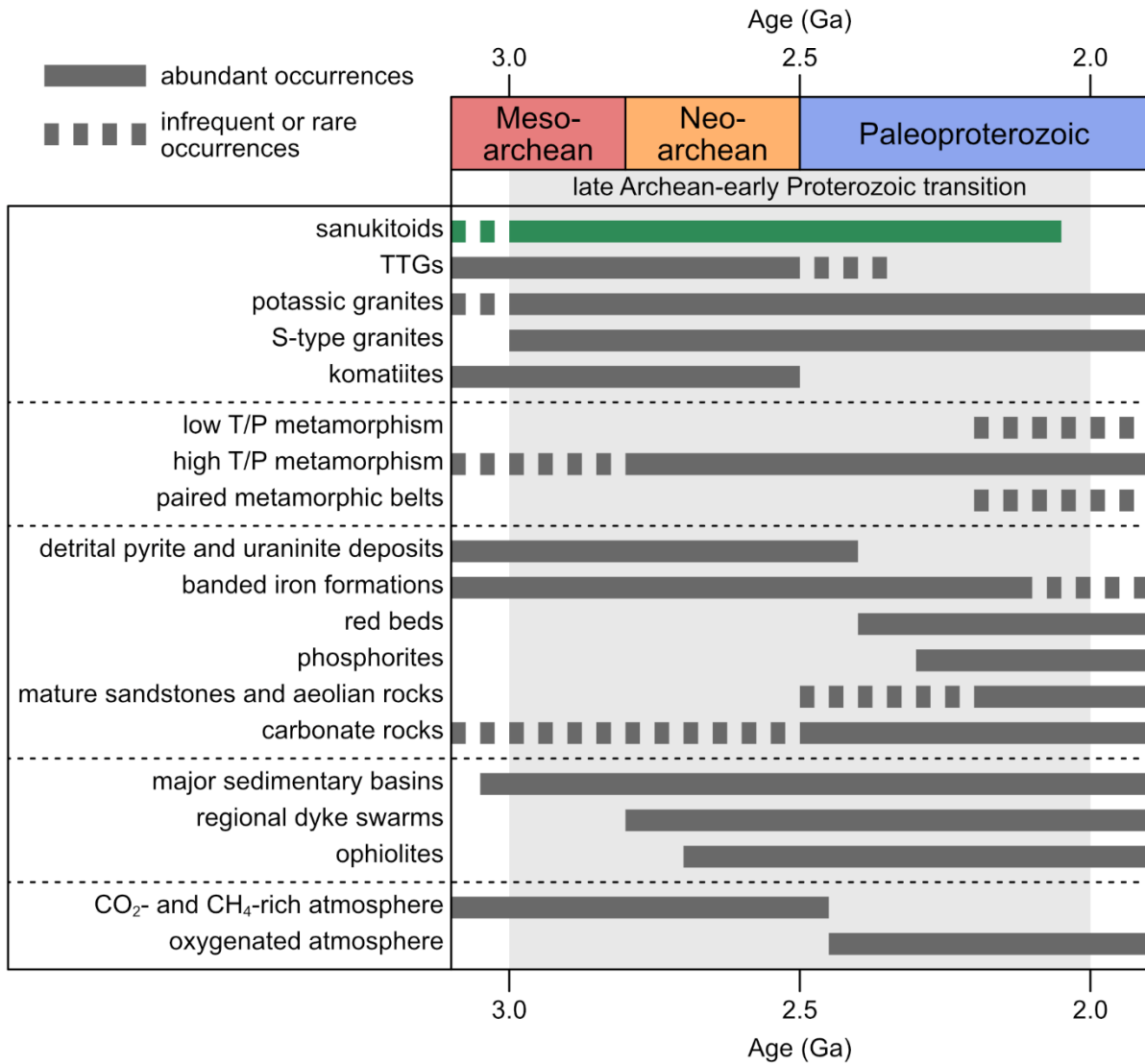
Figure 1.1: Simplified summary of the key changes to the igneous, metamorphic and sedimentary rock records, structural features and atmospheric composition across the late Archean-early Proterozoic transition (~3.0 to 2.0 Ga). Solid lines show abundant occurrences, while dashed lines show infrequent or rare occurrences. The occurrence of sanukitoids almost exclusively during this period is highlighted in green, and their temporal distribution is from my own compilation of reported sanukitoid occurrences in published literature. Other temporal distributions are based on Brown and Johnson (2019), Bucholz and Spencer (2019), Condie and Stern (2023), Cosgrove et al. (2024), Hawkesworth et al. (2024), Holder et al. (2019), Moyen and Laurent (2018), Pufahl and Hiatt (2012) and Veizer and Mackenzie (2014).

Many of the changes described above are proposed to be linked to secular cooling of the Earth, and in particular to its influence on terrestrial geodynamics (e.g. Brown et al., 2020; Hawkesworth et al., 2024; Keller and Schoene, 2012; Moyen and Laurent, 2018). The geodynamic regime of the modern Earth is plate tectonics, where rigid lithospheric plates separated by continuous boundaries move laterally across the planet's surface as an expression of mantle convection, generating new crust where

they diverge at mid-ocean ridges, and recycling old crust into the mantle where they converge at subduction zones. There is a consensus that modern-style plate tectonics would not have operated on a hotter, younger Earth (e.g. Gunawardana et al., 2024; Sizova et al., 2010; van Hunen and Moyen, 2012; van Hunen and van den Berg, 2008), raising the questions of *what* geodynamic regime preceded modern-style plate tectonics, *when* the transition to modern-style plate tectonics was, and *how* this transition occurred. Studying the late Archean-early Proterozoic transition is therefore crucial for improving our understanding of geodynamics and the impact of its evolution on biogeochemical cycles. This topic is of particular importance as the Earth is the only known planet with active plate tectonics and felsic continental crust, as well as the only one to host life. Constraining the Earth's geodynamic evolution may therefore have implications for understanding our planet's habitability and the development of life.

The granitoids that make up the continental crust provide one of the best-preserved, albeit incomplete, records of the late Archean-early Proterozoic transition, and are the geological archive that I utilise in this thesis. These granitoids are preserved globally in cratons, which are ancient, stable blocks of continental lithosphere. In the following section I review the compositional evolution of continental crust-forming granitoids across the late Archean-early Proterozoic transition. I then discuss current constraints and theories on mantle temperature and potential geodynamic changes during this time, as well as briefly describing the evolution of atmospheric oxygenation across this transition.

1.1.1. Evolution of continental crust composition

Preserved early Archean (4.0 – 3.0 Ga) continental crust is dominated by TTG suites which are the lithological association of three sodic plutonic rocks called tonalites, trondhjemites and granodiorites (e.g. Jahn et al., 1981; Moyen, 2011; Moyen and Martin, 2012). These rocks are characterised by low proportions of alkali feldspar – 10 – 35% of total feldspars in granodiorites and ≤ 10% in tonalites and trondhjemites (fig. 1.2a). Their remaining mineralogy consists of plagioclase, quartz and biotite with lesser amphibole (hornblende) (Moyen and Martin, 2012), and in trondhjemites the
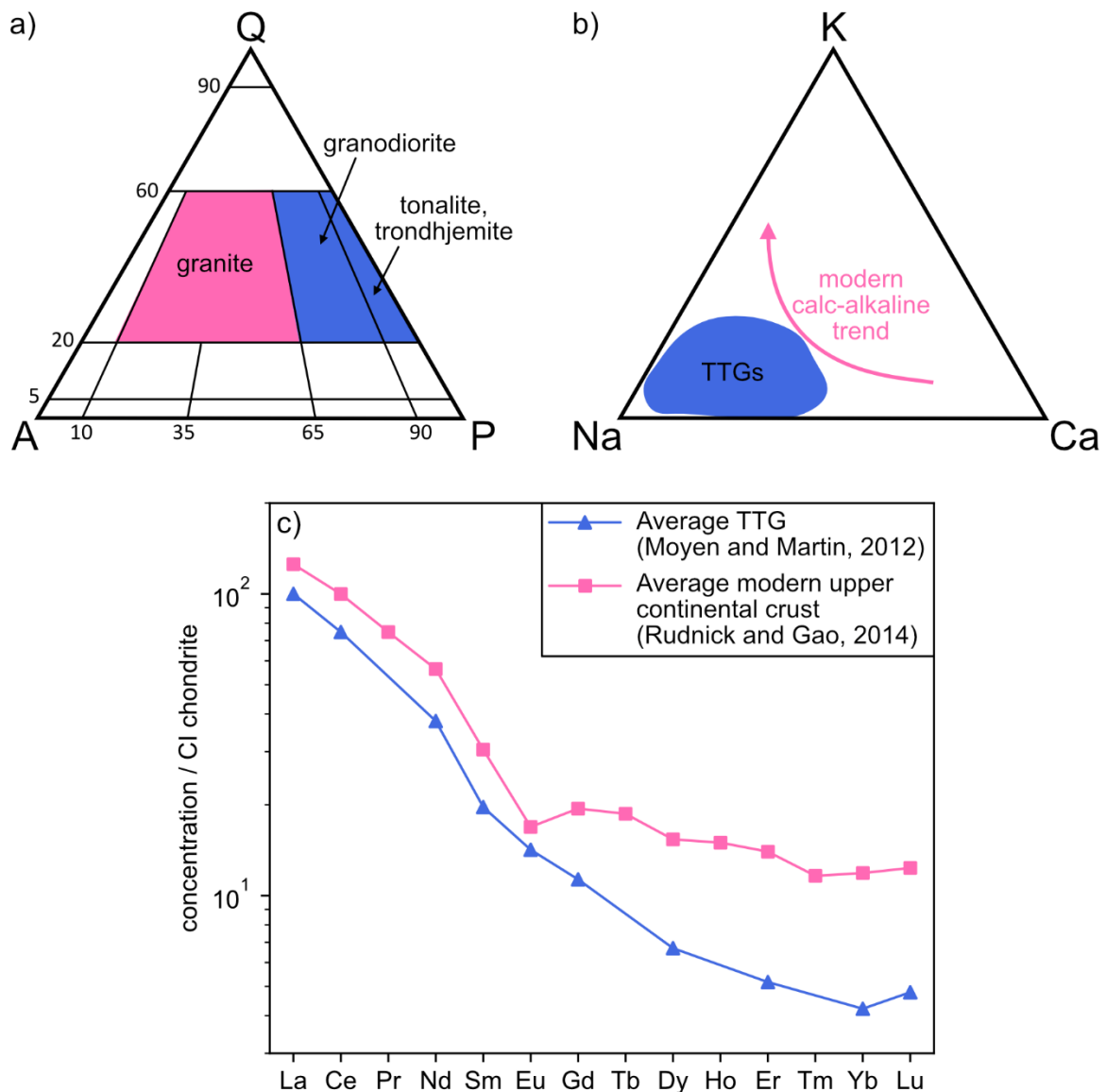
Figure 1.2: Comparison of Archean TTG compositions (blue) to modern granites and upper continental crust (pink). a) QAP ternary diagram comparing the mineralogy of TTG lithologies and granite. Q = quartz, A = alkali feldspar, P = plagioclase feldspar. b) Molar K-Na-Ca ternary diagram comparing TTGs to the modern calc-alkaline magma series differentiation trend, after figure 4b from Moyen and Martin (2012). c) CI chondrite-normalised REE patterns for the average TTG composition from Moyen and Martin (2012) and the average modern upper continental crust composition from Rudnick and Gao (2014). REE concentrations are normalised to the CI chondrite values from O'Neill (2016).

plagioclase is mostly oligoclase (10 – 30% anorthite). They are geochemically distinguished from modern upper continental crust by being sodic ($K_2O/Na_2O < 0.6$ (Moyen and Martin, 2012) compared to $K_2O/Na_2O \approx 0.9$ for modern upper continental crust (Rudnick and Gao, 2014)), by having highly fractionated CI chondrite-normalised rare earth element (REE) patterns due to elevated light rare earth element (LREE) but low heavy rare earth element (HREE) concentrations, and by lacking any europium

(Eu) (fig. 1.2) or strontium (Sr) anomalies (e.g. Condie, 1993; Moyen and Martin, 2012). These geochemical features are thought to reflect their petrogenesis by partial melting of hydrated, likely incompatible element-enriched, metabasites in the garnet stability field without significant residual plagioclase, which was constrained by geochemical modelling (e.g. Arth and Hanson, 1972; Condie and Hunter, 1976; Johnson et al., 2017; O'Nions and Pankhurst, 1974; Palin et al., 2016; Smithies et al., 2009) and partial melting experiments (e.g. Moyen and Stevens, 2006; Rapp et al., 1991; Sen and Dunn, 1994; Winther, 1996; Zhang et al., 2013). TTGs display systematic variations in their trace element compositions, particularly their HREE concentrations, that are traditionally interpreted to reflect metabasite partial melting over a range of pressures (~1 – >2 GPa; e.g. Halla et al., 2009; Moyen, 2011; Moyen and Stevens, 2006). They were consequently categorised into three geochemical groups – "low pressure" (high HREE) TTGs that formed at ~1 – 1.2 GPa, "high pressure" (low HREE) TTGs that formed at ≥ 2 GPa, and "medium pressure" TTGs that formed at intermediate pressures (Halla et al., 2009; Moyen, 2011). Recent studies propose that mineral fractional crystallisation and/or accumulation (Ding et al., 2024; Kendrick et al., 2021; Laurent et al., 2020; Liou and Guo, 2019; Mathieu, 2022; Rollinson, 2021; Smithies et al., 2019), fluid-fluxed melting (Pourteau et al., 2020), silicification of the metabasite protolith (André et al., 2022, 2019; Murphy et al., 2024), and hybridisation of multiple melt fractions (Hernández-Montenegro et al., 2021) may also have been important for generating TTGs and their observed geochemical variability.

In contrast to the early Archean, the late Archean (3.0 – 2.5 Ga) saw a significant diversification in granitoid magmas (e.g. Laurent et al., 2014a; Moyen, 2020). Classification and nomenclature of these late Archean granitoids have been developed by multiple studies, in particular Champion and Sheraton (1997), Moyen et al. (2003), Laurent et al. (2014a) and Moyen (2020). The key petrological and geochemical characteristics and proposed petrogenesis of the main types of Archean granitoid are summarised in table 1.1. TTGs continued to be emplaced until the end of the Archean (2.5 Ga), and in some places into the early Paleoproterozoic (e.g. Bruno et al., 2020; Wang and Long, 2024), but were now joined by a variety of other granitoids. Sanukitoids are igneous rocks enriched in both compatible and

Table 1.1: Summary of the key petrological and geochemical characteristics and proposed petrogenesis of the main types of late Archean granitoids. Characteristics taken from Laurent et al. (2014a), Martin et al. (2009), Moyen (2020), Moyen et al. (2003) and Moyen and Martin (2012). Mineral abbreviations: Pl = plagioclase, Qz = quartz, Bt = biotite, Hbl = hornblende, Ep = epidote, Kfs = K-feldspar, Px = pyroxene, Ms = muscovite, Grt = garnet. [a]A/CNK = molar Al_2O_3 / (CaO + Na_2O + K_2O). [b]FeO_T = total iron expressed as FeO.

		TTGs	Sanukitoids	Biotite Granites	Two-Mica Granites
Lithologies		Tonalite, trondhjemite, granodiorite	Diorite, quartz diorite, monzodiorite, granodiorite, rare granite	Granite, granodiorite	Granite, leucogranite
Mineralogy		Pl + Qz + Bt ± Hbl ± Ep with scare Kfs	Pl + Qz + Hbl + Bt + Kfs ± Px ± Ep	Pl + Ksf + Qz + Bt	Pl + Kfs + Qz + Bt + Ms ± Grt
Geochemistry	K_2O/Na_2O	< 0.6 Sodic	Variable but on average ≈ 0.7 Moderately potassic	> 0.6 Potassic	> 0.6 Potassic
	Aluminium saturation (A/CNK[a])	≈ 0.9 – 1.1 Slightly metaluminous to slightly peraluminous	≈ 0.7 – 1.0 Metaluminous	≥ 1.0 Peraluminous	≥ 1.3 Strongly peraluminous
	Ferromagnesian major oxides (FeO_T[b] + MgO + MnO + TiO_2)	≤ 5 wt%	5 – 25 wt%	≤ 4 wt%	≤ 4 wt%
	CI chondrite-normalised REE patterns	Steeply fractionated Limited Eu anomaly	Steeply fractionated Limited to slightly negative Eu anomaly	Variably fractionated Strong negative Eu anomaly	Variably fractionated Strong negative Eu anomaly
	Other distinguishing characteristics		High Mg# Enriched in both compatible (Ni, Cr) and incompatible (Ba, Sr, LREE) trace elements	Relatively enriched in highly incompatible trace elements (e.g. Rb, Th)	Enriched in highly incompatible trace elements (e.g. Rb, Th)
Proposed petrogenesis		Mainly partial melting of hydrous metabasite in the garnet stability field	Interaction between mantle peridotite and a component derived from recycled crustal material	Mainly partial melting of pre-existing TTG crust	Partial melting of metasediments

incompatible elements whose formation requires recycling of crustal material into the mantle (e.g. Martin et al., 2009; Shirey and Hanson, 1984). Sanukitoids are a minor but distinctive component of late Archean-early Proterozoic terranes (e.g. Heilimo et al., 2010; Laurent et al., 2014a; Martin et al., 2009) and, as they are the main focus of this thesis, they are discussed in detail in section 1.2. Potassic granitoids, primarily biotite and two-mica granites, also started to become a significant component of continental crust. Biotite granites are the second most abundant granitoids in Archean terranes after TTGs (e.g. Laurent et al., 2014a; Moyen et al., 2003), and are generally thought to have formed by intracrustal melting of pre-existing TTG crust (e.g. Dey et al., 2012; Frost et al., 2006; Moyen et al., 2003; Skjerlie and Johnston, 1993; Watkins et al., 2007; Whalen et al., 2004), although a couple of recent studies propose that some biotite granites formed by partial melting of metabasites enriched in potassium by low-temperature hydrothermal alteration (André et al., 2022; Li et al., 2021). Strongly peraluminous two-mica (biotite-muscovite) granites are less common than biotite granites. They show many similarities to modern S-type granites and formed by intracrustal melting of a variety of metasediments (e.g. Breaks and Moore, 1992; Feng and Kerrich, 1992; Li et al., 2020), and they possibly tapped increasingly diverse sedimentary sources across the late Archean-early Proterozoic transition (Bucholz and Spencer, 2019; Moyen and Laurent, 2018). Syenites and alkaline granites also make rare appearances in late Archean terranes (e.g. Bourne and L'Heureux, 1991; Champion and Sheraton, 1997; Moyen, 2020), and hybrid granitoids were generated by interaction between the various granitoid magmas described above (e.g. Almeida et al., 2010; Laurent et al., 2014a; Moyen, 2020). Globally, the diversification of granitoid magmatism was a diachronous change, occurring as early as ~3.3 Ga in the Singhbhum Craton (e.g. Chaudhuri et al., 2022) and as late as ~2.1 Ga in the São Francisco Craton (e.g. Bruno et al., 2020). For individual cratons, this wide range of granitoids was emplaced over a relatively short period of ~20 – 50 million years (myr), in comparison to the longer period of TTG generation that preceded it (~200 – 500 myr) (Laurent et al., 2014a).

The evolution of granitoid magmatism described above significantly impacted the chemical composition of continental crust across the late Archean-early Proterozoic transition. The upper continental crust became more potassic (e.g. Condie, 1993; Keller and Schoene, 2012) and was enriched in heat-producing elements (e.g. U, Th,

K), which may have been crucial for the thermochemical stabilisation of cratons (e.g. Reimink and Smye, 2024; Schoene et al., 2008). Concentrations of incompatible trace elements, including REE, large ion lithophile elements (LILE, e.g. Ba, Rb) and high field strength elements (HFSE e.g. Hf, Nb, Ta), increased at ~2.5 – 2.0 Ga, while trace element ratios like Sr/Y and La/Yb decreased and Eu anomalies became more strongly negative (e.g. Condie, 1993; Condie et al., 2023; Gaschnig et al., 2016). The upper continental crust may also have become more felsic during this transition (Chen et al., 2020; Dhuime et al., 2015; Large et al., 2018; Tang et al., 2016; Tian et al., 2023), although the magnitude of this change, and even the existence of a significant change in upper crustal SiO_2 at this time, are debated (Garçon, 2021; Greber et al., 2017; Greber and Dauphas, 2019; Keller and Harrison, 2020; Ptáček et al., 2020; Saji et al., 2023). In addition, TTG geochemistry evolved across this period, with increasing LILE contents (Sr, Ba, Sr/Y) and compatible element concentrations (Ni, Cr, Mg# [= $100*Mg / (Mg + Fe^{2+})$]) observed (T. E. Johnson et al., 2019; Martin and Moyen, 2002; Moyen and Laurent, 2018). These changes in part reflect the increased abundance of "high pressure" TTGs in the late Archean (Moyen, 2020; Moyen and Laurent, 2018). Additionally, shifts in the stable isotopic compositions of TTGs and of the bulk upper continental crust are seen during the late Archean-early Proterozoic transition. Increases in oxygen isotope compositions ($\delta^{18}O$) are reported at both craton (e.g. Mole et al., 2021; Smithies et al., 2021) and global (e.g. Bindeman et al., 2024; Gaschnig et al., 2016; Valley et al., 2005) scales. For silicon isotopes, the $\delta^{30}Si$ values of TTGs appear to decrease from the Neoarchean to the early Paleoproterozoic (Zhou et al., 2024).

The compositions of igneous rocks primarily depend on the composition of their source and the conditions (pressure, temperature, H_2O) of melting, and are also influenced by any subsequent differentiation (e.g. mineral fractionation/accumulation, assimilation) of these primary magmas (e.g. Moyen and Laurent, 2018; Rollinson and Pease, 2021). The changes observed in granitoids across the late Archean-early Proterozoic transition must therefore reflect changes in these variables. The increased diversity of granitoids, particularly regarding their major element compositions, indicates that a greater variety of source compositions were involved in forming granitoid magmas in the late Archean than in the early Archean. In addition to partial melting of metabasites to form TTGs, the mantle, metasediments and TTGs

themselves started being involved in granitoid magma genesis, forming sanukitoids, two-mica granites and biotite granites respectively (e.g. Laurent et al., 2014a; Moyen, 2020; Moyen and Laurent, 2018). This range of sources in part records increased crustal reworking at this time, which gradually concentrated incompatible trace elements, including heat-producing elements, in the upper continental crust (e.g. Moyen and Laurent, 2018; Reimink and Smye, 2024). Continental emergence above sea level likely contributed to this diversity as abundant sediments started being produced by weathering of this emerged crust (e.g. Arndt, 2023; Bucholz and Spencer, 2019; Reimink and Smye, 2024). The increases in $\delta^{18}O$ indicate that source materials that had interacted with the shallow hydrosphere became more involved in granitoid petrogenesis (e.g. Bindeman et al., 2024; Smithies et al., 2021). Changes in the compositions of TTGs appear to record an increase in high pressure melting towards the end of the Archean, while higher compatible element concentrations may suggest greater extents of interaction between TTG melts and the mantle (T. E. Johnson et al., 2019; Martin and Moyen, 2002; Moyen and Laurent, 2018). In contrast, changes in the trace element composition of the bulk upper continental crust, such as lower Sr/Y and La/Yb, document a shift to shallower depths of melting (e.g. Condie, 1993; Condie et al., 2023; Keller and Schoene, 2012). These conclusions drawn from changes in granitoid composition can help constrain late Archean-early Proterozoic geodynamics.

1.1.2. Late Archean-early Proterozoic geodynamics

The geochemical compositions of igneous rocks, including of granitoids, are an important line of evidence used to constrain Precambrian geodynamics. However, the link between a magma's geochemistry and its geodynamic setting of formation is not straightforward, and it is unlikely to have a unique solution (e.g. Moyen and Laurent, 2018; Rollinson and Pease, 2021). This problem, as well as uncertainty about how much hotter than present Archean mantle temperatures were (e.g. Ganne and Feng, 2017; Herzberg et al., 2010), significantly contribute to the debate about the nature of early Earth geodynamics and when plate tectonics began. In this section I first provide an overview of constraints on mantle temperature at this time, before discussing current theories about geodynamics during the late Archean-early Proterozoic transition.
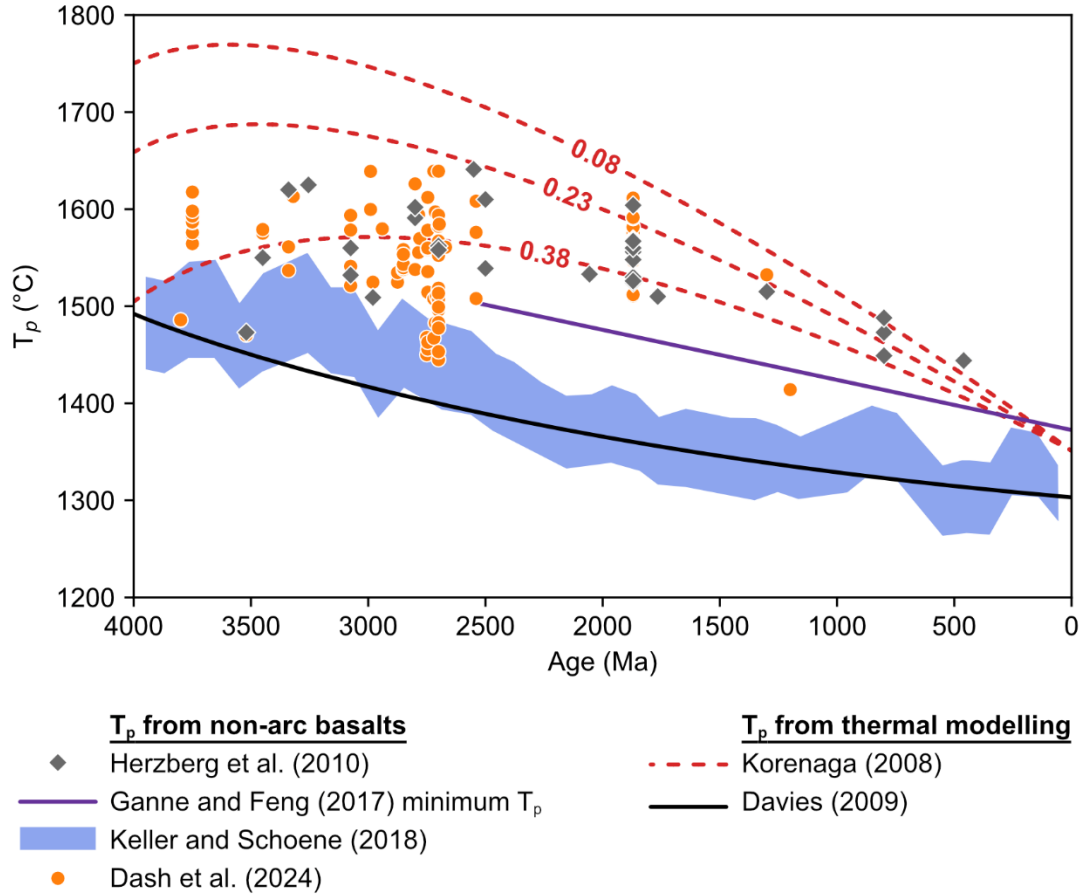
Figure 1.3: Proposed evolution of ambient mantle potential temperature (T_p) over the Earth's history. T_p estimates from non-arc basalts are from Dash et al. (2024), Ganne and Feng (2017) (values calculated using Fe^{2+}/Fe_{total} = 0.9), Herzberg et al. (2010) and Keller and Schoene (2018). T_p estimates from thermal modelling are from Davies (2009) and Korenaga (2008). Modelled T_p for three different Urey ratio (the ratio of the Earth's internal heat production to its surface heat flux) values (0.08, 0.23, 0.38) from Korenaga (2008) are shown. In contrast, the T_p model from Davies (2009) uses a higher Urey ratio of 0.8.

The temperature of the Earth's mantle is the primary control on its geodynamic regime (e.g. Brown et al., 2020; Lenardic, 2018; S. Liu et al., 2022) and it has changed over the planet's history. Both geochemical constraints, primarily from non-arc basalts (e.g. Dash et al., 2024; Ganne and Feng, 2017; Herzberg et al., 2010; Keller and Schoene, 2018), and thermal modelling (e.g. Davies, 2009; Korenaga, 2008) have been used to reconstruct mantle potential temperature (T_p) through time (fig. 1.3). Some studies (e.g. Dash et al., 2024; Herzberg et al., 2010; Korenaga, 2008) favour T_p increasing through the early Archean to reach peak temperatures in the mid-late Archean, before cooling towards the present day T_p of ~1350°C. Estimates of this peak temperature are ~200 – 300°C hotter than present. The other school of thought is that mantle temperatures were more moderate in the mid-late Archean (~50 – 150°C hotter than

10

present) and have been steadily cooling since the start of the Archean (e.g. Davies, 2009; Ganne and Feng, 2017; Keller and Schoene, 2018).

Hotter mantle temperatures would have reduced mantle viscosity and generated mafic crust that was thicker, and possibly weaker, than present day oceanic crust (e.g. Sizova et al., 2010; van Hunen and Moyen, 2012; van Hunen and van den Berg, 2008). There is debate about whether this oceanic lithosphere was more positively buoyant (e.g. Davies, 1992; van Hunen and Moyen, 2012) or had greater negative buoyancy (e.g. Weller et al., 2019) than present. These changes alter the forces that drive plate tectonics (e.g. slab pull, mantle convection), and hence affect the dynamics, and possibly the viability, of subduction and modern-style plate tectonics. Thermomechanical modelling is used to investigate the effect of hotter mantle temperatures on geodynamics. Some studies have determined that subduction was unable to operate until temperatures fell to < ~200 – 250°C higher than present (e.g. Gunawardana et al., 2024; Sizova et al., 2010), while others find that it was still feasible at these conditions (e.g. Hynes, 2014; van Hunen and van den Berg, 2008; Weller et al., 2019). Non-plate tectonic regimes proposed for the hotter early Earth are mostly "sluggish" or "squishy lid" modes with some degree of lateral movement but no defined plate boundaries (e.g. Lourenço et al., 2020; Rozel et al., 2017). Vertical crustal motion may have dominated over the lateral motion characteristic of modern-style plate tectonics, with features like crustal drips (also referred to as "sagduction") and lower crustal delamination (e.g. Capitanio et al., 2019; Johnson et al., 2014; Nebel et al., 2018; Rozel et al., 2017; Sizova et al., 2015). Alternatively, numerous studies find that some form of subduction may have operated on a hotter Earth, but that the style differed from modern "Benioff-style" subduction. Many models suggest that Archean subduction was intermittent and short-lived, with frequent slab break-off (e.g. Gunawardana et al., 2024; Moyen and van Hunen, 2012; O'Neill et al., 2007; Perchuk et al., 2019; van Hunen and van den Berg, 2008). The lower plate might have been subducted at a shallower angle, creating a situation akin to underthrusting (e.g. Perchuk et al., 2025; Sizova et al., 2010). Some studies support faster subduction on a hotter Earth (e.g. O'Neill et al., 2007; Perchuk et al., 2019), while others propose that it was more sluggish than present (e.g. Foley, 2024, 2018). Overall, geodynamic models support the onset and stabilisation of deep, sustained subduction and modern-

style plate tectonics as mantle temperatures cooled (e.g. Gunawardana et al., 2024; Perchuk et al., 2025; Sizova et al., 2010).

Given the diversity of geodynamic scenarios proposed for the early Earth, it is no surprise that there are multiple different interpretations of how geodynamics may have changed during the late Archean-early Proterozoic transition. From analysis of the literature, the dominant viewpoint emerging appears to be that, while some form of subduction may have occurred in the early Archean, it was a short-lived and relatively uncommon phenomenon until the late Archean-early Proterozoic when it became more stable and widespread (e.g. Gunawardana et al., 2024; Hawkesworth et al., 2024; Moyen and Laurent, 2018; Nebel et al., 2024; Sizova et al., 2010). This change may signal the beginning of modern-style plate tectonics at this time, initiating subduction-collision (Wilson) cycles on a global scale (e.g. Laurent et al., 2014a), although discerning when subduction changed from a localised event to being representative of a global network of plate boundaries (i.e. modern-style plate tectonics) is difficult to tell (e.g. Hawkesworth et al., 2024; Nebel et al., 2024). A somewhat related theory is that the geodynamic regime of the Earth changed during this transition from a "sluggish lid" or vertical tectonic mode to one more similar to plate tectonics, with the onset of subduction occurring at this time (e.g. Ackerman et al., 2022; Brown et al., 2020; Smithies and Champion, 2000). This model is supported by geochemical evidence that deep recycling of supracrustal materials began at this time (e.g. Cui et al., 2022; Mole et al., 2021). The variables controlling the onset and stability of subduction (e.g. lithospheric thickness, radiogenic heat production, lithospheric mantle-asthenospheric mantle density contrast) were likely not homogeneous across the whole planet, which could explain the diachronous nature of this transition (e.g. Huang et al., 2022; Martin et al., 2009).

Another common opinion is that many magmatic changes during the late Archean-early Proterozoic transition reflect secular cooling of the mantle altering the style and thermal structure of subduction zones. This cooling may have caused subduction angles to steepen (e.g. Perchuk et al., 2025; Sizova et al., 2010) or subduction to become faster (e.g. Foley, 2024, 2018), and these changes, in combination with overall colder mantle and slab temperatures, resulted in lower geothermal gradients during subduction. The locus of slab melting was consequently moved to greater

depths, making ascending melts interact with a greater thickness of mantle wedge (e.g. Martin and Moyen, 2002; Moyen and Laurent, 2018), and may also have shifted it from melting metabasites to melting sediments (e.g. Laurent et al., 2011). Cooler geotherms would result in lower degrees of slab melting, and hence these melts interacted more extensively with the mantle and might have been completely consumed by metasomatic reactions (e.g. Martin et al., 2009; Moyen et al., 2003). The subducting slab may even have become too cold to melt, with slab dehydration becoming the dominant process instead (Laurie et al., 2013; Martin, 1986). Consequently, it is often proposed that subduction geometry and processes began to resemble modern subduction more closely by the end of the late Archean-early Proterozoic transition.

A few studies advocate for a geodynamic transition unrelated to plate tectonics and subduction. These authors invoke the evolution of long-lived crustal drips, which gradually descended into the mantle and may have become asymmetric due to lithospheric flow, resembling a subduction zone geometry (e.g. Nebel et al., 2018; Smithies et al., 2021). Stalling of hot, mantle-derived sanukitoid magmas at the base of the crust may have provided heat to melt the overlying crust (Nebel et al., 2018). An alternative opinion is that the late Archean-early Proterozoic transition does not require a geodynamic change at all. While decreasing mantle and crustal temperatures are still significant factors influencing this transition, other processes, such as the emergence of continental crust above sea level and changing surface conditions, may be more important than geodynamics for explaining the changes in igneous rock, and particularly granitoid, compositions at this time (e.g. Arndt, 2023; Bédard, 2024; Reimink and Smye, 2024).

In summary, there are multiple theories about how geodynamic changes may have been involved in the late Archean-early Proterozoic transition. This period might mark the onset of subduction (e.g. Brown et al., 2020; Smithies and Champion, 2000), the stabilisation of global, modern-style plate tectonics (e.g. Hawkesworth et al., 2024; Laurent et al., 2014a) or a change in the style of subduction (e.g. Martin et al., 2009; Moyen and Laurent, 2018). Alternatively, it represents a transition not related to subduction and plate tectonics (e.g. Nebel et al., 2018; Smithies et al., 2021), or possibly there was no geodynamic change at all (e.g. Arndt, 2023). New constraints

are therefore needed to elucidate the causes of the late Archean-early Proterozoic transition.

1.1.3. Changes in atmospheric oxygenation
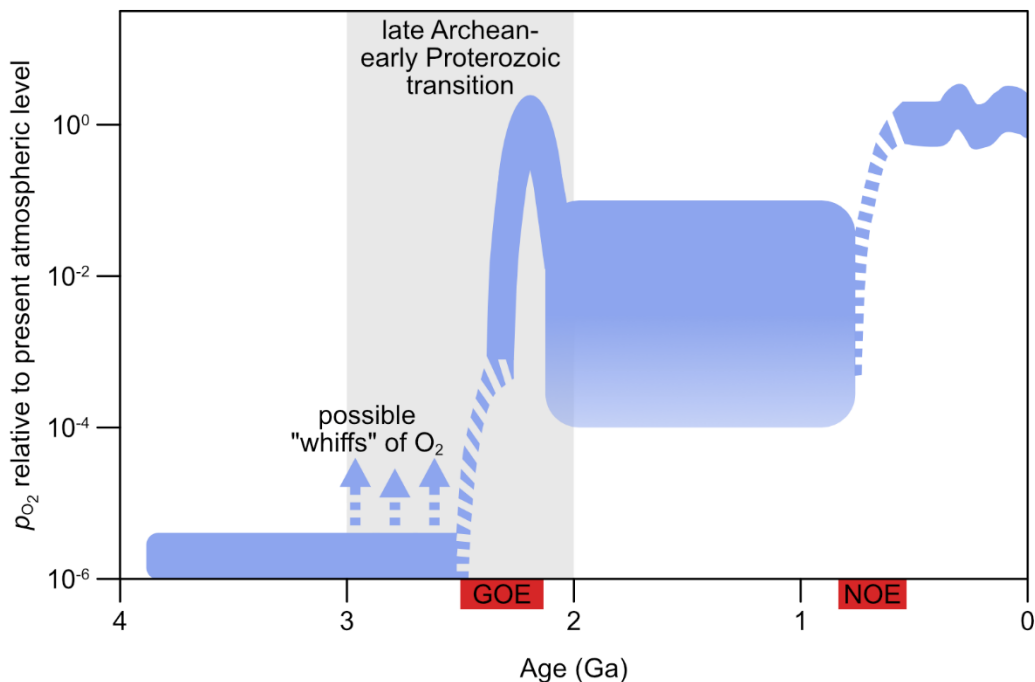
Figure 1.4: The blue curve shows the evolution of atmospheric partial pressure of O_2 (p_{O2}), relative to the present atmospheric level, over the Earth's history. Based on figure 1 from Lyons et al. (2014). The dashed sections indicate that the detailed structures of the Great Oxidation Event (GOE) and Neoproterozoic Oxygenation Event (NOE) need to be further constrained. The dashed arrows indicate possible "whiffs" of O_2 before the GOE. The grey region shows the late Archean-early Proterozoic transition from ~3.0 to 2.0 Ga.

At a similar time to the changes in granitoid magmatism and potential geodynamic transition, the composition of the Earth's atmosphere was significantly altered. Between ca. 2.45 and 2.05 Ga (e.g. Bekker et al., 2004; Gumsley et al., 2017; Poulton et al., 2021) global atmospheric molecular oxygen (O_2) levels rose for the first time from neglibile amounts (<0.001% of the modern level; Pavlov and Kasting, 2002) to up to ~10% of the modern level (e.g. Holland, 2006; Kanzaki and Murakami, 2016) in what has been labelled the "Great Oxidation Event" or "GOE" (Holland, 2002) (fig. 1.4). The timing, tempo and magnitude of the O_2 increase at the GOE are primarily constrained by geochemical signatures in sedimentary rocks, particularly by the disappearance of mass-independent sulfur isotope fractionation (e.g. Bekker et al.,

2004; Farquhar et al., 2000; Luo et al., 2016; Poulton et al., 2021). There is some disagreement about the exact timing of the GOE (e.g. Bekker et al., 2004; Poulton et al., 2021) and whether the rise in O_2 was a single event (e.g. Luo et al., 2016) or happened stepwise (e.g. Gumsley et al., 2017), but there is a consensus that O_2 levels had finished increasing by ~2.05 Ga.

The rise in atmospheric O_2 at the GOE is primarily attributed to the emergence of cyanobacteria, which produce O_2 via photosynthesis (e.g. Kasting, 2013; Olejarz et al., 2021). However, evidence supports the existence of photosynthesising cyanobacteria in the Archean (e.g. Brocks et al., 1999; Farquhar et al., 2011; Schirrmeister et al., 2015), meaning photosynthesis likely evolved several hundred million years before the GOE. There are numerous proposals that changes in crustal composition and geodynamics during the late Archean-early Proterozoic transition may have also influenced the accumulation of O_2 in the atmosphere. The shift towards more felsic crustal compositions and decrease in ultramafic komatiite abundance would have reduced rates of H_2 production via serpentinisation (e.g. Leong et al., 2021; Smit and Mezger, 2017) and decreased the abundance of crustal reductants (e.g. Fe^{2+}, S^{2-}) (e.g. Lee et al., 2016), diminishing the magnitude of these O_2 sinks. This shift in crustal composition might have also affected nutrient fluxes, for example by reducing the availability of nickel which is an important nutrient for some methanogens (e.g. Konhauser et al., 2009). Endogenic oxidation of TTG magmas by retention of Fe^{2+} over Fe^{3+} in residual garnet may have generated oxidised continental crust and helped shift the redox balance of the Earth's surface (Tang et al., 2024). Establishing subduction and plate tectonics globally would lead to increased subduction rates of oxidised material, such as mid ocean ridge-altered oceanic crust and carbon- and sulfur-rich sediments, causing a gradual increase in the oxidation state of volcanic gases (e.g. Holland, 2009, 2002; Nebel et al., 2024). Coupling this process with loss of reduced H_2 gas to space might have helped cause net oxidation of the Earth's surface and crust (e.g. Catling et al., 2001; Claire et al., 2006). The composition of volcanic gases may have also changed due to the emergence of continents above sea level. This caused a shift from submarine volcanism to subaerial volcanism, for which degassing occurs at lower pressures and releases more oxidised sulfur (e.g. Gaillard et al., 2011; Kump and Barley, 2007). Continental emergence would have also generated increased weathering fluxes of important nutrients (e.g.

phosphorous, molybdenum) to the oceans, enhancing biological productivity (e.g. Hao et al., 2020; Scott et al., 2011). The evolution of the solid Earth and the atmosphere were hence likely closely linked during the late Archean-early Proterozoic transition.

The GOE hugely affected chemical processes on the Earth as widespread oxidation could now occur, which significantly altered the biogeochemical cycling of redox-sensitive elements such as sulfur (e.g. Lyons and Gill, 2010), iron (e.g. Watanabe et al., 2023), arsenic (e.g. Chi Fru et al., 2019) and uranium (e.g. Cuney, 2010). Consequently, the chemical and isotopic compositions of near-surface materials (seafloor-altered oceanic crust, sediments) being recycled into the mantle changed, meaning the GOE impacted not only the Earth's surface but also its interior. As these recycled materials can end up in the mantle source regions of igneous rocks, increasing atmospheric O_2 may have affected magma compositions. Several recent studies report differences in the chemical and isotopic compositions of igneous rocks that are interpreted as recording secular changes in the compositions of recycled materials due to increasing atmospheric oxygenation (Ahmad et al., 2023, 2022; Andersen et al., 2015; Liu et al., 2019; Moreira et al., 2023; Stolper and Bucholz, 2019). The igneous rock record therefore provides an opportunity to investigate how the GOE impacted the deeper parts of biogeochemical cycles and potentially influenced magmatism during the late Archean-early Proterozoic transition.

1.2. Sanukitoids

Sanukitoid magmatism is a distinctive feature of the late Archean-early Proterozoic transition (fig. 1.1). Sanukitoids are a type of igneous rock characterised by enrichment in both compatible (e.g. Mg, Ni, Cr) and incompatible (e.g. Ba, Sr, LREE) elements, reflecting the involvement of both mantle and recycled crustal components in their formation (e.g. Heilimo et al., 2010; Martin et al., 2009; Shirey and Hanson, 1984; Stern et al., 1989). The geochemical composition of sanukitoids is regarded as being transitional between those of Archean TTG suites and post-Archean granites (e.g. Martin et al., 2009). They display highly fractionated CI chondrite-normalised REE patterns similar to those of TTGs (fig. 1.5a, c) (e.g. Smithies and Champion, 2000;
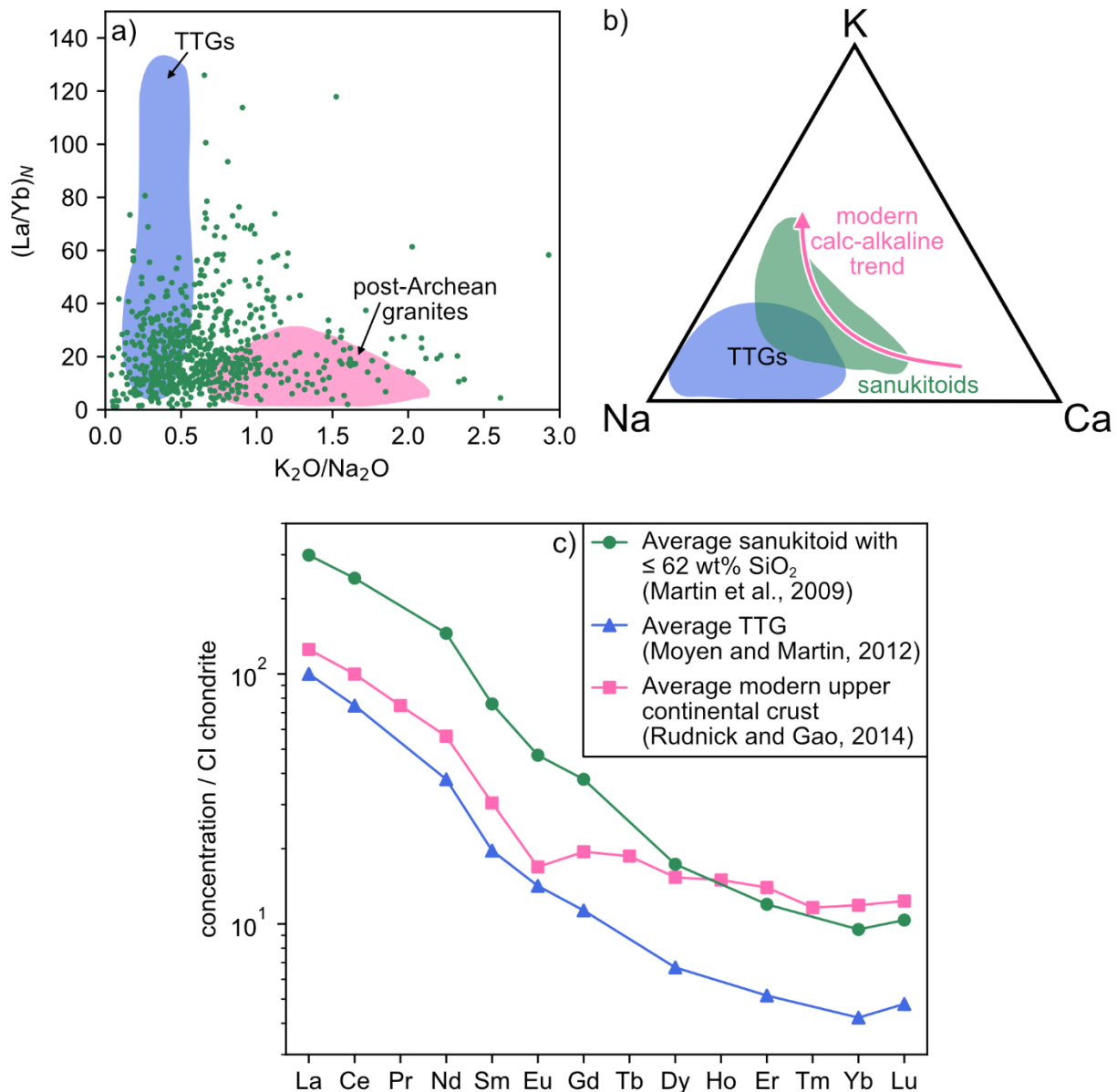
Figure 1.5: Comparison of Archean-Paleoproterozoic sanukitoids (green) to Archean TTGs (blue) and post-Archean granites and upper continental crust (pink). a) (La/Yb)$_N$ vs K$_2$O/Na$_2$O where REE concentrations are normalised to the CI chondrite values from O'Neill (2016). After figure 2.8 from Laurent (2012). The geochemical compositions of rocks described as "sanukitoid" in published literature are taken from my own compilation of published sanukitoid geochemical data. Following Martin et al. (2009), this dataset was filtered for samples with ≤ 62 wt% SiO$_2$ to exclude samples with geochemical compositions significantly affected by differentiation. b) Molar K-Na-Ca ternary diagram comparing sanukitoids to TTGs and the modern calc-alkaline differentiation trend. After figure 4 from Martin et al. (2009). c) CI chondrite-normalised REE patterns for average sanukitoids with ≤ 62 wt% SiO$_2$ from Martin et al. (2009), the average TTG composition from Moyen and Martin (2012) and the average modern upper continental crust composition from Rudnick and Gao (2014). REE concentrations are normalised to the CI chondrite values from O'Neill (2016).

Stern et al., 1989), but follow a calc-alkaline-like differentiation trend similar to post-Archean granites (fig. 1.5b) (e.g. de Oliveira et al., 2009; Martin et al., 2009). In

general, sanukitoids are moderately potassic (average $K_2O/Na_2O \approx 0.7$; Moyen, 2020), making them intermediate between the sodic TTGs and potassic granites (fig. 1.5a). Constraints from mineral chemistry suggest that sanukitoid parental magmas were water-rich and oxidised, with > 7 wt% H_2O and oxygen fugacity (fO_2) of NNO +0.3 to NNO +2.5 (log units relative to the nickel-nickel oxide buffer) comparable to modern arc magmas (de Oliveira et al., 2010; do Nascimento et al., 2023, 2021). As a result of their temporally and geochemically transitional nature, sanukitoids are interpreted to reflect the evolution of continental crust composition and changing geodynamics during the late Archean-early Proterozoic transition (e.g. Laurent et al., 2014a; Martin et al., 2009; Smithies and Champion, 2000).
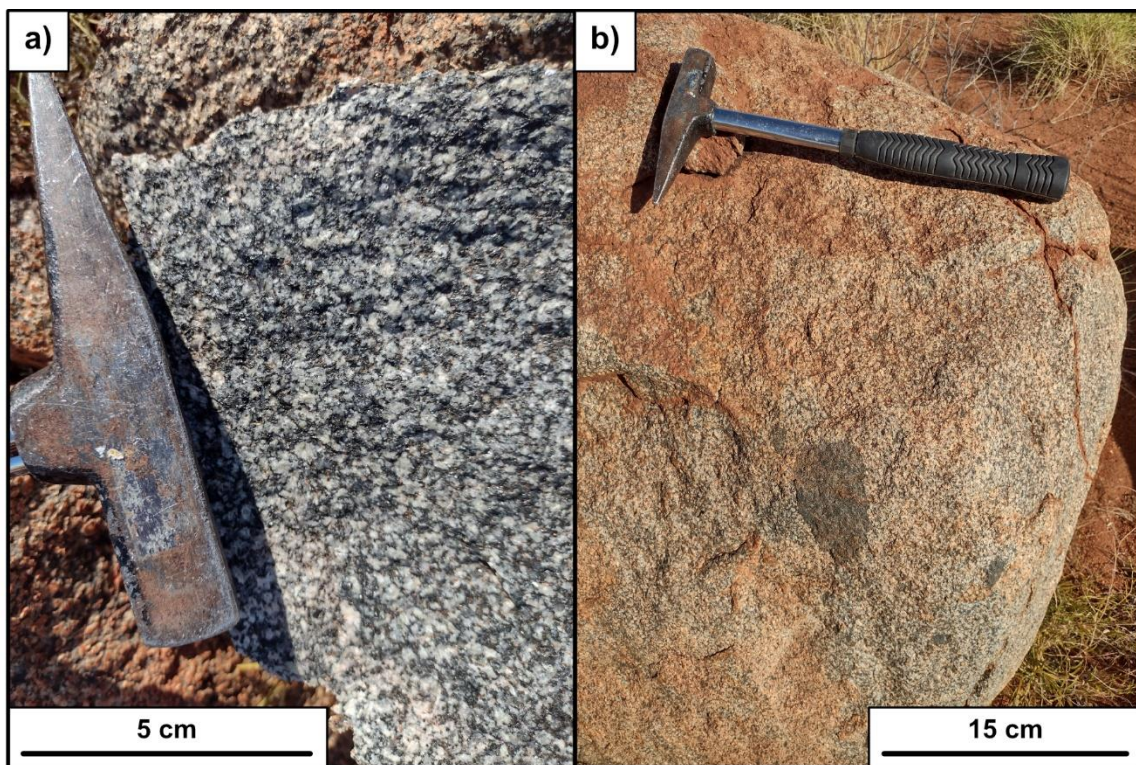
Figure 1.6: Field photographs of sanukitoid from the Wallareenya granodiorite high-Mg diorite suite, Pilbara Craton. Photographs taken by Laura Spencer. a) Close-up of a fresh surface of medium-grained, equigranular biotite-hornblende diorite sanukitoid. b) Diorite-granodiorite sanukitoid outcrop containing a microgranular mafic enclave.

The vast majority of sanukitoid occurrences are plutonic, but instances of volcanic and subvolcanic sanukitoid magmatism have been identified (e.g. Dey et al., 2015; Guo et al., 2017; Shirey and Hanson, 1984; Smithies et al., 2019; Wang et al., 2022). Sanukitoids cover a wide silica range and vary lithologically from diorites and quartz diorites to monzodiorites and granodiorites plus rare granites (fig. 1.6) (e.g. Heilimo et

al., 2010; Martin et al., 2009; Stern and Hanson, 1991). Their mineralogy consists of a quartz- and plagioclase-dominated matrix with lesser K-feldspar that contains "clots" or "clusters" of mafic minerals – mainly hornblende and biotite with occasional pyroxene – and sometimes K-feldspar phenocrysts (e.g. Martin et al., 2009; Smithies and Champion, 2000; Stern et al., 1989). Accessory phases found in sanukitoids are mainly magnetite, ilmenite, titanite, apatite, zircon, epidote and allanite (e.g. de Oliveira et al., 2010; Laurent et al., 2014a; Lobach-Zhuchenko et al., 2005). Microgranular mafic, generally dioritic to monzodioritic, enclaves are also common (fig. 1.6b) (e.g. Heilimo et al., 2010; Martin et al., 2009; Smithies and Champion, 2000).
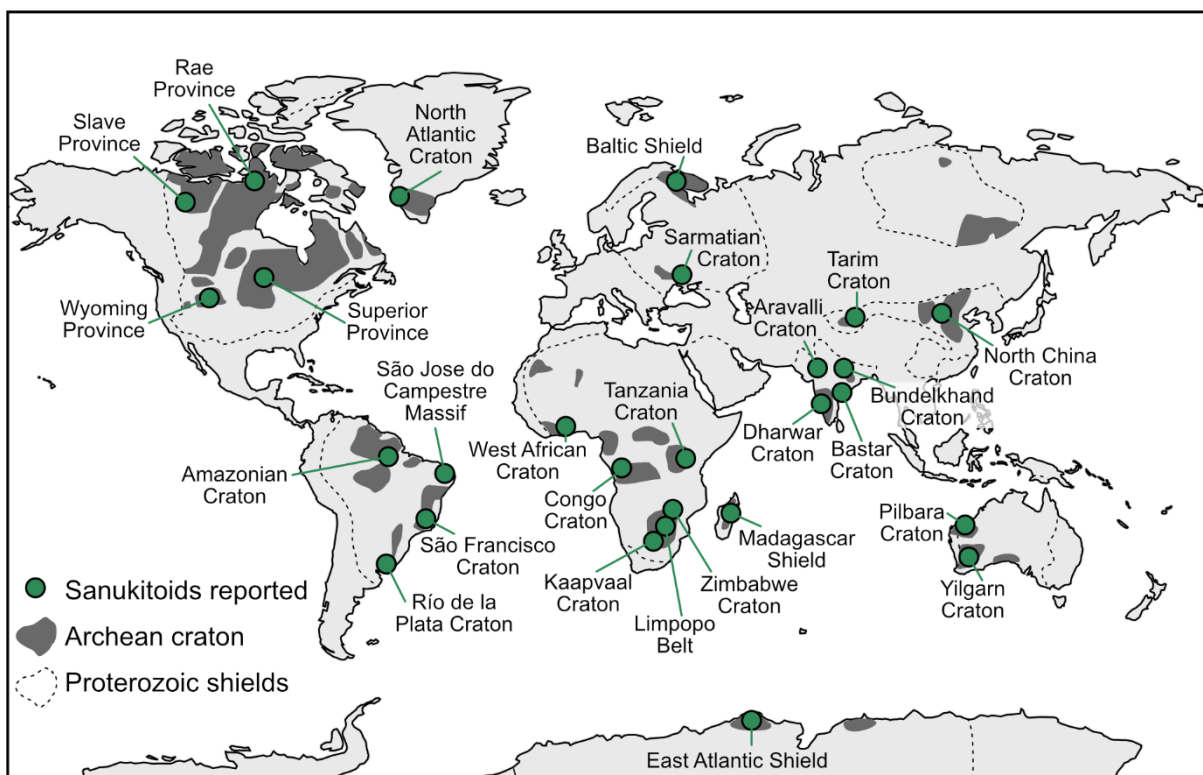
Figure 1.7: Spatial distribution of Archean and Paleoproterozoic sanukitoid occurrences reported in published literature. Simplified distribution of Archean cratons and Proterozoic shields is after Bleeker (2003) and Groves and Santosh (2021).

Sanukitoids are a minor but ubiquitous component of late Archean-early Proterozoic terranes and have been reported on the majority of cratons (fig. 1.7). Most sanukitoid magmatism occurred during the Neoarchean (2.8 – 2.5 Ga) when it was the most widespread, but it was also fairly common in the late Mesoarchean (3.0 – 2.8 Ga) and earliest Paleoproterozoic (2.5 – 2.4 Ga) (fig. 1.8). A few older occurrences of sanukitoids have also been reported, dating as far back as the Paleoarchean (~3.3 –

3.4 Ga) on the Pilbara Craton (Vandenburg et al., 2023). A small burst of sanukitoid magmatism appears to have occurred towards the end of the late Archean-early Proterozoic transition at ~2.20 – 2.05 Ga when sanukitoids are again described on multiple cratons (e.g. Aidoo et al., 2020; Angeletti et al., 2021; Bruno et al., 2020; Terentiev and Santosh, 2017). After ~2 Ga, sanukitoids practically disappear from the rock record. Several studies have identified potential Phanerozoic analogues to Archean-Paleoproterozoic sanukitoids, primarily high Ba-Sr granite suites from syn- to post-collisional settings (e.g. Fowler and Rollinson, 2012; C.-Y.-H. Liu et al., 2022; W. Wang et al., 2018; Zhang et al., 2019) and low-silica adakites (also referred to as high-Mg andesites) from volcanic arcs (e.g. Chiaradia et al., 2014; Martin et al., 2005; Qian and Hermann, 2010; Tatsumi, 2006).

In the following sections, I first review how previous studies have defined and classified sanukitoids in order to distinguish them from other late Archean-early Proterozoic granitoids. I also detail the terminology relating to sanukitoids that has been introduced since their initial identification. After this I describe the current state of research into the formation and differentiation of sanukitoid magmas, and the questions that remain about their petrogenesis.
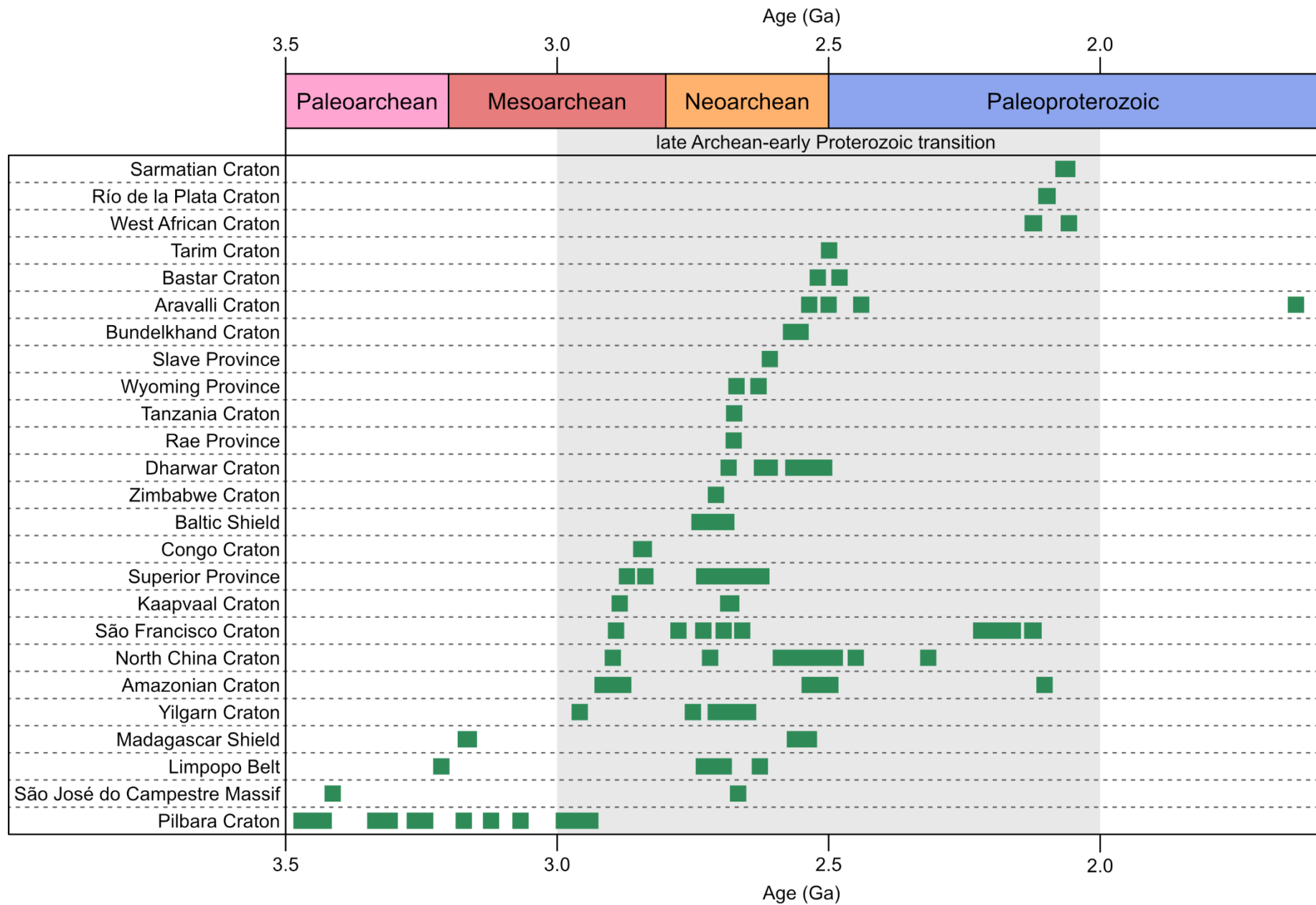
Figure 1.8: Temporal distribution of Archean and Paleoproterozoic sanukitoid occurrences reported in published literature. The green rectangles show the ages of reported sanukitoid magmatism for each location.

1.2.1. Defining and identifying sanukitoids

Sanukitoids were first recognised as a distinct component of Archean terranes, separate from TTGs, by Shirey and Hanson (1984), who described mantle-derived monzodiorites and trachyandesites from the Rainy Lake region of the Superior Province. Shirey and Hanson called these rocks "sanukitoids" because they shared distinctive geochemical characteristics – silica-oversaturation with high Mg# and high Ni, Cr and LILE concentrations – with Miocene high-Mg andesites from the Setouchi volcanic belt, Japan (e.g. Tatsumi, 2006; Tatsumi and Ishizaka, 1982), which were originally named "sanukitoids" by Koto (1916). However, sanukitoid lithologies had been described before this, particularly elsewhere in the Superior Province (Arth and Hanson, 1975; Beakhouse, 1983; Longstaffe et al., 1980) and in the Finnish part of the Baltic Shield (e.g. Martin et al., 1983; Vidal et al., 1980).

Following their identification, Stern et al. (1989) proposed the first quantitative geochemical definition for Archean-Paleoproterozoic sanukitoids based on rocks from the southwestern Superior Province (table 1.2). Their definition restricted the term "sanukitoid" to relatively primitive (SiO_2 = 55 – 60 wt%) diorites and monzodiorites, but was expanded by Stern and Hanson (1991) to include the more differentiated high-Mg granodiorites derived from them, collectively called the "sanukitoid suite". Since then, "sanukitoid" has remained a primarily geochemical term. "High-Mg diorite" was proposed as an alternative name for Archean sanukitoids by Smithies and Champion (2000) because of geochemical differences between the Archean rocks and the Setouchi high-Mg andesites, namely that the Archean rocks have higher Ba and Sr concentrations and La/Yb ratios than the high-Mg andesites. However, "high-Mg diorite" has not been used as widely as "sanukitoid" in subsequent publications.

Over the past two decades, the geochemical definition of "sanukitoid" has further evolved, with an emphasis on distinguishing sanukitoids from other late Archean-early Proterozoic granitoids (i.e. TTGs, biotite granites etc.) (table 1.2) (Halla et al., 2009; Heilimo et al., 2010; Laurent et al., 2014a; Lowrey et al., 2023; Martin et al., 2009; Moyen, 2020). Classification diagrams for late Archean granitoids were developed by Halla et al. (2009), Heilimo et al. (2010) (fig. 1.9) and Laurent et al. (2014a) (fig. 1.10).
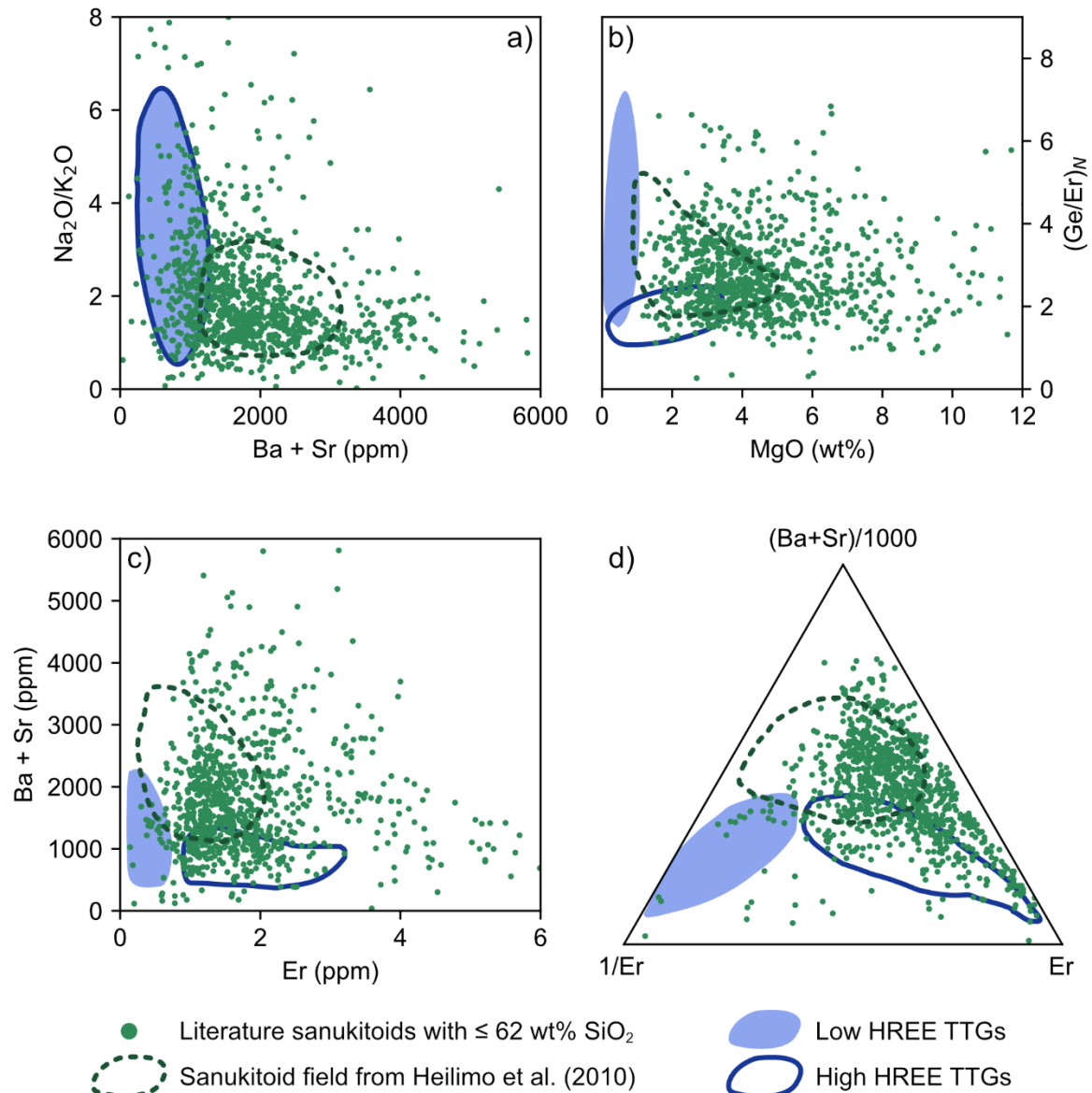
Figure 1.9: Classification diagrams for sanukitoids and TTGs proposed by Halla et al. (2009) and Heilimo et al. (2010), after figure 10 from Heilimo et al. (2010). TTGs are divided into low HREE and high HREE subgroups. The geochemical compositions of rocks described as "sanukitoid" in published literature, plotted in green, are taken from my own compilation of published sanukitoid geochemical data. Following Martin et al. (2009), this dataset was filtered for samples with ≤ 62 wt% SiO_2 to exclude samples with geochemical compositions significantly affected by differentiation.

In these diagrams, sanukitoids are separated from TTGs by their significant enrichment in Ba and Sr, their high MgO contents (these features are captured by Laurent et al. in the combined parameter "2 FMSB" (= 2 * [FeO_T + MgO] * [Sr + Ba]), fig. 1.10), and their slightly more potassic nature (lower Na_2O/K_2O). Sanukitoids are distinguished from biotite and two-mica granites again by their marked enrichments in Ba, Sr and Mg, but also by their lower Al content (captured by lower A/CNK (= molar

Table 1.2: The geochemical characteristics used in literature definitions of Archean-Paleoproterozoic sanukitoids, and comparison of the average values of geochemical parameters used to distinguish between low-Ti and high-Ti sanukitoids from Martin et al. (2009). The subscript X_N refers to the CI chondrite-normalised REE concentration. Eu/Eu* is the Eu anomaly of a CI-chondrite normalised REE pattern.

Paper / Term	Stern et al. (1989) Sanukitoid	Stern and Hanson (1991) Sanukitoid suite	Heilimo et al. (2010) Sanukitoid series	Laurent et al. (2014a) Sanukitoid *sensu lato*	Lowrey et al. (2023) Sanukitoid (at 60 wt% SiO₂)	Martin et al. (2009) Average composition at ≤ 62 wt% SiO₂ Low-Ti sanukitoid	Martin et al. (2009) Average composition at ≤ 62 wt% SiO₂ High-Ti sanukitoid
Major Elements — SiO_2 (wt%)	55 – 60	55 – 73	55 – 70	45 – 70	60	≤ 62	≤ 62
TiO_2 (wt%)						0.69	1.21
MgO (wt%)			1.5 – 9	1.5 – 9		4.33	3.39
Mg#	> 60	43 – 62	45 – 65	45 – 65	> 50	58	47
FeO* + MgO + MnO + TiO_2 (wt%)				5 – 25			
Na_2O (wt%)		4 – 5.5				4.49	4.09
K_2O (wt%)	> 1	0.5 – 4	1.5 – 5	1.5 – 5		3.04	3.20
K_2O/Na_2O		< 1	0.33 – 2	≥ 0.5		0.68	0.78
P_2O_5		≤ 0.5				0.42	0.72
Mantle-compatible trace elements — V (ppm)				> 50			
Cr (ppm)	> 200	≤ 150		20 – 500	> 80	143	58
Ni (ppm)	> 100			15 – 200	> 50	69	36
Large ion lithophile elements (LILE) — Sr (ppm)	> 500	500 – 2000		> 400		1202	994
Ba (ppm)	> 500	500 – 2000		> 1000		1493	1445
Ba + Sr (ppm)			> 1400				
Rb/Sr	< 0.1	≤ 0.1					
Sr/Y					≥ 30		

24

Table 1.2 continued:

	Paper	Stern et al. (1989)	Stern and Hanson (1991)	Heilimo et al. (2010)	Laurent et al. (2014a)	Lowrey et al. (2023)	Martin et al. (2009) Average composition at ≤ 62 wt% SiO_2	
	Name	Sanukitoid	Sanukitoid suite	Sanukitoid series	Sanukitoid *sensu lato*	Sanukitoid (at 60 wt% SiO_2)	Low-Ti sanukitoid	High-Ti sanukitoid
High field strength elements (HFSE)	Y						20	35
	Zr						172	316
	Nb						10	17
Rare Earth elements (REE)	Chondrite-normalised REE pattern	Strongly enriched in LREE	Steeply fractionated					
	Ce_N		65 – 170					
	Yb_N		3 – 6					
	Eu/Eu*	~1	~1		0.5 – 1			
	$(La/Yb)_N$				10 – 75, most > 25		29.2	31.5
	$(Gd/Er)_N$			2 – 6				

Al$_2$O$_3$ / [CaO + Na$_2$O + K$_2$O])) and less potassic nature (higher Na$_2$O/K$_2$O) (Laurent et al., 2014a) (fig. 1.10). Linear discriminant analysis done by Moyen (2020) on major elements in Archean granitoids determined that K/Na is most effective at separating potassic granitoids (including sanukitoids) from TTGs, while Fe/Mg segregates sanukitoids from other potassic granites.
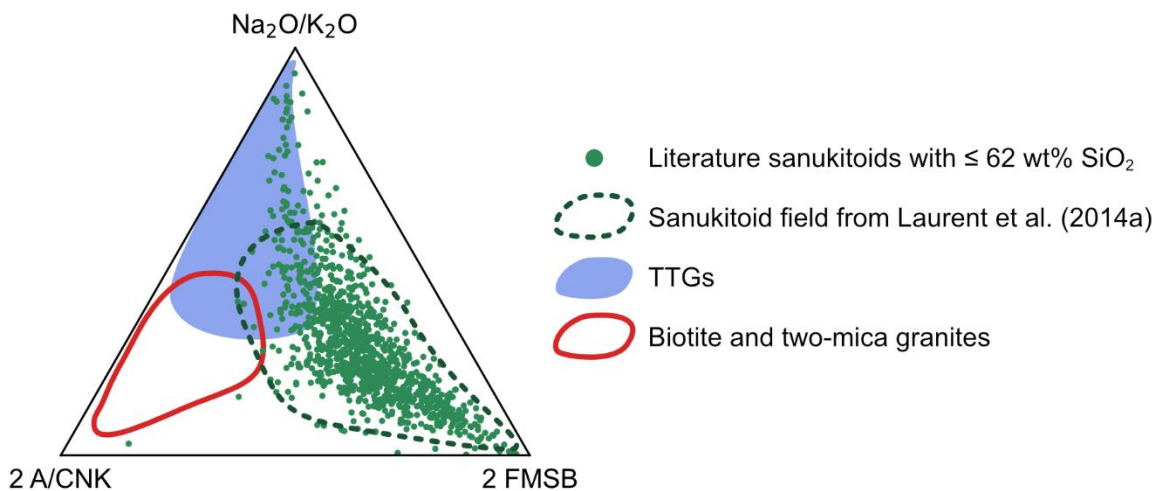
*Figure 1.10: Classification diagram for late Archean granitoids (sanukitoids, TTGs and biotite and two-mica granites) proposed by Laurent et al. (2014a), after figure 7 from Laurent et al. (2014a). 2 A/CNK = 2 * molar Al$_2$O$_3$ / [CaO + Na$_2$O + K$_2$O]. 2 FMSB = 2 * [FeO$_T$ + MgO] * [Sr + Ba]. The geochemical compositions of rocks described as "sanukitoid" in published literature, plotted in green, are taken from my own compilation of published sanukitoid geochemical data. Following Martin et al. (2009), this dataset was filtered for samples with ≤ 62 wt% SiO$_2$ to exclude samples with geochemical compositions significantly affected by differentiation.*

Lowrey et al. (2023) produced a systematic, albeit more complex, classification procedure for granitoids from the Yilgarn Craton (table 1.2, fig. 1.11). Sanukitoids are included as part of the mafic granite group (Champion and Sheraton, 1997), which are primarily separated from other granitoids by their high Mg# (fig. 1.11a and b; see Lowrey et al. (2023) for the full classification procedure). Sanukitoids are then distinguished from other mafic granites by their high Sr/Y ≥ 30 (fig. 1.11c). They also introduced the new term of "sanukitoid-like rocks" to describe rocks which display many of the key characteristics of sanukitoids but have slightly lower Mg#, Ni and Cr concentrations (fig. 1.11d-f). Lowrey et al. based the location of the boundary between sanukitoids and sanukitoid-like rocks on the definition of Stern et al. (1989). As can be seen in figures 1.11d-f, many samples that have been described as "sanukitoids" in
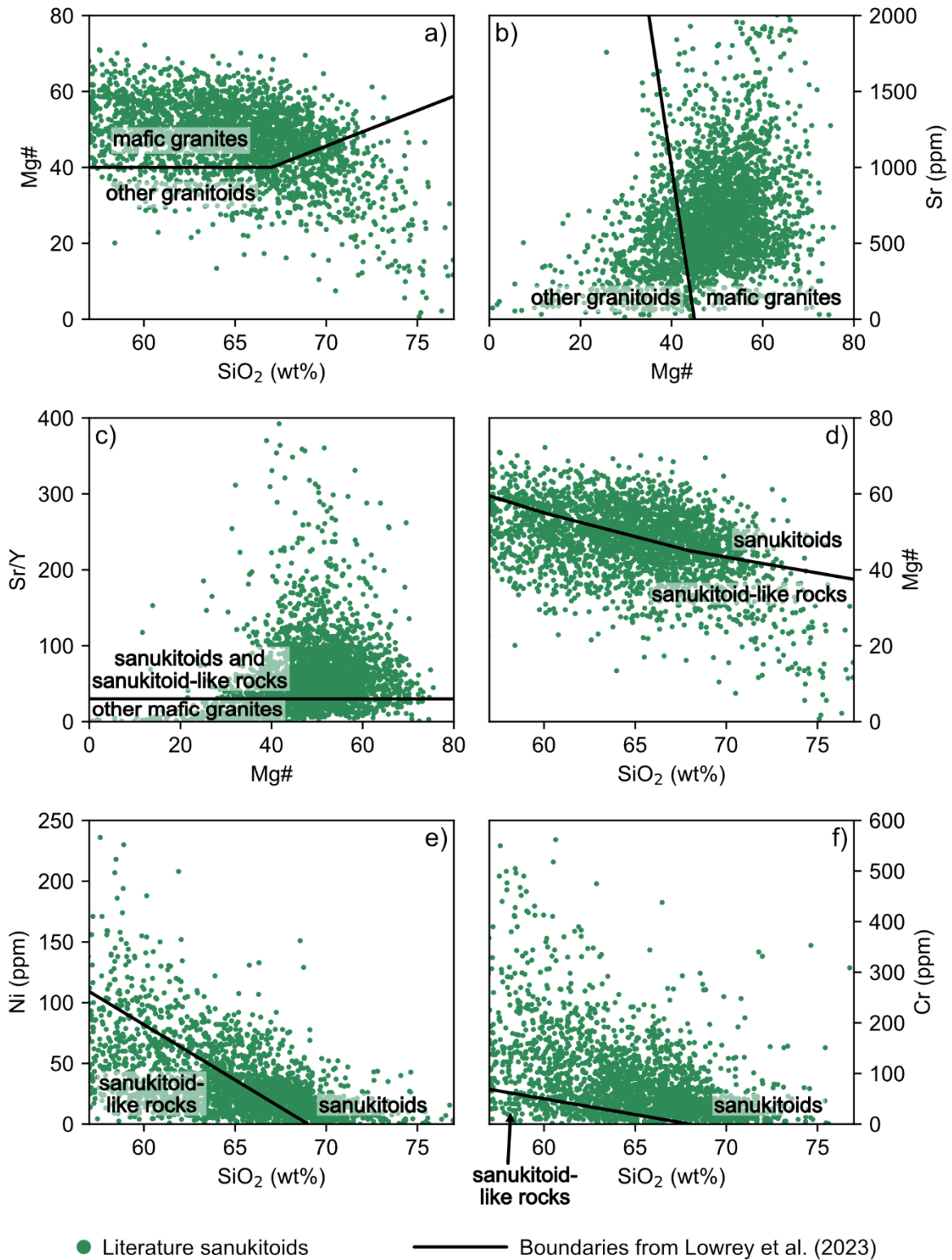
Figure 1.11: Selected figures from Lowrey et al. (2023)'s granitoid classification procedure. The equations of the boundary lines are given in Lowrey et al. (2023). The geochemical compositions of rocks described as "sanukitoid" in published literature, plotted in green, are taken from my own compilation of published sanukitoid geochemical data. a) Mg# vs SiO₂ (wt%) separating mafic granites from other granitoids, after figure 25 from Lowrey et al.; b) Sr (ppm) vs Mg# separating mafic granites from other granitoids, after figure 34 from Lowrey et al.; c) Sr/Y vs Mg# separating sanukitoids and sanukitoid-like rocks from other mafic granites after figure 53 from Lowrey et al.. Figures d), e) and f) separate sanukitoids from sanukitoid-like rocks: d) Mg# vs SiO₂ (wt%) after figure 54 from Lowrey et al.; e) Ni (ppm) vs SiO₂ (wt%) after figure 56 from Lowrey et al.; f) Cr (ppm) vs SiO₂ (wt%) after figure 55 from Lowrey et al..

published literature fall into the field of sanukitoid-like rocks, being less enriched in compatible elements than the original definitions of sanukitoid require.

Multiple studies (e.g. Laurent et al., 2014a; Moyen, 2020; Steenfelt et al., 2005) have observed that the term "sanukitoid" has been applied to a more diverse range of rocks than those originally described by Shirey and Hanson (1984) and Stern et al. (1989). To try to address this, Laurent et al. (2014a) introduced the terms "sanukitoids *sensu stricto* (s.s.)" to refer to sanukitoids that fit Stern et al. (1989)'s definition and "sanukitoids *sensu lato* (s.l.)" to refer to a wider group of rocks that have a similar petrogenesis to sanukitoids s.s. but differ in geochemical composition (table 1.2). Further work is needed to investigate the various heterogeneous rocks that have been labelled "sanukitoid" as the fluctuating and gradually broadening definition of this group may obscure important details of the formation of mantle-derived late Archean-early Proterozoic granitoids and their potential link to geodynamic changes during this period.
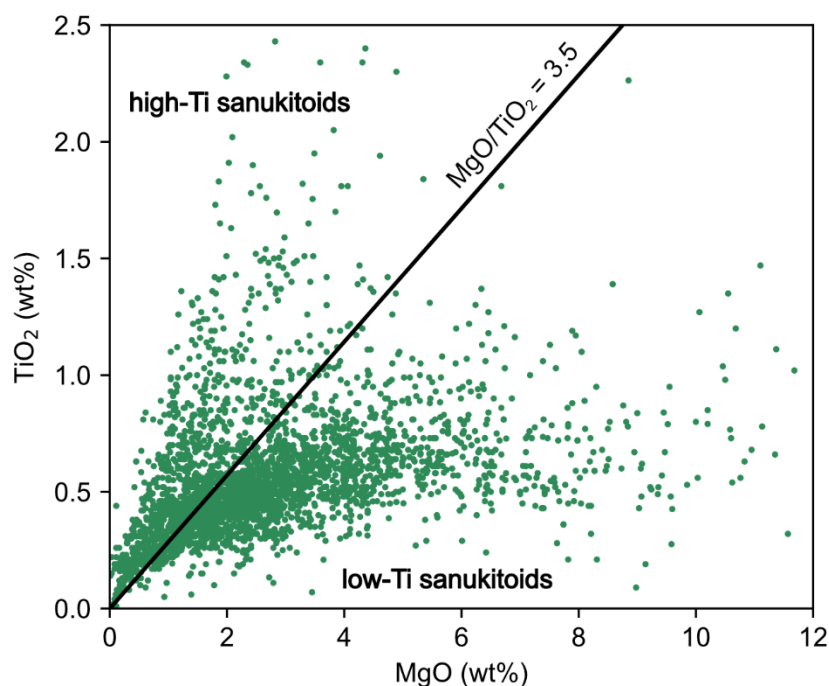
Figure 1.12: Plot of TiO$_2$ (wt%) vs MgO (wt%), with MgO/TiO$_2$ = 3.5 used to divide low-Ti sanukitoids from high-Ti sanukitoids after Martin et al. (2009). The geochemical compositions of rocks described as "sanukitoid" in published literature, plotted in green, are taken from my own compilation of published sanukitoid geochemical data.

Further terminology relating to Archean-Paleoproterozoic sanukitoids and closely associated rocks has been added to the lexicon. Moyen et al. (2003) identified a unique type of late Archean granitoid in the Dharwar Craton, which they named "Closepet-type granite" after the type locality. Closepet-type granites display many of the key characteristics of sanukitoids, such as relatively high Mg#, steeply fractionated chondrite-normalised REE patterns and Ba and Sr enrichment. However, Closepet-type granites differ from typical sanukitoids (i.e. the Stern et al. (1989) and Heilimo et al. (2010) definitions) by being more potassic, less aluminous, having higher HFSE (e.g. Ti, Zr, Nb), REE and P_2O_5 contents and lower Mg# and Mg, Cr and Ni concentrations (Martin et al., 2009; Moyen et al., 2003) (table 1.2). Martin et al. (2009) encouraged grouping Closepet-type granites with sanukitoids. They introduced the terms "low-Ti sanukitoid" to describe the typical sanukitoids of Stern et al. (1989) and "high-Ti sanukitoid" to describe Closepet-type granites, using a plot of TiO_2 vs MgO to distinguish between the two types (fig. 1.12). The name "high-Ti sanukitoid" is now most commonly used in published literature to describe these rocks. They are included in sanukitoids s.l. by Laurent et al. (2014a), and high-Ti sanukitoids have also been referred to as "high-K calc-alkaline granitoids" (HKCA granitoids) by Moyen (2020), although this group is broader than the typical high-Ti sanukitoids and likely includes some hybrid granitoids and granitoids of crustal origin. High-Ti sanukitoids have been identified on multiple cratons, including the Amazonian Craton (Silva-Silva et al., 2020), Limpopo Belt (Laurent et al., 2011), Madagascar Shield (Schofield et al., 2010), North China Craton (Wang et al., 2024) and Sarmatian Craton (Terentiev and Santosh, 2018).

While the exact geochemical parameters used to define sanukitoids have varied over the past four decades, some features are shared by almost all definitions (table 1.2). These geochemical characteristics provide key constraints on how sanukitoid magmas formed:

1. High Mg# and high concentrations of mantle-compatible elements (e.g. Ni, Cr), which show that sanukitoids need a significant ultramafic mantle component in their source (e.g. Martin et al., 2009; Shirey and Hanson, 1984).

2. Enrichment in Ba and Sr, including in the less evolved members of the sanukitoid suite, which requires that this mantle source component was

enriched in incompatible elements, likely by a component derived from recycled crustal material (e.g. Shirey and Hanson, 1984; Stern et al., 1989).

3. Enrichment in LREE and highly fractionated chondrite-normalised REE patterns parallel to those of TTGs, which suggest a petrogenetic link between sanukitoids and TTGs (e.g. Martin et al., 2009; Smithies and Champion, 2000).

1.2.2. Petrogenesis of sanukitoid magmas

The distinctive geochemical characteristics of sanukitoids show that recycling of crustal material into the mantle, followed by interaction between a component derived from this crustal material (i.e. melt, aqueous fluid) and mantle peridotite, is needed to form their parental magmas. This model is consistent with the near-chondritic to suprachondritic Nd radiogenic isotope compositions ($\varepsilon Nd(t)$) of sanukitoids that indicate a juvenile source (e.g. Heilimo et al., 2013; Laurent et al., 2014a; Ma et al., 2013; Seixas et al., 2013; Smithies et al., 2004).

The recycled crust-derived component is most commonly proposed to be a TTG-like melt generated by metabasite partial melting in the garnet stability field due to the similarity between sanukitoid and TTG REE patterns (fig. 1.5c) (e.g. Martin et al., 2009; Smithies and Champion, 2000). Experimental studies (Rapp et al., 2010, 1999) and geochemical modelling (e.g. de Oliveira et al., 2011; Seixas et al., 2013; Semprich et al., 2015; Smithies and Champion, 2000) provide further support for a metabasite-derived component. However, various other sources have also been proposed for this incompatible element-enriched component, which may be particularly pertinent to explaining the unique geochemical features of specific sanukitoid intrusions. A recycled sediment-derived component is often suggested, either on its own (e.g. Halla, 2005; Laurent et al., 2011; Raza et al., 2021) or alongside a metabasite-derived component (e.g. Scandolara et al., 2024; Sun et al., 2020; Wang et al., 2024). Chemical characteristics such as relatively high K_2O/Na_2O (e.g. Sun et al., 2020; Wang et al., 2024), HFSE ratios (e.g. low Zr/Ta; Sun et al., 2020; Xu et al., 2019), enrichment in U and Th (e.g. Li et al., 2024) and high zircon $\delta^{18}O$ (e.g. King et al., 1998; Moreira et al., 2023; Wang et al., 2024) have been used to argue for sediment involvement in sanukitoid petrogenesis. Laurent et al. (2019) proposed that a plot of total LREE concentrations ($\Sigma LREE = La + Ce + Pr + Nd$) vs [Sr + Ba] (fig. 1.13) could

be used to distinguish between sanukitoids formed by mantle-metabasite interaction and those formed by mantle-sediment interaction as the latter have high ΣLREE but relatively low [Sr + Ba] (e.g. Laurent et al., 2011). A carbonatite melt component has been implicated for sanukitoids from West Greenland (Steenfelt et al., 2005) and the Superior Province (Semprich et al., 2015) because these intrusions are more enriched in Sr, Ba, P, K and REE than the majority of sanukitoids. Finally, Heilimo et al. (2010) proposed that an alkaline melt generated from upwelling asthenospheric mantle was additionally involved in forming sanukitoids from the Baltic Shield in order to explain why their high K-Ba-Sr signature is not correlated with Nd-Hf isotopic evidence for a crustal component.

- Literature sanukitoids with ≤ 62 wt% SiO_2
- Sanukitoids formed by mantle-TTG interaction
- Sanukitoids formed by mantle-sediment interaction
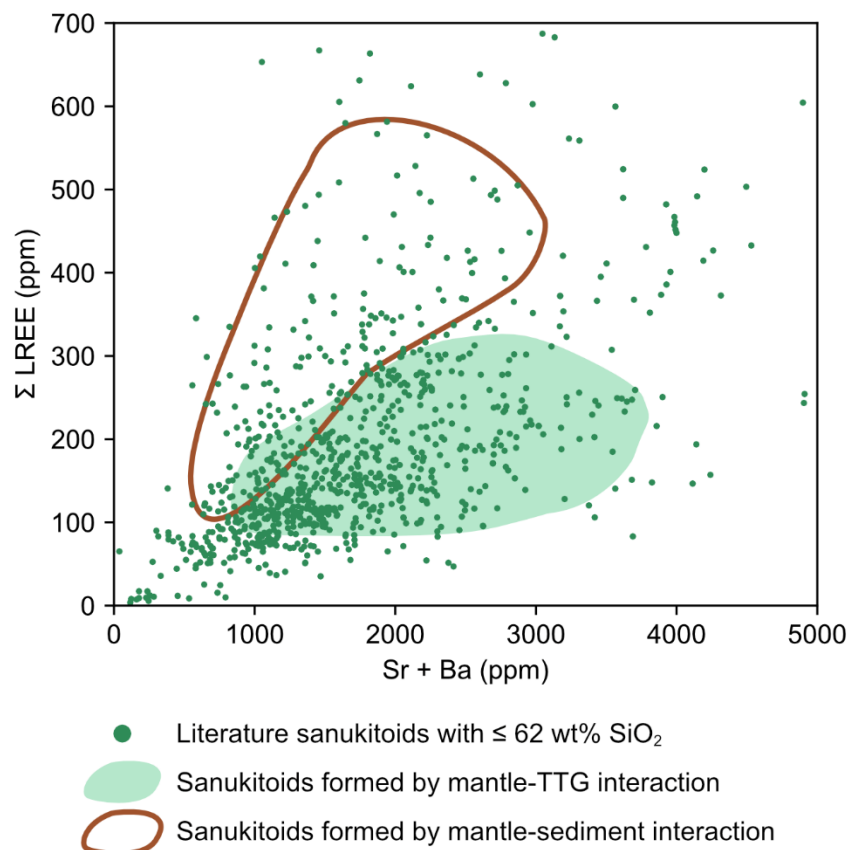
Figure 1.13: Plot of total LREE concentrations (ΣLREE = La + Ce + Pr + Nd) (ppm) vs [Sr + Ba] (ppm) after figure 13 from Laurent et al. (2019). Laurent et al. (2019) proposed that this graph can be used to distinguish between sanukitoids formed by mantle-TTG interaction (light green field) and sanukitoids formed by mantle-sediment interaction (brown field). The geochemical compositions of rocks described as "sanukitoid" in published literature are taken from my own compilation of published sanukitoid geochemical data. Following Martin et al. (2009), this dataset was filtered for samples with ≤ 62 wt% SiO_2 to exclude samples with geochemical compositions significantly affected by differentiation.
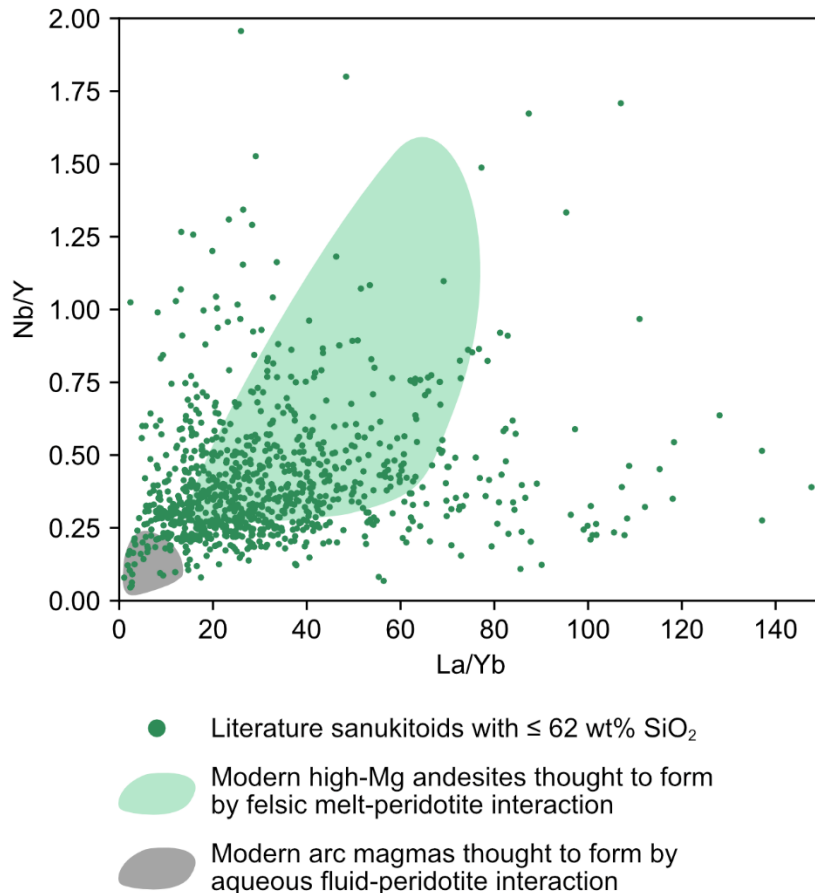
Figure 1.14: Plot of Nb/Y vs La/Yb comparing sanukitoids (green circles) to modern high-Mg andesites that are thought to form by felsic melt-peridotite interaction (light green field) and modern arc magmas that are thought to form by aqueous fluid-peridotite interaction (grey field). After figure 7a from Martin et al. (2009). The geochemical compositions of rocks described as "sanukitoid" in published literature are taken from my own compilation of published sanukitoid geochemical data. Following Martin et al. (2009), this dataset was filtered for samples with ≤ 62 wt% SiO_2 to exclude samples with geochemical compositions significantly affected by differentiation.

There is some disagreement about whether the incompatible element-enriched component was a melt (e.g. Martin et al., 2009; Rapp et al., 2010; Semprich et al., 2015; Smithies and Champion, 2000) or an aqueous fluid generated by dehydration of metabasites and/or sediments (e.g. Ahmad et al., 2018; Halla, 2005; Lobach-Zhuchenko et al., 2008; Stern et al., 1989). Support for a silicate melt comes from the elevated La/Yb, Nb/Y and Sr/Y of sanukitoids in comparison to most modern arc magmas, which are thought to primarily record fluid-mantle interaction (fig. 1.14) (e.g. Martin et al., 2009; Smithies and Champion, 2000). On the other hand, some studies favour an aqueous fluid component because sanukitoids display depletions in fluid-immobile HFSE alongside enrichments in fluid-mobile LILE (Halla, 2005; Stern et al., 1989). These fluids might also have been CO_2-rich (Lobach-Zhuchenko et al., 2008).

The nature of the incompatible element-enriched component may affect the crystallisation pathway followed by sanukitoid magmas during differentiation as higher H_2O contents stabilise amphibole over biotite (e.g. Bucholz et al., 2014; C.-Y.-H. Liu et al., 2022). Determining whether a melt or fluid component was more important for generating sanukitoid magmas has significant geodynamic implications because partial melting and dehydration of metabasite/sediment lithologies occur under different P-T conditions (e.g. Hernández-Uribe et al., 2019; Johnson and Plank, 2000; Martin, 1986).

While it is well-established that sanukitoids formed by interaction between a recycled crustal component and mantle peridotite, the nature of this interaction is debated. A two-stage process via mantle metasomatism is most commonly invoked (e.g. Kovalenko et al., 2005; Shirey and Hanson, 1984; Smithies and Champion, 2000) and appears to have become the default petrogenesis proposed in the literature. In this model, the mantle is first metasomatised by the crust-derived component, meaning the melt/fluid is completely consumed during reactions with mantle peridotite, altering its composition and likely forming new minerals such as phlogopite and pargasitic amphibole (e.g. Heilimo et al., 2010; Kovalenko et al., 2005; Laurent et al., 2011; Lobach-Zhuchenko et al., 2008). This metasomatised mantle source subsequently melts to generate sanukitoid parental magma. However, experimental studies (Rapp et al., 2010, 1999) and geochemical modelling (e.g. Laurent, 2012; Martin et al., 2009; Semprich et al., 2015) demonstrate that a one-stage process where a metabasite-derived melt assimilates mantle peridotite can also create sanukitoid magmas. In this scenario, olivine is the main mineral consumed by the metabasite-derived melt (Rapp et al., 2010, 1999). The key difference between these processes is the melt/fluid-to-rock ratio – in the one-stage process the melt-to-rock ratio is high and the crustal component dominates, whereas in the two-stage process the melt/fluid-to-rock ratio is low and mantle peridotite dominates volumetrically (e.g. Martin et al., 2009; Rapp et al., 2010). More recently, Smithies et al. (2019, 2018) proposed that sanukitoid magmas can evolve from lamprophyric magmas by amphibole-dominated fractional crystallisation. This model, which is based on sanukitoids from the Yilgarn Craton, is a variation on the two-stage process described above as calc-alkaline lamprophyres form by low- to moderate-degree partial melting of metasomatised mantle (e.g. Choi et al., 2020; Rock, 1991). Again, determining the nature of crust-derived component-

mantle interaction has geodynamic implications as the two-stage petrogenetic model requires an additional thermal trigger to start melting the metasomatised mantle (e.g. Heilimo et al., 2010). Furthermore, the P-T conditions of this interaction are poorly constrained (e.g. Martin et al., 2009; Semprich et al., 2015).

The variables detailed above have the potential to generate chemical heterogeneity among sanukitoids. A key topic of debate is what is responsible for the compositional differences between low-Ti and high-Ti sanukitoids. Martin et al. (2009) and Laurent (2012) proposed that low-Ti sanukitoids formed via a one-stage process while high-Ti sanukitoids formed via a two-stage process as the latter mechanism creates greater enrichments in HFSE and REE. The P-T conditions of the mantle-crustal component interaction may also be an important factor. Geochemical modelling by Laurent (2012) suggested that high-Ti sanukitoids formed at relatively low pressures and temperatures (< 2 GPa, 900 – 1100°C) within the amphibole and phlogopite stability fields while low-Ti sanukitoids formed at higher P-T conditions (> 2.5 GPa, 1000 – 1200°C). In contrast, modelling by Wang et al. (2024) supports high-Ti sanukitoids forming at higher pressures (~3 – 4 GPa) than low-Ti sanukitoids (~2 GPa) due to the control of pressure on melt TiO_2 content. Alternatively, different crustal components may be involved. Wang et al. (2024) proposed that the mantle source of high-Ti sanukitoids was metasomatised solely by sediment melts, while low-Ti sanukitoids required a significant metabasite-derived melt component. A dominant sediment component has been implicated for several other high-Ti sanukitoid intrusions, including the Bulai pluton, Limpopo Belt (Laurent et al., 2011), the Anjana and Amet granites, Aravalli Craton (Raza et al., 2021), and monzogranites from the Jinzhou area, North China Craton (Xu et al., 2019). However, modelling by Laurent (2012) determined that the composition of the metasomatic agent has only a secondary control on sanukitoid geochemistry. Mixing between metasomatised mantle-derived melts and magma from crustal sources may also be an important process for generating high-Ti sanukitoids (e.g. Jayananda et al., 1995; Moyen et al., 2001; Terentiev and Santosh, 2018).

A few studies suggest that there may be secular changes in sanukitoid compositions across the late Archean-early Proterozoic transition. Moyen et al. (2003) observed that

there may be a temporal relationship between low-Ti sanukitoids and high-Ti sanukitoids in the Dharwar Craton as the high-Ti Closepet granite was emplaced at ~2520 Ma, after most low-Ti sanukitoid magmatism in the region. However, this temporal relationship does not hold across all cratons – for example, in the Aravalli Craton emplacement of the high-Ti Jhiri granite at ~2530 Ma (Raza et al., 2022) precedes the majority of low-Ti sanukitoid magmatism on the craton (e.g. Ahmad et al., 2018; Mondal and Raza, 2013; Rahaman and Mondal, 2015), and contemporaneous low-Ti and high-Ti sanukitoids have also been reported on some cratons (e.g. Terentiev and Santosh, 2017; Wang et al., 2024). Mauri et al. (2023) found that Paleoproterozoic sanukitoids from the São Francisco Craton generally have lower $(La/Yb)_N$ than typical Archean sanukitoids. They interpreted this as reflecting lower degrees of interaction between the crustal component and mantle peridotite in the Paleoproterozoic, which may record a transition from typical sanukitoid magmatism towards modern BADR (basalt-andesite-dacite-rhyolite) magmatism. Secular changes in the geochemistry of Archean intermediate rocks, which include dioritic sanukitoids, have also been reported (Wang et al., 2024; Yao et al., 2023). This dataset shows increasing K_2O/Na_2O, (Sr + Ba), TiO_2 and Fe^* (= FeO_T / [FeO_T + MgO]) during the late Archean (< 3 Ga) (Wang et al., 2024). On the whole, however, the secular evolution of sanukitoid compositions remains largely unexplored, despite them having been emplaced over an approximately one-billion-year time period (fig. 1.8). Investigating the temporal evolution of sanukitoid chemistry may provide further insight into changing processes during the late Archean-early Proterozoic transition. In particular, the compositions of crustal materials (i.e. altered oceanic crust, sediments) recycled into the mantle likely changed across this transition, and sanukitoid compositions potentially provide a record of this evolution.

Following their formation, sanukitoid parental magmas differentiated to create the wide range of SiO_2 contents displayed by the sanukitoid suite (e.g. Heilimo et al., 2010; Stern and Hanson, 1991). Sanukitoids follow a differentiation pathway similar to the calc-alkaline series (fig. 1.5c), showing a slight increase in K_2O/Na_2O and no Fe enrichment during their evolution, but have slightly lower CaO contents than the modern calc-alkaline trend (e.g. de Oliveira et al., 2009; Gómez-Frutos and Castro, 2022; Martin et al., 2009). Major and trace element modelling shows that this evolution was primarily driven by amphibole- and plagioclase-dominated fractional

crystallisation (e.g. Laurent et al., 2013; Seixas et al., 2013; Smithies et al., 2019). Other minerals, namely biotite, K-feldspar and pyroxenes, may have also crystallised during differentiation, alongside accessory phases such as apatite, titanite, zircon, allanite and Fe-Ti oxides (e.g. Seixas et al., 2013; Smithies et al., 2019; Stern and Hanson, 1991). This process produced diorite-hornblendite cumulates that are sometimes found entrained as xenoliths in the more evolved sanukitoid magma (Smithies et al., 2019). Mineral thermobarometry for sanukitoids from the Amazonian Craton determined that they crystallised at ~700 – 950°C and were emplaced at relatively shallow crustal levels (P ≈ 100 – 300 MPa), with some intrusions also recording a high pressure (~600 – 900 MPa) crystallisation stage (de Oliveira et al., 2009; do Nascimento et al., 2023, 2021). These studies also indicate that sanukitoid crystallisation likely occurred under high fO_2 conditions. In addition, mixing between primitive sanukitoid magmas and felsic magmas may have contributed to the differentiation of some sanukitoids (e.g. Laurent et al., 2013; Sun et al., 2019). Gómez-Frutos and Castro (2022) conducted crystallisation experiments on materials analogous to Archean sanukitoids, and based on these experiments proposed that the compositional range of the sanukitoid suite was generated by self-contamination of primitive sanukitoid magmas by pyroxene-rich cumulates formed during the early stages of differentiation. However, these experiments may not be particularly relevant to the differentiation of natural sanukitoid magmas because the starting materials contain either low amounts of H_2O (3 wt%) or no H_2O, unlike natural sanukitoid magmas that contained > 5 wt% H_2O (de Oliveira et al., 2009; do Nascimento et al., 2023, 2021), which likely inhibited crystallisation of hydrous minerals such as amphibole and biotite during Gómez-Frutos and Castro's experiments.

Recent studies have proposed a new petrogenetic link between sanukitoids and TTGs. Smithies et al. (2019) observed that in the eastern Yilgarn Craton, the evolved end of the sanukitoid differentiation trend intersects with a subset of "high pressure" TTGs characterised by very high Sr/Y and Sr concentrations (fig. 1.15). They demonstrated that these TTGs could have formed by amphibole-dominated fractional crystallisation of sanukitoid magmas. Similarly, Liou and Guo (2019) proposed that some "high pressure" TTGs in the North China Craton evolved from metasomatised mantle-derived diorites with similar geochemical compositions to sanukitoids via amphibole

fractional crystallisation. C.-Y.-H. Liu et al. (2022) suggested that only sanukitoids which formed from aqueous fluid-metasomatised mantle sources have the potential to evolve into TTGs because abundant amphibole crystallisation requires water-rich magmas. This alternative petrogenetic model for "high pressure" TTGs is significant because it implies that some TTGs were ultimately derived from a mantle source, rather than being generated directly by high pressure metabasite partial melting.
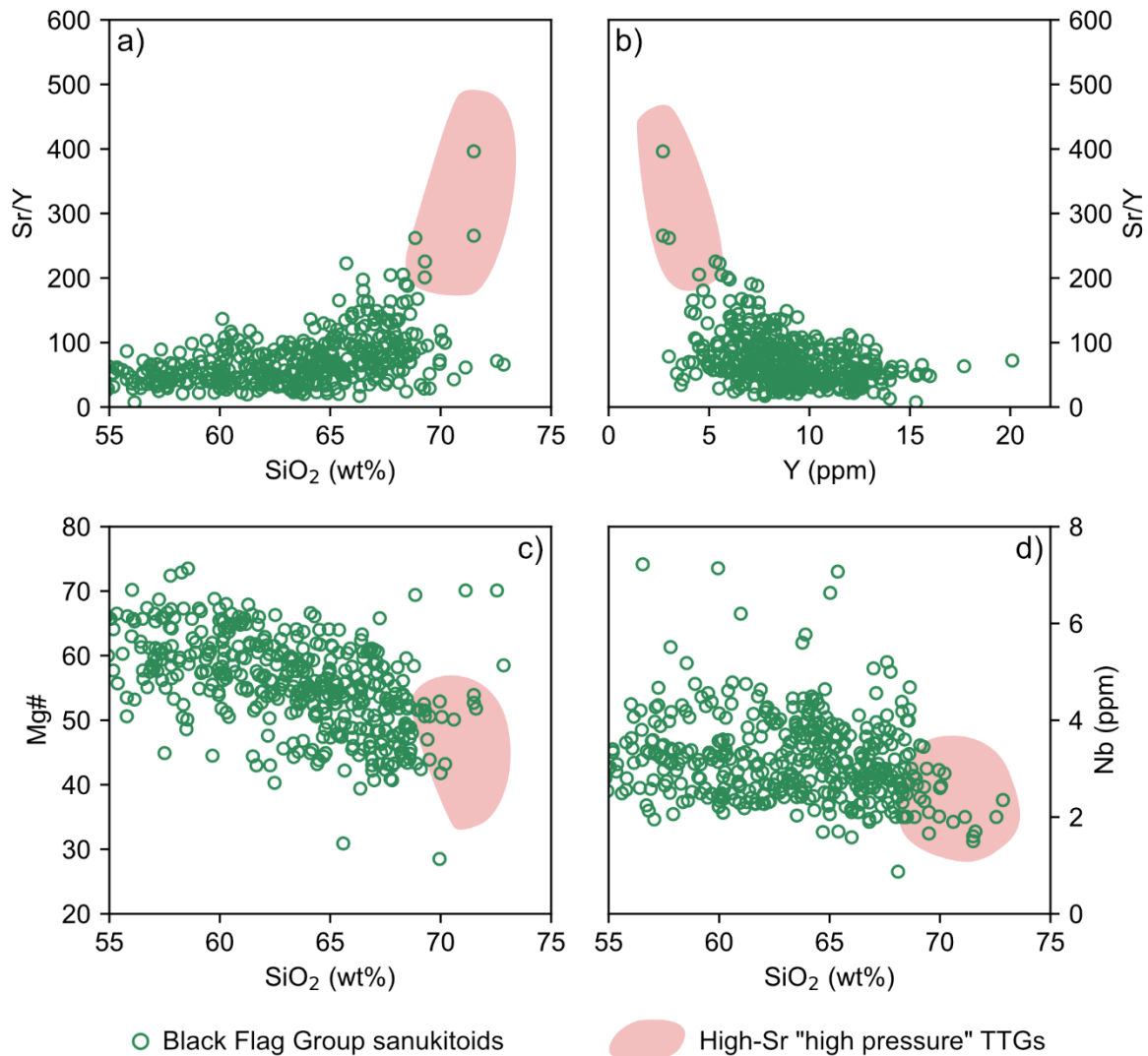
Figure 1.15: Comparison between sanukitoids (the Black Flag Group, green) and high-Sr "high pressure" TTGs (light red field) from the Eastern Goldfields Superterrane, Yilgarn Craton, after figures 4 and 6 from Smithies et al. (2019). a) Sr/Y vs SiO$_2$ (wt%), b) Sr/Y vs Y (ppm), c) Mg# vs SiO$_2$ (wt%), and d) Nb (ppm) vs SiO$_2$ (wt%). Black Flag Group geochemical compositions are from Smithies et al. (2022).

In summary, the dominant model for sanukitoid formation is interaction between a TTG-like melt and mantle peridotite via either a one-stage (assimilation) or two-stage

(metasomatism) process. Sanukitoid parental magmas then underwent amphibole- and plagioclase-dominated fractional crystallisation to generate the sanukitoid suite. Multiple different geodynamic scenarios that fit this petrogenetic model have been proposed. As sanukitoid formation requires burial of crustal materials to mantle depths, most studies link sanukitoids, or at least the creation of their metasomatised mantle source, to a subduction zone setting. The transition from TTG to sanukitoid magmatism may have been caused by decreasing degrees of slab melting as the mantle cools, causing mantle metasomatism/assimilation processes to dominate (e.g. Martin et al., 2009; Moyen et al., 2003), or by the onset of deep subduction with a significant mantle wedge overlying the downgoing slab (e.g. Rapp et al., 2010; Smithies and Champion, 2000). Some studies that favour a different crust-derived component to TTG melts suggest that the appearance of sanukitoids reflects a change from metabasite melting to sediment melting as subduction geothermal gradients decreased in the late Archean (e.g. Laurent et al., 2011). Alternatively, the sanukitoid mantle source might have formed in an intraplate setting that replicates the geometry of subduction zones, such as delamination of dense lower crustal eclogite (e.g. Bédard, 2006) or dripping of crust into the mantle (sagduction) (e.g. Nebel et al., 2018; Smithies et al., 2019). In these scenarios the onset of sanukitoid magmatism may record development of asymmetric crustal drips (Nebel et al., 2018) or strengthening of the lithosphere and creation of lithospheric structures (e.g. shear zones) that facilitated extraction of sanukitoid magmas from the mantle (Smithies et al., 2019).

For the two-stage process a subsequent thermal trigger is needed to melt the metasomatised mantle source of sanukitoids. Many proposed triggers occur in a subduction-collision setting. Slab breakoff leads to upwelling of hot asthenospheric mantle through the newly created gap in the slab, providing heat to melt metasomatised mantle (e.g. Heilimo et al., 2010; Lobach-Zhuchenko et al., 2008; Moreira et al., 2020; Whalen et al., 2004). Slab breakoff may have been more frequent on a hotter, younger Earth when subduction was less stable (e.g. Gunawardana et al., 2024; van Hunen and van den Berg, 2008), or have occurred following attempted subduction of buoyant continental lithosphere or oceanic plateaus (e.g. Davies and von Blanckenburg, 1995). Slab rollback can cause extension in the overlying plate which might have triggered mantle melting (e.g. Chen et al., 2022; Sun et al., 2019; Yu et al., 2021). In a collisional setting, crustal thickening followed by lithospheric

delamination or late- to post-collisional thermal relaxation and extension might have melted the sanukitoid mantle source (e.g. Kovalenko et al., 2005; Laurent et al., 2014a; Whalen et al., 2004), hence the appearance of sanukitoid magmatism in the late Archean may reflect the stabilisation of global plate tectonics and the onset of continental collision (Laurent et al., 2014a). In an intraplate setting the thermal trigger for melting metasomatised mantle may have been provided by plume-like mantle upwelling (e.g. Jayananda et al., 2000; Kovalenko et al., 2005; Smithies et al., 2019) or lithospheric extension and rifting (e.g. Smithies et al., 2019). In the latter case, the onset of sanukitoid magmatism might be related to increasing lithospheric strength as the planet cooled, allowing rifting to begin (Hawkesworth et al., 2024).

Overall, while the broad-scale petrogenetic model for sanukitoid magmatism is well-established (e.g. Martin et al., 2009), details of their formation, such as the source and nature (i.e. melt vs aqueous fluid) of the recycled crust-derived component(s), the character of crustal component-mantle interaction and the P-T conditions of melting, remain debated or poorly constrained. Consequently, there are many different interpretations of the significance of sanukitoid magmatism, and their genesis has been linked to a variety of geodynamic settings (e.g. Bédard, 2006; Laurent et al., 2014a; Nebel et al., 2018; Smithies and Champion, 2000). There are also currently aspects of sanukitoid magmatism that require further exploration, including their proposed link to "high pressure" TTGs (Liou and Guo, 2019; Smithies et al., 2019) and potential secular evolution (e.g. Mauri et al., 2023; Wang et al., 2024), that may provide new insights into the late Archean-early Proterozoic transition. Novel analytical techniques present an exciting opportunity to provide new constraints on sanukitoid formation and evolution, and to improve our understanding of continental crust evolution and geodynamics during the late Archean-early Proterozoic transition.

1.3. Application of novel stable isotopes to investigating sanukitoid petrogenesis

"Novel" or "non-traditional" stable isotope geochemistry is a rapidly developing area of research that uses variations in the stable isotope compositions of a wide range of elements to study natural processes. This growth was facilitated by advances in mass

spectrometry over the past few decades, which expanded the isotopic systems that could be measured at high precision from just the light, abundant, non-metallic "traditional" isotopes (H, C, N, O, S) to virtually the entire periodic table. Novel stable isotopes have successfully been used to trace numerous high- and low-temperature geochemical processes, with different elements being sensitive to different processes. In magmatic systems, novel stable isotopes have been used to trace partial melting (e.g. Ti, Klaver et al. (2024); Fe, Williams et al. (2009)), magma differentiation (e.g. Ti, Hoare et al. (2020); Si, Savage et al. (2011)), recycling of near-surface materials into the source regions of igneous rocks (e.g. Ba, Wu et al. (2020); U, Andersen et al. (2015)), redox processes (e.g. Fe, Sossi and Debret (2021); Sn, Roskosz et al. (2020)) and magmatic-hydrothermal interactions (e.g. Mo, Kaufmann et al. (2021); Ba, Deng et al. (2024)). Therefore, novel stable isotopes may provide new constraints on sanukitoid formation and evolution, and help further our understanding of changes in granitoid magmatism across the late Archean-early Proterozoic transition.

Isotope fractionation is the relative partitioning of isotopes of a particular element between two coexisting phases, creating variations in the isotopic compositions of such substances. High-temperature stable isotope fractionation often occurs at equilibrium, where mass-dependent isotope fractionation is driven by variations in bond stiffness (e.g. Bigeleisen and Mayer, 1947; Urey, 1947). Heavy isotopes tend to concentrate in strong, stiff bonds where valence state is high and/or coordination number is low (e.g. Schauble, 2004; Young et al., 2015). The magnitude of equilibrium isotope fractionation depends on temperature, scaling with $1/T^2$ (Urey, 1947), as well as on the relative mass difference between the isotopes, making it smaller at high temperatures and for heavier elements. However, very heavy elements (e.g. U, Tl, Hg) are also significantly affected by a different kind of equilibrium isotope fractionation called nuclear field shift effects that arise from differences in nuclear size and shape between isotopes (e.g. Bigeleisen, 1996; Schauble, 2007). Isotopic fractionation resulting from nuclear field shift effects scales with $1/T$, and hence can generate mas-independent isotope fractionations that have greater magnitudes than equilibrium mass-dependent isotope fractionations (e.g. Bigeleisen, 1996; Fujii et al., 2009). Kinetic processes can also cause mass-dependent isotope fractionation during unidirectional processes. This is driven by differences in the amount of energy isotopes need to react or move, which is lower for lighter isotopes (e.g. Schauble, 2004). Kinetic

isotope fractionation is common in biologically mediated reactions and evaporation/condensation processes, and helps create large isotope fractionations in near-surface materials, but it has also been observed on small length scales at higher temperatures due to diffusion (e.g. Watkins et al., 2017).

Over the past few years, various novel stable isotope systems have started being used to investigate the formation and evolution of Archean-Paleoproterozoic granitoids, with efforts mainly focussed on TTGs. The silicon (Si) isotope compositions of TTGs have been most extensively studied using both whole rock samples (André et al., 2022, 2019; Deng et al., 2019a; Murphy et al., 2024; Zhou et al., 2024) and individual minerals (Lei et al., 2023; Murphy et al., 2024). The heavy Si isotope compositions of Archean TTGs provide evidence of a seawater silicified metabasite protolith (André et al., 2022, 2019; Lei et al., 2023; Murphy et al., 2024), while a possible shift towards lighter Si isotope compositions seen in Paleoproterozoic TTGs from the North China Craton is interpreted as reflecting interaction of the metabasite protolith with meteoric water, (Zhou et al., 2024). Titanium and iron stable isotopes generally support TTG genesis by metabasite partial melting followed by fractional crystallisation (Aarons et al., 2020; Hoare et al., 2023; Z.J. Zhang et al., 2023), although the iron isotope compositions of some TTGs have been interpreted as more consistent with them forming by fractional crystallisation of mantle-derived magmas (Doucet et al., 2020; Liou et al., 2022). Calcium isotope fractionations in TTGs were used as a proxy for geothermal gradient by Antonelli et al. (2021), who calculated gradients of 500 – 750°C/GPa similar to modern "hot" subduction zones. In contrast, a combined iron-zinc (Fe-Zn) isotope investigation by Doucet et al. (2020) found no evidence in TTGs from the Kaapvaal Craton of the Fe-Zn isotope decoupling that is generated by various processes in modern subduction zones.

Some novel stable isotope systems have been used to study other types of Archean granitoids. Li et al. (2020) identified two distinct magnesium isotope compositions among Neoarchean potassic granites from the North China Craton, suggesting they formed by partial melting of two different sources – igneous rocks and weathered sediments. Si isotopes coupled with Ge/Si ratios demonstrated that the source of potassic granites in the Kaapvaal Craton changed from K-enriched, silicified mafic

rocks to pre-existing TTGs at ~3.1 Ga (André et al., 2022). Currently, novel stable isotope data for sanukitoids are limited to Fe and Zn isotope compositions, which are intermediate between mantle-derived rocks and crustal granitoids and hence reflect the involvement of both crustal and mantle components in their formation (Doucet et al., 2020, 2018; Li et al., 2024). Li et al. (2024) observed that the Zn isotope compositions of sanukitoids from the Kaapvaal and North China Cratons positively correlate with Th/Yb and Th/Nb and therefore appear to be tracing a recycled sediment component. However, while Li et al. (2024) and Doucet et al. (2020, 2018) refer to these rocks as "sanukitoids", their geochemical compositions differ significantly from the original geochemical definitions of Archean sanukitoid (e.g. Heilimo et al., 2010; Stern et al., 1989) as they are more Fe-rich, have lower Mg# and less fractionated REEs, and are not as strongly enriched in Ba (Laurent et al., 2014b; Li et al., 2024). Typical Archean-Paleoproterozoic sanukitoids therefore remain unexplored using novel stable isotopes, despite being a distinctive component of late Archean-early Proterozoic terranes.

Novel stable isotopes have the potential to help answer and resolve some of the remaining questions and debates surrounding Archean-Paleoproterozoic sanukitoids, and the aim of this thesis is to do precisely that. Selecting appropriate isotope systems to use for this investigation is crucial because different isotope systems are sensitive to different processes, and our current level of understanding about how these isotope systems behave varies between elements. In this thesis I use titanium (Ti) and uranium (U) isotope compositions to provide insights into sanukitoid formation and evolution.

1.3.1. Titanium stable isotope systematics

Titanium is a transition metal that is abundant in the Earth's crust and mantle. Mass dependent Ti stable isotope variations are expressed in delta notation as $\delta^{49}Ti$ relative to the Origins Laboratory Titanium standard (OL-Ti), using the ratio of ^{49}Ti to ^{47}Ti (equation 1.1) (Millet and Dauphas, 2014).

$$\delta^{49}Ti = 10^3 \left(\frac{\left(\frac{^{49}Ti}{^{47}Ti}\right)_{sample}}{\left(\frac{^{49}Ti}{^{47}Ti}\right)_{OL-Ti}} - 1 \right) \quad (1.1)$$

A particularly attractive quality of Ti is that it is a HFSE, so it has very low mobility in aqueous fluids, even at high salinities (e.g. Rustioni et al., 2021). Consequently, Ti isotopes are regarded as being resistant to alteration and metamorphism, meaning the Ti isotope compositions of ancient, often altered rocks such as sanukitoids are expected to be robust. It also means that Ti isotopes are not significantly affected by fluid-driven processes (Millet et al., 2016), although the recent studies by Emproto et al. (2025, 2022) and Jiang et al. (2024) suggest that some fluid-mineral Ti isotope fractionation might occur in hydrothermal ore systems with ligand-rich brines.
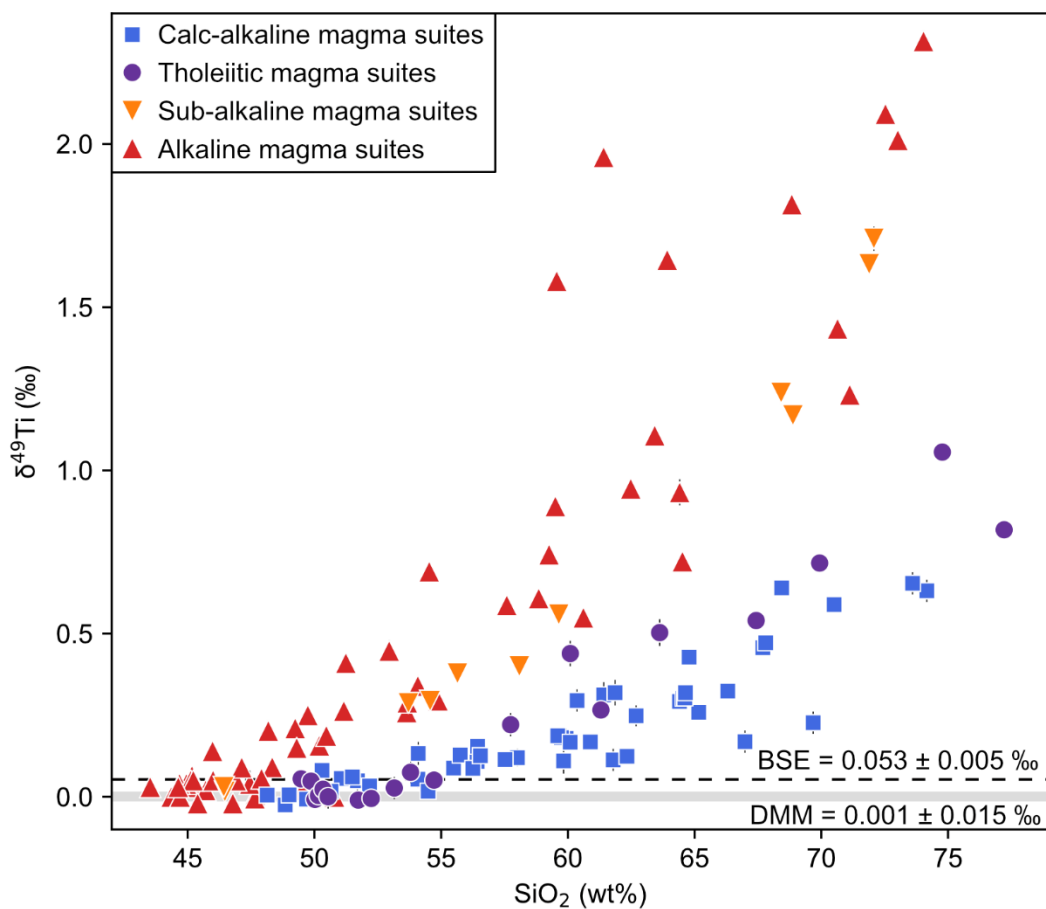
Figure 1.16: $\delta^{49}Ti$ (‰) vs SiO₂ (wt%) showing the evolution of $\delta^{49}Ti$ during differentiation of calc-alkaline, tholeiitic, sub-alkaline and alkaline magma suites. Uncertainty in $\delta^{49}Ti$ is shown as the 95% confidence interval. The bulk silicate Earth (BSE) composition of 0.053 ± 0.005‰ (black dashed line) is from Deng et al. (2023), and the depleted MORB mantle (DMM) composition of 0.001 ± 0.015‰ (grey rectangle) is from Klaver et al. (2024). Ti isotope data are from Deng et al. (2019b), Greber et al. (2021), Hoare et al. (2020), Johnson et al. (2023), Millet et al. (2016) and Zhao et al. (2024).

Ti isotope behaviour in igneous rocks is generally well-understood. Mineral-melt Ti isotope fractionation is the main cause of $\delta^{49}Ti$ variability in terrestrial magmas, and is

driven by differences in the coordination of Ti between silicate melts (mainly 5-fold coordination, e.g. Farges et al., 1996; Farges and Brown, 1997) and Ti-bearing minerals (either 6-fold or 4-fold coordination). *Ab initio* density functional theory (DFT) calculations (Aarons et al., 2021; Leitzke et al., 2018; W. Wang et al., 2020), measurements of experimental (Prissel et al., 2024; Rzehak et al., 2022, 2021) and naturally occurring mineral separates (Greber et al., 2021; A.C. Johnson et al., 2023, 2019; Mandl, 2019; Nie et al., 2021), and measurements of micro-milled individual crystals (Hoare et al., 2022) have been used to constrain mineral-melt Ti isotope fractionation factors. Magmatic suites show increasing $\delta^{49}Ti$ during differentiation due to fractional crystallisation of minerals enriched in light Ti isotopes, particularly of Fe-Ti oxides (fig. 1.16) (Aarons et al., 2020; Deng et al., 2019b; Greber et al., 2021; Hoare et al., 2020; A. C. Johnson et al., 2023, 2019; Millet et al., 2016; Zhao et al., 2024, 2020). This process produces complementary low $\delta^{49}Ti$ cumulates (Storck et al., 2023). Different magma series display varying magnitudes of Ti isotope fractionation during differentiation due to them crystallising different modal abundances and compositions of Fe-Ti oxides (Deng et al., 2019b; Hoare et al., 2020), as well as different proportions of Ti-bearing silicate minerals (Johnson et al., 2023) (fig. 1.16). The alkaline magma series displays the greatest increase in $\delta^{49}Ti$ during differentiation, while the calc-alkaline series shows the smallest increase. Furthermore, magma H_2O content and oxygen fugacity (fO_2) affect the timing of Fe-Ti oxide saturation and hence the onset of the $\delta^{49}Ti$ increase during differentiation (Hoare et al., 2020), which may enable Ti isotopes to be used as a proxy for magma H_2O content and fO_2 (Hoare, 2021).

Ti isotope fractionation is also observed during partial melting processes. While Ti isotopes are not significantly fractionated during melting of typical mantle lithologies (i.e. lherzolite, harzburgite) (Millet et al., 2016), partial melting of metabasites and metasediments generates melts with higher $\delta^{49}Ti$ then their protoliths due to retention of light Ti isotopes in residual Fe-Ti oxides (e.g. rutile) and amphibole (Hoare et al., 2023; Klaver et al., 2024; Z.J. Zhang et al., 2023). This process is proposed to explain the Ti isotope compositions of both Archean TTGs (Hoare et al., 2023; Z.J. Zhang et al., 2023) and modern arc lavas (Klaver et al., 2024). Recycling of isotopically light melting residues generated by formation of the early continental crust into the upper mantle during the Archean may have lowered the $\delta^{49}Ti$ of the upper mantle from the

chondritic value of 0.053 ± 0.005‰ (Deng et al., 2023) to its present-day value of 0.001 ± 0.015‰ (Klaver et al., 2024), with some modern ocean island basalts (OIB) still sampling a primordial, high $\delta^{49}Ti$ lower mantle reservoir (Deng et al., 2023).

Overall, Ti stable isotopes are a well-understood isotopic system that is capable of tracing multiple magmatic processes. The sensitivity of $\delta^{49}Ti$ to metabasite partial melting but not to aqueous fluid-driven processes means that measuring Ti stable isotopes in sanukitoids may be able to distinguish between the involvement of silicate melt and aqueous fluid components in their petrogenesis. Ti isotopes are sensitive to magma differentiation and hence can be used to test the proposed petrogenetic link between sanukitoids and "high pressure" TTGs (Liou and Guo, 2019; Smithies et al., 2019). Finally, as Ti isotope fractionation during differentiation is affected by the H_2O content and fO_2 of magmas, measuring the Ti isotope compositions of sanukitoid suites might provide further constraints on the water content and oxidation of sanukitoid magmas.

1.3.2. Uranium isotope systematics

Uranium is a radioactive actinide series metal with atomic number 92. While there are no stable isotopes of U, it does have two long-lived isotopes – ^{238}U (half-life $t_{1/2} = 4.468$ Gyr) and ^{235}U ($t_{1/2} = 0.704$ Gyr) (Villa et al., 2016) – that can be fractionated by non-radiogenic processes in the same way as stable isotopes. This fractionation creates variations in the $^{238}U/^{235}U$ of geological materials, which are reported in delta notation relative to the CRM145 standard as $\delta^{238}U$ (equation 1.2) (e.g. Andersen et al., 2017).

$$\delta^{238}U = 10^3 \left(\frac{\left(\frac{^{238}U}{^{235}U} \right)_{sample}}{\left(\frac{^{238}U}{^{235}U} \right)_{CRM145}} - 1 \right) \quad (1.2)$$

^{234}U has a much shorter half-life of 246,000 years (Cheng et al., 2013), and measurement of variations in $^{234}U/^{238}U$ ($\delta^{234}U$, equation 1.3) can be used to determine whether the ^{238}U-^{234}U system has been disturbed from secular equilibrium ($\delta^{234}U = 0$) within the last ~1.5 Myr. Measuring $\delta^{234}U$ alongside $\delta^{238}U$ can be helpful for assessing whether U isotopes in a sample have been disturbed by recent U mobility due to

weathering and alteration (e.g. Andersen et al., 2015; Charbonnier et al., 2023; Pavia et al., 2023).

$$\delta^{234}U = 10^3 \left(\frac{\left(\frac{^{234}U}{^{238}U} \right)_{sample}}{\left(\frac{^{234}U}{^{238}U} \right)_{CRM145}} - 1 \right) + \delta^{234}U_{CRM145} \quad (1.3)$$

U and its isotopes are particularly sensitive to redox processes as U primarily occurs in two oxidation states – fluid-immobile U^{4+} and fluid-mobile U^{6+} – on the Earth. Because U is a very heavy element, its isotopes are affected by nuclear field shift effects. For isotope substitutions involving a change in redox state, isotope fractionation due to nuclear field shift effects dominates and concentrates light ^{235}U in U^{6+} (e.g. Bigeleisen, 1996; Fujii et al., 2006), which is the opposite direction to that expected for mass-dependent equilibrium isotope fractionation (e.g. Bigeleisen and Mayer, 1947; Young et al., 2015). On the present-day Earth, redox-related U isotope fractionation has been observed during alteration of oceanic crust at mid-ocean ridges (Andersen et al., 2024, 2015; Noordmann et al., 2016), U reduction and accumulation in sediments (e.g. Andersen et al., 2014; Weyer et al., 2008), and mobilisation of U from the slab in subduction zones (Freymuth et al., 2019) (fig. 1.17). The U isotope compositions of surface reservoirs (e.g. sediments, altered oceanic crust, seawater) on the modern Earth are summarised in figure 1.17a. Changes in the oxygenation of the Earth's surface during its history, such as the GOE, had a huge impact on terrestrial U cycling (e.g. Cuney, 2010) as well as U isotope fractionation. Consequently, the U isotope compositions of sediments (e.g. Chen et al., 2021; X. Wang et al., 2018) and altered oceanic crust (Rodney et al., 2024, Preprint) varied through time, with generally less U isotope fractionation occurring when the surface was less oxidised and hence U mobility was limited. These observations mean that the $\delta^{238}U$ of materials being recycled into the Earth's mantle likely changed over the Earth's history. Andersen et al. (2015) proposed that such a change is captured by the U isotope compositions of recent mid-ocean ridge basalts (MORB) and OIB, both of which have low Th/U ratios indicating addition of recycled U to their sources. MORB have slightly higher $\delta^{238}U$ than the bulk Earth due to addition of high $\delta^{238}U$ altered oceanic crust, similar to that found at present-day mid-ocean ridges, to their mantle source. OIB, on the other hand,
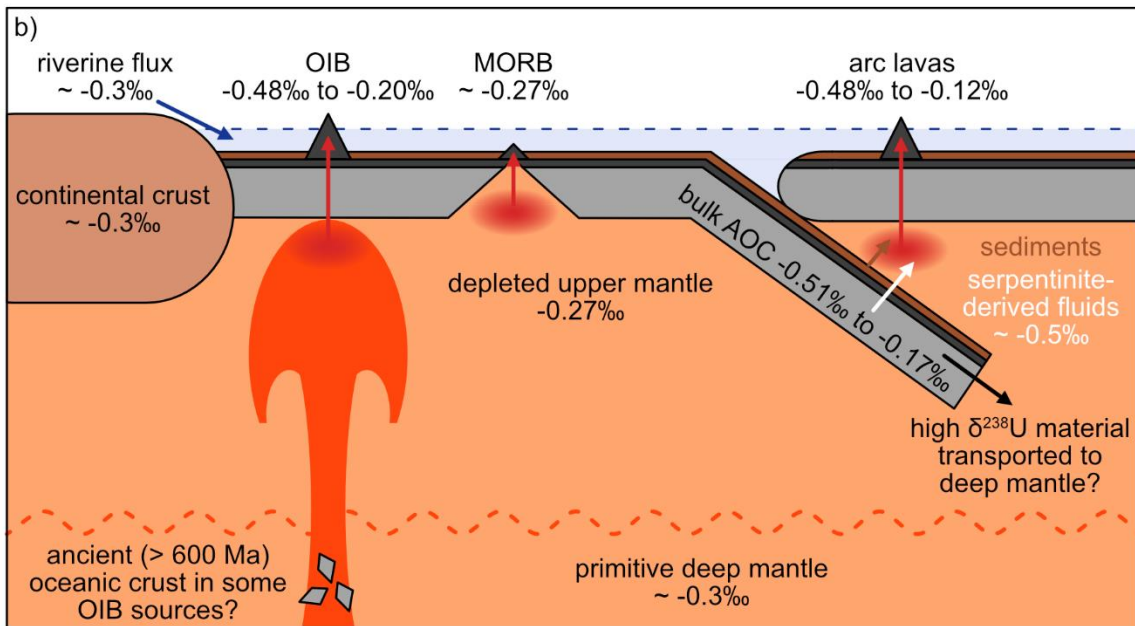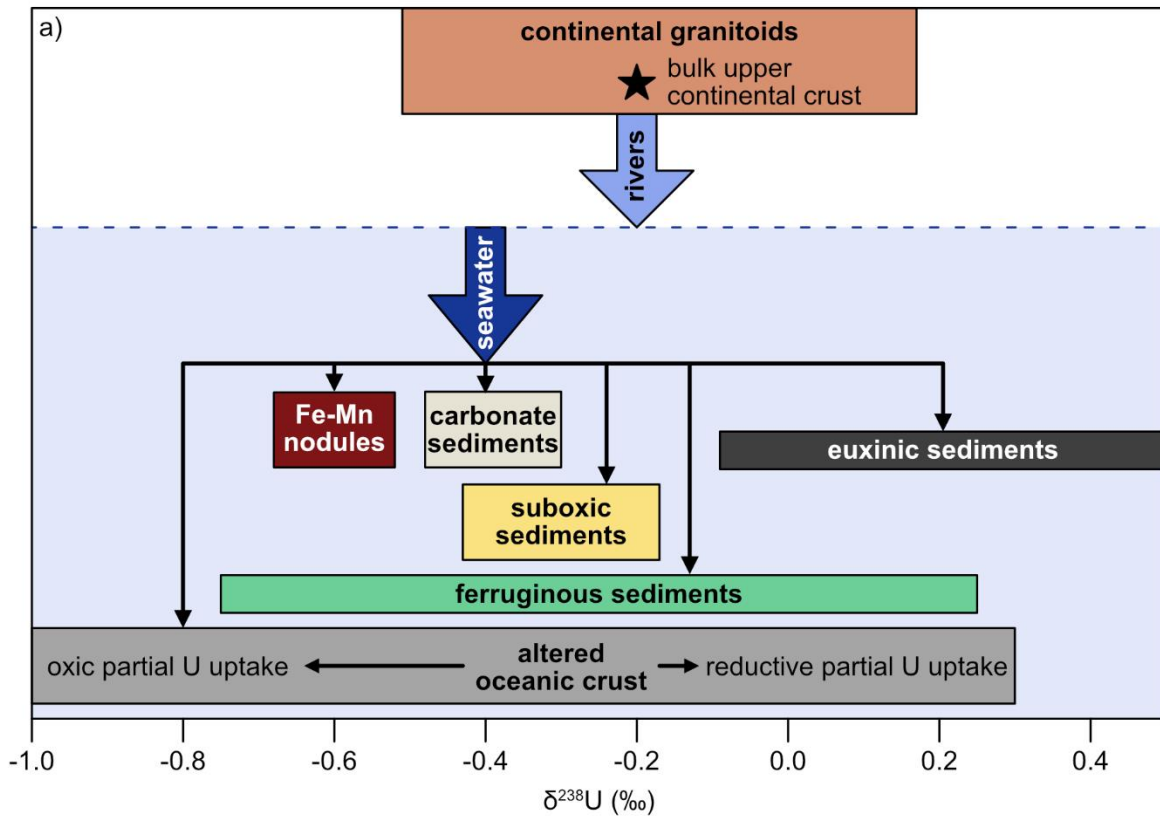
Figure 1.17: a) Modern U isotope compositions of the Earth's surface reservoirs, modified from figure 1 from Cole et al. (2020). Altered oceanic crust δ238U is from Andersen et al. (2024). Bulk upper continental crust δ238U (black star) is from Noordmann et al. (2016) and Tissot and Dauphas (2015). b) Schematic diagram (not to scale) of the modern terrestrial U isotope cycle, modified from figure 2c from Andersen et al. (2015). Arc lava δ238U values are from Andersen et al. (2015), Avanzinelli et al. (2018) and Freymuth et al. (2019), and serpentinite-derived fluid δ238U is from Freymuth et al. (2019). Ocean island basalt (OIB) δ238U values are from Andersen et al. (2015), Gaschnig et al. (2021a, 2021b) and Goldmann et al. (2015). Bulk altered oceanic crust (AOC) δ238U values are from Andersen et al. (2015, 2024) and Noordmann et al. (2016). Average mid-ocean ridge basalt (MORB) δ238U is from Andersen et al. (2015).

have identical $\delta^{238}U$ to the bulk Earth which suggests that the recycled altered oceanic crust in their source had unfractionated $\delta^{238}U$ and hence likely formed before the second major increase in surface oxygenation during the Neoproterozoic Oxygenation Event at ~0.8 – 0.55 Ga (e.g. Fike et al., 2006; Scott et al., 2008).

High-temperature fractionation of U isotopes during magmatic processes is more poorly constrained than it is for Ti isotopes. No significant U isotope fractionation is thought to occur during mantle partial melting because U is a highly incompatible element and partitions almost entirely into the melt phase (Andersen et al., 2017). Most unaltered igneous rocks have $\delta^{238}U$ values that are close to the bulk Earth composition (-0.306 ± 0.026‰; Andersen et al., 2015), and the present-day continental crust is also estimated to have indistinguishable $\delta^{238}U$ to the bulk Earth at ~-0.3‰ (Noordmann et al., 2016; Tissot and Dauphas, 2015). No correlation between $\delta^{238}U$ and indices of magma differentiation (e.g. SiO_2, MgO) has been observed in terrestrial igneous rocks (Gaschnig et al., 2021a; Noordmann et al., 2016; Sheng et al., 2025; Telus et al., 2012), implying that limited U isotope fractionation occurs during magmatic differentiation. However, Tissot et al. (2017) reported variation of $\delta^{238}U$ with REE concentrations in angrite meteorites which they proposed was caused by pyroxene accumulation. The U isotope compositions of some igneous and metamorphic mineral separates and single zircon crystals have also been measured, and were found to have significantly variable $\delta^{238}U$ (Hiess et al., 2012; Livermore et al., 2018; Tissot et al., 2019), suggesting that some high-temperature mineral-melt U isotope fractionation does occur on the Earth. U isotope variations in bulk igneous rocks are instead dominated by the involvement of recycled crustal materials with heterogeneous $\delta^{238}U$ in their formation. Arc lavas in particular display variable $\delta^{238}U$ due to addition of oxidised, serpentinite-derived fluids with low $\delta^{238}U$ (Andersen et al., 2015; Freymuth et al., 2019) or recycled sediments (Avanzinelli et al., 2018) to their mantle source. OIB from St. Helena and Samoa have low $\delta^{238}U$ which may reflect an ancient altered oceanic crust component in their sources (Gaschnig et al., 2021b). However, Telus et al. (2012) found that I-, S- and A-type granites from the Lachlan fold belt had indistinguishable U isotope compositions, despite them having very different sources. U isotopes may also trace magmatic-hydrothermal interactions, which are proposed to have generated low $\delta^{238}U$ in pegmatites from the Tibetan Plateau (Sheng et al., 2025). Figure 1.17b summarises the modern terrestrial U isotope cycle.

Overall, the U isotope compositions of igneous rocks mainly record the presence of recycled crustal materials with distinct δ^{238}U in their sources (e.g. Andersen et al., 2015; Gaschnig et al., 2021b). As the U isotope compositions of crustal materials are particularly sensitive to changes in redox processes (e.g. Chen et al., 2021; Rodney et al., 2024, Preprint) and terrestrial U cycling was significantly altered by the GOE (e.g. Cuney, 2010), U isotopes are well-suited to investigating whether sanukitoids record a change in the composition of crustal materials being recycled into the mantle across the GOE. While U is more mobile than Ti during weathering and alteration processes, and hence the U isotope compositions of Archean-Paleoproterozoic rocks are less robust, measuring δ^{234}U alongside δ^{238}U will help monitor for the effects of recent U mobility.

1.4. Thesis outline

The late Archean-early Proterozoic transition saw numerous significant changes occur on the Earth, many of which might be related to geodynamic changes at this time. Sanukitoid magmatism is a distinctive feature of this period and marks a major shift in continental crust composition, but many aspects of sanukitoid formation, such as the nature (melt vs fluid) and source of the recycled crustal component, are debated, which has led to multiple different interpretations of their link to geodynamics. Furthermore, there are aspects of sanukitoid magmatism, such as its proposed petrogenetic link to some TTGs and the potential temporal evolution of sanukitoid compositions, that have not been extensively investigated. The aim of this thesis is to use novel stable isotopes, specifically titanium and uranium isotopes, to gain new insights into the formation and evolution of sanukitoid magmas. This investigation aims to improve our understanding of sanukitoid magmatism and further constrain the nature of geodynamic changes that occurred during the late Archean-early Proterozoic transition.

The chapters of this thesis each focus on investigating different aspects of sanukitoid magmatism:
- In Chapter 3 I use Ti stable isotopes to determine whether the recycled crustal component involved in sanukitoid formation was a silicate melt or an aqueous

fluid, as well as to provide additional constraints on the differentiation and H_2O content/fO_2 of sanukitoid magmas. I achieve this by measuring the Ti isotope compositions of sanukitoids from multiple cratons with ages spanning across the late Archean-early Proterozoic transition, and by comparing these to Phanerozoic high Ba-Sr granites from Scotland that are proposed to be recent sanukitoid analogues. This is accompanied by modelling of the Ti isotope compositions of experimental melts to investigate the effect of different melting conditions on the magnitude of Ti isotope fractionation during metabasite partial melting. I find that sanukitoids show a muted $\delta^{49}Ti$ increase during differentiation due to removal of significant proportions of Ti in hornblende during fractional crystallisation, which fractionates Ti isotopes less than Fe-Ti oxides. Their Ti isotope systematics record early Fe-Ti oxide saturation, implying sanukitoid parental magmas were as water-rich and oxidised as modern arc magmas. Primitive (pre-oxide saturation) sanukitoids have significantly heavier $\delta^{49}Ti$ than the mantle and modern arc basalts, which requires the involvement of a metabasite partial melt. I favour formation of this metabasite melt by fluid-fluxed eclogite partial melting, supporting generation of the sanukitoid mantle source by a subduction-like process in the late Archean.

- In Chapter 4 I use Ti stable isotopes to investigate the proposed formation of high-Sr "high pressure" TTGs by amphibole-dominated fractional crystallisation of sanukitoids in the Neoarchean Eastern Goldfields Superterrane, Yilgarn Craton. I achieve this by measuring the Ti isotope compositions of high-Sr "high pressure" TTG samples and comparing these data with the Ti isotope compositions of the Yilgarn Craton sanukitoids they are proposed to have evolved from, which are presented in Chapter 3. I also analyse TTGs with different trace element compositions (i.e. low pressure, medium pressure and other high pressure TTGs) from the region to compare the Ti isotope compositions of TTGs that are proposed to have formed by different mechanisms. Additionally, I use published geochemical data for TTGs and sanukitoids to identify other occurrences of high-Sr "high pressure" TTGs and hence assess the potential global significance of this mechanism of forming "high pressure" TTGs across the late Archean-early Proterozoic transition. I find that the $\delta^{49}Ti$ values of high-Sr "high pressure" TTGs plot at the evolved end of

the Yilgarn sanukitoid differentiation trend and Rayleigh fractionation model, providing strong support for their generation by fractional crystallisation of sanukitoid magmas. The Ti isotope and trace element compositions of the other TTGs are best explained by partial melting of hydrous metabasite, sometimes followed by fractional crystallisation, demonstrating the diverse petrogenesis of TTGs in the Neoarchean Yilgarn Craton. High-Sr "high pressure" TTGs are temporally and spatially associated with sanukitoids on many Archean cratons, implying that formation of TTGs by fractional crystallisation of metasomatised mantle-derived sanukitoid magmas was likely a global phenomenon that emerged in the late Archean due to a geodynamic transition which promoted interaction between metabasite melts and mantle peridotite.

- In Chapter 5 I use U isotopes to investigate whether the composition of the recycled crustal component involved in sanukitoid formation changed across the GOE as a result of changing surface oxygenation. I achieve this by measuring the U isotope compositions of sanukitoids with ages spanning across the entire late Archean-early Proterozoic transition, as well as of the Phanerozoic high Ba-Sr granites from Scotland that are proposed to be recent sanukitoid analogues. I supplement these data by measuring the U isotope compositions of Archean TTGs to improve constraints on the U isotope composition of the main constituent of Archean continental crust. I show that $\delta^{238}U$ variations in TTGs and sanukitoids are primarily driven by apatite fractional crystallisation. Archean sanukitoid samples not affected by this process display distinct $\delta^{238}U$-Th/U systematics to modern arc magmas and hence show no evidence for addition of oxidised aqueous fluids or sediments to the sanukitoid mantle source. This result implies that sanukitoid parental magmas were likely oxidised via a different mechanism to modern arc magmas. Data for sanukitoid and granitoid samples not affected by apatite fractional crystallisation are too limited to confidently discern any secular evolution in their U isotope compositions.

Details of the analytical methodology used to measure Ti and U isotope compositions and descriptions of the samples analysed in this thesis are provided in Chapter 2.

2. Analytical methods and samples

This chapter first details the analytical methods used in this thesis. It then describes the rock samples that were analysed using these methods for the work presented in the following chapters.

2.1. Analytical methods

Multi-collector inductively coupled plasma mass spectrometry (MC-ICP-MS) is the principal analytical technique for measuring non-traditional stable isotope compositions and was used to measure titanium (Ti) and uranium (U) isotope compositions for this thesis. This section first gives an overview of how MC-ICP-MS works, and then describes the specific methods used to purify Ti and U from silicate rock samples and analyse their isotopic compositions via MC-ICP-MS.

2.1.1. Overview of multi-collector inductively coupled plasma mass spectrometry (MC-ICP-MS)

MC-ICP-MS is a relatively recent development in the field of mass spectrometry, with the first measurements from a MC-ICP-MS reported by Walder et al. (1993). It has proven particularly useful for measurement of "non-traditional" or "novel" stable isotope systems (e.g. Ti, Millet and Dauphas, 2014; Cu and Zn, Maréchal et al., 1999; Zr, Inglis et al., 2018) as the plasma source can efficiently ionize a wider range of elements than a thermal ionisation mass spectrometer (TIMS) (Albarède and Beard, 2004). The higher supply of ions from the plasma also makes measurements quicker for MC-ICP-MS than for TIMS. However, there is low transmission of ions from the plasma to the mass spectrometer, and this contributes to the significant instrumental mass bias (mass-dependent isotope fractionation that occurs in the instrument during measurement) associated with MC-ICP-MS (e.g. Albarède and Beard, 2004; Balaram et al., 2022). The plasma gas, most commonly argon (Ar), can also introduce isobaric interferences that need to be corrected for.

A MC-ICP-MS consists of several key parts – a sample introduction system, a plasma source, an interface and focussing lenses, an analyser, and multiple collectors. Figure 2.1 shows a schematic diagram of a MC-ICP-MS based on the Nu Plasma II used in this thesis. Typically, liquid samples are analysed and are introduced to the instrument using a nebuliser to form an aerosol. The inductively coupled plasma is generated in a torch using an electromagnetic coil to heat and partially ionise Ar gas. The sample aerosol passes through the centre of the torch, and the extreme temperatures of the plasma cause the sample to split into individual atoms (atomisation) which are then ionised via collisions with electrons from the plasma, forming predominantly singly-charged, positive ions. The ionised sample then proceeds through the mass spectrometer interface which consists of two cones – the sampler cone and the skimmer cone. The interface enables the mass spectrometer to be kept under vacuum while the samples are at atmospheric pressure, but a substantial fraction of the ions are lost during transfer across the interface. The ions are accelerated using a high voltage applied to the cones and are focussed using a series of lenses to create a beam of positive ions that passes into the analyser. The Nu Plasma II is double-focussing, meaning its analyser consists of two sectors. First is the electrostatic sector which only makes sure that only ions with specific kinetic energies enter the magnet. Next is the magnetic sector which uses a magnetic field to separate ions based on their mass/charge ratio. The separated beams then need to be directed into the collectors. Some MC-ICP-MS instruments achieve this by moving the collectors themselves to align with each ion beam, whereas the Nu Plasma II uses a zoom lens system to align the beams with fixed collectors. At the collectors the ions are counted by a combination of Faraday detectors and electron multipliers.

The resolution of a mass spectrometer describes its ability to distinguish adjacent peaks in a mass spectrum. The mass resolution of an MC-ICP-MS instrument is defined as the relative difference in mass between 5% and 95% peak height (ΔM) across the peak edge, while the resolving power is determined by dividing the mass being measured (M) by ΔM. The resolution of an MC-ICP-MS can be altered by passing the ion beam through a slit of changeable width (source defining slit). A narrower slit samples a smaller portion of the beam so that beam intensity is averaged over a narrower mass interval, giving sharper peak edges and hence higher resolution. The cost of measuring at higher resolution is that ions are lost when the beam is

clipped, resulting in lower sensitivity. Clipping also creates aberrations at the edges of the beam – on the Nu Plasma II alpha slits are used to correct for these. For this thesis, U isotope measurements were performed in low resolution mode (M/ΔM ≈ 500), while Ti isotope measurements were performed in medium resolution mode (M/ΔM ≈ 4000) to help resolve polyatomic interferences such as $^{30}Si^{16}O$ and $^{28}Si^{19}F$ (Millet and Dauphas, 2014).
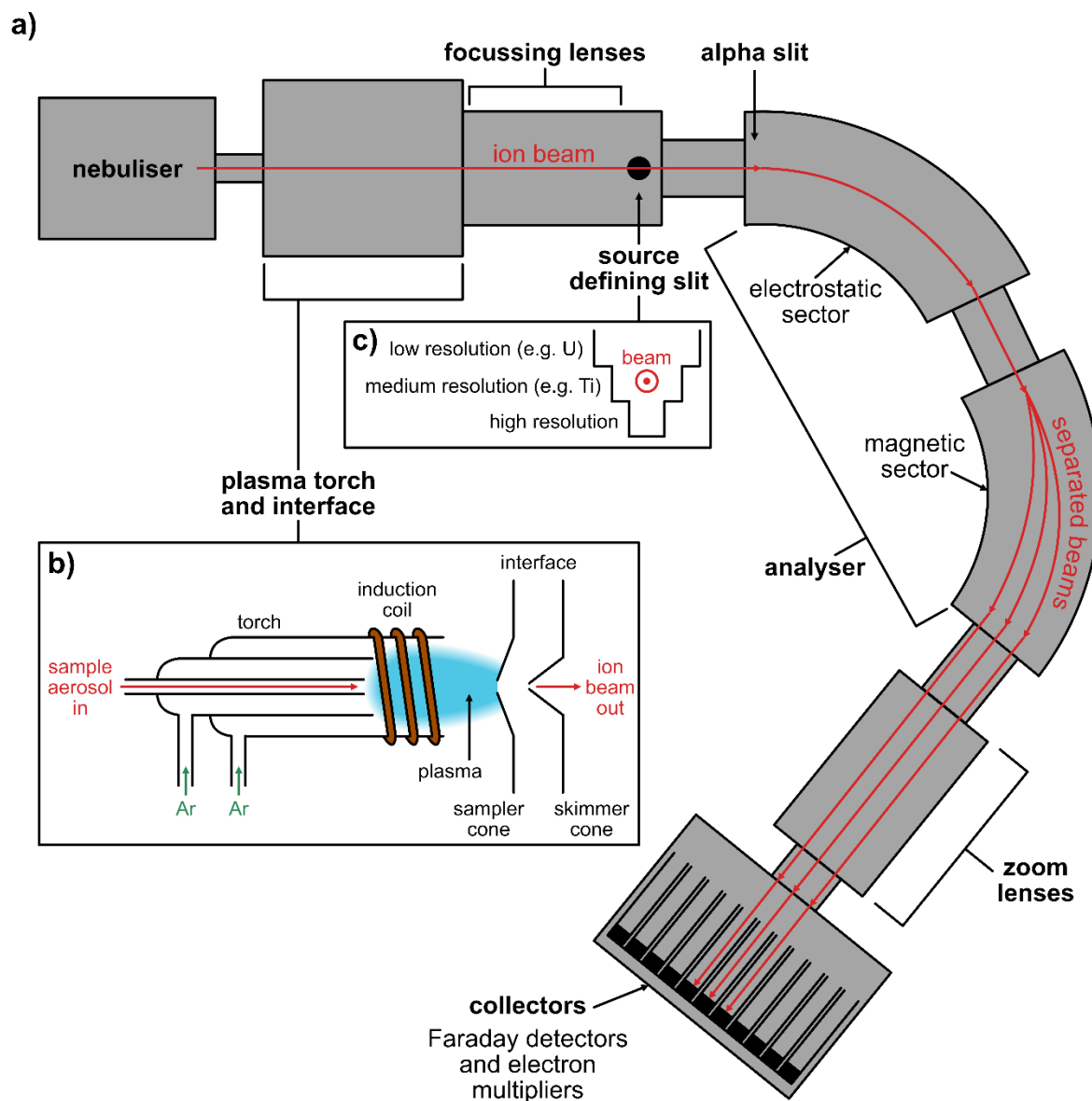
Figure 2.1: a) Schematic diagram of a MC-ICP-MS based on the Nu Plasma II. b) Schematic diagram of the plasma torch and interface of a MC-ICP-MS. c) Schematic diagram showing how the width of the entrance slit can be changed to alter the beam resolution.

Transmission of a sample through a MC-ICP-MS is non-quantitative, particularly through the instrument interface. This is thought to be the main cause of instrumental mass bias, and results in heavier ions being transmitted more efficiently through the mass spectrometer (e.g. Albarède and Beard, 2004; Balaram et al., 2022). High precision isotope analysis using MC-ICP-MS hence requires correction for this instrumental mass bias. Two common methods for doing this are standard-sample bracketing and double spiking. Standard-sample bracketing involves interpolating the mass bias for an unknown sample from the mass bias of preceding and succeeding runs of a standard of known composition. In contrast, the double spike method adds known artificial enrichments ("spikes") of two isotopes of the element being analysed to the sample in order to trace instrumental mass fractionation. Double spiking is used in both Ti and U isotope analysis and is described in detail in section 2.1.1.1.

High precision isotope analysis using MC-ICP-MS also requires purification of the desired element from a sample to remove interfering species. These interferences can be spectral (isobaric) or non-spectral (also called "matrix effects"). Section 2.1.2 describes how sample purification is achieved for Ti and U. However, corrections for other interferences may still be necessary. These include isobaric interferences introduced by the plasma gas (such as Ar-bearing compounds) or by the analyte solution. The specific corrections used for Ti and U isotope analysis are detailed in section 2.1.3.

2.1.1.1. The double spike method

Double spiking is a popular method for correcting for instrumental mass bias in mass spectrometry. This technique involves measuring the relative amounts of at least four isotopes of an element, two of which have been artificially enriched by adding isotopic "spikes" of known abundances to the sample. The composition of the double spike and the sample:spike ratio are typically optimised to produce data with small uncertainties (Rudge et al., 2009), although practical concerns, such as whether a particular isotope is affected by isobaric interferences or mass-independent fractionation (e.g. nucleosynthetic anomalies), must additionally be taken into account (e.g. Klaver and Coath, 2019). The use of triple spikes to correct for mass bias has also been proposed, but whether they provide smaller uncertainties than double spikes is debated (e.g.

Galer, 1999; Rudge et al., 2009). A big advantage of the double spike method is that if the sample and spike are mixed and equilibrated beforehand, it can also be used to correct for any mass-dependent fractionation that occurs during chemical purification. This alleviates the need for quantitative yields from sample purification.

The theoretical basis of the double spike method is that if the composition of the double spike is known, it is possible to invert the measured isotope ratios to the true, mass bias-corrected isotope ratios. From the four isotopes involved we can make three isotope ratios that all share a common denominator. For each isotope ratio (i) three equations can be written (equations 2.1, 2.2 and 2.3). Equations 2.1 and 2.2 are the discrimination or mass fractionation laws. They can take different forms, but for Ti and U isotopes it is assumed that instrumental mass fractionation follows the exponential mass fractionation law (e.g. Andersen et al., 2015; Millet and Dauphas, 2014). Equation 2.1 expresses the isotope ratio of the sample (N_i) in terms of mass-dependent fractionation by fractionation factor α from the isotopic composition of a reference standard (n_i). P_i is the natural logarithm of the ratio of the atomic masses of the isotopes.

$$N_i = n_i e^{-\alpha P_i} \quad (2.1)$$

Equation 2.2 describes the mass-dependent fractionation of the sample-spike mixture due to instrumental mass bias (m_i) away from its original isotopic composition (M_i) by fractionation factor β.

$$M_i = m_i e^{-\beta P_i} \quad (2.2)$$

Equation 2.3 is the mixing law, showing how the sample (N_i) and double spike (T_i) are combined to give the sample-spike mixture (M_i). λ is a parameter that describes the proportion of the double spike in the mixture.

$$M_i = \lambda T_i + (1 - \lambda)N_i \quad (2.3)$$

Equations 2.1, 2.2 and 2.3 can be combined into a single equation (equation 2.4):

$$F_i(\lambda, \alpha, \beta, n_i, m_i, T_i) = \lambda T_i + (1 - \lambda)n_i e^{-\alpha P_i} - m_i e^{-\beta P_i} = 0 \quad (2.4)$$

Equation 2.4 can be written for each isotope ratio, giving three non-linear simultaneous equations. The values of n_i and T_i are known, while m_i is the measured sample-spike mixture composition, leaving only three unknowns − λ, α and β. Double spike deconvolution involves solving these three simultaneous equations via iterative

methods to determine the values of the three unknowns, and then using equation 2.1 to calculate the true, mass bias-corrected isotope composition of the sample.

The above method is used to correct Ti stable isotope measurements for instrumental mass bias. Titanium has five stable isotopes (^{46}Ti, ^{47}Ti, ^{48}Ti, ^{49}Ti, ^{50}Ti), but ^{50}Ti is affected by mass-independent nucleosynthetic anomalies so it is not well-suited to use for double spike deconvolution. ^{46}Ti also shows mass-independent fractionation in meteorites, but these variations are small in comparison to ^{50}Ti and no ^{46}Ti anomalies are seen among terrestrial samples, making ^{46}Ti suitable to use for double spike deconvolution. Taking into account the unsuitability of ^{50}Ti, Millet and Dauphas (2014) used Monte Carlo simulations in ^{46}Ti-^{47}Ti-^{48}Ti-^{49}Ti space to determine that the optimum Ti double spike is a 1:1 mixture of ^{47}Ti and ^{49}Ti, while the optimum sample:spike ratio is 52:48.

Double spike deconvolution for U isotopes presents a special case. The double spike IRMM-3636 containing 50% ^{233}U and 50% ^{236}U is used (Richter et al., 2008). There is virtually no ^{233}U or ^{236}U present in natural samples, meaning that the measured ^{236}U/^{233}U of the sample-spike mixture is equivalent to the ^{236}U/^{233}U of the spike after undergoing mass-dependent fractionation in the MC-ICP-MS. As we know the original double spike composition, we can directly solve the exponential mass fractionation law to find β (equation 2.5), the fractionation factor associated with instrumental mass bias, and then use β to calculate the true, mass bias-corrected isotope ratios of the sample (equation 2.6).

$$\beta = \ln\left(\frac{\left(\frac{^{236}U}{^{233}U}\right)_{measured}}{\left(\frac{^{236}U}{^{233}U}\right)_{double\ spike}}\right) \Big/ \ln\left(\frac{236.045566}{233.039632}\right) \quad (2.5)$$

$$\left(\frac{^{238}U}{^{235}U}\right)_{\substack{mass\ bias \\ corrected}} = \left(\frac{^{238}U}{^{235}U}\right)_{measured} e^{-\beta \ln\left(\frac{238.050708}{235.0493242}\right)} \quad (2.6)$$

The amount of IRMM-3636 double spike added to each sample aims to achieve a ^{238}U/^{236}U ratio of ~30 as this results in ^{233}U and ^{236}U concentrations intermediate between those of ^{238}U and ^{235}U. IRMM-3636 also contains minute amounts of ^{234}U, ^{235}U and ^{238}U which need to be corrected for when processing data.

2.1.2. Sample preparation and purification

Before MC-ICP-MS analysis, whole rock samples must be digested in strong acids and then purified to isolate the element of interest from the sample matrix. This is usually achieved via ion exchange chromatography, as is the case for Ti and U.

2.1.2.1. Titanium purification

50 – 70 mg of finely powdered silicate rock samples were digested in a mixture of 1 ml concentrated HNO_3 and 1 ml concentrated HF at 120°C for at least 72 hours. Then an additional 2 ml of concentrated HNO_3 was added before the samples were dried down at 100°C. Each sample was taken up in 500 µl concentrated HNO_3 and immediately dried down at 120°C three times, before being dissolved in 5 ml 6M HCl. 400 µl of saturated boric acid solution was then added to dissolve any fluorides, as their formation can remove Ti from the sample solution and cause Ti isotope fractionation. The samples were refluxed overnight at 120°C, before an aliquot containing 5 µg Ti was taken from each sample solution. 21.8 µl of the ^{47}Ti-^{49}Ti double spike was added to each sample aliquot to achieve the optimum sample:spike ratio of 52:48 (Millet and Dauphas, 2014). The sample-spike mixtures were dried down, then taken up in 300 µl concentrated HNO_3 and immediately dried down twice to help equilibrate the spike and sample.

Separation of Ti from the sample matrix was achieved by cation exchange chromatography using 2 ml Eichrom DGA resin cartridges, following the established method of Zhang et al. (2011) and Millet and Dauphas (2014). A vacuum box was used to help regulate the flow of reagents through the resin cartridges. Most samples (all those presented in Chapter 3) were purified via two identical passes of the sample through the resin following the procedure in table 2.1. Some studies have performed an alternative second stage of purification using AG1-X8 resin. The main purpose of this stage is to ensure removal of molybdenum (Mo) from the Ti fraction for Mo-rich samples, as double-charged Mo is an isobaric interference on Ti during mass spectrometry (Millet and Dauphas, 2014; Zhang et al., 2011). This stage was not required for the samples in this thesis as they have low Mo/Ti of generally < 0.01. Following purification, the samples were dried down, then refluxed in a mixture of 150

µl concentrated HNO_3 and 150 µl 30% H_2O_2 at 120°C for at least a few hours to remove any organic material, before being dried down again.

Table 2.1: Procedure for a single pass of a sample through 2 ml Eichrom DGA resin cartridges to purify Ti for MC-ICP-MS analysis (Millet and Dauphas, 2014; Zhang et al., 2011). This procedure is done twice to achieve a double pass of the samples through the resin cartridges.

Step	Reagent	Volume (ml)
Cleaning	MQ water	20
Cleaning	3M HNO_3	10
Conditioning	12M HNO_3	10
Sample loading	12M HNO_3	5
Matrix elution	12M HNO_3	20
Ti elution	12M HNO_3 + 1 wt% H_2O_2	10
Cleaning	3M HNO_3	10
Cleaning	MQ water	20

Table 2.2: Revised procedure for a single pass of a sample through 2 ml Eichrom DGA resin cartridges to purify Ti for MC-ICP-MS analysis. Sufficient purification of Ti is achieved after a single pass of the sample through the resin.

Step	Reagent	Volume (ml)
Wetting agent	20% ethanol (left to soak the resin for ~1 hour)	3
Cleaning	MQ water	20
Cleaning	3M HNO_3	10
Conditioning	12M HNO_3	10
Sample loading	12M HNO_3	5
Matrix elution	12M HNO_3	15
Ti elution	12M HNO_3 + 1 wt% H_2O_2	10
Cleaning	3M HNO_3	10
Cleaning	MQ water	20
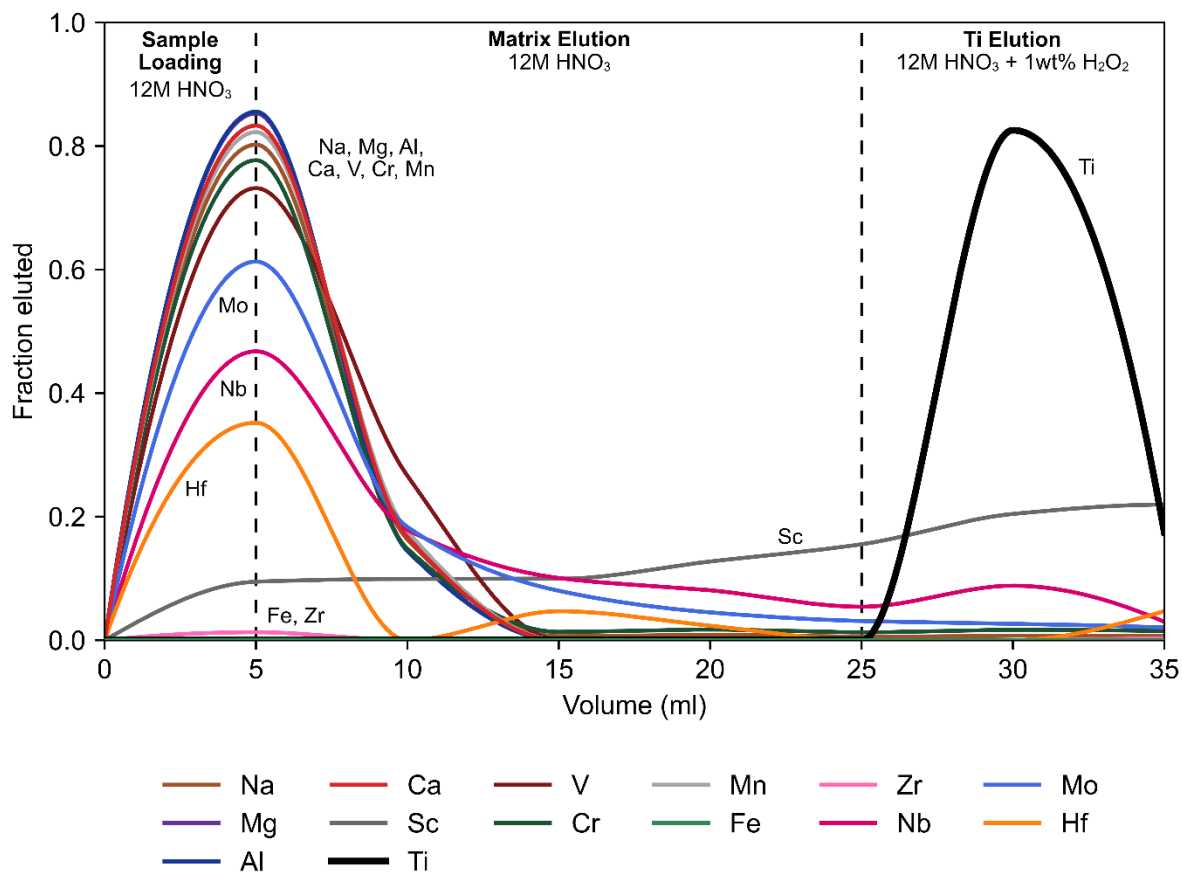
Figure 2.2: Elution curve for geological reference material JB-2 from a 2ml Eichrom DGA resin cartridge.

Over the duration of my PhD, it was observed that Ti yields following purification were decreasing. For a while this remained satisfactory, as the samples were spiked prior to purification so double spike deconvolution could correct for any mass-dependent fractionation that occurred due to Ti loss during purification. However, yields continued to decrease until almost no Ti was being collected after cation exchange chromatography. Following communication with TrisKem, the manufacturer of the resin cartridges, it was suggested that 20% ethanol was used as a wetting agent before the chromatography in order to improve wetting of the DGA resin. I recalibrated the Ti cation exchange chromatography with new DGA resin cartridges, now soaking the resin in 20% ethanol for approximately 1 hour before starting to clean the columns. The recalibration shows that this method achieves separation of Ti from key matrix elements (e.g. Ca, V, Cr, Mo) in a single pass of the sample through the DGA resin, and with elution of the matrix in 15 ml 12M HNO_3 rather than 20 ml (fig. 2.2). The

procedure for this revised method is presented in table 2.2 and was used for the samples in Chapter 4. Ti yields of ~85 – 95% were obtained for these samples.

2.1.2.2. Uranium purification

30 – 205 mg of finely powdered silicate rock samples, weighed to contain ~150 ng of U, were digested in a mixture of 1 ml concentrated HNO_3 and 2 ml concentrated HF at 120°C for at least 72 hours. The IRMM-3636 ^{233}U-^{236}U double spike was added to each sample before dissolution, aiming for a $^{238}U/^{236}U$ ratio of ~30. The samples were dried down at 100°C, then taken up in 5 ml 6M HCl and refluxed at 120°C for ~24 hours before being dried down again. Next, each sample was taken up in 500 µl concentrated HNO_3 and immediately dried down twice.

Table 2.3: Procedure for a single pass of a sample through 1 ml TRU resin in a Bio-Rad column to purify U for MC-ICP-MS analysis.

Step	Reagent	Volume (ml)
Cleaning	0.1N HCl + 0.3N HF	10
Cleaning	MQ water	5
Conditioning	1.5N HNO_3	10
Sample loading	1.5N HNO_3	10
Matrix elution	1.5N HNO_3	20
U elution	0.1N HCl + 0.3N HF	10

Separation of U from the sample matrix was done by two-stage ion exchange chromatography. When U concentrations are high enough, and hence U:matrix ratios are low enough, this can be achieved via two identical passes through ~0.6 ml of UTEVA resin (100 – 150 µm particle size) loaded in self-shrink Teflon columns (e.g. Tissot and Dauphas, 2015; Weyer et al., 2008). The alternative, which is a necessity for samples with high matrix volumes, is to first pass the sample through 1 ml of TRU resin loaded in a 10 ml Bio-Rad column, and then do a single pass through UTEVA resin for the second stage (Andersen et al., 2015). The procedures for the TRU resin and UTEVA resin chromatography stages are presented in tables 2.3 and 2.4 respectively. Following purification, the samples were dried down, then refluxed in a

mixture of 500 µl concentrated HNO₃ and 500 µl 30% H₂O₂ at 120°C for at least a few hours to remove any organic material, before being dried down again.

Table 2.4: Procedure for a single pass of a sample through ~0.6 ml UTEVA resin in a self-shrink Teflon column to purify U for MC-ICP-MS analysis.

Step	Reagent	Volume (ml)
Cleaning	0.1N HCl + 0.3N HF	8
Cleaning	MQ water	2
Conditioning	3N HNO₃	5
Sample loading	3N HNO₃	5
Matrix elution	3N HNO₃	15
Matrix elution (Th)	3N HCl	9
U elution	0.1N HCl + 0.3N HF	10

2.1.3. Isotopic analysis using MC-ICP-MS

Ti and U isotope compositions were measured using the Nu Plasma II MC-ICP-MS at the Cardiff Earth Laboratory for Trace Element and Isotope Chemistry (CELTIC), Cardiff University. Samples were introduced to the mass spectrometer through an Aridus II desolvating nebuliser used with Ar gas.

2.1.3.1. Titanium stable isotope analysis

Samples were taken up in 2% HNO₃ + trace HF (2.5 ml concentrated HF per litre of 2% HNO₃) for analysis and introduced to the MC-ICP-MS at concentrations of 1 – 1.3 ppm. Measurements were performed in medium resolution mode, and each sample analysis consisted of one block of 50 measurements each with an integration time of 10 seconds. The cup configuration used is given in table 2.5, and Ca interference on ^{46}Ti and ^{48}Ti was monitored at mass 44. Ti isotope compositions are given in delta notation relative to the Origins Laboratory Titanium standard (OL-Ti) (equation 2.7).

$$\delta^{49}Ti = 10^3 \left(\frac{\left(\frac{^{49}Ti}{^{47}Ti}\right)_{sample}}{\left(\frac{^{49}Ti}{^{47}Ti}\right)_{OL-Ti}} - 1 \right) \quad (2.7)$$

To account for small polyatomic interferences than cannot be resolved, such as $^{28}Si^{19}F$ on ^{47}Ti (Si comes from the mass spectrometer torch, while F is from the sample solution), all sample measurements were bracketed by measurements of double-spiked OL-Ti standard.

Table 2.5: Cup configuration used on the Nu Plasma II at Cardiff University for measurement of Ti stable isotope compositions.

Collector	H10	H9	H7	H4	L2
Mass	49	48	47	46	44
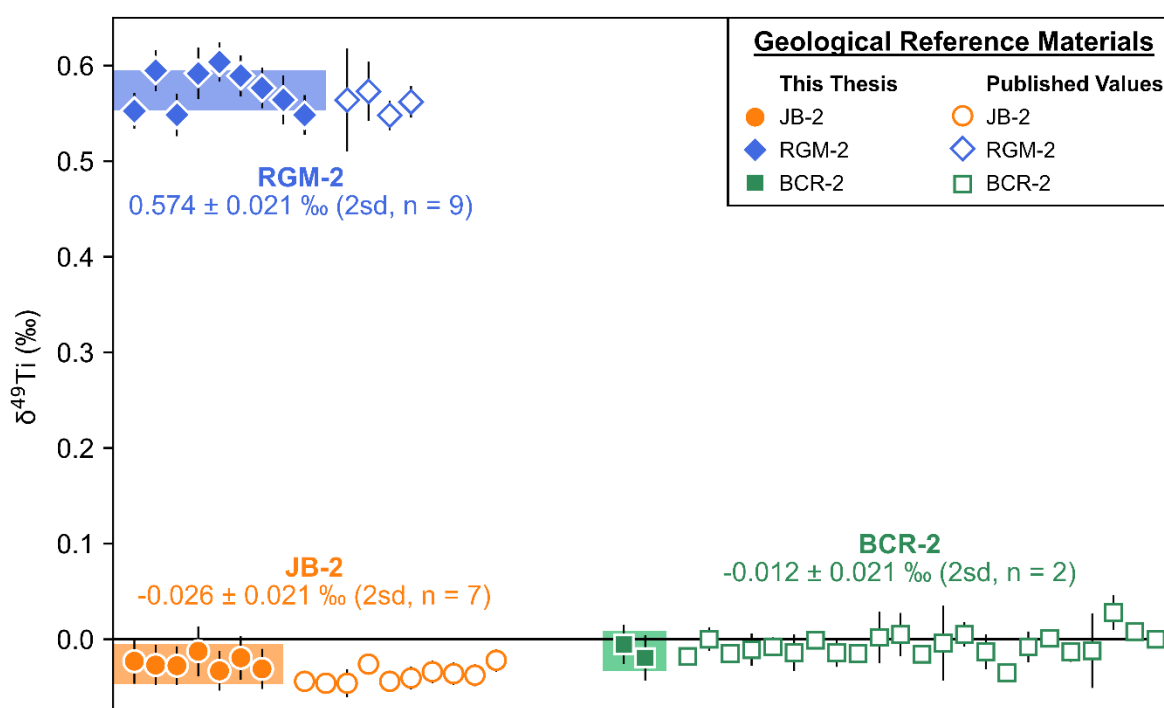
Figure 2.3: Measured δ^{49}Ti (‰) of geological reference materials JB-2, RGM-2 and BCR-2. Filled symbols are measurements made over the duration of this thesis and the errors are the 95% confidence intervals. The weighted mean values of these measurements are given, and the shaded boxes show the 2sd of this weighted mean. Open symbols are values published in the literature (Anguelova et al., 2024; Deng et al., 2018a, 2018b, 2019b, 2020, 2023; Greber et al., 2021; He et al., 2020, 2022; Hoare et al., 2020, 2022, 2023; Klaver et al., 2021, 2024; Kommescher et al., 2020; Li et al., 2022; Mandl, 2019; Millet & Dauphas, 2014; Millet et al., 2016; Saji et al., 2023; Storck et al., 2023; Williams, 2015; Williams et al., 2021; Zhao et al., 2020) and the errors are given as 2se.

Data reduction was performed offline using the algebraic method of Millet and Dauphas (2014), via code written in Python using the NumPy, SciPy and OpenPyXl libraries (Hoare, 2021). First, isobaric Ca interferences on ^{46}Ti and ^{48}Ti were corrected

for. Then outliers were removed using a 2σ filter, and the mean of the filtered data was calculated. Double spike deconvolution was done on the mean isotope ratios using Newton Raphson iteration, and Monte-Carlo simulations were used to estimate the internal error as a 95% confidence interval. Finally, the standard-bracketed $\delta^{49}Ti$ values were calculated.

Repeated measurements of geological reference materials (JB-2, RGM-2, BCR-2) made over the duration of this PhD are in good agreement with previously published values (fig. 2.3, Appendix A). The total procedural blank was ~1 ng Ti which is negligible in comparison to the ~10 µg Ti processed for each sample-spike mixture. To assess the long-term reproducibility of the Ti isotope measurements, a compilation of individual measurements of the OL-Ti standard made during this PhD is presented in figure 2.4. These data give a mean $\delta^{49}Ti$ of -0.002 ± 0.024‰ (2sd, n = 76).
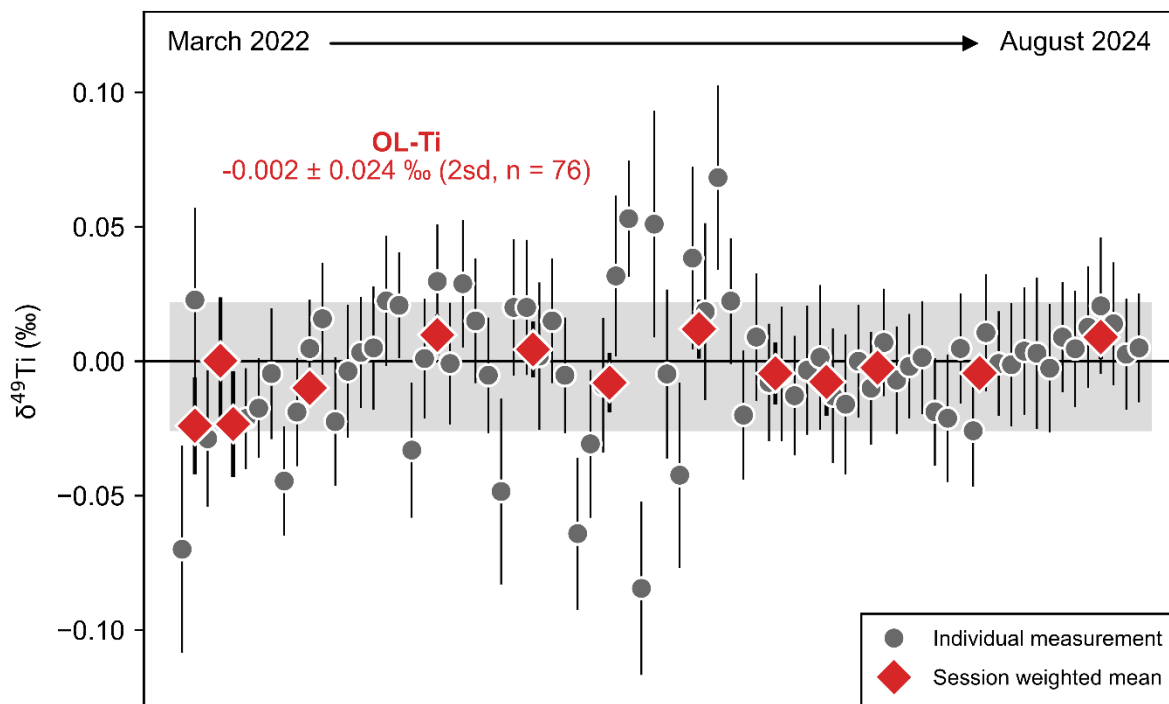
Figure 2.4: Compilation of $\delta^{49}Ti$ (‰) measurements of OL-Ti made over the duration of this PhD. Errors on the individual measurements are the 95% confidence intervals, while errors on the session weighted means are 2se. The weighted mean of all the OL-Ti measurements is -0.002 ± 0.024 ‰ (2sd, n = 76), and the shaded box shows the 2sd of this weighted mean.

2.1.3.2. Uranium isotope analysis

Samples were taken up in 2% HNO_3 for analysis and introduced to the MC-ICP-MS at concentrations of 50 – 100 ppb. Measurements were performed in low resolution mode. On-peak zeroes were measured for 60 seconds prior to each sample, while each sample analysis consisted of one block of 60 measurements each with an integration time of 5 seconds. The cup configuration used is given in table 2.6. Mass 238 was monitored on H6 as this cup is fitted with a 10^{10} Ω resistor. This means it can accommodate a larger ion beam than the other cups (which are fitted with 10^{11} Ω resistors), which is necessary because of the high abundance of ^{238}U (> 99% of natural U) compared to the other isotopes. Thorium (Th) was monitored on mass 232. U isotope compositions are given in delta notation relative to the CRM145 standard (equations 2.8 and 2.9). Every two samples were bracketed by measurements of double-spiked CRM145 standard.

$$\delta^{238}U = 10^3 \left(\frac{\left(\frac{^{238}U}{^{235}U}\right)_{sample}}{\left(\frac{^{238}U}{^{235}U}\right)_{CRM145}} - 1 \right) \quad (2.8)$$

$$\delta^{234}U = 10^3 \left(\frac{\left(\frac{^{234}U}{^{238}U}\right)_{sample}}{\left(\frac{^{234}U}{^{238}U}\right)_{CRM145}} - 1 \right) + \delta^{234}U_{CRM145} \quad (2.9)$$

Table 2.6: Cup configuration used on the Nu Plasma II at Cardiff University for measurement of U isotope compositions.

Collector	H6	H4	H3	H2	H1	Ax
Resistor (Ω)	10^{10}	10^{11}	10^{11}	10^{11}	10^{11}	10^{11}
Mass	238	236	235	234	233	232

Data reduction was performed offline in a Microsoft Excel spreadsheet. First the data were zero-corrected by subtracting the on-peak zero from the sample measurements. Next the data were corrected for tail effects. Collisions in the flight tube create a tail of low energy molecules that overlap with lower masses (e.g. Andersen et al., 2004). ^{238}U and ^{236}U are the main sources of the tails, so ^{236}U needs to be corrected for interference from the ^{238}U tail while all lower masses are corrected for interference

from both the ^{238}U and ^{236}U tails. Tail correction was done using the method of Hiess et al. (2012), which estimates the tail contribution at a given mass using an exponential decay function. The data were then corrected for hydride (MH$^+$) formation during measurement. Isobaric interferences from ^{232}ThH$^+$ on ^{233}U and from ^{233}UH$^+$ on ^{234}U need to be corrected for, while the contributions of ^{234}UH$^+$ and ^{235}UH$^+$ are insignificant in comparison to the ^{235}U and ^{236}U beams respectively. The rate of hydride production (UH$^+$/U) has previously been measured to be ~5 x 10^{-6} and is assumed to be stable across all measurements. Following this, the isotope ratios for each cycle were calculated from the corrected values and were used in the double spike deconvolution to correct for mass bias as described in section 2.1.1.1. Minute contributions to ^{234}U, ^{235}U and ^{238}U from the IRMM-3636 double spike were then subtracted from the mass bias-corrected ratios. Outliers were removed using a 1σ filter, and the mean isotope ratio was calculated from the filtered data. Finally, standard-bracketed δ^{238}U and δ^{234}U values were calculated using weighted contributions of the bracketing measurements of double-spiked CRM145. Uncertainties on δ^{238}U and δ^{234}U were estimated from the external reproducibility (2se) of repeated measurements of the CZ reference material from the same session(s) as the sample measurements.

Repeated measurements of the δ^{238}U of geological reference materials (BCR-2, HU-1, CZ-1) made over the duration of this PhD are in excellent agreement with previously published values (fig. 2.5a, Appendix A). Measured δ^{234}U of BCR-2 and CZ-1 are also in good agreement with published values (fig. 2.5b, Appendix A). The δ^{234}U of HU-1 is higher than published values (fig. 2.5b), although the δ^{234}U of HU-1 has only been reported twice previously (Cheng et al., 2013; Hiess et al., 2012) and hence is poorly constrained. Total procedural blanks were ≤ 75 pg U which is negligible in comparison to the ~150 ng U processed for each sample. The repeated measurements of the CZ-1 secondary standard are used to assess the long-term reproducibility of the U isotope measurements, and these data give a mean δ^{238}U of -0.05 ± 0.04‰ and a mean δ^{234}U of 2 ± 1‰ (2sd, n = 16) (fig. 2.5).
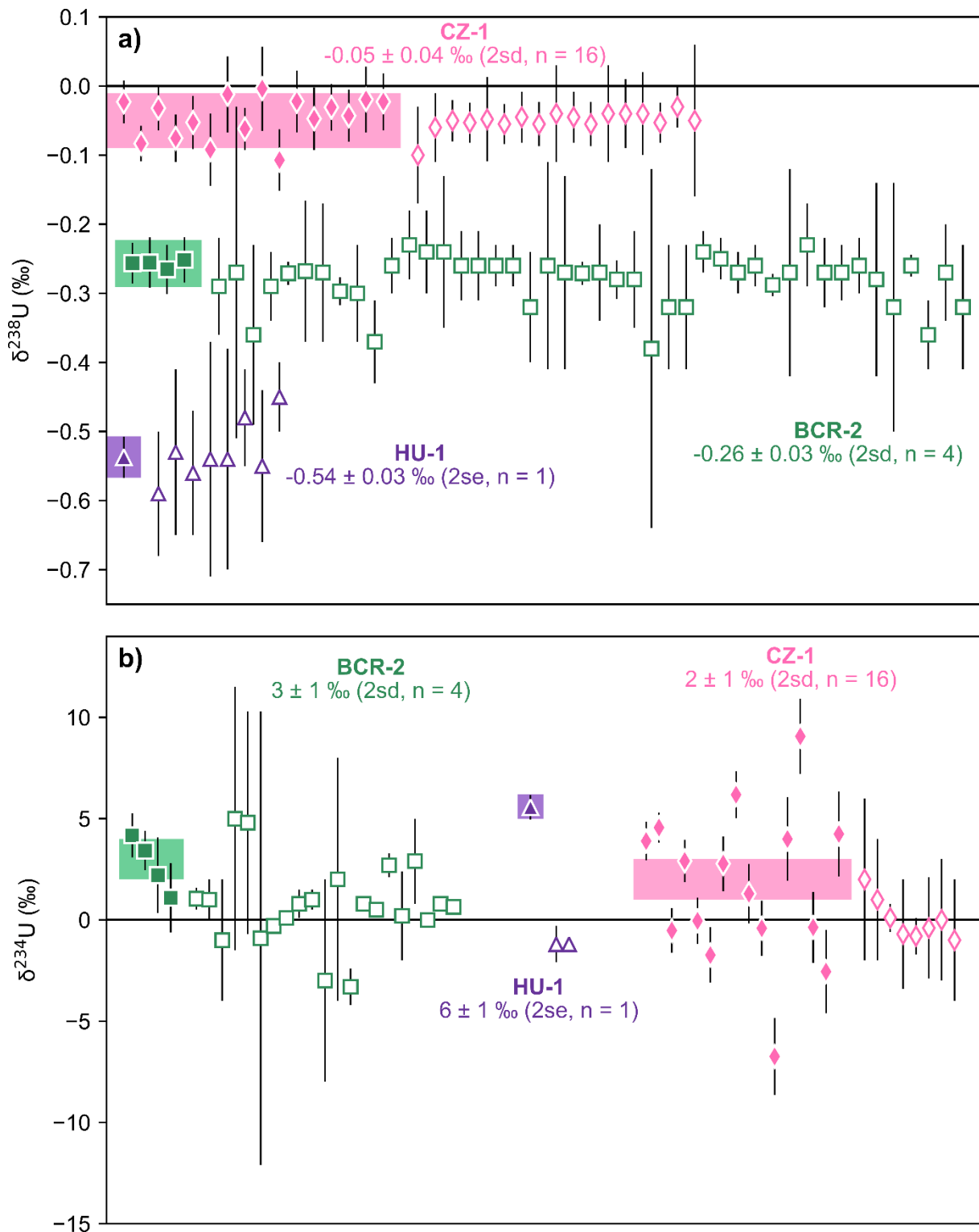
Figure 2.5: a) Measured δ²³⁸U (‰) and b) measured δ²³⁴U (‰) of geological reference materials BCR-2, HU-1 and CZ-1. Filled symbols are measurements made over the duration of this thesis and the errors are 2se. The weighted mean values of these measurements are given, and the shaded boxes show the 2sd of this weighted mean (2se for HU-1). Open symbols are values published in the literature (Andersen et al., 2014, 2015, 2016, 2018, 2020, 2024; Avanzinelli et al., 2018; Brennecka et al., 2015, 2018; Brennecka & Wadhwa, 2012; Bura-Nakić et al., 2018; Casalini, 2018; Cheng et al., 2013; Clarkson et al., 2021; Condon et al., 2010; Dahl et al., 2014, 2017; Dang et al., 2018a, 2018b, 2022; Freymuth et al., 2019; Goldmann et al., 2015; He et al., 2021; Hiess et al., 2012; Hinojosa et al., 2016; Holmden et al., 2015; Iizuka et al., 2014; Keatley et al., 2021; Kipp et al., 2022; Lau et al., 2016, 2017, 2022; Lefebvre et al., 2019, 2021; Murphy et al., 2014; Stirling et al., 2005, 2007; Tissot et al., 2016, 2018, 2019; Tissot & Dauphas, 2015; X. Wang et al., 2018; Weyer et al., 2008).

2.2. Sample descriptions

Whole rock samples of Archean-Paleoproterozoic sanukitoids, Paleozoic sanukitoid analogues and Archean TTGs were analysed using the techniques described in section 2.1. Both the Ti and U isotope compositions of many of these samples were measured, hence their data are presented across multiple chapters of this thesis. To avoid repetition, this section provides detailed descriptions and geological context for all the samples analysed for this thesis. The major and trace element compositions of all samples have been previously published and their references are compiled in Appendix C. Where available, references for radiogenic and stable isotope compositions of the samples are also compiled in Appendix C.
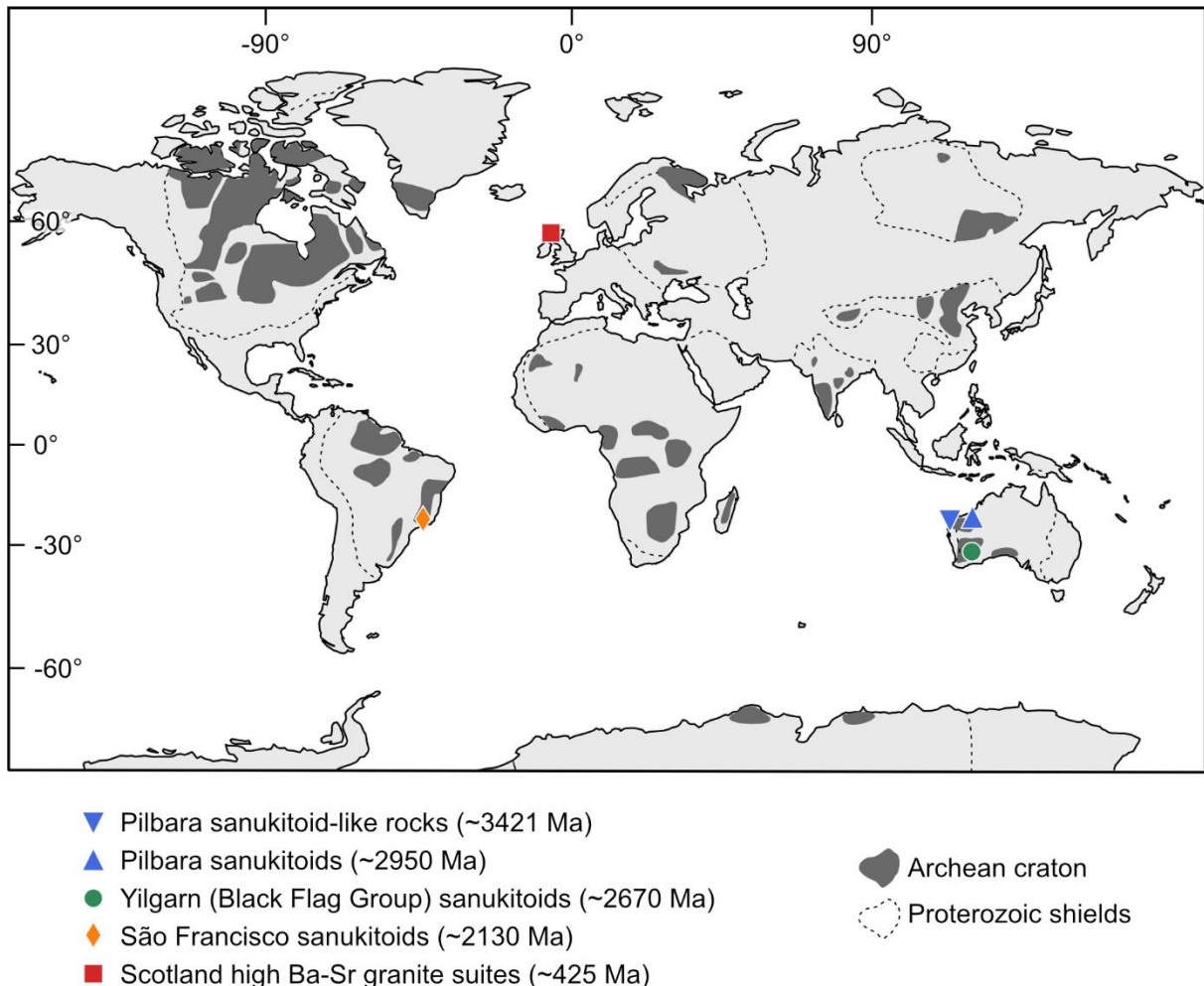
Figure 2.6: Location of Archean and Paleoproterozoic sanukitoid suites and Paleozoic high Ba-Sr granite suites analysed in this thesis. Simplified distribution of Archean cratons and Proterozoic shields is after Bleeker (2003) and Groves and Santosh (2021).

2.2.1. Sanukitoids and analogues

The sanukitoid samples come from Archean-Paleoproterozoic sanukitoid suites that were selected to cover a range of ages spanning across the late Archean-early Proterozoic transition, as well as different locations globally (fig. 2.6). These sanukitoid suites can all be described as "low-Ti sanukitoids" because they have $MgO/TiO_2 > 3.5$ (Martin et al., 2009). The Black Flag Group (BFG) from the Yilgarn Craton in particular was selected because it continuously covers a wide SiO_2 range (44 – 73 wt%), including primitive sanukitoids and calc-alkaline lamprophyres as well as the more felsic rocks that evolved from them (Smithies et al., 2022, 2019, 2018). Furthermore, the BFG was targeted because it is proposed to be petrogenetically linked to high-Sr "high pressure" TTGs, representing the liquid line of descent connecting the TTGs to mantle-derived parental magmas (Smithies et al., 2019). In addition to the Archean-Paleoproterozoic sanukitoids, I analysed samples of Paleozoic high Ba-Sr granite suites from the Caledonian Orogeny in Scotland which are proposed to be Phanerozoic sanukitoid analogues (Fowler and Rollinson, 2012).

2.2.1.1. Pilbara Craton

The Pilbara Craton (fig. 2.7a), Western Australia, is one of the best-preserved blocks of Archean continental crust. Its eastern half, called the East Pilbara Terrane, is dominated by Paleoarchean granitoid domes and greenstone keels that are typically interpreted to have formed by vertical geodynamic processes (e.g. Smithies et al., 2009; Van Kranendonk et al., 2004; Wiemer et al., 2018). West of this terrane is the Central Pilbara Tectonic Zone (CPTZ) which formed by rifting at ~3.2 Ga (e.g. Van Kranendonk et al., 2010) and separates the East Pilbara Terrane from the West Pilbara Superterrane.

The sanukitoid samples from the Pilbara Craton are approximately 2950 Ma and belong to the high-Mg diorite suite of Smithies and Champion (2000). They were intruded as small stocks (most covering < 20 km^2 in area) into turbidites in the Mallina Basin, CPTZ (fig. 2.7b), and their emplacement may have been controlled by pre-existing basin structures (Smithies and Champion, 2000). The high-Mg diorite suite displays the key geochemical characteristics of Archean sanukitoids, including high Mg# (42 – 61), high concentrations of compatible trace elements such as Cr (20 – 210
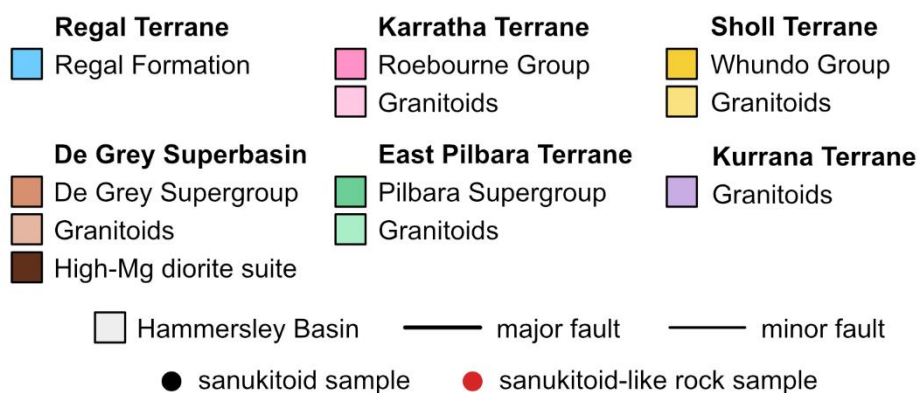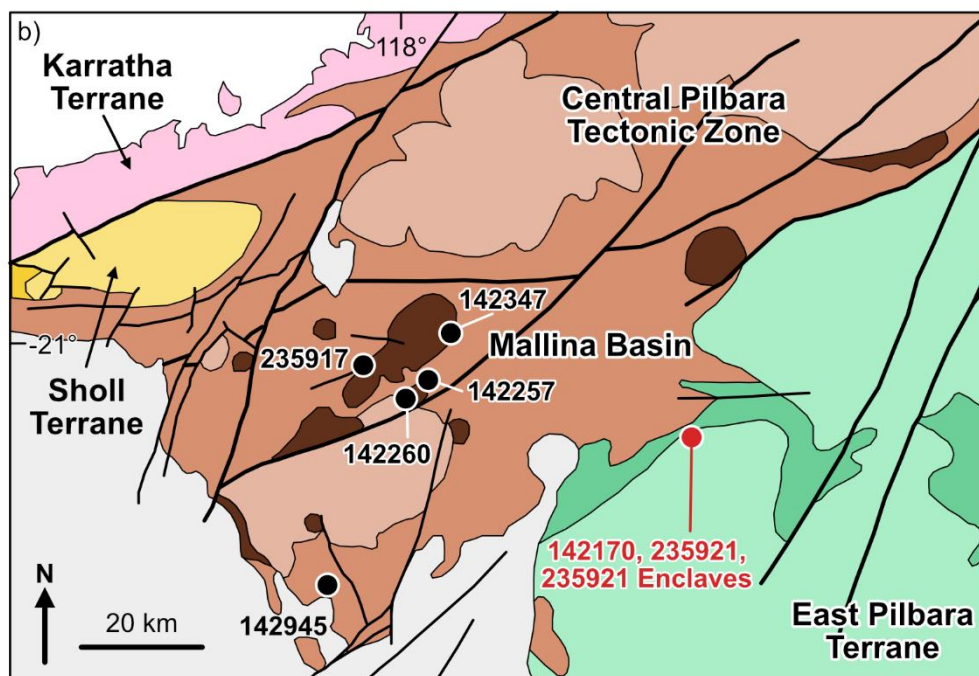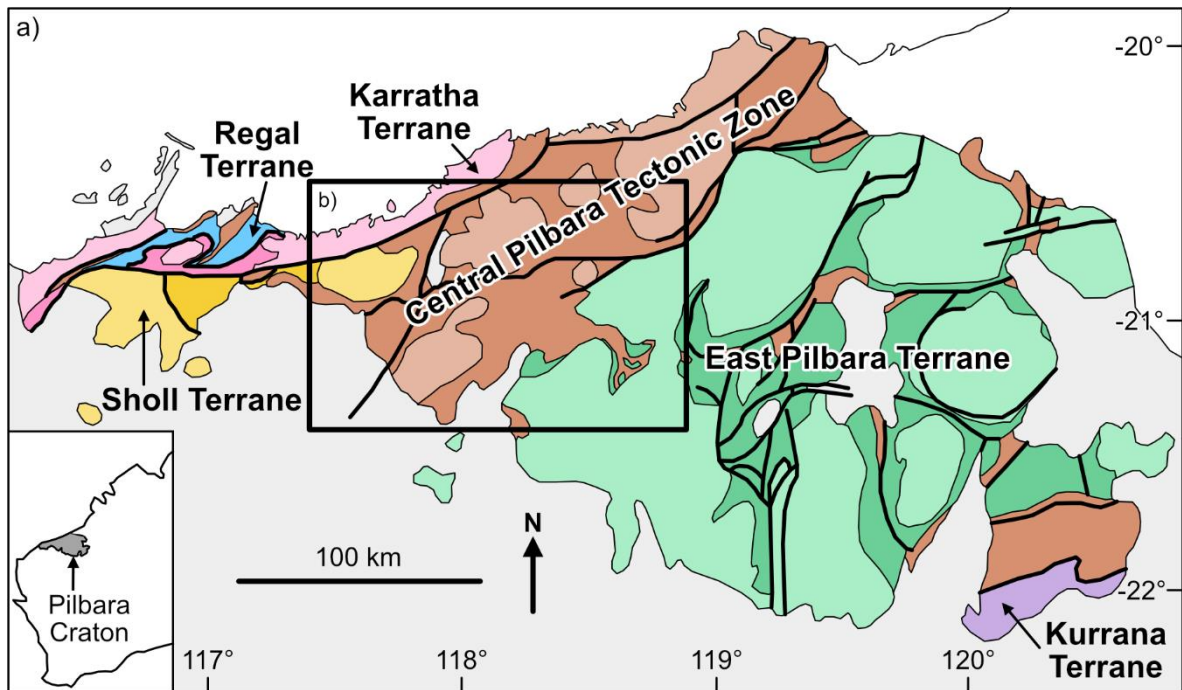
Figure 2.7: a) Simplified geological map of the Pilbara Craton, showing the terranes and major faults. After figure 1 from Van Kranendonk (2010). b) Simplified geological map of the Mallina Basin, showing the locations of sanukitoid (high-Mg diorite suite) and sanukitoid-like rock samples analysed in this thesis. Modified from figure 1 from Smithies and Champion (2000).

ppm) and Ni (15 – 100 ppm), and enrichment in Ba (450 – 1600 ppm) and Sr (300 – 950 ppm). It has strongly fractionated CI chondrite-normalised rare earth element (REE) patterns, with increasing La/Yb as the rocks evolve due to decreasing heavy rare earth element (HREE) concentrations, and $\varepsilon Nd_{(2950\ Ma)}$ of -0.1 to 0.8 (Smithies et al., 2004). Smithies and Champion (2000) and Smithies et al. (2004) favour a two-stage model for the formation of the high-Mg diorite suite, with a mantle source that was metasomatised by addition of ~40% TTG-like metabasite melt component subsequently undergoing ~25% partial melting. Geochemical composition varies slightly between individual intrusions which may be due to variable source composition and degree of partial melting (Smithies and Champion, 2000). Formation of this mantle source has been linked to both subduction (e.g. Smithies et al., 2004; Smithies and Champion, 2000) and intraplate sagduction (e.g. Smithies et al., 2021; Vandenburg et al., 2023) settings. The timing of sanukitoid magmatism is late- to post-kinematic with respect to the first regional deformation of the Mallina Basin, and melting of their metasomatised mantle source may have been triggered by a plume, rifting or lithospheric detachment. Following their emplacement, the parental magmas then differentiated by hornblende ± clinopyroxene fractional crystallisation to generate the more evolved members of the suite (Smithies and Champion, 2000). Smithies and Champion (2000) proposed that the melanodiorite found as chilled margins on some of the high-Mg diorite intrusions may be closest in composition to the parental magma as it has been least affected by magma differentiation.

Five sanukitoid samples belonging to the high-Mg diorite suite were analysed for this thesis (fig. 2.7b). Samples 142347 and 235917 are, respectively, a melanodiorite and a quartz diorite from the Peawah Granodiorite (Smithies and Champion, 2000; Vandenburg et al., 2023). Sample 142260 is a melanodiorite from Jones Well Stock, 142257 is a granodiorite from Stock 1, and 142945 is a metafelsic volcanic rock (Smithies et al., 2004; Smithies and Champion, 2000). Hornblende is the dominant mafic mineral with lesser biotite, and, in the case of melanodiorite, also some pyroxenes. Textures range from equigranular to feldspar-porphyritic, and accessory minerals present are magnetite, titanite, apatite and zircon. All high-Mg diorite suite rocks have undergone recrystallisation at lower- to middle-greenschist facies conditions, causing primary mafic minerals to start being replaced by actinolite and chlorite, while epidote and sericite are beginning to replace primary plagioclase

(Smithies et al., 2004). The major and trace element data for samples 142260, 142347 and 142257 are reported in Smithies and Champion (2000), and for sample 142945 are taken from the Western Australian Geochemistry Database (WACHEM; Geological Survey of Western Australia, 2025). Data for sample 235917 are reported by Vandenburg et al. (2023).

In addition to the ~2950 Ma sanukitoids, I have analysed ~3421 Ma granitoids from the northwest margin of the Yale dome, East Pilbara Terrane (fig. 2.7b). These samples are best considered to be "sanukitoid-like" rocks (Lowrey et al., 2023), as while they show many of the key geochemical characteristics of sanukitoids (e.g. high Ba and Sr concentrations, moderately potassic with K_2O/Na_2O of 0.7-1.0), they have lower Mg# (37 – 40) and Ni (15 – 19 ppm) and Cr (20 – 40 ppm) concentrations, and slightly shallower CI chondrite-normalised REE patterns ($(La/Yb)_N \approx 15$) than typical Archean sanukitoids (Smithies et al., 2021; Vandenburg et al., 2023). Three samples of Paleoarchean "sanukitoid-like" rock were analysed for this thesis. Sample 142170 is a foliated biotite granite which has experienced epidote alteration of its feldspars. Sample 235921 is a foliated biotite-hornblende granite with altered feldspars, while 235921 enclaves is taken from the mafic microgranular enclaves (MME) hosted by this granite. Their lithological descriptions and major and trace element compositions are reported by Vandenburg et al. (2023).

2.2.1.2. Yilgarn Craton

The Yilgarn Craton is a large block of dominantly late Archean (< 3 Ga) crust located in Western Australia and is divided into seven terranes (fig. 2.8). The largest one is the Youanmi Terrane which likely represents a protocraton nucleus onto which other terranes accreted in the Neoarchean (e.g. Cassidy et al., 2006; Czarnota et al., 2010). The easternmost four terranes are separated by large-scale shear zones and collectively make up the Eastern Goldfields Superterrane (EGST). Geochemical and isotopic data from the EGST are most consistent with it having formed by rifting of Youanmi Terrane basement, creating a series of discrete, north-south-trending basins (e.g. Barnes et al., 2012; Masurel et al., 2022; Smithies et al., 2023).
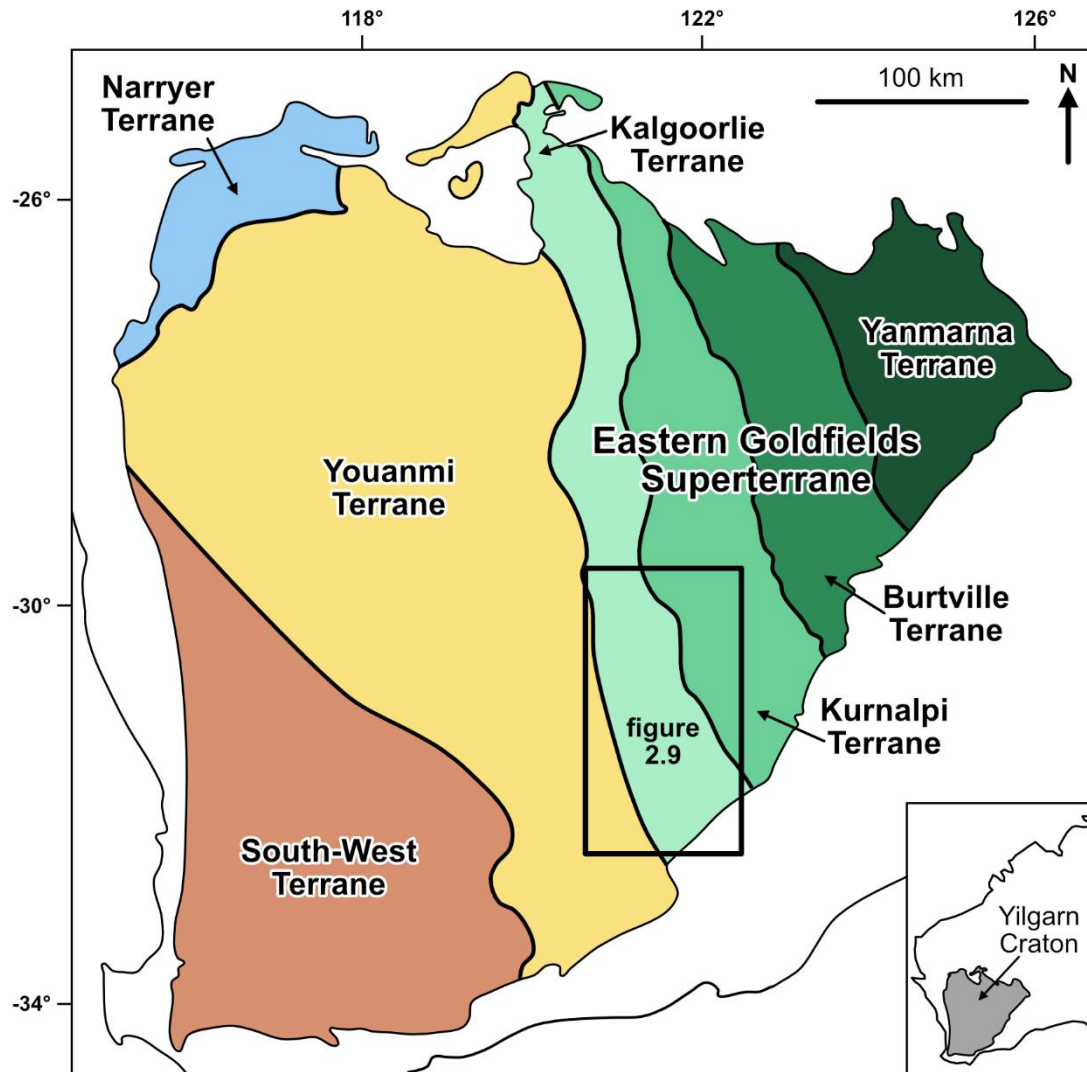
Figure 2.8: Map showing the tectonic division of the Yilgarn Craton into terranes, after Cassidy et al. (2006). The Eastern Goldfields Superterrane consists of the Kalgoorlie, Kurnalpi, Burtville and Yanmarna Terranes. The black rectangle is the area of the southern Kalgoorlie Terrane that is shown in more detail in figure 2.9.

For this thesis I analysed samples from the Black Flag Group, which is a cogenetic suite of sanukitoids and calc-alkaline lamprophyres that were emplaced in the southern Kalgoorlie Terrane, EGST (fig. 2.9), between approximately 2700 and 2650 Ma (Smithies et al., 2022, 2019, 2018; Squire et al., 2010; Tripp, 2013). BFG magmatism is spatially and temporally associated with gold mineralisation in the EGST, both of which tend to occur along regional-scale shear zones (Smithies et al., 2022, 2018). The BFG differs from the majority of sanukitoid suites as it consists of a significant volume of volcanic and volcaniclastic rocks, in addition to subvolcanic dykes
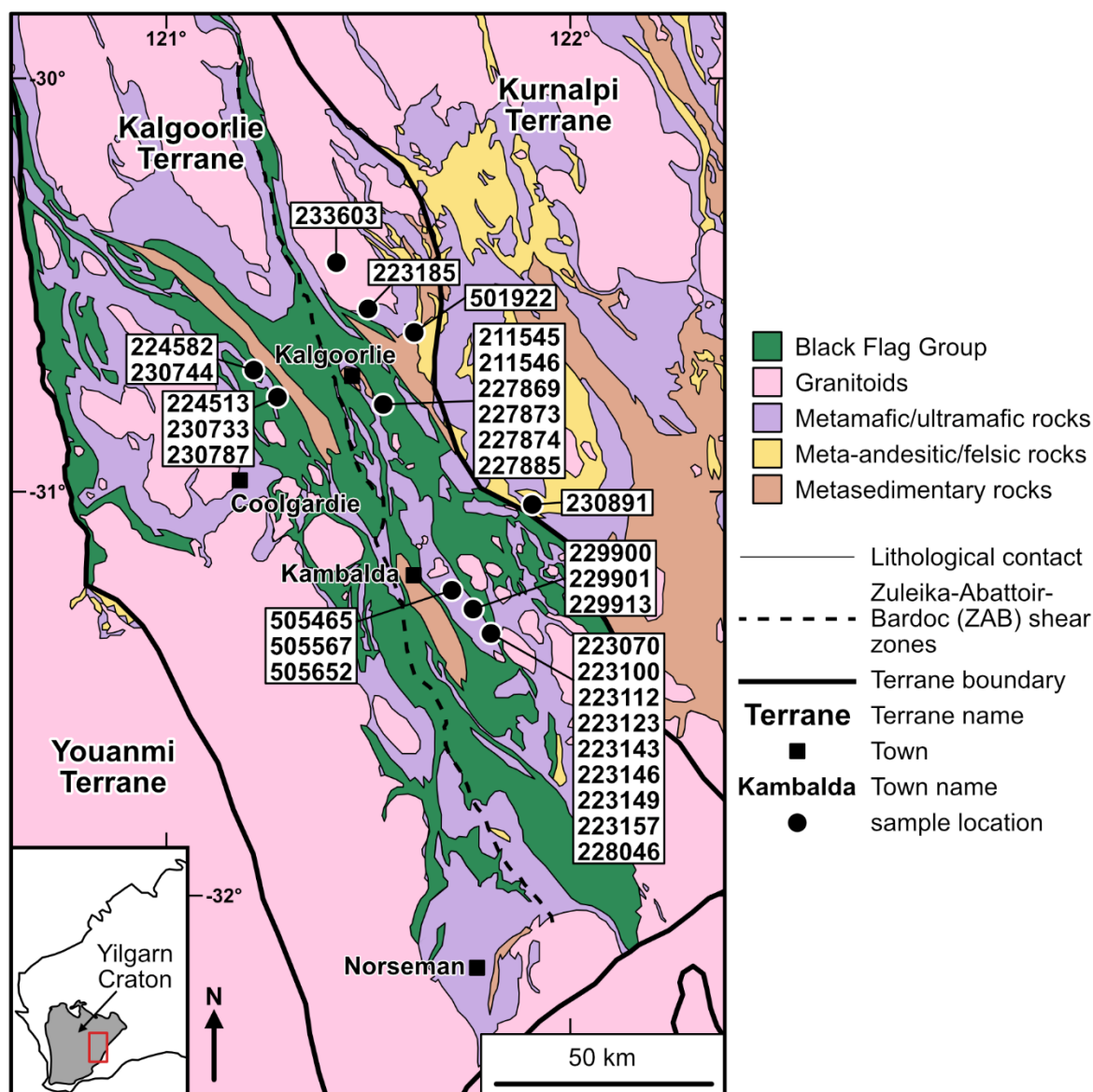
Figure 2.9: Simplified geological map of the southern Kalgoorlie Terrane, showing the locations of Black Flag Group (BFG) sanukitoid samples analysed in this thesis. The green areas show the surface outcrop of the BFG. Based on the "1:500,000 State interpreted bedrock geology of Western Australia" map (Geological Survey of Western Australia, 2020).

and intrusions. Smithies et al. (2022) found that emplacement mechanism did not significantly modify geochemistry. The BFG continuously covers a wide SiO_2 range, with lithologies varying from primitive basalts and lamprophyres, to intermediate andesites and diorites, and finally to evolved dacites, granodiorites and granites. They are generally hornblende ± plagioclase porphyritic, but the abundance and size of crystals, as well as the rock texture, vary depending on emplacement mechanism. All samples have undergone greenschist facies metamorphism along with variable degrees of whole-rock silicification and weak-to-moderate feldspar-destructive

alteration. The samples analysed in this thesis are primarily taken from diamond drill cores, and figure 2.10 shows the range of textures displayed by the samples.

The geochemistry of the BFG fits literature definitions of "sanukitoid", with high Ba and Sr concentrations generally > 500 ppm, strongly fractionated REEs, and in the less evolved members of the suite Mg# > 50 and Ni and Cr concentrations > 100 ppm (Smithies et al., 2022, 2018). Metasomatism of the BFG mantle source is proposed to have been dominantly fluid-mediated due to the strong negative HFSE anomalies and relatively low Zr/Sm and La/Nb of the lamprophyres, and may have occurred during incipient/failed subduction or surrounding dense, lower crustal drips (Smithies et al., 2019). This metasomatised mantle likely underwent partial melting during the late stages of extension related to rifting of the Yilgarn Craton to form the Eastern Goldfields Superterrane, which may have been caused by a mantle plume (Smithies et al., 2023, 2022). Geochemical modelling suggests that the primitive lamprophyric magmas differentiated by hornblende ± plagioclase (plus minor apatite and zircon) fractional crystallisation to form the wide SiO_2 range of the BFG (Perring and Rock, 1991; Smithies et al., 2019).

The BFG has been divided into two main groups based on its geochemistry – a high La/Th (≥ 4.9) group and a low La/Th (< 4.9) group (fig. 2.11a) – with the former group slightly more enriched in LREE and some HFSE (e.g. Nb, Zr) than the latter (Smithies et al., 2022). A key difference between the groups is that the high La/Th group has higher, more radiogenic $\varepsilon Nd_{(2690\ Ma)}$ and younger two-stage depleted mantle Nd model ages (T_{2DM}) than the low La/Th group, suggesting that their mantle sources differ. Formation of the high La/Th group source hence appears to have involved a younger and slightly more incompatible trace element-enriched crustal component than for the low La/Th group source (Smithies et al., 2022). The difference between the groups is not only geochemical, but also temporal and spatial. The low La/Th group is typically older (mostly > 2680 Ma) than the high La/Th group (mostly < 2670 Ma), although they are locally found to be mutually intrusive and interlayered showing they were sometimes emplaced concurrently (Smithies et al., 2022). High La/Th BFG are exclusively found to the east of the Zuleika-Abattoir-Bardoc (ZAB) shear zones, while low La/Th BFG are more widespread and are found both sides of the ZAB shear zones
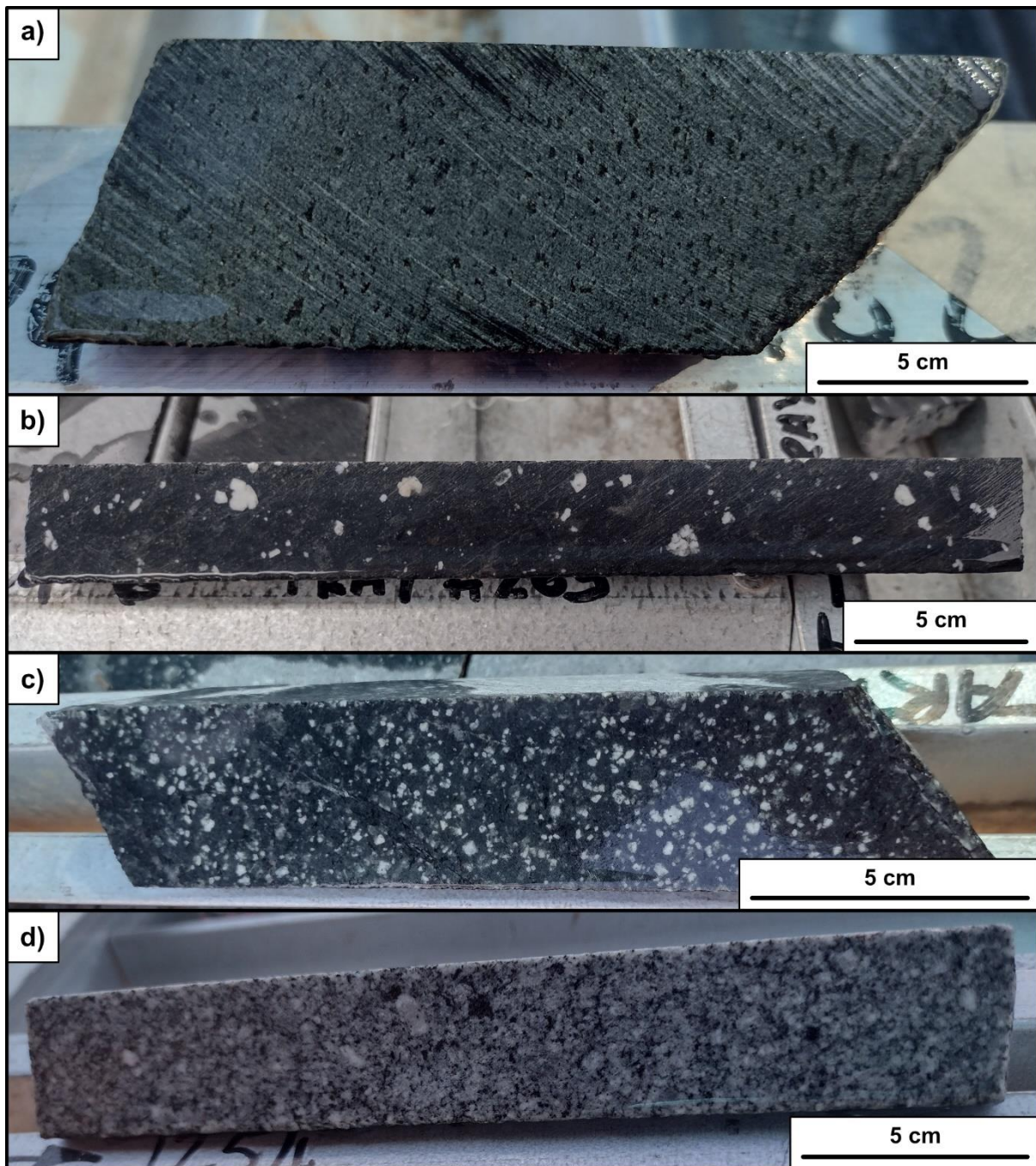
Figure 2.10: Photographs of the diamond drill core sections that some of the Black Flag Group samples are taken from, demonstrating the range of textures displayed by the samples. Photographs taken by Laura Spencer at the Geological Survey of Western Australia's Joe Lord Core Library, Kalgoorlie, WA. a) Sample 223149 – fine-grained metabasalt containing small, amphibole-bearing clots of mafic minerals that form a weak fabric across the width of the core (approximately top to bottom in the photograph). b) Sample 211546 – porphyritic meta-andesite consisting of a very fine-grained to vitric groundmass containing relatively sparse, euhedral to subhedral plagioclase phenocrysts up to ~1 cm in length with no preferred orientation. c) Sample 223123 – porphyritic dacite consisting of a very fine-grained to vitric groundmass containing abundant, small (< 4mm length), subhedral plagioclase phenocrysts with no preferred orientation. d) Sample 223146 – fine- to medium-grained granodiorite consisting of plagioclase, quartz, amphibole and lesser biotite, containing sparse, subhedral plagioclase phenocrysts 1 – 2 cm in length that are sometimes zoned and a few small (< 1 cm) fragments of very fine-grained, more mafic rock.

(fig. 2.9). Smithies et al. (2022) proposed that the ZAB shear zones may be a surface expression of a lower lithospheric boundary separating the sources of the high La/Th and low La/Th groups. In addition to this, the high La/Th group has been further divided by Ni content to create "high Ni" and "low Ni" subgroups which are indistinguishable except for the former having higher Ni, Cr and MgO contents and higher Mg# than the latter (fig. 2.11b) (Smithies et al., 2022). There is significant overlap of the "high Ni" and "low Ni" subgroups at high SiO2 contents.
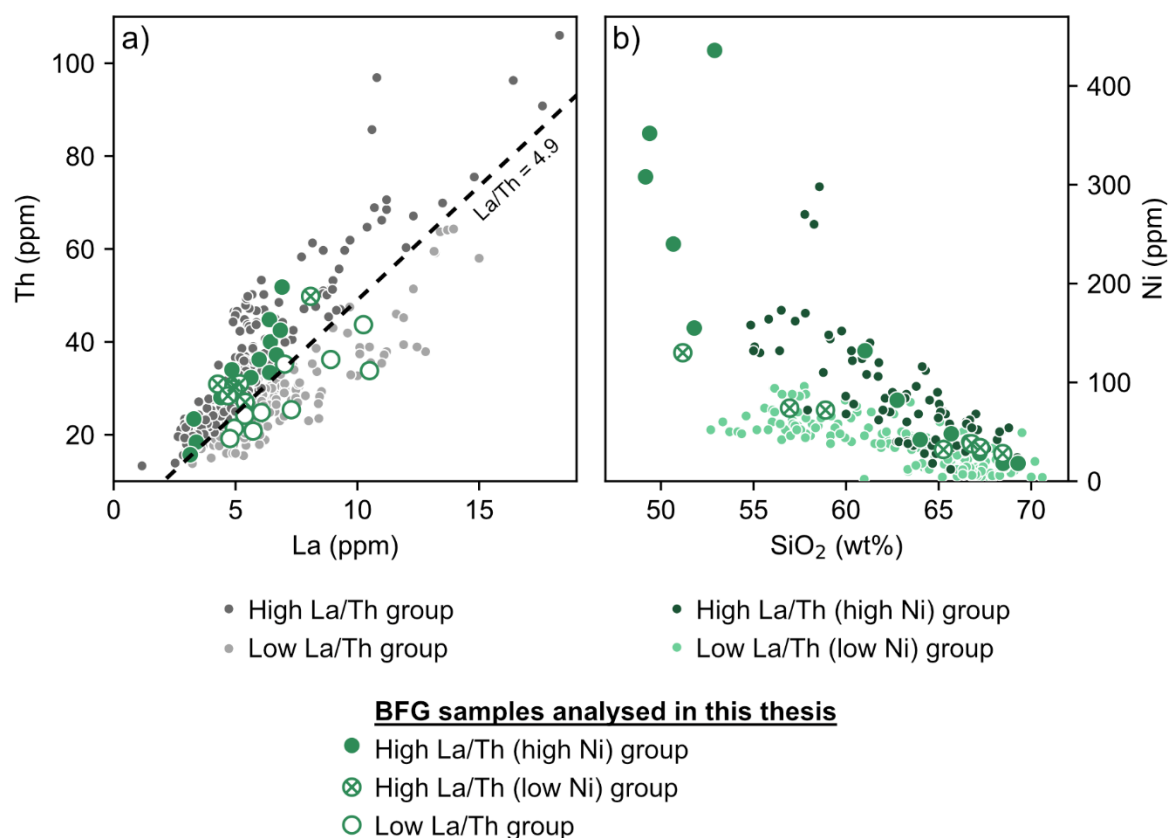
Figure 2.11: a) Th (ppm) vs La (ppm), showing division of the Black Flag Group (BFG) into a high La/Th (≥ 4.9) group and a low La/Th (< 4.9) group, after figure 40 from Smithies et al. (2022). b) Ni (ppm) vs SiO2 (wt%) showing division of the high La/Th BFG group into high Ni (dark green) and low Ni (light green) subgroups. The BFG geochemical data are from Smithies et al. (2022). Large green symbols show the compositions of BFG samples analysed in this thesis.

I selected samples from all three geochemical subgroups of the BFG – high La/Th (high Ni), high La/Th (low Ni) and low La/Th – for analysis (fig. 2.11), ensuring that the selected samples from each subgroup covered the full compositional range. All samples are from the Kalgoorlie-Kambalda region of the southern Kalgoorlie Terrane (fig. 2.9). Thirteen samples belong to the high La/Th (high Ni) group with SiO2 contents

of 49.2 – 69.3 wt%, while seven samples with SiO_2 of 51.2 – 68.5 wt% were selected from the high La/Th (low Ni) group. Ten samples were taken from the low La/Th group and these cover a slightly wider SiO_2 range of 43.8 – 70.1 wt%. The full list of samples from each BFG subgroup and their lithological descriptions are given in Appendix B. For samples taken from diamond drill cores, the core name and depths that the sample was taken from are provided in Appendix C. The elemental and radiogenic isotope compositions are reported by Smithies et al. (2022, 2019) and in the Western Australia Geochemistry Database (WACHEM; Geological Survey of Western Australia, 2025).

2.2.1.3. São Francisco Craton and Paleocontinent

The São Francisco Craton and Paleocontinent are located in eastern Brazil (fig. 2.12). The São Francisco Craton refers to the ancient, stable crustal block that was not significantly affected by Neoproterozoic deformation and metamorphism, while the São Francisco Paleocontinent consists of the São Francisco Craton plus the Archean-Paleoproterozoic blocks affected by Neoproterozoic deformation and metamorphism that amalgamated to it (Bruno et al., 2020). The southern São Francisco Craton consists of several Archean gneiss complexes which are proposed to have formed by subduction followed by continental collision (e.g. Marimon et al., 2022; Simon et al., 2021). In the Paleoproterozoic, multiple crustal blocks collided with the southeastern edge of the craton and accreted to it, forming the Minas Orogen (e.g. Bruno et al., 2021). For this thesis I analysed Paleoproterozoic sanukitoids from the Mineiro Belt, which is the northwesternmost block of the Minas Orogen (fig. 2.12).

The Alto Maranhão Suite is a 2130 ± 2 Ma (Noce, 1995) cogenetic sanukitoid suite located in the northeast of the Mineiro Belt (fig. 2.12). It consists of biotite-hornblende tonalites and quartz diorites that contain abundant dioritic microgranular mafic enclaves, and was metamorphosed to greenschist-low amphibolite facies (Seixas et al., 2013). Moreira et al. (2018) found that this metamorphism did not affect the large, euhedral titanites which preserve igneous textures and ages of ~2130 Ma, although a few small titanites yielded younger ages (~2050 Ma) that may be related to thermal overprinting. As it was not affected by Neoproterozoic deformation and metamorphism, the Alto Maranhão Suite and this section of the Mineiro Belt are considered part of the
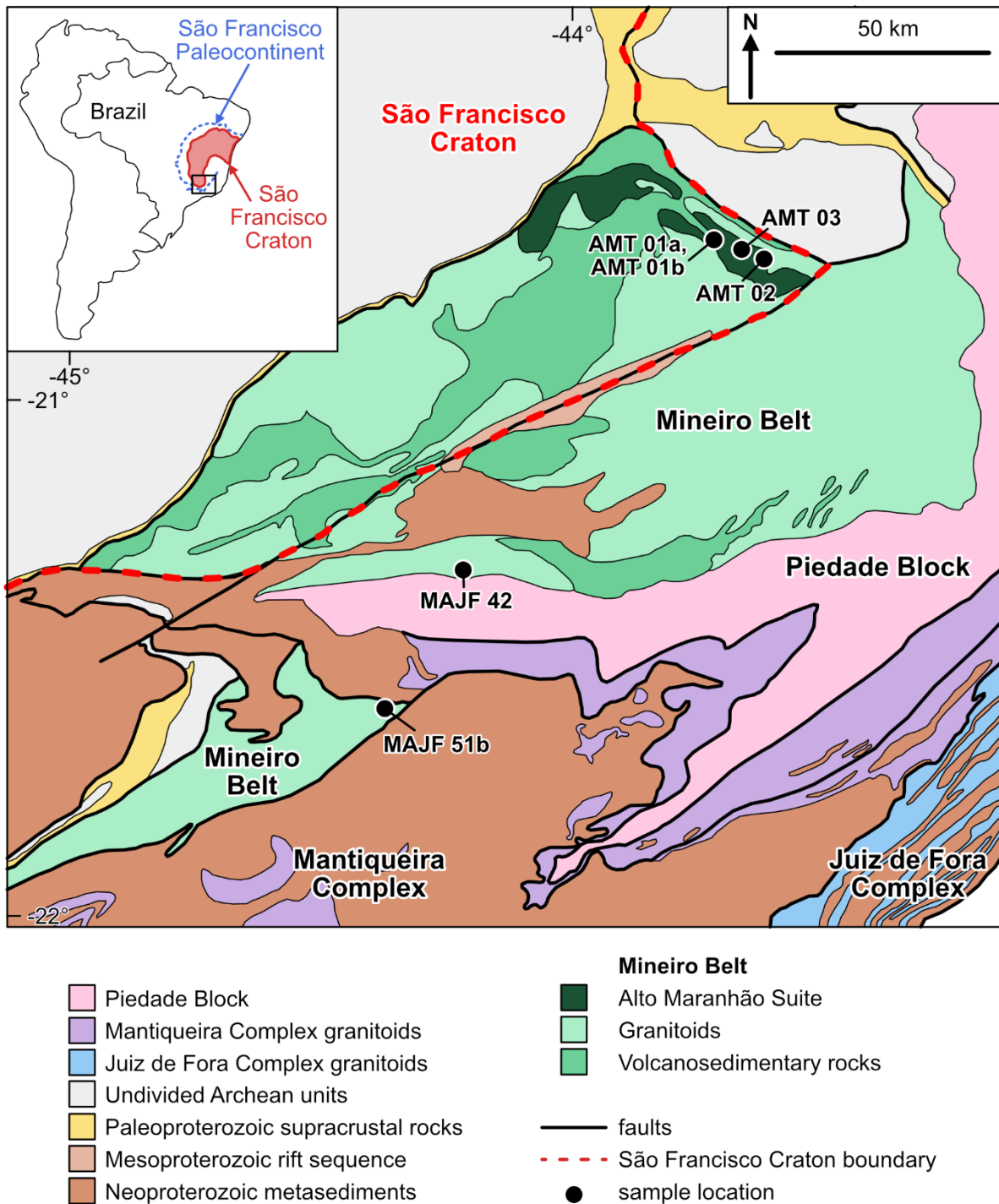
Figure 2.12: Simplified geological map of the Minas Orogen in the southern São Francisco Craton (extent shown in red) and Paleocontinent (extent shown in blue), showing the locations of sanukitoid samples analysed in this thesis. The outcrop of the Alto Maranhão sanukitoid suite in the Mineiro Belt is shown in dark green. Modified from figure 2 from Bruno et al. (2021), figure 1 from Moreira et al. (2018) and figure 1 from de Morisson Valeriano et al. (2022).

São Francisco Craton (fig. 2.12). The Alto Maranhão Suite is classified as low-Ti sanukitoid and has high Ba and Sr contents generally > 700 ppm, relatively high Mg# ≥ 46 and Cr > 50 ppm, and steep CI chondrite-normalised REE patterns (Moreira et

al., 2018; Seixas et al., 2013). It has $\varepsilon Nd_{(2130\ Ma)}$ of -1.0 to +0.9, showing it was derived from a juvenile source (Moreira et al., 2018; Seixas et al., 2013). The Alto Maranhão Suite is proposed to have formed by partial melting of mantle that was metasomatised by slab melts in a subduction setting (Moreira et al., 2018; Seixas et al., 2013). REE modelling by Seixas et al. (2013) supports ~13% partial melting of a source consisting of ~50% metabasite melt with a TTG-like composition and ~50% primitive mantle to form the Alto Maranhão Suite parental magmas. Zircons from the Alto Maranhão Suite have $\delta^{18}O$ values of 6.18 to 6.68‰ (Moreira et al., 2020) which are slightly heavier than the mantle (5.3 ± 0.3‰; Valley et al., 1998), while sulfur speciation and trace elements in apatite-hosted zircon inclusions record oxidised conditions with fO_2 of FMQ +0.80 ± 0.16 to +1.24 ± 0.36 (log units relative to the fayalite-magnetite-quartz buffer) (Moreira et al., 2023). Moreira et al. (2023, 2020) interpreted these characteristics as recording an oxidised sediment component in the Alto Maranhão Suite mantle source. Trace element modelling demonstrates that fractional crystallisation of hornblende + plagioclase ± biotite plus accessory allanite, apatite and zircon from parental magmas can generate the full compositional range of the suite (Seixas et al., 2013).

I analysed four samples (AMT 01a, AMT 01b, AMT 02 and AMT 03) from the Alto Maranhão Suite. Moreira et al. (2018) described these samples and reported their major and trace element and radiogenic isotope compositions. The zircon Hf and O isotope compositions of AMT 03 are reported by Moreira et al. (2020), and the sulfur speciation and trace element compositions of apatite-hosted zircon inclusions from AMT 02 and AMT 03 are reported by Moreira et al. (2023). These samples are all biotite-hornblende tonalites that cover a relatively narrow SiO_2 range of 62.4 – 67.2 wt% (Moreira et al., 2018). AMT 01a and AMT 01b contain significant accessory epidote while AMT 03 contains large titanite grains, and samples AMT 01a and AMT 01b are slightly more altered than samples AMT 02 and AMT 03 (Moreira et al., 2018).

I also analysed two additional sanukitoid samples from the southern Mineiro Belt (fig. 2.12), MAJF 42 and MAJF 51b, which have zircon U-Pb crystallisation ages of 2114 ± 10 Ma and 2117 ± 24 Ma respectively (Bruno et al., 2021). Sample descriptions, major and trace element and radiogenic isotope compositions are reported by Bruno et al. (2021). Both samples are granodioritic hornblende-biotite orthogneisses that were

affected by Neoproterozoic deformation and are hence part of the São Francisco Paleocontinent. MAJF 42 has been metamorphosed to greenschist facies, while MAJF 51b has been metamorphosed to epidote-amphibolite facies and is banded with migmatitic textures. These samples both have relatively high Mg# > 48 and Ni and Cr concentrations > 70 ppm, and MAJF 42 is more strongly enriched in Ba and Sr than MAJF 51b. Bruno et al. (2021) proposed that the mantle source of these sanukitoids was metasomatised by sediment-derived aqueous fluids in a subduction zone setting. MAJF 42 has $\varepsilon Nd_{(t)}$ of +1.3 which may reflect the involvement of coeval (~2.1 Ga) sediments, while MAJF 51b has negative $\varepsilon Nd_{(t)}$ of -5 which Bruno et al. (2021) attribute to an Archean-aged sediment component in their mantle source.

2.2.1.4. Caledonian Orogeny, Scotland

During the early Paleozoic Caledonian Orogeny, numerous high Ba-Sr granite and syenite suites were generated and emplaced in the Northern Highland Terrane, Scotland. Fowler et al. (2008) and Fowler and Rollinson (2012) observed close petrological and geochemical similarity between the high Ba-Sr granite suites and Archean sanukitoids. Both the high Ba-Sr granite suites and sanukitoids are amphibole- and biotite-bearing granitoids that are found in association with lamprophyres and their plutonic equivalents appinites, although granite lithologies are more abundant in the high Ba-Sr granite suites. Like sanukitoids, the high Ba-Sr granite suites clearly have high LILE concentrations, as well as high incompatible element (e.g. Mg, Ni, Cr) concentrations and steeply fractionated CI-chondrite normalised REE curves. Their major element compositions largely overlap, although the primitive members of the high Ba-Sr granite suites have slightly higher P_2O_5 and slightly lower Fe_2O_3 and MnO contents than sanukitoids (Fowler and Rollinson, 2012). These similarities led Fowler and Rollinson (2012) to label the Paleozoic high Ba-Sr granite suites as "Phanerozoic analogues of Neoarchean sanukitoids". Elemental and isotopic data suggest that the high Ba-Sr granite suites formed by partial melting of lithospheric mantle enriched by a small amount (< 5%) of subducted sediment melts, with melting possibly triggered by slab breakoff (Fowler et al., 2008; Zhu et al., 2024).
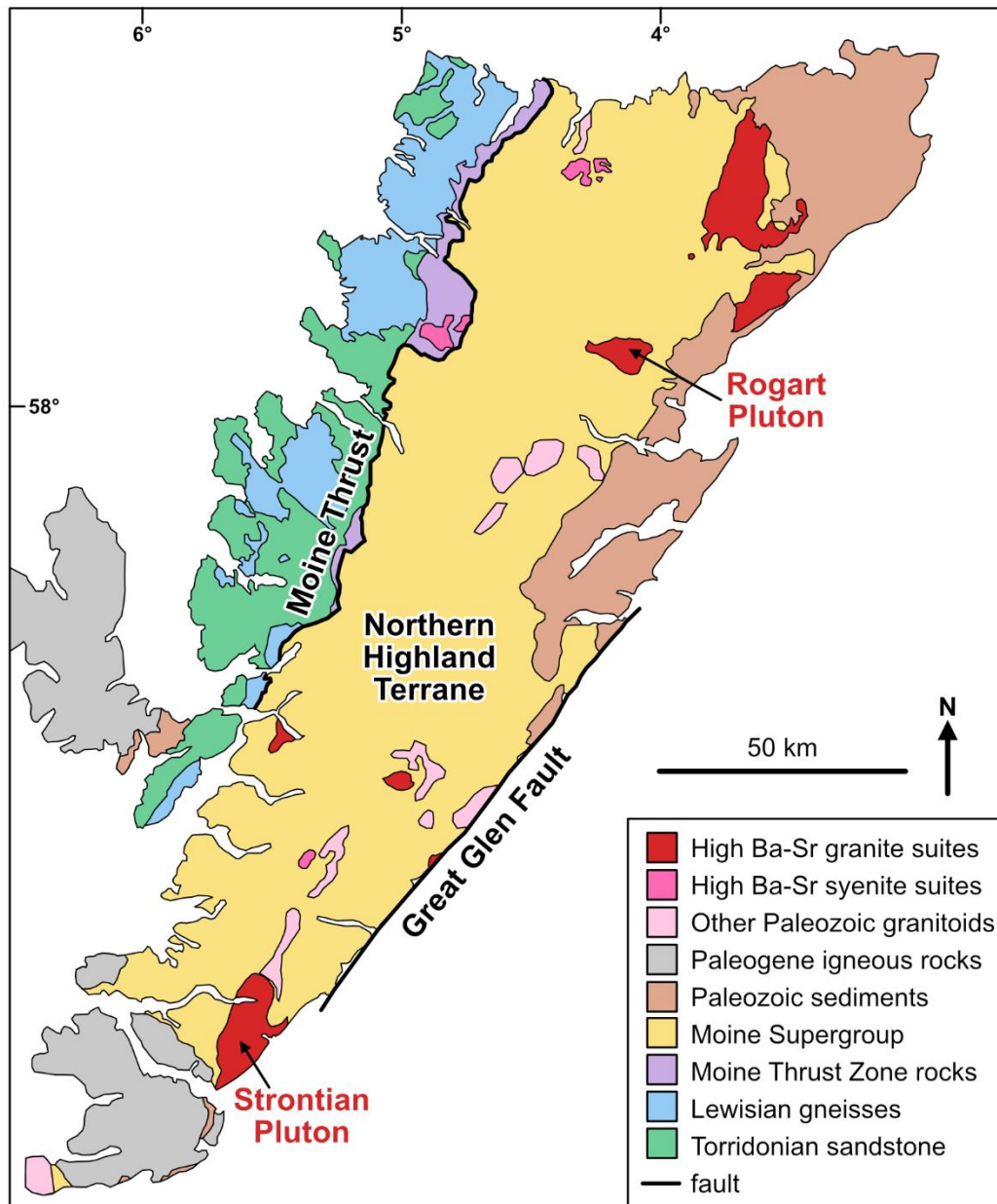
Figure 2.13: Simplified geological map of the Northern Highland Terrane, Scotland, showing the locations of the Rogart and Strontian high Ba-Sr granite suite plutons. Modified from figure 1 from Fowler et al. (2008).

The samples analysed for this thesis come from the Rogart and Strontian plutons, which have been dated at 425 ± 1.5 Ma and 425 ± 3 Ma respectively (Kocks et al., 2014; Rogers and Dunning, 1991). The Rogart pluton is situated in the north of the Northern Highland Terrane (fig. 2.13) and is a concentrically zoned intrusion which transitions from outer tonalite (sample RT1) to granodiorite (RHG2) and then to granite in the centre (Fowler et al., 2001). The Strontian pluton lies at the southern end of the Northern Highland Terrane (fig. 2.13) and consists of hornblende-biotite granodiorite

(samples SR1, SR3 and SR4). Both plutons contain enclaves of appinite (RA1, RA2, SR2) which the granitoids are proposed to have evolved from by clinopyroxene- and biotite-dominated fractionation, with plagioclase and amphibole becoming significant fractionating phases later on (Fowler et al., 2008, 2001). These high Ba-Sr granite suites show some feldspar alteration but have not been affected by later metamorphism (e.g. Bruand et al., 2023; Fowler et al., 2008). The petrology and whole-rock elemental and isotopic compositions of the Rogart pluton are reported by Fowler et al. (2001), while the Strontian pluton samples are described by Fowler et al. (2008). A more comprehensive re-analysis of sample trace element concentrations was done by Zhu et al. (2024), and these concentrations are used where data were previously not available. Detailed accessory mineral chemistry and isotopic compositions for both plutons are described in Bruand et al. (2023, 2014), while their whole-rock Mg and Ba stable isotope compositions are reported by Zhu et al. (2024).

The elemental compositions of the Rogart and Strontian plutons are similar except for the slightly greater LREE and LILE enrichments in the Rogart pluton (Fowler et al., 2008). Their radiogenic and stable isotope compositions show clear differences. The Rogart pluton displays clearly enriched Sr and Nd isotope compositions, while the Strontian pluton has Sr-Nd isotope compositions closer to depleted mantle values (Fowler et al., 2008). Similarly, the Strontian pluton exhibits a narrow range of δ^{26}Mg and δ^{138}Ba values that largely overlap with mantle compositions, while the Rogart pluton has lower δ^{26}Mg and δ^{138}Ba (Zhu et al., 2024). This combined Mg-Ba-Sr-Nd isotope evidence suggests that the mantle source of the Rogart pluton was more significantly contaminated by subducted sediment than the mantle source of the Strontian pluton (Fowler et al., 2008; Zhu et al., 2024). This sediment component is thought to be pelagic sediment, with the low δ^{26}Mg of some Rogart pluton samples possibly indicating carbonate sediment involvement (Zhu et al., 2024). Apatites and titanites from the Strontian pluton have well-defined rims with low REE and HFSE concentrations that likely record a mixing event with a more mafic magma (Bruand et al., 2014). No such feature is observed in the Rogart pluton, but their radiogenic isotopes do record assimilation of surrounding Moine metasediments (Fowler et al., 2001).

2.2.2. TTGs

The TTG samples analysed for this thesis primarily come from the Eastern Goldfields Superterrane (EGST), Yilgarn Craton, to enable investigation of the proposed genetic link between high-Sr "high pressure" TTGs and sanukitoids in this region (Smithies et al., 2019). Additional TTG samples from the Youanmi Terrane, Yilgarn Craton, and the Pilbara Craton were selected to cover a range of ages across the Archean. These additional samples were collected in September/October 2019 as part of the YiPi (Yilgarn-Pilbara) sampling campaign led by O. Nebel, R.H. Smithies, E. Bruand and M-A. Millet.

2.2.2.1. Yilgarn Craton

I analysed seventeen TTG samples from the EGST, Yilgarn Craton (fig. 2.14), which were selected to cover the full range of trace element compositions exhibited by TTGs (fig. 2.15). I used the Bayesian classifier of Moyen (2011) to classify the TTGs into high pressure, medium pressure and low pressure groups. I then used the geochemical criteria from Smithies et al. (2019) to divide the high pressure TTGs into a high-Sr "high pressure" TTG group that is proposed to be petrogenetically linked to the Black Flag Group sanukitoids, and a medium pressure-like "high-pressure" TTG group. The high-Sr "high pressure" TTGs have $K_2O/Na_2O < 0.5$, $Sr > 700$ ppm, $Sr/Y >$ 100, $Yb < 0.4$ ppm and $La/Yb > 60$ (Smithies et al., 2019), while the medium pressure-like "high pressure" TTGs do not meet all these criteria. Three samples (227968, 502247 and 505481) are classified as high-Sr "high pressure" TTGs, four samples (230558, 501894, 504718 and 233734) as medium pressure-like "high pressure" TTGs, four samples (222660, 240405, 502533 and 234000) as medium pressure TTGs, and six samples (500854, 240623, 501345, 504940, 501356 and 233699) as low pressure TTGs. Figure 2.15 shows the distinct trace element characteristics of these groups. These samples are estimated to be of mid-Neoarchean age (~2700 – 2650 Ma). Most of the selected EGST TTG samples are from the Kalgoorlie-Kambalda region of the Kalgoorlie Terrane (fig. 2.16), but three low pressure TTG samples (501345, 504940 and 501356) are from further north in the Kalgoorlie Terrane near Wiluna, and one low pressure TTG sample (500854) is from the Kurnalpi Terrane (fig. 2.15). Brief lithological descriptions of these samples are given in Appendix B and are

taken from the Western Australian Geochemistry Database (WACHEM; Geological Survey of Western Australia, 2025).
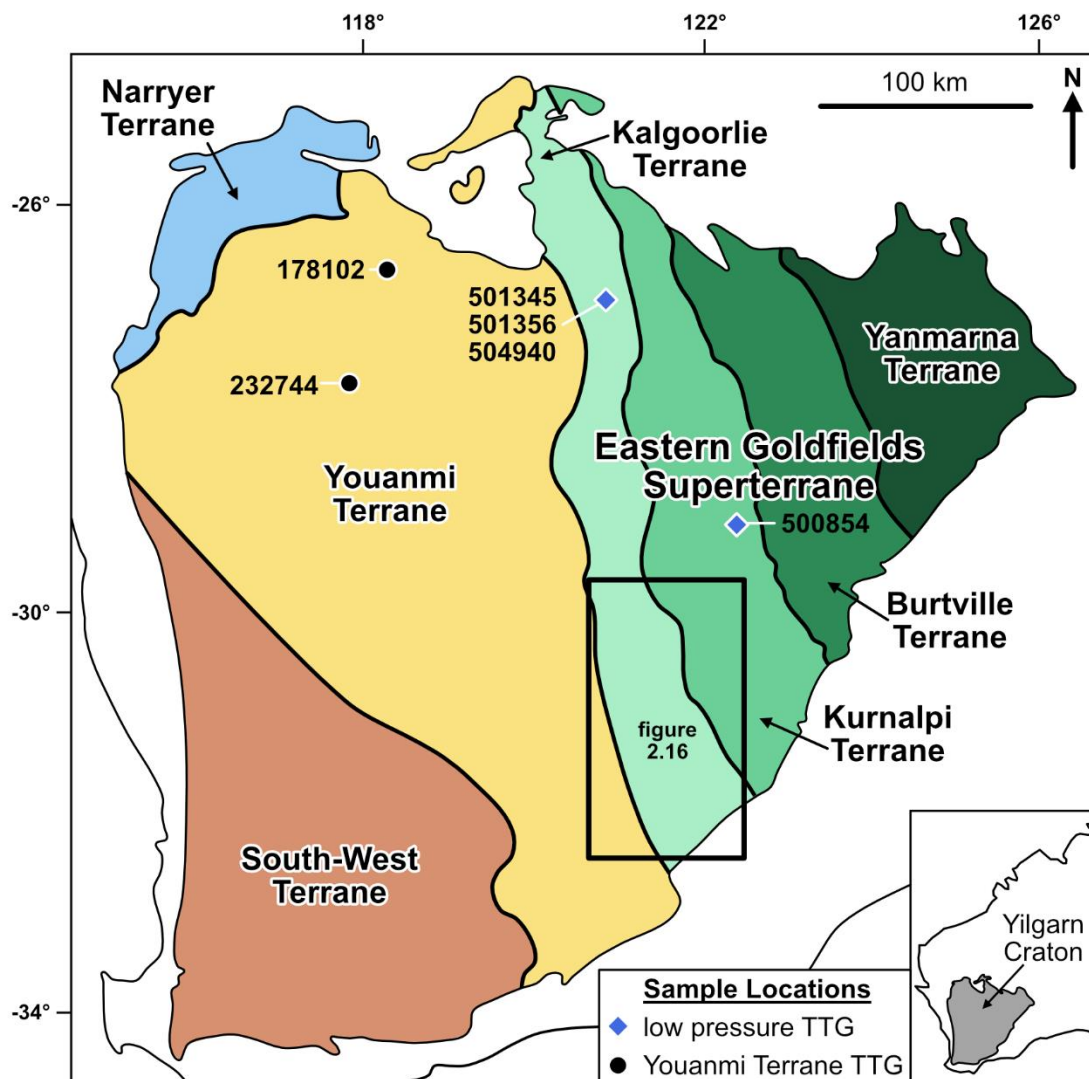
Figure 2.14: Map of the Yilgarn Craton showing the locations of TTG samples analysed in this thesis. After Cassidy et al. (2006). The black rectangle is the area of the southern Kalgoorlie Terrane that is shown in more detail in figure 2.16.

I analysed two additional TTG samples from the Youanmi Terrane of the Yilgarn Craton. Sample 178102 is a ~2787 Ma coarse-grained biotite-amphibole granodiorite from the Meekatharra area, and sample 232744 is a weakly foliated biotite tonalite from the Mount Magnet area that is inferred to be ~2696 Ma (fig. 2.14). Both samples are classified as medium pressure TTGs.
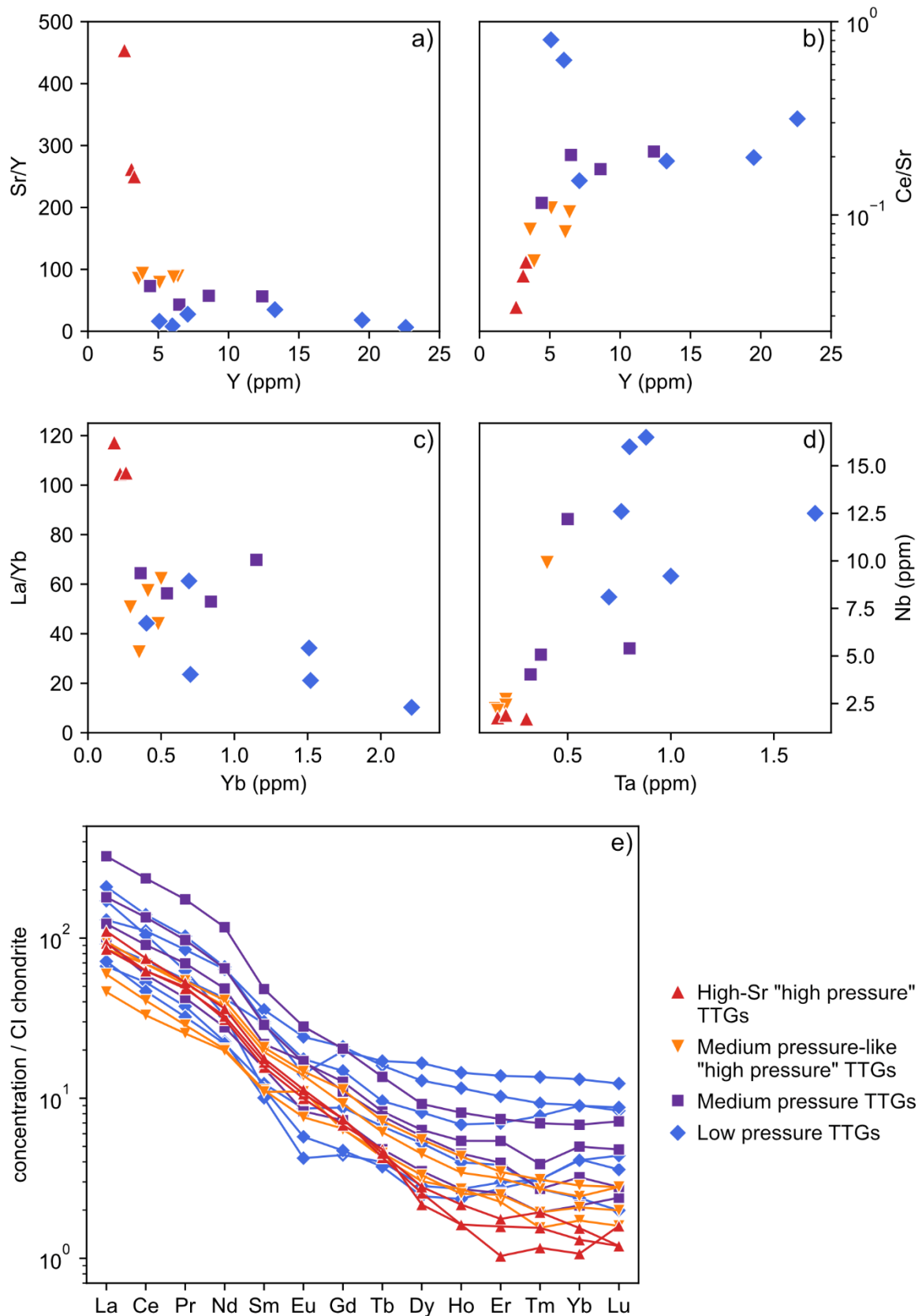
Figure 2.15: Plots showing the differences in trace element composition between the geochemical groups of Eastern Goldfields Superterrane TTGs analysed in this thesis. a) Sr/Y vs Y (ppm), b) Ce/Sr vs Y (ppm), c) La/Yb vs Yb (ppm), d) Nb (ppm) vs Ta (ppm), e) CI chondrite-normalised REE patterns, where REE concentrations are normalised to the CI chondrite values from O'Neill (2016)
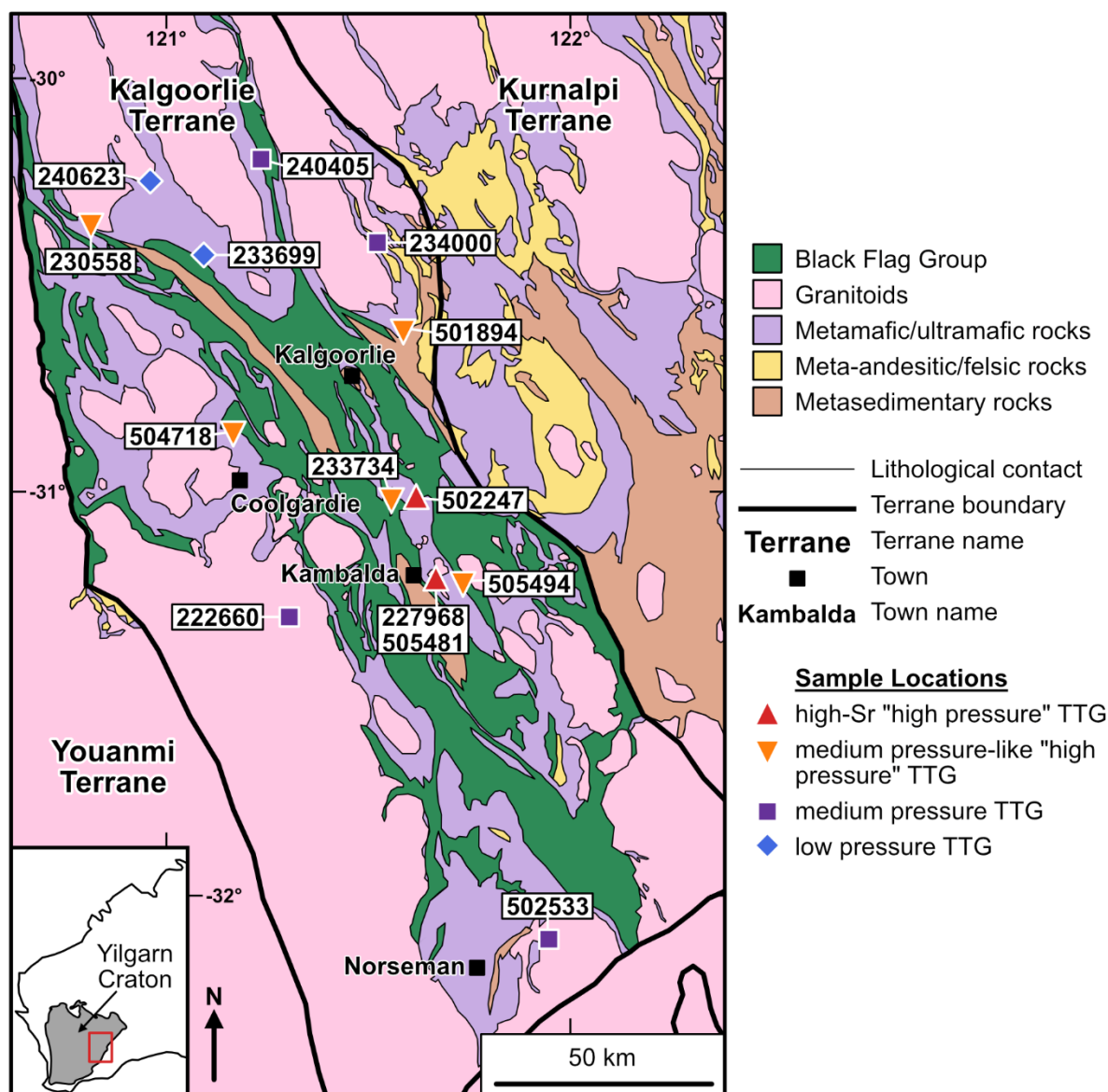
Figure 2.16: Simplified geological map of the southern Kalgoorlie Terrane, showing the locations of TTG samples analysed in this thesis. Based on the "1:500,000 State interpreted bedrock geology of Western Australia" map (Geological Survey of Western Australia, 2020).

2.2.2.2. Pilbara Craton

Four TTG samples from the Pilbara Craton were analysed for this thesis and were selected to sample different ages of magmatism on the craton. Their lithological descriptions and major and trace element compositions are reported in Vandenburg et al. (2023). Three samples are from the East Pilbara Terrane (fig. 2.17). Sample 235965 is a fine-grained, moderately foliated, biotite-bearing mesosomatic gneiss from the western margin of the Shaw Dome that is estimated to be ~3425 Ma and is classified as a medium pressure TTG. Samples 142870 and 235945 are both from the

Warrawagine Dome and are classified as low pressure TTGs. 142870 is a ~3500 Ma medium-grained, weakly foliated biotite tonalite, while 235945 is a medium-grained, equigranular biotite granodiorite from a younger phase of magmatism (~3303 Ma) on the southern margin of the complex. Finally, sample 235913 is a medium-grained, weakly foliated biotite granodiorite with secondary epidote from the Karratha granitoid complex in the Karratha Terrane (fig. 2.17). It is inferred to be ~3270 Ma and is classified as a medium pressure TTG.
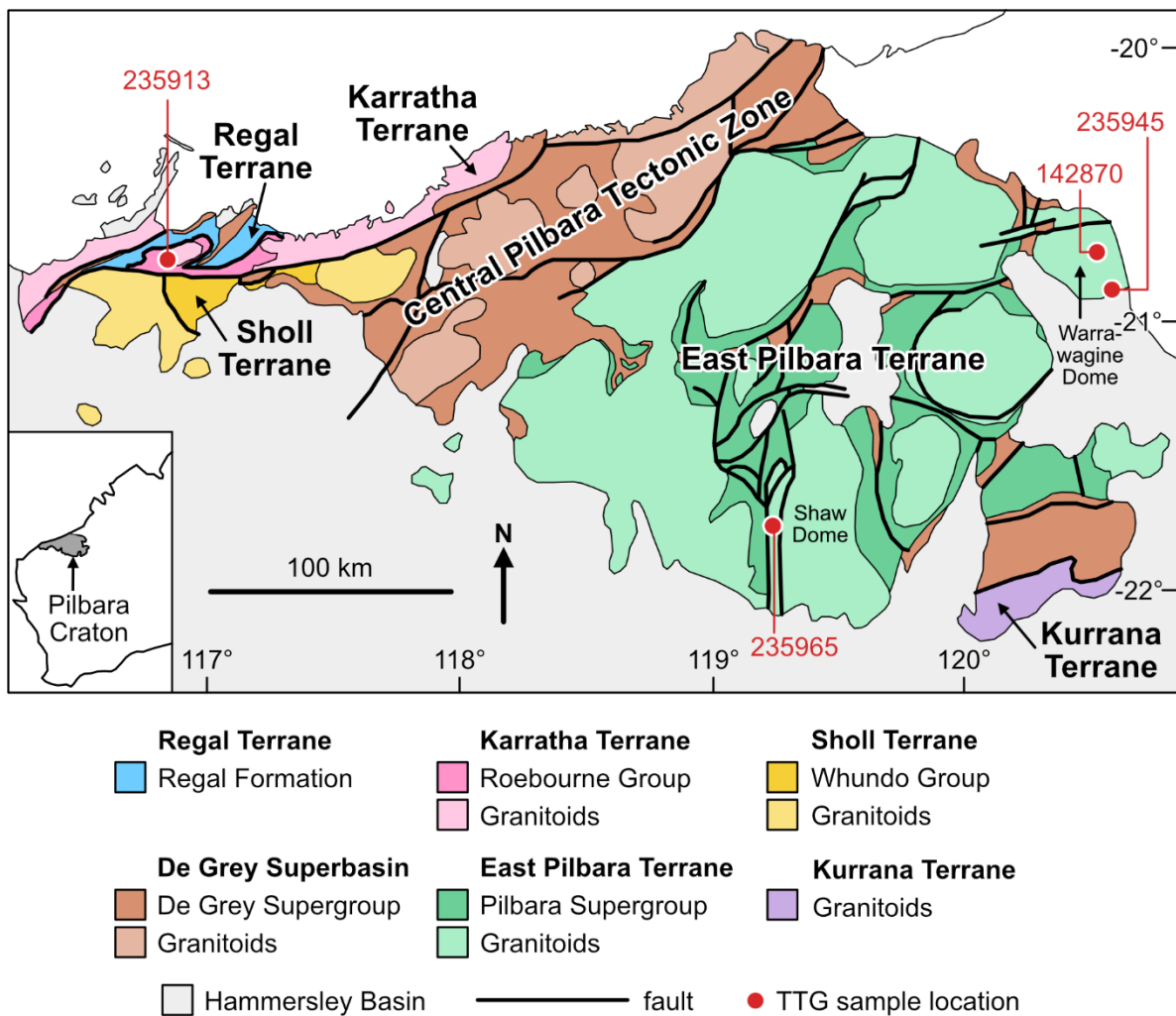
Figure 2.17: Simplified geological map of the Pilbara Craton, showing the locations of TTG samples analysed in this thesis. After figure 1 from Van Kranendonk (2010).

3. Tracing hydrous eclogite melts in the source of sanukitoids with titanium stable isotopes

3.1. Abstract

Sanukitoids are unique Archean and early Proterozoic igneous rocks. They contain high amounts of Mg, Ni and Cr, showing they are mantle-derived melts, while they are also enriched in Sr and Ba and have relatively high K contents, requiring the involvement of an incompatible element-enriched component likely derived from recycled crustal material. The appearance of sanukitoids in the geological record coincides with a shift in continental crust composition, and both events have been linked to a change in geodynamic processes on Earth. However, uncertainties remain about sanukitoid petrogenesis, in particular whether their mantle source was metasomatised by a metabasite-derived silicate melt or by an aqueous fluid. Titanium (Ti) stable isotopes can trace magmatic processes where silicate melts are in equilibrium with Fe-Ti oxides and amphibole but are insensitive to fluid-driven processes, making them a suitable tool to investigate not only the formation of sanukitoid magmas but also their subsequent evolution. Here I present Ti isotope data (δ^{49}Ti) for a series of Neoarchean sanukitoids from the Yilgarn Craton that continuously covers the full compositional range of sanukitoids. These are complemented by Mesoarchean sanukitoids and Paleoarchean "sanukitoid-like" rocks from the Pilbara Craton, and by Paleoproterozoic sanukitoids from the São Francisco Craton/Paleocontinent. In addition, I analysed Paleozoic high Ba-Sr granite suites from Scotland, which are proposed to be Phanerozoic sanukitoid analogues.

I show that evolved sanukitoids, which formed after Fe-Ti oxide saturation, display a more muted δ^{49}Ti increase during differentiation compared to currently analysed modern calc-alkaline suites. This difference is best explained by removal of significant

proportions of Ti during sanukitoid differentiation by magmatic hornblende, which fractionates Ti isotopes less strongly than Fe-Ti oxides. Combined with early oxide saturation at high Mg#, this suggests that sanukitoid parental magmas had H_2O contents and fO_2 at least as high as modern arc magmas. Primitive (pre-oxide saturation) sanukitoids, however, have significantly higher $\delta^{49}Ti$ (0.11 – 0.20‰) than modern arc basalts, the depleted mantle and the bulk silicate Earth (BSE). Their elevated $\delta^{49}Ti$ values cannot be explained by aqueous fluids alone in their mantle source, and instead require the involvement of a hydrous eclogite melt component formed in equilibrium with residual rutile. I favour generation of this metasomatic melt by fluid-fluxed eclogite partial melting, demonstrating that both metabasite melts and aqueous fluids are important for sanukitoid formation. The Ti isotope compositions of Archean and Paleoproterozoic sanukitoids therefore favour formation of the sanukitoid mantle source by a subduction-like process at least ~2.7 Ga.

3.2. Introduction

The appearance of sanukitoid magmas in the geological record in the late Archean to early Proterozoic marks an important transition in Earth evolution. During this period the composition of continental crust-forming magmas changed from the sodic tonalites, trondhjemites and granodiorites (TTG suites) characteristic of Archean (4.0 to 2.5 Ga) cratons, to the potassic granites that have dominated upper continental crust ever since. This shift in composition is thought to reflect a change in geodynamic processes towards modern day plate tectonics, and as a result, sanukitoid occurrence has often been linked to the onset of subduction (e.g. Smithies and Champion, 2000) or a change in subduction style (e.g. Laurent et al., 2014a; Martin et al., 2009).

Sanukitoids are also compositionally transitional between Archean TTG suites and post-Archean granites (Martin et al., 2009). On average they are moderately potassic, and are enriched in both compatible (e.g. Mg, Ni, Cr) and incompatible (e.g. Ba, Sr, light rare earth elements (LREE)) elements, which shows they formed by interaction between mantle peridotite and an incompatible element-enriched component likely derived from recycled crustal material (e.g. Shirey and Hanson, 1984; Stern et al., 1989). Similar to TTGs, they display highly fractionated rare earth element (REE)

patterns, while also showing calc-alkaline differentiation trends similar to post-Archean granites (e.g. de Oliveira et al., 2009; Martin et al., 2009).

Our understanding of the link between sanukitoids and a potential global geodynamic transition is limited by uncertainties about their petrogenesis. In particular, the source and nature (i.e. melt or aqueous fluid) of the incompatible element-enriched component(s) in sanukitoid source regions are debated. A recycled, garnet-bearing metabasite (amphibolite or eclogite) derived source component is commonly inferred due to the similarity between sanukitoid and TTG REE compositions (e.g. Martin et al., 2009, 2005). Some studies favour a metabasite-derived silicate melt because of the elevated La/Yb, Nb/Y and Sr/Y of sanukitoids relative to most modern arc magmas (e.g. Martin et al., 2009; Smithies and Champion, 2000). Other studies argue instead for a metabasite-derived aqueous fluid because sanukitoids display strong depletions in fluid-immobile high field strength elements (HFSE, e.g. Ti, Nb, Ta) coupled with enrichments in fluid-mobile large ion lithophile elements (LILE, e.g. Sr, Ba) (e.g. Lobach-Zhuchenko et al., 2008; Stern et al., 1989). Sediment-derived melts/fluids (e.g. Halla, 2005), carbonatitic melts (e.g. Steenfelt et al., 2005) and alkaline melts (e.g. Heilimo et al., 2010) have additionally been proposed as incompatible element-enriched components.

A second uncertainty concerns the mechanisms and timing of interaction between the enriched component(s) and mantle peridotite. The generally favoured model is a two-stage process where mantle peridotite is first metasomatised by the incompatible element-enriched component and then undergoes partial melting to form sanukitoid parental magmas (e.g. Shirey and Hanson, 1984; Smithies and Champion, 2000). However, experimental petrology has shown that a one-stage process where TTG-like melts assimilate predominantly olivine from peridotite as they ascend through the mantle can also generate magmas with sanukitoid compositions (Rapp et al., 2010, 1999). Recently, it has been proposed that sanukitoid magmas can evolve from lamprophyric magmas by amphibole-dominated fractional crystallisation (Smithies et al., 2019, 2018), which is a variation on the two-stage model as calc-alkaline lamprophyres form by low- to moderate-degree partial melting of metasomatised mantle.

Titanium (Ti) stable isotopes are proving to be a valuable tracer of magmatic processes, and Fe-Ti oxide-melt and amphibole-melt equilibria in particular (e.g. Deng et al., 2019b; Hoare et al., 2022, 2020; A.C. Johnson et al., 2023, 2019; Millet et al., 2016; Zhao et al., 2020). By contrast, Ti isotopes are insensitive to fluid-driven processes, because Ti is insoluble in aqueous fluids. These properties have already provided significant insights into the role mafic lithologies play in forming continental crust. Most notably, Z.J. Zhang et al. (2023) and Hoare et al. (2023) showed that the Ti isotope compositions of Archean TTGs can be explained by partial melting of metabasites with Ti-bearing oxides and amphibole as residual phases, followed by fractional crystallisation. In modern settings, Klaver et al. (2024) demonstrated the occurrence of slab melting in subduction zones by tracing rutile as a residual phase.

Here I present the Ti stable isotope compositions ($\delta^{49}Ti = 10^3 \times [(^{49}Ti/^{47}Ti)_{sample} / (^{49}Ti/^{47}Ti)_{OL-Ti} - 1]$) of Archean and Paleoproterozoic sanukitoids as well as of Paleozoic sanukitoid analogues to test models of the formation and evolution of sanukitoids. Full sample descriptions are given in Chapter 2, section 2.2.1, and the Ti isotope measurements were made via the methods described in Chapter 2, section 2.1. I find that primitive sanukitoids have significantly heavier Ti isotope compositions than the depleted mantle, the bulk silicate Earth (BSE) and modern arc basalts, which cannot be explained by metasomatism of their mantle source via aqueous fluids alone. Instead, primitive sanukitoids require the involvement of a metabasite melt component enriched in heavy Ti isotopes, which likely formed by fluid-fluxed partial melting of eclogite, favouring formation of the sanukitoid mantle source by a subduction-like process.

3.3. Results

The $\delta^{49}Ti$ values of Archean and Paleoproterozoic sanukitoid samples are presented in table 3.1 and figure 3.1, and vary from 0.108 ± 0.023‰ to 0.291 ± 0.021‰. The relatively primitive samples ($SiO_2 < 58$ wt%, MgO > 5.5 wt%) precede oxide saturation; hence, they cover a more limited range (0.108 – 0.197‰) and their $\delta^{49}Ti$ is not correlated with indices of differentiation (fig. 3.1). These values are significantly higher than estimates of the $\delta^{49}Ti$ of the BSE (0.053 ± 0.005‰, 2se; Deng et al., 2023) and

depleted MORB (mid-ocean ridge basalt) mantle (DMM) (0.001 ± 0.015‰, 2sd; Klaver et al., 2024). At SiO_2 > 58 wt% (i.e., after oxide saturation) $\delta^{49}Ti$ positively covaries with SiO_2 content (fig. 3.1a), similar to the differentiation trends seen in modern magma suites (e.g. Deng et al., 2019b; Hoare et al., 2020; Millet et al., 2016). The Yilgarn sanukitoids extend to higher SiO_2 contents (> 70 wt%) and $\delta^{49}Ti$ values (0.291‰) than the Pilbara and São Francisco sanukitoids (67 wt% and ~0.23‰, respectively).
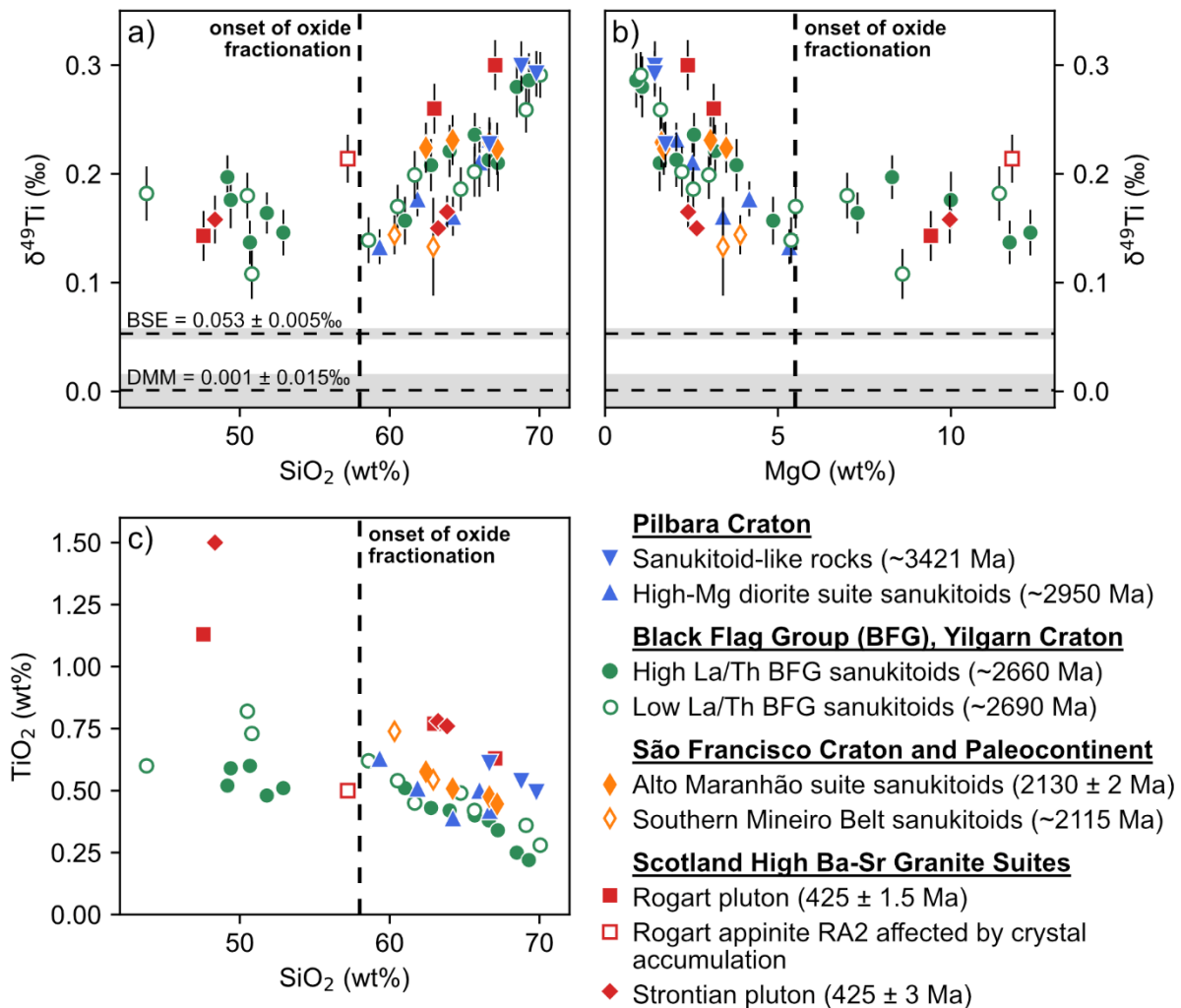
Figure 3.1: a) $\delta^{49}Ti$ (‰) vs SiO_2 (wt%), b) $\delta^{49}Ti$ (‰) vs MgO (wt%), and c) TiO_2 (wt%) vs SiO_2 (wt%) of Archean and Paleoproterozoic sanukitoids, Paleoarchean sanukitoid-like rocks and Paleozoic high Ba-Sr granites. Uncertainty in $\delta^{49}Ti$ is shown as the 95% confidence interval. BSE and DMM $\delta^{49}Ti$ values are from Deng et al. (2023) and Klaver et al. (2024) respectively, and the 2 standard error uncertainty is shown by the grey rectangles. The onset of oxide fractionation is determined from the inflection in the TiO_2 vs SiO_2 trend.

The ~3.42 Ga sanukitoid-like rocks from the Pilbara Craton plot on the same $\delta^{49}Ti$ vs SiO_2 trend as the sanukitoids (fig. 3.1a). These samples cover a limited compositional

Table 3.1: $\delta^{49}Ti$ data for the Archean-Paleoproterozoic sanukitoid samples and Paleozoic high Ba-Sr granite suite samples analysed in this chapter. Key elemental concentrations and geochemical parameters are also given. The sources of the major and trace element data for the samples are given in Appendix C. 95% ci = 95% confidence interval, calculated via the method described in Chapter 2. n = number of measurements made. Mg# = 100 * (Mg / (Mg + Fe^{2+})). λ_1 is the shape coefficient that describes the steepness of CI chondrite-normalised REE patterns (O'Neill, 2016). For (La/Yb)$_N$, (Dy/Yb)$_N$ and λ_1, REE concentrations are normalised to the CI chondrite values from O'Neill (2016).

Sample	Age	Location	Suite	$\delta^{49}Ti$	95% ci	n	TiO$_2$	SiO$_2$	Mg#	(La/Yb)$_N$	(Dy/Yb)$_N$	λ_1
	Ma			‰	‰		wt%	wt%				
235921 Enclaves	~3421	Pilbara	Sanukitoid-like rocks	0.227	0.021	1	0.61	66.65	38.2	11.63	1.26	14.34
235921	~3421	Pilbara	Sanukitoid-like rocks	0.299	0.023	1	0.54	68.78	37.0	16.50	1.16	16.49
142170	~3421	Pilbara	Sanukitoid-like rocks	0.292	0.021	1	0.49	69.79	40.2	15.11	1.27	15.73
235917	~2948	Pilbara	High-Mg diorite suite	0.211	0.032	2	0.50	65.99	49.0	39.87	1.55	21.83
142945	~2950	Pilbara	High-Mg diorite suite	0.232	0.015	1	0.42	66.69	51.8	16.49	1.39	16.97
142260	~2950	Pilbara	High-Mg diorite suite	0.177	0.016	1	0.51	61.86	54.0	22.54	1.44	18.47
142347	2498 ± 5	Pilbara	High-Mg diorite suite	0.133	0.016	1	0.63	59.33	53.1			
142257	~2950	Pilbara	High-Mg diorite suite	0.161	0.018	1	0.39	64.22	59.3	15.16	1.33	16.07
227869	~2660	Yilgarn	High La/Th (high Ni) BFG	0.197	0.020	1	0.52	49.17	74.3	49.32	1.91	22.27
227873	~2660	Yilgarn	High La/Th (high Ni) BFG	0.176	0.026	1	0.59	49.39	73.2	34.60	1.82	21.28
223149	~2660	Yilgarn	High La/Th (high Ni) BFG	0.137	0.020	1	0.60	50.67	71.7	21.46	1.49	20.03
505567	~2660	Yilgarn	High La/Th (high Ni) BFG	0.164	0.019	1	0.48	51.80	69.0	31.46	1.77	21.21
505652	~2660	Yilgarn	High La/Th (high Ni) BFG	0.146	0.021	1	0.51	52.90	76.2	19.44	1.48	17.93
229900	~2660	Yilgarn	High La/Th (high Ni) BFG	0.157	0.022	1	0.51	61.02	65.2	30.08	1.83	20.55
228046	~2660	Yilgarn	High La/Th (high Ni) BFG	0.208	0.024	1	0.43	62.76	62.6	34.88	1.16	21.91
223100	~2660	Yilgarn	High La/Th (high Ni) BFG	0.221	0.024	1	0.42	64.00	59.5	22.71	1.33	20.20
229913	2666 ± 7	Yilgarn	High La/Th (high Ni) BFG	0.236	0.020	1	0.40	65.68	57.7	32.91	1.63	22.50
223123	~2660	Yilgarn	High La/Th (high Ni) BFG	0.213	0.025	1	0.38	66.62	57.7	35.49	1.92	22.00
223112	~2660	Yilgarn	High La/Th (high Ni) BFG	0.210	0.026	1	0.34	67.22	55.6	31.17	1.77	20.22
223146	~2660	Yilgarn	High La/Th (high Ni) BFG	0.280	0.028	1	0.25	68.48	51.8	27.25	1.83	20.18

Table 3.1 continued:

Sample	Age Ma	Location	Suite	δ^{49}Ti ‰	95% ci ‰	n	TiO$_2$ wt%	SiO$_2$ wt%	Mg#	(La/Yb)$_N$	(Dy/Yb)$_N$	λ$_1$
223143	~2660	Yilgarn	High La/Th (high Ni) BFG	0.286	0.025	1	0.22	69.29	51.5	39.61	2.80	20.39
223157	~2660	Yilgarn	High La/Th (low Ni) BFG	0.157	0.024	1	0.71	51.18	66.3	22.32	1.64	19.86
229901	~2660	Yilgarn	High La/Th (low Ni) BFG	0.126	0.020	1	0.59	56.95	58.1	14.03	1.10	16.70
227885	~2660	Yilgarn	High La/Th (low Ni) BFG	0.123	0.020	1	0.57	58.89	60.5	19.48	1.36	18.89
211546	~2660	Yilgarn	High La/Th (low Ni) BFG	0.233	0.018	1	0.36	65.26	52.6	37.71	1.78	20.86
230891	~2660	Yilgarn	High La/Th (low Ni) BFG	0.207	0.020	1	0.40	66.78	54.1	30.76	1.54	21.57
211545	~2660	Yilgarn	High La/Th (low Ni) BFG	0.233	0.020	1	0.36	67.25	53.6	36.50	1.83	21.88
223070	~2660	Yilgarn	High La/Th (low Ni) BFG	0.268	0.020	1	0.28	68.46	53.3	38.32	2.00	21.34
227874	~2690	Yilgarn	Low La/Th BFG	0.182	0.025	1	0.60	43.77	74.1	24.47	1.90	19.74
501922	~2690	Yilgarn	Low La/Th BFG	0.180	0.021	1	0.82	50.50	67.1	24.60	1.75	19.68
505465	~2690	Yilgarn	Low La/Th BFG	0.108	0.023	1	0.73	50.80	68.3	10.57	1.37	14.28
230733	~2690	Yilgarn	Low La/Th BFG	0.139	0.021	1	0.62	58.59	58.7	13.00	1.18	15.79
224582	~2690	Yilgarn	Low La/Th BFG	0.170	0.020	1	0.54	60.53	66.5	17.15	1.26	17.03
224513	~2690	Yilgarn	Low La/Th BFG	0.199	0.022	1	0.45	61.67	57.6	15.24	1.10	15.21
230774	~2690	Yilgarn	Low La/Th BFG	0.186	0.020	1	0.49	64.74	55.2	21.90	1.51	18.27
230787	~2690	Yilgarn	Low La/Th BFG	0.202	0.023	1	0.42	65.66	55.7	34.25	1.60	21.82
233603	~2690	Yilgarn	Low La/Th BFG	0.259	0.021	1	0.36	69.10	51.6	45.15	1.86	22.48
223185	~2690	Yilgarn	Low La/Th BFG	0.291	0.021	1	0.28	70.05	50.5	33.54	2.02	21.10
AMT 03	2130 ± 2	São Francisco	Alto Maranhão suite	0.224	0.023	1	0.58	62.42	58.4	44.41	2.12	21.84
AMT 02	2130 ± 2	São Francisco	Alto Maranhão suite	0.231	0.023	1	0.51	64.20	58.0	29.38	1.39	20.82
AMT 01a	2130 ± 2	São Francisco	Alto Maranhão suite	0.229	0.023	1	0.47	66.65	47.4	12.94	1.16	16.23
AMT 01b	2130 ± 2	São Francisco	Alto Maranhão suite	0.223	0.024	1	0.45	67.18	49.9			19.41
MAJF 51b	2117 ± 24	São Francisco		0.144	0.018	1	0.74	60.32	48.5	8.54	1.17	11.32

Table 3.1 continued:

Sample	Age Ma	Location	Suite	$\delta^{49}Ti$ ‰	95% ci ‰	n	TiO_2 wt%	SiO_2 wt%	Mg#	$(La/Yb)_N$	$(Dy/Yb)_N$	λ_1
MAJF 42	2114 ± 10	São Francisco		0.133	0.045	2	0.54	62.91	58.6	23.54	1.84	18.27
RA1	425 ± 1.5	Scotland	Rogart pluton	0.143	0.023	1	1.13	47.57	70.0	57.64	2.55	24.20
RA2	425 ± 1.5	Scotland	Rogart pluton	0.214	0.022	1	0.50	57.20	81.4	55.74	2.39	24.70
RT1	425 ± 1.5	Scotland	Rogart pluton	0.260	0.023	1	0.77	62.98	56.9	29.38	1.77	19.79
RHG2	425 ± 1.5	Scotland	Rogart pluton	0.300	0.023	1	0.63	67.04	55.0	27.75	1.79	19.03
SR2	425 ± 3	Scotland	Strontian pluton	0.150	0.004	2	1.50	48.34	68.9	19.68	1.78	18.67
SR3	425 ± 3	Scotland	Strontian pluton	0.165	0.015	2	0.78	63.23	55.3	31.60	2.04	18.88
SR4	425 ± 3	Scotland	Strontian pluton	0.176	0.023	1	0.76	63.83	54.4	25.51	1.52	18.65

range at the upper end of this trend of 66.7 to 69.8 wt% SiO_2, and consequently have relatively high $\delta^{49}Ti$ values of 0.227 ± 0.021‰ to 0.299 ± 0.023‰. The Paleozoic high Ba-Sr granite suites cover a similar $\delta^{49}Ti$ range to the Archean and Paleoproterozoic sanukitoids, varying between 0.143 ± 0.023‰ and 0.300 ± 0.023‰. Appinites from both the Rogart and Strontian plutons have indistinguishable $\delta^{49}Ti$ values of 0.143 ± 0.023‰ and 0.158 ± 0.022‰ respectively, similar to the more primitive sanukitoid samples.

3.4. Discussion

3.4.1. Effects of alteration, metamorphism and post-emplacement processes

The majority of Archean and Paleoproterozoic samples have experienced later metamorphism and/or alteration that may have affected their chemical and isotopic compositions (Bruno et al., 2021; Moreira et al., 2018; Smithies et al., 2019, 2004). Titanium is a HFSE with very low mobility in aqueous fluids (even at high salinities, see Rustioni et al., 2021) so protolith $\delta^{49}Ti$ values are expected to be largely unaffected by metamorphism and alteration involving aqueous fluids and brines. This is supported by the absence of correlation between $\delta^{49}Ti$ and LOI (loss on ignition), Ce anomaly (Ce/Ce*) and fluid mobile elements (e.g. Pb) in the samples studied here (fig. 3.2). Silicate melts, on the other hand, can transport significant amounts of Ti, and partial melting in the presence of residual Ti-bearing oxides can cause Ti isotope fractionation and produce melts with high $\delta^{49}Ti$ (e.g. Klaver et al., 2024). Two samples (MAJF 42 and 51b) from the São Francisco Paleocontinent have migmatitic textures showing they have undergone partial melting during metamorphism (Bruno et al., 2021). At comparable SiO_2 contents (60 – 63 wt%) these samples have $\delta^{49}Ti$ values nearly 0.1‰ lower than the unmigmatised Alto Maranhão suite from nearby in the Mineiro Belt (fig. 3.1a). However, these samples still broadly plot on the same overall trend as the other sanukitoids and their geochemical compositions show no obvious evidence of significant melt extraction, so I consider their Ti isotope compositions to be robust. The Paleozoic high Ba-Sr granite suites have not been affected by any later metamorphism

(e.g. Fowler et al., 2008). The similarity of their Ti isotope compositions to those of the Archean and Paleoproterozoic sanukitoids therefore adds strength to the argument that $\delta^{49}Ti$ is not significantly affected by metamorphic processes.
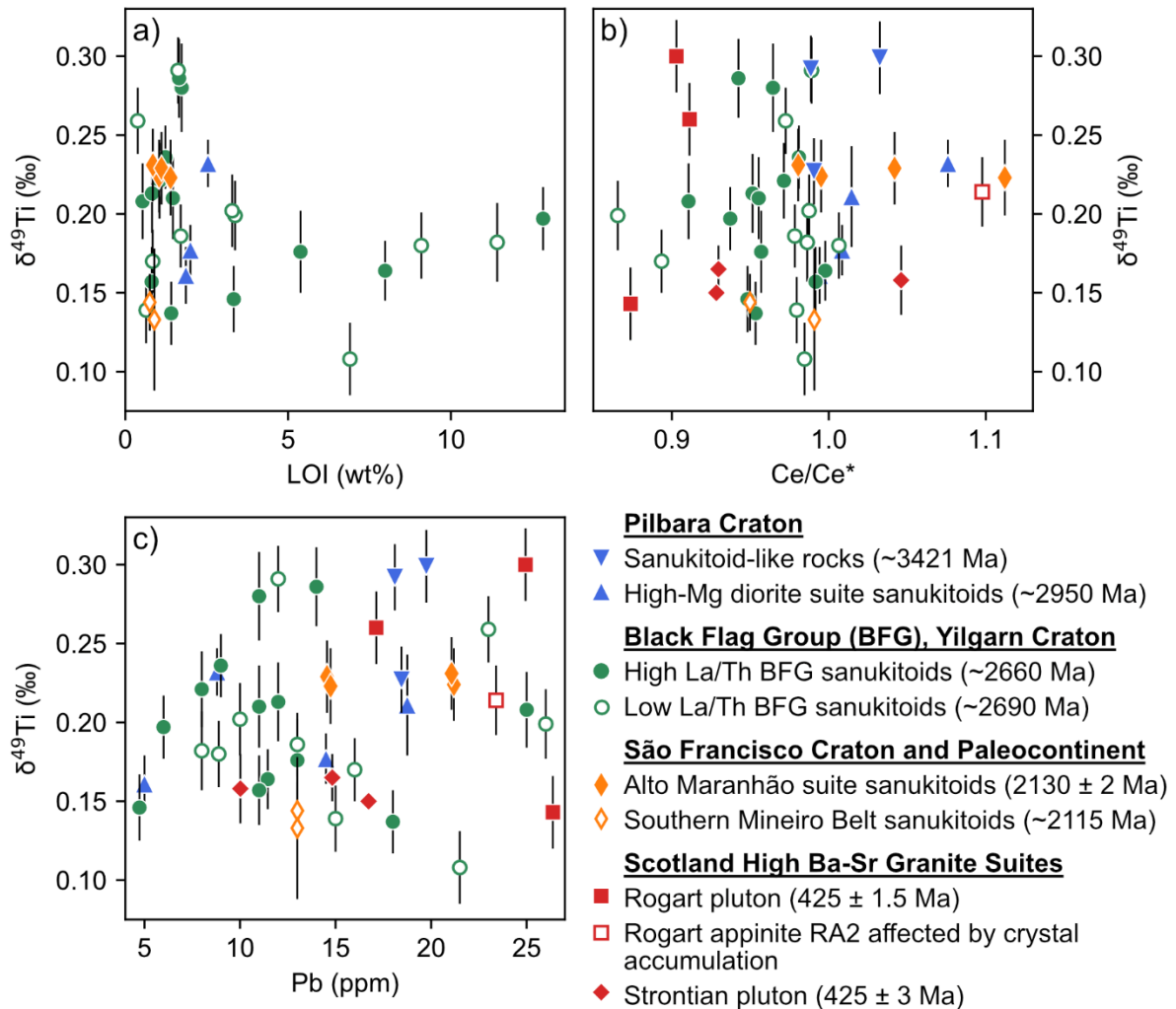
Figure 3.2: $\delta^{49}Ti$ (‰) vs a) loss on ignition (LOI) (wt%); b) Ce anomaly Ce/Ce* (= Ce$_N$ / (La$_N$ * Pr$_N$)$^{1/2}$, where REE concentrations are normalised to the CI chondrite values from O'Neill, 2016). Removal of Ce by aqueous fluids during alteration decreases Ce/Ce*; c) Pb (ppm). Uncertainty in $\delta^{49}Ti$ is shown as the 95% confidence interval.

Sample RA2 from the Rogart pluton has unusually high MgO and CaO for its SiO$_2$ content. This composition suggests that it has been affected by pyroxene-dominated crystal accumulation and may be significantly displaced from a true melt composition. No significant Ti isotope fractionation between pyroxene and silicate melt is expected (Leitzke et al., 2018; Rzehak et al., 2021; W. Wang et al., 2020), but RA2 shows slightly elevated $\delta^{49}Ti$ and may have been affected by accumulation of other minerals; hence, it is excluded from further discussion.

3.4.2. Differentiation of sanukitoids

While less evolved sanukitoids and appinites (< 58 wt% SiO₂) show scattered but fairly constant δ⁴⁹Ti values between 0.1 and 0.2‰, the δ⁴⁹Ti values of the more evolved sanukitoids are correlated with indices of magma differentiation (SiO₂, MgO; fig. 3.1), with the highest δ⁴⁹Ti measured in the most differentiated samples. The onset of this δ⁴⁹Ti increase coincides with TiO₂ content beginning to decrease (fig. 3.1c). This observation supports the conclusion of previous studies that Ti isotope fractionation during magma differentiation is primarily caused by fractional crystallisation of Fe-Ti oxides such as titanomagnetite and ilmenite (e.g. Deng et al., 2019b; Hoare et al., 2020; Millet et al., 2016).

Increasing δ⁴⁹Ti during differentiation has been observed in alkaline, tholeiitic and calc-alkaline magma series but the magnitude of this increase depends on the composition and abundance of Fe-Ti oxides, which themselves are a reflection of the TiO₂ concentration, water content and oxidation state of the magma (Aarons et al., 2020; Deng et al., 2019b; Hoare et al., 2022, 2020; Johnson et al., 2023; Millet et al., 2016). Of these magma series, the calc-alkaline series shows the smallest increase in δ⁴⁹Ti during differentiation (fig. 1.16) due to crystallisation of relatively small amounts of Ti-poor oxides and removal of significant proportions of Ti from the melt by silicates such as clinopyroxene, which do not significantly fractionate Ti isotopes (Hoare et al., 2020; Johnson et al., 2023). Sanukitoid magmas tend to follow a differentiation pathway akin to calc-alkaline magmas (e.g. de Oliveira et al., 2009; Martin et al., 2009). However, they display an even more muted δ⁴⁹Ti increase during differentiation than the modern calc-alkaline suites (fig. 3.3a). This feature is also observed in the Paleoarchean sanukitoid-like rocks and Paleozoic high Ba-Sr granite suites (see section 3.4.2.1 for a detailed discussion of the differentiation of the high Ba-Sr granite suites). I modelled the Ti isotope composition of evolving sanukitoid magmas using Rayleigh fractionation and the BFG sanukitoid suite, which is unique among sanukitoid occurrences as it covers a large and continuous range in SiO₂ content. The value of the bulk mineral-melt Ti isotope fractionation factor ($\alpha_{solid-melt}$) and the 2σ uncertainty were determined by weighted curve fitting to the measured δ⁴⁹Ti and calculated fraction of Ti remaining in the melt (F_{melt}^{Ti}) of the samples (a detailed description of the method used is provided in Appendix D). The modelled $\alpha_{solid-melt}$ values for the BFG

subgroups are distinctly closer to 1 than those of modern calc-alkaline suites at comparable SiO_2 contents (Hoare et al., 2020; Johnson et al., 2023) (fig. 3.3b), thus indicating that the magnitude of Ti isotope fractionation during differentiation of sanukitoids is smaller than that of modern calc-alkaline magmas.
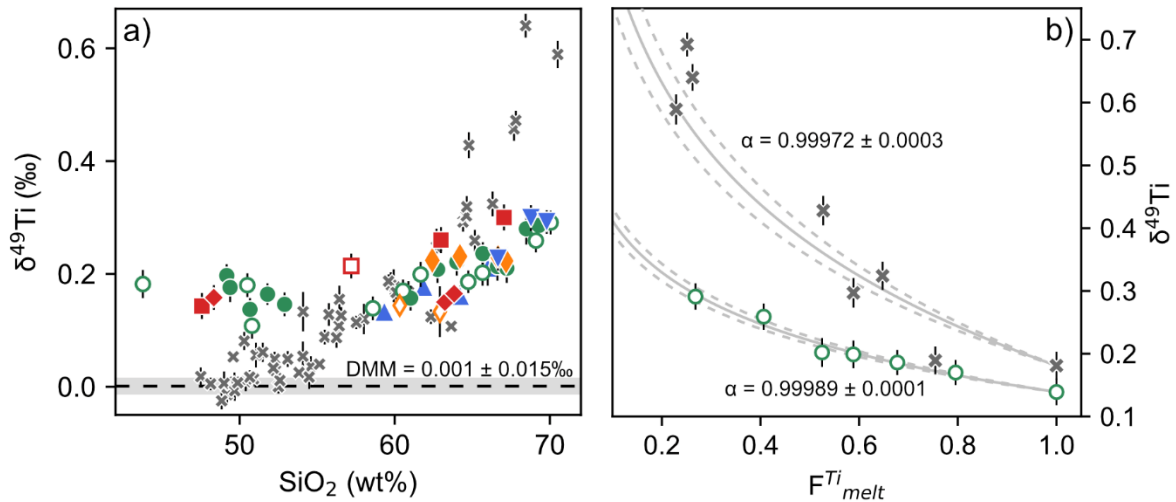
Pilbara Craton
▼ Sanukitoid-like rocks (~3421 Ma)
▲ High-Mg diorite suite sanukitoids (~2950 Ma)

Black Flag Group (BFG), Yilgarn Craton
● High La/Th BFG sanukitoids (~2660 Ma)
○ Low La/Th BFG sanukitoids (~2690 Ma)

Modern Magmatic Suites
✖ Calc-alkaline suites

São Francisco Craton and Paleocontinent
◆ Alto Maranhão suite sanukitoids (2130 ± 2 Ma)
◇ Southern Mineiro Belt sanukitoids (~2115 Ma)

Scotland High Ba-Sr Granite Suites
■ Rogart pluton (425 ± 1.5 Ma)
□ Rogart appinite RA2 affected by crystal accumulation
◆ Strontian pluton (425 ± 3 Ma)

Figure 3.3: Comparison between Archean and Paleoproterozoic sanukitoid suites and modern calc-alkaline suites. a) $\delta^{49}Ti$ (‰) vs SiO_2 (wt%). Calc-alkaline suite data are from the New Britain arc (Millet and Dauphas, 2014), the Mariana arc (Millet et al., 2016), Agung volcano (Millet et al., 2016), the Tonga-Kermadec arc (Mandl et al., 2019), Santorini volcano (Hoare et al., 2020) and Rindjani Volcano (Johnson et al., 2023). DMM $\delta^{49}Ti$ value is from Deng et al. (2023) and the 2 standard error uncertainty is shown by the grey rectangle. b) $\delta^{49}Ti$ (‰) vs the fraction of Ti remaining in the melt (F_{melt}^{Ti}) for the low La/Th subgroup of the Black Flag Group sanukitoids and for Santorini. Rayleigh isotope fractionation models are shown in grey, with the dashed lines showing the 2σ uncertainty. Santorini $\delta^{49}Ti$ data and $\alpha_{solid-melt}$ are from Hoare et al. (2020).

This difference is best explained by the fact that fractionating mineral assemblages in sanukitoids and their analogue suites are dominated by amphibole (Fowler et al., 2001; Seixas et al., 2013; Smithies et al., 2019; Smithies and Champion, 2000). This contrasts with the calc-alkaline differentiation suites for which Ti isotope data are available, which contain either no (Agung, Santorini) or "trace" amounts (Rindjani) of hornblende (Johnson et al., 2023). Up to ~2 wt% TiO_2 can be incorporated in

octahedral sites in igneous hornblende (e.g. Makino and Tomita, 1989). It is therefore expected to have lower δ^{49}Ti than melt, as confirmed by Mandl (2019) who measured a $\Delta^{49}Ti_{amphibole-melt}$ of -0.210‰ at ~775°C. Mass balance calculations by Greber et al. (2021) also support amphibole having lower δ^{49}Ti than melt, with $\Delta^{49}Ti_{amphibole-melt}$ of -0.30‰ at ~780°C. Taken together, these results indicate that hornblende fractionates Ti isotopes more strongly than other Ti-bearing silicates such as clinopyroxene (Rzehak et al., 2021; W. Wang et al., 2020), but not as strongly as Fe-Ti oxides (e.g. Hoare et al., 2022). This implies that removal of a significant proportion of Ti by hornblende instead of oxides would reduce Ti isotope fractionation during differentiation and increase the bulk $\alpha_{solid-melt}$ to be closer to 1. Hornblende is proposed to be an early crystallising phase in the BFG (Smithies et al., 2019, 2018). The absence of clear correlation between δ^{49}Ti and SiO$_2$ or MgO contents in pre-oxide saturation (SiO$_2$ < 58 wt, MgO > 5.5 wt%) samples (figs. 3.1a and b) further suggests that hornblende fractional crystallisation did not cause significant Ti isotope fractionation in the BFG. I therefore propose that the more muted δ^{49}Ti increase seen during sanukitoid magma differentiation is due to removal of significant proportions of Ti by hornblende with limited associated isotope fractionation.

Hoare et al. (2020) found that δ^{49}Ti starts to increase at higher Mg# (= 100 * Mg / [Mg + Fe^{2+}]) in more water-rich, oxidised arc magmas because these conditions promote earlier oxide saturation. As discussed earlier, this inflection in sanukitoid δ^{49}Ti marks the onset of Fe-Ti oxide crystallisation, so this relationship can provide insights into the water content and oxidation of sanukitoid parental magmas. Sanukitoid δ^{49}Ti starts to increase at high Mg# (~60 – 70), suggesting early oxide saturation relative to modern arc suites (fig. 3.4). This implies that sanukitoid parental magmas had high water contents and oxygen fugacity (fO$_2$) comparable to modern arc magmas. This conclusion is in agreement with the findings of de Oliveira et al. (2010) and do Nascimento et al. (2023, 2021) from mineral chemistry that sanukitoid parental magmas contained > 7wt% H$_2$O and had fO$_2$ of NNO +0.3 to NNO +2.5 (log units relative to the nickel-nickel oxide buffer). High magma Ti and Fe contents may also drive earlier oxide saturation, but as the primitive sanukitoids here have low TiO$_2$ contents (< 0.9 wt%) this is unlikely to be an important factor. Both early oxide

fractionation and abundant hornblende crystallisation are consistent with sanukitoid parental magmas being water-rich and as such they require a H_2O-rich mantle source.
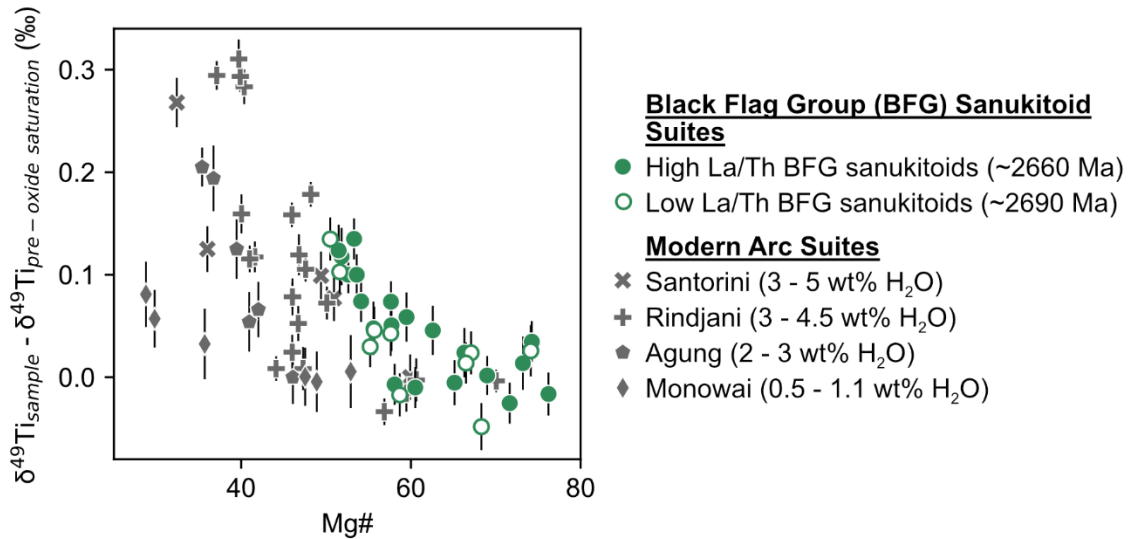
Figure 3.4: $\delta^{49}Ti$ (‰) vs Mg# of the Black Flag Group sanukitoids and modern arc magmatic suites, based on figure 8 from Hoare et al. (2020). The y-axis is plotted as sample $\delta^{49}Ti$ minus the weighted mean $\delta^{49}Ti$ of pre-oxide saturation samples (where $\alpha_{solid-melt} \approx 1$) from that suite, to enable better comparison between suites. Modern arc magmatic suites are from Santorini volcano and Monowai seamount (Hoare et al., 2020), Rindjani Volcano (Johnson et al., 2023) and Agung Volcano (Millet et al., 2016).

3.4.2.1. Differentiation of the high Ba-Sr granite suites

The two high Ba-Sr granite suite plutons show distinct trends in $\delta^{49}Ti$ during differentiation (fig. 3.5a). The Rogart samples show a similar muted increase in $\delta^{49}Ti$ during differentiation to the sanukitoids, but displaced to slightly higher $\delta^{49}Ti$ at a given SiO_2 content. Negative correlation of $^{143}Nd/^{144}Nd$ with SiO_2 is observed in the Rogart pluton and is proposed to be caused by assimilation of Moine metasediments (Fowler et al., 2008). However, a $\delta^{49}Ti$-Nd isotope binary mixing model of bulk Moine metasediments with Rogart appinite shows that this process alone cannot explain the $\delta^{49}Ti$ increase during differentiation (fig. 3.5b). The $\delta^{49}Ti$ increase in the Rogart high Ba-Sr granite pluton therefore likely records fractional crystallisation of significant amphibole alongside Fe-Ti oxides like the Archean and Paleoproterozoic sanukitoids. The small displacement to higher $\delta^{49}Ti$ may be due to the Rogart magmas having slightly higher TiO_2 contents than the sanukitoids analysed here (fig. 3.1c), and as a result crystallising slightly more abundant and/or Ti-rich oxides.
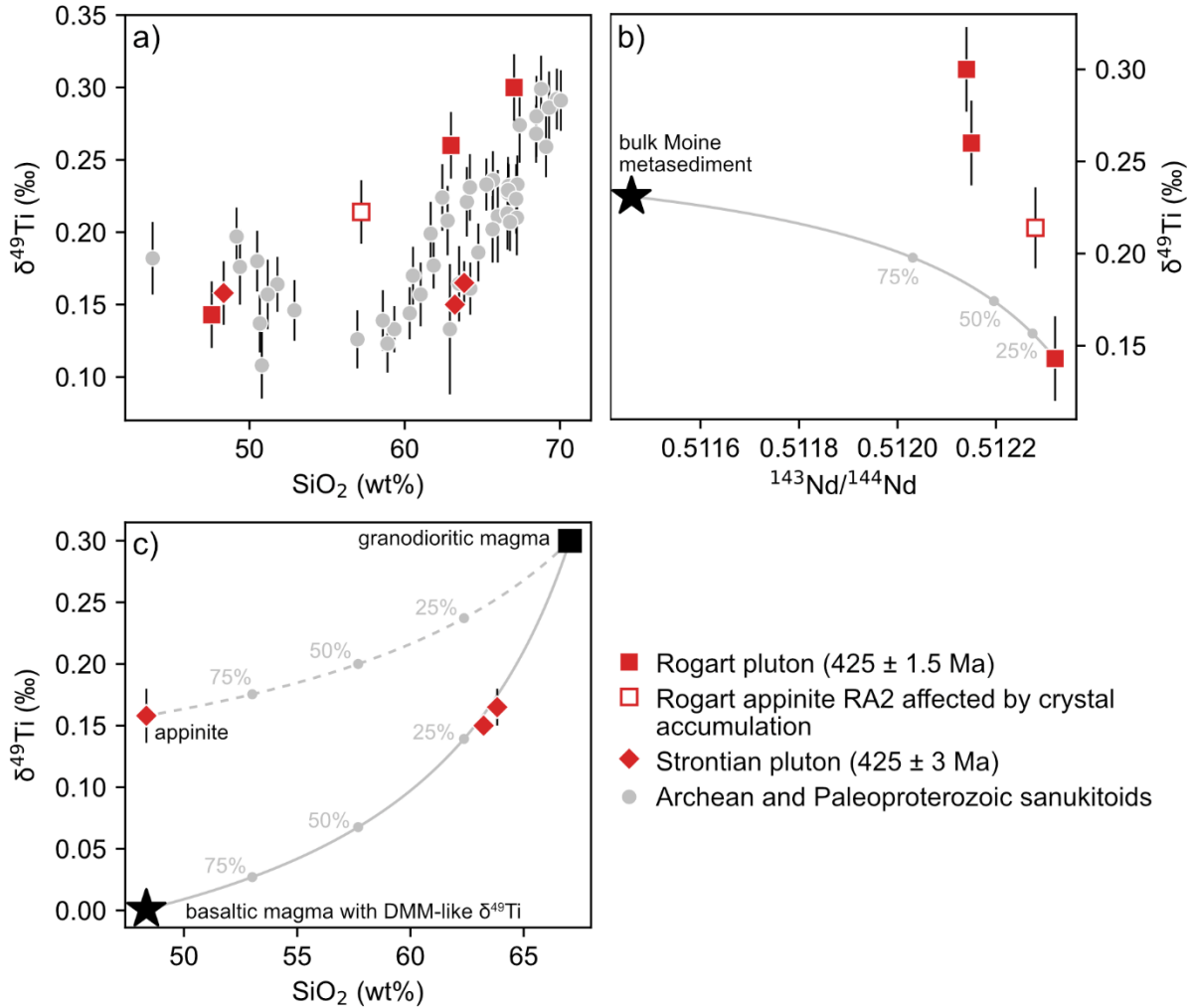
Figure 3.5: a) $\delta^{49}Ti$ (‰) vs SiO₂ (wt%) for the Rogart and Strontian plutons and Archean and Paleoproterozoic sanukitoids. b) Ti-Nd isotope binary mixing model between appinite from the Rogart pluton (RA1) and bulk Moine metasediment. Moine metasediment $^{143}Nd/^{144}Nd$ (0.51146) is from Fowler et al. (2008), Nd (27 ppm) and Ti (3716 ppm) concentrations are global subducting sediment (GLOSS) values from Plank & Langmuir (1998), and $\delta^{49}Ti$ is the weighted mean of Paleozoic sediments (0.231‰, Deng et al., 2019b; Saji et al., 2023). c) $\delta^{49}Ti$-SiO₂ binary mixing models between granodioritic magma (RHG2) and appinitic magma (SR2) (dashed line), and between granodioritic magma and N-MORB-like basaltic magma (solid line). The $\delta^{49}Ti$ of the basaltic magma with DMM-like $\delta^{49}Ti$ is the average N-MORB value from Klaver et al. (2024) of 0.001‰.

In contrast, $\delta^{49}Ti$ remains constant during differentiation of the Strontian pluton, and at ~63 wt% SiO₂ it has $\delta^{49}Ti$ ~0.1‰ lower than in the Rogart pluton (fig. 3.5a). Trace element concentrations in titanite and apatite from Strontian granites record a late mixing event with a mafic magma (Bruand et al., 2014). The mafic magma would likely have lower $\delta^{49}Ti$ and higher TiO₂ content than the granitic magma it is mixing with, so late mixing with a mafic magma may explain the difference between the Ti isotope systematics of the Rogart and Strontian plutons. Binary mixing models show that

mixing between a granodioritic magma and a basaltic magma with similar Ti isotope composition to the DMM ($\delta^{49}Ti$ = 0.001 ± 0.015‰, Klaver et al., 2024) can reproduce the Ti isotope compositions of the Strontian granodiorites, whereas mixing of a granodioritic magma with appinite cannot (fig. 3.5c).

3.4.3. Formation of sanukitoid parental magmas
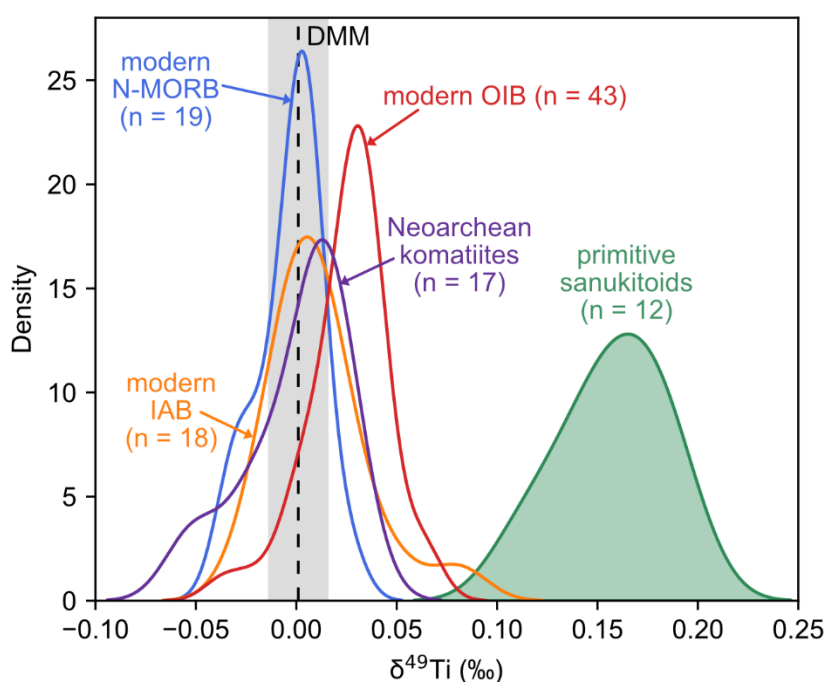
Figure 3.6: Kernel density plots comparing the distribution of primitive (pre-oxide saturation) sanukitoid $\delta^{49}Ti$ (‰) to other primitive terrestrial magmas – modern N-MORB, ocean island basalts (OIB) and island arc basalts (IAB), and Neoarchean komatiites. Primitive terrestrial magma $\delta^{49}Ti$ data are from Deng et al. (2018a, 2019b, 2023), Greber et al. (2017); Hoare et al. (2020), A.C. Johnson et al. (2019, 2023), Millet & Dauphas (2014), Millet et al. (2016) and Zhao et al. (2020). The DMM $\delta^{49}Ti$ value is from Klaver et al. (2024) and the 2 standard error uncertainty is shown by the grey rectangle.

Sanukitoid and appinite samples with SiO_2 < 58 wt% and MgO > 5.5 wt% display near constant, if slightly scattered, Ti isotope compositions. These samples precede Fe-Ti oxide saturation (fig. 3.1) and their Ti isotope compositions were not affected by amphibole crystallisation. Their $\delta^{49}Ti$ values have therefore not been affected by fractional crystallisation and are likely representative of the Ti isotope composition of their parental melts. The $\delta^{49}Ti$ values of primitive sanukitoids range from 0.108 ± 0.023‰ to 0.197 ± 0.020‰. No Ti isotope fractionation is expected during partial

melting of typical mantle lithologies (i.e. lherzolite, harzburgite) due to the absence of minerals such as Ti-bearing oxides (Millet et al., 2016), so melts would be expected to have δ^{49}Ti similar to the DMM (0.001 ± 0.015‰, Klaver et al., 2024) or intermediate between the DMM and primordial mantle (0.053 ± 0.005‰, Deng et al., 2023) for samples older than ~2.7 Ga. This is indeed the case for modern arc basalts, ocean island basalts (OIB), N- (normal-) MORB and Neoarchean komatiites (fig. 3.6). However, primitive sanukitoids display significantly heavy Ti isotope compositions compared to ambient mantle and its melting products (fig. 3.6). The mantle source of sanukitoids is widely considered to form by interaction between mantle peridotite and an incompatible element-enriched melt or aqueous fluid derived from recycled metabasite (e.g. Martin et al., 2009; Shirey and Hanson, 1984; Smithies and Champion, 2000; Stern et al., 1989). The high δ^{49}Ti of primitive sanukitoids indicates that the enriched component may therefore have had a heavy Ti isotope composition and/or that there was significant Ti isotope fractionation during partial melting of the putative metasomatised mantle source. Below, I use the Ti isotope data to test these competing models for sanukitoid formation.

3.4.3.1. Metabasite-derived aqueous fluids

As previously discussed, sanukitoid parental magmas were water-rich, requiring a H_2O-rich mantle source which may have been created through metasomatism of peridotite by aqueous fluids or silicate melts. I first investigate whether addition of metabasite-derived aqueous fluid alone to ambient mantle can explain the high δ^{49}Ti of primitive sanukitoids.

Titanium is a HFSE and is highly insoluble in aqueous fluids, even at high salinities (e.g. Rustioni et al., 2021). Hence, very little Ti is expected to be transferred from metabasites to fluids even in the presence of residual rutile, preventing fluids from being able impart a distinct high δ^{49}Ti signature to the sanukitoid source. The low Ti content of aqueous fluids also means that no rutile or other phases containing significant amounts of Ti are stabilised during partial melting of aqueous fluid-fluxed mantle (Till et al., 2012). Aqueous fluid-fluxed peridotite melts formed at ~2.7 Ga should therefore have δ^{49}Ti indistinguishable from the late Archean ambient mantle (fig. 3.7, Klaver et al., 2024), which I estimate from the weighted mean of Neoarchean

komatiite δ⁴⁹Ti to be 0.001 ± 0.003‰ (2se, n = 17) (Deng et al., 2023; Greber et al., 2017). This is not what is observed for the primitive sanukitoids, hence demonstrating that addition of aqueous fluids alone cannot explain their high δ⁴⁹Ti signature.
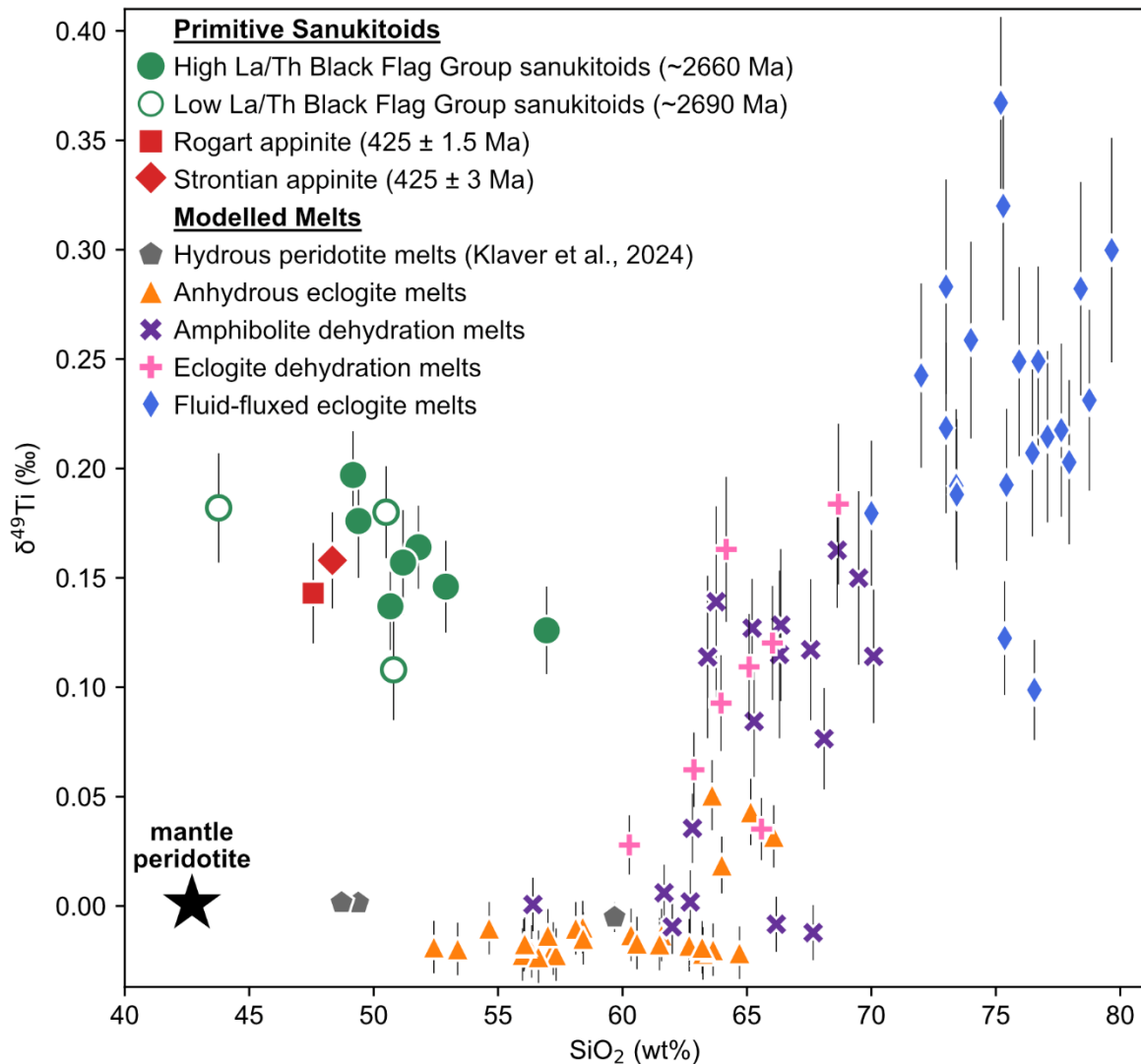
Figure 3.7: δ⁴⁹Ti (‰) vs SiO₂ (wt%) for primitive (pre-oxide saturation) Neoarchean sanukitoid samples and modelled partial melts of hydrous peridotite (Klaver et al., 2024) and metabasite. The δ⁴⁹Ti of the modelled melts was calculated using a mass balance approach via the method in Appendix E. Uncertainty in measured sanukitoid δ⁴⁹Ti is shown as the 95% confidence interval. Uncertainty in modelled partial melt δ⁴⁹Ti is shown as the 2σ, calculated by linear uncertainty propagation. The black star is Neoarchean mantle peridotite, for which δ⁴⁹Ti is estimated from the weighted mean of Neoarchean komatiites (0.001 ± 0.003‰, 2se, n = 17) (Deng et al., 2023; Greber et al., 2017). SiO₂ data for the modelled metabasite melts are from Carter et al. (2015), Kessel et al. (2005), Laurie and Stevens (2012), Martin & Hermann (2018), Massonne and Fockenberg (2022), Pertermann and Hirschmann (2003), Schmidt et al. (2004), Sen and Dunn (1994), Sisson and Kelemen (2018), Spandler et al. (2008), Wolf and Wyllie (1994), Yaxley and Green (1998) and Zhang et al. (2013).

3.4.3.2. Metabasite-derived partial melts

Silicate melts have much higher Ti concentrations than aqueous fluids and hence have a greater capacity to impart a distinct Ti isotope signature onto the mantle. In eclogites Ti is mainly hosted in Ti-bearing oxides (predominantly rutile), and in amphibolites significant amounts of Ti can also be found in amphibole. Minor amounts of Ti can be present in pyroxenes and garnet but these minerals do not significantly fractionate Ti isotopes (Rzehak et al., 2021; W. Wang et al., 2020). During metabasite partial melting, light Ti isotopes are preferentially retained in 6-fold coordinated sites in residual rutile ± amphibole, generating melts with higher δ^{49}Ti than the protolith. This phenomenon has been invoked to explain the Ti isotope compositions of Archean TTGs (Hoare et al., 2023; Z. J. Zhang et al., 2023) and some modern primitive arc magmas (Klaver et al., 2024). It is therefore possible that a metabasite melt component could be responsible for the high δ^{49}Ti of primitive sanukitoids.

I further investigate this hypothesis by modelling partial melting of eclogite and amphibolite. Specifically, I calculate the Ti isotope composition of experimental partial melts (see fig. 3.7 for references). $\Delta^{49}Ti_{melt-protolith}$ $(= \delta^{49}Ti_{melt} - \delta^{49}Ti_{protolith})$ was calculated using a mass balance approach following Klaver et al. (2024, 2021), and melt δ^{49}Ti was calculated using the average Neoarchean komatiite δ^{49}Ti (0.001 ± 0.003‰) as the metabasite protolith composition (see Appendix E for full method). I modelled three different metabasite partial melting scenarios:

1. Anhydrous eclogite melting, where there is no H_2O in the system.
2. Dehydration melting, where aqueous fluid is formed by the breakdown of hydrous minerals within the metabasite – amphibole in amphibolite and phengite or zoisite in eclogite – creating water-undersaturated conditions during melting.
3. Fluid-fluxed melting, where externally derived aqueous fluid creates water-saturated conditions during melting.

The results of this modelling are presented in Appendix F and figure 3.7.

Limited Ti isotope fractionation (δ^{49}Ti up to 0.051‰ at the smallest melt fractions) occurs during anhydrous eclogite melting, inconsistent with primitive sanukitoid data (fig. 3.7). This limited fractionation is due to two main factors. First, high temperatures

are required to cross the anhydrous solidus of eclogitic lithologies. For MORB-like compositions, this solidus lies between 1200 and 1350°C at 2 – 5 GPa (e.g. Pertermann and Hirschmann, 2003; Spandler et al., 2008). Equilibrium stable isotope fractionation scales with $1/T^2$ so these high temperatures restrict the magnitude of Ti isotope fractionation (e.g. Young et al., 2015). Second, rutile is significantly more soluble in silicate melts at high temperatures (Gaetani et al., 2008). As a result, rutile rapidly disappears from the eclogitic residue, shifting the balance of the Ti budget towards the melt and thus muting any isotope fractionation. Any Ti still in the residue is now hosted by clinopyroxene and garnet, both of which are expected to have a weak preference for incorporating heavy Ti isotopes (Leitzke et al., 2018; W. Wang et al., 2020). This fractionation results in melts generated in the absence of residual rutile having slightly lower $\delta^{49}Ti$ values than the metabasite protolith (fig. 3.7).

The presence of aqueous fluids lowers metabasite solidus temperatures significantly and hence promotes rutile stability (e.g. Gaetani et al., 2008). Phengite-bearing eclogite dehydration melting begins at ~970°C at 4 GPa (Massonne and Fockenberg, 2022), while zoisite-bearing eclogite dehydration occurs at < 1025°C (Skjerlie and Patiño Douce, 2002), meaning rutile remains stable at higher melt fractions during partial melting. Models of phengite-bearing eclogite dehydration melting show this results in melts with $\delta^{49}Ti$ values up to 0.184 ± 0.035‰, higher than anhydrous eclogite melts, and generates melts with comparable $\delta^{49}Ti$ to the primitive sanukitoids (fig. 3.7). Amphibolite dehydration melting, occurring at lower temperatures of 800 – 900°C at 1 – 2 GPa (Sen and Dunn, 1994; Zhang et al., 2013), generates melts with somewhat lower $\delta^{49}Ti$ up to 0.163 ± 0.023‰. The $\delta^{49}Ti$ of eclogite and amphibolite dehydration melts largely overlap (fig. 3.7), despite the main residual minerals hosting Ti (rutile and amphibole respectively) being different. While rutile fractionates Ti isotopes more strongly than amphibole, eclogite dehydration melting occurs at higher temperatures than amphibolite dehydration melting, restricting the overall magnitude of Ti isotope fractionation. These model results imply that amphibolite and eclogite dehydration melts might be suitable metasomatic agents to explain the high $\delta^{49}Ti$ of primitive sanukitoids.

Fluid-fluxed eclogite melting under water-saturated conditions lowers the MORB-eclogite solidus even further to 750 – 800°C at 2.2 – 4.5 GPa (e.g. Martin and

Hermann, 2018; Schmidt et al., 2004; Sisson and Kelemen, 2018). The combination of abundant residual rutile and relatively low melting temperatures leads to significant Ti isotope fractionation with melt δ^{49}Ti between 0.099 ± 0.020‰ and 0.367 ± 0.037‰, depending on the temperature and proportion of rutile in the protolith. These values are largely similar to those calculated by Klaver et al. (2024) but extend to heavier melt δ^{49}Ti due to the inclusion of experiments with higher proportions of residual rutile from Laurie and Stevens (2012). These results show that fluid-fluxed eclogite melting can readily generate melts with δ^{49}Ti comparable to and higher than primitive sanukitoids (fig. 3.7), and therefore mantle metasomatism by such melts would generate sanukitoid parental magmas enriched in heavy Ti isotopes.

Overall, the modelling demonstrates that the involvement of metabasite partial melt in the formation of sanukitoid parental magmas may be responsible for the heavy Ti isotope composition of primitive sanukitoids. However, the presence of aqueous fluid, either from the breakdown of hydrous minerals within metabasites or from an external source, is needed to generate melts with sufficiently high δ^{49}Ti.

3.4.3.3. Ti isotope fractionation during interaction with mantle peridotite

While significant Ti isotope fractionation occurs during metabasite melting, additional isotope fractionation may occur during interaction between the metabasite melts and mantle peridotite to form sanukitoid parental magmas. This interaction is generally thought to take place via a two-stage process where the mantle is metasomatised by metabasite melt and subsequently undergoes partial melting (e.g. Shirey and Hanson, 1984; Smithies and Champion, 2000), but a one-stage process where the metabasite melt assimilates peridotite has also been proposed (Rapp et al., 2010, 1999). Experimental studies show that interaction between metabasite melt and peridotite generally consumes olivine and the melt, and forms orthopyroxene and (if temperatures are low enough) phlogopite and/or sodic amphibole (e.g. pargasite) (e.g. Gervasoni et al., 2017; Prouteau et al., 2001; Rapp et al., 2010, 1999; Sen and Dunn, 1994). These results are consistent with suggestions that the LILE enrichment in some sanukitoids requires a phlogopite ± amphibole-bearing source (Heilimo et al., 2010; Kovalenko et al., 2005; Lobach-Zhuchenko et al., 2008). No Ti-bearing accessory

phases (e.g. oxides) were seen to form during the metabasite melt-peridotite reaction experiments, meaning that phlogopite and amphibole would be the main hosts of Ti in the sanukitoid mantle source. Pargasitic amphibole is the first phase to melt in this metasomatic assemblage, under both water-saturated and water-undersaturated conditions (Conceição and Green, 2004; Mengel and Green, 1989), so significant residual pargasite during sanukitoid parental magma genesis is unlikely. Phlogopite, on the other hand, is stable to higher temperatures and pressures than pargasite, particularly under water-saturated conditions when it can remain in the residue until > 100°C above the solidus (Conceição and Green, 2004). Multiple studies have proposed that a small amount of residual phlogopite during melting is needed to explain the LILE systematics of some sanukitoids, specifically their depletion in Rb alongside enrichment in Sr and Ba (Kovalenko et al., 2005; Laurent et al., 2011).

Titanium is predominantly incorporated into octahedral M2 sites in phlogopite but substitution into 4-fold coordinated sites may also be possible in Ti-rich compositions (e.g. Bendeliani et al., 2023). Similar to amphibole, at equilibrium the difference in Ti coordination is expected to give phlogopite lower δ^{49}Ti than co-existing silicate melt, consistent with data on a biotite mineral separate from the Kneeling Nun Tuff, which yielded $\Delta^{49}Ti_{biotite-melt}$ = -0.234 ± 0.060‰ at ~775°C (Mandl, 2019). While $\Delta^{49}Ti_{phlogopite-melt}$ is poorly constrained, this suggests that Ti isotope fractionation may occur during partial melting of metasomatised mantle peridotite if residual phlogopite is present. Titanium isotope fractionation during partial melting of phlogopite-bearing peridotite was modelled based on experiments from Condamine et al. (2016) (see Appendix E for method and Appendix F for results). Melts generated in equilibrium with small amounts (4 – 8 wt%) of residual phlogopite at 3 GPa and 1200 – 1300°C are up to 0.047 ± 0.012‰ (2sd) heavier than their metasomatised mantle protolith. While the melt compositions produced in these experiments are not analogous to parental sanukitoid magmas, these models demonstrate that the magnitude of Ti isotope fractionation due to residual phlogopite is small and will be limited by the low volume of phlogopite that can form from sodic metabasite melts (e.g. Prouteau et al., 2001). I therefore conclude that although small amounts of residual phlogopite in the sanukitoid mantle source can generate melts with higher δ^{49}Ti than their protolith, the magnitude of this fractionation is likely < 0.05‰. Hence, I consider

that formation of an isotopically heavy metabasite melt component in equilibrium with residual rutile ± amphibole is the main driver of high δ⁴⁹Ti in primitive sanukitoids.

3.4.3.4. Eclogite melts in the mantle source of sanukitoids
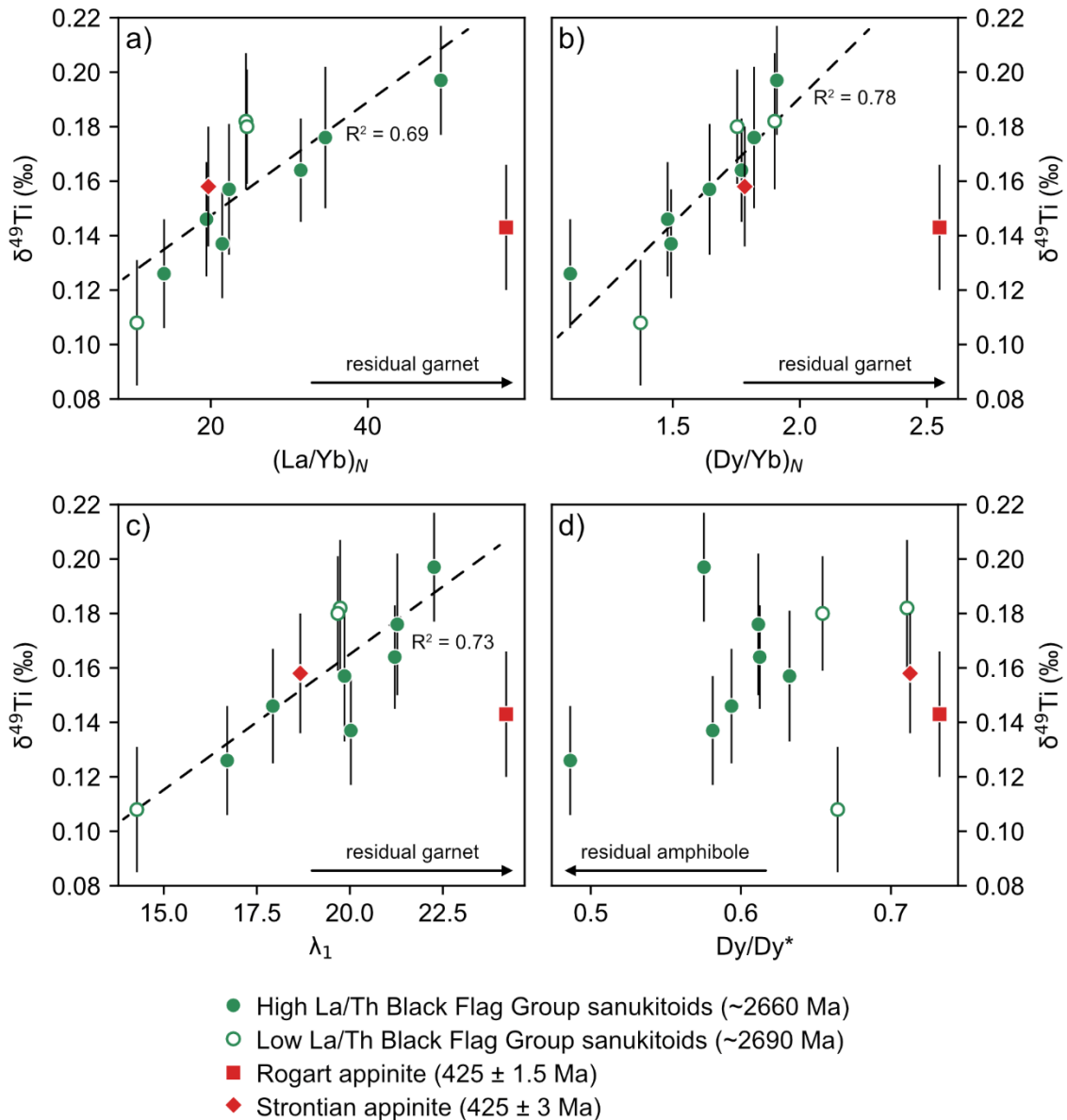
Figure 3.8: Primitive sanukitoid and appinite δ⁴⁹Ti (‰) vs a) (La/Yb)ₙ, b) (Dy/Yb)ₙ, c) λ₁ (O'Neill, 2016) and d) Dy/Dy (Davidson et al., 2013). The dashed lines are the least squares linear regressions of the Black Flag Group primitive sanukitoids and the Strontian appinite, with R² values for the regressions shown. REE concentrations are normalised to the CI chondrite values from O'Neill (2016).*

Both amphibolite and eclogite melts can match the Ti isotope fractionation observed in primitive sanukitoids. The δ⁴⁹Ti values of primitive sanukitoids, however, show

strong positive covariation with tracers of garnet fractionation such as the CI-chondrite normalised REE ratios $(La/Yb)_N$ and $(Dy/Yb)_N$ (figs. 3.8a and b). O'Neill (2016) demonstrated that polynomials can be fit to chondrite-normalised REE patterns to quantitatively describe their shape with shape coefficients (λ_n). λ_1 quantifies the steepness of REE patterns with higher values indicating a steeper slope. λ_1 is therefore a sensitive tracer of garnet fractionation, and positive covariation between λ_1 and $\delta^{49}Ti$ is also observed (fig. 3.8c). No such covariation is seen with tracers of amphibole fractionation like Dy/Dy^* $(=Dy_N / (La_N^{4/13} * Yb_N^{9/13})$, fig. 3.8d) which is a measure of the relative middle rare earth element (MREE) depletion $(Dy/Dy^* < 1)$ or enrichment $(Dy/Dy^* > 1)$ of chondrite-normalised REE patterns (Davidson et al., 2013). The samples with the highest $\delta^{49}Ti$ and $(La/Yb)_N$ also have the lowest Yb concentrations (fig. 3.9), demonstrating that this signature is associated with heavy rare earth element (HREE) depletion and hence most likely caused by retention of HREEs in residual garnet. I note that the covariations are only perturbed by the single Rogart appinite sample displaying elevated $(La/Yb)_N$, $(Dy/Yb)_N$ and λ_1. Such a steep REE pattern is likely due to the significant recycled sediment input to the Rogart pluton mantle source (Fowler et al., 2008). This strong correlation therefore implies that the heavy Ti isotope composition and the garnet signature in primitive sanukitoids share a common origin. In contrast there is no clear evidence for a link between high $\delta^{49}Ti$ and residual amphibole, suggesting that amphibolite is not a suitable source for the metabasite melt component in sanukitoids. The combined Ti isotope and trace element compositions of primitive sanukitoids thus favour the metasomatic agent being an eclogite melt formed in equilibrium with residual rutile and garnet. Critically, the Ti isotope composition of primitive sanukitoids implies that eclogite partial melting occurred during the late Archean.

However, sanukitoids are not pure eclogite melts, but rather magmas originating from a mantle metasomatised by such melts (e.g. Martin et al., 2009; Shirey and Hanson, 1984). The high $\delta^{49}Ti$ signature of the eclogite melts will hence be diluted by interaction with low $\delta^{49}Ti$ mantle (0.001 ± 0.003‰) and subsequent melting of the metasomatised source. It follows that the eclogite melt should have $\delta^{49}Ti$ significantly higher than the primitive sanukitoids: if not, and without significant additional Ti isotope fractionation due to residual phlogopite, the contribution of Ti from the mantle would have to be
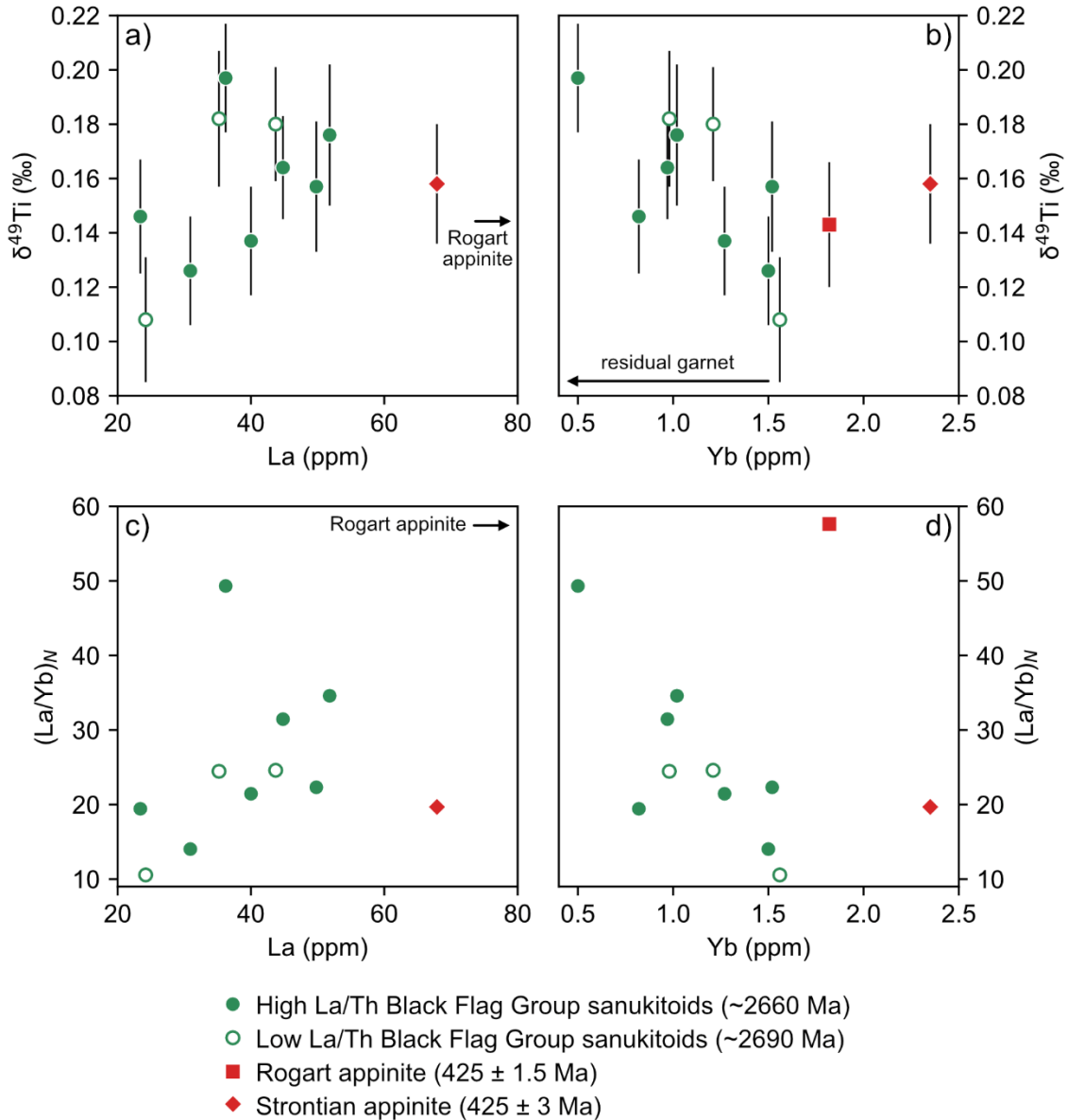
Figure 3.9: a) δ⁴⁹Ti (‰) vs La (ppm), b) δ⁴⁹Ti (‰) vs Yb (ppm), c) (La/Yb)ₙ vs La (ppm) and d) (La/Yb)ₙ vs Yb (ppm) for the primitive sanukitoids and appinites. Uncertainty in δ⁴⁹Ti is shown as the 95% confidence interval. For (La/Yb)ₙ, REE concentrations are normalised to the CI chondrite values from O'Neill (2016).

negligible for the high δ⁴⁹Ti signature of eclogite melts to be retained and transferred to the sanukitoid parental magmas. Sanukitoid major and trace element systematics rule out this scenario, with their high Mg# and Ni and Cr contents requiring a significant ultramafic peridotite component in their source (e.g. Martin et al., 2009). Hence, only eclogite melts with δ⁴⁹Ti significantly higher than the primitive sanukitoids can account for the data. My modelling shows that dehydration melting of eclogite generates melts with δ⁴⁹Ti that overlaps with the sanukitoids, whereas fluid-fluxed eclogite melting results in melts with δ⁴⁹Ti exceeding that of the sanukitoids. I thus favour mantle

peridotite metasomatised by fluid-fluxed eclogite melts as the likely origin of the heavy Ti isotope signature of primitive sanukitoids.

The Sr and Nd isotope compositions of the Paleozoic high Ba-Sr granite suites, and particularly of the Rogart pluton, are significantly enriched compared to the depleted mantle, suggesting contamination of their mantle source by subducted sediments (Fowler et al., 2008). Klaver et al. (2024) demonstrated that metasediment partial melting also generates melts enriched in heavy Ti isotopes due to the presence of residual Fe-Ti oxides during melting. However, the lower TiO_2 concentrations of metasediments than metabasites means that the resulting sediment melts will have lower Ti concentrations than metabasite melts, and generally the degree of Ti isotope fractionation during melting will be lower due to the lower abundance of residual Fe-Ti oxides. Ti stable isotopes are hence likely more sensitive to contributions from metabasite melts than metasediment melts, but they cannot definitively discriminate between metabasite and metasediment partial melt contributions for the Rogart pluton. However, the indistinguishable Ti isotope compositions of the Paleozoic appinites and the Archean and Paleoproterozoic primitive sanukitoids indicate they formed by similar processes.

3.4.4. Geodynamic Implications

Archean geodynamics are hotly debated and consequently multiple different geodynamic settings have been proposed for the formation of the sanukitoid mantle source (e.g. Bédard, 2006; Nebel et al., 2018; Stern et al., 1989). While geochemistry alone cannot pinpoint geodynamic setting, the results presented here provide new constraints on sanukitoid formation. The Ti stable isotope compositions of sanukitoids imply that they formed from water-rich, oxidised parental magmas that were likely generated from a mantle source metasomatised by fluid-fluxed eclogite partial melts. This result suggests that the mantle source of Archean and Paleoproterozoic sanukitoids must have formed in a geodynamic setting: 1) capable of recycling mafic rocks along low enough geothermal gradients (< ~12°C/km, e.g. Moyen, 2011) to high enough pressures (> ~1.8 GPa or > ~60 km depth, e.g. Chapman et al., 2019) to form eclogite; and 2) with a suitable external source of aqueous fluids to trigger fluid-fluxed melting.

On the present-day Earth, a Benioff-style subduction environment readily meets both these requirements. Numerous previous studies have proposed formation of the sanukitoid mantle source in a subduction setting (e.g. Martin et al., 2009; Smithies and Champion, 2000; Stern et al., 1989). Dehydration of abyssal serpentinites in the downgoing lithosphere is a source of voluminous aqueous fluid at subarc depths in modern subduction zones (Guillot and Hattori, 2013) and is proposed to trigger fluid-fluxed eclogite melting in modern arcs (e.g. Yogodzinski et al., 2017). I propose that the sanukitoid mantle source may have been formed by a similar process. The dynamics, and even the feasibility, of subduction in the late Archean are debated (e.g. van Hunen and Moyen, 2012), primarily because mantle potential temperatures may have been up to 150°C higher than present (e.g. Ganne and Feng, 2017). Numerical models show this would have caused higher geotherms in subduction zones and likely more frequent slab breakoff (e.g. van Hunen and van den Berg, 2008), both of which are conducive to the conditions for serpentinite-derived fluid-fluxed eclogite melting (e.g. Klaver et al., 2024). The constraints placed by an eclogitic protolith allow for slightly higher subduction geotherms of < ~12°C/km than present day (typically 5 – 8°C/km, e.g. Penniston-Dorland et al., 2015; Syracuse et al., 2010). As the mantle cooled during the Proterozoic and Phanerozoic, subduction geotherms decreased and subduction likely became more stable with less frequent slab breakoff (e.g. van Hunen and van den Berg, 2008), meaning conditions for fluid-fluxed eclogite melting in subduction zones may have become less common. This could explain why occurrences of sanukitoid magmatism became significantly rarer after the late Archean-early Proterozoic (Martin et al., 2009).

Alternatively, numerical models suggest that sinking crustal drips may have been capable of transporting hydrated, near-surface material to mantle depths along geothermal gradients < ~12°C/km (e.g. François et al., 2014; Sizova et al., 2015). Some models additionally favour a scenario where drips, triggered through lateral crustal movement and flow, are diverted and become asymmetric, creating a geometry that mimics, or may even represent, incipient subduction (Nebel et al., 2018). It is possible that such settings could generate eclogite, with dehydration of adjacent serpentinised komatiite/basalt releasing aqueous fluids to trigger fluid-fluxed eclogite melting (Hartnady et al., 2022; Tamblyn et al., 2023). Interaction of these melts with mantle peridotite could then generate the metasomatised mantle source of sanukitoids

(e.g. Nebel et al., 2018; Smithies et al., 2021). While crustal drips may provide an alternative setting to subduction for formation of the sanukitoid mantle source in the Archean, the viability of crustal drips (e.g. Korenaga, 2021) and their ability to transport hydrated, near-surface material to mantle depths (e.g. Roman and Arndt, 2020) are debated. If crustal drips were to only involve the lowermost crust (e.g. Johnson et al., 2014), which is likely to be largely anhydrous, it is difficult to reconcile with my results favouring fluid-fluxed eclogite melting due to the lack of an external source of aqueous fluids in this scenario. This is also the reason why I argue that my results are inconsistent with formation of the sanukitoid mantle source by delamination and then melting of dense lower crustal eclogites (Bédard, 2006).

My results therefore support the occurrence of fluid-fluxed eclogite melting and the formation of sanukitoid mantle sources by subduction-like processes at least as far back as ~2.7 Ga (the age of the oldest primitive sanukitoids in this study). In fact, as sanukitoids most likely formed by a two-stage process, the formation of the sanukitoid mantle source predates the age of magma emplacement, implying fluid-fluxed eclogite melting occurred before ~2.7 Ga. A later event – such as lithospheric extension (e.g. Laurent et al., 2014a; Smithies et al., 2019), slab breakoff (e.g. Heilimo et al., 2010) or lithospheric delamination (e.g. Kovalenko et al., 2005) – subsequently created a thermal anomaly and triggered melting of the metasomatised mantle to generate sanukitoid parental magmas. Furthermore, I note that the ~2950 Ma sanukitoids and ~3421 Ma sanukitoid-like rocks from the Pilbara Craton follow the same differentiation trend as the ~2670 Ma BFG sanukitoids. This observation may imply that they too formed by the same processes as the younger sanukitoids involving fluid-fluxed eclogite melting, but the lack of primitive samples prevents me from confidently extending my interpretations further back in the Archean. Nevertheless, this study clearly indicates that investigation of primitive sanukitoid and related magmas could prove useful for better understanding the geodynamic evolution of the Early Earth.

3.5. Conclusions

I present the Ti stable isotope compositions of late Archean-early Proterozoic sanukitoids and Paleozoic sanukitoid analogues. I use the δ^{49}Ti values of samples

formed before and after Fe-Ti oxide saturation to investigate the formation of the sanukitoid mantle source and the differentiation of sanukitoid magmas respectively. Post-Fe-Ti oxide saturation, sanukitoid suites show a more muted δ^{49}Ti increase during differentiation than currently analysed modern calc-alkaline suites. I ascribe this to the removal of significant proportions of Ti by hornblende, which fractionates Ti isotopes less than Fe-Ti oxides (Greber et al., 2021; Mandl, 2019). Furthermore, the onset of this δ^{49}Ti increase occurs at high Mg# compared to modern arc suites. This observation shows there was early oxide saturation in sanukitoid magmas and suggests that sanukitoid parental magmas had water contents and fO_2 at least as high as modern arc magmas.

Primitive (pre-Fe-Ti oxide saturation) sanukitoid samples have higher δ^{49}Ti values (0.11 – 0.20‰) than modern arc basalts, the depleted mantle and the BSE, which cannot be explained by aqueous fluids alone. Instead, the high δ^{49}Ti values of primitive sanukitoids require the involvement of a hydrous eclogite melt component formed in equilibrium with residual rutile. I favour generation of this metasomatic melt by fluid-fluxed eclogite partial melting, showing that both metabasite melts and aqueous fluids are important for sanukitoid formation. The Ti isotope compositions of primitive sanukitoids thus favour formation of the sanukitoid mantle source by a subduction-like process at least 2.7 Ga. The evidence supporting a subduction-like setting at ~2.7 Ga presented here gives further credence to models linking the widespread appearance of sanukitoids in the geological record to a global geodynamic transition.

4. Diverse petrogenesis of Neoarchean TTGs revealed by titanium stable isotopes

4.1. Abstract

Tonalite-trondhjemite-granodiorite (TTG) suites are the dominant constituent of Archean continental crust. Their trace element compositions show systematic variations typically interpreted to reflect metabasite partial melting at different pressures, with the low heavy rare earth element concentrations and high La/Yb, Sr/Y and Sr concentrations of some TTGs attributed to high pressure ($\geq$ 2 GPa) metabasite melting, and hence to deep subduction, in the Archean. Recent studies challenge this interpretation, and some suggest a subset of "high pressure" (HP) TTGs with very high Sr concentrations and Sr/Y instead formed by hornblende-dominated fractional crystallisation of metasomatised mantle-derived sanukitoid magmas. Titanium (Ti) stable isotopes are fractionated by crystallising Ti-bearing oxides and silicates (e.g. amphibole) during magma differentiation and can hence trace this proposed petrogenetic link between high-Sr HP TTGs and sanukitoids.

In this chapter I present the Ti stable isotope compositions (δ^{49}Ti) of Neoarchean (~2650 – 2700 million years ago) TTGs, including high-Sr HP TTGs, from the Eastern Goldfields Superterrane, Yilgarn Craton. They are spatially and temporally associated with the Black Flag Group (BFG) sanukitoids which are proposed to constitute the liquid line of descent linking these high-Sr HP TTGs to mantle-derived magmas, and were generated from a mantle source metasomatised by eclogite melts (Chapter 3). The high-Sr HP TTGs plot at the evolved end of the δ^{49}Ti differentiation trend and Rayleigh fractionation model for the BFG, providing strong support for formation of high-Sr HP TTGs by amphibole-dominated fractional crystallisation of sanukitoid magmas in the Yilgarn Craton. Conversely, the δ^{49}Ti values of the other TTGs can be

explained by the traditional model of partial melting of hydrous metabasite followed by fractional crystallisation. My results thus reveal the diverse petrogenesis of Neoarchean TTGs. High-Sr HP TTGs are almost ubiquitous in Archean cratons, became abundant and widespread after ~3 billion years ago, and most are spatially and temporally associated with sanukitoids. These observations imply that high-Sr HP TTG formation by fractional crystallisation of metasomatised mantle-derived sanukitoid magmas was a global phenomenon that emerged in the late Archean due to a geodynamic transition that promoted interaction between metabasite melts and mantle peridotite.

4.2. Introduction

Tonalite-trondhjemite-granodiorite (TTG) suites, which are the dominant constituent of Archean continental crust, show systematic variations in their trace element compositions, particularly in heavy rare earth element (HREE) and Sr concentrations. These variations have traditionally been linked to partial melting of metabasites at different pressures, and hence in the presence of different residual minerals (e.g. Halla et al., 2009; Moyen, 2011; Moyen and Stevens, 2006). Seminal work by Moyen (2011) categorised TTGs into three geochemical groups based on their apparent melting pressure – 1) low pressure (LP) TTGs which have high HREE and low Sr concentrations due to forming at low pressures (~1 – 1.2 GPa) in equilibrium with plagioclase-garnet amphibolite; 2) high pressure (HP) TTGs which were generated at high pressures (≥ 2 GPa) from a rutile-bearing eclogite, giving them low HREE and high Sr concentrations; 3) medium pressure (MP) TTGs which have intermediate HREE and Sr concentrations and formed from a plagioclase-poor, garnet-rich amphibolite source. This predominant interpretation that TTG geochemical compositions reflect melting metabasites over a range of pressures, including along relatively cool geothermal gradients capable of generating eclogite, has significantly influenced our understanding of what geodynamic setting TTGs formed in. For example, generation of TTG magmas over a large range of pressures supports Archean continental crust forming in multiple distinct geodynamic settings (e.g. Halla et al., 2009; Hernández-Montenegro et al., 2021; Moyen, 2011; Palin et al., 2016), while high pressure melting of rutile-bearing eclogite is often thought to imply that a

subduction-like process operated in the Archean (e.g. Halla et al., 2009; Moyen, 2011; Moyen and Stevens, 2006).

Recently, this straightforward interpretation of TTG compositional variations has been challenged. There is increasing recognition that the chemical compositions of TTGs do not directly correspond to magmatic liquids, which is an implicit assumption in the aforementioned model, and instead may have been modified during or after emplacement. Several studies have demonstrated the significant influence that mineral fractionation and/or accumulation during magma differentiation can have on TTG incompatible trace element concentrations. In particular, the low HREE concentrations and high La/Yb, Sr/Y and Sr concentrations characteristic of HP TTGs may have been generated by plagioclase accumulation (Kendrick et al., 2021; Laurent et al., 2020; Rollinson, 2021), hornblende fractional crystallisation (Liou et al., 2022; Liou and Guo, 2019; Mathieu, 2022; Rollinson, 2021; Smithies et al., 2019) or accessory mineral (e.g. apatite, titanite, zircon) fractional crystallisation (Ding et al., 2024), instead of by high pressure metabasite melting. This reinterpretation of TTG trace element signatures may have significant implications for models of Archean geodynamics as it creates uncertainty about the veracity of a key line of evidence used to argue for deep subduction in the Archean.

While metabasite melting followed by fractional crystallisation/mineral accumulation remains the prevailing model for TTG formation, an alternative petrogenesis is hornblende ± plagioclase fractional crystallisation of a hydrous, mantle-derived parental magma (e.g. Arth et al., 1978; Kamber et al., 2002; Kleinhanns et al., 2003; Smith et al., 1983). Although modern TTG analogues formed by this mechanism have been identified (e.g. Jagoutz et al., 2013; Martin and Sigmarsson, 2005), this model has generally been dismissed due to the absence of complementary hornblende-rich cumulates and the more mafic members of the liquid line of descent, as well as differences in the timing of mafic and TTG magmatism in Archean terranes (e.g. Moyen and Martin, 2012). Recently, Smithies et al. (2019) and Liou and Guo (2019) proposed that hornblende-dominated fractional crystallisation of metasomatised mantle-derived sanukitoid magmas can generate a subset of HP TTGs which have very high Sr and Sr/Y in the Yilgarn Craton and North China Craton respectively. Smithies et al. (2019) called these TTGs "high-Sr" HP TTGs, and they are characterised by $K_2O/Na_2O < 0.5$,

Sr > 500 ppm (but often > 700 ppm), Sr/Y > 100, Yb < 0.4 ppm and La/Yb > 60 at SiO_2 > 70 wt%. In both locations the more mafic members of the liquid line of descent and examples of complementary hornblendite cumulates were identified, supporting the viability of this mechanism. An implication of this model is again that so-called HP TTGs did not directly form by high pressure metabasite melting (Smithies et al., 2019). It is therefore evident that further work is needed to clarify how HP TTGs formed, and whether high pressure melting of metabasites occurred in the Archean.

Smithies et al. (2019) used trace element variations in the Black Flag Group (BFG) sanukitoids as evidence for formation of high-Sr HP TTGs by this mechanism in the Neoarchean (2.8 – 2.5 Ga) Eastern Goldfields Superterrane (EGST), Yilgarn Craton, arguing that the BFG constitutes the liquid line of descent from mantle-derived parental magma to evolved high-Sr HP TTGs. In Chapter 3, I presented the Ti stable isotope compositions ($\delta^{49}Ti = 10^3 \times [(^{49}Ti/^{47}Ti)_{sample} / (^{49}Ti/^{47}Ti)_{OL-Ti} - 1]$) of samples from the BFG. This sanukitoid suite displays shallowly increasing $\delta^{49}Ti$ with SiO_2 content due to fractional crystallisation of abundant hornblende alongside Fe-Ti oxides, meaning the Ti isotope evolution of the liquid line of descent proposed to form high-Sr HP TTGs is already constrained. Measuring the $\delta^{49}Ti$ of high-Sr HP TTGs from the EGST therefore provides a valuable opportunity to further investigate whether these TTGs did form by fractional crystallisation of metasomatised mantle-derived sanukitoid magmas. However, Ti stable isotopes are fractionated during metabasite partial melting (Chapter 3, Hoare et al., 2023; Klaver et al., 2024; Z.J. Zhang et al., 2023) due to retention of light Ti isotopes in residual Fe-Ti oxides (e.g. rutile) and amphibole, and previous studies have concluded that metabasite partial melting followed by fractional crystallisation is required to explain the Ti isotope compositions of TTGs (Hoare et al., 2023; Z.J. Zhang et al., 2023). Comparing the $\delta^{49}Ti$ of high-Sr HP TTGs to other TTGs from the same region but with different trace element compositions may provide insight into whether they have a distinct petrogenesis. It is of particular interest to compare the high-Sr HP TTGs to TTGs that are also classified as "high pressure" according to Moyen (2011) but have lower Sr and Sr/Y values. Smithies et al. (2019) describe this group of HP TTGs as having similar geochemical compositions to MP TTGs, hence I refer to these TTGs as "MP-like" HP TTGs.

In this chapter I measure the Ti stable isotope compositions of Neoarchean (~2650 – 2700 Ma) TTG samples from the EGST, Yilgarn Craton. These samples have been classified based on their geochemical compositions following Moyen (2011) and Smithies et al. (2019), and were selected to cover the full range of trace element compositions exhibited by TTGs. The samples analysed consist of three high-Sr HP TTGs, four MP-like HP TTGs, four MP TTGs and six LP TTGs. Full sample descriptions are given in Chapter 2, section 2.2.2.1. Most of the TTG samples are from the Kalgoorlie-Kambalda area of the Kalgoorlie Terrane – the region where the BFG sanukitoids are located – but three LP TTG samples are from further north in the Kalgoorlie Terrane near Wiluna, and one LP TTG sample is from the Kurnalpi Terrane (figs. 2.14 and 2.16). The Ti isotope measurements were made via the methods described in Chapter 2, section 2.1, and the resulting data are presented and discussed in the rest of this chapter.

4.3. Results

The δ^{49}Ti values of the EGST TTGs are presented in table 4.1 and range from 0.206 ± 0.022‰ to 1.385 ± 0.020‰ (95% confidence interval). δ^{49}Ti increases as the samples become more differentiated, with the most extreme values of > 1‰ found in two highly evolved LP TTGs with SiO_2 ≈ 76 wt% (fig. 4.1a). The remaining samples all have δ^{49}Ti values of ~0.2 – 0.6‰, similar to literature TTG data from the Kaapvaal Craton (Greber et al., 2017), Slave Craton (Aarons et al., 2020), Pilbara Craton (Z.J. Zhang et al., 2023) and southwest Greenland (Hoare et al., 2023; Z.J. Zhang et al., 2023) (fig. 4.1).

At SiO_2 ≈ 70 wt%, the different groups of EGST TTGs display distinct Ti isotope compositions (fig. 4.1b). The LP TTGs have the highest δ^{49}Ti values of ~0.4 – 0.6‰, while the MP TTGs have lower δ^{49}Ti of 0.23 – 0.30‰. The two subgroups of HP TTGs, subdivided following Smithies et al. (2019), also have different Ti isotope compositions. The "MP-like" HP TTGs are indeed MP-like – they have relatively low δ^{49}Ti values of 0.20 – 0.29‰ indistinguishable from the MP TTGs. In contrast, the high-Sr HP TTGs have distinctly higher δ^{49}Ti that increases from 0.329 ± 0.015‰ to 0.446 ± 0.022‰ as

the samples become more evolved. Their Ti isotope compositions fall in between those of the MP TTGs and the LP TTGs.
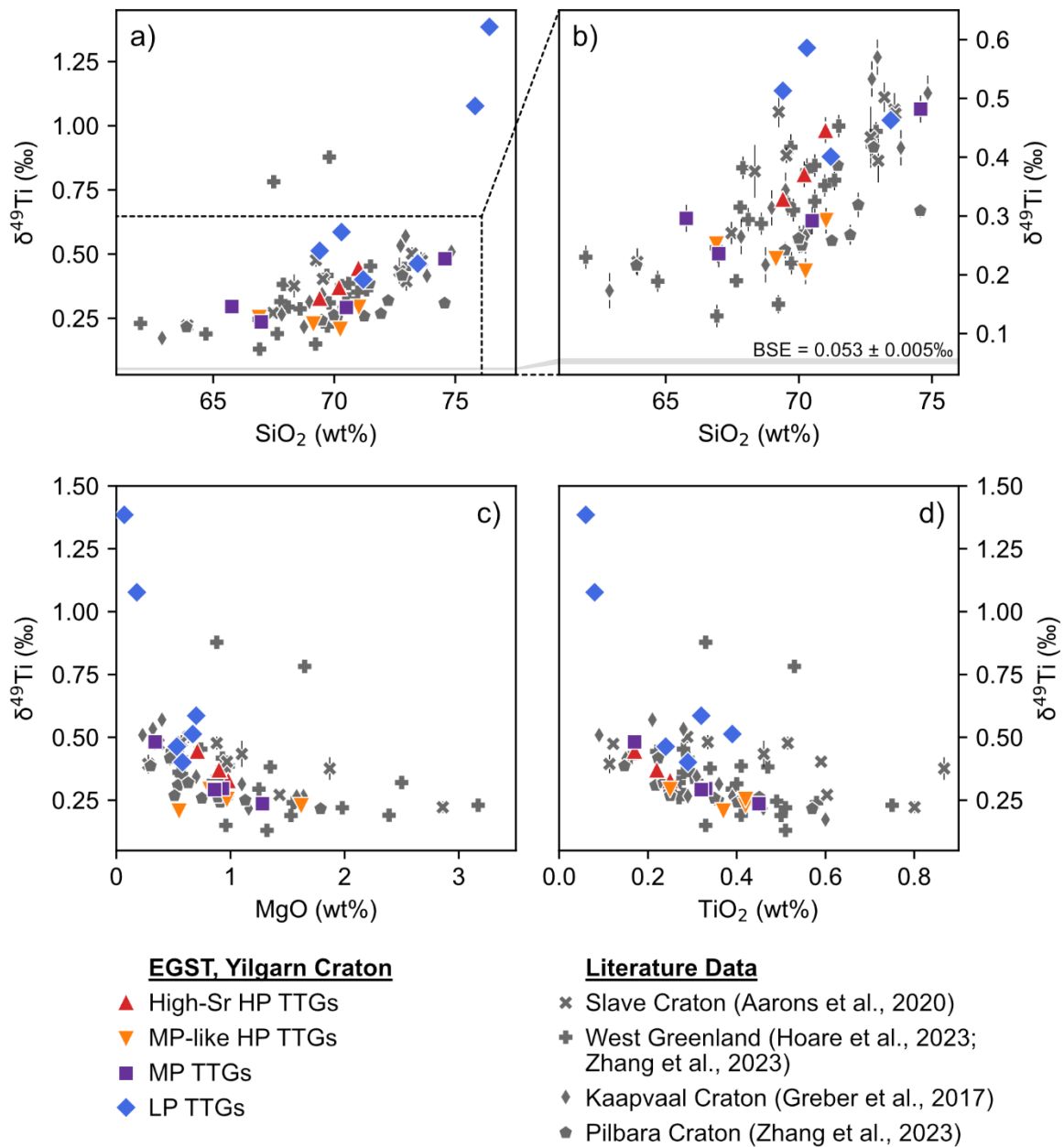
Figure 4.1: TTG δ⁴⁹Ti (‰) vs a) and b) SiO₂ (wt%), c) MgO (wt%), and d) TiO₂ (wt%). Coloured symbols are TTGs from the Eastern Goldfields Superterrane (EGST), Yilgarn Craton, while grey symbols are literature TTG data from Aarons et al. (2020), Greber et al. (2017), Hoare et al. (2023) and Z.J. Zhang et al. (2023). Uncertainty in δ⁴⁹Ti is shown as the 95% confidence interval. The grey line is the BSE value of 0.053 ± 0.005‰ from Deng et al. (2023).

Table 4.1: δ^{49}Ti data for the EGST TTG samples analysed in this chapter. Key elemental concentrations and geochemical parameters are also given. The sources of the major and trace element data for the samples are given in Appendix C. 95% ci = 95% confidence interval, calculated via the method described in Chapter 2. n = number of measurements made. For (La/Yb)$_N$, La and Yb concentrations are normalised to the CI chondrite values from O'Neill (2016).

Sample	Classification	δ^{49}Ti ‰	95% ci ‰	n	TiO$_2$ wt%	SiO$_2$ wt%	Sr ppm	Nb ppm	Yb ppm	K$_2$O/Na$_2$O	Sr/Y	La/Yb	(La/Yb)$_N$
227968	High-Sr HP TTG	0.329	0.015	2	0.25	69.4	812	1.76	0.22	0.41	262	105	71
502247	High-Sr HP TTG	0.446	0.022	1	0.17	71.0	1180	1.7	0.18	0.47	454	117	80
505481	High-Sr HP TTG	0.371	0.022	1	0.22	70.2	825	1.9	0.26	0.45	250	105	72
230558	MP-like HP TTG	0.227	0.014	2	0.42	69.14	401	2.22	0.41	0.45	79	57	39
501894	MP-like HP TTG	0.252	0.013	2	0.42	66.90	533	2.7	0.48	0.36	87	44	30
504718	MP-like HP TTG	0.292	0.022	1	0.25	71.02	306	2.4	0.29	0.31	85	51	35
233734	MP-like HP TTG	0.206	0.022	1	0.37	70.25	361	2.12	0.35	0.41	93	33	22
222660	MP TTG	0.482	0.023	1	0.17	74.57	323	4.03	0.36	0.64	73	64	44
240405	MP TTG	0.296	0.023	1	0.33	65.77	700	12.2	1.15	0.20	56	70	48
502533	MP TTG	0.292	0.023	1	0.32	70.55	493	5.4	0.84	0.68	57	53	36
234000	MP TTG	0.236	0.023	1	0.45	66.99	280	5.07	0.54	0.28	43	56	38
500854	LP TTG	0.513	0.016	2	0.39	69.4	353	8.1	1.52	0.50	18	21	14
240623	LP TTG	1.385	0.020	1	0.06	76.41	52.8	16.5	0.7	0.16	9	24	16
501345	LP TTG	0.586	0.016	2	0.32	70.3	195.5	16.0	0.4	0.25	28	44	30
504940	LP TTG	0.463	0.016	2	0.24	73.45	145	9.2	2.21	0.33	6	10	7
501356	LP TTG	0.401	0.015	2	0.29	71.2	465	12.5	1.51	0.59	35	34	23
233699	LP TTG	1.077	0.016	2	0.08	75.82	82	12.6	0.69	0.58	16	61	42

4.4. Discussion

4.4.1. Effects of alteration and metamorphism

Some TTGs in the EGST show evidence of post-emplacement deformation and metamorphism, such as gneissic textures (e.g. Champion and Sheraton, 1997), and may also have been affected by later alteration and weathering. Like other high field strength elements, Ti is highly immobile in aqueous fluids, even at high salinities (Rustioni et al., 2021). This is consistent with observations of highly limited Ti mobility during metamorphism and water-rock interaction, with only minor localised Ti redistribution seen (e.g. Brugger et al., 2024; Tilley and Eggleton, 2005). Recent studies suggest intensive chemical weathering may cause small degrees of Ti isotope fractionation (Aarons et al., 2023; He et al., 2022). The EGST TTGs show no evidence of such intensive weathering, with chemical index of alteration (CIA = [Al_2O_3 / (Al_2O_3 + CaO* + Na_2O + K_2O)] x 100) values of 48 to 54 that fall within the range of fresh granites and granodiorites (45 to 55; Nesbitt and Young, 1982). Their $\delta^{49}Ti$ values should hence be unaffected by metamorphism and alteration, which is supported by the absence of correlation between $\delta^{49}Ti$ and loss on ignition (LOI) or CIA (fig. 4.2). I therefore consider the Ti isotope compositions of the EGST TTGs to be representative of their igneous compositions.
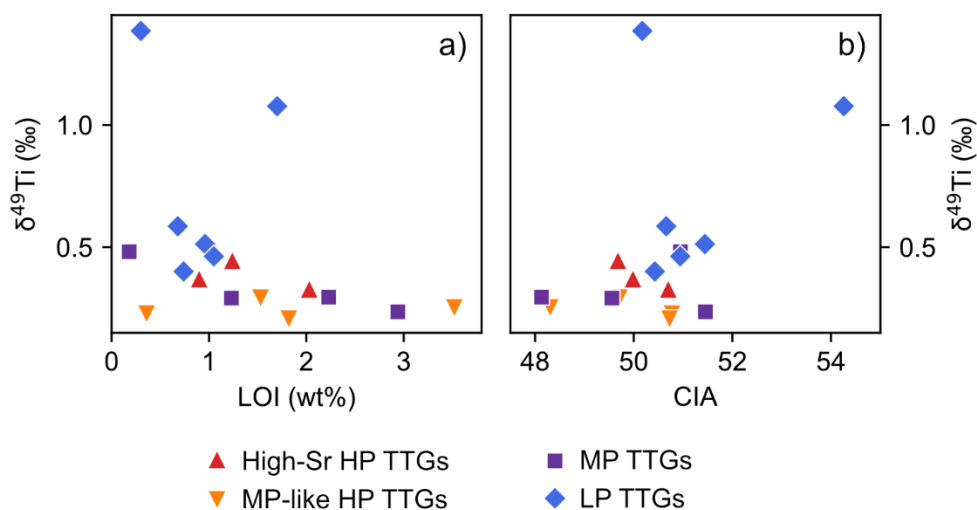
Figure 4.2: EGST TTG $\delta^{49}Ti$ (‰) vs a) loss on ignition (LOI) (wt%), and b) chemical index of alteration (CIA = [Al_2O_3 / (Al_2O_3 + CaO* + Na_2O + K_2O)] x 100).

4.4.2. Investigating the petrogenetic link between TTGs and sanukitoids in the Eastern Goldfields Superterrane
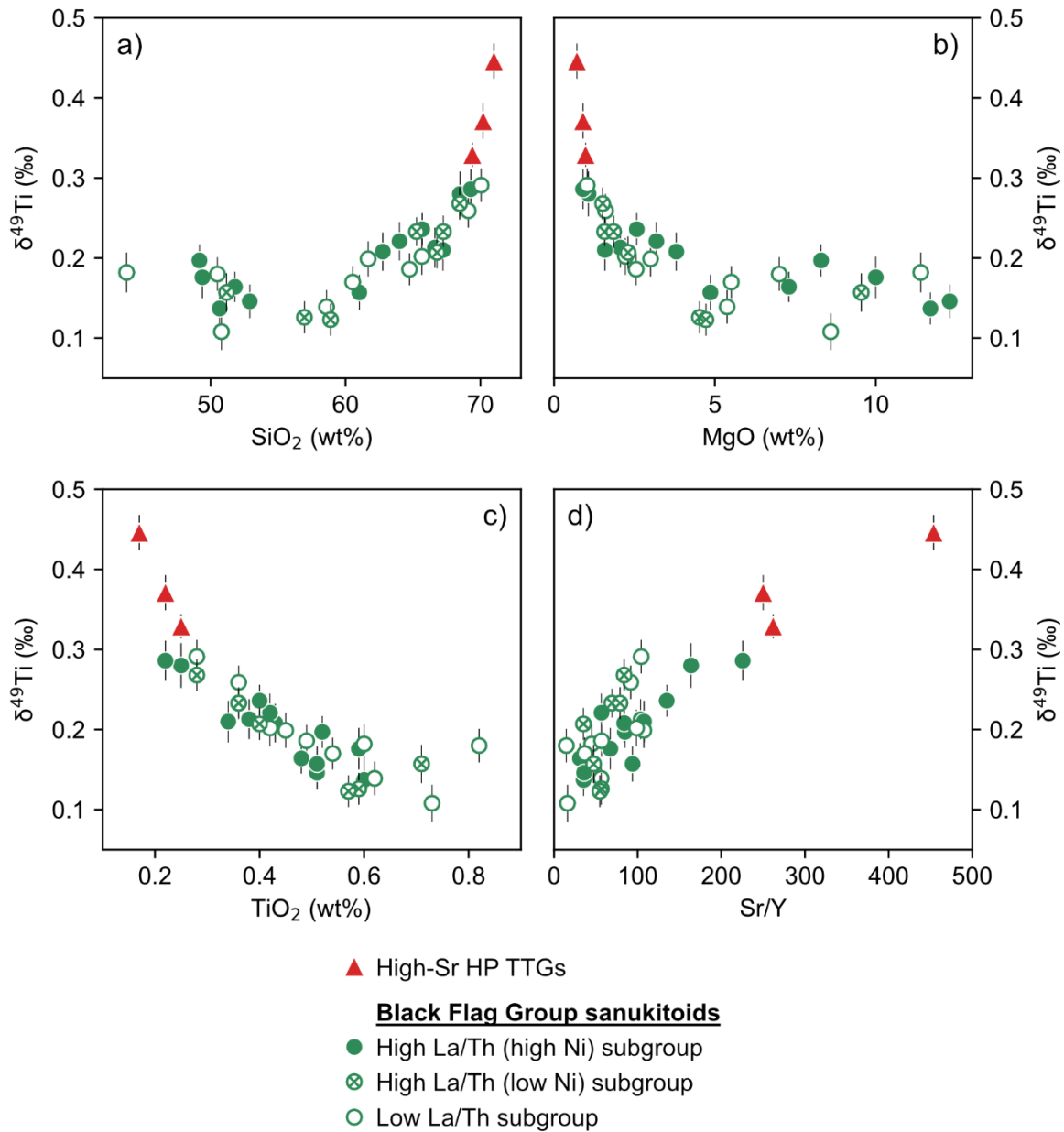
Figure 4.3: EGST high-Sr HP TTG and Black Flag Group sanukitoid δ⁴⁹Ti (‰) vs a) SiO₂ (wt%), b) MgO (wt%), c) TiO₂ (wt%), and d) Sr/Y. Ti isotope data for the Black Flag Group sanukitoids are presented in Chapter 3. Uncertainty in δ⁴⁹Ti is shown as the 95% confidence interval.

Smithies et al. (2019) proposed that in the EGST, high-Sr HP TTGs formed by hornblende-dominated fractional crystallisation of sanukitoid magmas instead of by high pressure metabasite melting, and are equivalent to the evolved members of the

Black Flag Group. In Chapter 3 I presented the Ti isotope compositions of the BFG sanukitoids, which form a differentiation trend with shallowly increasing δ⁴⁹Ti due to removal of Ti in hornblende alongside Fe-Ti oxides during fractional crystallisation. Figure 4.3 compares the Ti isotope compositions of the high-Sr HP TTGs to the BFG trend. The high-Sr HP TTGs plot at the evolved end of the BFG differentiation trend and extend it to higher δ⁴⁹Ti values of ~0.45‰.
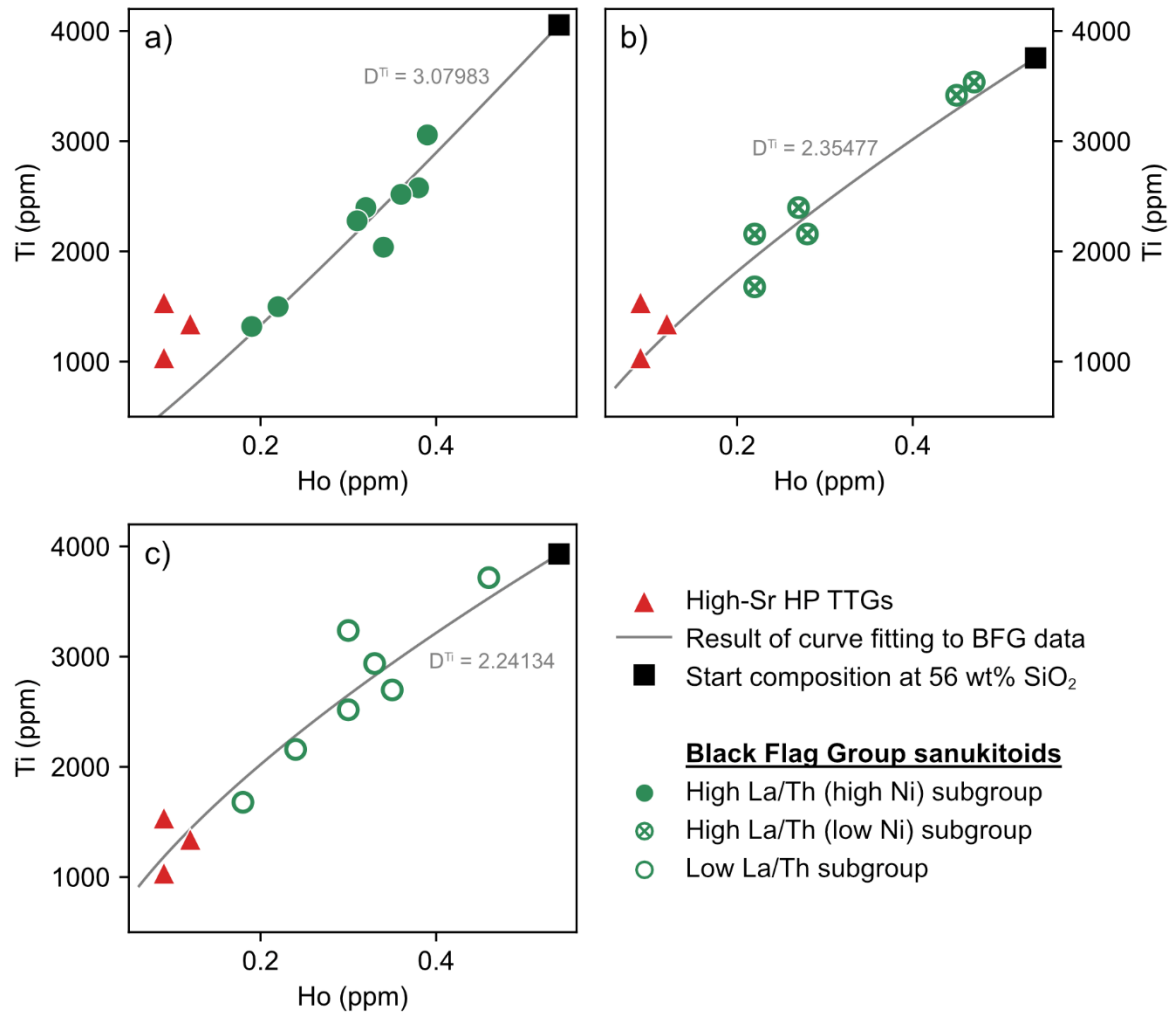
Figure 4.4: Ti (ppm) vs Ho (ppm) comparing the EGST high-Sr HP TTGs to the Black Flag Group sanukitoid subgroups – a) high La/Th (high Ni) BFG, b) high La/Th (low Ni) BFG, c) low La/Th BFG. The grey lines show the results of curve fitting equation D3 (Appendix D) to the Ti and Ho concentration data of the BFG sanukitoids.
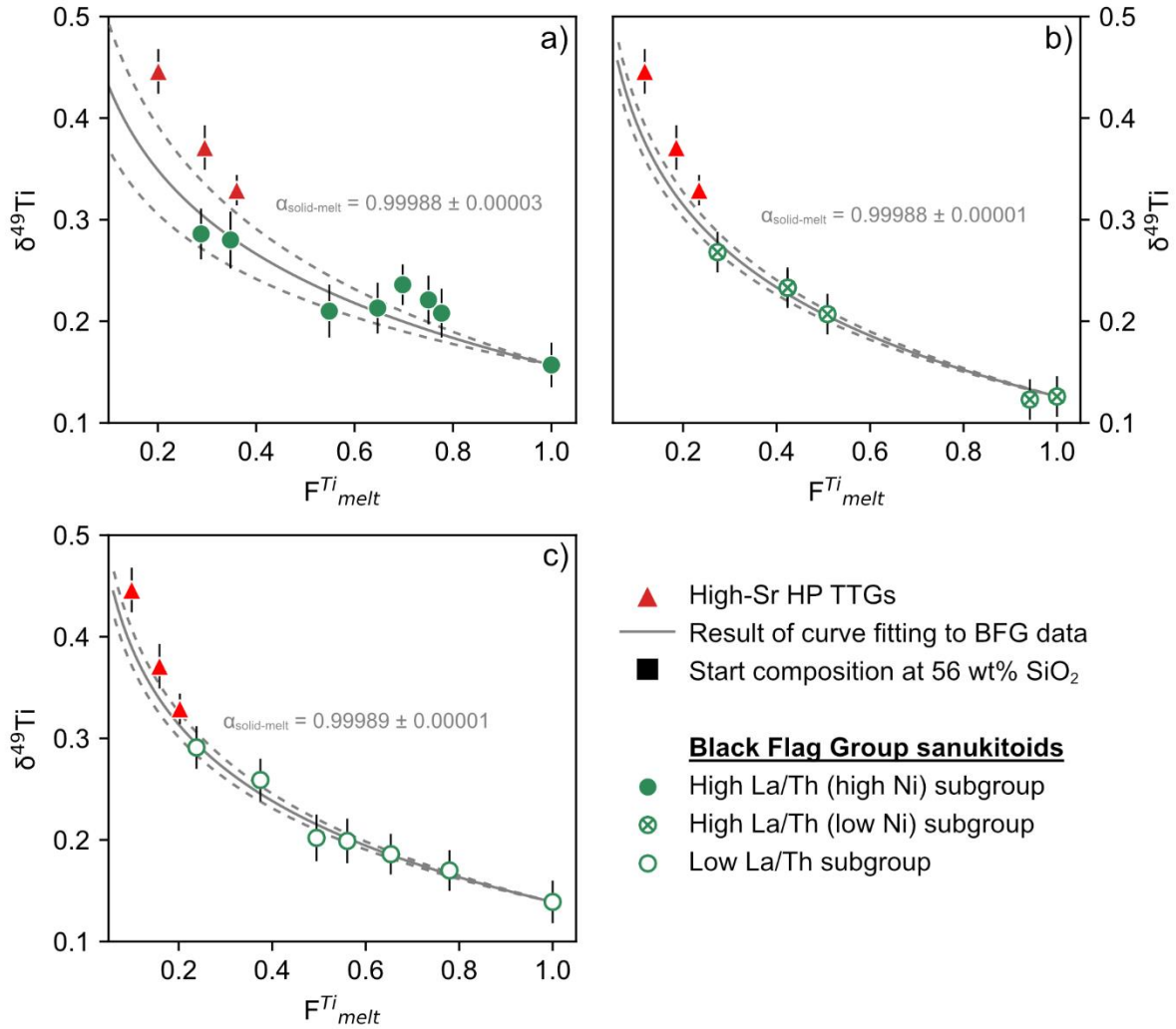
Figure 4.5: δ⁴⁹Ti (‰) vs calculated F_{melt}^{Ti} comparing the EGST high-Sr HP TTGs to the Rayleigh fractionation models for the Black Flag Group sanukitoid subgroups – a) high La/Th (high Ni) BFG, b) high La/Th (low Ni) BFG, c) low La/Th BFG. Uncertainty in the δ⁴⁹Ti of samples is shown as the 95% confidence interval. The solid grey lines show the Rayleigh fractionation models, and the dashed grey lines show the 2σ uncertainty on those models which was calculated using the method described in Appendix D.

To test the proposed petrogenetic link, I compare the Ti isotope compositions of the high-Sr HP TTGs to the Rayleigh fractionation models of evolving δ⁴⁹Ti during the differentiation of the BFG sanukitoids. These models were presented in Chapter 3, section 3.4.2, and the method used for this modelling is described in Appendix D. The BFG is divided into three geochemical subgroups – high La/Th (high Ni), high La/Th (low Ni) and low La/Th – which reflect slightly different mantle source compositions (Smithies et al., 2022), and I obtained slightly different modelled values for the bulk Ti partition coefficients (D_{bulk}^{Ti}) and solid-melt fractionation factors ($\alpha_{solid-melt}$) of these subgroups (see Appendix D). I therefore compare the high-Sr HP TTGs to each BFG

subgroup individually. The fraction of Ti remaining in the melt (F_{melt}^{Ti}) for each high-Sr HP TTG sample was calculated using the modelled optimum D_{bulk}^{Ti} for each subgroup, which itself was determined from the correlation between Ti and Ho concentrations via the method described in Appendix D. Figure 4.4 shows that the high-Sr HP TTGs plot on the Ti vs Ho trends and modelled curves of the low La/Th and high La/Th (low Ni) subgroups. However, the high-Sr HP TTGs plot above the Ti vs Ho trend defined by the high La/Th (high Ni) subgroup (fig. 4.4a), which suggests that this BFG subgroup is not a suitable predecessor for the high-Sr HP TTGs.
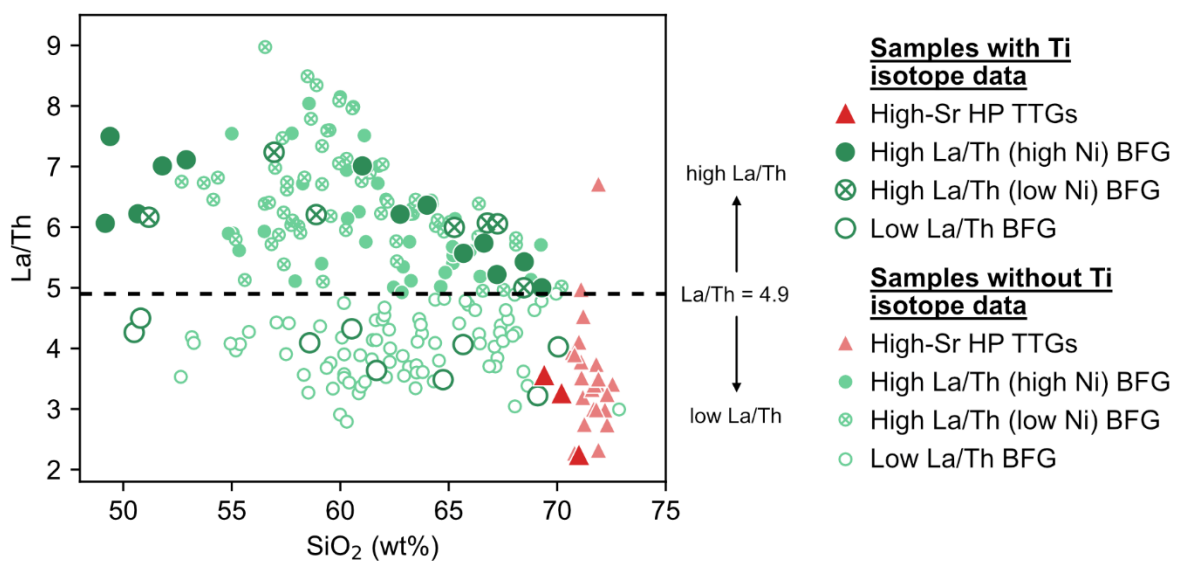
Figure 4.6: La/Th vs SiO₂ (wt%) comparing the EGST high-Sr HP TTGs to the different Black Flag Group sanukitoid subgroups. Larger, darker-coloured symbols are samples with Ti isotope data presented in this thesis, while smaller, lighter-coloured symbols are from wider datasets of samples which have not had their Ti stable isotope compositions measured. The wider BFG geochemical data are from Smithies et al. (2022), and the wider high-Sr HP TTG data are from the Western Australia Geochemistry Database (WACHEM, Geological Survey of Western Australia, 2025).

Figure 4.5 compares the high-Sr HP TTGs to the Rayleigh fractionation models of the BFG subgroups. Unsurprisingly, the high-Sr HP TTGs do not plot on the modelled fractionation trend of the high La/Th (high Ni) subgroup (fig. 4.5a). While they plot closer to the fractionation model of the high La/Th (low Ni) subgroup, the high-Sr HP TTGs still fall outside the 2σ uncertainty window on the model (fig. 4.5b). In contrast, the high-Sr HP TTGs plot on the evolved end of the modelled fractionation trend of the low La/Th BFG subgroup (fig. 4.5c), suggesting that the Ti isotope compositions of the
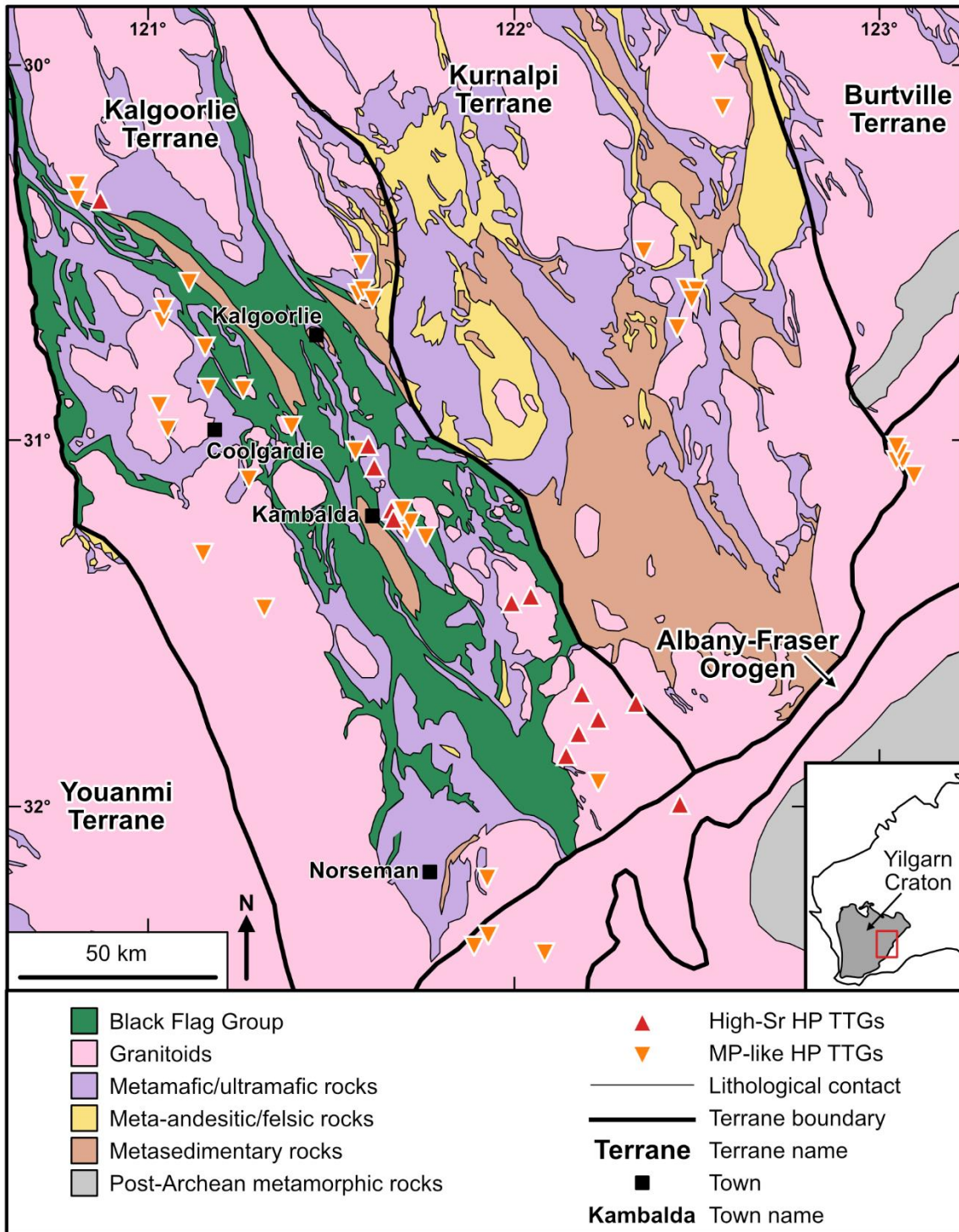
Figure 4.7: Simplified geological map of the southern Eastern Goldfields Superterrane, showing the locations of high-Sr HP TTG and MP-like HP TTG samples, and the spatial association of the high-Sr HP TTG occurrences with the Black Flag Group sanukitoid outcrops (green). Based on the "1:500,000 State interpreted bedrock geology of Western Australia" map (Geological Survey of Western Australia, 2020).

high-Sr HP TTGs can be explained by continued fractional crystallisation of the low La/Th BFG magmas. Most high-Sr HP TTGs from the EGST have low La/Th < 4.9 (fig. 4.6), further confirming that the low La/Th subgroup of the BFG represents the most likely liquid line of descent leading to high-Sr HP TTG formation. This result provides strong support for the formation of high-Sr HP TTGs by amphibole-dominated fractional crystallisation of sanukitoid magmas, specifically of low La/Th BFG sanukitoids, in the Neoarchean EGST, Yilgarn Craton.

The spatial distributions of the two types of "high pressure" TTGs in the EGST also support this petrogenetic model. Figure 4.7 reveals that the high-Sr HP TTGs are only found in a restricted, northwest-southeast-trending belt emplaced in close proximity to the BFG (green). In contrast, the MP-like HP TTGs are more widely distributed, with occurrences of this composition extending > 100 km further east than the BFG. The close spatial association of high-Sr HP TTGs and the BFG sanukitoids in the EGST is hence another argument in favour of them being petrogenetically linked.

In Chapter 3 I demonstrated that the parental magmas of the BFG formed by partial melting of mantle metasomatised by silicate melts that were most likely generated by fluid-fluxed eclogite partial melting. The evidence presented above confirms that the high-Sr HP TTGs constitute the evolved end of the BFG liquid line of descent, hence they share the same parental magmas. This result implies that the high-Sr HP TTGs ultimately had a metasomatised mantle source, contrasting with the hydrous metabasite source that is dominantly proposed for TTGs (e.g. Moyen and Martin, 2012; Moyen and Stevens, 2006). However, while the high-Sr HP TTGs did not directly form by high pressure metabasite melting, high pressure melting of eclogite in the presence of aqueous fluids is still a necessary step in their petrogenesis. This fluid-fluxed eclogite melt component favours formation of their metasomatised mantle source by a subduction-like process (see Chapter 3, section 3.4.4 for the full argument).

In Chapter 3, section 3.4.2, I showed that BFG δ^{49}Ti starts to increase at high Mg#, suggesting there was early oxide saturation and hence that the BFG magmas were H_2O-rich (fig. 3.4). The presence of significant magmatic H_2O suppresses plagioclase crystallisation, causing it to start forming later and in diminished quantities (e.g. Grove

et al., 2003; Sisson and Grove, 1993; Zimmer et al., 2010). Strontium is moderately compatible in plagioclase (e.g. Aigner-Torres et al., 2007; Brophy et al., 2011), so reduced plagioclase crystallisation will result in less Sr being removed from the melt during differentiation. Magmatic H_2O is also important as it helps stabilise amphibole as a crystallising phase. Yttrium is slightly compatible in calcic amphiboles (such as hornblende) (e.g. Brophy et al., 2011; Tiepolo et al., 2007), meaning amphibole fractional crystallisation should cause magma Y concentrations to decrease. Therefore, the high H_2O content of BFG magmas may play an important role in generating the characteristic high Sr concentrations and Sr/Y values of the high-Sr HP TTGs by suppressing plagioclase crystallisation, which helps maintain elevated magma Sr concentrations during differentiation, while promoting hornblende crystallisation, which reduces magma Y concentrations. Similarly, middle to heavy REEs are more compatible in amphibole than light REEs (e.g. Tiepolo et al., 2007), so stabilisation of amphibole by high magma H_2O content also helps create the low HREE concentrations and high La/Yb signature of high-Sr HP TTGs.

C.-Y.-H. Liu et al. (2022) proposed that sanukitoids followed two distinct crystallisation pathways which were controlled by the nature of the metasomatic agent involved in their formation – an aqueous fluid-metasomatised source generated H_2O-rich magmas that mainly crystallised amphibole, while a melt-metasomatised source formed magmas with lower H_2O contents that instead crystallised biotite and plagioclase. They consequently concluded that only sanukitoids derived from fluid-dominated metasomatised mantle sources were capable of undergoing significant amphibole fractional crystallisation to form high-Sr HP TTGs. My results agree that the parental magmas of high-Sr HP TTGs were H_2O-rich which, as discussed above, was important for creating their distinct geochemical signature. However, the Ti stable isotope evidence presented in this thesis supports the involvement of a significant metabasite melt component in forming the sanukitoid parental magmas of high-Sr HP TTGs. As this metabasite melt was most likely generated by fluid-fluxed eclogite melting, the resulting melt was probably H_2O-rich, and the flux of this melt into the mantle may also have been accompanied by a flux of aqueous fluids. These processes would have created a H_2O-rich mantle source capable of generating H_2O-rich sanukitoid parental magmas. The dependence of sanukitoid crystallisation pathway on the metasomatic agent involved may therefore not be as binary as C.-Y.-H. Liu et al. (2022) imply, and

the involvement of both metabasite-derived melts and aqueous fluids is likely necessary to form high-Sr HP TTGs.

4.4.3. The diverse petrogenesis of TTGs in the Neoarchean Eastern Goldfields Superterrane

The LP, MP and MP-like HP TTGs from the EGST have Ti isotope and trace element compositions distinct from the high-Sr HP TTGs (figs. 4.1 and 4.8), so they may have a different origin. Previous studies (Aarons et al., 2020; Greber et al., 2017; Hoare et al., 2023; Z.J. Zhang et al., 2023) have investigated the Ti isotope compositions of Eo-Paleoarchean (4.0 – 3.2 Ga) TTGs with similar elemental compositions to these EGST TTGs (figs. 4.1 and 4.8), and have used thermodynamics-based Ti isotope fractionation modelling to demonstrate that their δ^{49}Ti values are best explained by metabasite partial melting followed by fractional crystallisation (Hoare et al., 2023; Z.J. Zhang et al., 2023). To facilitate comparison between these samples and the EGST TTGs, I classified these TTGs into LP, MP, MP-like HP and high-Sr HP TTGs after Moyen (2011) and Smithies et al. (2019). I was unable to confidently classify the TTGs from the Kaapvaal Craton that were analysed by Greber et al. (2017) and two TTGs from the Itsaq Gneiss Complex measured by Z.J. Zhang et al. (2023) as these samples did not have sufficient trace element concentration data available. The remaining TTG samples were all classified as MP TTGs and MP-like HP TTGs. None of the Eo-Paleoarchean TTGs are classified as LP TTGs or high-Sr HP TTGs.

While in the EGST, high-Sr HP TTGs have distinct, higher δ^{49}Ti than MP and MP-like TTGs at ~70 wt% SiO_2 content, this observation does not hold when global TTG data are also considered (fig. 4.8a). MP and MP-like HP TTGs form a broad, shallowly increasing trend with SiO_2, with δ^{49}Ti rising from ~0.2‰ at 65 wt% SiO_2 to ~0.5‰ at 75 wt% SiO_2, which fully overlaps with the EGST high-Sr HP TTGs. This observation is consistent with previous findings that metabasite partial melting and calc-alkaline-like differentiation – which is followed by the BFG and high-Sr HP TTGs – produce similar δ^{49}Ti vs SiO_2 trends (Hoare et al., 2023; Z.J. Zhang et al., 2023). Consequently, Ti isotopes alone cannot distinguish between mechanisms of TTG formation, and
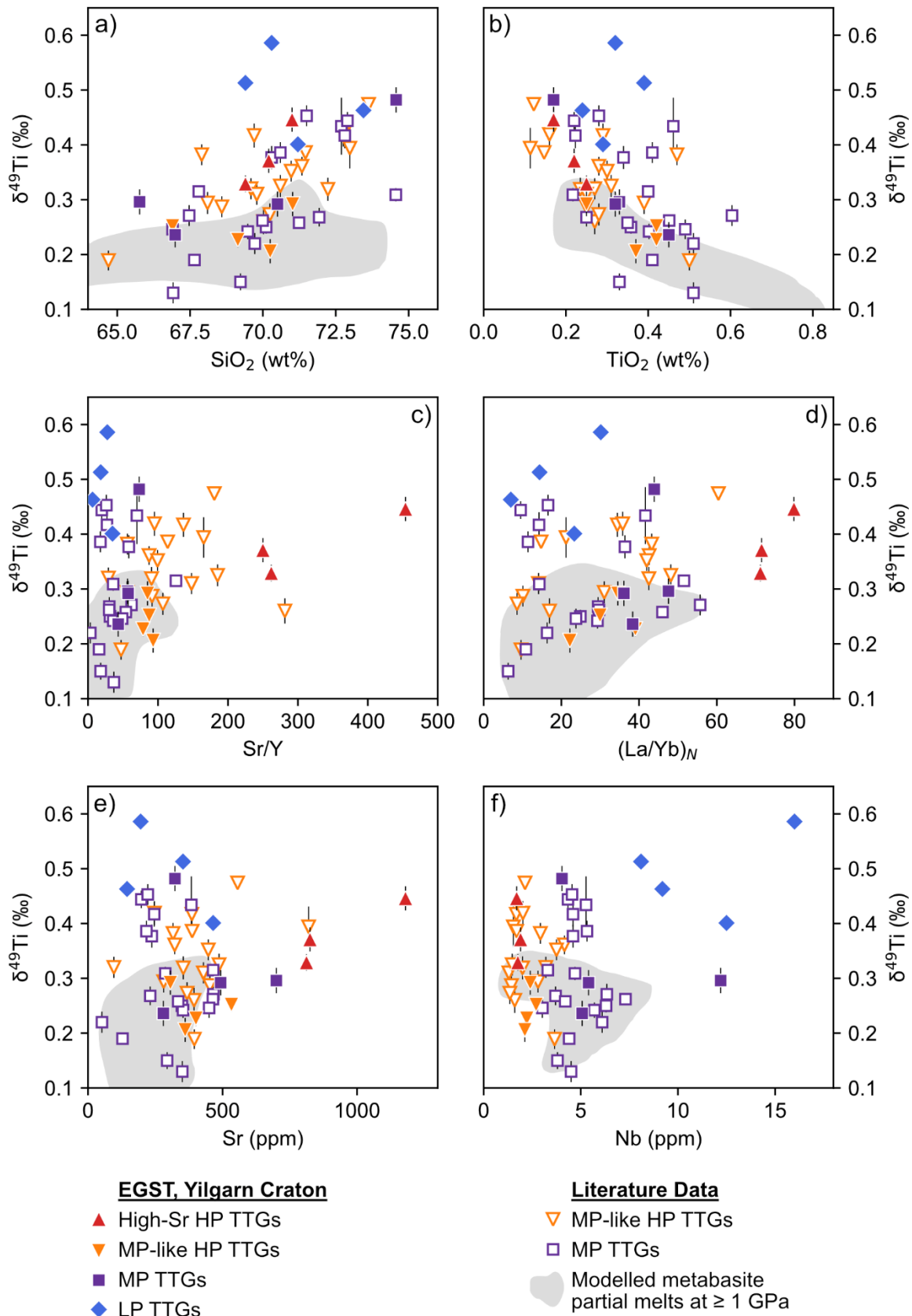
Figure 4.8: EGST TTG (solid symbols) and global TTG (open symbols) δ⁴⁹Ti (‰) vs a) SiO₂ (wt%), b) TiO₂ (wt%), c) Sr/Y, d) (La/Yb)ₙ where REE concentrations are normalised to CI-chondrite values from O'Neill (2016) e) Sr (ppm), and f) Nb (ppm). Literature TTG data are from Aarons et al. (2020), Hoare et al. (2023) and Z.J. Zhang et al. (2023), and were classified after Moyen (2011) and Smithies et al. (2019). Uncertainty in δ⁴⁹Ti is shown as the 95% confidence interval. The grey shading shows modelled metabasite partial melt elemental and isotopic compositions at ≥ 1 GPa and 10 – 40% melting, after modelling by Hoare et al. (2023) and Z.J. Zhang et al. (2023).

having the full liquid line of descent, as I do here with the BFG sanukitoids, is necessary to conclusively prove TTGs formed by fractional crystallisation of mantle-derived magmas using Ti isotopes. It is when looking at incompatible trace element compositions that the high-Sr HP TTGs are revealed to be distinct to the other analysed TTGs, with higher Sr concentrations, Sr/Y and (La/Yb)$_N$ (chondrite-normalised REE concentration ratio) (figs. 4.8c-e). The LP TTGs appear to generally have higher δ^{49}Ti than the other TTGs, but whether this is a global signature is unclear as the only Ti isotope data available are from EGST LP TTGs.

The elemental and Ti isotope compositional similarity between the EGST MP TTGs and MP-like HP TTGs and the literature MP TTGs and MP-like HP TTGs respectively suggests that they may have a common petrogenesis. Metabasite partial melting at moderate-high pressures (≥ 1 GPa) can readily generate melts with δ^{49}Ti values of 0.2 – 0.3‰ due to retention of light Ti isotopes in residual amphibole and Fe-Ti oxides (Chapter 3 of this thesis, section 3.4.3.2; Hoare et al., 2023; Klaver et al., 2024; Z.J. Zhang et al., 2023), which can explain the composition of almost all the EGST MP and MP-like HP TTGs. The heavier Ti isotope composition (0.482 ± 0.023‰) of the most evolved MP TTG sample (222660) was likely generated by fractional crystallisation of Fe-Ti oxides and Ti-bearing silicate minerals from less evolved TTG magmas (Hoare et al., 2020, 2023; Z.J. Zhang et al., 2023).

Modelling by Z.J. Zhang et al. (2023) demonstrated that Ti isotope fractionation during metabasite partial melting is expected to have a small pressure dependence. This is because rutile replaces amphibole as the dominant host of Ti in the residue at high pressures (~2 GPa). Rutile fractionates Ti isotopes more than amphibole (Hoare et al., 2022; Mandl, 2019; W. Wang et al., 2020), hence high pressure melting generates melts with δ^{49}Ti values up to 0.1‰ higher than low-medium pressure melting. However, while the trace element compositions of MP and HP TTGs imply they formed by melting at different pressures, they have indistinguishable Ti isotope compositions, both within the EGST and globally (fig. 4.8). This similarity may be because pressure is not the only factor controlling the balance between amphibole and Fe-Ti oxides in the residual assemblage. Hoare et al. (2023) modelled melting of a range of metabasite compositions and showed that protolith TiO_2 content is also important as it controls the abundance of residual Fe-Ti oxides. At high metabasite TiO_2 contents

the pressure effect modelled by Z.J. Zhang et al. (2023) can even be reversed as ilmenite, which fractionates Ti isotopes more than rutile, becomes stable alongside amphibole at low pressures. The effect of variable protolith TiO_2 content on Ti isotope fractionation during metabasite melting may therefore be obscuring any variation of TTG $\delta^{49}Ti$ with pressure of melting.

While two EGST LP TTGs with $\delta^{49}Ti$ of 0.40 – 0.46‰ (504940 and 501356) plot at the evolved end of the TTG differentiation trend, another two LP TTG samples with SiO_2 $\approx$ 70 wt% (500854 and 501345) plot ~0.1‰ above this trend (fig. 4.8a), with $\delta^{49}Ti$ values of 0.513 ± 0.016‰ and 0.586 ± 0.016‰ respectively. Crustal reworking involving a second stage of intra-crustal anatexis is one way to further elevate $\delta^{49}Ti$ at lower SiO_2 and higher TiO_2 contents, and this effect has been observed in migmatised TTGs and Archean intra-crustal differentiates (Hoare et al., 2023; Z.J. Zhang et al., 2023). However, both these LP TTG samples display primary igneous textures, such as rhythmic layering and feldspar phenocrysts, with no evidence for migmatisation or gneissic banding, suggesting they have not experienced a second stage of melting. As mentioned previously, melting a Ti-rich source at low pressures can generate isotopically heavier melts due to the presence of residual ilmenite (Hoare et al., 2023). However, melting Ti-rich sources also produces parental melts that are comparatively richer in Ti than those from lower-Ti sources. These LP TTGs have low TiO_2 contents of 0.3 – 0.4 wt% and are not notably enriched in Ti relative to other EGST TTGs (fig. 4.8b), hence it is unlikely that their metabasite protoliths had significantly elevated TiO_2 contents.

An alternative possibility is that these samples have experienced more extensive crystallisation from their parental magmas than other TTGs with similar SiO_2 contents. If these LP TTGs had relatively low-Si parental magmas compared to the other LP TTGs, they may have undergone more crystallisation by ~70 wt% SiO_2 than other TTGs with comparable SiO_2. Hoare et al. (2023) modelled crystallisation pathways for low-Si tonalite (~67 wt% SiO_2) which demonstrated that crystallisation of such a magma, and fractional crystallisation in particular, can produce magmas with $\delta^{49}Ti >$ 0.5‰ at ~70 wt% SiO_2 (fig. 4.9a). I therefore propose that the elevated $\delta^{49}Ti$ of these LP TTGs most likely results from them having a low-SiO_2 parental magma that has undergone relatively extensive crystallisation in comparison to other TTGs of similar

136

composition. This effect may have been supplemented by them having a slightly – but not significantly – more Ti-rich source.
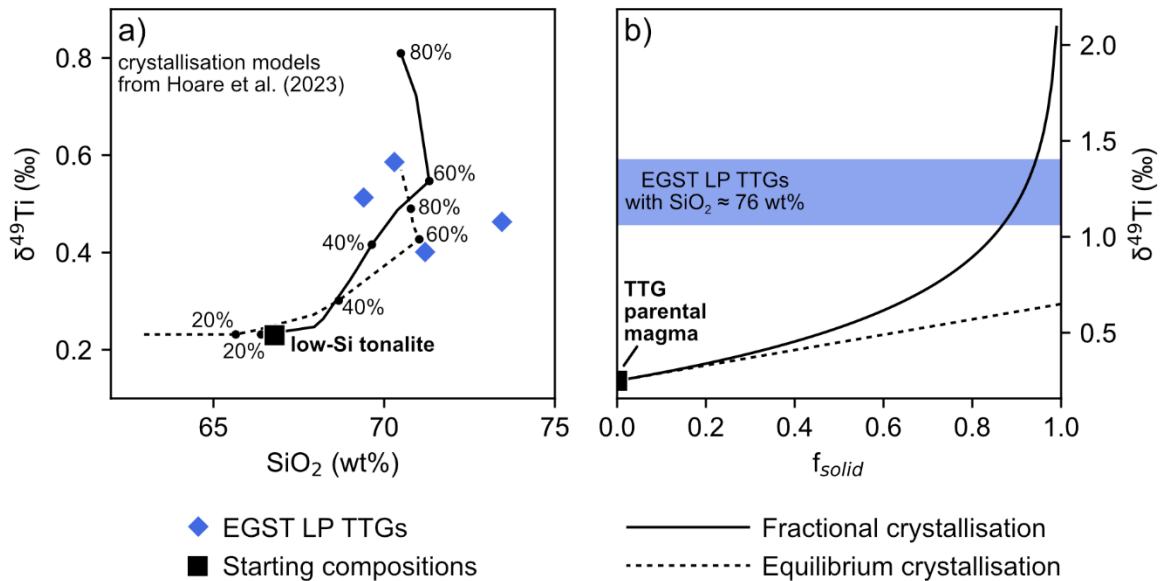
Figure 4.9: a) $\delta^{49}Ti$ (‰) vs SiO_2 (wt%) comparing the EGST LP TTGs to modelled melt compositions from the low-Si tonalite crystallisation models of Hoare et al. (2023). The low-Si tonalite starting composition is SiO_2 = 66.79 wt% and $\delta^{49}Ti$ = 0.23‰. b) Simplified models of melt $\delta^{49}Ti$ evolution vs the fraction of melt that has crystallised (f_{solid}) during equilibrium and fractional crystallisation with $\alpha_{solid-melt}$ = 0.99960 from a TTG parental magma with $\delta^{49}Ti$ = 0.25‰. The blue rectangle shows the $\delta^{49}Ti$ compositions (including 95% ci) of the most evolved ($SiO_2 \approx 76$ wt%) EGST LP TTG samples – 233699 and 240623.

The most evolved TTGs are two LP TTG samples, 233699 and 240623, with $SiO_2 \approx$ 76 wt%. The samples have very high $\delta^{49}Ti$ values of 1.007 ± 0.016‰ and 1.385 ± 0.020‰ respectively, and likely formed by intra-crustal crystallisation of TTG parental magmas. To investigate the crystallisation conditions responsible for their Ti isotope compositions, I modelled Ti isotope fractionation of a TTG parental magma with a starting $\delta^{49}Ti$ value ($\delta^{49}Ti_0$) of 0.25‰ during equilibrium and fractional crystallisation. The Ti budget of the mineral assemblage crystallising from tonalitic magmas is dominated by hornblende + ilmenite ± biotite ± titanomagnetite (e.g. Hoare et al., 2023; Moyen and Martin, 2012; Z.J. Zhang et al., 2023). Very small amounts of Ti can also be hosted in plagioclase but this does not result in significant Ti isotope fractionation (Greber et al., 2021; Mandl, 2019). Hoare et al. (2023) and Z.J. Zhang et al. (2023) calculated that such crystallising mineral assemblages result in solid-melt fractionation factors ($\alpha_{solid-melt}$) < 1, with values down to 0.99960 when abundant ilmenite forms in the latter stages of crystallisation. I hence use $\alpha_{solid-melt}$ = 0.99960 in my

calculations to estimate the upper limit of how melt δ^{49}Ti may increase during TTG crystallisation. Equilibrium crystallisation is an example of closed-system behaviour, so the evolution of melt Ti isotope composition ($\delta^{49}Ti_{melt}$) can be calculated using equation 4.1, where ε is given by equation 4.2 and f_{solid} is the fraction of melt that has crystallised.

$$\delta^{49}Ti_{melt} = \varepsilon f_{solid} + \delta^{49}Ti_0 \quad (4.1)$$

$$\varepsilon = (\alpha_{solid-melt} - 1) \times 1000 \quad (4.2)$$

Fractional crystallisation, on the other hand, is an open-system process that can be modelled using the Rayleigh fractionation equation (equation 4.3).

$$\delta^{49}Ti_{melt} = \left(\left(1000 + \delta^{49}Ti_0\right) \times \left((1 - f_{solid})^{(\alpha_{solid-melt}-1)}\right) \right) - 1000 \quad (4.3)$$

The results of the modelling are plotted in figure 4.9b. Although these are simplified models in that they use a single $\alpha_{solid-melt}$ value and hence ignore any potential changes in the crystallising assemblage, they demonstrate that equilibrium crystallisation is incapable of generating melts with high enough δ^{49}Ti values to explain the most evolved LP TTGs from the EGST. In contrast, extensive (f_{solid} > 0.8) fractional crystallisation can produce melts with comparable δ^{49}Ti to these samples. Higher $\alpha_{solid-melt}$ values (i.e. closer to 1) due to less ilmenite crystallising would require greater extents of fractional crystallisation to generate the most evolved LP TTGs, while melts formed by equilibrium crystallisation would have even lower δ^{49}Ti values. Therefore, the Ti isotope compositions of the most evolved LP TTGs from the EGST require differentiation of TTG magmas via extensive fractional crystallisation.

Overall, Ti stable isotopes provide evidence for contemporaneous formation of TTGs by multiple different mechanisms in the Neoarchean EGST, Yilgarn Craton. LP, MP and MP-like HP TTGs formed by partial melting of hydrous metabasites over a range of pressures, followed by fractional crystallisation. In contrast, the parental magmas of the high-Sr HP TTGs had a mantle source that was metasomatised by fluid-fluxed eclogite melts. These magmas then evolved via hornblende-dominated fractional crystallisation to form the high-Sr HP TTGs. Generation of TTGs by two distinct mechanisms at the same time and in the same location demonstrates that TTG-forming processes were likely more diverse and complex than is generally appreciated.

4.4.4. Global significance of high-Sr HP TTGs

In the prior discussion I have provided further support for the formation of high-Sr HP TTGs by fractional crystallisation of sanukitoid magmas, and demonstrated the contemporaneous petrogenesis of TTGs by two distinct mechanisms in the Neoarchean EGST, Yilgarn Craton. In this section I investigate the potential global significance of high-Sr HP TTGs, and hence of TTG formation from mantle-derived sanukitoid magmas. To do this, I searched for occurrences of TTGs with similar geochemical compositions to the EGST high-Sr HP TTGs on other Archean cratons. These global high-Sr HP TTGs exhibit the key geochemical characteristics listed by Smithies et al. (2019) – $K_2O/Na_2O < 0.5$, Sr > 500 ppm (but ideally > 700 ppm), Sr/Y > 100, Yb < 0.4 ppm and La/Yb > 60 at SiO_2 > 70 wt%. I used literature compilations of global TTG geochemical analyses by Moyen (2011) and T.E. Johnson et al. (2019), as well as the GEOROC Database compilation for Archean cratons (DIGIS Team, 2024) and regional compilations for the Pilbara Craton (Vandenburg et al., 2023), southern São Francisco Craton (Simon et al., 2021) and south-east Superior Province (Mole et al., 2021), to help identify these occurrences. My resulting compilation of high-Sr HP TTG occurrences is presented in table 4.2. I then used my own compilation of published Archean-Paleoproterozoic sanukitoid geochemical data to determine whether the high-Sr HP TTGs are temporally and spatially associated with sanukitoid magmatism to help assess the likelihood of their petrogenesis via the sanukitoid fractional crystallisation model.

While temporal and spatial association with sanukitoids supports formation of high-Sr HP TTGs by fractional crystallisation of metasomatised mantle-derived parental magmas, more detailed investigation is necessary to confirm this petrogenesis for each individual high-Sr HP TTG occurrence. The presence of complementary hornblendite cumulate xenoliths, which formed by accumulation of the fractionated minerals, can provide additional support for the fractional crystallisation origin of high-Sr HP TTGs (Liou and Guo, 2019; Rollinson, 2021; Smithies et al., 2019), and reported occurrences of such cumulates are also recorded in table 4.2. Furthermore, it is important to note that the absence of associated sanukitoids does not preclude the formation of high-Sr HP TTGs by fractional crystallisation of sanukitoid magmas. Sanukitoids are only a minor component of late Archean terranes (e.g. Laurent et al.,
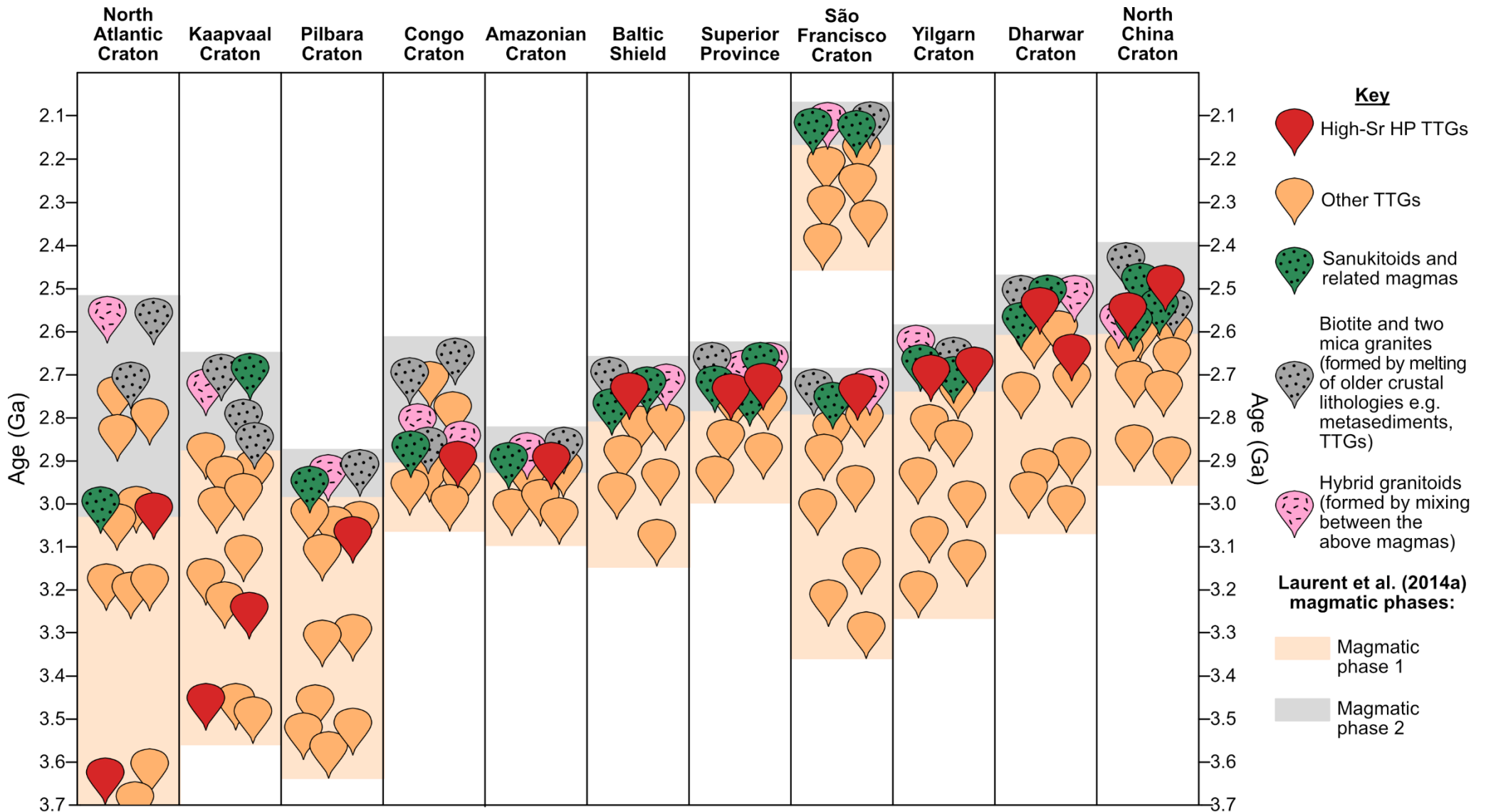
Figure 4.10: Simplified age distributions of high-Sr HP TTG, sanukitoid and other granitoid occurrences on Archean cratons where high-Sr HP TTGs are identified in this chapter. Archean granitoid types and magmatic phases are from Laurent et al. (2014a). This figure is modified from figures in Bruno et al. (2020), Cawood et al. (2018), Heilimo et al. (2011) and Laurent et al. (2014a). Granitoid magma evolution of the North Atlantic Craton was constructed from Garde et al. (2020), Næraa et al. (2014), Olierook et al. (2021) and Steenfelt et al. (2005). Granitoid magma evolution of the Congo Craton was constructed from Akame et al. (2024), Blein et al. (2024), Shang et al. (2004, 2010), Tchameni et al. (2000) and Turnball et al. (2021).

Table 4.2: List of high-Sr HP TTG occurrences on Archean cratons worldwide, sanukitoid occurrences temporally and spatially associated with them, and reports of associated hornblendite cumulates. The full list of references[a] is provided at the end of the table.

Craton	Location	High-Sr HP TTG occurrences			Hornblendite cumulates?	Temporally and spatially associated sanukitoids		
		Suite	Age (Ma)	Refs.[a]		Suite	Age (Ma)	Refs.[a]
Amazonian Craton	Carajás Province	Equigranular granodiorite, Tucumã area	2870	[1]		Rio Maria granodiorite	2872 ± 5	[2]
Baltic Shield	Eastern Finland	Sample H34 from the Naavala grey gneiss	~2700	[3]		Arola intrusion Loso intrusion Siikalahti intrusion	2734 ± 3 2719 ± 19 ~2680	[4]
Congo Craton	Chaillu massif	High La/Yb TTG suite	~2910 – 2840	[5]		Mesocratic to melanocratic gneisses	~2850 – 2830	[5]
Dharwar Craton	Western block	Trondhjemite from the Sargur region	~2650	[6]				
	Central block	Sample KG27 (exact location unclear)	2540	[7, 8]		e.g. Belur granodiorite suite Closepet granite Gajendragarh granodiorite-granite suite	2527 ± 4 ~2560 – 2510 2517 ± 8	[9] e.g. [10] [9]
Kaapvaal Craton	Barberton Greenstone Belt	Stolzberg pluton Weergevonden pluton Badplaas pluton Nelshoogte pluton	~3450 3434 ± 18 ~3260 3236 ± 1	[11] [12] [11, 13] [13]				
North Atlantic Craton	West Greenland	Itsaq gneiss complex Uivak I gneiss suite Igánánguit granodiorite	> 3700 > 3600 3023	[14] [15] [16]		Qeretaussaq diorite	3050	[16]

Table 4.2 continued:

Craton	Location	High-Sr HP TTG occurrences			Hornblendite cumulates?	Temporally and spatially associated sanukitoids		
		Suite	Age (Ma)	Refs.[a]		Suite	Age (Ma)	Refs.[a]
North China Craton	Eastern Block	Granodiorite from the Jiubing area, Northern Liaoning Block	2550 ± 4	[17]		Quartz diorite-monzodiorite from the Jiubing area	~2550	[20]
		Trondhjemite from the Shiwen area, Eastern Liaoning province	~2547 – 2517	[18]		Quartz diorite-granodiorite from the Shiwen area	~2550	[18, 21]
		Trondhjemite from the Zuamenzi-Gualanyu area, Eastern Hebei terrane	~2500	[19]	Yes	Petrogenetically-linked diorites from the Zuamenzi-Gualanyu area	~2500	[19]
	Trans-North China Orogen	Multiple TTG gneisses from the Datong-Huai'an Complex	~2500 – 2450	[22, 23]	Mention of hbl-accumulation melanosomes by [22], but absence noted by [23]	Coeval dioritic gneisses from the Datong-Huai'an Complex	~2526 – 2485	[22, 23]
	Western Block	Tonalite-granodiorite from the Siziwangqi area, Yinshan Block	~2500	[24]		Diorites from the Yinshan Block, e.g. Dajitu pluton, Banshentu pluton	~2525 – 2480	[25-27]
Pilbara Craton	Sholl Terrane	Granodiorite from the Whundo area	~3070	[28]				
São Francisco Craton	Southern São Francisco Craton	Tonalitic gneiss from the Bação complex	2778 ± 2	[29]		Absence in the Bação complex noted by [29]		
		TTG gneisses from the Campo Belo complex	~2730	[30, 31]		Granodioritic-tonalitic gneisses from the Campo Belo Complex		[30-32]

Table 4.2 continued:

Craton	Location	High-Sr HP TTG occurrences			Hornblendite cumulates?	Temporally and spatially associated sanukitoids		
		Suite	Age (Ma)	Refs.[a]		Suite	Age (Ma)	Refs.[a]
Superior Province	Southeast Superior Province	TTGs from the Abitibi Subprovince, e.g. Round Lake Batholith, Kenogamissi Batholith, Hope Lake Stock	~2740 – 2660	[33]		Multiple intrusions from the Abitibi Subprovince, e.g. Otto Lake Stock, O'Brien Stock, Abitibi Batholith	~2690 – 2670	e.g. [34, 35]
		Various TTGs from the Opatica Subprovince		[33]		Multiple intrusions from the Opatica Subprovince, e.g. Lac au Bout Intrusion, Théodat Complex, La Sicotière Suite	~2830 – 2690	e.g. [36]
		Various TTGs from the Pontiac Subprovince		[33]		Multiple intrusions from the Pontiac Subprovince, e.g. Lac Fréchette Pluton, Lac Fournière Pluton, Rémigny Batholith	~2685 – 2675	e.g. [37]
Yilgarn Craton	Youanmi Terrane	Lady Lydia granitoid, Yalgoo area, Murchinson domain	~2760 – 2750	[38]		Cagacaroon syenogranite, Yalgoo Dome, Murchinson domain	~2747	[39]
	Eastern Goldfields Superterrane	TTGs from the southern Kalgoorlie Terrane (fig. 4.7)	~2700 – 2650	[40]	Yes	Black Flag Group, southern Kalgoorlie Terrane	~2700 – 2650	[40, 41]

[a]References: [1] Silva-Silva et al. (2020); [2] de Oliveira et al. (2009); [3] Martin (1987); [4] Heilimo et al. (2010); [5] Blein et al. (2024); [6] Ranjan et al. (2020); [7] T.E. Johnson et al. (2019); [8] Moyen (2011); [9] Dey et al. (2017); [10] Moyen et al. (2001); [11] Clemens et al. (2006); [12] Laurent et al. (2020); [13] André et al. (2019); [14] Liu et al. (2016); [15] Hoffmann et al. (2011); [16] Garde (1997); [17] Wang et al. (2017); [18] Liu et al. (2020); [19] Liou and Guo (2019); [20] Sun et al. (2020); [21] Bao et al. (2022); [22] Chen et al. (2022); [23] J. Zhang et al. (2023); [24] Chen et al. (2017); [25] Ma et al. (2013); [26] D. Wang et al. (2018); [27] Wang et al. (2024); [28] Vandenburg et al. (2023); [29] Farina et al. (2015); [30] Miranda et al. (2018); [31] Simon et al. (2021); [32] Engler et al. (2002); [33] Mole et al. (2021); [34] Sutcliffe et al. (1990); [35] Fayol & Jébrak (2017); [36] Pedreira Pérez et al. (2024); [37] Godet et al. (2023); [38] Mahbubul Ameen and Wilde (2018); [39] Clos et al. (2018); [40] Smithies et al. (2019); [41] Smithies et al. (2022).

2014a), and on many cratons, such as the Pilbara Craton (e.g. Smithies and Champion, 2000), the Superior Craton (e.g. Stern et al., 1989) and the Baltic Shield (e.g. Heilimo et al., 2010), they primarily occur as relatively small intrusions of < 10 km in length. It is possible that the sanukitoids in a given region have simply not been preserved. Alternatively, in regions with poor exposure, that have not been mapped in detail, or that lack geochemical data, sanukitoids might not yet have been discovered or recognised as such.

High-Sr HP TTGs are found on many cratons globally and range from Eoarchean to early Paleoproterozoic in age (fig. 4.10). However, high-Sr HP TTGs become more abundant and widespread after ~3 Ga, with > 3.2 Ga occurrences limited to the Kaapvaal and North Atlantic Cratons (André et al., 2019; Clemens et al., 2006; Hoffmann et al., 2011; T. E. Johnson et al., 2019; Laurent et al., 2020; Liu et al., 2016; Yearron, 2003). This temporal distribution of high-Sr HP TTGs mirrors that of sanukitoids (e.g. Laurent et al., 2014a; Martin et al., 2009), and the majority of the < 3 Ga high-Sr HP TTG occurrences are spatially and temporally associated with sanukitoid magmatism (table 4.2, fig. 4.10). For example, Blein et al. (2024) report coeval ~2910 – 2840 Ma high-Sr HP TTGs and sanukitoids in the Chaillu Massif, Congo Craton, while both sanukitoids and high-Sr HP TTGs are documented in the ~2730 Ma Campo Belo Complex, São Francisco Craton (Engler et al., 2002; Miranda et al., 2018; Simon et al., 2021). Several instances of contemporaneous high-Sr HP TTGs and sanukitoids are found in the North China Craton between 2540 – 2440 Ma (see table 4.2). It is therefore viable that these high-Sr HP TTGs formed by a similar mechanism to the EGST high-Sr HP TTGs, and ultimately had a metasomatised mantle source.

The above findings suggest that mechanisms for forming TTG magmas may have globally diversified in the late Archean (< 3 Ga). This shift might have arisen from secular geodynamic changes that facilitated metabasite melt-mantle interaction, enabling the metasomatised mantle sources of sanukitoids and high-Sr HP TTGs to form. Many studies have proposed a geodynamic transition in response to secular cooling of the Earth as the reason behind the observed diversification and compositional evolution of granitoids in the late Archean (e.g. Cawood et al., 2022; T.E. Johnson et al., 2019; Laurent et al., 2014a), although the exact nature of this

change varies depending on when subduction is considered to have begun. If subduction is thought to have already been operating in the early Archean, this change may be increasing depth and decreasing degree of slab melting in response to mantle cooling (e.g. Martin et al., 2009; Martin and Moyen, 2002), making melt-mantle interaction and mantle metasomatism more favourable. Some studies also suggest that mantle cooling can steepen the subduction angle (e.g. Sizova et al., 2010; van Hunen and Moyen, 2012), again resulting in greater interaction between slab melts and mantle peridotite. An opposing view is that this geodynamic transition represents the onset of subduction and modern-style plate tectonics (e.g. Cui et al., 2022; Smithies and Champion, 2000). After this, crustal materials could be readily recycled into the mantle, leading to the formation of metasomatised mantle. Meanwhile, intraplate geodynamic models proposed for the late Archean invoke crustal drips developing asymmetric, subduction-like shapes due to intra-crustal flow, enabling interaction between crustal melts and the mantle (Nebel et al., 2018; Vandenburg et al., 2023). An alternative perspective is that metasomatised mantle and sanukitoid magmas were generated continually throughout the Archean, but that these magmas could not be efficiently extracted and emplaced at upper crustal levels until the lithosphere strengthened and trans-lithospheric structures such as shear zones could develop (Smithies et al., 2019). In this model, these structures facilitated extraction and shallow emplacement of the deep-sourced sanukitoid (and by extension high-Sr HP TTG) magmas. Regardless of the exact geodynamic change involved, the increased abundance of high-Sr HP TTGs in the late Archean likely reflects greater crust-mantle interaction from this time onwards.

T.E. Johnson et al. (2019) investigated secular changes in TTG compositions and observed increasing maximum values for Sr concentration and Sr/Y with decreasing age. T.E. Johnson et al. attributed this to an increase in the depth of metabasite melting in the mid-late Archean, with more residual garnet (which sequesters Y) and less/no residual plagioclase (which sequesters Sr) present during TTG genesis. However, in light of the results presented in this chapter, the onset of high-Sr HP TTG formation by fractional crystallisation of metasomatised mantle melts may contribute significantly to generating the increasing trends in Sr and Sr/Y seen by T.E. Johnson et al. (2019). Consequently, the straight-forward interpretation that secular evolution of TTG

compositions primarily reflects changes in melting depth is complicated by the multiple mechanisms for forming TTG magmas.

Derivation of high-Sr HP TTGs from a metasomatised mantle source instead of from recycled metabasite means that some late Archean TTGs represent net addition of material to the continental crust, instead of only recording reworking of pre-existing crust. Therefore, while the late Archean was a period of increasing intra-crustal reworking which generated potassic granitoids through melting of pre-existing TTGs and metasediments (e.g. Laurent et al., 2014a; Li et al., 2020), it also saw a rise in addition of new material to the continental crust through sanukitoids and high-Sr HP TTGs. This result may have implications for crustal growth models as they might have underestimated juvenile input in the late Archean. However, only ~20% of TTGs are classified as HP TTGs (Moyen, 2011), of which high-Sr HP TTGs form only a subset. High-Sr HP TTGs therefore constitute a relatively minor proportion of TTG magmatism and their contribution to crustal growth is likely limited.

While metasomatised mantle appears to be a viable source for the parental magmas of many high-Sr HP TTGs, this petrogenesis is unlikely to account for all high-Sr HP TTG occurrences. The Eo- and Paleoarchean high-Sr HP TTGs from the Kaapvaal and North Atlantic Cratons were emplaced long before any sanukitoids or sanukitoid-like rocks were in those locations (André et al., 2019; Clemens et al., 2006; Hoffmann et al., 2011; T. E. Johnson et al., 2019; Laurent et al., 2020; Liu et al., 2016; Yearron, 2003). Unlike the younger high-Sr HP TTG occurrences, which were emplaced during Laurent et al. (2014a)'s magmatic phase 2 when diverse granitoid magmas formed over a short period of time, these TTGs formed during the long-lasting initial period of TTG generation on these cratons (magmatic phase 1, fig. 4.10). The distinctive "high-Sr high pressure" geochemical signature of these TTGs may instead record intra-crustal mineral fractional crystallisation/accumulation of tonalitic magmas formed by partial melting of hydrous metabasite. Indeed, Laurent et al. (2020) proposed that the high-Sr HP TTGs from the ~3450 Ma Stolzburg pluton, Kaapvaal Craton, were generated by the combined effects of plagioclase accumulation and loss of interstitial liquid of a tonalitic parental magma, that itself was likely generated by metabasite partial melting at moderate pressures.
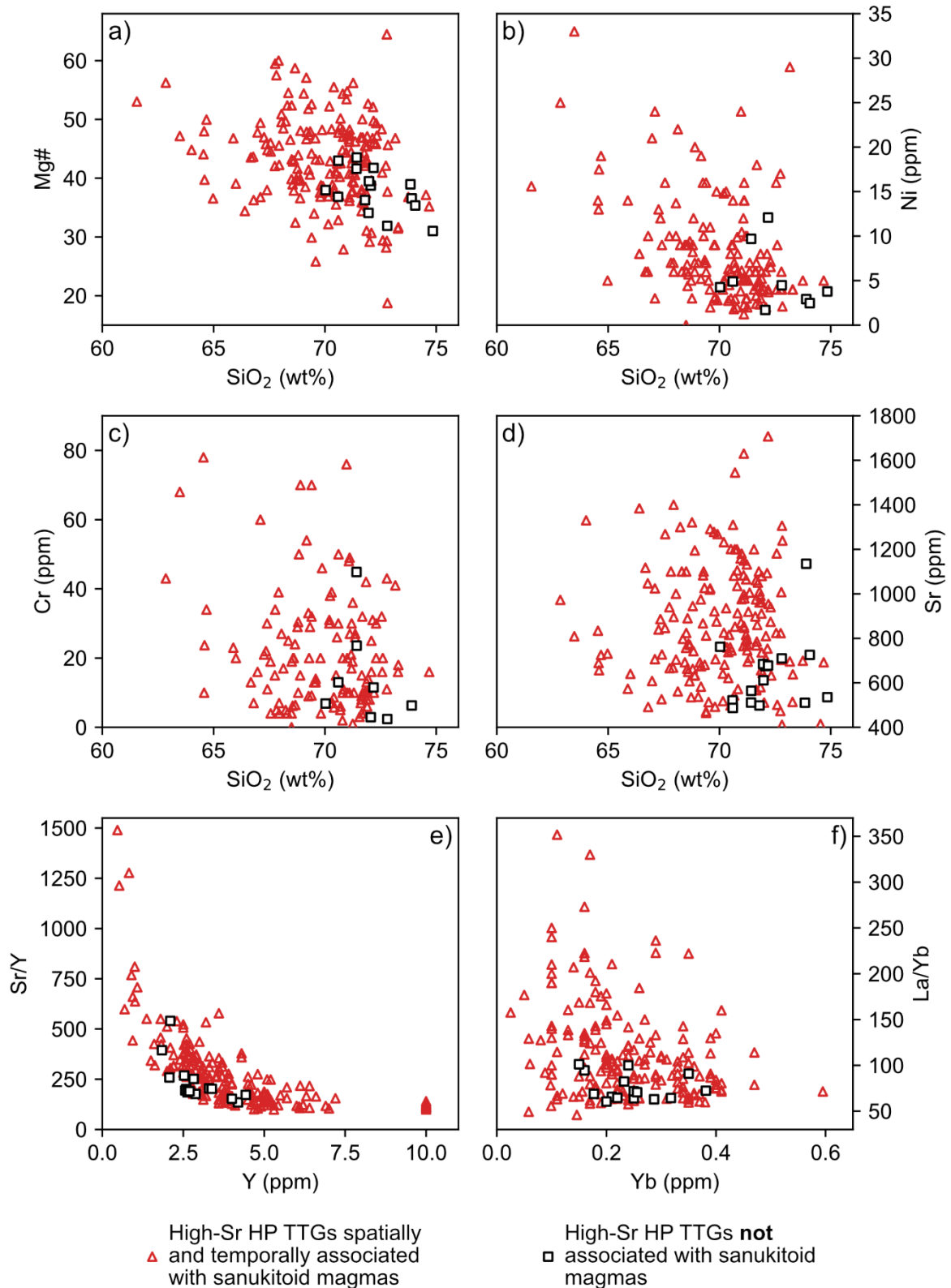
Figure 4.11: Comparison between global high-Sr HP TTGs spatially and temporally associated with sanukitoid magmas and those high-Sr HP TTG occurrences not spatially and/or temporally associated with sanukitoid magmas. a) Mg# vs SiO₂ (wt%), b) Ni (ppm) vs SiO₂ (wt%), c) Cr (ppm) vs SiO₂ (wt%), d) Sr (ppm) vs SiO₂ (wt%), e) Sr/Y vs Y (ppm), and f) La/Yb vs Yb (ppm). The full list of references for the data is given in table 4.2.

Furthermore, not all Meso-Neoarchean high-Sr HP TTGs are clearly associated with sanukitoid magmatism. One example is a ~2650 Ma trondhjemite from the Western Dharwar Craton (Ranjan et al., 2020) where no sanukitoid occurrences have been reported. Additionally, this high-Sr HP TTG predates the earliest sanukitoid magmatism in the Dharwar Craton by ~20 Myr (Balakrishnan and Rajamani, 1987; Krogstad et al., 1991). Fractional crystallisation of sanukitoid parental magmas may hence seem to be an unlikely petrogenesis for this trondhjemite. The situation is similar for a ~3068 Ma high-Sr HP TTG from the Sholl Terrane of the Pilbara Craton (Vandenburg et al., 2023) and a 2778.2 ± 1.5 Ma high-Sr HP TTG from the Bação Complex in the São Francisco Craton (Farina et al., 2015), neither of which are spatially associated with sanukitoids. However, as mentioned earlier, the absence of associated sanukitoids does not mean that they never existed – it is possible that in these regions the sanukitoids were not preserved or that their occurrence has just not been reported yet.

Although there is no clear compositional difference between high-Sr HP TTGs associated with sanukitoids and high-Sr HP TTGs *not* associated with sanukitoids, some minor distinctions can be made. High-Sr HP TTGs associated with sanukitoids generally extend to higher concentrations of compatible trace elements (Ni, Cr) and higher Mg# than those of comparable SiO_2 content that are not associated with sanukitoids (figs. 4.11a-c), which may reflect the mantle source of the former TTGs. Occurrences associated with sanukitoids also extend to more extreme Sr concentrations and Sr/Y and La/Yb values, particularly in comparison to the Eo- and Paleoarchean high-Sr HP TTGs (figs. 4.11d-f).

Taken altogether, it appears that high-Sr HP TTGs show a similar temporal distribution to sanukitoids, becoming significantly more widespread in the late Archean (< 3 Ga). This observation may imply that formation of TTGs by fractional crystallisation of metasomatised mantle-derived magmas became a global phenomenon at this time due to a geodynamic transition than promoted metabasite melt-mantle interaction. Therefore, contemporaneous formation of TTGs by multiple distinct mechanisms could have occurred on many cratons in the late Archean. However, while it is important to recognise that some Archean TTGs ultimately had a mantle source and hence represent net addition of material to the continental crust, high-Sr HP TTGs are

relatively uncommon, so this mechanism likely accounts for only a minor amount of TTG magmatism and crustal growth. On top of that, it seems improbable that this petrogenesis can explain all high-Sr HP TTG occurrences, particularly those from the Eo- and Paleoarchean, so the geochemical compositions of these TTGs may instead record high pressure melting of hydrous metabasite or mineral fractional crystallisation/accumulation of magmas formed by melting metabasite at lower pressures (Ding et al., 2024; Kendrick et al., 2021; Laurent et al., 2020; Mathieu, 2022; Rollinson, 2021).

4.5. Conclusions

In this chapter I present the Ti stable isotope compositions of Neoarchean TTGs from the Eastern Goldfields Superterrane, Yilgarn Craton. The δ^{49}Ti values of the high-Sr HP TTGs plot at the evolved end of the Black Flag Group sanukitoid differentiation trend and Rayleigh fractionation models, demonstrating that they formed by hornblende-dominated fractional crystallisation of low La/Th BFG magmas. This result provides further support for the formation of these TTGs by fractional crystallisation of metasomatised mantle-derived sanukitoid magmas. The Ti isotope compositions of other TTGs from the EGST can be explained by partial melting of hydrous metabasites sometimes followed by fractional crystallisation. Ti stable isotopes therefore provide evidence for contemporaneous formation of TTGs by multiple mechanisms – hydrous metabasite partial melting *and* fractional crystallisation of mantle-derived magmas – in the Neoarchean Yilgarn Craton.

TTGs with similar geochemical compositions to the EGST high-Sr HP TTGs are reported on many Archean cratons, and their temporal distribution largely mirrors that of sanukitoids, becoming more abundant and widespread after ~3 Ga. Many of these global high-Sr HP TTGs are spatially and temporally associated with sanukitoids, implying that formation of TTGs by fractional crystallisation of metasomatised mantle-derived magmas was a global phenomenon that emerged in the late Archean due to a geodynamic transition that promoted interaction between metabasite melts and mantle peridotite. These high-Sr HP TTGs represent newly identified, albeit volumetrically minor, juvenile additions to the continental crust in the late Archean.

5. Constraints on the uranium isotope compositions of sanukitoids and TTGs

5.1. Abstract

Surface oxygenation has significantly increased over the Earth's history, impacting the biogeochemical cycling of redox-sensitive elements such as uranium (U). The resulting changes in the elemental and isotopic compositions of near-surface materials – seafloor-altered oceanic crust (AOC) and sediments – can be recorded by secular variations in the geochemistry of mantle-derived igneous rocks. Terrestrial U isotope fractionation is primarily driven by redox changes, meaning the U isotope compositions ($\delta^{238}U$) of these materials are particularly sensitive to varying surface oxygenation. Sanukitoids are mantle-derived rocks that contain an AOC-derived melt component and were emplaced across the Great Oxidation Event (GOE, ca. 2.45 – 2.05 Ga). In this chapter I present the U isotope compositions of Archean and Paleoproterozoic sanukitoids and Paleozoic sanukitoid analogues, aiming to investigate whether the $\delta^{238}U$ of AOC recycled into the mantle changed over the Earth's history in response to increasing surface oxygenation. These data are supplemented by analyses of tonalites-trondhjemites-granodiorites (TTGs) to better constrain the U isotope composition of the dominant constituent of Archean continental crust.

I show that $\delta^{238}U$ variations in TTGs and sanukitoids are primarily driven by apatite fractional crystallisation, which causes a decrease in $\delta^{238}U$ during magmatic differentiation. These data provide the first evidence of high-temperature U isotope fractionation influencing the $\delta^{238}U$ of bulk terrestrial igneous rocks. Archean sanukitoids not affected by fractional crystallisation display distinctly higher $\delta^{238}U$ and Th/U than most modern arc magmas and hence show no evidence of U^{6+} addition to their mantle sources by oxidised aqueous fluids, implying that Archean sanukitoids

were oxidised by different mechanisms to modern arc magmas. A Paleoproterozoic sanukitoid and the Rogart high Ba-Sr granite pluton have elevated $\delta^{238}U$ values, likely due to an isotopically heavy recycled sediment component. Overall, data for sanukitoids and their analogues are too limited to confidently discern any secular evolution in their U isotope compositions. Comparison with literature granitoid $\delta^{238}U$ data reveals that Neoarchean granitoids not affected by apatite fractional crystallisation have indistinguishable $\delta^{238}U$ (-0.27 ± 0.02‰) to Phanerozoic granitoids. They may have marginally heavier $\delta^{238}U$ than the bulk silicate Earth (BSE, -0.306 ± 0.026‰) but improved constraints on the U isotope composition of the BSE are needed to confirm this observation. Eoarchean granitoids appear to have considerably lighter $\delta^{238}U$ (~-0.38‰) than Neoarchean granitoids and the BSE, although available Eoarchean data are very limited and further work is necessary to investigate whether granitoid, and hence potentially mantle, $\delta^{238}U$ increased over the Archean.

5.2. Introduction

Atmospheric and oceanic oxygenation have significantly changed over the Earth's history (e.g. Canfield, 2005; Holland, 2006; Lyons et al., 2014; Reinhard and Planavsky, 2022), hugely impacting the biogeochemical cycling of redox-sensitive elements. The first major increase in atmospheric molecular oxygen (O_2) occurred during the "Great Oxidation Event" or "GOE" at ca. 2.45 – 2.05 Ga (e.g. Bekker et al., 2004; Gumsley et al., 2017; Holland, 2002; Poulton et al., 2021), when O_2 levels increased from negligible (< 0.001% of the modern level; Pavlov and Kasting, 2002) to up to ~10% of the modern level (e.g. Holland, 2006; Kanzaki and Murakami, 2016). A second major increase in surface oxygenation, called the "Neoproterozoic Oxygenation Event" or "NOE", followed at ca. 0.8 – 0.55 Ga (e.g. Fike et al., 2006; Och and Shields-Zhou, 2012; Scott et al., 2008; Shields-Zhou and Och, 2011). Atmospheric O_2 increased towards modern levels (e.g. Krause et al., 2022; Sperling et al., 2015) and the oceans are thought to have become fully oxygenated at this time (e.g. Canfield, 1998; Canfield et al., 2007; Reinhard and Planavsky, 2022; Sahoo et al., 2012).

Increasing surface oxygenation also affected the deep Earth as the chemical and isotopic compositions of near-surface materials – seafloor-altered oceanic crust (AOC) and sediments – being recycled into the mantle changed. Some of these recycled crustal materials end up in the mantle source regions of igneous rocks, meaning that mantle-derived rocks can record changes in Earth's surface oxygenation (Ahmad et al., 2023, 2022; Andersen et al., 2015; Liu et al., 2019; Moreira et al., 2023; Stolper and Bucholz, 2019). Sanukitoids are mantle-derived rocks that contain a recycled crustal component – most likely a metabasite-derived melt (see Chapter 3 of this thesis) – and crucially were emplaced across the GOE during the late Archean-early Proterozoic transition (fig. 1.8; e.g. Askkour et al., 2023; Bruno et al., 2020; Laurent et al., 2014a). Sanukitoid geochemistry may therefore record changes in the composition of crustal materials, in particular of AOC, being recycled into the mantle across the GOE. As high Ba-Sr granite suites are proposed to be Phanerozoic analogues of Archean and Paleoproterozoic sanukitoids (e.g. Fowler and Rollinson, 2012), it might be possible to extend this record to additionally investigate changes in the composition of recycled crustal materials across the NOE.

Terrestrial cycling of uranium (U) was greatly impacted by changes in surface oxygenation. U has two major valence states – fluid-mobile U^{6+} and fluid-immobile U^{4+} (e.g. Langmuir, 1978). Consequently, the GOE significantly increased U mobility on Earth as U^{4+} could be oxidised to U^{6+} and liberated from U-bearing minerals by aqueous fluids for the first time (e.g. Cuney, 2010). This process established a continental weathering-derived flux of dissolved U to the oceans and addition of U from seawater to AOC during seafloor alteration began, fractionating U from thorium (Th) to give AOC low Th/U ratios. Liu et al. (2019) observed variations in the Th/U of arc igneous rocks through time in response to changes in the Th/U of recycled AOC at the GOE and NOE. The changes in surface oxygenation also affected U isotopes as redox changes are the primary driver of terrestrial U isotope fractionation (e.g. Andersen et al., 2017). Multiple studies of sediments report changes in U isotope composition (expressed in delta notation as $\delta^{238}U = 10^3 \times [(^{238}U/^{235}U)_{sample} / (^{238}U/^{235}U)_{CRM145} - 1]$) across the GOE (Brüske et al., 2020; Chen et al., 2021; X. Wang et al., 2018) and NOE (e.g. Chen et al., 2021; Wei et al., 2021). Ophiolites appear to only show evidence of significant U isotope fractionation during U addition after the NOE, as U addition to oceanic crust during seafloor alteration before the NOE was

likely near-quantitative because it occurred under relatively U-poor, anoxic deep ocean conditions (Rodney et al., 2024, Preprint). Andersen et al. (2015) and Gaschnig et al. (2021b) propose that the difference in $\delta^{238}U$ between normal mid-ocean ridge basalts (N-MORB) and some ocean island basalts (OIB), both of which have low Th/U indicating addition of recycled U to their mantle sources, records a change in the U isotope composition of AOC being recycled into the mantle across the NOE. These studies demonstrate that U isotopes are an effective tracer of secular redox changes on the Earth's surface, and that these signatures can be preserved in igneous rocks.

In this chapter I measure the U isotope compositions of Archean and Paleoproterozoic sanukitoids and their Phanerozoic analogues, aiming to trace changes in the composition of crustal materials being recycled into the mantle across the GOE and NOE, as well as changes in the processes involved in this recycling. Pre-GOE samples consist of ~3421 Ma "sanukitoid-like" rocks and ~2950 Ma sanukitoids from the Pilbara Craton, and ~2670 Ma sanukitoids from the Black Flag Group (BFG), Yilgarn Craton. The post-GOE sanukitoids are from the São Francisco Craton and Paleocontinent and are ~2130 Ma. The ~425 Ma high Ba-Sr granite suites from Scotland represent post-NOE sanukitoid analogues. I measure $\delta^{234}U$ (= 10^3 x [$(^{234}U/^{238}U)_{sample}$ / $(^{234}U/^{238}U)_{CRM145}$ − 1] + $\delta^{234}U_{CRM145}$) alongside $\delta^{238}U$ to help assess the extent of recent U mobility due to weathering and alteration in these samples as these processes may modify $\delta^{238}U$ (e.g. Andersen et al., 2015; Charbonnier et al., 2023; Pavia et al., 2023).

The study of U isotopes in sanukitoids is supplemented by analysis of Archean TTGs (tonalites-trondhjemites-granodiorites) from the Pilbara and Yilgarn Cratons, Western Australia. These measurements are made to help constrain the U isotope composition of the main constituent of Archean continental crust. TTGs are compositionally distinct to modern continental crust as they are sodic ($K_2O/Na_2O < 0.6$) with highly fractionated rare earth elements (REEs) and no negative europium (Eu) anomaly (e.g. Moyen and Martin, 2012). The change in continental crust composition from sodic Archean TTGs to the potassic granites that dominate younger upper continental crust (UCC) occurred at a similar time to the GOE in the late Archean-early Proterozoic, and is thought to reflect a change in continental crust forming processes resulting from a geodynamic transition towards modern-style plate tectonics (e.g. Hawkesworth et al., 2020; Laurent et al., 2014a; Taylor and McLennan, 1995). Whether these changes had any effect on

the U isotope composition of the continental crust is not currently known. Noordmann et al. (2016) is the only study to report U isotope measurements of Archean granitoids, but they only analysed a limited number of samples and did not measure $\delta^{234}U$ or discuss whether the $\delta^{238}U$ of these samples had been modified by later alteration. Constraining the evolution of granitoid $\delta^{238}U$ is important for studies that use U isotopes in marine sedimentary rocks to trace surface redox processes over the Earth's history as weathering of the continental crust is the dominant source of U in the oceans (e.g. Dunk et al., 2002; Tissot and Dauphas, 2015). At the moment, such studies have to make the assumption that the $\delta^{238}U$ of Archean UCC is identical to that of Phanerozoic UCC (e.g. Chen et al., 2021; X. Wang et al., 2018). Measuring the U isotope compositions of TTGs will therefore not only provide a useful comparison to sanukitoids but will also help test the validity of this assumption.

The U isotope measurements of sanukitoids and TTGs were made via the methods described in Chapter 2, section 2.1, and full sample descriptions are given in Chapter 2, section 2.2. The resulting data are presented and discussed in the rest of this chapter. However, I first briefly discuss the U isotope compositions of the bulk Earth and bulk silicate Earth (BSE) which are referred to throughout this chapter.

5.2.1. U isotope compositions of the bulk Earth and the bulk silicate Earth

The isotopic compositions of the bulk Earth and the bulk silicate Earth are important points of comparison when interpreting isotope data from terrestrial igneous rocks, as deviation from bulk Earth or BSE values implies that isotope fractionation has occurred during the formation of the rock or during post-emplacement processes. It is therefore crucial that bulk Earth and BSE isotopic compositions are well constrained. There is currently some uncertainty about the $\delta^{238}U$ of the bulk Earth – Andersen et al. (2015) calculated bulk Earth $\delta^{238}U$ of -0.306 ± 0.026‰ based on high precision measurements of two meteorites, while Andersen et al. (2017) estimated bulk Earth $\delta^{238}U$ to be -0.34‰ based on a larger number of meteorite analyses taken from Andersen et al. (2015), Connelly et al. (2012) and Goldmann et al. (2015).

A common approach for estimating the isotopic composition of the bulk Earth is to measure primitive chondritic meteorites. For U isotopes this comes with multiple difficulties. First, U concentrations in chondrites are low, meaning large masses of chondrite sample are needed to make high precision $\delta^{238}U$ measurements. This was done by Andersen et al. (2015) who obtained high precision (2se = 0.02 – 0.05‰) $\delta^{238}U$ measurements from large chondrite samples of 5 – 25 g. In contrast, Goldmann et al. (2015) measured chondrite samples mostly weighing < 1 g and as a result their data have lower precisions (typical 2se = 0.06 – 0.18‰). However, it is difficult to obtain large samples of meteorites due to their limited volume, meaning Andersen et al. were able to analyse fewer meteorite samples than Goldmann et al.. Another drawback of measuring low sample masses is that U is concentrated in minor phases (e.g. apatite, oldhamite) in chondrites and is therefore susceptible to the "nugget effect" (Tissot and Dauphas, 2015). The abundance of these minor phases can vary significantly between small samples, translating into U isotope measurements that are not representative of the bulk sample composition.

Additionally, the $\delta^{238}U$ of meteorites, and in particular of meteorite finds, may have been affected by aqueous alteration on Earth, which can mobilise U and fractionate its isotopes (Andersen et al., 2015). Recent (within the last ~1.5 Myr) disturbance can be assessed using $\delta^{234}U$ as U loss or gain shifts $\delta^{234}U$ away from secular equilibrium ($\delta^{234}U = 0$). Andersen et al. (2015) measured $\delta^{234}U$ alongside $\delta^{238}U$ in meteorites and used the combination of $\delta^{234}U$ and Th/U to assess the effects of terrestrial weathering on the meteorites. They subsequently calculated their bulk Earth value using only samples at secular equilibrium. No $\delta^{234}U$ measurements of chondrites were made by Goldmann et al. (2015) or Connelly et al. (2012).

Considering the above, I favour the bulk Earth $\delta^{238}U$ value of -0.306 ± 0.026‰ (2se, n = 2) calculated by Andersen et al. (2015). While it is based on a very limited number of meteorite samples, it is calculated from high precision measurements of large samples and only includes samples not affected by terrestrial weathering. Further support for this bulk Earth value comes from its agreement with the independently calculated bulk Earth $\delta^{238}U$ value of -0.29 ± 0.02‰ from Tissot and Dauphas (2015). This value was calculated using a mass balance between the crustal and mantle U reservoirs, assuming the bulk Earth has a chondritic U concentration.

The BSE includes the Earth's mantle and crust but not its core. Metal-silicate partitioning experiments predict that negligible U is present in the Earth's core (e.g. Faure et al., 2020; Wheeler et al., 2006), hence virtually all terrestrial U is found in the BSE, and we can assume that the U isotope composition of the BSE is identical to that of the bulk Earth. I therefore use the -0.306 ± 0.026‰ as the δ^{238}U value for both the bulk Earth and the BSE in this chapter.

5.3. Results
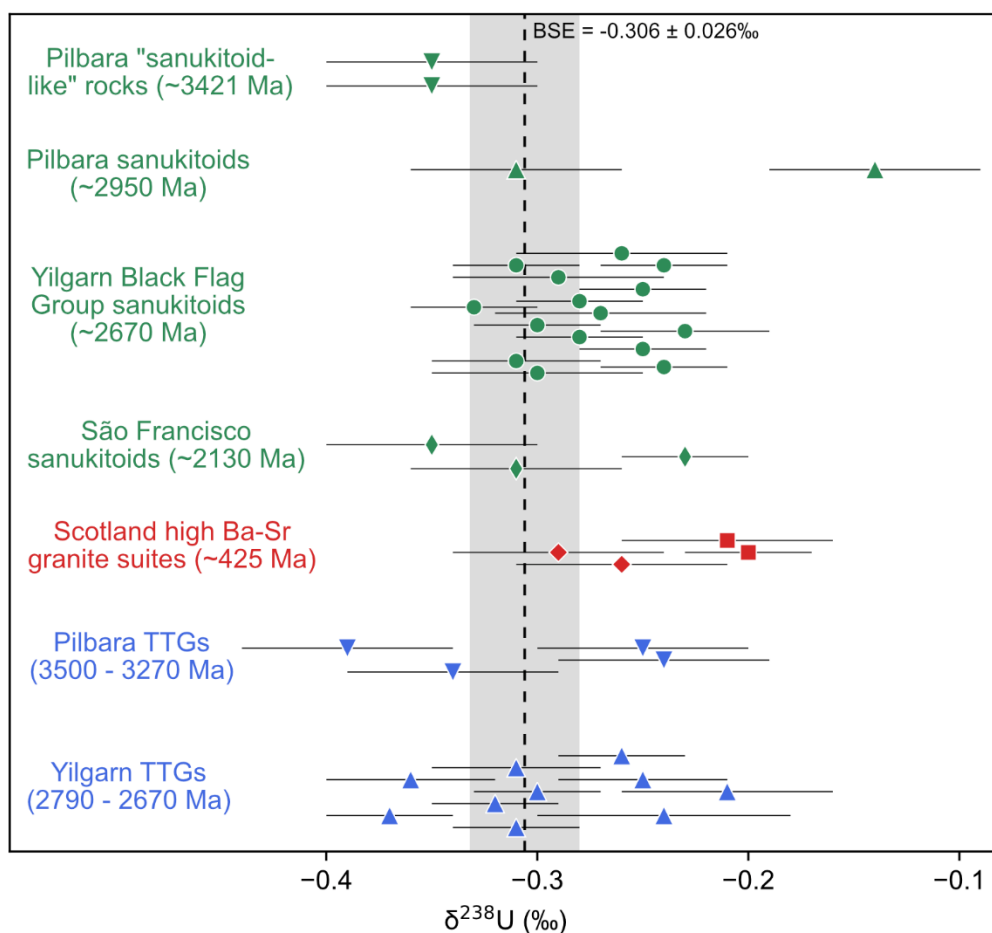
Figure 5.1: δ^{238}U (‰) of Archean and Paleoproterozoic sanukitoids (green), Paleozoic high Ba-Sr granite suites proposed to be Phanerozoic sanukitoid analogues (red) and Archean TTGs (blue). Uncertainty on δ^{238}U is shown as 2se. The black dashed line is the BSE δ^{238}U value of -0.306 ± 0.026‰ (Andersen et al., 2015) and the grey box is the 2se uncertainty on this value.

The U isotope compositions of the samples analysed for this chapter are presented in table 5.1 and figures 5.1 and 5.2. The $\delta^{238}U$ values of most Archean and Paleoproterozoic sanukitoids vary from -0.35 to -0.23‰ (fig. 5.1). The lower end of this range is slightly lighter than the $\delta^{238}U$ of the BSE (-0.306 ± 0.026; Andersen et al., 2015), while the upper end extends to slightly heavier $\delta^{238}U$ values than the BSE. One 2.95 Ga sanukitoid from the Pilbara Craton (sample 235917) has distinctly higher $\delta^{238}U$ of -0.14 ± 0.05‰. There is $\delta^{238}U$ heterogeneity among sanukitoid samples from the same suite – the fifteen samples from the Black Flag Group have $\delta^{238}U$ from -0.33 ± 0.03‰ to -0.23 ± 0.04‰, while the two samples from the Alto Maranhão suite have distinct $\delta^{238}U$ values of -0.35 ± 0.05‰ and -0.23 ± 0.03‰. There is no clear covariation between sanukitoid $\delta^{238}U$ and indices of magma differentiation (e.g. SiO_2, MgO) (figs. 5.2e and f).

The Paleozoic high Ba-Sr granite suites have $\delta^{238}U$ values that overlap with the Archean and Paleoproterozoic sanukitoids and extend to slightly heavier values (-0.29 ± 0.05‰ to -0.20 ± 0.03‰). The Rogart pluton has distinctly higher $\delta^{238}U$ (-0.21 ± 0.05‰ to -0.20 ± 0.03‰) than the Strontian pluton (-0.29 ± 0.05‰ to -0.26 ± 0.05‰). There is no obvious covariation between $\delta^{238}U$ and indices of differentiation or U concentration across both high Ba-Sr granite plutons (fig. 5.2).

The $\delta^{238}U$ values of Archean TTGs cover a similar range to the sanukitoids of -0.39 ± 0.05‰ to -0.21 ± 0.05‰. Most TTGs have $\delta^{238}U$ within error of the BSE – only two samples (235945, 500854) are lighter than it and one sample (232744) is heavier than it. There is no clear difference between the U isotope compositions of TTGs from the Pilbara Craton and TTGs from the Yilgarn Craton, and no clear covariation between $\delta^{238}U$ and indices of differentiation or U concentration (fig. 5.2).

27 out of 40 samples (68%) display $\delta^{234}U$ values within error of zero and are therefore at secular equilibrium. Samples not at secular equilibrium tend to have $\delta^{234}U < 0$, extending down to -85 ± 5‰. A few samples have $\delta^{234}U$ significantly higher than zero, reaching +149 ± 5‰ in TTG sample 235965. The BFG sanukitoids cover a limited $\delta^{234}U$ range from -13 to +7‰, and 14 out of 15 samples have $\delta^{234}U$ within error of zero. TTGs show more heterogeneous $\delta^{234}U$ (-85 to +149‰) than sanukitoids (-60 to +7‰). All high Ba-Sr granite suite samples have $\delta^{234}U$ within error of zero and are

hence at secular equilibrium. There is no overall covariation between δ^{234}U and δ^{238}U or U concentration (figs. 5.2a and b), and samples at secular equilibrium cover a similar range in δ^{238}U to those not at secular equilibrium. The only exception to this is the previously mentioned sanukitoid sample 235917 with δ^{238}U of -0.14 ± 0.05‰, which also has the lowest δ^{234}U value of all the sanukitoid samples of -60 ± 5‰.

Figure 5.2: a) and b) δ^{238}U (‰) vs δ^{234}U (‰), c) δ^{238}U (‰) vs U (ppm), d) δ^{234}U (‰) vs U (ppm), e) δ^{238}U (‰) vs SiO$_2$ (wt%), and f) δ^{238}U (‰) vs MgO (wt%). Uncertainty on δ^{238}U and δ^{234}U is shown as 2se. The dashed lines mark secular equilibrium (δ^{234}U = 0).

Table 5.1: $\delta^{238}U$ and $\delta^{234}U$ data for the samples analysed in this chapter. Key elemental concentrations and geochemical parameters are also given. The sources of the major and trace element data for the samples are given in Appendix C. 2se = 2 standard errors. $P/P^* = P_N / (Ce_N * Nd_N)^{0.5}$ where elemental concentrations are normalised to primitive mantle values from Palme & O'Neill (2014).

Sample	Age	Location	Suite	$\delta^{238}U$	2se	$\delta^{234}U$	2se	U	SiO$_2$	Zr	Hf	Th/U	Ce/Mo	P/P*
	Ma			‰	‰	‰	‰	ppm	wt%	ppm	ppm			
Sanukitoids and analogues														
235921 Enclaves	~3421	Pilbara	Sanukitoid-like rocks	-0.35	0.05	-2	5	4.21	66.65	209	5.6	4.82	102	0.18
235921	~3421	Pilbara	Sanukitoid-like rocks	-0.35	0.05	-10	5	4.29	68.78	253	6.8	5.48	102	0.14
235917	2948	Pilbara	High-Mg diorite suite	-0.14	0.05	-60	5	3.15	65.99	163	4.3	4.95	632	0.27
142347	2498 ± 5	Pilbara	High-Mg diorite suite	-0.31	0.05	1	5	3	59.33	145		4.33		
227869	~2660	Yilgarn	High La/Th (high Ni) BFG	-0.33	0.03	-1	9	1.51	49.17	114	3.35	3.95	73	0.39
227873	~2660	Yilgarn	High La/Th (high Ni) BFG	-0.24	0.03	-3	9	1.01	49.39	110	2.83	6.84	172	0.38
223149	~2660	Yilgarn	High La/Th (high Ni) BFG	-0.31	0.03	0	9	1.44	50.67	92.5	2.46	4.47	70	0.45
505567	~2660	Yilgarn	High La/Th (high Ni) BFG	-0.25	0.03	3	9	1.29	51.80	105	2.8	4.95	117	0.35
505652	~2660	Yilgarn	High La/Th (high Ni) BFG	-0.25	0.03	2	9	0.73	52.90	87	2.3	4.51	12	0.42
227863	~2660	Yilgarn	High La/Th (high Ni) BFG	-0.30	0.03	-3	9	1.09	54.85	104	2.78	4.05	84	0.51
211213	~2660	Yilgarn	High La/Th (high Ni) BFG	-0.23	0.04	5	9	0.81	55.82	102	3.04	4.30	124	0.46
229900	~2660	Yilgarn	High La/Th (high Ni) BFG	-0.29	0.05	2	5	1.31	61.02	111	2.93	3.70	51	0.32
223157	~2660	Yilgarn	High La/Th (low Ni) BFG	-0.24	0.03	5	9	1.71	51.18	118	3.08	4.73	16	0.44
229901	~2660	Yilgarn	High La/Th (low Ni) BFG	-0.28	0.03	2	9	1.03	56.95	113	2.98	4.15	43	0.46
230891	~2660	Yilgarn	High La/Th (low Ni) BFG	-0.26	0.05	1	5	1.28	66.78	129	3.49	3.84	75	0.35
227874	~2690	Yilgarn	Low La/Th BFG	-0.30	0.05	0	9	1.34	43.77	110	2.64	5.23	129	0.50
501922	~2690	Yilgarn	Low La/Th BFG	-0.28	0.03	1	9	2.17	50.50	147	3.7	4.72	265	0.38
505465	~2690	Yilgarn	Low La/Th BFG	-0.31	0.04	7	9	2.75	50.80	121	3.4	1.96	34	1.43
230733	~2690	Yilgarn	Low La/Th BFG	-0.27	0.05	-13	5	1.4	58.59	104	2.8	4.33	121	0.39
AMT02	2130 ± 2	São Francisco	Alto Maranhão suite	-0.35	0.05	-27	5	4	64.20	172		5.68		0.27

Table 5.1 continued:

Sample	Age Ma	Location	Suite	δ²³⁸U ‰	2se ‰	δ²³⁴U ‰	2se ‰	U ppm	SiO₂ wt%	Zr ppm	Hf ppm	Th/U	Ce/Mo	P/P*
Sanukitoids and analogues														
AMT03	2130 ± 2	São Francisco	Alto Maranhão suite	-0.23	0.03	-3	9	3	62.42	191		6.45		0.30
MAJF 51b	2117 ± 24	São Francisco		-0.31	0.05	-13	5	1.3	60.32	91	2.1	5.54		0.23
RA2	425 ± 1.5	Scotland	Rogart pluton	-0.20	0.03	2	9	3.04	57.20	127	3.34	6.28		0.17
RT1	425 ± 1.5	Scotland	Rogart pluton	-0.21	0.05	3	5	1.51	62.98	69.6	1.82	6.13		0.33
SR3	425 ± 3	Scotland	Strontian pluton	-0.29	0.05	4	5	2.11	63.23	218	4.83	3.64		0.37
SR4	425 ± 3	Scotland	Strontian pluton	-0.26	0.05	1	5	2.48	63.83	109	2.78	2.91		0.32
TTGs														
235965	3425	Pilbara		-0.34	0.05	149	5	1.36	71.48	130	3.5	3.89	748	0.23
142870	3500	Pilbara		-0.24	0.05	3	5	4.71	74.21	169	4.7	2.96	520	0.03
235913	~3270	Pilbara		-0.25	0.05	-59	5	1.32	68.24	127	3.4	3.58	720	0.33
235945	3303	Pilbara		-0.39	0.05	11	5	2.85	68.55	351	8.4	3.56	373	0.15
178102	2787	Yilgarn		-0.24	0.06	-85	5	1.13	64.73	110	2.9	4.93	89	0.41
232744	~2696	Yilgarn		-0.21	0.05	6	5	3.49	72.0	154	3.9	3.47	912	0.17
502247	~2670	Yilgarn		-0.31	0.03	19	9	3.54	71.0	109	3.3	2.65	34	0.22
505481	~2670	Yilgarn		-0.25	0.04	-4	9	2.54	70.2	121	3.1	3.29	96	0.27
230558	~2670	Yilgarn		-0.26	0.03	-4	9	1.47	69.14	109	3.02	3.88	218	0.31
504718	~2670	Yilgarn		-0.30	0.03	-31	9	1.22	71.02	107	2.9	4.13	73	0.29
240405	~2680	Yilgarn		-0.32	0.03	0	9	3.44	65.77	201	4.6	4.45	75	0.19
502533	~2670	Yilgarn		-0.31	0.04	2	9	5.25	70.5	133	3.8	3.85	123	0.16
500854	~2670	Yilgarn		-0.37	0.03	4	9	1.35	69.4	225	5.5	3.60	58	0.22
501356	~2670	Yilgarn		-0.36	0.04	-70	9	7.98	71.2	183	4.5	2.62	128	0.13

5.4. Discussion

5.4.1. Weathering and alteration

Uranium is mobile in aqueous fluids in its oxidised U^{6+} state, making it susceptible to processes like oxidative weathering and hydrothermal alteration. It is therefore essential to first determine whether such processes have modified bulk rock $\delta^{238}U$ from its original value.
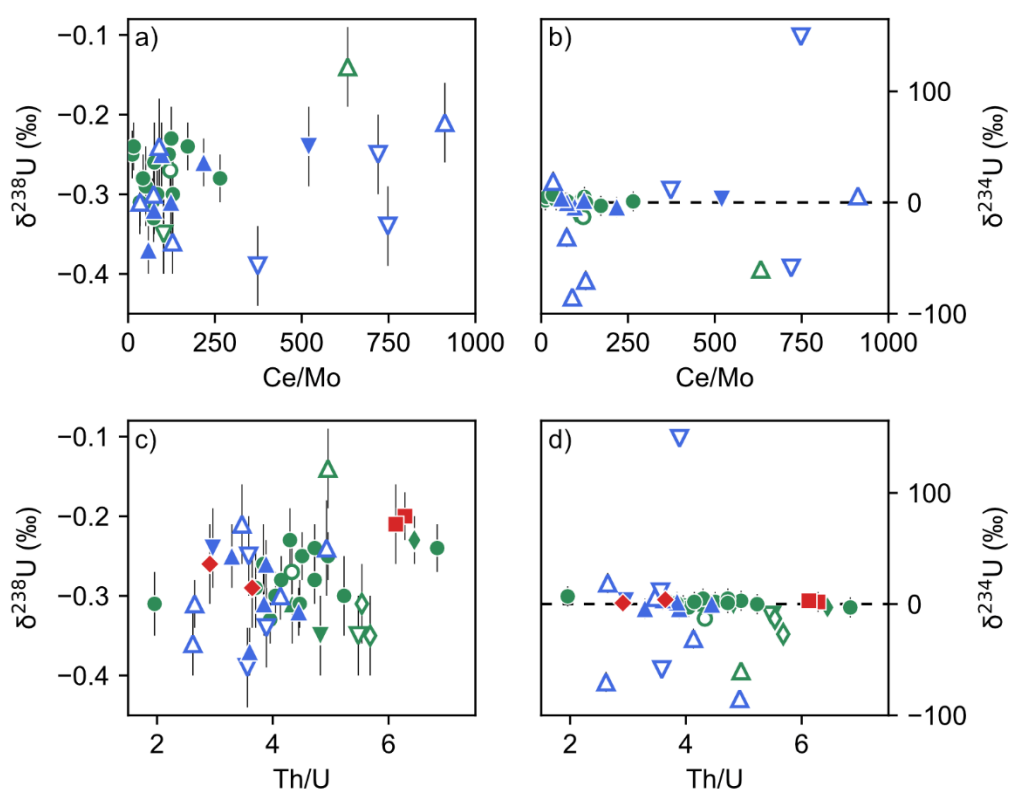
Figure 5.3: a) $\delta^{238}U$ (‰) vs Ce/Mo, b) $\delta^{234}U$ (‰) vs Ce/Mo, c) $\delta^{238}U$ (‰) vs Th/U and d) $\delta^{234}U$ (‰) vs Th/U. The dashed lines mark secular equilibrium ($\delta^{234}U = 0$).

Sample δ234U can be used to assess whether the 238U-234U system has been disturbed from secular equilibrium (δ234U = 0) in the last ~1.5 Myr, approximately five times the half-life of 234U (246,000 years; Cheng et al., 2013). U loss or gain within this time period will cause deviation from secular equilibrium (δ234U ≠ 0). As mentioned previously, only ~70% of the samples analysed here are at secular equilibrium. The main process that may have recently disturbed U in a sample is chemical weathering. U loss during chemical weathering preferentially mobilises 234U as the daughter atoms sit in damaged recoil sites, leaving the rock with δ234U < 0 (e.g. Chabaux et al., 2003). Oxidative weathering may also affect δ238U as light U isotopes concentrate in the U^{6+} state and are preferentially removed by aqueous fluids (e.g. Stirling et al., 2007; Wang et al., 2015). Samples affected by weathering are therefore expected to have low δ234U and high δ238U (Charbonnier et al., 2023; Pavia et al., 2023). This is observed for sanukitoid sample 235917 which has the highest δ238U value of -0.14 ± 0.05‰ accompanied by low δ234U of -60 ± 5‰ (figs. 5.2a and b). Four additional sanukitoid samples and four TTG samples also have δ234U < 0, but it is not clear if their δ238U has been significantly affected by weathering as their δ238U values all fall within the range of samples at secular equilibrium and no correlation between δ238U and δ234U is observed (figs. 5.2a and b). However, δ234U is only sensitive to U mobilisation within the last ~1.5 Myr, so samples currently at secular equilibrium could have been affected by weathering/alteration > 1.5 Ma. Interestingly, the majority of BFG samples (14 out of 15) are at secular equilibrium. Most of these samples are taken from drill cores meaning they have not been exposed subaerially, which may explain why their U isotope systematics show little evidence of recent disturbance.

Trace element ratios can also trace oxidative weathering and are not restricted to the last 1.5 Myr. Mo and Ce have similar compatibilities during mantle melting, but Mo is preferentially lost during oxidative weathering while Ce is not, causing Ce/Mo to increase (Gaschnig et al., 2021b). Two samples display elevated Ce/Mo and negative δ234U – one is 235917 which was previously discussed and the other is TTG sample 235913 (fig 5.3b). TTG samples 232744 and 142870 have δ234U near secular equilibrium, but they also have significantly elevated Ce/Mo of 912 and 520 respectively, as well as some of the highest δ238U values of the TTGs (-0.21 ± 0.05‰ and -0.24 ± 0.05‰ respectively) (fig. 5.3), which implies that their U isotope systematics may have been affected by weathering >1.5 Myr. Several other TTG

samples have high Ce/Mo but there is no obvious covariation between this and $\delta^{238}U$, so it is unclear if their U isotope systematics have been affected by oxidative weathering. Th/U is also sensitive to weathering processes. Soluble U^{6+} is removed while Th remains immobile, hence weathering causes Th/U to increase. The utility of Th/U for assessing chemical weathering among the samples analysed here is limited as I avoided selecting samples with high Th/U specifically because this characteristic implies that they likely experienced U loss due to weathering which may have affected their $\delta^{238}U$. As a result, the Th/U of the samples in this study covers a relatively narrow range from 2 to 7, and no overall covariation between $\delta^{238}U$ or $\delta^{234}U$ and Th/U is observed (figs. 5.3c and d).

Six samples have $\delta^{234}U > 0$, indicating U gain within the last ~1.5 Myr. Most of these deviations are relatively small (+6 ± 5‰ to +19 ± 9‰), but sample 235965, a ~3425 Ma TTG from the Pilbara Craton, has very high $\delta^{234}U$ of +149 ± 5‰. This is the largest deviation from secular equilibrium observed among the samples analysed here. Groundwaters are enriched in ^{234}U primarily due to alpha recoil processes enabling ^{234}U to be more readily mobilised from minerals (Dunk et al., 2002; Osmond and Cowart, 1976). Groundwaters can display extremely high $\delta^{234}U$ typically of ~+50 to +1000‰ (Osmond and Cowart, 1976), meaning they have the potential to significantly increase $\delta^{234}U$ while only slightly increasing U concentration. Addition of U from high $\delta^{234}U$ groundwaters could therefore explain the high $\delta^{234}U$ of sample 235965, even with its relatively low U concentration of 1.36 ppm. The $\delta^{238}U$ of groundwaters away from U ore deposits are unknown (Andersen et al., 2017). Modelling by Rodney et al. (2024, Preprint) suggests that U addition from groundwater does not significantly affect $\delta^{238}U$ unless a large amount of U is added. As sample 235965 has a relatively low U concentration and $\delta^{238}U$ of -0.34 ± 0.05‰ indistinguishable from the BSE, I propose that there is no clear evidence for significant modification of this sample's $\delta^{238}U$ by interaction with groundwater. Other samples with $\delta^{234}U > 0$ represent comparatively minor deviations from secular equilibrium, and hence potential for recent modification of $\delta^{238}U$ by groundwaters is even more limited.

To summarise, four samples (Yilgarn Craton TTG 232744, and Pilbara Craton sanukitoid 235917 and TTGs 235913 and 142870) show isotopic and trace element evidence for modification by oxidative weathering. As processes involving U oxidation

can alter $\delta^{238}U$, these samples are excluded from further discussion. Other samples also show $\delta^{234}U < 0$, but as there is no clear evidence that this was associated with oxidative processes, there is nothing to suggest that the $\delta^{238}U$ of these samples has been significantly modified from their original values. To reflect some degree of uncertainty about the $\delta^{238}U$ values of these samples, they are plotted as open symbols on subsequent figures. Samples with $\delta^{234}U > 0$ may have experienced U addition from high $\delta^{234}U$ groundwaters, in particular Pilbara Craton TTG 235965. However, there is no evidence suggesting that this process has altered sample $\delta^{238}U$, so these samples are also plotted as open symbols on subsequent figures.

5.4.2. U isotope fractionation by magmatic differentiation

In this section I investigate whether the U isotope compositions of TTGs and sanukitoids have been affected by magmatic differentiation. While no correlation between $\delta^{238}U$ and indices of magma differentiation (e.g. SiO_2, MgO) is observed for sanukitoids or TTGs (figs. 5.2e and f), $\delta^{238}U$ does show some correlation with trace element concentrations and elemental anomalies (fig. 5.4). All samples, but especially TTGs, display negative correlation between $\delta^{238}U$ and Zr and Hf concentrations (figs. 5.4a and b). The $\delta^{238}U$ of TTGs is also positively correlated with phosphorus (P) anomaly ($P/P^* = P_N / (Ce_N * Nd_N)^{0.5}$, where elemental concentrations are normalised to primitive mantle values from Palme and O'Neill, 2014) (fig. 5.4c). Some sanukitoid samples, particularly those with relatively low $\delta^{238}U$, also plot on this trend. Additionally, there appears to be some degree of covariation of $\delta^{238}U$ with europium (Eu) anomaly ($Eu/Eu^* = Eu_N / (Sm_N * Gd_N)^{0.5}$, where elemental concentrations are normalised to CI chondrite values from O'Neill, 2016) (fig. 5.4d). Most of these geochemical parameters are sensitive to the crystallisation of accessory minerals from magmas. The Zr and Hf concentrations trace zircon, while P/P^* traces the phosphate mineral apatite. In contrast, Eu/Eu^* is primarily used to look at plagioclase fractionation as Eu is particularly compatible in plagioclase. Accessory minerals such as zircon, apatite, titanite and allanite are the main hosts of U in TTGs and sanukitoids (e.g. Cuney, 2010; Martin et al., 2009; Moyen and Martin, 2012), so the trends in figure 5.4 suggest that the U isotope compositions of TTGs and sanukitoids have been fractionated by accessory minerals during magma differentiation. The most primitive samples are BFG sanukitoids with $SiO_2 < 55$ wt% which all plot towards the high $\delta^{238}U$

end of the trends, suggesting that accessory mineral fractionation during magma differentiation drove rock compositions towards lower $\delta^{238}U$ values.
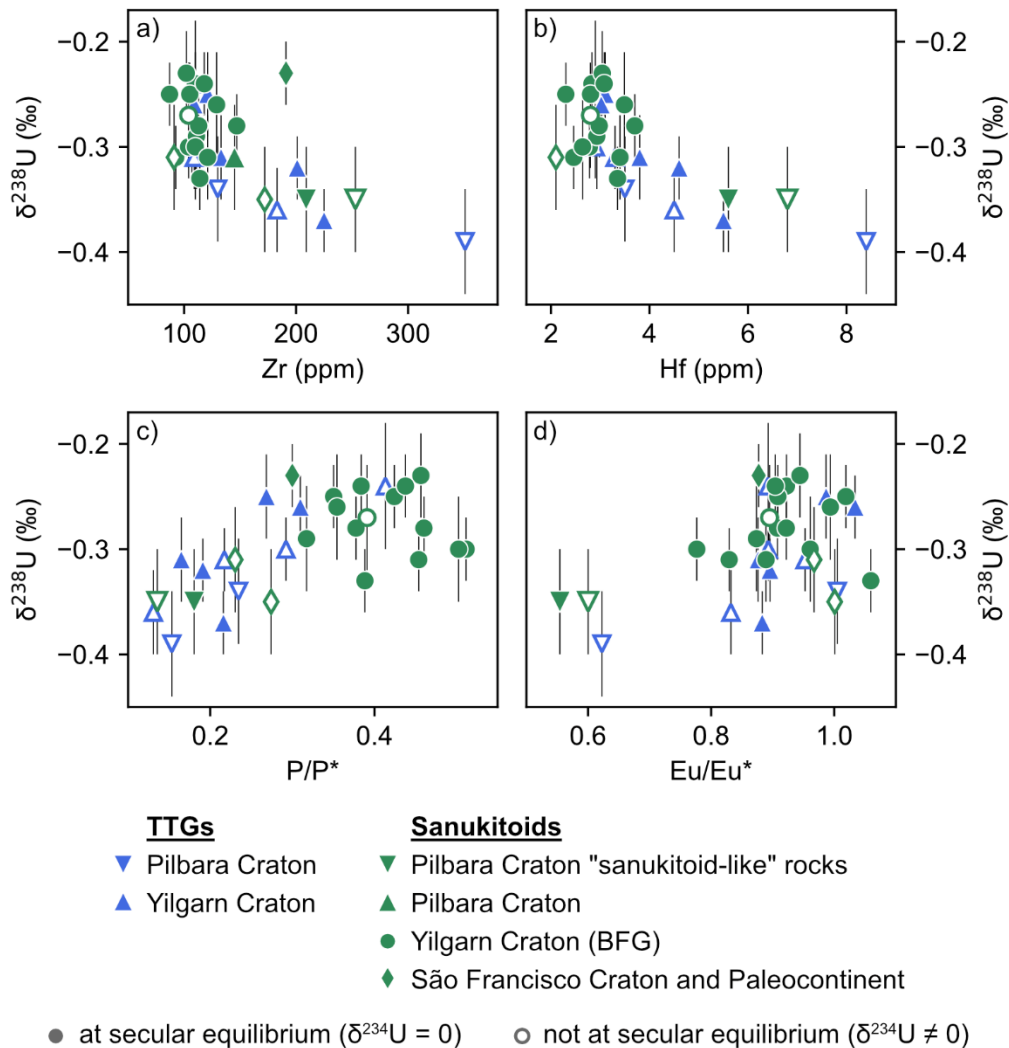
Figure 5.4: TTG and Archean-Paleoproterozoic sanukitoid $\delta^{238}U$ (‰) vs a) Zr (ppm), b) Hf (ppm), c) phosphorus anomaly P/P* (= P_N / (Ce_N * Nd_N)$^{0.5}$ where elemental concentrations are normalised to primitive mantle concentrations from Palme and O'Neill (2014)) and d) europium anomaly Eu/Eu* (= Eu_N / (Sm_N * Gd_N)$^{0.5}$ where elemental concentrations are normalised to CI chondrite values from O'Neill (2016)).

One possible interpretation of the trends in figure 5.4 is that they were generated by zircon accumulation as zircon is the main host of Zr and Hf in felsic rocks (e.g. Hoskin and Schaltegger, 2003). In this scenario, the negative direction of the correlations between $\delta^{238}U$ and Zr and Hf concentrations implies that the accumulated zircons preferentially incorporated ^{235}U over ^{238}U and hence had low $\delta^{238}U$. However, this inference is inconsistent with analyses of zircon mineral separates that find zircon to have average $\delta^{238}U$ of -0.13‰ (Hiess et al., 2012; Livermore et al., 2018), which is

significantly heavier than modern upper continental crust ($\delta^{238}U \approx$ -0.3‰, Noordmann et al., 2016; Tissot and Dauphas, 2015). Tissot et al. (2019) found slightly lighter average $\delta^{238}U$ of ~-0.3‰ for individual Hadean-Paleoarchean zircon crystals from the Jack Hills conglomerate, but this is still inconsistent with the trends in the TTGs and sanukitoids as it suggests zircons have indistinguishable $\delta^{238}U$ to silicate magmas. Therefore, it appears that accumulation of zircons is unable to explain $\delta^{238}U$ variations in TTGs and sanukitoids.

The conflicting observations described above could be reconciled if the correlations in my data are instead caused by incomplete dissolution of isotopically heavy zircon during sample preparation. To investigate this possibility, I compare the expected amount (mass in ng) of U in the fully dissolved sample, calculated from published U concentrations and the mass of sample dissolved, to the actual amount of U in the analysed sample solution. The latter value was calculated from the measured $^{238}U/^{236}U$ ratio. All the ^{236}U in the analysed sample solution comes from the IRMM-3636 double spike, so the mass of ^{236}U in the sample is known. Multiplication of the $^{238}U/^{236}U$ ratio by the mass of ^{236}U gives the mass of ^{238}U in the sample. As ^{238}U makes up ~99% of naturally occurring U, the mass of ^{238}U can be used as an estimate of the total non-spike U content of the analysed sample solution. Figure 5.5 plots the expected U content of the fully dissolved sample against the measured U content of the analysed sample. The majority of samples have a U yield within 10% of the expected yield. This suggests that there was no significant U loss from samples due to incomplete sample dissolution, and therefore this cannot be the cause of $\delta^{238}U$ variations. A mass balance calculation can be done to provide further support for this conclusion. For dissolution of a sample the following mass balance between the bulk sample, dissolved material and undissolved zircon can be written (equation 5.1):

$$\delta^{238}U_{bulk} = X_{zircon}\delta^{238}U_{zircon} + (1 - X_{zircon})\delta^{238}U_{dissolved} \quad (5.1)$$

X_{zircon} is the proportion of sample U hosted in undissolved zircon. $\delta^{238}U_{zircon}$ is taken to be the mean zircon $\delta^{238}U$ of -0.13‰ from Hiess et al. (2012) and Livermore et al. (2018). To change the U isotope composition of a sample from the average $\delta^{238}U$ of UCC ($\delta^{238}U_{bulk}$= -0.3‰, Noordmann et al., 2016; Tissot and Dauphas, 2015) to the lightest TTG $\delta^{238}U$ value ($\delta^{238}U_{dissolved}$= -0.39‰), approximately 35% of sample U needs to be lost in undissolved, isotopically heavy zircon. If the heaviest TTG $\delta^{238}U$

value of -0.24‰ is instead used for $\delta^{238}U_{bulk}$, the proportion of sample U that needs to be lost rises to ~58%. I have shown above that none of the samples show evidence for this magnitude of U loss (fig. 5.5), again demonstrating that incomplete sample dissolution cannot explain the observed δ238U trends my samples.
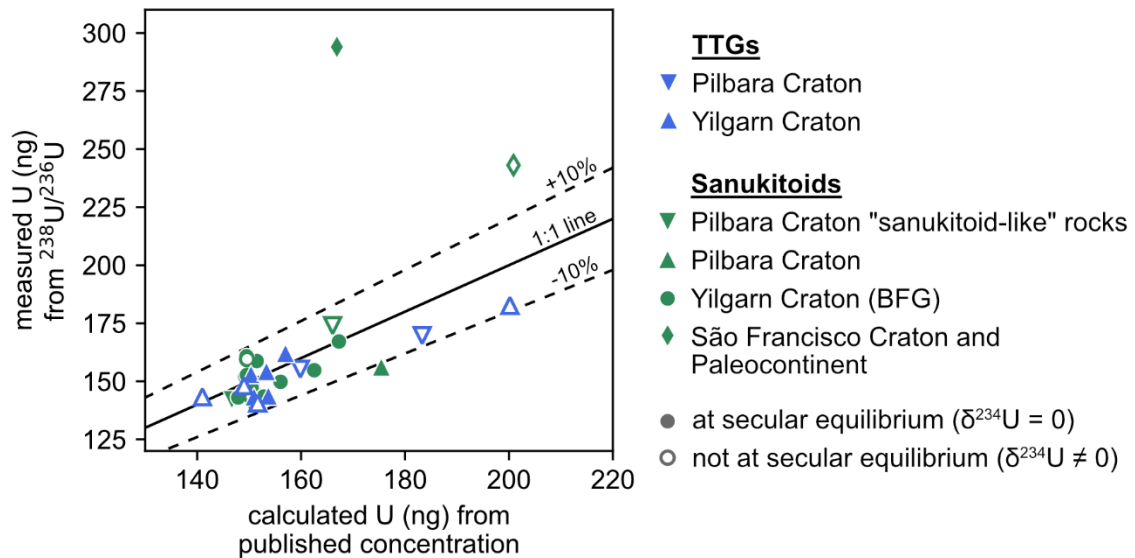
Figure 5.5: The mass of U in the analysed sample solution calculated from the measured 238U/236U (ng) vs the expected mass of U calculated from the published U concentration (ng). The solid line is the 1:1 line while the dashed lines show when the mass of U calculated from 238U/236U is between +10% and -10% from the 1:1 line.

Alternatively, the variations in TTG and sanukitoid δ238U may have been generated by fractional crystallisation of an isotopically heavy mineral assemblage. The correlation between δ238U and P/P* (fig. 5.4c) implicates apatite. The U isotope compositions of two igneous apatite mineral separates have been measured, and both have higher δ238U than the BSE (Hiess et al., 2012; Livermore et al., 2018). Hiess et al. (2012) analysed apatite from a carbonatite that has δ238U of -0.17 ± 0.11‰ (2se, n = 2), while Livermore et al. (2018) measured δ238U of -0.04 ± 0.04 (2se, n = 1) in apatite from a 1341 Ma leucogabbro. These data suggest that apatites preferentially incorporate heavy U isotopes to give them higher δ238U than the BSE. Fractional crystallisation of isotopically heavy apatite would drive the remaining melt to lower δ238U and P/P* and can hence explain the positive correlation between δ238U and P/P* for samples with P/P* ≤ 0.3 (fig. 5.4c). However, as neither Hiess et al. (2012) or Livermore et al. (2018) measured the bulk U isotope composition of the host rock, I cannot be completely certain of the direction of U isotope fractionation between apatite and

167

silicate/carbonatite melt. To provide additional support for preferential incorporation of ^{238}U over ^{235}U into apatite, I consider whether this direction of fractionation is consistent with stable isotope theory. In silicate magmas with oxygen fugacity (fO$_2$) similar to TTG magmas (fO$_2$ ≈ ΔFMQ -1 ± 1.1, given in log units relative to the fayalite-magnetite-quartz buffer, Ge et al., 2023), U is predominantly present as 6-fold coordinated U^{4+} with average U-O bond lengths of 2.26 – 2.29 Å (Farges et al., 1992; Halse, 2014). On incorporation into apatite, U preferentially partitions onto Ca sites which are either 7- or 9-fold coordinated, and hence have longer, weaker bonds (e.g. Luo et al., 2009). Traditional equilibrium isotope theory predicts that heavy isotopes concentrate in the phase with the stronger, stiffer bonds (e.g. Bigeleisen and Mayer, 1947; Young et al., 2015), which in this case is the silicate melt. Apatite preferentially incorporating heavy U isotopes is therefore inconsistent with traditional equilibrium isotope fractionation of stable isotopes.

Mass-dependent isotope fractionation can also be caused by non-equilibrium, kinetic processes. Kinetic isotope fractionation occurs during unidirectional processes where isotope exchange is incomplete. In the scenario of apatite crystallisation, kinetic U isotope fractionation could arise from faster diffusion of the lighter isotope (^{235}U) through the melt than the heavier isotope (^{238}U). This process would generate apatite crystals enriched in ^{235}U, so kinetic isotope fractionation cannot explain why apatite appears to preferentially incorporate heavy U isotopes. Additionally, it is unlikely that significant kinetic fractionation of U isotopes occurs in gabbros and TTGs. These are plutonic rocks that cooled slowly, making it likely that equilibrium was obtained, and in TTGs no kinetic isotope fractionation has been observed for lighter elements (e.g. Ca, Fe) that are more susceptible to large kinetic isotope fractionations (Antonelli et al., 2021; Doucet et al., 2020; Liou et al., 2022; Z. J. Zhang et al., 2023).

The discussion above shows that mass-dependent isotope fractionation cannot explain why apatite appears to be enriched in ^{238}U over ^{235}U. But apatite is not alone in displaying this characteristic – U coordination also increases during incorporation from silicate melt (6-fold coordination) into other igneous accessory minerals (e.g. 8-fold in zircon, e.g. Bea, 1996; 7-fold in titanite, Tiepolo et al., 2002), and the available data suggest that these minerals are also dominantly enriched in ^{238}U over ^{235}U (Hiess et al., 2012; Livermore et al., 2018; Tissot et al., 2019). Something must therefore be

consistently driving U isotope fractionation due to changes in U coordination/bond length in the opposite direction to that expected from mass-dependent fractionation. Nuclear field shift (NFS) effects may provide the answer. As U is a heavy element with a high atomic number (Z = 92), it also experiences mass-independent equilibrium isotope fractionation due to NFS effects. While traditional equilibrium isotope fractionation results from the mass differences between isotopes, NFS effects arise from differences in nuclear size and shape between isotopes and can generate larger magnitudes of fractionation than traditional equilibrium mass-dependent fractionation (e.g. Bigeleisen, 1996; Fujii et al., 2009). NFS effects cause odd neutron number nuclei to be displaced to lower energies – for U this results in the ground state of ^{235}U having lower electronic energy than ^{238}U (Bigeleisen, 1996). Consequently, in isotope substitutions involving a change in U redox state, isotope fractionation due to NFS effects results in heavy U isotopes concentrating in U^{4+} over U^{6+} (e.g. Bigeleisen, 1996; Fujii et al., 2006) – the opposite direction to fractionation predicted by traditional equilibrium isotope theory (e.g. Bigeleisen and Mayer, 1947; Young et al., 2015). It is therefore possible that NFS effects may also cause a change in the direction of U isotope fractionation for isotopic substitutions only involving a change in U coordination/bond length. This could explain why apatite and other igneous accessory minerals appear to preferentially incorporate ^{238}U over ^{235}U.

I propose that δ^{238}U variations in Archean igneous rocks are mainly caused by fractional crystallisation of apatite, which is enriched in ^{238}U as a result of NFS effects. The δ^{238}U values of samples with P/P* ≤ 0.3 were lowered by fractional crystallisation of isotopically heavy apatite, while the U isotope compositions of samples with P/P* > 0.3 were not significantly affected by apatite fractional crystallisation. Apatite is a near-ubiquitous accessory mineral in silicic igneous rocks (Webster and Piccoli, 2015), and is the main phosphate mineral in TTGs (e.g. Moyen and Martin, 2012) and sanukitoids (e.g. Martin et al., 2009), hence apatite exerts a dominant control on P concentrations during magma evolution. Global geochemical datasets for both TTGs and Archean-Paleoproterozoic sanukitoids show decreasing P_2O_5 contents as SiO_2 contents increase (fig. 5.6). For the Alto Maranhão suite sanukitoids from the São Francisco Craton, which plot on the δ^{238}U vs P/P* trend, Rayleigh fractional crystallisation modelling has demonstrated that apatite fractional crystallisation is required to explain the evolution of their REE concentrations (Seixas et al., 2013). These pieces of

evidence demonstrate that apatite crystallisation, and hence apatite fractional crystallisation, likely occurred during the differentiation of TTG and sanukitoid magmas. In contrast, while trace element modelling suggests apatite fractional crystallisation also occurred in the BFG sanukitoids (Smithies et al., 2019), the majority of BFG samples that I analysed are relatively primitive (SiO_2 < 58 wt%) and likely have not experienced significant amounts of apatite crystallisation, as demonstrated by their high P/P*, hence their $\delta^{238}U$ is unaffected by apatite fractional crystallisation.
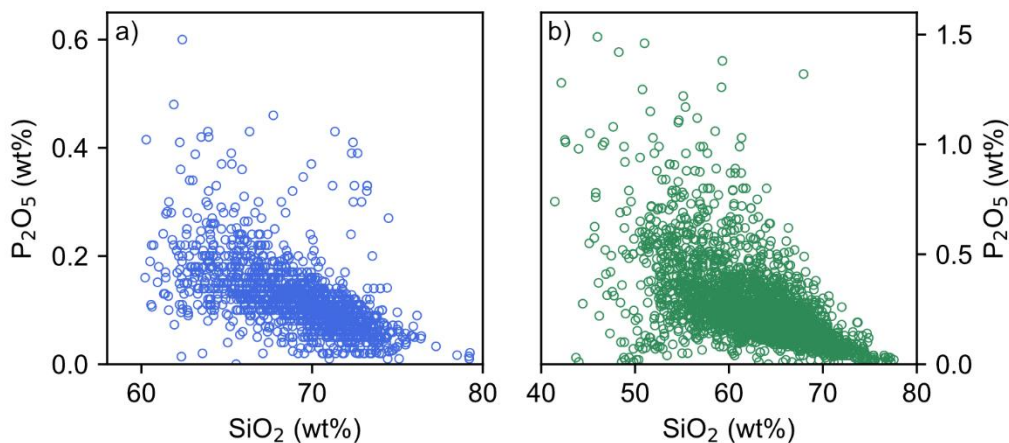
Figure 5.6: P_2O_5 (wt%) vs SiO_2 (wt%) for a global dataset of a) TTGs from Moyen (2011), and b) Archean and Paleoproterozoic sanukitoids from my own compilation of published geochemical data of rocks described as "sanukitoid" in published literature.

In addition, figure 5.7 shows that the $\delta^{238}U$ of TTGs from the Eastern Goldfields Superterrane, Yilgarn Craton, is broadly negatively correlated with their titanium (Ti) isotope composition ($\delta^{49}Ti$), and in particular TTGs with the lowest $\delta^{238}U$ have the highest $\delta^{49}Ti$. It is well understood that magma $\delta^{49}Ti$ increases during differentiation due to fractional crystallisation of isotopically light Fe-Ti oxides and Ti-bearing silicates (e.g. amphibole) (e.g. Hoare et al., 2020; Millet et al., 2016), so the fact that the most differentiated TTG samples from a Ti isotope perspective also have the lowest $\delta^{238}U$ supports my proposal that it is apatite fractional crystallisation, rather than mineral accumulation, that is responsible for the observed trend.
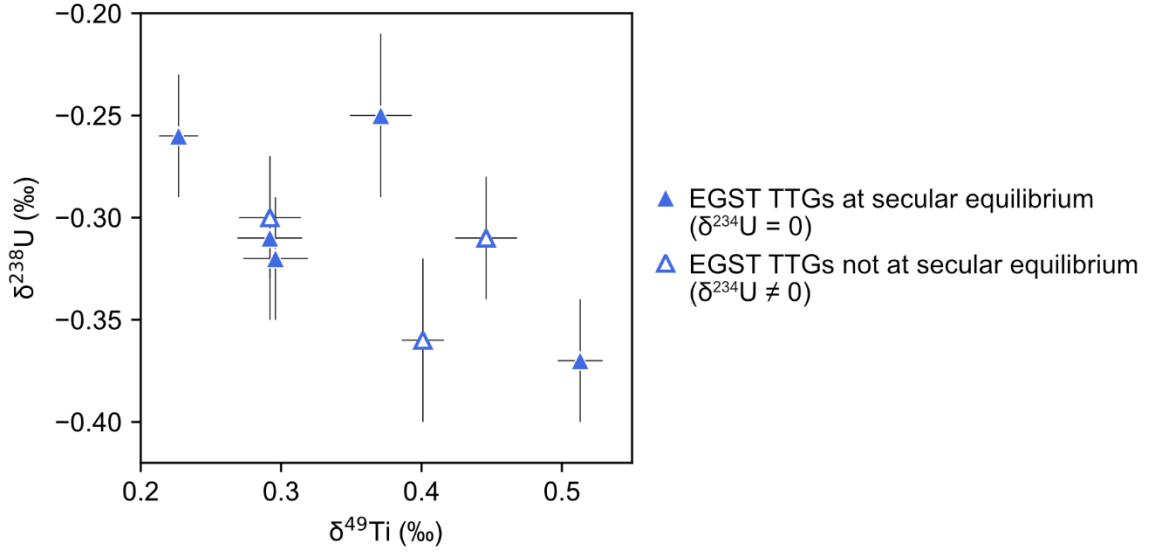
Figure 5.7: Eastern Goldfields Superterrane TTG δ²³⁸U (‰) vs δ⁴⁹Ti (‰). Uncertainty on δ²³⁸U is shown as 2se, and uncertainty on δ⁴⁹Ti is shown as the 95% confidence interval. The Ti stable isotope data are presented in Chapter 4 of this thesis.

To investigate the feasibility of apatite fractional crystallisation generating the observed magnitude of U isotope fractionation, I use Rayleigh fractionation modelling (equation 5.2). The weighted mean δ²³⁸U of unfractionated Archean samples with P/P* > 0.3 (-0.27 ± 0.01‰, 2sd, n = 18) was used as the starting composition ($\delta^{238}U_0$). F_{melt}^{U} is the fraction of U remaining in the melt.

$$\delta^{238}U = 10^3 \left(F_{melt}^{U}{}^{(\alpha_{apatite-melt}-1)} - 1 \right) + \delta^{238}U_0 \quad (5.2)$$

I use the U isotope composition of the ~1341 Ma leucogabbro apatite (δ²³⁸U = -0.04 ± 0.04‰, Livermore et al., 2018) to constrain the apatite-silicate melt fractionation factor ($\alpha_{apatite-melt}$). As the δ²³⁸U of the bulk leucogabbro has not been measured, an assumption must be made about the U isotope composition of the melt the apatite crystallised from. Before ~600 Ma, the mantle is thought to have had uniform U isotope composition identical to the chondritic bulk Earth (Andersen et al., 2015), so I assume that the leucogabbro apatite crystallised from a melt with δ²³⁸U = -0.306 ± 0.037‰ (2sd). I therefore estimate Δ²³⁸U$_{apatite-melt}$ (= δ²³⁸U$_{apatite}$ - δ²³⁸U$_{melt}$) to be +0.27 ± 0.08‰ (2sd), which is equivalent to $\alpha_{apatite-melt}$= 1.00027 ± 0.00008 (2sd). Figure 5.8 presents the results of the Rayleigh fractionation modelling. To generate the U isotope composition of the lightest TTG sample (δ²³⁸U = -0.39 ± 0.05‰), around 20 – 60% of total U needs to be removed by apatite fractional crystallisation. As mentioned previously, other common accessory phases in TTGs and sanukitoids, such as titanite

and zircon, are also predominantly enriched in [238]U (Hiess et al., 2012; Livermore et al., 2018; Tissot et al., 2019), so fractional crystallisation of these minerals alongside apatite may additionally help drive magma δ^{238}U to lighter values during differentiation. This simple modelling hence demonstrates that fractional crystallisation of isotopically heavy apatite is a viable cause of observed δ^{238}U variability in TTGs and sanukitoids.
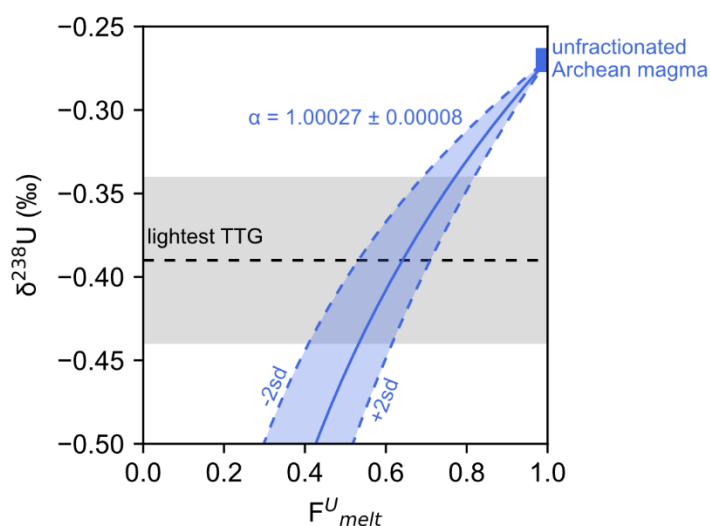
Figure 5.8: δ^{238}U (‰) vs the fraction of U remaining in the melt (F^U_{melt}), showing Rayleigh fractionation modelling of apatite fractional crystallisation in TTG magmas. The apatite-melt fractionation factor ($\alpha_{apatite-melt}$) is constrained by the leucogabbro apatite from Livermore et al. (2018) to be 1.00027 ± 0.00008 (2sd). The Rayleigh fractionation models are shown in blue, with the dashed lines and shaded blue region showing the 2sd uncertainty. The black dashed line marks the lightest TTG δ^{238}U value and the grey shaded region shows the 2se uncertainty on this value (-0.39 ± 0.05‰, sample 235945).

Overall, these data add to growing evidence of U isotope fractionation at high temperatures in igneous rocks (Hiess et al., 2012; Livermore et al., 2018; Tissot et al., 2019, 2017). They also provide the first demonstration that U isotope fractionation by magmatic processes can influence the δ^{238}U of bulk terrestrial igneous rocks. However, there are currently few data available on mineral separate U isotope compositions, particularly for non-zircon minerals as previous studies have focussed on geochronological applications of these data (Hiess et al., 2012; Livermore et al., 2018). There are also very limited constraints on mineral-melt U isotope fractionation factors. The best way to determine these would be direct measurements of coexisting glass and mineral phases, but measuring the δ^{238}U of the bulk rock sample that mineral separates are taken from would also prove valuable.

5.4.3. U isotope variations in sanukitoids

In this section I investigate $\delta^{238}U$ variations in Archean and Paleoproterozoic sanukitoids, as well as in the Paleozoic high Ba-Sr granite suites, their Phanerozoic analogues. I first discuss sanukitoid $\delta^{238}U$-Th/U compositions and compare these to modern arc magmas to investigate crustal recycling processes, before focussing on $\delta^{238}U$ variations within individual rock suites. Then I assess whether there was any temporal evolution in the U isotope compositions of sanukitoids and their analogues, particularly across the GOE and NOE when significant changes in terrestrial U cycling likely occurred (e.g. Andersen et al., 2015; Cuney, 2010; Partin et al., 2013). Finally, I discuss the implications of these findings for the creation of oxidised sanukitoid magmas in the Archean and Paleoproterozoic.

5.4.3.1. $\delta^{238}U$ – Th/U systematics

The ratio of thorium (Th) to uranium (Th/U) is a powerful tool to use in combination with $\delta^{238}U$, particularly when investigating crustal recycling processes. Th and U are both present as tetravalent cations of similar radius in the mantle and are hence not significantly fractionated during melting processes. In contrast, soluble U^{6+} can form under oxidising conditions, meaning mobilisation of U^{6+} in aqueous fluids can fractionate U from immobile Th and modify Th/U from the BSE value of 3.77 (Faure et al., 2020; Wipperfurth et al., 2018). Sanukitoid magmas formed by interaction between mantle peridotite and an incompatible element-enriched component derived from recycled crustal material(s), most likely a metabasite-derived melt (see Chapter 3; e.g. Martin et al., 2009; Smithies and Champion, 2000). On the present-day Earth, crustal materials are predominantly recycled into the mantle at subduction zones, and components derived from them (e.g. melts, fluids) migrate into the mantle source regions of arc magmas. Comparison of sanukitoids to modern arc magmas can hence help with interpreting the $\delta^{238}U$-Th/U systematics of sanukitoids, as well as provide insight into how crustal recycling processes have changed over the Earth's history.

Figure 5.9: Th/U vs δ²³⁸U (‰) of Archean and Paleoproterozoic sanukitoid samples not affected by apatite fractional crystallisation (P/P* > 0.3) and high Ba-Sr granite suites, compared to modern arc lavas. Modern arc lava data from Andersen et al. (2015), Avanzinelli et al. (2018) and Freymuth et al. (2019). BSE Th/U from Faure et al. (2020) and Wipperfurth et al. (2018). BSE δ²³⁸U from Andersen et al. (2015).
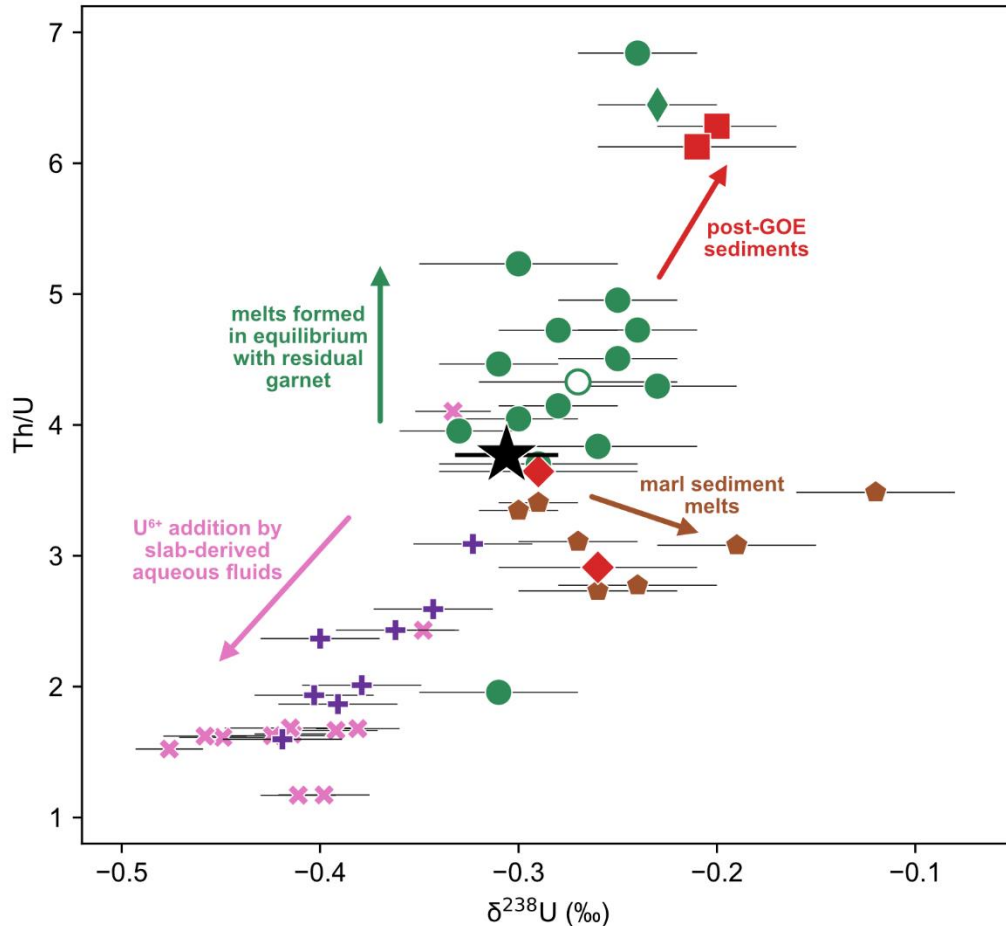
Currently, the U isotope compositions of lavas from three modern arcs – the Mariana arc (Andersen et al., 2015), the Izu arc (Freymuth et al., 2019) and the Campanian arc (Mount Vesuvius, Avanzinelli et al., 2018) – have been measured. Izu and Mariana arc lavas form a trend extending away from the BSE towards lower δ²³⁸U and Th/U values (fig. 5.9). This reflects the influence of oxidised, slab-derived aqueous fluids, which preferentially mobilise and transport U over Th and hence generate magmas with low

Th/U ratios. U can only be mobilised by aqueous fluids if it is oxidised (U^{6+}), and Freymuth et al. (2019) proposed that the oxidation of U^{4+} to U^{6+} in unaltered sections of subducted oceanic crust is associated with a U isotope fractionation of ~-0.2‰, creating low $\delta^{238}U$ fluids. In contrast, lavas from Mount Vesuvius have higher $\delta^{238}U$ than the BSE which is thought to be due to the involvement of isotopically heavy marl melt in their formation (fig. 5.9) (Avanzinelli et al., 2018).

Archean and Paleoproterozoic sanukitoids with $\delta^{238}U$ not affected by apatite fractional crystallisation (P/P* > 0.3) are also plotted on figure 5.9. They display distinct $\delta^{238}U$-Th/U systematics to the modern arc lavas. The sanukitoids have $\delta^{238}U$ ranging from similar to the BSE to slightly higher values, and their weighted average $\delta^{238}U$ of -0.27 ± 0.01‰ (2se, n = 17) is slightly heavier than the BSE (-0.306 ± 0.026‰; Andersen et al., 2015). Sanukitoid Th/U is also generally higher than the BSE value, excepting one BFG sample with Th/U of ~2. The sanukitoid compositions therefore contrast with the low $\delta^{238}U$ and Th/U of modern fluid-dominated arc magmas. A Welch's unequal variances t-test confirms that the difference between the U isotope compositions of sanukitoids (mean $\delta^{238}U$ = -0.27‰, σ = 0.03‰, n = 16) and fluid-dominated arc magmas (mean $\delta^{238}U$ = -0.40‰, σ = 0.04‰, n = 20) is statistically significant, $t(34)$ = 10.2, p < 0.001. This result suggests that the processes transferring U from recycled crust to the mantle source of magmas may have changed since the end of the Archean.

The low $\delta^{238}U$ and Th/U signature of modern arc magmas is generated by oxidation of U^{4+} in the subducted slab to fluid-mobile U^{6+} by oxidising aqueous fluids, followed by transfer of this ^{235}U-enriched fluid to the mantle wedge (Freymuth et al., 2019). There is hence no evidence for addition of U^{6+} to the mantle source of sanukitoids by oxidised aqueous fluids. The absence of this process in the Mesoarchean-Paleoproterozoic can be explained by temporal changes in the redox state of the crustal materials being recycled into the mantle. Before the first major increase in atmospheric O_2 at the GOE (~2.45 – 2.05 Ga; e.g. Bekker et al., 2004; Gumsley et al., 2017; Poulton et al., 2021), atmospheric O_2 levels were much lower than present at < 0.001% of the modern level (e.g. Pavlov and Kasting, 2002), resulting in anoxic deep ocean waters. These anoxic conditions likely prevailed until the NOE (~800 – 550 Ma; e.g. Och and Shields-Zhou, 2012; Scott et al., 2008) when further significant increase

in atmospheric O_2 enabled oxygenation of the deep ocean (e.g. Canfield, 1998; Canfield et al., 2007; Reinhard and Planavsky, 2022). At a similar time, seawater sulfate concentrations increased to be similar to modern levels, leading to addition of sulfate as anhydrite and oxidation of Fe^{2+} by sulfate during seafloor alteration (e.g. Fakhraee et al., 2019; Farquhar et al., 2010). These conditions meant that seafloor-altered oceanic crust likely did not become substantially oxidised until the early Phanerozoic (Stolper and Keller, 2018), a change that is reflected by the concurrent increase in the fO_2 of island arc magmas (Stolper and Bucholz, 2019). As the redox budget of Archean and Proterozoic AOC was low and dominated by relatively low solubility Fe^{3+} from magnetite in serpentinised mantle, aqueous fluids derived from such recycled AOC were not significantly oxidising (Evans and Tomkins, 2011). Hence transformation of U^{4+} to U^{6+} by oxidised aqueous fluids in recycled crust, and its associated low $\delta^{238}U$ and Th/U signature (Freymuth et al., 2019), did not appear until after the NOE.

The sanukitoid samples mostly have Th/U values of ~4 – 6, higher than the BSE (3.77, Faure et al., 2020; Wipperfurth et al., 2018). Two samples have even higher Th/U of ~6.5, while only one sample has Th/U lower than the BSE value (BFG sanukitoid 505465). Primitive sanukitoids from the BFG show general positive covariation between Th/U and tracers of garnet fractionation (fig. 5.10a and b), such as the CI-chondrite normalised ratio $(La/Yb)_N$, and the shape coefficient λ_1 which quantifies the steepness of their chondrite-normalised REE pattern (O'Neill, 2016). The heavy Ti stable isotope compositions (high $\delta^{49}Ti$ values) of primitive BFG sanukitoids trace residual rutile during eclogite partial melting (see Chapter 3 of this thesis), and figure 5.10c shows that their Th/U also positively covaries with $\delta^{49}Ti$. These trends suggest that the high Th/U of BFG sanukitoids may originate from the eclogite-derived melt component that metasomatised the sanukitoid mantle source, which formed in equilibrium with residual garnet and rutile. Th^{4+} is slightly more incompatible than U^{4+} in garnet due to it having a slightly larger ionic radius (e.g. Blundy and Wood, 2003; Elkins et al., 2008). The elevated Th/U of these primitive sanukitoids may therefore be explained by preferential retention of U over Th in residual minerals such as garnet during formation of the eclogite melt component. The high Th/U signature was then transferred to the BFG sanukitoid mantle source alongside high $\delta^{49}Ti$ during metasomatism.
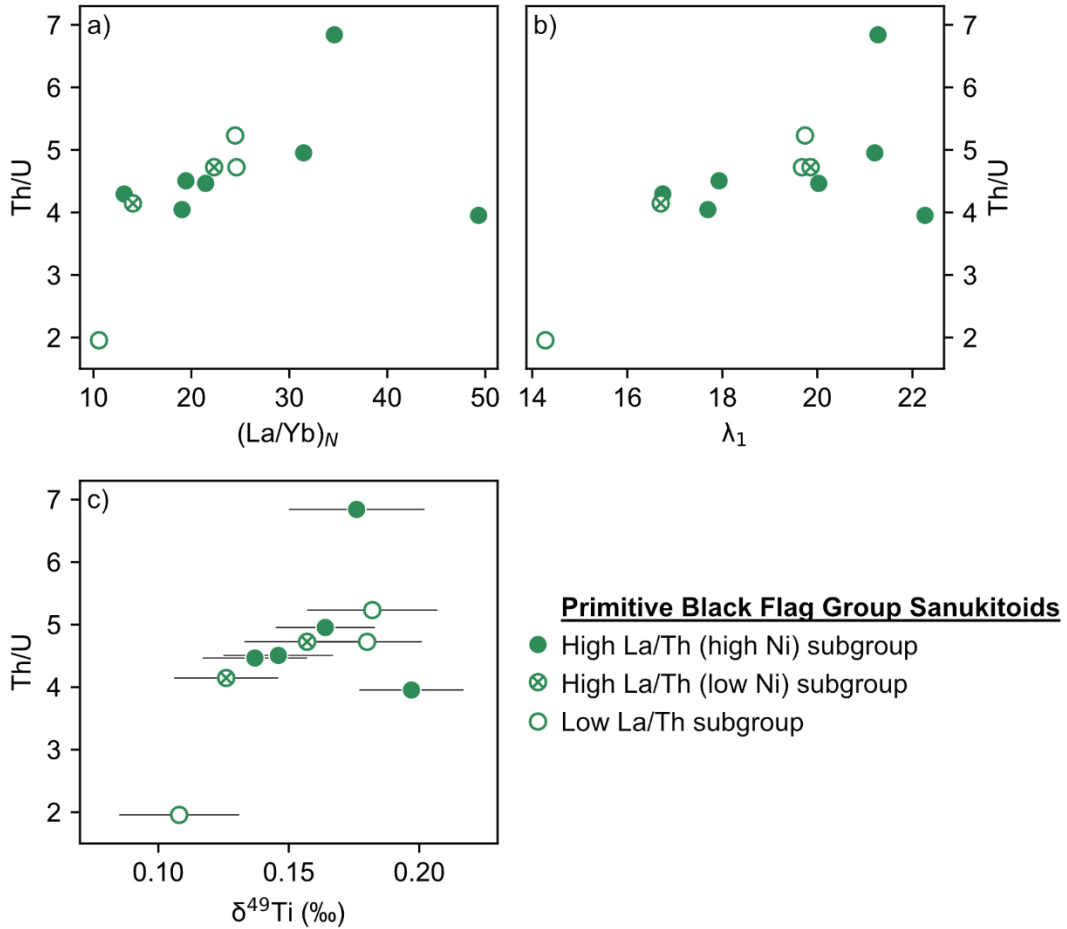
Figure 5.10: Primitive (SiO₂ < 58 wt%) Black Flag Group sanukitoid Th/U vs a) (La/Yb)ₙ, b) λ₁ (O'Neill, 2016) and c) δ⁴⁹Ti (‰). REE concentrations are normalised to the CI chondrite values from O'Neill (2016). The Ti stable isotope data are presented in Chapter 3 of this thesis, and uncertainty on δ⁴⁹Ti is shown as the 95% confidence interval.

Sanukitoids not affected by apatite fractional crystallisation (P/P* > 0.3) display $\delta^{238}U$ values that are on average (weighted mean = -0.27 ± 0.03‰, 2sd) slightly heavier than the BSE (-0.306 ± 0.026‰), hence there may have been a small U isotope fractionation during sanukitoid parental magma formation in the opposite direction to mobilisation of U^{6+} by oxidising aqueous fluids. The limited magnitude of U isotope fractionation supports there being no redox change during transfer of U from recycled crustal material to the sanukitoid mantle source. As U^{4+} is insoluble in aqueous fluids, I propose that a melt component is responsible for any U addition to the sanukitoid mantle source. This process is consistent with the Ti stable isotope compositions of primitive sanukitoids which require the involvement of a metabasite-derived melt component in sanukitoid formation (Chapter 3). In contrast to Th/U, no correlation is observed between $\delta^{238}U$ and (La/Yb)ₙ, λ₁ or δ⁴⁹Ti for primitive BFG sanukitoids. It

therefore appears that, while residual silicate minerals such as garnet can fractionate U from Th, they do not cause significant U isotope fractionation. Consequently, the origin of the slightly heavier U isotope composition of sanukitoids relative to the BSE is not immediately evident, and possible explanations for it are discussed in section 5.4.4.4.

5.4.3.2. The high Ba-Sr granite suites
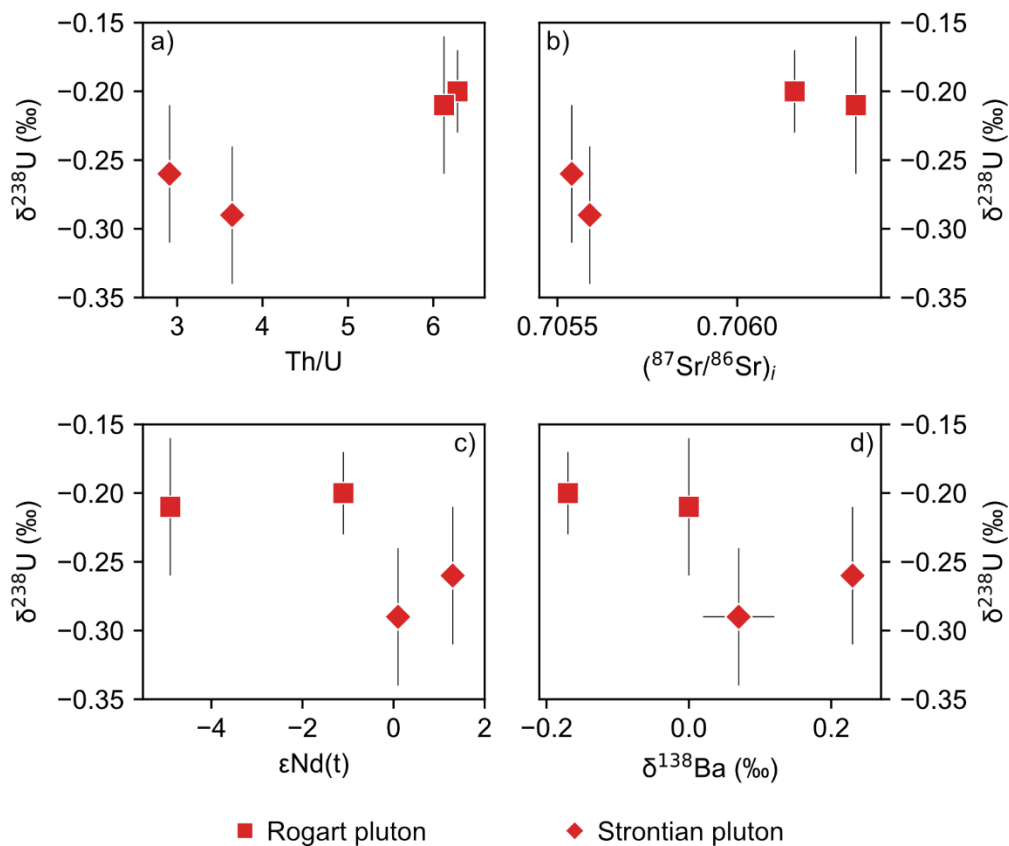
Figure 5.11: High Ba-Sr granite suite $\delta^{238}U$ (‰) vs a) Th/U, b) initial Sr isotope composition ($^{87}Sr/^{86}Sr)_i$, c) $\epsilon Nd(t)$, and d) $\delta^{138}Ba$ (‰). Radiogenic isotope compositions are from Fowler et al. (2001, 2008) and Ba stable isotope compositions are from Zhu et al. (2024). Uncertainty on $\delta^{138}Ba$ is shown as 2sd.

While data are limited, the two high Ba-Sr granite suite plutons display distinct $\delta^{238}U$-Th/U systematics – the Strontian pluton has $\delta^{238}U$ within error of the BSE and similar to unaltered N-MORB ($\delta^{238}U$ = -0.268 ± 0.011‰, Andersen et al., 2015) as well as Th/U values similar to slightly lower than the BSE, while the Rogart pluton has significantly higher $\delta^{238}U$ and Th/U (fig. 5.11a). In addition, the Rogart and Strontian plutons have different radiogenic isotope compositions. The Rogart pluton has higher

(^{87}Sr/^{86}Sr)$_i$ and lower ϵNd(t) (deviation of ^{143}Nd/^{144}Nd from the chondritic uniform reservoir (CHUR) composition) than the Strontian pluton, meaning the Rogart pluton originated from a more isotopically enriched mantle source (Fowler et al., 2008, 2001). Fowler et al. (2008) attributed this to variable amounts of a pelagic sediment component in the Paleozoic Caledonian mantle, with a greater sediment contribution for the Rogart pluton. Ba-Mg-O stable isotope systematics also support this conclusion (Fowler et al., 2008; Zhu et al., 2024). These isotopic data suggest addition of up to 5% pelagic sediment component to the mantle source of the Rogart pluton (Zhu et al., 2024). In the high Ba-Sr granite plutons, δ^{238}U is positively correlated with (^{87}Sr/^{86}Sr)$_i$ and negatively correlated with ϵNd and δ^{138}Ba (fig. 5.11). The geochemical data therefore imply that the high δ^{238}U and Th/U of the Rogart pluton are due to a pelagic sediment component in its mantle source.

The Th/U and U isotope compositions of pelagic sediments are highly variable (e.g. Gama and Schwark, 2022; Li and Tissot, 2023). High Th/U is primarily associated with significant detrital input which increases the Th concentration of the sediment (e.g. Carpentier et al., 2013; Hillaire-Marcel et al., 1990). The δ^{238}U of the detrital component in marine sediments is poorly constrained as studies have focused instead on carbonate sediments and organic-rich shales/mudrocks that are used for paleoredox reconstructions. Its U isotope composition is often assumed to be equal to the average crustal δ^{238}U in order to correct for detrital input, and is generally found to be lighter than the authigenic component (e.g. Andersen et al., 2016; Asael et al., 2013; Holmden et al., 2015). However, it is possible to imagine a detrital component with high δ^{238}U – oxidative chemical weathering may preferentially mobilise ^{235}U, leaving the residual rock with high δ^{238}U to be incorporated in detrital sediment (Charbonnier et al., 2023; Pavia et al., 2023). Alternatively, Th/U and δ^{238}U may not trace the same component of the pelagic sediment. Bulk Th/U is likely dominated by Th from the detrital component, while bulk δ^{238}U is a mixture of the detrital and authigenic components, and it may be the authigenic component that is enriched in heavy U isotopes.

The light Mg isotope compositions of some Rogart pluton samples may indicate the involvement of carbonate sediments (Zhu et al., 2024). Marine carbonates can exhibit relatively high Th/U. The amount of U in carbonate depends on seawater U

concentrations, and during increased ocean anoxia seawater U content decreases. High marine carbonate Th/U can hence be seen during periods of extensive ocean anoxia (Brennecka et al., 2011; Marenco et al., 2016). However, current studies suggest that this effect only causes limited elevation of carbonate Th/U of < 4 (Marenco et al., 2016), which is lower than the Th/U of the Rogart pluton (~6). The compiled carbonate data in the Uranium Isotope Database (UID; Li and Tissot, 2023) do extend to higher Th/U values (> 10), but these more extreme values are generally associated with elevated Th concentrations rather than diminished U concentrations, suggestive of contamination by a detrital component. I therefore favour that the Th/U-δ^{238}U systematics of the Rogart pluton are best explained by contamination of its mantle source with pelagic sediment containing a significant detrital component.

The Strontian pluton has δ^{238}U of -0.29 ± 0.05‰ to -0.26 ± 0.05‰, within error of both the BSE (-0.306 ± 0.026‰) and the modern upper mantle estimated from N-MORBs (-0.268 ± 0.011‰; Andersen et al., 2015). Its mantle-like U isotope composition is in agreement with its Ba and Mg stable isotope compositions and relatively depleted Sr and Nd isotope compositions. This supports previous conclusions that the mantle source of the Strontian pluton contains significantly less recycled sediment than the Rogart pluton source (Fowler et al., 2008; Zhu et al., 2024).

5.4.3.3. δ^{238}U variations in the Black Flag Group sanukitoids

The δ^{238}U of the Neoarchean Black Flag Group sanukitoids varies from -0.33 ± 0.03‰ to -0.23 ± 0.04‰, and this variation does not appear to be generated by apatite fractional crystallisation or other processes during differentiation (fig. 5.12a). Their δ^{238}U is broadly correlated with La/Th (fig. 5.12b), the geochemical parameter used to divide the BFG into subgroups. The low La/Th subgroup has relatively low and homogeneous δ^{238}U with a weighted mean of -0.29 ± 0.02‰ (2se) that is similar to the BSE. Meanwhile, the high La/Th subgroups display more variable δ^{238}U that extends to values slightly heavier than the BSE, and in the case of the high La/Th (high Ni) subgroup δ^{238}U is positively correlated with La/Th (fig. 5.12b).

The compositional differences between BFG subgroups are interpreted to reflect compositionally distinct lithospheric mantle sources, and the component responsible

for enriching the source of the high La/Th subgroups was likely younger and more enriched in incompatible trace elements than the component in the low La/Th subgroup source (Smithies et al., 2022). It is hence possible that the variable δ^{238}U of the BFG sanukitoids is related to their mantle source compositions. However, the weighted means of the low La/Th subgroup (-0.29 ± 0.04‰, 2sd, n = 4) and high La/Th subgroups (-0.27 ± 0.03‰, 2sd, n = 11) are indistinguishable, and a Welch's unequal variances t-test confirms that the difference between the subgroups is not large enough to be statistically significant, t(10.1) = 1.41, p = 0.19. The current resolution of the U isotope data is therefore not good enough to properly examine δ^{238}U variability on this scale, and it is not possible to confidently determine the origin of δ^{238}U variability among the BFG sanukitoids.
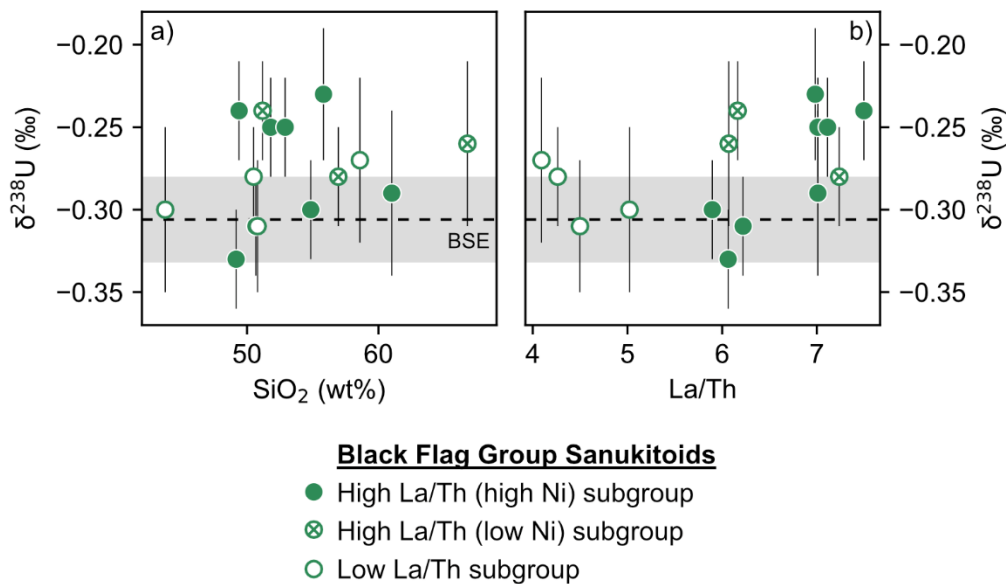
Figure 5.12: Black Flag Group sanukitoid subgroup δ^{238}U (‰) vs a) SiO$_2$ (wt%) and b) La/Th. The black dashed line is the BSE δ^{238}U value of -0.306 ± 0.026‰ (Andersen et al., 2015) and the grey box is the 2se uncertainty on this value.

5.4.3.4. Secular evolution of sanukitoid δ^{238}U

Archean and Paleoproterozoic sanukitoids and their Paleozoic high Ba-Sr granite suite analogues were emplaced across the GOE and NOE and contain a component derived from recycled crust, most likely a metabasite-derived melt (Chapter 3; e.g. Martin et al., 2009; Smithies and Champion, 2000). The evolution of sanukitoid δ^{238}U through time (fig. 5.13) may therefore record changes in the U isotope composition of this recycled material resulting from increasing atmosphere and ocean oxygenation.

Once samples affected by apatite fractionation (P/P* ≤ 0.3) have been removed, the sanukitoid data outside of the ~2660 – 2690 Ma Black Flag Group are very limited. The weighted mean of the BFG data suggests that Archean sanukitoids had average δ^{238}U of -0.28 ± 0.01‰ (2se, n = 15), similar to the BSE.
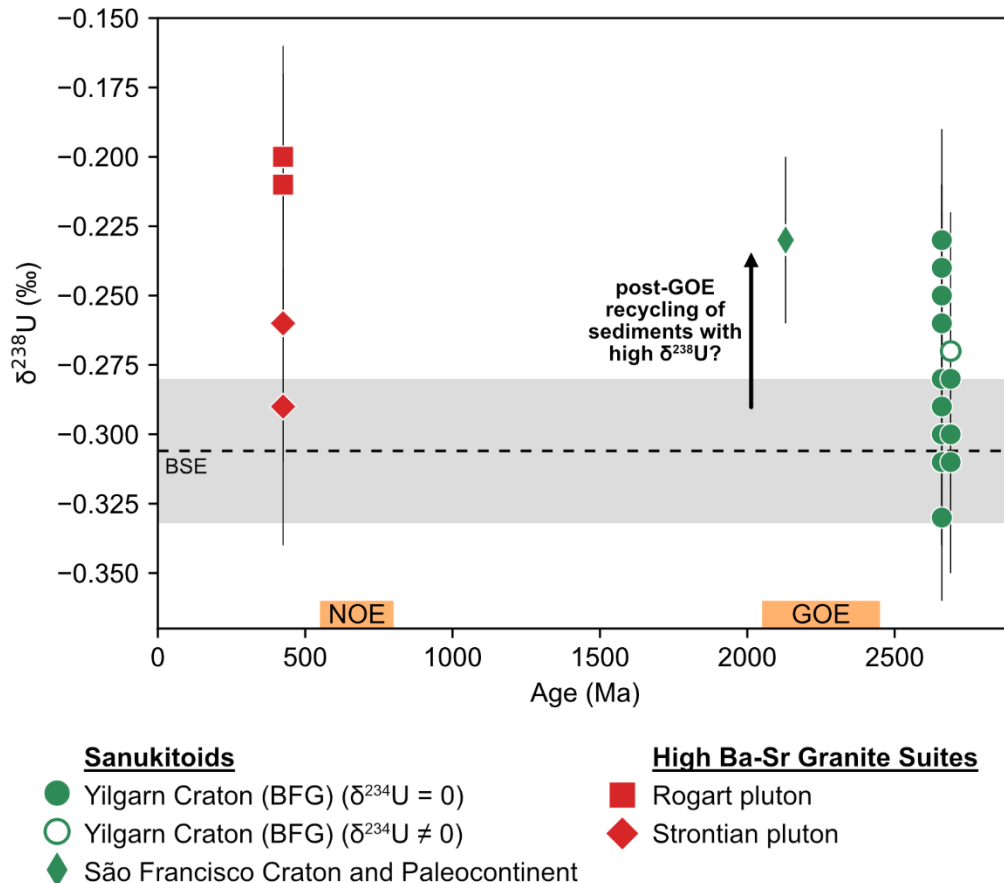
Figure 5.13: Evolution of sanukitoid and Phanerozoic analogue (high Ba-Sr granite suite) δ^{238}U (‰) through time. Only samples not affected by apatite fractional crystallisation (P/P* > 0.3) are plotted. The black dashed line is the BSE δ^{238}U value of -0.306 ± 0.026‰ (Andersen et al., 2015) and the grey box is the 2se uncertainty on this value.

The Alto Maranhão suite sanukitoid from the São Francisco Craton formed at 2130 ± 2 Ma (Noce, 1995), after the first major rise in atmospheric O_2 at the GOE, and has δ^{238}U of -0.23 ± 0.03‰. This value falls right at the upper end of the BFG range, and is slightly heavier than the average δ^{238}U of Archean sanukitoids. Moreira et al. (2020) found that most zircons from the Alto Maranhão suite have slightly higher δ^{18}O (~6 – 6.7‰) than the mantle (5.3 ± 0.6‰; Valley, 2003). They proposed that this shows a recycled sediment component was involved in the formation of these sanukitoids in addition to a metabasite melt component. The Alto Maranhão suite sample also has

high Th/U of 6.4, and on figure 5.9 it plots near the Rogart Pluton, the sediment component in which is well-established. The relatively high $\delta^{238}U$ of the Alto Maranhão suite sanukitoid may therefore reflect an isotopically heavy recycled sediment component in its source, similar to the Rogart Pluton. Multiple studies have found evidence for increased $\delta^{238}U$ variability in sediments after the GOE due to oxidative weathering processes starting (Brüske et al., 2020; Chen et al., 2021; X. Wang et al., 2018). The onset of recycling sediments with distinct $\delta^{238}U$ into the mantle, followed by incorporation of these sediments into the source region of sanukitoids such as the 2130 Ma Alto Maranhão suite, may have caused a shift to higher $\delta^{238}U$ in sanukitoids following the GOE. However, this conclusion is based on a single sanukitoid sample with a U isotope composition that still falls in the range of Archean sanukitoids, so this conclusion is speculative at best. Measurement of additional Paleoproterozoic sanukitoid samples, using P/P* to filter for apatite fractionation, is needed to provide more robust constraints on the possible changes to sanukitoid $\delta^{238}U$ across the GOE.

The Scottish high Ba-Sr granite suites were emplaced at ~425 Ma, after the second major rise in atmospheric O_2 at the NOE. As discussed in section 5.4.3.2., a recycled pelagic sediment component is thought to be responsible for the high $\delta^{238}U$ of the Rogart Pluton. The Strontian Pluton, which does not contain a significant sediment component (Fowler et al., 2008; Zhu et al., 2024), has weighted mean $\delta^{238}U$ of -0.28 ± 0.04‰ (2se, n = 2), indistinguishable from the average composition of Archean sanukitoids (-0.28 ± 0.01‰). These data suggest that despite a significant change in U cycling at the NOE, the U isotope composition of the recycled crust-derived component did not significantly change. I discuss two possible explanations for this observation below. However, it is again important to note that sample numbers are relatively limited, and that there is a large temporal gap between the ~2130 Ma sanukitoid and the ~425 Ma high Ba-Sr granite suites.

The first possible explanation is that, as the high Ba-Sr granite suites were emplaced relatively shortly after the NOE (~800 – 550 Ma) at ~425 Ma, they could be sampling older AOC that formed before changes to U addition during seafloor alteration at the NOE. Generation of $\delta^{238}U$ variations in recent AOC require either reductive (high $\delta^{238}U$) or oxic (low $\delta^{238}U$) partial U uptake from U-rich, oxidised, seawater-derived fluid (Andersen et al., 2024). Multiple studies have proposed that deep ocean oxygenation

was only achieved relatively late, during the early Paleozoic (e.g. Dahl et al., 2019; Gill et al., 2011; Reinhard and Planavsky, 2022). Some studies suggest an even more extreme scenario where deep oceans may not have been fully oxygenated until later in the Paleozoic < 425 Ma (e.g. Dahl et al., 2010; Sperling et al., 2015; Stolper and Keller, 2018). Hence the deep ocean conditions required to create $\delta^{238}U$ variability in AOC may have only developed shortly before the emplacement of the high Ba-Sr granite suites. The age of subducting slabs on the modern Earth ranges from ~0 to 160 Ma (e.g. Cruciani et al., 2005), and there may have been further time delay between enrichment of the high Ba-Sr granite mantle source and its melting (e.g. Fowler et al., 2008). It is therefore possible that the high Ba-Sr granite suites are either too old or contain too old a recycled AOC component to record a change in the $\delta^{238}U$ of AOC following the NOE and extensive deep ocean oxygenation. A recent study of U isotopes in ophiolites through time found evidence of significant U uptake and variable $\delta^{238}U$ in oceanic crust since at least 540 Ma (Rodney et al., 2024, Preprint). This finding suggests that the AOC component in the high Ba-Sr granites would likely have had variable $\delta^{238}U$, although Rodney et al. note that the spatial and temporal extents of deep ocean oxygenation recorded by these data are not clear.

An alternative explanation for the similar $\delta^{238}U$ of Archean sanukitoids and the post-NOE Strontian pluton is that the metabasite melt component had indistinguishable $\delta^{238}U$ to unaltered N-MORB and the mantle, despite its AOC source having variable $\delta^{238}U$. Seafloor alteration of oceanic crust produces heterogeneous $\delta^{238}U$ values, with the magnitude and direction of fractionation depending on redox conditions during U addition and how quantitative U uptake is (Andersen et al., 2024, 2015; Noordmann et al., 2016). Slab melting may be most likely to affect the uppermost AOC as temperatures are highest near the slab-mantle interface (e.g. Syracuse et al., 2010; van Keken et al., 2011). The uppermost part of AOC generally shows low $\delta^{238}U$ due to oxic U uptake but the vertical extent of this signature varies – in young AOC low $\delta^{238}U$ extends through the whole 750m section of lavas (Andersen et al., 2024), while in older (> 100 Ma) AOC a switch to reductive U uptake and high $\delta^{238}U$ is observed below ~100m (Andersen et al., 2015; Noordmann et al., 2016). If slab melting samples a mixture of high $\delta^{238}U$ and low $\delta^{238}U$ AOC, the resulting melt could have similar $\delta^{238}U$ to unaltered MORB and hypothetical Archean altered crust. Additionally, while on average the uppermost AOC has low $\delta^{238}U$, all cores also show some bulk samples

from this region with $\delta^{238}U$ indistinguishable from fresh MORB (Andersen et al., 2024, 2015; Noordmann et al., 2016). The heterogeneous U isotope composition of AOC may therefore have led to the generation of slab-derived melts with indistinguishable $\delta^{238}U$ to unaltered MORB and hypothetical Archean altered crust, resulting in no observable difference in the average $\delta^{238}U$ of Archean sanukitoids and Paleozoic high Ba-Sr granites.

In summary, there is no clear secular trend in the U isotope composition of sanukitoids through time, despite major changes to the U geochemical cycle across the GOE and NOE. Slightly higher average sanukitoid $\delta^{238}U$ after the GOE may reflect the onset of recycling sediments with variable $\delta^{238}U$ due to oxidative weathering, but this conclusion is based on a single Paleoproterozoic sanukitoid sample so it is not robust. For samples without a significant sediment component, Neoarchean sanukitoids have indistinguishable average $\delta^{238}U$ to their mid-Paleozoic analogues. This may be due to heterogeneous $\delta^{238}U$ in Paleozoic upper AOC or due to the AOC component having formed before extensive deep ocean oxygenation.

5.4.3.5. Implications for the oxidation of sanukitoid magmas

Ti stable isotopes (Chapter 3), mineral chemistry (de Oliveira et al., 2010; do Nascimento et al., 2023, 2021) and S speciation in apatite (Meng et al., 2022; Moreira et al., 2023) support oxidised parental magmas for Archean and Paleoproterozoic sanukitoids, with fO_2 of ΔFMQ +0.77 to +1.24 which is comparable to modern arc magmas (average ΔFMQ of ~+1; Cottrell et al., 2021). The mechanism(s) by which modern subduction processes generate oxidised magmas are debated, but there is a growing consensus that neither degassing nor crystal fractionation can cause a large enough increase in fO_2, and that the mantle source regions of arc magmas are themselves oxidised (see Evans and Tomkins (2021) for a recent review). The dominant model is that modern arc magmas are oxidised by inputs of oxidised material (e.g. fluids, melts) from the subducted slab (e.g. Evans and Tomkins, 2021). This mechanism is supported by observations that the fO_2 of arc magmas changes with the spatial (Hu et al., 2024) and temporal (Stolper and Bucholz, 2019) distributions of oxidised crustal materials. Oxidised aqueous fluids generated during slab devolatilisation are the most commonly invoked source of redox budget (the number

of moles of elements that can reduce or oxidise other elements; Evans, 2006) (e.g. Duan et al., 2022; Kelley and Cottrell, 2009; Zhang et al., 2021), and solutes within these fluids are required to transport the redox budget to the subarc mantle (Evans and Tomkins, 2021). While reduction of Fe^{3+} during dehydration of serpentinised lithospheric mantle may form oxidised fluids (e.g. Debret and Sverjensky, 2017, although this is disputed e.g. Piccoli et al., 2019), Fe itself is generally not considered a significant vector of redox budget due to its low solubility in aqueous fluids (e.g. Evans and Tomkins, 2011; Kelley and Cottrell, 2009). Instead sulfate, which is primarily added to the oceanic crust and lithospheric mantle from seawater during seafloor alteration, is thought to be the main species responsible for transferring redox budget from the slab to the subarc mantle (e.g. Alt et al., 2013; Bénard et al., 2018; Pons et al., 2016). Oxidised sediments may also contribute, either by oxidising slab-derived fluids (Ague et al., 2022; Padrón-Navarta et al., 2023) or by transferring redox budget in sediment melts (e.g. Canil and Fellows, 2017).

While U isotopes and Th/U demonstrate U^{6+} addition by oxidised aqueous fluids in modern arc magmas (Andersen et al., 2015; Freymuth et al., 2019), there is no evidence for this process having occurred in Archean and Paleoproterozoic sanukitoids. This may not be particularly surprising – as previously detailed, seafloor-altered oceanic crust was not substantially oxidised until after the NOE (e.g. Stolper and Keller, 2018; Rodney et al., 2024, Preprint). Seawater sulfate concentrations were also low until a similar time (e.g. Fakhraee et al., 2025; Farquhar et al., 2010), meaning there was limited sulfate present in oceanic lithosphere and hence that the main vector of redox budget in aqueous fluids was absent in the Archean and most of the Proterozoic. This evidence suggests that, unlike for modern arc magmas, oxidising, sulfate-bearing aqueous fluids were probably not responsible for the oxidised nature of sanukitoid magmas. Therefore, the mechanisms by which mantle-derived magmas are oxidised, or at least their relative importances, may have changed over the Earth's history.

One possible mechanism for the oxidation of sanukitoid magmas is the presence of a component derived from recycled oxidised sediments in their mantle source. Moreira et al. (2023) proposed that this process is the cause of the high fO_2 (ΔFMQ +0.80 to +1.24) of the Alto Maranhão suite sanukitoids, which I have presented the U isotope

compositions of in this chapter. These sanukitoids are ~2130 Ma (Noce, 1995; Seixas et al., 2013) and hence formed after the rise in atmospheric O_2 at the GOE. The combination of higher apatite S^{6+}/S_{total} and zircon $\delta^{18}O$ and U/Yb compositions in the sanukitoids than older (~2350 Ma) TTGs from the same region led Moreira et al. to conclude that recycled oxidised sediments, which were only able to form after the start of the GOE, are responsible for the high fO_2 of the Alto Maranhão suite. However, unlike these Paleoproterozoic samples, most sanukitoids formed in the Meso-Neoarchean, before the GOE, when atmospheric O_2 was lower and consequently sediments were not significantly oxidised (e.g. Lyons et al., 2014; Pufahl and Hiatt, 2012). Some studies have found evidence for "whiffs" of oxygen before the GOE, possibly as far back as 2.95 Ga (Anbar et al., 2007; Planavsky et al., 2014; X. Wang et al., 2020), which may have locally generated oxidised sediments. Wu et al. (2024) proposed that such sediments may have contributed to the oxidation of late Neoarchean (~2.5 Ga) metasomatised mantle peridotite xenoliths. However, I consider it unlikely that localised recycling of oxidised sediments before the GOE can account for the widespread distribution of sanukitoids in the late Archean.

Alternative mechanisms for producing oxidised mantle without the involvement of oxidised slab inputs or sulfate have been proposed, with hydrogen playing an important role. Iacovino et al. (2020) suggested that hydrogen in aqueous fluids may be an important oxidant. H^+ in the fluid is reduced to H_2 while Fe^{2+} in the surrounding mantle is oxidised to Fe^{3+} via the following reaction:

$$2Fe^{2+}_{(s)} + 2H^+_{(aq)} \rightarrow 2Fe^{3+}_{(s)} + H_{2\,(aq)}$$
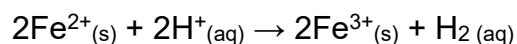
Tollan and Hermann (2019) and Brandon and Draper (1996) proposed a different model involving dissociation of H_2O in slab-derived melt/fluid as it ascends through the mantle. A coupled hydroxylation-oxidation reaction with mantle minerals (mainly orthopyroxene) occurs, in which H^+ reacts with Fe^{2+} in the mineral to form Fe^{3+}, while OH^- is also added to the mineral. The H_2 formed is then diffusively lost to leave locally oxidised mantle. Meng et al. (2022) suggested that one of these mechanisms may be responsible for the formation of oxidised, sulfur-rich magmas, including sanukitoids, in the Neoarchean Superior Craton. Similarly, Wu et al. (2024) proposed that these processes may have contributed to the oxidation of ~2.5 Ga peridotite xenoliths from the North China Craton which were metasomatised by adakite-like melts. A major difference between these two mechanisms involving H^+ as the oxidant is the volume

of fluid they require. Modelling done by Iacovino et al. (2020) suggests that the former method requires high fluid:rock ratios of ~1 – 10 to elevate mantle fO_2 sufficiently in modern arcs. In contrast, Brandon and Draper (1996) calculated that the latter mechanism requires only ~0.1 – 0.2 g of H_2O per kilogram of peridotite to raise its fO_2 by 1 – 2 log units. This consideration caused Meng et al. (2022) to view the dissociation mechanism of Tollan and Hermann (2019) and Brandon and Draper (1996) as more viable than the one proposed by Iacovino et al. (2020). However, as discussed in Chapter 3, the Ti isotope compositions of primitive sanukitoid magmas are best explained by addition of an eclogite melt formed by fluid-fluxed melting to their mantle source. This result implies that the metabasite-derived melt flux to the sanukitoid mantle source may have been accompanied by a significant aqueous fluid flux, which could potentially oxidise the sanukitoid mantle source via Iacovino et al. (2020)'s proposed mechanism.

Another possibility is that the metabasite melt component oxidised the mantle source of sanukitoids. Fe^{2+} is more compatible than Fe^{3+} in garnet (Holycross and Cottrell, 2023), meaning that retention of Fe^{2+} in residual garnet during partial melting could generate relatively oxidised melts with high $Fe^{3+}/\Sigma Fe$. Tang et al. (2024) proposed that this process created oxidised medium pressure and high pressure TTG magmas in the Neoarchean North China Craton. This model for forming oxidised melts is a variation on one proposed for modern arc magmas in which melt oxidation is driven by high pressure fractional crystallisation of garnet (e.g. Tang et al., 2019, 2018). A recent study by Holycross and Cottrell (2023) concluded that this mechanism can only cause limited melt fO_2 increase of < 1 log unit due to the garnet-melt partition coefficients for Fe^{2+} ($D_{Fe^{2+}}^{grt/melt}$) and Fe^{3+} ($D_{Fe^{3+}}^{grt/melt}$) converging at the conditions of high pressure garnet fractional crystallisation (1.5 GPa, > 1100°C). However, formation of the metabasite melt component in sanukitoids would have occurred under different P-T conditions. The Ti isotope data presented in Chapter 3 favour fluid-fluxed eclogite melting to generate this component, which occurs at higher pressures (2 – 4 GPa) but lower temperatures (750 – 900°C) than garnet fractional crystallisation (e.g. Martin and Hermann, 2018; Schmidt et al., 2004; Sisson and Kelemen, 2018). The experimental data from Holycross and Cottrell demonstrate that decreasing the temperature increases $D_{Fe^{2+}}^{grt/melt}$ more rapidly than $D_{Fe^{3+}}^{grt/melt}$. While data are more

limited, they also suggest that increasing the pressure increases $D^{grt/melt}_{Fe^{2+}}$ but decreases $D^{grt/melt}_{Fe^{3+}}$. Hence at the conditions of fluid-fluxed eclogite melting, Fe^{2+} is expected to be distinctly more compatible in garnet than Fe^{3+}, enhancing the oxidation change imparted by garnet-melt fractionation. Indeed, when Tang et al. (2024) modelled metabasite partial melting at 900°C using the partition coefficients from Holycross and Cottrell (2023) they found that residual garnet modes of > 0.2 can increase melt fO_2 by > 2 log units. It is therefore viable that Fe^{2+} retention in residual garnet may have generated oxidised metabasite-derived melts which oxidised the mantle source of sanukitoids during metasomatism.

Overall, sanukitoid magmas display similar fO_2 to modern arc magmas, but their U isotope and Th/U compositions show no evidence for addition of oxidised aqueous fluids to their mantle source. While the oxidation of Paleoproterozoic sanukitoids can be explained by recycling of oxidised sediments into their source (Moreira et al., 2023), this process is unable to account for the widespread occurrence of oxidised sanukitoid magmas in the late Archean. In the absence of oxidised surface materials being recycled into the mantle, alternative mechanisms are needed to form oxidised sanukitoid parental magmas. I propose that the mantle source of Archean sanukitoids may have been oxidised by reaction of H^+ from aqueous fluids/hydrous melts (Brandon and Draper, 1996; Iacovino et al., 2020; Tollan and Hermann, 2019) or by an oxidised eclogite partial melt with high $Fe^{3+}/\Sigma Fe$ due to Fe^{2+} retention in residual garnet (Tang et al., 2024). This conclusion implies that the dominant mechanisms for generating oxidised, mantle-derived magmas have likely changed over the Earth's history. The onset of recycling oxidised sediments into the mantle at the GOE may represent a change towards modern-style processes in which recycled, oxidised crustal materials are the main source of redox budget.

5.4.4. The U isotope compositions of granitoids

Prior to this study, the only $\delta^{238}U$ measurements of Archean granitoids were two samples from the Isukaia terrane, Greenland, and three samples from Eswatini analysed by Noordmann et al. (2016). The work presented in this chapter therefore significantly increases the amount of Archean granitoid $\delta^{238}U$ data available. In this

section I combine my data with literature data to investigate whether the U isotope compositions of granitoid magmas (SiO_2 > 57 wt%) have changed over time. However, it is important to first assess whether the $\delta^{238}U$ values of literature granitoid samples have been affected by weathering and alteration (see section 5.4.1; e.g. Andersen et al., 2015; Charbonnier et al., 2023; Pavia et al., 2023). Many previous studies reporting granitoid U isotope data do not discuss the possibility that their $\delta^{238}U$ values may have been altered from the original values, despite U being mobile in aqueous fluids, and did not measure $\delta^{234}U$ alongside $\delta^{238}U$. Additionally, the findings presented in section 5.4.2 of this chapter demonstrate that it is also necessary to consider the effects of mineral fractional crystallisation/accumulation during magmatic differentiation as these processes can modify bulk rock $\delta^{238}U$ away from the composition of the parental melt.

5.4.4.1. Assessing the impact of weathering, alteration and magmatic differentiation on literature granitoid $\delta^{238}U$

Literature Archean granitoid data are from Noordmann et al. (2016), who did not measure $\delta^{234}U$ alongside $\delta^{238}U$. I therefore use elemental concentration data to assess whether weathering/alteration may have modified the $\delta^{238}U$ of these samples. Unfortunately, I was unable to obtain the full major and trace element data for the Eswatini granitoids, and hence I am unable to evaluate the impact of these processes on their U isotope compositions. The Eoarchean granitoids from Greenland have Th/U of 3.96 – 4.38, only slightly higher than the BSE, which suggests they did not experience significant U loss or addition during alteration. No Mo data are available for these samples, so I am unable to use Ce/Mo as a proxy for oxidative weathering. To gain additional information about how altered these samples are I calculated their chemical index of alteration (CIA = [Al_2O_3 / (Al_2O_3 + CaO* + Na_2O + K_2O)] x 100, Nesbitt and Young, 1982). The tonalite and quartz dioritic gneiss have CIA values of 50.4 and 46.7 respectively, both within the range of fresh granites and granodiorites (45 to 55, Nesbitt and Young, 1982), hence they do not appear to have been significantly altered. Additionally, these samples have P/P* > 0.35 so they show no clear evidence for apatite fractional crystallisation when compared to the other Archean samples from this chapter. Therefore, the U isotope compositions of the Greenland granitoids have likely not been significantly modified by

weathering/alteration or by fractional crystallisation, although I cannot be completely confident in this conclusion given the lack of $\delta^{234}U$ data.

Once samples affected by oxidative weathering (see section 5.4.1) and apatite fractional crystallisation (P/P* ≤ 0.3, see section 5.4.2) have been excluded, the remaining Archean granitoid data presented in this chapter are limited to 5 samples that are all Neoarchean granitoids from the Yilgarn Craton. To expand the dataset, I include some unpublished U isotope data of Neoarchean granitoids from the Carajás Province in the Amazonian Craton, Brazil (Carneiro et al., 2023). Two samples of the ~2739 Ma Curral granite show no evidence for modification by weathering or apatite fractional crystallisation and have $\delta^{238}U$ of -0.26 ± 0.05‰ and -0.29 ± 0.05‰.

In addition to the high Ba-Sr granites analysed in this chapter, the U isotope compositions of Paleozoic granitoids from the South Bohemian Massive (Weinsberg granites; Noordmann et al., 2016) and Lachlan Fold Belt (Telus et al., 2012) have been measured. The potential impact of weathering and alteration on the U isotope compositions of these samples was not discussed by Noordmann et al. or Telus et al., despite the latter study measuring $\delta^{234}U$ and reporting values that are mostly not at secular equilibrium ($\delta^{234}U \neq 0$). I have attempted to filter for the effects of later U mobilisation during alteration/weathering for the Lachlan Fold Belt granitoids by excluding samples with $\delta^{234}U > 20$ or < -20, representing significant departures from secular equilibrium. However, there are shortcomings to this approach – it is insensitive to U mobilisation before ~1.5 Ma, and not all U mobilisation significantly modifies $\delta^{238}U$ (e.g. Rodney et al., 2024, Preprint). No $\delta^{234}U$ data are available for the Weinsberg granites, but one sample displays high Th/U of ~12 which may indicate U loss and was therefore excluded. Unfortunately, I could not locate the full major and trace element compositions of two of the Weinsberg granite samples analysed by Noordmann et al. (2016) so I was unable to assess whether these samples had been affected by later U mobilisation. Consequently, only one Weinsberg granite sample, Wb 11-94, is considered to have not been affected by weathering/alteration and is included on figure 5.14. Due to the diverse compositions of the Paleozoic granitoids and the fact that the major and trace element data of multiple samples are incomplete, I feel I am unable to confidently assess whether these samples have experienced fractional crystallisation of U-bearing accessory minerals. Some of the Paleozoic

samples plotted on figure 5.14 may therefore have undergone U isotope fractionation due to fractional crystallisation.

5.4.4.2. The temporal evolution of granitoid δ^{238}U
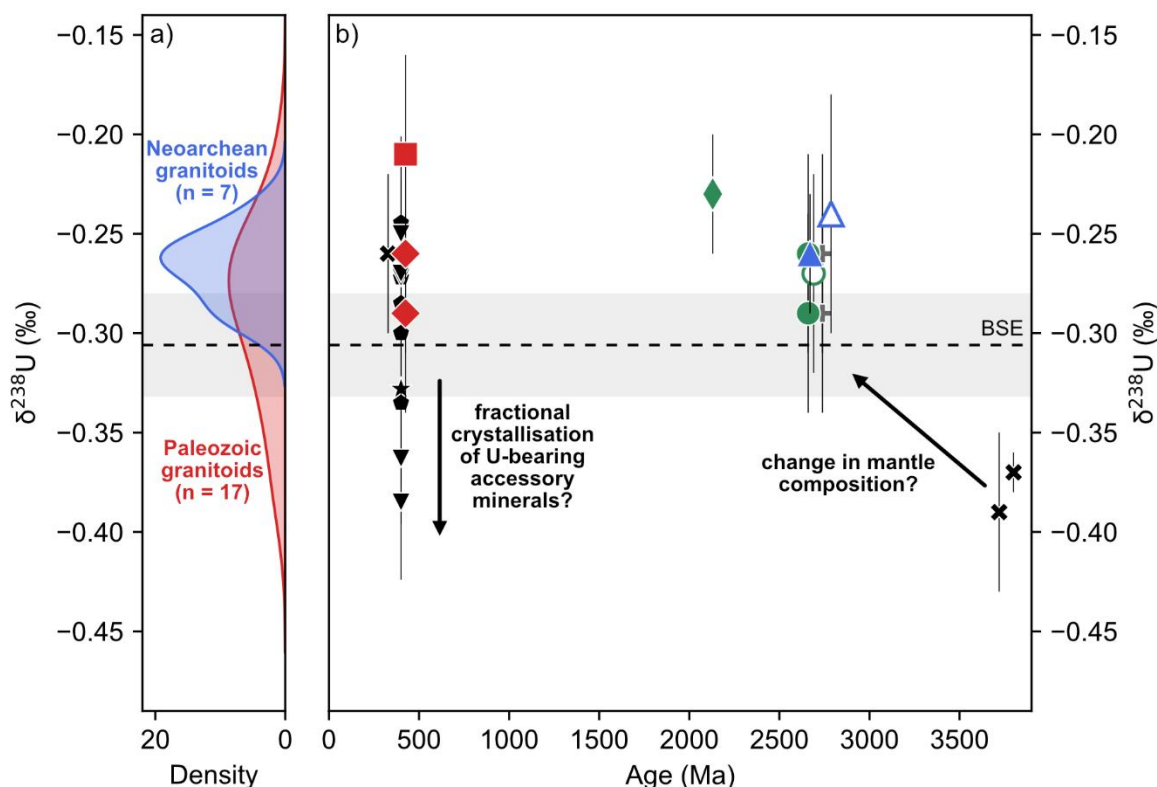
Figure 5.14: a) Kernel density plot comparing Neoarchean granitoid δ^{238}U (‰) to Paleozoic granitoid δ^{238}U. b) Evolution of granitoid δ^{238}U (‰) through time, plotting data from this chapter, unpublished granitoid data from the Carajás Province, Amazonian Craton, and literature data from Telus et al. (2012) and Noordmann et al. (2016). Paleozoic data have been filtered to exclude samples with U isotope compositions likely affected by weathering/alteration, while Archean and Paleoproterozoic data have additionally been filtered to exclude samples likely affected by apatite fractional crystallisation. The black dashed line is the BSE δ^{238}U value of -0.306 ± 0.026‰ (Andersen et al., 2015) and the grey box is the 2se uncertainty on this value.

Figure 5.14b plots the $\delta^{238}U$ of granitoids likely not affected by oxidative weathering, alteration or fractional crystallisation against their age, while figure 5.14a compares the distribution of Neoarchean (2800 – 2500 Ma) granitoid $\delta^{238}U$ to that of Paleozoic (541 – 252 Ma) granitoid $\delta^{238}U$. There are several key observations that can be made about the temporal evolution of granitoid $\delta^{238}U$:

1. The two Eoarchean (4.0 – 3.6 Ga) granitoids have $\delta^{238}U$ of -0.37 ± 0.01‰ and -0.39 ± 0.04‰ (2se) (Noordmann et al., 2016) which are significantly lighter than the BSE and are ~0.1‰ lower than the Neoarchean granitoids, which have weighted mean $\delta^{238}U$ of -0.27 ± 0.02‰ (2se, n = 7). Possible origins of the light U isotope composition of Eoarchean granitoids are discussed in section 5.4.4.3.

2. On average, Neoarchean granitoids have slightly heavier $\delta^{238}U$ (-0.27 ± 0.02‰) than the BSE (-0.306 ± 0.026‰; Andersen et al., 2015). Possible explanations for this difference are discussed in section 5.4.4.4.

3. The kernel density plot (fig. 5.14a) shows that the distributions of Neoarchean and Paleozoic granitoid $\delta^{238}U$ peak at similar $\delta^{238}U$ values of ~-0.26 to -0.28‰. However, the Paleozoic granitoids display a broader distribution than the Neoarchean granitoids. These observations and their implications are discussed in more detail below.

The Paleozoic granitoids appear to have more variable $\delta^{238}U$ than the Neoarchean and Paleoproterozoic granitoids (fig. 5.14a). Their extension towards lighter $\delta^{238}U$ values than the Neoarchean granitoids is likely because the Paleozoic granitoids have not been filtered for the effects of mineral fractionation during differentiation – Archean granitoids also show light $\delta^{238}U$ values down to -0.39‰ but in section 5.4.2. I demonstrated that this is due to apatite fractional crystallisation, hence these samples are excluded from figure 5.14. However, more detailed investigation is needed to confirm this interpretation of the light Paleozoic granitoid U isotope compositions. The Paleozoic granitoids also extend to slightly heavier $\delta^{238}U$ values than the Neoarchean granitoids, primarily because of the Rogart pluton tonalite with $\delta^{238}U$ = -0.21 ± 0.05‰. In section 5.4.3.2 I concluded that the heavy U isotope compositions of the Rogart pluton and Paleoproterozoic sanukitoid were caused by recycled sediments in their mantle sources, hence recycled sediments can explain the high $\delta^{238}U$ values observed. However, the S-type granites from the Lachlan Fold Belt do not share this

characteristic, despite them having a sedimentary source that has been exposed to chemical weathering (Telus et al., 2012).

Figure 5.14a shows that the distributions of Neoarchean and Paleozoic granitoid $\delta^{238}U$ peak at similar values. A Welch's unequal variances t-test indicates there is no statistically significant difference between the Neoarchean granitoids (mean $\delta^{238}U$ = -0.27‰, σ = 0.02‰, n = 7) and Paleozoic granitoids (mean $\delta^{238}U$ = -0.29‰, σ = 0.04‰, n = 17), $t(22.0)$ = 1.79, p = 0.09. Aside from the high Ba-Sr granites analysed in this thesis, the I-type granites from the Lachlan Fold Belt are most analogous to the Archean granitoids, particularly to TTGs, as they too formed by partial melting of metaigneous rocks (e.g. Telus et al., 2012). Excluding two samples (I1 and I8) with low $\delta^{238}U$ (-0.363 ± 0.033‰ and -0.385 ± 0.039‰ respectively) that was likely generated by fractional crystallisation, the Paleozoic I-type granites have weighted mean $\delta^{238}U$ of -0.28 ± 0.02‰ (2se, n = 4). This value is indistinguishable from the average Neoarchean granitoid value (-0.27 ± 0.02‰) and further demonstrates that the average U isotope composition of granitoid magmas has likely not significantly changed since the Neoarchean.

The continental crust is a key reservoir in the U geochemical cycle as weathering of upper continental crust (UCC) is the main source of U in seawater. Constraining the U isotope composition of the UCC through time is therefore important for studies that use the $\delta^{238}U$ of marine sediments to look at environmental changes (e.g. in redox conditions) throughout the Earth's history. Noordmann et al. (2016) estimated that the present day UCC has average $\delta^{238}U$ = -0.30 ± 0.05‰ (2se, n = 41), while Tissot and Dauphas (2015) calculated the $\delta^{238}U$ of bulk continental crust to be -0.29 ± 0.03‰ (2sd). However, constraints on the U isotope composition of Archean UCC are limited, and previous studies investigating the $\delta^{238}U$ of Archean sediments have had to assume that the $\delta^{238}U$ of Archean UCC is the same as modern UCC (e.g. Chen et al., 2021; X. Wang et al., 2018). The new granitoid data presented in this chapter demonstrate that Neoarchean granitoids have indistinguishable $\delta^{238}U$ to Paleozoic granitoids and to estimates of modern continental crust $\delta^{238}U$ (Noordmann et al., 2016; Tissot and Dauphas, 2015), which suggests that the U isotope composition of UCC has likely not varied significantly since ~2.8 Ga. These data therefore help validate the assumption of invariant UCC $\delta^{238}U$ through time made by past studies of U isotope

variations in Archean sediments (e.g. Chen et al., 2021; X. Wang et al., 2018), at least as far back as the Neoarchean.

5.4.4.3. Origin of the low $\delta^{238}U$ of Eoarchean granitoids

The Eoarchean tonalite and quartz dioritic gneiss from Greenland have $\delta^{238}U$ values of -0.37 ± 0.01‰ and -0.39 ± 0.04‰ respectively (Noordmann et al., 2016), significantly lighter than both the BSE (-0.306 ± 0.026‰) and Neoarchean granitoids (-0.27 ± 0.02‰). In this section I investigate possible origins of the light $\delta^{238}U$ of Eoarchean granitoids. TTGs, such as the Eoarchean tonalite and the Neoarchean TTGs from the Yilgarn craton, predominantly formed by partial melting of metabasites in the garnet stability field (e.g. Moyen and Martin, 2012), while the Neoarchean BFG sanukitoids formed by partial melting of mantle metasomatised by hydrous eclogite melts (see Chapter 3 of this thesis). The petrogenesis of the 3720 Ma quartz dioritic gneiss is not as well constrained but it has previously been grouped with TTGs from the Isukaia terrane so may share a similar petrogenesis to them (Hoffmann et al., 2011; Nutman et al., 1999). The change in granitoid $\delta^{238}U$ from the Eoarchean to the Neoarchean may therefore reflect a change in the composition of the mantle and mantle-derived magmas (basalts). I consider the viability of three possible mechanisms for changing Archean mantle composition for explaining the apparent change in mantle $\delta^{238}U$:

1. Mixing of the late veneer into the upper mantle.
2. Mixing of residues from crust formation into the mantle over time.
3. Mixing of recycled crustal materials into the mantle over time.

One possibility is that the increase in $\delta^{238}U$ between the Eoarchean and Neoarchean reflects gradual mixing of a late veneer into the mantle. The isotopic compositions of siderophile elements have previously been used to argue for a "missing" late veneer component in the Isua source mantle (e.g. W isotopes, Dale et al., 2017; Willbold et al., 2011; Ru isotopes, Fischer-Gödde et al., 2020; Ni isotopes, Xu et al., 2023). The late veneer hypothesis was developed to explain why highly siderophile elements are more abundant in the BSE than is predicted by metal-silicate partitioning experiments, with late addition of meteorite material after core formation elevating their concentrations (e.g. Chou, 1978; Li, 2022). In contrast, U is a lithophile element, and

experiments predict that negligible U partitioned into the core (e.g. Faure et al., 2020; Wheeler et al., 2006). Therefore, addition of only a small proportion of the Earth's total U during the late veneer should not have significantly modified the $\delta^{238}U$ of the BSE. An additional problem with this mechanism for modifying the $\delta^{238}U$ of the mantle is that it would require the BSE to have initially had a non-chondritic U isotope composition.

A second possible mechanism to explain changing Archean mantle $\delta^{238}U$ is mixing of the residues from crust formation into the mantle. If the source of the Eoarchean granitoids had the same U isotope composition as the BSE, it implies that forming the Eoarchean granitoids generated residues with high $\delta^{238}U$. Recycling these isotopically heavy residues into the mantle over the Archean could have slightly elevated the $\delta^{238}U$ of the Neoarchean granitoid sources. However, the Eoarchean granitoids are proposed to have the same petrogenesis as the younger TTGs – partial melting of garnet-bearing metabasite (Nutman et al., 1999) – so it would be expected that any U isotope fractionation during formation of the Eoarchean granitoids also occurred during formation of the Neoarchean TTGs. This inference would imply Neoarchean mantle was > 0.1‰ heavier than the BSE, for which there is no evidence, hence I consider that this mechanism is unable to account for the change in granitoid $\delta^{238}U$.

Recycling of crustal materials with distinct $\delta^{238}U$ into the mantle over the Archean may have raised its $\delta^{238}U$ slightly by the Neoarchean. Modern U cycling is thought to result in a flux of isotopically heavy U into the mantle, largely from recycled AOC, which has slightly elevated the $\delta^{238}U$ of the modern upper mantle relative to the BSE (Andersen et al., 2015). This heavy U isotope signature of AOC exists because the Earth's surface is currently oxidised (Andersen et al., 2024, 2015; Rodney et al., 2024, Preprint). In contrast, surface U isotope fractionation under low atmospheric O_2 and anoxic ocean conditions in the Archean was limited (e.g. Brüske et al., 2020; Chen et al., 2021; Rodney et al., 2024, Preprint; X. Wang et al., 2018). Recycled crustal materials likely did not have distinct $\delta^{238}U$ compared to the mantle until at least after the start of the GOE at ~2.45 Ga, hence this process would not have been able to significantly modify the U isotope composition of the Archean mantle. Furthermore, this mechanism would again imply that the BSE initially had a non-chondritic U isotope composition.

Alternatively, as there does not appear to be a viable mechanism for changing the $\delta^{238}U$ of the mantle in the Archean, the $\delta^{238}U$ of the Eoarchean granitoids may have been modified from their parental magma compositions by a process such as fractional crystallisation. Their light $\delta^{238}U$ values of -0.37‰ and -0.39‰ are identical to those of the TTG and sanukitoid samples that have experienced significant apatite fractional crystallisation (fig. 5.4). While these samples have high P/P* > 0.35, which seems to imply that they formed before significant apatite crystallisation from TTG magmas occurs (P/P* ≈ 0.3, fig. 5.4c), using solely comparison of their P/P* to that of other Archean igneous rocks to assess the extent of apatite fractionation may not be valid if they did not have similar parental magma elemental compositions. In the absence of a viable mechanism for modifying the U isotope composition of the mantle, and hence of mantle-derived rocks (basalts), I consider this explanation of the light $\delta^{238}U$ of Eoarchean granitoids to be the most likely. However, further work is still necessary to verify whether there is a genuine increase in the $\delta^{238}U$ of granitoids, and potentially of the mantle and mantle-derived igneous rocks, over the Archean, or whether the apparently light U isotope composition of Eoarchean granitoids is just the result of fractional crystallisation. Measurement of additional Eoarchean samples, as well as of Paleo-Mesoarchean granitoids, would be useful for this purpose. Improving constraints on U isotope fractionation during magma differentiation would also help with interpreting $\delta^{238}U$ variations in granitoids such as this.

5.4.4.4. Origin of the slightly elevated $\delta^{238}U$ of Neoarchean granitoids

Neoarchean granitoids with U isotope compositions that are not modified by weathering/alteration or apatite fractional crystallisation have average $\delta^{238}U$ of -0.27 ± 0.02‰, which is marginally higher than the current best estimate for the BSE composition of -0.306 ± 0.026‰ (Andersen et al., 2015). The peak in the distribution of Paleozoic granitoid $\delta^{238}U$ also appears to be slightly heavier than the BSE (fig. 5.14a). These observations imply that the parental melts of Neoarchean granitoids, and possibly also of Paleozoic granitoids, were slightly enriched in ^{238}U relative to the BSE. In this section I explore possible explanations for this apparent small difference in U isotope compositions.

There is growing evidence for mineral-melt U isotope fractionation at high temperatures (Hiess et al., 2012; Livermore et al., 2018; Tissot et al., 2019, 2017), and in section 5.4.2, I demonstrated that this process generated δ^{238}U variations in Archean granitoids. It is therefore possible that high temperature mineral-melt U isotope fractionation may be responsible for the heavy δ^{238}U of Neoarchean granitoids. The petrogenesis of both TTGs and sanukitoids is thought to involve metabasite partial melting (e.g. Martin et al., 2009; Moyen and Martin, 2012), hence U isotope fractionation may have occurred during this process. Garnet may be the main residual host of U during metabasite partial melting as U is slightly more compatible in garnet than in other major metabasite-forming minerals (clinopyroxene, amphibole) (e.g. Blundy and Wood, 2003; Elkins et al., 2008). However, as was discussed in section 5.4.3.1, the primitive sanukitoid samples from the BFG show no clear covariation of δ^{238}U with tracers of garnet fractionation (($La/Yb)_N$ and λ_1) despite some degree of correlation of Th/U with these tracers (fig. 5.10). It consequently appears that residual garnet does not cause significant U isotope fractionation. U is only marginally more incompatible in clinopyroxene than in garnet. Tissot et al. (2017) proposed that accumulation of isotopically light pyroxenes can explain why plutonic angrites have lower δ^{238}U than volcanic angrites. Retention of ^{235}U in residual clinopyroxene during metabasite partial melting might hence be able to generate melts with slightly higher δ^{238}U than their protolith.

Alternatively, the granitoids' parental melts might have already crystallised out minerals with low δ^{238}U deeper in the crust, forming isotopically light cumulates in the lower crust. As mentioned above, pyroxenes may have lower δ^{238}U than the melt they crystallised from (Tissot et al., 2017). However, pyroxenes are rare in TTGs and unlikely to crystallise in notable quantities from an already felsic parental magma. Small amounts of ortho- and clinopyroxene can be found in clots of mafic minerals in sanukitoids (e.g. Laurent et al., 2014a; Martin et al., 2009). Therefore, there is a possibility that early pyroxene crystallisation could increase the δ^{238}U of sanukitoids, although most studies favour amphibole and plagioclase as the main phases crystallising from sanukitoid magmas (e.g. de Oliveira et al., 2010; Lobach-Zhuchenko et al., 2005; Seixas et al., 2013; Smithies et al., 2019). Further to this, because TTGs also display elevated δ^{238}U and U is very incompatible in pyroxenes ($D_U^{px/melt}$ < 0.02,

Blundy and Wood, 2003), I consider it unlikely that early pyroxene fractional crystallisation can explain the uniformly high δ^{238}U of Neoarchean granitoids.

Hornblende and plagioclase are generally thought to be the main phases crystallising from TTG and sanukitoid magmas (e.g. Laurent et al., 2020, 2013; Moyen and Martin, 2012; Smithies et al., 2019). U partitioning in plagioclase is poorly constrained but it is likely highly incompatible ($D_U^{plag/melt}$ < 0.001; Blundy and Wood, 2003; Sun et al., 2017) and hence plagioclase fractionation is unlikely to affect U isotopes. U may be slightly more compatible in hornblende than in pyroxenes (Nandedkar et al., 2016), but whether it fractionates U isotopes is completely unknown. However, hornblende is proposed to be an early crystallising phase in the BFG sanukitoids (Smithies et al., 2019, 2018) and no variation of δ^{238}U with SiO_2 is seen for the BFG (fig. 5.12a), implying that hornblende fractional crystallisation does not significantly affect U isotopes. While the aforementioned silicate phases dominate the crystallising mineral assemblage, U is highly incompatible in them, so U-bearing accessory phases such as apatite, zircon and titanite are likely far more important controls on the U budget during differentiation. Mineral separate measurements suggest these phases all preferentially incorporate ^{238}U over ^{235}U (Hiess et al., 2012; Livermore et al., 2018; Tissot et al., 2019), so early fractional crystallisation of U-bearing accessory phases would likely generate the opposite U isotope fractionation. Overall, it appears that deep, early fractional crystallisation of ^{235}U-enriched minerals cannot readily explain the high δ^{238}U of Neoarchean granitoids, although further work constraining mineral-melt U isotope fractionation, particularly for silicate minerals, would help strengthen this conclusion.

Another conceivable explanation is that the δ^{238}U of the Earth's mantle was modified early in the Earth's history. Possible mechanisms for changing mantle δ^{238}U were discussed in the previous section in relation to increasing granitoid δ^{238}U across the Archean. While the difference in δ^{238}U between Neoarchean granitoids and the BSE (~0.04‰) is smaller than between Neoarchean and Eoarchean granitoids (~0.1‰), the previous discussion concluded that none of the proposed mechanisms appear to be feasible for modifying the U isotope composition of the mantle in the Archean. It is

hence unlikely that a change in mantle δ^{238}U is responsible for the elevated δ^{238}U of Neoarchean granitoids relative to the BSE.

Finally, the apparent difference in U isotope composition between Neoarchean granitoids and the BSE may not be significant and may be a consequence of the average δ^{238}U of one or both reservoirs being poorly constrained. Due to many samples being affected by either weathering or apatite fractional crystallisation, the average δ^{238}U of Neoarchean granitoids is constrained by only seven samples from two locations (the Yilgarn and Amazonian cratons), all of similar age (~2.7 Ga). Meanwhile, the BSE value is based on high precision measurements of just two large, unaltered meteorite samples (Andersen et al., 2015). The difference between Neoarchean granitoids (-0.27 ± 0.02‰) and the BSE (-0.306 ± 0.026‰) is minimal and their 2se uncertainty windows do overlap by 0.01‰. It can therefore be argued that Neoarchean granitoids and the BSE do not have distinct U isotope compositions, and that measurement of additional samples for either reservoir could easily change their average δ^{238}U values to be even more similar.

Overall, further sample measurements are needed to better constrain the U isotope compositions of both the BSE and Neoarchean granitoids before a clear conclusion can be drawn on whether they have distinct δ^{238}U or not. Efforts to constrain the bulk Earth/BSE composition should focus on high-precision measurements of large meteorite samples, using geochemical parameters such as Th/U and δ^{234}U to check for modification by terrestrial weathering. Future studies of U isotopes in Archean granitoids would benefit from careful sample selection to avoid samples affected by apatite fractional crystallisation, while measuring δ^{234}U alongside δ^{238}U is essential to thoroughly assess the effects of alteration on bulk rock U isotope compositions. If, however, the slightly elevated δ^{238}U of Neoarchean granitoids relative to the BSE is a genuine signature, I consider retention of ^{235}U in residual clinopyroxene during metabasite partial melting to be the most likely explanation.

5.5. Conclusions

In this chapter I present the U isotope compositions of Archean and Paleoproterozoic sanukitoids and Paleozoic sanukitoid analogues, aiming to investigate whether the $\delta^{238}U$ of AOC recycled into the mantle changed in response to increasing atmospheric and oceanic oxygenation across the GOE and NOE. These data are supplemented by analyses of TTGs to better constrain the U isotope composition of the dominant constituent of Archean continental crust. These data instead provide the first evidence of high-temperature mineral-melt U isotope fractionation influencing the $\delta^{238}U$ of bulk terrestrial igneous rocks. TTGs and Archean-Paleoproterozoic sanukitoids show a decrease in $\delta^{238}U$ during magmatic differentiation which appears to be caused by apatite fractional crystallisation. Similar processes may also contribute to observed $\delta^{238}U$ variability in Phanerozoic granitoids. Future work should focus on determining mineral-melt U isotope fractionation factors and measuring the $\delta^{238}U$ of cogenetic differentiation suites to improve our understanding of high-temperature U isotope fractionation.

As the U isotope compositions of a significant proportion of the TTG and sanukitoid samples analysed here have been affected by apatite fractional crystallisation, the data suitable for investigating the original aim of this chapter are rather limited. Sanukitoids not affected by fractional crystallisation display distinctly higher $\delta^{238}U$ and Th/U than most modern arc magmas, showing no evidence of addition of U^{6+} to their mantle sources by oxidised aqueous fluids. Instead, they appear to be more consistent with addition of a melt component to their mantle source, involving no significant U isotope fractionation while slightly increasing Th/U. These findings imply that Archean sanukitoids were oxidised by different mechanisms to modern arc magmas, with oxidation of the sanukitoid mantle source by reaction with H^+ from aqueous fluids/hydrous melts or with an eclogite partial melt that was itself oxidised by Fe^{2+} retention in residual garnet being possible methods. Data for sanukitoids and their analogues are too limited to confidently discern any secular evolution in their U isotope compositions, but they may hint at $\delta^{238}U$ expanding to higher values after the GOE due to the onset of recycling sediments with variable $\delta^{238}U$ into the mantle.

Neoarchean granitoids not affected by fractional crystallisation have indistinguishable $\delta^{238}U$ to Phanerozoic granitoids, although the available data are again quite limited and it is difficult to thoroughly assess the impact of weathering, alteration and fractional crystallisation on literature granitoid U isotope compositions. The Neoarchean granitoids appear to have slightly heavier $\delta^{238}U$ (-0.27 ± 0.02‰) than the BSE (-0.306 ± 0.026‰; Andersen et al., 2015), but improving constraints on the U isotope compositions of both reservoirs is essential to determine if this is a significant difference. Two Eoarchean granitoids have $\delta^{238}U$ of ~-0.38‰, considerably lighter than both the BSE and Neoarchean granitoids. Additional analyses of Archean granitoid U isotope compositions are needed to discern the cause of this difference.

6. Synthesis and outlook

Sanukitoid magmatism is a distinctive feature of the late Archean-early Proterozoic transition (~3.0 – 2.0 Ga) that marks a major shift in continental crust composition, and sanukitoid generation may be linked to a geodynamic change at this time. The work presented in this thesis uses the novel stable isotope compositions of sanukitoids, specifically their titanium (Chapters 3 and 4) and uranium (Chapter 5) isotope compositions, to provide new constraints on the formation of sanukitoid parental magmas, their magmatic differentiation and petrogenetic link to high-Sr "high pressure" (HP) TTGs, and the origin of their oxidised nature. These results further our understanding of petrogenetic and geodynamic processes across the late Archean-early Proterozoic transition.

While it is well-established that sanukitoid parental magmas formed by interaction between mantle peridotite and a component derived from recycled crustal materials (e.g. Martin et al., 2009; Shirey and Hanson, 1984), the nature (i.e. fluid vs melt) and exact source of this crust-derived component are debated. The Ti stable isotope compositions of primitive (pre-Fe-Ti oxide saturation) sanukitoids presented in Chapter 3 are significantly heavier than the mantle and modern arc basalts. This elevated δ^{49}Ti signature cannot be explained by an aqueous fluid component alone and instead requires a metabasite melt component. Modelling conducted to investigate Ti isotope fractionation during metabasite melting leads me to favour a link to fluid-fluxed eclogite partial melting. This result demonstrates that both metabasite melts and aqueous fluids were important for sanukitoid formation, and may help explain why conflicting petrogenetic interpretations of sanukitoid geochemical compositions exist. However, there is still significant geochemical heterogeneity among sanukitoids, some of which may be related to the involvement of additional incompatible element-enriched components in their formation. In particular, recycled sediments are proposed to be present in the mantle source of some sanukitoid intrusions (e.g. Halla, 2005; Laurent et al., 2011; Sun et al., 2020), and it is possible that the importance of this sediment component in sanukitoids changed across the late Archean-early Proterozoic

transition as emergence of the continents above sea level led to subaerial weathering (e.g. Chowdhury et al., 2025; Reimink and Smye, 2024) and increasing atmospheric oxygenation allowed widespread oxidative weathering to occur (e.g. Brüske et al., 2020; Gaschnig et al., 2014). Ti stable isotopes can be fractionated during metasediment partial melting, generating melts enriched in heavy Ti isotopes similar to metabasite partial melting (Klaver et al., 2024). However, sediments mostly have lower TiO_2 concentrations than metabasites, resulting in lower melt TiO_2 contents as well as generally lower $\delta^{49}Ti$ due to the lower abundance of residual Fe-Ti oxides. Ti isotopes are therefore not particularly sensitive tracers of sediment melts and they cannot effectively discriminate between the relative contributions of metabasite and metasediment melts to sanukitoid formation. The possible increase in average sanukitoid $\delta^{238}U$ after the GOE may hint at the onset of recycling sediments with variable $\delta^{238}U$ due to oxidative weathering at this time, but this conclusion is not robust as it is based on very limited data. Furthermore, tracing a recycled sediment component with U isotopes is complicated by the fact that sediments have highly variable $\delta^{238}U$ (Li and Tissot, 2023) Other geochemical parameters, such as zircon $\delta^{18}O$ (e.g. Moreira et al., 2023; Wang et al., 2024), are more sensitive tracers of recycled sediments and are hence better suited to investigating the involvement of a sediment component in sanukitoid formation across the late Archean-early Proterozoic transition. Novel stable isotope systems where metabasite-derived and metasediment-derived components are expected to have distinct isotopic compositions – for example barium stable isotopes (e.g. Nielsen et al., 2020; Shu et al., 2025) – might also be useful for such an investigation.

While there is indeed significant geochemical heterogeneity among Archean-Paleoproterozoic sanukitoids, this variability may in part be due to the gradually broadening definition of "sanukitoid" (e.g. Laurent et al., 2014a; Martin et al., 2009) and its application to a more diverse range of rocks than those originally described by Shirey and Hanson (1984) and Stern et al. (1989) (e.g. Moyen, 2020; Steenfelt et al., 2005). Grouping all these rocks with diverse geochemical compositions and potentially diverse origins under a single name – one that is implicitly linked to derivation of the rock from an incompatible element-enriched mantle source (e.g. Laurent et al., 2014a) – may be obscuring details of their petrogenesis and hence of geodynamic processes during the late Archean-early Proterozoic transition. For example, figure 1.10 shows

that many rocks that have been described as "sanukitoids" in the literature have considerably lower Mg# and Ni and Cr concentrations than literature geochemical definitions of sanukitoid (Heilimo et al., 2010; Lowrey et al., 2023; Stern et al., 1989), which may imply that their formation did not involve as significant a mantle component. A thorough review of the heterogeneous Archean-Paleoproterozoic rocks labelled "sanukitoid" in the literature is needed to unscramble the origin of their variability and discern what information these rocks can provide about petrogenetic and geodynamic processes during the late Archean-early Proterozoic transition. Future work to refine and clarify the geochemical definition of "sanukitoid" may help ensure the terminology is consistently applied in future publications.

The δ^{49}Ti of sanukitoids increases as they differentiate due to fractional crystallisation of isotopically light Fe-Ti oxides and hornblende. In Chapter 3 I show that their δ^{49}Ti starts to increase at high Mg# of ~60 – 70, indicating that there was early oxide saturation in sanukitoid magmas and hence that sanukitoid parental magmas had H_2O contents and fO_2 at least as high as modern arc magmas. My results add to existing evidence from mineral chemistry (de Oliveira et al., 2010; do Nascimento et al., 2023, 2021) and S speciation in apatite (Meng et al., 2022; Moreira et al., 2023) that supports Archean and Paleoproterozoic sanukitoid magmas being similarly oxidised to Phanerozoic arc magmas. Modern subduction processes are generally thought to create oxidised magmas via transfer of oxidised recycled materials (slab-derived aqueous fluids, sediment melts) to the mantle sources of arc magmas (e.g. Ague et al., 2022; Evans and Tomkins, 2021; Kelley and Cottrell, 2009). This process is reflected in the low δ^{238}U and Th/U of modern arc magmas which record U^{6+} addition by oxidised fluids (Andersen et al., 2015; Freymuth et al., 2019). The data presented in Chapter 5, however, show that Archean sanukitoids have δ^{238}U and Th/U values similar to slightly higher than the BSE, hence there is no evidence for addition of oxidised U^{6+}-bearing surface materials to their mantle sources. The absence of oxidised surface materials being recycled into their mantle source implies that sanukitoid magmas were oxidised by a different mechanism to modern arc magmas. Using constraints on the conditions of sanukitoid parental magma formation provided by the Ti isotope data, I propose two possible mechanisms for generating oxidised sanukitoid magmas in the Archean. First, as I favour an eclogite protolith for the metabasite melt component, this metabasite melt may have been oxidised by retention

of Fe^{2+} over Fe^{3+} in abundant residual garnet (Tang et al., 2024). Second, as I favour formation of the metabasite melt component by fluid-fluxed eclogite melting, this metabasite melt was likely hydrous and its flux into the mantle may have been accompanied by a significant aqueous fluid flux. Reaction of H^+ from the aqueous fluid/hydrous melt might have then oxidised the sanukitoid mantle source (Brandon and Draper, 1996; Iacovino et al., 2020; Tollan and Hermann, 2019). Further investigation into possible mechanisms for generating oxidised magmas, including sanukitoids, in the Archean is needed and could include improving constraints on the magnitude of fO_2 changes that can be imparted by the mechanisms described above. Such research would provide insights into how the dominant processes for generating oxidised magmas have changed over the Earth's history.

Sanukitoids show close spatial and temporal associations with gold mineralisation in multiple Archean cratons, for example in the Yilgarn Craton (Witt et al., 2013) and the Superior Province (Fayol and Jébrak, 2017). There is debate about whether this relationship is just coincidental, with the distributions of both features relying on a common structural control (e.g. Smithies et al., 2018), or whether there is a direct genetic link between sanukitoid magmatism and gold mineralisation (e.g. Fayol and Jébrak, 2017). The results presented in this thesis may contribute to improving our understanding of the link between sanukitoids and gold mineralisation. If a genetic relationship does exist between the two, it would likely be via the exsolution of large volumes of volatile-rich, oxidised magmatic aqueous fluids from sanukitoid magmas as they underwent fractional crystallisation (e.g. Fayol and Jébrak, 2017; Smithies et al., 2018). The oxidised nature of the magma is important for generating such oxidised magmatic-hydrothermal fluids and may also have contributed to high gold solubility, and hence gold transport, in the magma itself (e.g. Cameron and Hattori, 1987; Fayol and Jébrak, 2017). As described above, the Ti and U isotope data demonstrate that sanukitoid parental magmas were oxidised and water-rich, and they also help to constrain the possible origins of this oxidation and water. These results might provide insights into the source of gold in sanukitoid-associated gold deposits, and help add to models of Archean sanukitoid intrusion-related gold deposit formation.

Sanukitoids follow a differentiation pathway very similar to the modern calc-alkaline series (e.g. de Oliveira et al., 2010; Martin et al., 2009). In Chapter 3 I demonstrate

that sanukitoid suites show a more muted δ^{49}Ti increase during differentiation than currently analysed modern calc-alkaline suites. I propose that this is caused by fractional crystallisation of abundant hornblende alongside Fe-Ti oxides from H_2O-rich sanukitoid magmas, as amphibole fractionates Ti isotopes less than Fe-Ti oxides (Greber et al., 2021; Mandl, 2019). This result demonstrates that hydrous silicate minerals such as amphibole can play a significant role in controlling magma δ^{49}Ti evolution during differentiation. In addition, amphibole and phlogopite are important Ti-bearing residual phases during partial melting of various lithologies (e.g. metabasites, metasomatised mantle). However, constraints on the magnitude of amphibole-melt and phlogopite-melt Ti isotope fractionation factors, which I use in the experimental melt modelling presented in Chapter 3 and Appendices E and F, are limited and primarily come from single mineral separates from the Kneeling Nun Tuff analysed by Mandl (2019). This contrasts with the detailed *ab initio* density functional theory (DFT) calculations (Aarons et al., 2021; Leitzke et al., 2018; W. Wang et al., 2020) and empirical studies (Hoare et al., 2022) used to determine mineral-melt Ti isotope fractionation factors for Fe-Ti oxides and non-hydrous silicate minerals. Further work is therefore needed to better constrain mineral-melt Ti isotope fractionation factors for Ti-bearing hydrous silicates such as amphibole and phlogopite. This work will make more accurate fractionation factors available for use in models of Ti isotope fractionation during various processes, including partial melting of metamorphic rocks (e.g. amphibolites, gneisses) and metasomatised mantle lithologies (e.g. the MARID (mica-amphibole-rutile-ilmenite-diopside) and PIC (phlogopite-ilmenite-clinopyroxene) suites), and fractional crystallisation of hydrous magmas.

Recent studies by Smithies et al. (2019) and Liou and Guo (2019) suggest that a subset of "high pressure" TTGs with very high Sr concentrations and Sr/Y formed by hornblende-dominated fractional crystallisation of metasomatised mantle-derived sanukitoid magmas, instead of by the predominantly favoured model of high pressure (≥ 2 GPa) metabasite partial melting (e.g. Moyen, 2011). In Chapter 3 I present the Ti stable isotope compositions of the Black Flag Group (BFG) sanukitoids, which Smithies et al. (2019) propose constitute the liquid line of descent linking high-Sr HP TTGs to mantle-derived magmas in the Eastern Goldfields Superterrane, Yilgarn Craton. These data constrain the δ^{49}Ti evolution of the BFG during magma differentiation, and I model the differentiation trends of the different geochemical

subgroups of the BFG using Rayleigh fractionation. In Chapter 4 I show that the Ti isotope compositions of high-Sr HP TTGs from the Eastern Goldfields Superterrane plot at the evolved end of the BFG sanukitoid differentiation trend and Rayleigh fractionation models, demonstrating that they formed by hornblende-dominated fractional crystallisation of low La/Th BFG magmas and ultimately had a hydrous eclogite melt-metasomatised mantle source. In contrast, the δ^{49}Ti values of other TTGs from the Eastern Goldfields Superterrane, which have different trace element compositions to the high-Sr HP TTGs, can be explained by the traditional petrogenetic model for TTGs where hydrous metabasite undergoes partial melting in the garnet stability field. While TTG formation via fractional crystallisation of hydrous mafic magma has been proposed multiple times over the past few decades (e.g. Arth et al., 1978; Kamber et al., 2002; Kleinhanns et al., 2003; Smith et al., 1983), this petrogenetic model has generally been dismissed in favour of a metabasite melting origin (e.g. Moyen and Martin, 2012). My results provide strong support for the derivation of some Archean TTGs from mantle-sourced sanukitoid magmas. They also record the contemporaneous, diverse petrogenesis of Neoarchean TTGs in the Yilgarn Craton, demonstrating that TTG-forming processes were likely more varied than previously appreciated.

From published geochemical data of global TTGs, I identify high-Sr HP TTGs on many Archean cratons. The temporal distribution of global high-Sr HP TTGs largely mirrors that of sanukitoids as they become more abundant and widespread in the late Archean, after ~3 Ga. Furthermore, within individual cratons many high-Sr HP TTGs are spatially and temporally associated with sanukitoid magmatism. These findings imply that formation of high-Sr HP TTGs by fractional crystallisation of metasomatised mantle-derived sanukitoid magmas was a global phenomenon, and that mechanisms for forming TTG magmas may have globally diversified in the late Archean. As high-Sr HP TTGs were derived from metasomatised mantle sources rather than exclusively from recycled metabasite, they represent net addition of material to the continental crust. Crustal growth models may therefore have previously underestimated juvenile input in the late Archean, although high-Sr HP TTGs appear to constitute a relatively minor proportion of TTG magmatism. Future work may want to further constrain the magnitude of the contribution from high-Sr HP TTGs to TTG magmatism and crustal growth in the late Archean.

The results presented in this thesis place new constraints on geodynamic processes during the late Archean-early Proterozoic transition. The emergence of metasomatised mantle-sourced high-Sr HP TTGs alongside sanukitoids in the late Archean was likely the result of a geodynamic transition at this time that promoted interaction between metabasite melts and mantle peridotite. Generation of the metabasite melt component involved in sanukitoid petrogenesis by fluid-fluxed eclogite melting is most consistent with formation of the sanukitoid mantle source by a subduction-like process, and shows that deep burial of hydrated near-surface material along relatively low geothermal gradients occurred at least as far back as ~2.7 Ga. This process may have been either some form of subduction or sinking crustal drips that brought hydrated near-surface material to mantle depths. On the other hand, formation of the sanukitoid mantle source via delamination of lower crustal eclogite or crustal drips involving only anhydrous lower crust is not compatible with my results.

Shifting the focus away from sanukitoid petrogenesis, the data presented in Chapter 5 have significant implications for our understanding of uranium isotope systematics. TTGs and Archean-Paleoproterozoic sanukitoids show a decrease in $\delta^{238}U$ during magmatic differentiation which appears to be caused by apatite fractional crystallisation. This work provides the first demonstration of high-temperature mineral-melt U isotope fractionation influencing the $\delta^{238}U$ of bulk igneous rocks, and adds to growing evidence of high-temperature U isotope fractionation (Hiess et al., 2012; Livermore et al., 2018; Tissot et al., 2019, 2017). However, our understanding of this process is currently hindered by the incredibly limited constraints on mineral-melt U isotope fractionation factors, hence future work investigating high-temperature U isotope fractionation is imperative. The best way to determine mineral-melt U isotope fractionation factors would be direct measurements of coexisting glass and mineral phases, with a focus on U-bearing accessory minerals (e.g. apatite, zircon, titanite, allanite) that are the main hosts of U in igneous rocks. Measuring the $\delta^{238}U$ of the bulk rock sample that any mineral separates are taken from would also provide valuable insights into the direction and magnitude of high-temperature U isotope fractionation, as previous studies of U isotope compositions in mineral separates did not make such analyses (Hiess et al., 2012; Livermore et al., 2018; Tissot et al., 2019). In addition, targeted analysis of cogenetic differentiation suites, as opposed to disparate igneous

samples, would improve our understanding of $\delta^{238}U$ evolution during magma differentiation.

Although my data are limited, they hint at possible secular variation of granitoid, and potentially mantle, U isotope compositions over the Archean. Eoarchean granitoids have considerably lighter $\delta^{238}U$ (~-0.38‰; Noordmann et al., 2016) than Neoarchean granitoids (average $\delta^{238}U$ = -0.27 ± 0.02‰) and the BSE (-0.306 ± 0.026‰; Andersen et al., 2015). However, as Eoarchean granitoid data are limited to just two samples and there does not appear to be an obviously viable mechanism for changing the $\delta^{238}U$ of the mantle and mantle-derived igneous rocks at this time, further work is needed to determine whether there was a genuine increase in the $\delta^{238}U$ of granitoids in the Archean or whether the low $\delta^{238}U$ of the Eoarchean granitoids were produced by magmatic differentiation. Future work should involve measuring the U isotope compositions of additional Eoarchean granitoid samples, as well as of Paleo-Mesoarchean granitoids, and should measure $\delta^{234}U$ alongside $\delta^{238}U$ to help assess the extent of recent U mobility due to weathering and alteration. These results also suggest that Neoarchean granitoids may have slightly heavier average $\delta^{238}U$ than the BSE. However, the U isotope compositions of both Neoarchean granitoids and the BSE are constrained by relatively few samples. Future work to better constrain the $\delta^{238}U$ of the BSE and bulk Earth is necessary, and efforts should focus on high precision measurements of large meteorite samples, using parameters such as Th/U and $\delta^{234}U$ to check for modification of their U isotope compositions by terrestrial weathering.

Finally, my data suggest that the U isotope compositions of oxidised, largely subduction-related, magmas have changed over the Earth's history. While modern arc magmas mostly have low Th/U and low $\delta^{238}U$ down to ~-0.5‰ due to addition of oxidised, slab-derived aqueous fluids to their mantle source (Andersen et al., 2015; Freymuth et al., 2019), Archean sanukitoids have significantly higher $\delta^{238}U$ of -0.33‰ to -0.23‰, similar to the BSE composition. Additionally, some oxidised igneous rocks – the Rogart high Ba-Sr granite suite pluton and Paleoproterozoic Alto Maranhão suite sanukitoid (Chapter 5), Mount Vesuvius (Avanzinelli et al., 2018) – have higher $\delta^{238}U$ than the BSE due to a recycled sediment component. Liu et al. (2019) observed secular changes in the Th/U of arc magmas over the last 3 Gyr, and found a significant

decrease in their average Th/U during the NOE at ~0.65 Ga. Future work could investigate whether this shift in Th/U was accompanied by a change in the δ^{238}U of oxidised arc magmas to help constrain exactly how U cycling processes in subduction zones changed across the NOE. It could also explore when in the Earth's history the low δ^{238}U and Th/U signature, and hence significant transfer of U^{6+} in oxidised, slab-derived aqueous fluids, is first recorded in oxidised magmas, helping us understand how subduction zone processes and mechanisms of magma oxidation have changed though time.

Bibliography

Aarons, S.M., Dauphas, N., Blanchard, M., Zeng, H., Nie, N.X., Johnson, A.C., Greber, N.D., Hopp, T., 2021. Clues from Ab Initio Calculations on Titanium Isotopic Fractionation in Tholeiitic and Calc-Alkaline Magma Series. ACS Earth Space Chem. 5, 2466–2480. https://doi.org/10.1021/acsearthspacechem.1c00172

Aarons, S.M., Dauphas, N., Greber, N.D., Roskosz, M., Bouchez, J., Carley, T., Liu, X.-M., Rudnick, R.L., Gaillardet, J., 2023. Titanium transport and isotopic fractionation in the Critical Zone. Geochimica et Cosmochimica Acta 352, 175–193. https://doi.org/10.1016/j.gca.2023.05.008

Aarons, S.M., Reimink, J.R., Greber, N.D., Heard, A.W., Zhang, Z., Dauphas, N., 2020. Titanium isotopes constrain a magmatic transition at the Hadean-Archean boundary in the Acasta Gneiss Complex. Science Advances 6, eabc9959. https://doi.org/10.1126/sciadv.abc9959

Ackerman, L., Žák, J., Kachlík, V., Svojtka, M., Tomek, F., Santolík, V., Sláma, J., Trubač, J., Strnad, L., Vacek, F., 2022. The diversity of sources of late Archean granites reflects a transition from plume-dominated to plate tectonics in the Superior Province, Canada. Precambrian Research 370, 106525. https://doi.org/10.1016/j.precamres.2021.106525

Ague, J.J., Tassara, S., Holycross, M.E., Li, J.-L., Cottrell, E., Schwarzenbach, E.M., Fassoulas, C., John, T., 2022. Slab-derived devolatilization fluids oxidized by subducted metasedimentary rocks. Nat. Geosci. 15, 320–326. https://doi.org/10.1038/s41561-022-00904-7

Ahmad, I., Mondal, M.E.A., Bhutani, R., Satyanarayanan, M., 2018. Geochemical evolution of the Mangalwar Complex, Aravalli Craton, NW India: Insights from elemental and Nd-isotope geochemistry of the basement gneisses. Geoscience Frontiers, Greenstone belts and their mineral endowment 9, 931–942. https://doi.org/10.1016/j.gsf.2017.07.003

Ahmad, Q., Wille, M., Labidi, J., König, S., Devey, C., Mezger, K., 2023. Heavy Mo isotope enrichment in the Pitcairn plume: Implications for the subduction cycle

of anoxic sediments. Earth and Planetary Science Letters 624, 118466. https://doi.org/10.1016/j.epsl.2023.118466

Ahmad, Q., Wille, M., Rosca, C., Labidi, J., Schmid, T., Mezger, K., König, S., 2022. Molybdenum isotopes in plume-influenced MORBs reveal recycling of ancient anoxic sediments. Geochem. Persp. Let. 23, 43–48. https://doi.org/10.7185/geochemlet.2236

Aidoo, F., Sun, F.-Y., Liang, T., Nude, P.M., 2020. New insight into the Dahomeyide Belt of southeastern Ghana, West Africa: Evidence of arc-continental collision and Neoarchaean crustal reworking. Precambrian Research 347, 105836. https://doi.org/10.1016/j.precamres.2020.105836

Aigner-Torres, M., Blundy, J., Ulmer, P., Pettke, T., 2007. Laser Ablation ICPMS study of trace element partitioning between plagioclase and basaltic melts: an experimental approach. Contrib Mineral Petrol 153, 647–667. https://doi.org/10.1007/s00410-006-0168-2

Akame, J.M., Oliveira, E.P., Debaille, V., Poujol, M., Schulz, B., Bisso, D., Humbert, F., Koah Na Lebogo, S.P., Zo'o Zame, P., 2024. Mesoarchean synchronous emplacement of TTG gneisses and potassic granitoids in the Nyabessane granite-greenstone terranes, NW Congo Craton (southern Cameroon): Zircon UPb geochronology, petrogenesis and tectonic implications. Lithos 464–465, 107429. https://doi.org/10.1016/j.lithos.2023.107429

Albarède, F., Beard, B., 2004. Analytical Methods for Non-Traditional Isotopes. Reviews in Mineralogy and Geochemistry 55, 113–152. https://doi.org/10.2138/gsrmg.55.1.113

Almeida, J. de A.C., Dall'Agnol, R., Dias, S.B., Althoff, F.J., 2010. Origin of the Archean leucogranodiorite–granite suites: Evidence from the Rio Maria terrane and implications for granite magmatism in the Archean. Lithos 120, 235–257. https://doi.org/10.1016/j.lithos.2010.07.026

Alt, J.C., Schwarzenbach, E.M., Früh-Green, G.L., Shanks, W.C., Bernasconi, S.M., Garrido, C.J., Crispini, L., Gaggero, L., Padrón-Navarta, J.A., Marchesi, C., 2013. The role of serpentinites in cycling of carbon and sulfur: Seafloor serpentinization and subduction metamorphism. Lithos, Serpentinites from mid-oceanic ridges to subduction 178, 40–54. https://doi.org/10.1016/j.lithos.2012.12.006

Anbar, A.D., Duan, Y., Lyons, T.W., Arnold, G.L., Kendall, B., Creaser, R.A., Kaufman, A.J., Gordon, G.W., Scott, C., Garvin, J., Buick, R., 2007. A Whiff of Oxygen Before the Great Oxidation Event? Science 317, 1903–1906. https://doi.org/10.1126/science.1140325

Andersen, M.B., Elliott, T., Freymuth, H., Sims, K.W.W., Niu, Y., Kelley, K.A., 2015. The terrestrial uranium isotope cycle. Nature 517, 356–359. https://doi.org/10.1038/nature14062

Andersen, M.B., Matthews, A., Bar-Matthews, M., Vance, D., 2020. Rapid onset of ocean anoxia shown by high U and low Mo isotope compositions of sapropel S1. Geochem. Persp. Let. 15, 10–14. https://doi.org/10.7185/geochemlet.2027

Andersen, M.B., Matthews, A., Vance, D., Bar-Matthews, M., Archer, C., de Souza, G.F., 2018. A 10-fold decline in the deep Eastern Mediterranean thermohaline overturning circulation during the last interglacial period. Earth and Planetary Science Letters 503, 58–67. https://doi.org/10.1016/j.epsl.2018.09.013

Andersen, M.B., Rodney, J.B., Freymuth, H., Vils, F., Harris, M., Cooper, K., Teagle, D.A.H., Elliott, T., 2024. Time scales and mechanisms of uranium uptake in altered ocean crust; observations from the ~15 million year-old site 1256 in the eastern equatorial Pacific. Geochimica et Cosmochimica Acta 382, 142–159. https://doi.org/10.1016/j.gca.2024.07.028

Andersen, M.B., Romaniello, S., Vance, D., Little, S.H., Herdman, R., Lyons, T.W., 2014. A modern framework for the interpretation of 238U/235U in studies of ancient ocean redox. Earth and Planetary Science Letters 400, 184–194. https://doi.org/10.1016/j.epsl.2014.05.051

Andersen, M.B., Stirling, C.H., Potter, E.-K., Halliday, A.N., 2004. Toward epsilon levels of measurement precision on 234U/238U by using MC-ICPMS. International Journal of Mass Spectrometry 237, 107–118. https://doi.org/10.1016/j.ijms.2004.07.004

Andersen, M.B., Stirling, C.H., Weyer, S., 2017. Uranium Isotope Fractionation. Reviews in Mineralogy and Geochemistry 82, 799–850. https://doi.org/10.2138/rmg.2017.82.19

Andersen, M.B., Vance, D., Morford, J.L., Bura-Nakić, E., Breitenbach, S.F.M., Och, L., 2016. Closing in on the marine 238U/235U budget. Chemical Geology 420, 11–22. https://doi.org/10.1016/j.chemgeo.2015.10.041

André, L., Abraham, K., Hofmann, A., Monin, L., Kleinhanns, I.C., Foley, S., 2019. Early continental crust generated by reworking of basalts variably silicified by seawater. Nat. Geosci. 12, 769–773. https://doi.org/10.1038/s41561-019-0408-5

André, L., Monin, L., Hofmann, A., 2022. The origin of early continental crust: New clues from coupling Ge/Si ratios with silicon isotopes. Earth and Planetary Science Letters 582, 117415. https://doi.org/10.1016/j.epsl.2022.117415

Angeletti, M., Chichorro, M., Castro, A., Frisicale, M.C., Solá, R., Dimieri, L.V., 2021. New geochemical, U–Pb SIMS geochronology and Lu–Hf isotopic data in zircon from Tandilia basement rocks, Río de la Plata craton, Argentina: Evidence of a sanukitoid precursor for some Paleoproterozoic granitoids. Journal of South American Earth Sciences 108, 103199. https://doi.org/10.1016/j.jsames.2021.103199

Anguelova, M., Vilela, N., Kommescher, S., Greber, N.D., Fehr, M.A., Schönbächler, M., 2024. Constraining the mass-dependent Ti isotope composition of the chondritic reservoir – An inter-laboratory comparison study. Geochimica et Cosmochimica Acta 372, 171-180. https://doi.org/10.1016/j.gca.2024.01.026

Antonelli, M.A., Kendrick, J., Yakymchuk, C., Guitreau, M., Mittal, T., Moynier, F., 2021. Calcium isotope evidence for early Archaean carbonates and subduction of oceanic crust. Nat Commun 12, 2534. https://doi.org/10.1038/s41467-021-22748-2

Arndt, N., 2023. How did the continental crust form: No basalt, no water, no granite. Precambrian Research 397, 107196. https://doi.org/10.1016/j.precamres.2023.107196

Arth, J.G., Barker, F., Peterman, Z.E., Friedman, I., 1978. Geochemistry of the Gabbro—Diorite—Tonalite—Trondhjemite Suite of southwest Finland and its Implications for the Origin of Tonalitic and Trondhjemitic Magmas. Journal of Petrology 19, 289–316. https://doi.org/10.1093/petrology/19.2.289

Arth, J.G., Hanson, G.N., 1975. Geochemistry and origin of the early Precambrian crust of northeastern Minnesota. Geochimica et Cosmochimica Acta 39, 325–362. https://doi.org/10.1016/0016-7037(75)90200-8

Arth, J.G., Hanson, G.N., 1972. Quartz diorites derived by partial melting of eclogite or amphibolite at mantle depths. Contr. Mineral. and Petrol. 37, 161–174. https://doi.org/10.1007/BF00371074

Asael, D., Tissot, F.L.H., Reinhard, C.T., Rouxel, O., Dauphas, N., Lyons, T.W., Ponzevera, E., Liorzou, C., Chéron, S., 2013. Coupled molybdenum, iron and uranium stable isotopes as oceanic paleoredox proxies during the Paleoproterozoic Shunga Event. Chemical Geology, Special Issue dedicated to H.D. Holland: Evolution of the atmosphere and ocean through time 362, 193–210. https://doi.org/10.1016/j.chemgeo.2013.08.003

Askkour, F., Ikenne, M., Chelle-Michou, C., Cousens, B.L., Markovic, S., Ousbih, M., Souhassou, M., El Bilali, H., Ernst, R., 2023. Geochronology and petrogenesis of granitoids from the Bas Draa inlier (Western Anti-Atlas, Morocco): Revived debate on the tectonic regime operating during early Paleoproterozoic at the NW edge of the West African Craton. Geochemistry 84.1, 126044. https://doi.org/10.1016/j.chemer.2023.126044

Avanzinelli, R., Casalini, M., Elliott, T., Conticelli, S., 2018. Carbon fluxes from subducted carbonates revealed by uranium excess at Mount Vesuvius, Italy. Geology 46, 259–262. https://doi.org/10.1130/G39766.1

Balakrishnan, S., Rajamani, V., 1987. Geochemistry and Petrogenesis of Granitoids around the Kolar Schist Belt, South India: Constraints for the Evolution of the Crust in the Kolar Area. The Journal of Geology 95, 219–240. https://doi.org/10.1086/629121

Balaram, V., Rahaman, W., Roy, P., 2022. Recent advances in MC-ICP-MS applications in Earth and environmental sciences: Challenges and solutions. Geosystems and Geoenvironment 1, 100019. https://doi.org/10.1016/j.geogeo.2021.100019

Bao, H., Liu, S., Wan, Y., Wang, M., Sun, G., Gao, L., Wang, W., Guo, R., Fu, J., 2022. Neoarchean granitoids and tectonic regime of lateral growth in northeastern North China Craton. Gondwana Research 107, 176–200. https://doi.org/10.1016/j.gr.2022.02.015

Barnes, S.J., Van Kranendonk, M.J., Sonntag, I., 2012. Geochemistry and tectonic setting of basalts from the Eastern Goldfields Superterrane. Australian Journal of Earth Sciences 59, 707–735. https://doi.org/10.1080/08120099.2012.687398

Bea, F., 1996. Residence of REE, Y, Th and U in Granites and Crustal Protoliths; Implications for the Chemistry of Crustal Melts. Journal of Petrology 37, 521–552. https://doi.org/10.1093/petrology/37.3.521

Beakhouse, G.P., 1983. Geological, Geochemical and Rb-Sr and U-Pb Zircon
      Geochronological Investigations of Granitoid Rocks from the Winnipeg River
      Belt, Northwestern Ontario and Southeastern Manitoba (PhD Thesis).
      McMaster University.

Bédard, J.H., 2024. A gradual Proterozoic transition from an unstable stagnant lid to
      the modern plate tectonic system. Journal of the Geological Society 181,
      jgs2024-023. https://doi.org/10.1144/jgs2024-023

Bédard, J.H., 2006. A catalytic delamination-driven model for coupled genesis of
      Archaean crust and sub-continental lithospheric mantle. Geochimica et
      Cosmochimica Acta 70, 1188–1214. https://doi.org/10.1016/j.gca.2005.11.008

Bekker, A., Holland, H.D., Wang, P.-L., Rumble, D., Stein, H.J., Hannah, J.L.,
      Coetzee, L.L., Beukes, N.J., 2004. Dating the rise of atmospheric oxygen.
      Nature 427, 117–120. https://doi.org/10.1038/nature02260

Bénard, A., Klimm, K., Woodland, A.B., Arculus, R.J., Wilke, M., Botcharnikov, R.E.,
      Shimizu, N., Nebel, O., Rivard, C., Ionov, D.A., 2018. Oxidising agents in sub-
      arc mantle melts link slab devolatilisation and arc magmas. Nat Commun 9,
      3500. https://doi.org/10.1038/s41467-018-05804-2

Bendeliani, A.A., Eremin, N.N., Bobrov, A.V., 2023. Mechanisms and conditions of Ti
      and Cr incorporation in mantle phlogopite: the results of atomistic simulation.
      Phys Chem Minerals 50, 8. https://doi.org/10.1007/s00269-023-01232-x

Bigeleisen, J., 1996. Nuclear Size and Shape Effects in Chemical Reactions. Isotope
      Chemistry of the Heavy Elements. J. Am. Chem. Soc. 118, 3676–3680.
      https://doi.org/10.1021/ja954076k

Bigeleisen, J., Mayer, M.G., 1947. Calculation of Equilibrium Constants for Isotopic
      Exchange Reactions. J. Chem. Phys. 15, 261–267.
      https://doi.org/10.1063/1.1746492

Bindeman, I.N., Rudnick, R.L., Gaschnig, R.M., Hofmann, A., Schmitt, A.K., 2024.
      Triple oxygen and hydrogen isotopes of glacial diamictites record crustal
      maturation and changing surface conditions through geologic time. Chemical
      Geology 670, 122458. https://doi.org/10.1016/j.chemgeo.2024.122458

Bleeker, W., 2003. The late Archean record: a puzzle in ca. 35 pieces. Lithos, A Tale
      of Two Cratons: The Slave-Kaapvaal Workshop 71, 99–134.
      https://doi.org/10.1016/j.lithos.2003.07.003

Blein, O., Fullgraf, T., Padel, M., Melleton, J., Chevillard, M., Gloaguen, E., Boudzoumou, F., Cagnard, F., Le Bayon, B., Djama, L.-M., Callec, Y., 2024. Geochemical and geochronological signatures of granitoids from the Chaillu massif, Congo Craton: Insights into Mesoarchean crustal growth. Precambrian Research 409, 107435. https://doi.org/10.1016/j.precamres.2024.107435

Blundy, J., Wood, B., 2003. Mineral-Melt Partitioning of Uranium, Thorium and Their Daughters. Reviews in Mineralogy and Geochemistry 52, 59–123. https://doi.org/10.2113/0520059

Bourne, J.H., L'Heureux, M., 1991. The petrography and geochemistry of the Clericy Pluton: an ultrapotassic pyroxenite-syenite suite of late Archaean age from the Abitibi region, Quebec. Precambrian Research 52, 37–51. https://doi.org/10.1016/0301-9268(91)90012-Y

Brandon, A.D., Draper, D.S., 1996. Constraints on the origin of the oxidation state of mantle overlying subduction zones: An example from Simcoe, Washington, USA. Geochimica et Cosmochimica Acta 60, 1739–1749. https://doi.org/10.1016/0016-7037(96)00056-7

Breaks, F.W., Moore, J.M., 1992. The Ghost Lake Batholith, Superior Province of northwestern Ontario; a fertile, S-type, peraluminous granite-rare-element pegmatite system. The Canadian Mineralogist 30, 835–875.

Brennecka, G.A., Amelin, Y., Kleine, T., 2018. Uranium isotope ratios of Muonionalusta troilite and complications for the absolute age of the IVA iron meteorite core. Earth and Planetary Science Letters 490, 1–10. https://doi.org/10.1016/j.epsl.2018.03.010

Brennecka, G.A., Budde, G., Kleine, T., 2015. Uranium isotopic composition and absolute ages of Allende chondrules. Meteoritics & Planetary Science 50, 1995–2002. https://doi.org/10.1111/maps.12567

Brennecka, G.A., Herrmann, A.D., Algeo, T.J., Anbar, A.D., 2011. Rapid expansion of oceanic anoxia immediately before the end-Permian mass extinction. Proceedings of the National Academy of Sciences 108, 17631–17634. https://doi.org/10.1073/pnas.1106039108

Brennecka, G.A., Wadhwa, M., 2012. Uranium isotope compositions of the basaltic angrite meteorites and the chronological implications for the early Solar

System. Proceedings of the National Academy of Sciences 109, 9299–9303. https://doi.org/10.1073/pnas.1114043109

Brocks, J.J., Logan, G.A., Buick, R., Summons, R.E., 1999. Archean Molecular Fossils and the Early Rise of Eukaryotes. Science 285, 1033–1036. https://doi.org/10.1126/science.285.5430.1033

Brophy, J.G., Ota, T., Kunihro, T., Tsujimori, T., Nakamura, E., 2011. In situ ion-microprobe determination of trace element partition coefficients for hornblende, plagioclase, orthopyroxene, and apatite in equilibrium with natural rhyolitic glass, Little Glass Mountain Rhyolite, California. American Mineralogist 96, 1838–1850. https://doi.org/10.2138/am.2011.3857

Brown, M., Johnson, T.E., 2019. Metamorphism and the evolution of subduction on Earth. American Mineralogist 104, 1065–1082. https://doi.org/10.2138/am-2019-6956

Brown, M., Johnson, T.E., Gardiner, N.J., 2020. Plate Tectonics and the Archean Earth. Annual Review of Earth and Planetary Sciences 48, 291–320. https://doi.org/10.1146/annurev-earth-081619-052705

Bruand, E., Storey, C., Fowler, M., 2014. Accessory Mineral Chemistry of High Ba–Sr Granites from Northern Scotland: Constraints on Petrogenesis and Records of Whole-rock Signature. Journal of Petrology 55, 1619–1651. https://doi.org/10.1093/petrology/egu037

Bruand, E., Storey, C., Fowler, M., Dhuime, B., Doucelance, R., 2023. Mineral-whole rock isotope fidelity? A comparative study of Hf-Nd-O from high Ba-Sr granitoids. Chemical Geology 624, 121425. https://doi.org/10.1016/j.chemgeo.2023.121425

Brugger, J., Cuchet, S., van der Burgt, A., Crumbach, M., Etschmann, B., Xing, Y., Ram, R., Michaut, P., Nebel, O., Raveggi, M., Maas, R., Pearce, M.A., Howard, D.L., 2024. Titanite and allanite as a record of multistage co-mobility of Ti-REE-Nb-As during metamorphism in the Central Alps. American Mineralogist. https://doi.org/10.2138/am-2024-9378

Bruno, H., Elizeu, V., Heilbron, M., de Morisson Valeriano, C., Strachan, R., Fowler, M., Bersan, S., Moreira, H., Dussin, I., Guilherme do Eirado Silva, L., Tupinambá, M., Almeida, J., Neto, C., Storey, C., 2020. Neoarchean and Rhyacian TTG-Sanukitoid suites in the southern São Francisco Paleocontinent, Brazil: Evidence for diachronous change towards modern

tectonics. Geoscience Frontiers 11, 1763–1787.
https://doi.org/10.1016/j.gsf.2020.01.015

Bruno, H., Heilbron, M., de Morisson Valeriano, C., Strachan, R., Fowler, M., Bersan, S., Moreira, H., Motta, R., Almeida, J., Almeida, R., Carvalho, M., Storey, C., 2021. Evidence for a complex accretionary history preceding the amalgamation of Columbia: The Rhyacian Minas-Bahia Orogen, southern São Francisco Paleocontinent, Brazil. Gondwana Research 92, 149–171. https://doi.org/10.1016/j.gr.2020.12.019

Brüske, A., Martin, A.N., Rammensee, P., Eroglu, S., Lazarov, M., Albut, G., Schuth, S., Aulbach, S., Schoenberg, R., Beukes, N., Hofmann, A., Nägler, T., Weyer, S., 2020. The onset of oxidative weathering traced by uranium isotopes. Precambrian Research 338, 105583. https://doi.org/10.1016/j.precamres.2019.105583

Bucholz, C.E., Jagoutz, O., Schmidt, M.W., Sambuu, O., 2014. Fractional crystallization of high-K arc magmas: biotite- versus amphibole-dominated fractionation series in the Dariv Igneous Complex, Western Mongolia. Contrib Mineral Petrol 168, 1072. https://doi.org/10.1007/s00410-014-1072-9

Bucholz, C.E., Spencer, C.J., 2019. Strongly Peraluminous Granites across the Archean–Proterozoic Transition. Journal of Petrology 60, 1299–1348. https://doi.org/10.1093/petrology/egz033

Bura-Nakić, E., Andersen, M.B., Archer, C., de Souza, G.F., Marguš, M., Vance, D., 2018. Coupled Mo-U abundances and isotopes in a small marine euxinic basin: Constraints on processes in euxinic basins. Geochimica et Cosmochimica Acta 222, 212–229. https://doi.org/10.1016/j.gca.2017.10.023

Butterfield, N.J., 2015. Early evolution of the Eukaryota. Palaeontology 58, 5–17. https://doi.org/10.1111/pala.12139

Cameron, E.M., Hattori, K., 1987. Archean gold mineralization and oxidized hydrothermal fluids. Economic Geology 82, 1177–1191. https://doi.org/10.2113/gsecongeo.82.5.1177

Canfield, D.E., 2005. The Early History of Atmospheric Oxygen: Homage to Robert M. Garrels. Annual Review of Earth and Planetary Sciences 33, 1–36. https://doi.org/10.1146/annurev.earth.33.092203.122711

Canfield, D.E., 1998. A new model for Proterozoic ocean chemistry. Nature 396, 450–453. https://doi.org/10.1038/24839

Canfield, D.E., Poulton, S.W., Narbonne, G.M., 2007. Late-Neoproterozoic Deep-Ocean Oxygenation and the Rise of Animal Life. Science 315, 92–95. https://doi.org/10.1126/science.1135013

Canil, D., Fellows, S.A., 2017. Sulphide–sulphate stability and melting in subducted sediment and its role in arc mantle redox and chalcophile cycling in space and time. Earth and Planetary Science Letters 470, 73–86. https://doi.org/10.1016/j.epsl.2017.04.028

Capitanio, F.A., Nebel, O., Cawood, P.A., Weinberg, R.F., Chowdhury, P., 2019. Reconciling thermal regimes and tectonics of the early Earth. Geology 47, 923–927. https://doi.org/10.1130/G46239.1

Carneiro, L. de S., Moreto, C.P.N., Monteiro, L.V.S., Xavier, R.P., 2023. Geochemical signatures of the Neoarchean and Paleoproterozoic copper systems in the Carajás Mineral Province, NW Brazil: Implications for metal endowment. Journal of Geochemical Exploration 254, 107306. https://doi.org/10.1016/j.gexplo.2023.107306

Carpentier, M., Weis, D., Chauvel, C., 2013. Large U loss during weathering of upper continental crust: The sedimentary record. Chemical Geology 340, 91–104. https://doi.org/10.1016/j.chemgeo.2012.12.016

Carter, L.B., Skora, S., Blundy, J.D., De Hoog, J.C.M., Elliott, T., 2015. An Experimental Study of Trace Element Fluxes from Subducted Oceanic Crust. Journal of Petrology 56, 1585–1606. https://doi.org/10.1093/petrology/egv046

Casalini, M., 2018. 98Mo/95Mo and 238U/235U in Lamproites, shoshonites, and high-K calc-alkaline rocks from Western Alps: Inferences on their genesis. Italian Journal of Geosciences 173, 465–477. https://doi.org/10.3301/IJG.2018.20

Cassidy, K.F., Champion, D.C., Krapež, B., Barley, M.E., Brown, S.J.A., Blewett, R.S., Groenewald, P.B., Tyler, I.M., 2006. A revised geological framework for the Yilgarn Craton, Western Australia (No. 2006/8). Geological Survey of Western Australia.

Catling, D.C., Zahnle, K.J., McKay, C.P., 2001. Biogenic Methane, Hydrogen Escape, and the Irreversible Oxidation of Early Earth. Science 293, 839–843. https://doi.org/10.1126/science.1061976

Cawood, P.A., Chowdhury, P., Mulder, J.A., Hawkesworth, C.J., Capitanio, F.A., Gunawardana, P.M., Nebel, O., 2022. Secular Evolution of Continents and the

Earth System. Reviews of Geophysics 60, e2022RG000789.
https://doi.org/10.1029/2022RG000789

Cawood, P.A., Hawkesworth, C.J., Pisarevsky, S.A., Dhuime, B., Capitanio, F.A.,
Nebel, O., 2018. Geological archive of the onset of plate tectonics.
Philosophical Transactions of the Royal Society A: Mathematical, Physical
and Engineering Sciences 376, 20170405.
https://doi.org/10.1098/rsta.2017.0405

Cerri, R.I., Spencer, C., Caxito, F. de A., Luvizotto, G.L., Moraes, R., Riccomini, C.,
Puetz, S.J., 2024. Earth's metamorphic secular evolution accessed by rutile.
Precambrian Research 411, 107530.
https://doi.org/10.1016/j.precamres.2024.107530

Chabaux, F., Riotte, J., Dequincey, O., 2003. U-Th-Ra Fractionation During
Weathering and River Transport. Reviews in Mineralogy and Geochemistry
52, 533–576. https://doi.org/10.2113/0520533

Champion, D.C., Sheraton, J.W., 1997. Geochemistry and Nd isotope systematics of
Archaean granites of the Eastern Goldfields, Yilgarn Craton, Australia:
implications for crustal growth processes. Precambrian Research, Archaean
Granite-Greenstone Geology of the Eastern Goldfields 83, 109–132.
https://doi.org/10.1016/S0301-9268(97)00007-7

Chapman, T., Clarke, G.L., Daczko, N.R., 2019. The role of buoyancy in the fate of
ultra-high-pressure eclogite. Sci Rep 9, 19925.
https://doi.org/10.1038/s41598-019-56475-y

Charbonnier, Q., Clarkson, M.O., Hilton, R.G., Vance, D., 2023. Source versus
weathering processes as controls on the Mackenzie river uranium isotope
signature. Chemical Geology 625, 121409.
https://doi.org/10.1016/j.chemgeo.2023.121409

Chaudhuri, T., Kamei, A., Das, M., Mazumder, R., Owada, M., 2022. Evolution of the
Archean felsic crust of Singhbhum Craton, India: A reassessment. Earth-
Science Reviews 231, 104067.
https://doi.org/10.1016/j.earscirev.2022.104067

Chen, K., Rudnick, R.L., Wang, Z., Tang, M., Gaschnig, R.M., Zou, Z., He, T., Hu, Z.,
Liu, Y., 2020. How mafic was the Archean upper continental crust? Insights
from Cu and Ag in ancient glacial diamictites. Geochimica et Cosmochimica

Acta, The continents: Origin, evolution and interactions with other reservoirs 278, 16–29. https://doi.org/10.1016/j.gca.2019.08.002

Chen, N.H.-C., Zhao, G., Sun, M., Zhou, H., 2017. Geochemistry of ~2.5 Ga granitoids at the northern margin of the Yinshan Block: Implications for the crustal evolution of the North China Craton. Precambrian Research, Archean to Proterozoic Evolution of the North China Craton 303, 673–686. https://doi.org/10.1016/j.precamres.2017.08.022

Chen, X., Tissot, F.L.H., Jansen, M.F., Bekker, A., Liu, C.X., Nie, N.X., Halverson, G.P., Veizer, J., Dauphas, N., 2021. The uranium isotopic record of shales and carbonates through geologic time. Geochimica et Cosmochimica Acta 300, 164–191. https://doi.org/10.1016/j.gca.2021.01.040

Chen, Y., Zhang, J., Gao, P., Liu, J., Yin, C., Qian, J., Liu, X., Wang, X., 2022. Modern-style plate tectonics manifested by the late Neoarchean TTG-sanukitoid suite from the Datong-Huai'an Complex, Trans-North China Orogen. Lithos 430–431, 106843. https://doi.org/10.1016/j.lithos.2022.106843

Cheng, H., Lawrence Edwards, R., Shen, C.-C., Polyak, V.J., Asmerom, Y., Woodhead, J., Hellstrom, J., Wang, Y., Kong, X., Spötl, C., Wang, X., Calvin Alexander, E., 2013. Improvements in 230Th dating, 230Th and 234U half-life values, and U–Th isotopic measurements by multi-collector inductively coupled plasma mass spectrometry. Earth and Planetary Science Letters 371–372, 82–91. https://doi.org/10.1016/j.epsl.2013.04.006

Chi Fru, E., Somogyi, A., El Albani, A., Medjoubi, K., Aubineau, J., Robbins, L.J., Lalonde, S.V., Konhauser, K.O., 2019. The rise of oxygen-driven arsenic cycling at ca. 2.48 Ga. Geology 47, 243–246. https://doi.org/10.1130/G45676.1

Chiaradia, M., Müntener, O., Beate, B., 2014. Quaternary Sanukitoid-like Andesites Generated by Intracrustal Processes (Chacana Caldera Complex, Ecuador): Implications for Archean Sanukitoids. Journal of Petrology 55, 769–802. https://doi.org/10.1093/petrology/egu006

Choi, E., Fiorentini, M.L., Giuliani, A., Foley, S.F., Maas, R., Taylor, W.R., 2020. Subduction-related petrogenesis of Late Archean calc-alkaline lamprophyres in the Yilgarn Craton (Western Australia). Precambrian Research 338, 105550. https://doi.org/10.1016/j.precamres.2019.105550

Chou, C.-L., 1978. Fractionation of siderophile elements in the earth's upper mantle, in: Proceedings of the 9th Lunar and Planetary Science Conference 1. pp. 219–230.

Chowdhury, P., Cawood, P.A., Mulder, J.A., 2025. Subaerial Emergence of Continents on Archean Earth. Annual Review of Earth and Planetary Sciences 53. https://doi.org/10.1146/annurev-earth-040722-093345

Claire, M.W., Catling, D.C., Zahnle, K.J., 2006. Biogeochemical modelling of the rise in atmospheric oxygen. Geobiology 4, 239–269. https://doi.org/10.1111/j.1472-4669.2006.00084.x

Clarkson, M.O., Lenton, T.M., Andersen, M.B., Bagard, M.-L., Dickson, A.J., Vance, D., 2021. Upper limits on the extent of seafloor anoxia during the PETM from uranium isotopes. Nat Commun 12, 399. https://doi.org/10.1038/s41467-020-20486-5

Clemens, J.D., Yearron, L.M., Stevens, G., 2006. Barberton (South Africa) TTG magmas: Geochemical and experimental constraints on source-rock petrology, pressure of formation and tectonic setting. Precambrian Research 151, 53–78. https://doi.org/10.1016/j.precamres.2006.08.001

Clos, F., Weinberg, R., Zibra, I., 2018. Building the Archean continental crust: 300 Ma of felsic magmatism in the Yalgoo dome (Yilgarn Craton) (No. 186). Geological Survey of Western Australia, Perth, Australia.

Cole, D.B., Planavsky, N.J., Longley, M., Böning, P., Wilkes, D., Wang, X., Swanner, E.D., Wittkop, C., Loydell, D.K., Busigny, V., Knudsen, A.C., Sperling, E.A., 2020. Uranium Isotope Fractionation in Non-sulfidic Anoxic Settings and the Global Uranium Isotope Mass Balance. Global Biogeochemical Cycles 34, e2020GB006649. https://doi.org/10.1029/2020GB006649

Conceição, R.V., Green, D.H., 2004. Derivation of potassic (shoshonitic) magmas by decompression melting of phlogopite+pargasite lherzolite. Lithos 72, 209–229. https://doi.org/10.1016/j.lithos.2003.09.003

Condamine, P., Médard, E., Devidal, J.-L., 2016. Experimental melting of phlogopite-peridotite in the garnet stability field. Contrib Mineral Petrol 171, 95. https://doi.org/10.1007/s00410-016-1306-0

Condie, K.C., 1993. Chemical composition and evolution of the upper continental crust: Contrasting results from surface samples and shales. Chemical Geology 104, 1–37. https://doi.org/10.1016/0009-2541(93)90140-E

Condie, K.C., Hunter, D.R., 1976. Trace element geochemistry of Archean granitic rocks from the Barberton region, South Africa. Earth and Planetary Science Letters 29, 389–400. https://doi.org/10.1016/0012-821X(76)90144-8

Condie, K.C., Puetz, S.J., Spencer, C.J., Roberts, N.M.W., 2023. Four billion years of secular compositional change in granitoids. Chemical Geology 644, 121868. https://doi.org/10.1016/j.chemgeo.2023.121868

Condie, K.C., Puetz, S.J., Spencer, C.J., Roberts, N.M.W., 2022. Secular compositional changes in hydrated mantle: The record of arc-type basalts. Chemical Geology 607, 121010. https://doi.org/10.1016/j.chemgeo.2022.121010

Condie, K.C., Stern, R.J., 2023. Ophiolites: Identification and tectonic significance in space and time. Geoscience Frontiers 14, 101680. https://doi.org/10.1016/j.gsf.2023.101680

Condon, D.J., McLean, N., Noble, S.R., Bowring, S.A., 2010. Isotopic composition (238U/235U) of some commonly used uranium reference materials. Geochimica et Cosmochimica Acta 74, 7127–7143. https://doi.org/10.1016/j.gca.2010.09.019

Connelly, J.N., Bizzarro, M., Krot, A.N., Nordlund, Å., Wielandt, D., Ivanova, M.A., 2012. The Absolute Chronology and Thermal Processing of Solids in the Solar Protoplanetary Disk. Science 338, 651–655. https://doi.org/10.1126/science.1226919

Cosgrove, G.I.E., Colombera, L., Mountney, N.P., 2024. The Precambrian continental record: A window into early Earth environments. Precambrian Research 402, 107286. https://doi.org/10.1016/j.precamres.2023.107286

Cottrell, E., Birner, S.K., Brounce, M., Davis, F.A., Waters, L.E., Kelley, K.A., 2021. Oxygen Fugacity Across Tectonic Settings, in: Magma Redox Geochemistry. American Geophysical Union (AGU), pp. 33–61. https://doi.org/10.1002/9781119473206.ch3

Cruciani, C., Carminati, E., Doglioni, C., 2005. Slab dip vs. lithosphere age: No direct function. Earth and Planetary Science Letters 238, 298–310. https://doi.org/10.1016/j.epsl.2005.07.025

Cui, Z., Xia, X.-P., Huang, X.-L., Xu, J., Yang, Q., Zhang, W.-F., Zhang, L., Lai, C.-K., Wang, X., 2022. Meso- to Neoarchean geodynamic transition of the North

China Craton indicated by H2O-in-zircon for TTG suite. Precambrian Research 371, 106574. https://doi.org/10.1016/j.precamres.2022.106574

Cuney, M., 2010. Evolution of Uranium Fractionation Processes through Time: Driving the Secular Variation of Uranium Deposit Types. Economic Geology 105, 553–569. https://doi.org/10.2113/gsecongeo.105.3.553

Czarnota, K., Champion, D.C., Goscombe, B., Blewett, R.S., Cassidy, K.F., Henson, P.A., Groenewald, P.B., 2010. Geodynamics of the eastern Yilgarn Craton. Precambrian Research, Geodynamics and architecture of a world class mineral province: the Archean eastern Yilgarn Craton, Western Australia 183, 175–202. https://doi.org/10.1016/j.precamres.2010.08.004

Dahl, T.W., Connelly, J.N., Kouchinsky, A., Gill, B.C., Månsson, S.F., Bizzarro, M., 2017. Reorganisation of Earth's biogeochemical cycles briefly oxygenated the oceans 520 Myr ago. Geochem. Persp. Let. 3, 210–220. https://doi.org/10.7185/geochemlet.1724

Dahl, T.W., Connelly, J.N., Li, D., Kouchinsky, A., Gill, B.C., Porter, S., Maloof, A.C., Bizzarro, M., 2019. Atmosphere–ocean oxygen and productivity dynamics during early animal radiations. Proceedings of the National Academy of Sciences 116, 19352–19361. https://doi.org/10.1073/pnas.1901178116

Dahl, T.W., Hammarlund, E.U., Anbar, A.D., Bond, D.P.G., Gill, B.C., Gordon, G.W., Knoll, A.H., Nielsen, A.T., Schovsbo, N.H., Canfield, D.E., 2010. Devonian rise in atmospheric oxygen correlated to the radiations of terrestrial plants and large predatory fish. Proceedings of the National Academy of Sciences 107, 17911–17915. https://doi.org/10.1073/pnas.1011287107

Dale, C.W., Kruijer, T.S., Burton, K.W., 2017. Highly siderophile element and 182W evidence for a partial late veneer in the source of 3.8 Ga rocks from Isua, Greenland. Earth and Planetary Science Letters 458, 394–404. https://doi.org/10.1016/j.epsl.2016.11.001

Dang, D.H., Evans, R.D., Wang, W., Omanović, D., El Houssainy, A., Lenoble, V., Mullot, J.-U., Mounier, S., Garnier, C., 2018a. Uranium isotope geochemistry in modern coastal sediments: Insights from Toulon Bay, France. Chemical Geology 481, 133–145. https://doi.org/10.1016/j.chemgeo.2018.01.032

Dang, D.H., Wang, W., Gibson, T.M., Kunzmann, M., Andersen, M.B., Halverson, G.P., Evans, R.D., 2022. Authigenic uranium isotopes of late Proterozoic

black shale. Chemical Geology 588, 120644.
https://doi.org/10.1016/j.chemgeo.2021.120644

Dang, D.H., Wang, W., Pelletier, P., Poulain, A.J., Evans, R.D., 2018b. Uranium dispersion from U tailings and mechanisms leading to U accumulation in sediments: Insights from biogeochemical and isotopic approaches. Science of The Total Environment 610–611, 880–891.
https://doi.org/10.1016/j.scitotenv.2017.08.156

Dash, S., Babu, E.V.S.S.K., Ganne, J., Mukherjee, S., 2024. Plate tectonics through Earth's history: constraints from the thermal evolution of Earth's upper mantle. International Geology Review 67, 500–533.
https://doi.org/10.1080/00206814.2024.2394994

Davidson, J., Turner, S., Plank, T., 2013. Dy/Dy*: Variations Arising from Mantle Sources and Petrogenetic Processes. Journal of Petrology 54, 525–537.
https://doi.org/10.1093/petrology/egs076

Davies, G.F., 2009. Effect of plate bending on the Urey ratio and the thermal evolution of the mantle. Earth and Planetary Science Letters 287, 513–518.
https://doi.org/10.1016/j.epsl.2009.08.038

Davies, G.F., 1992. On the emergence of plate tectonics. Geology 20, 963–966.
https://doi.org/10.1130/0091-7613(1992)020<0963:OTEOPT>2.3.CO;2

Davies, J.H., von Blanckenburg, F., 1995. Slab breakoff: A model of lithosphere detachment and its test in the magmatism and deformation of collisional orogens. Earth and Planetary Science Letters 129, 85–102.
https://doi.org/10.1016/0012-821X(94)00237-S

de Morisson Valeriano, C., Turbay, C.V.G., Bruno, H., Simonetti, A., Heilbron, M., Bersan, S.M., Strachan, R., 2022. Paleo- and Mesoarchean TTG-sanukitoid to high-K granite cycles in the southern São Francisco craton, SE Brazil. Geoscience Frontiers 13, 101372. https://doi.org/10.1016/j.gsf.2022.101372

de Oliveira, M.A., Dall'Agnol, R., Almeida, J. de A.C. de, 2011. Petrology of the Mesoarchean Rio Maria suite and the discrimination of sanukitoid series. Lithos 127, 192–209. https://doi.org/10.1016/j.lithos.2011.08.017

de Oliveira, M.A., Dall'Agnol, R., Althoff, F.J., da Silva Leite, A.A., 2009. Mesoarchean sanukitoid rocks of the Rio Maria Granite-Greenstone Terrane, Amazonian craton, Brazil. Journal of South American Earth Sciences,

Magmatism, Crustal Evolution, and Metallogenesis of Carajás and adjacent provinces 27, 146–160. https://doi.org/10.1016/j.jsames.2008.07.003

de Oliveira, M.A., Dall'Agnol, R., Scaillet, B., 2010. Petrological Constraints on Crystallization Conditions of Mesoarchean Sanukitoid Rocks, Southeastern Amazonian Craton, Brazil. Journal of Petrology 51, 2121–2148. https://doi.org/10.1093/petrology/egq051

Debret, B., Sverjensky, D.A., 2017. Highly oxidising fluids generated during serpentinite breakdown in subduction zones. Sci Rep 7, 10351. https://doi.org/10.1038/s41598-017-09626-y

Deng, G., Jiang, D., Huang, F., Li, G., Xu, Z., 2024. Barium isotope evidence for a magmatic fluid-dominated petrogenesis of LCT-type pegmatites. Geochemical Perspectives Letters 31, 14–20. https://doi.org/10.7185/geochemlet.2426

Deng, Z., Chaussidon, M., Guitreau, M., Puchtel, I.S., Dauphas, N., Moynier, F., 2019a. An oceanic subduction origin for Archaean granitoids revealed by silicon isotopes. Nature Geoscience 12, 774–778. https://doi.org/10.1038/s41561-019-0407-6

Deng, Z., Chaussidon, M., Savage, P., Robert, F., Pik, R., Moynier, F., 2019b. Titanium isotopes as a tracer for the plume or island arc affinity of felsic rocks. PNAS 116, 1132–1135. https://doi.org/10.1073/pnas.1809164116

Deng, Z., Moynier, F., Sossi, P.A., Chaussidon, M., 2018a. Bridging the depleted MORB mantle and the continental crust using titanium isotopes. Geochem. Persp. Let. 11–15. https://doi.org/10.7185/geochemlet.1831

Deng, Z., Moynier, F., van Zuilen, K., Sossi, P.A., Pringle, E.A., Chaussidon, M., 2018b. Lack of resolvable titanium stable isotopic variations in bulk chondrites. Geochimica et Cosmochimica Acta 239, 409–419. https://doi.org/10.1016/j.gca.2018.06.016

Deng, Z., Moynier, F., Villeneuve, J., Jensen, N.K., Liu, D., Cartigny, P., Mikouchi, T., Siebert, J., Agranier, A., Chaussidon, M., Bizzarro, M., 2020. Early oxidation of the martian crust triggered by impacts. Science Advances 6, eabc4941. https://doi.org/10.1126/sciadv.abc4941

Deng, Z., Schiller, M., Jackson, M.G., Millet, M.-A., Pan, L., Nikolajsen, K., Saji, N.S., Huang, D., Bizzarro, M., 2023. Earth's evolving geodynamic regime recorded by titanium isotopes. Nature 621, 100–104. https://doi.org/10.1038/s41586-023-06304-0

Dey, S., Halla, J., Kurhila, M., Nandy, J., Heilimo, E., Pal, S., 2017. Geochronology of Neoarchaean granitoids of the NW eastern Dharwar craton: implications for crust formation. Geological Society, London, Special Publications 449, 89–121. https://doi.org/10.1144/SP449.9

Dey, S., Nandy, J., Choudhary, A.K., Liu, Y., Zong, K., 2015. Neoarchaean crustal growth by combined arc–plume action: evidence from the Kadiri Greenstone Belt, eastern Dharwar craton, India. Geological Society, London, Special Publications 389, 135–163. https://doi.org/10.1144/SP389.3

Dey, S., Pandey, U.K., Rai, A.K., Chaki, A., 2012. Geochemical and Nd isotope constraints on petrogenesis of granitoids from NW part of the eastern Dharwar craton: Possible implications for late Archaean crustal accretion. Journal of Asian Earth Sciences 45, 40–56. https://doi.org/10.1016/j.jseaes.2011.09.013

Dhuime, B., Wuestefeld, A., Hawkesworth, C.J., 2015. Emergence of modern continental crust about 3 billion years ago. Nature Geosci 8, 552–555. https://doi.org/10.1038/ngeo2466

DIGIS Team, 2024. GEOROC Compilation: Archaean Cratons. [Database] https://doi.org/10.25625/1KRR1P (Accessed: December 2024)

Ding, N., Wang, X.-L., Du, D.-H., Wang, D., Anhaeusser, C., 2024. Compositional diversity of TTGs controlled by heterogeneous accumulation of accessory minerals. Lithos 482–483, 107718. https://doi.org/10.1016/j.lithos.2024.107718

do Nascimento, A.C., de Oliveira, D.C., da Silva, L.R., Lamarão, C.N., 2021. Mineral thermobarometry and its implications for petrological constraints on Mesoarchean granitoids from the Carajás Province, Amazonian Craton (Brazil). Journal of South American Earth Sciences 109, 103271. https://doi.org/10.1016/j.jsames.2021.103271

do Nascimento, A.C., de Oliveira, D.C., Gabriel, E.O., Marangoanha, B., Ribeiro da Silva, L., Aleixo, E. da C., 2023. Mineral chemistry of the Água Limpa suite: Insights into petrological constraints and magma ascent rate of Mesoarchean sanukitoids from the Sapucaia terrane (Carajás Province, southeastern Amazonian Craton, Brazil). Journal of South American Earth Sciences 132, 104683. https://doi.org/10.1016/j.jsames.2023.104683

Doucet, L.S., Laurent, O., Ionov, D.A., Mattielli, N., Debaille, V., Debouge, W., 2020. Archean lithospheric differentiation: Insights from Fe and Zn isotopes. Geology 48, 1028–1032. https://doi.org/10.1130/G47647.1

Doucet, L.S., Laurent, O., Mattielli, N., Debouge, W., 2018. Zn isotope heterogeneity in the continental lithosphere: New evidence from Archean granitoids of the northern Kaapvaal craton, South Africa. Chemical Geology 476, 260–271. https://doi.org/10.1016/j.chemgeo.2017.11.022

Duan, W.-Y., Li, X.-P., Schertl, H.-P., Willner, A.P., 2022. C-O-H-S fluids released by oceanic serpentinite in subduction zones: Implications for arc-magma oxidation. Earth and Planetary Science Letters 594, 117709. https://doi.org/10.1016/j.epsl.2022.117709

Dunk, R.M., Mills, R.A., Jenkins, W.J., 2002. A reevaluation of the oceanic uranium budget for the Holocene. Chemical Geology, Geochemistry of Crustal Fluids-Fluids in the Crust and Chemical Fluxes at the Earth's Surface 190, 45–67. https://doi.org/10.1016/S0009-2541(02)00110-9

Elkins, L.J., Gaetani, G.A., Sims, K.W.W., 2008. Partitioning of U and Th during garnet pyroxenite partial melting: Constraints on the source of alkaline ocean island basalts. Earth and Planetary Science Letters 265, 270–286. https://doi.org/10.1016/j.epsl.2007.10.034

Emproto, C., Mathur, R., Simon, A.C., Bindeman, I., Godfrey, L., Dhnaram, C., Lisitsin, V., 2022. Integrated O, Fe, and Ti isotopic analysis elucidates multiple metal and fluid sources for magnetite from the Ernest Henry Iron oxide copper gold (IOCG) Deposit, Queensland, Australia. Ore Geology Reviews 150, 105170. https://doi.org/10.1016/j.oregeorev.2022.105170

Emproto, C., Mathur, R., Sun, M., Simon, A.C., Godfrey, L., 2025. Fluid-mineral titanium isotope fractionation: Computational and empirical results with implications for mineral deposits. Geochimica et Cosmochimica Acta 390, 251–263. https://doi.org/10.1016/j.gca.2024.12.007

Engler, A., Koller, F., Meisel, T., Quéméneur, J., 2002. Evolution of the archean/proterozoic crust in the southern São Francisco craton near Perdões, Minas Gerais, Brazil: petrological and geochemical constraints. Journal of South American Earth Sciences 15, 709–723. https://doi.org/10.1016/S0895-9811(02)00113-X

Evans, K.A., 2006. Redox decoupling and redox budgets: Conceptual tools for the study of earth systems. Geology 34, 489–492. https://doi.org/10.1130/G22390.1

Evans, K.A., Tomkins, A.G., 2021. Redox Variables and Mechanisms in Subduction Magmatism and Volcanism, in: Magma Redox Geochemistry. American Geophysical Union (AGU), pp. 63–91. https://doi.org/10.1002/9781119473206.ch4

Evans, K.A., Tomkins, A.G., 2011. The relationship between subduction zone redox budget and arc magma fertility. Earth and Planetary Science Letters 308, 401–409. https://doi.org/10.1016/j.epsl.2011.06.009

Fakhraee, M., Crockford, P.W., Bauer, K.W., Pasquier, V., Sugiyama, I., Katsev, S., Raven, M.R., Gomes, M., Philippot, P., Crowe, S.A., Tarhan, L.G., Lyons, T.W., Planavsky, N., 2025. The history of Earth's sulfur cycle. Nat Rev Earth Environ 6, 106–125. https://doi.org/10.1038/s43017-024-00615-0

Fakhraee, M., Hancisse, O., Canfield, D.E., Crowe, S.A., Katsev, S., 2019. Proterozoic seawater sulfate scarcity and the evolution of ocean–atmosphere chemistry. Nat. Geosci. 12, 375–380. https://doi.org/10.1038/s41561-019-0351-5

Farges, F., Brown, G.E., 1997. Coordination chemistry of titanium (IV) in silicate glasses and melts: IV. XANES studies of synthetic and natural volcanic glasses and tektites at ambient temperature and pressure. Geochimica et Cosmochimica Acta 61, 1863–1870. https://doi.org/10.1016/S0016-7037(97)00050-1

Farges, F., Brown, G.E., Navrotsky, A., Gan, H., Rehr, J.J., 1996. Coordination chemistry of Ti(IV) in silicate glasses and melts: II. Glasses at ambient temperature and pressure. Geochimica et Cosmochimica Acta 60, 3039–3053. https://doi.org/10.1016/0016-7037(96)00145-7

Farges, F., Ponader, C.W., Calas, G., Brown, G.E., 1992. Structural environments of incompatible elements in silicate glass/melt systems: II. UIV, UV, and UVI. Geochimica et Cosmochimica Acta 56, 4205–4220. https://doi.org/10.1016/0016-7037(92)90261-G

Farina, F., Albert, C., Lana, C., 2015. The Neoarchean transition between medium- and high-K granitoids: Clues from the Southern São Francisco Craton (Brazil).

Precambrian Research 266, 375–394.
https://doi.org/10.1016/j.precamres.2015.05.038

Farquhar, J., Bao, H., Thiemens, M., 2000. Atmospheric Influence of Earth's Earliest Sulfur Cycle. Science 289, 756–758.
https://doi.org/10.1126/science.289.5480.756

Farquhar, J., Wu, N., Canfield, D.E., Oduro, H., 2010. Connections between Sulfur Cycle Evolution, Sulfur Isotopes, Sediments, and Base Metal Sulfide Deposits. Economic Geology 105, 509–533.
https://doi.org/10.2113/gsecongeo.105.3.509

Farquhar, J., Zerkle, A.L., Bekker, A., 2011. Geological constraints on the origin of oxygenic photosynthesis. Photosynth Res 107, 11–36.
https://doi.org/10.1007/s11120-010-9594-0

Faure, P., Bouhifd, M.A., Boyet, M., Manthilake, G., Clesi, V., Devidal, J.-L., 2020. Uranium and thorium partitioning in the bulk silicate Earth and the oxygen content of Earth's core. Geochimica et Cosmochimica Acta 275, 83–98.
https://doi.org/10.1016/j.gca.2020.02.010

Fayol, N., Jébrak, M., 2017. Archean Sanukitoid Gold Porphyry Deposits: A New Understanding and Genetic Model from the Lac Bachelor Gold Deposit, Abitibi, Canada. Economic Geology 112, 1913–1936.
https://doi.org/10.5382/econgeo.2017.4534

Feng, R., Kerrich, R., 1992. Geochemical evolution of granitoids from the Archean Abitibi Southern Volcanic Zone and the Pontiac subprovince, Superior Province, Canada: Implications for tectonic history and source regions. Chemical Geology 98, 23–70. https://doi.org/10.1016/0009-2541(92)90090-R

Fike, D.A., Grotzinger, J.P., Pratt, L.M., Summons, R.E., 2006. Oxidation of the Ediacaran Ocean. Nature 444, 744–747. https://doi.org/10.1038/nature05345

Fischer-Gödde, M., Elfers, B.-M., Münker, C., Szilas, K., Maier, W.D., Messling, N., Morishita, T., Van Kranendonk, M., Smithies, H., 2020. Ruthenium isotope vestige of Earth's pre-late-veneer mantle preserved in Archaean rocks. Nature 579, 240–244. https://doi.org/10.1038/s41586-020-2069-3

Foley, B.J., 2024. Generation of Archean TTGs via sluggish subduction. Geology 52, 656–660. https://doi.org/10.1130/G52196.1

Foley, B.J., 2018. The dependence of planetary tectonics on mantle thermal state: applications to early Earth evolution. Philosophical Transactions of the Royal

Society A: Mathematical, Physical and Engineering Sciences 376, 20170409. https://doi.org/10.1098/rsta.2017.0409

Fowler, M.B., Henney, P.J., Darbyshire, D.P.F., Greenwood, P.B., 2001. Petrogenesis of high Ba–Sr granites: the Rogart pluton, Sutherland. Journal of the Geological Society 158, 521–534. https://doi.org/10.1144/jgs.158.3.521

Fowler, M.B., Kocks, H., Darbyshire, D.P.F., Greenwood, P.B., 2008. Petrogenesis of high Ba–Sr plutons from the Northern Highlands Terrane of the British Caledonian Province. Lithos 105, 129–148. https://doi.org/10.1016/j.lithos.2008.03.003

Fowler, M.B., Rollinson, H., 2012. Phanerozoic sanukitoids from Caledonian Scotland: Implications for Archean subduction. Geology 40, 1079–1082. https://doi.org/10.1130/G33371.1

François, C., Philippot, P., Rey, P., Rubatto, D., 2014. Burial and exhumation during Archean sagduction in the East Pilbara Granite-Greenstone Terrane. Earth and Planetary Science Letters 396, 235–251. https://doi.org/10.1016/j.epsl.2014.04.025

Freymuth, H., Andersen, M.B., Elliott, T., 2019. Uranium isotope fractionation during slab dehydration beneath the Izu arc. Earth and Planetary Science Letters 522, 244–254. https://doi.org/10.1016/j.epsl.2019.07.006

Frost, C.D., Frost, B.R., Kirkwood, R., Chamberlain, K.R., 2006. The tonalite–trondhjemite–granodiorite (TTG) to granodiorite–granite (GG) transition in the late Archean plutonic rocks of the central Wyoming Province. Can. J. Earth Sci. 43, 1419–1444. https://doi.org/10.1139/e06-082

Fujii, T., Moynier, F., Albarède, F., 2009. The nuclear field shift effect in chemical exchange reactions. Chemical Geology, Advances in experimental and theoretical isotope geochemistry 267, 139–156. https://doi.org/10.1016/j.chemgeo.2009.06.015

Fujii, Y., Higuchi, N., Haruno, Y., Nomura, M., Suzuki, T., 2006. Temperature Dependence of Isotope Effects in Uranium Chemical Exchange Reactions. Journal of Nuclear Science and Technology 43, 400–406. https://doi.org/10.1080/18811248.2006.9711111

Gaetani, G.A., Asimow, P.D., Stolper, E.M., 2008. A model for rutile saturation in silicate melts with applications to eclogite partial melting in subduction zones

and mantle plumes. Earth and Planetary Science Letters 272, 720–729. https://doi.org/10.1016/j.epsl.2008.06.002

Gaillard, F., Scaillet, B., Arndt, N.T., 2011. Atmospheric oxygenation caused by a change in volcanic degassing pressure. Nature 478, 229–232. https://doi.org/10.1038/nature10460

Galer, S.J.G., 1999. Optimal double and triple spiking for high precision lead isotopic measurement. Chemical Geology 157, 255–274. https://doi.org/10.1016/S0009-2541(98)00203-4

Gama, J., Schwark, L., 2022. Lithofacies of early Jurassic successions derived from spectral gamma ray logging in the Mandawa Basin, SE Tanzania. Arab J Geosci 15, 1373. https://doi.org/10.1007/s12517-022-10622-4

Ganne, J., Feng, X., 2017. Primary magmas and mantle temperatures through time. Geochemistry, Geophysics, Geosystems 18, 872–888. https://doi.org/10.1002/2016GC006787

Garçon, M., 2021. Episodic growth of felsic continents in the past 3.7 Ga. Science Advances 7, eabj1807. https://doi.org/10.1126/sciadv.abj1807

Garde, A.A., 1997. Accretion and evolution of an Archaean high-grade grey gneiss – amphibolite complex: the Fiskefjord area, southern West Greenland. Geology of Greenland Survey Bulletin 177, 1–115. https://doi.org/10.34194/ggub.v179.5075

Garde, A.A., Windley, B.F., Kokfelt, T.F., Keulen, N., 2020. Archaean Plate Tectonics in the North Atlantic Craton of West Greenland Revealed by Well-Exposed Horizontal Crustal Tectonics, Island Arcs and Tonalite-Trondhjemite-Granodiorite Complexes. Front. Earth Sci. 8, 540997. https://doi.org/10.3389/feart.2020.540997

Gaschnig, R.M., Rader, S.T., Reinhard, C.T., Owens, J.D., Planavsky, N., Wang, X., Asael, D., Greaney, A., Helz, R., 2021a. Behavior of the Mo, Tl, and U isotope systems during differentiation in the Kilauea Iki lava lake. Chemical Geology 574, 120239. https://doi.org/10.1016/j.chemgeo.2021.120239

Gaschnig, R.M., Reinhard, C.T., Planavsky, N.J., Wang, X., Asael, D., Jackson, M.G., 2021b. The impact of primary processes and secondary alteration on the stable isotope composition of ocean island basalts. Chemical Geology 581, 120416. https://doi.org/10.1016/j.chemgeo.2021.120416

Gaschnig, R.M., Rudnick, R.L., McDonough, W.F., Kaufman, A.J., Hu, Z., Gao, S., 2014. Onset of oxidative weathering of continents recorded in the geochemistry of ancient glacial diamictites. Earth and Planetary Science Letters 408, 87–99. https://doi.org/10.1016/j.epsl.2014.10.002

Gaschnig, R.M., Rudnick, R.L., McDonough, W.F., Kaufman, A.J., Valley, J.W., Hu, Z., Gao, S., Beck, M.L., 2016. Compositional evolution of the upper continental crust through time, as constrained by ancient glacial diamictites. Geochimica et Cosmochimica Acta 186, 316–343. https://doi.org/10.1016/j.gca.2016.03.020

Ge, R.-F., Wilde, S.A., Zhu, W.-B., Wang, X.-L., 2023. Earth's early continental crust formed from wet and oxidizing arc magmas. Nature 623, 334–339. https://doi.org/10.1038/s41586-023-06552-0

Geological Survey of Western Australia, 2025. Western Australian Geochemistry Database (WACHEM). [Database] Available at: http://geochem.dmp.wa.gov.au/geochem/ (Accessed: January 2025)

Geological Survey of Western Australia, 2020. 1:500,000 State interpreted bedrock geology of Western Australia, 2020. [Map]

Gervasoni, F., Klemme, S., Rohrbach, A., Grützner, T., Berndt, J., 2017. Experimental constraints on mantle metasomatism caused by silicate and carbonate melts. Lithos 282–283, 173–186. https://doi.org/10.1016/j.lithos.2017.03.004

Gill, B.C., Lyons, T.W., Young, S.A., Kump, L.R., Knoll, A.H., Saltzman, M.R., 2011. Geochemical evidence for widespread euxinia in the Later Cambrian ocean. Nature 469, 80–83. https://doi.org/10.1038/nature09700

Godet, A., Guilmette, C., Marsh, J.H., Rottier, B., Tinkham, D., Siles Malta, I., Rehm, A., Jørgensen, T.R.C., Hamilton, M.A., Ribeiro, D., Beaudoin, G., 2023. Origin, nature, and evolution of the northern Pontiac subprovince, Canada: Insights from the intrusive record. Precambrian Research 396, 107169. https://doi.org/10.1016/j.precamres.2023.107169

Goldmann, A., Brennecka, G., Noordmann, J., Weyer, S., Wadhwa, M., 2015. The uranium isotopic composition of the Earth and the Solar System. Geochimica et Cosmochimica Acta 148, 145–158. https://doi.org/10.1016/j.gca.2014.09.008

Gómez-Frutos, D., Castro, A., 2022. Sanukitoid crystallization relations at 1.0 and 0.3 GPa. Lithos 414–415, 106632. https://doi.org/10.1016/j.lithos.2022.106632

Greber, N.D., Dauphas, N., 2019. The chemistry of fine-grained terrigenous sediments reveals a chemically evolved Paleoarchean emerged crust. Geochimica et Cosmochimica Acta 255, 247–264. https://doi.org/10.1016/j.gca.2019.04.012

Greber, N.D., Dauphas, N., Bekker, A., Ptáček, M.P., Bindeman, I.N., Hofmann, A., 2017. Titanium isotopic evidence for felsic crust and plate tectonics 3.5 billion years ago. Science 357, 1271–1274. https://doi.org/10.1126/science.aan8086

Greber, N.D., Pettke, T., Vilela, N., Lanari, P., Dauphas, N., 2021. Titanium isotopic compositions of bulk rocks and mineral separates from the Kos magmatic suite: Insights into fractional crystallization and magma mixing processes. Chemical Geology 578, 120303. https://doi.org/10.1016/j.chemgeo.2021.120303

Grove, T.L., Elkins-Tanton, L.T., Parman, S.W., Chatterjee, N., Müntener, O., Gaetani, G.A., 2003. Fractional crystallization and mantle-melting controls on calc-alkaline differentiation trends. Contributions to Mineralogy and Petrology 145, 515–533. https://doi.org/10.1007/s00410-003-0448-z

Groves, D.I., Santosh, M., 2021. Craton and thick lithosphere margins: The sites of giant mineral deposits and mineral provinces. Gondwana Research 100, 195–222. https://doi.org/10.1016/j.gr.2020.06.008

Guillot, S., Hattori, K., 2013. Serpentinites: Essential Roles in Geodynamics, Arc Volcanism, Sustainable Development, and the Origin of Life. Elements 9, 95–98. https://doi.org/10.2113/gselements.9.2.25

Gumsley, A.P., Chamberlain, K.R., Bleeker, W., Söderlund, U., de Kock, M.O., Larsson, E.R., Bekker, A., 2017. Timing and tempo of the Great Oxidation Event. Proceedings of the National Academy of Sciences 114, 1811–1816. https://doi.org/10.1073/pnas.1608824114

Gunawardana, P.M., Chowdhury, P., Morra, G., Cawood, P.A., 2024. Correlating mantle cooling with tectonic transitions on early Earth. Geology 52, 230-234. https://doi.org/10.1130/G51874.1

Guo, R., Liu, S., Gong, E., Wang, W., Wang, M., Fu, J., Qin, T., 2017. Arc-generated metavolcanic rocks in the Anshan–Benxi greenstone belt, North China Craton:

Constraints from geochemistry and zircon U–Pb–Hf isotopic systematics. Precambrian Research, Archean to Proterozoic Evolution of the North China Craton 303, 228–250. https://doi.org/10.1016/j.precamres.2017.03.028

Halla, J., 2005. Late Archean high-Mg granitoids (sanukitoids) in the southern Karelian domain, eastern Finland: Pb and Nd isotopic constraints on crust−mantle interactions. Lithos, Geodynamic Controls on Adakite, TTG and Sanukitoid Genesis: Implications for Models of Crust Formation 79, 161–178. https://doi.org/10.1016/j.lithos.2004.05.007

Halla, J., van Hunen, J., Heilimo, E., Hölttä, P., 2009. Geochemical and numerical constraints on Neoarchean plate tectonics. Precambrian Research 174, 155–162. https://doi.org/10.1016/j.precamres.2009.07.008

Halse, H.R., 2014. Using synchrotron radiation to determine the oxidation state of uranium in magmas (PhD Thesis). Imperial College London.

Hao, J., Knoll, A.H., Huang, F., Schieber, J., Hazen, R.M., Daniel, I., 2020. Cycling phosphorus on the Archean Earth: Part II. Phosphorus limitation on primary production in Archean ecosystems. Geochimica et Cosmochimica Acta 280, 360–377. https://doi.org/10.1016/j.gca.2020.04.005

Hartnady, M.I.H., Johnson, T.E., Schorn, S., Hugh Smithies, R., Kirkland, C.L., Richardson, S.H., 2022. Fluid processes in the early Earth and the growth of continents. Earth and Planetary Science Letters 594, 117695. https://doi.org/10.1016/j.epsl.2022.117695

Hawkesworth, C.J., Cawood, P.A., Dhuime, B., 2020. The Evolution of the Continental Crust and the Onset of Plate Tectonics. Frontiers in Earth Science 8, 326. https://doi.org/10.3389/feart.2020.00326

Hawkesworth, C.J., Cawood, P.A., Dhuime, B., Kemp, T., 2024. Tectonic processes and the evolution of the continental crust. Journal of the Geological Society 181, jgs2024-027. https://doi.org/10.1144/jgs2024-027

He, X., Ma, J., Wei, G., Wang, Z., Zhang, L., Zeng, T., Zhang, Z., 2022. Mass-dependent fractionation of titanium stable isotopes during intensive weathering of basalts. Earth and Planetary Science Letters 579, 117347. https://doi.org/10.1016/j.epsl.2021.117347

He, X., Ma, J., Wei, G., Zhang, L., Wang, Z., Wang, Q., 2020. A new procedure for titanium separation in geological samples for 49 Ti/ 47 Ti ratio measurement

by MC-ICP-MS. Journal of Analytical Atomic Spectrometry 35, 100–106. https://doi.org/10.1039/C9JA00316A

He, Z., Clarkson, M.O., Andersen, M.B., Archer, C., Sweere, T.C., Kraal, P., Guthauser, A., Huang, F., Vance, D., 2021. Temporally and spatially dynamic redox conditions on an upwelling margin: The impact on coupled sedimentary Mo and U isotope systematics, and implications for the Mo-U paleoredox proxy. Geochimica et Cosmochimica Acta 309, 251–271. https://doi.org/10.1016/j.gca.2021.06.024

Heilimo, E., Halla, J., Andersen, T., Huhma, H., 2013. Neoarchean crustal recycling and mantle metasomatism: Hf–Nd–Pb–O isotope evidence from sanukitoids of the Fennoscandian shield. Precambrian Research 228, 250–266. https://doi.org/10.1016/j.precamres.2012.01.015

Heilimo, E., Halla, J., Hölttä, P., 2010. Discrimination and origin of the sanukitoid series: Geochemical constraints from the Neoarchean western Karelian Province (Finland). Lithos 115, 27–39. https://doi.org/10.1016/j.lithos.2009.11.001

Heilimo, E., Halla, J., Huhma, H., 2011. Single-grain zircon U–Pb age constraints of the western and eastern sanukitoid zones in the Finnish part of the Karelian Province. Lithos 121, 87–99. https://doi.org/10.1016/j.lithos.2010.10.006

Hernández-Montenegro, J.D., Palin, R.M., Zuluaga, C.A., Hernández-Uribe, D., 2021. Archean continental crust formed by magma hybridization and voluminous partial melting. Sci Rep 11, 5263. https://doi.org/10.1038/s41598-021-84300-y

Hernández-Uribe, D., Hernández-Montenegro, J.D., Cone, K.A., Palin, R.M., 2019. Oceanic slab-top melting during subduction: Implications for trace-element recycling and adakite petrogenesis. Geology 48, 216–220. https://doi.org/10.1130/G46835.1

Herzberg, C., Condie, K., Korenaga, J., 2010. Thermal history of the Earth and its petrological expression. Earth and Planetary Science Letters 292, 79–88. https://doi.org/10.1016/j.epsl.2010.01.022

Hiess, J., Condon, D.J., McLean, N., Noble, S.R., 2012. 238U/235U Systematics in Terrestrial Uranium-Bearing Minerals. Science 335, 1610–1614. https://doi.org/10.1126/science.1215507

Hillaire-Marcel, C., Aksu, A., Causse, C., Vernal, A. de, Ghaleb, B., 1990. Response of Th/U in deep Labrador Sea sediments (ODP Site 646 to changes in sedimentation rates and paleoproductivities. Geology 18, 162–165. https://doi.org/10.1130/0091-7613(1990)018<0162:ROTUID>2.3.CO;2

Hinojosa, J.L., Stirling, C.H., Reid, M.R., Moy, C.M., Wilson, G.S., 2016. Trace metal cycling and 238U/235U in New Zealand's fjords: Implications for reconstructing global paleoredox conditions in organic-rich sediments. Geochimica et Cosmochimica Acta 179, 89–109. https://doi.org/10.1016/j.gca.2016.02.006

Hoare, L., 2021. Mechanics and applications of titanium isotope fractionation in terrestrial magmas (PhD Thesis). Cardiff University.

Hoare, L., Klaver, M., Muir, D.D., Klemme, S., Barling, J., Parkinson, I.J., Johan Lissenberg, C., Millet, M.-A., 2022. Empirical and Experimental Constraints on Fe-Ti Oxide-Melt Titanium Isotope Fractionation Factors. Geochimica et Cosmochimica Acta 326, 253-272. https://doi.org/10.1016/j.gca.2022.02.011

Hoare, L., Klaver, M., Saji, N.S., Gillies, J., Parkinson, I.J., Lissenberg, C.J., Millet, M.-A., 2020. Melt chemistry and redox conditions control titanium isotope fractionation during magmatic differentiation. Geochimica et Cosmochimica Acta 282, 38–54. https://doi.org/10.1016/j.gca.2020.05.015

Hoare, L., Rzehak, L.J.A., Kommescher, S., Jansen, M., Rosing, M.T., Nagel, T., Millet, M.-A., Hoffmann, J.E., Fonseca, R.O.C., 2023. Titanium isotope constraints on the mafic sources and geodynamic origins of Archean crust. Geochemical Perspectives Letters 28, 37–42. https://doi.org/10.7185/geochemlet.2340

Hoffmann, J.E., Münker, C., Næraa, T., Rosing, M.T., Herwartz, D., Garbe-Schönberg, D., Svahnberg, H., 2011. Mechanisms of Archean crust formation inferred from high-precision HFSE systematics in TTGs. Geochimica et Cosmochimica Acta 75, 4157–4178. https://doi.org/10.1016/j.gca.2011.04.027

Holder, R.M., Viete, D.R., Brown, M., Johnson, T.E., 2019. Metamorphism and the evolution of plate tectonics. Nature 572, 378–381. https://doi.org/10.1038/s41586-019-1462-2

Holland, H.D., 2009. Why the atmosphere became oxygenated: A proposal. Geochimica et Cosmochimica Acta 73, 5241–5255. https://doi.org/10.1016/j.gca.2009.05.070

Holland, H.D., 2006. The oxygenation of the atmosphere and oceans. Philosophical Transactions of the Royal Society B: Biological Sciences 361, 903-915. https://doi.org/10.1098/rstb.2006.1838

Holland, H.D., 2002. Volcanic gases, black smokers, and the great oxidation event. Geochimica et Cosmochimica Acta 66, 3811–3826. https://doi.org/10.1016/S0016-7037(02)00950-X

Holmden, C., Amini, M., Francois, R., 2015. Uranium isotope fractionation in Saanich Inlet: A modern analog study of a paleoredox tracer. Geochimica et Cosmochimica Acta 153, 202–215. https://doi.org/10.1016/j.gca.2014.11.012

Holycross, M., Cottrell, E., 2023. Garnet crystallization does not drive oxidation at arcs. Science 380, 506–509. https://doi.org/10.1126/science.ade3418

Hoskin, P.W.O., Schaltegger, U., 2003. The Composition of Zircon and Igneous and Metamorphic Petrogenesis. Reviews in Mineralogy and Geochemistry 53, 27–62. https://doi.org/10.2113/0530027

Hu, F., Jiang, H., Wan, B., Ducea, M.N., Gao, L., Wu, F.-Y., 2024. Latitude-dependent oxygen fugacity in arc magmas. Nat Commun 15, 6050. https://doi.org/10.1038/s41467-024-50337-6

Huang, G., Mitchell, R.N., Palin, R.M., Spencer, C.J., Guo, J., 2022. Barium content of Archaean continental crust reveals the onset of subduction was not global. Nat Commun 13, 6553. https://doi.org/10.1038/s41467-022-34343-0

Hynes, A., 2014. How feasible was subduction in the Archean? Can. J. Earth Sci. 51, 286–296. https://doi.org/10.1139/cjes-2013-0111

Iacovino, K., Guild, M.R., Till, C.B., 2020. Aqueous fluids are effective oxidizing agents of the mantle in subduction zones. Contrib Mineral Petrol 175, 36. https://doi.org/10.1007/s00410-020-1673-4

Iizuka, T., Amelin, Y., Kaltenbach, A., Koefoed, P., Stirling, C.H., 2014. U–Pb systematics of the unique achondrite Ibitira: Precise age determination and petrogenetic implications. Geochimica et Cosmochimica Acta 132, 259–273. https://doi.org/10.1016/j.gca.2014.02.017

Inglis, E.C., Creech, J.B., Deng, Z., Moynier, F., 2018. High-precision zirconium stable isotope measurements of geological reference materials as measured by double-spike MC-ICPMS. Chemical Geology 493, 544–552. https://doi.org/10.1016/j.chemgeo.2018.07.007

Jagoutz, O., Schmidt, M.W., Enggist, A., Burg, J.-P., Hamid, D., Hussain, S., 2013. TTG-type plutonic rocks formed in a modern arc batholith by hydrous fractionation in the lower arc crust. Contrib Mineral Petrol 166, 1099–1118. https://doi.org/10.1007/s00410-013-0911-4

Jahn, B.-M., Glikson, A.Y., Peucat, J.J., Hickman, A.H., 1981. REE geochemistry and isotopic data of Archean silicic volcanics and granitoids from the Pilbara Block, Western Australia: implications for the early crustal evolution. Geochimica et Cosmochimica Acta 45, 1633–1652. https://doi.org/10.1016/S0016-7037(81)80002-6

James, H.L., 1983. Chapter 12 Distribution of Banded Iron-Formation in Space and Time, in: Trendall, A.F., Morris, R.C. (Eds.), Developments in Precambrian Geology, Iron-Formation Facts and Problems. Elsevier, pp. 471–490. https://doi.org/10.1016/S0166-2635(08)70053-7

Jayananda, M., Martin, H., Peucat, J.-J., Mahabaleswar, B., 1995. Late Archaean crust-mantle interactions: geochemistry of LREE-enriched mantle derived magmas. Example of the Closepet batholith, southern India. Contr. Mineral. and Petrol. 119, 314–329. https://doi.org/10.1007/BF00307290

Jayananda, M., Moyen, J.-F., Martin, H., Peucat, J.-J., Auvray, B., Mahabaleswar, B., 2000. Late Archaean (2550–2520 Ma) juvenile magmatism in the Eastern Dharwar craton, southern India: constraints from geochronology, Nd–Sr isotopes and whole rock geochemistry. Precambrian Research 99, 225–254. https://doi.org/10.1016/S0301-9268(99)00063-7

Jiang, X., Chen, X., Hoare, L., Schertl, H.-P., Palmer, M.R., Zhang, W., Cai, P., Liu, H., Zheng, Y., Gao, S., 2024. Substantial in situ Ti isotope variations in rutile record source and fluid evolution of porphyry copper mineralization systems. GSA Bulletin 137, 1763-1776. https://doi.org/10.1130/B37798.1

Johnson, A.C., Aarons, S.M., Dauphas, N., Nie, N.X., Zeng, H., Helz, R.T., Romaniello, S.J., Anbar, A.D., 2019. Titanium isotopic fractionation in Kilauea Iki lava lake driven by oxide crystallization. Geochimica et Cosmochimica Acta 264, 180–190. https://doi.org/10.1016/j.gca.2019.08.022

Johnson, A.C., Zhang, Z.J., Dauphas, N., Rudnick, R.L., Foden, J.D., Toc, M., 2023. Redox and mineral controls on Fe and Ti isotopic fractionations during calc-alkaline magmatic differentiation. Geochimica et Cosmochimica Acta 355, 1–12. https://doi.org/10.1016/j.gca.2023.06.016

Johnson, M.C., Plank, T., 2000. Dehydration and melting experiments constrain the fate of subducted sediments. Geochemistry, Geophysics, Geosystems 1. https://doi.org/10.1029/1999GC000014

Johnson, T.E., Brown, M., Gardiner, N.J., Kirkland, C.L., Smithies, R.H., 2017. Earth's first stable continents did not form by subduction. Nature 543, 239–242. https://doi.org/10.1038/nature21383

Johnson, T.E., Brown, M., Kaus, B.J.P., VanTongeren, J.A., 2014. Delamination and recycling of Archaean crust caused by gravitational instabilities. Nature Geosci 7, 47–52. https://doi.org/10.1038/ngeo2019

Johnson, T.E., Kirkland, C.L., Gardiner, N.J., Brown, M., Smithies, R.H., Santosh, M., 2019. Secular change in TTG compositions: Implications for the evolution of Archaean geodynamics. Earth and Planetary Science Letters 505, 65–75. https://doi.org/10.1016/j.epsl.2018.10.022

Kamber, B.S., Ewart, A., Collerson, K.D., Bruce, M.C., McDonald, G.D., 2002. Fluid-mobile trace element constraints on the role of slab melting and implications for Archaean crustal growth models. Contrib Mineral Petrol 144, 38–56. https://doi.org/10.1007/s00410-002-0374-5

Kanzaki, Y., Murakami, T., 2016. Estimates of atmospheric O2 in the Paleoproterozoic from paleosols. Geochimica et Cosmochimica Acta 174, 263–290. https://doi.org/10.1016/j.gca.2015.11.022

Kasting, J.F., 2013. What caused the rise of atmospheric O2? Chemical Geology, Special Issue dedicated to H.D. Holland: Evolution of the atmosphere and ocean through time 362, 13–25. https://doi.org/10.1016/j.chemgeo.2013.05.039

Kaufmann, A.K.C., Pettke, T., Wille, M., 2021. Molybdenum isotope fractionation at upper-crustal magmatic-hydrothermal conditions. Chemical Geology 578, 120319. https://doi.org/10.1016/j.chemgeo.2021.120319

Keatley, A.C., Dunne, J.A., Martin, T.L., Nita, D.C., Andersen, M.B., Scott, T.B., Richards, D.A., Awbery, R.P., 2021. Uranium isotope variation within vein-type uranium ore deposits. Applied Geochemistry 131, 104977. https://doi.org/10.1016/j.apgeochem.2021.104977

Keller, C.B., Harrison, T.M., 2020. Constraining crustal silica on ancient Earth. Proceedings of the National Academy of Sciences 117, 21101–21107. https://doi.org/10.1073/pnas.2009431117

Keller, C.B., Schoene, B., 2018. Plate tectonics and continental basaltic geochemistry throughout Earth history. Earth and Planetary Science Letters 481, 290–304. https://doi.org/10.1016/j.epsl.2017.10.031

Keller, C.B., Schoene, B., 2012. Statistical geochemistry reveals disruption in secular lithospheric evolution about 2.5 Gyr ago. Nature 485, 490–493. https://doi.org/10.1038/nature11024

Kelley, K.A., Cottrell, E., 2009. Water and the Oxidation State of Subduction Zone Magmas. Science 325, 605–607. https://doi.org/10.1126/science.1174156

Kendrick, J., Duguet, M., Yakymchuk, C., 2021. Diversification of Archean tonalite-trondhjemite-granodiorite suites in a mushy middle crust. Geology 50, 76–80. https://doi.org/10.1130/G49287.1

Kessel, R., Ulmer, P., Pettke, T., Schmidt, M.W., Thompson, A.B., 2005. The water–basalt system at 4 to 6 GPa: Phase relations and second critical endpoint in a K-free eclogite at 700 to 1400 °C. Earth and Planetary Science Letters 237, 873–892. https://doi.org/10.1016/j.epsl.2005.06.018

King, E.M., Valley, J.W., Davis, D.W., Edwards, G.R., 1998. Oxygen isotope ratios of Archean plutonic zircons from granite–greenstone belts of the Superior Province: indicator of magmatic source. Precambrian Research 92, 365–387. https://doi.org/10.1016/S0301-9268(98)00082-5

Kipp, M.A., Li, H., Ellwood, M.J., John, S.G., Middag, R., Adkins, J.F., Tissot, F.L.H., 2022. 238U, 235U and 234U in seawater and deep-sea corals: A high-precision reappraisal. Geochimica et Cosmochimica Acta 336, 231–248. https://doi.org/10.1016/j.gca.2022.09.018

Klaver, M., Coath, C.D., 2019. Obtaining Accurate Isotopic Compositions with the Double Spike Technique: Practical Considerations. Geostandards and Geoanalytical Research 43, 5–22. https://doi.org/10.1111/ggr.12248

Klaver, M., MacLennan, S.A., Ibañez-Mejia, M., Tissot, F.L.H., Vroon, P.Z., Millet, M.-A., 2021. Reliability of detrital marine sediments as proxy for continental crust composition: The effects of hydrodynamic sorting on Ti and Zr isotope systematics. Geochimica et Cosmochimica Acta 310, 221–239. https://doi.org/10.1016/j.gca.2021.05.030

Klaver, M., Yogodzinski, G., Albert, C., Camejo-Harry, M., Elburg, M., Hoernle, K., Macpherson, C., Nowell, G., Rushmer, T., Williams, H., Millet, M.-A., 2024.

Widespread slab melting in modern subduction zones. Earth and Planetary Science Letters 626, 118544. https://doi.org/10.1016/j.epsl.2023.118544

Kleinhanns, I.C., Kramers, J.D., Kamber, B.S., 2003. Importance of water for Archaean granitoid petrology: a comparative study of TTG and potassic granitoids from Barberton Mountain Land, South Africa. Contributions to Mineralogy and Petrology 145, 377–389. https://doi.org/10.1007/s00410-003-0459-9

Kocks, H., Strachan, R.A., Evans, J.A., Fowler, M., 2014. Contrasting magma emplacement mechanisms within the Rogart igneous complex, NW Scotland, record the switch from regional contraction to strike-slip during the Caledonian orogeny. Geological Magazine 151, 899–915. https://doi.org/10.1017/S0016756813000940

Kommescher, S., Fonseca, R.O.C., Kurzweil, F., Thiemens, M.M., Münker, C., Sprung, P., 2020. Unravelling lunar mantle source processes via the Ti isotope composition of lunar basalts. Geochem. Persp. Let. 13, 13–18. https://doi.org/10.7185/geochemlet.2007

Konhauser, K.O., Pecoits, E., Lalonde, S.V., Papineau, D., Nisbet, E.G., Barley, M.E., Arndt, N.T., Zahnle, K., Kamber, B.S., 2009. Oceanic nickel depletion and a methanogen famine before the Great Oxidation Event. Nature 458, 750–753. https://doi.org/10.1038/nature07858

Korenaga, J., 2021. Hadean geodynamics and the nature of early continental crust. Precambrian Research 359, 106178. https://doi.org/10.1016/j.precamres.2021.106178

Korenaga, J., 2008. Urey ratio and the structure and evolution of Earth's mantle. Reviews of Geophysics 46. https://doi.org/10.1029/2007RG000241

Koto, B., 1916. On the Volcanoes of Japan V. The Journal of the Geological Society of Japan 23, 95–127. https://doi.org/10.5575/geosoc.23.279_95

Kovalenko, A., Clemens, J.D., Savatenkov, V., 2005. Petrogenetic constraints for the genesis of Archaean sanukitoid suites: geochemistry and isotopic evidence from Karelia, Baltic Shield. Lithos, Geodynamic Controls on Adakite, TTG and Sanukitoid Genesis: Implications for Models of Crust Formation 79, 147–160. https://doi.org/10.1016/j.lithos.2004.05.006

Krause, A.J., Mills, B.J.W., Merdith, A.S., Lenton, T.M., Poulton, S.W., 2022. Extreme variability in atmospheric oxygen levels in the late Precambrian. Science Advances 8, eabm8191. https://doi.org/10.1126/sciadv.abm8191

Krogstad, E.J., Hanson, G.N., Rajamani, V., 1991. U-Pb Ages of Zircon and Sphene for Two Gneiss Terranes Adjacent to the Kolar Schist Belt, South India: Evidence for Separate Crustal Evolution Histories. The Journal of Geology 99, 801–815. https://doi.org/10.1086/629553

Kump, L.R., Barley, M.E., 2007. Increased subaerial volcanism and the rise of atmospheric oxygen 2.5 billion years ago. Nature 448, 1033–1036. https://doi.org/10.1038/nature06058

Langmuir, D., 1978. Uranium solution-mineral equilibria at low temperatures with applications to sedimentary ore deposits. Geochimica et Cosmochimica Acta 42, 547–569. https://doi.org/10.1016/0016-7037(78)90001-7

Large, R.R., Mukherjee, I., Zhukova, I., Corkrey, R., Stepanov, A., Danyushevsky, L.V., 2018. Role of upper-most crustal composition in the evolution of the Precambrian ocean–atmosphere system. Earth and Planetary Science Letters 487, 44–53. https://doi.org/10.1016/j.epsl.2018.01.019

Lau, K.V., Hancock, L.G., Severmann, S., Kuzminov, A., Cole, D.B., Behl, R.J., Planavsky, N.J., Lyons, T.W., 2022. Variable local basin hydrography and productivity control the uranium isotope paleoredox proxy in anoxic black shales. Geochimica et Cosmochimica Acta 317, 433–456. https://doi.org/10.1016/j.gca.2021.10.011

Lau, K.V., Macdonald, F.A., Maher, K., Payne, J.L., 2017. Uranium isotope evidence for temporary ocean oxygenation in the aftermath of the Sturtian Snowball Earth. Earth and Planetary Science Letters 458, 282–292. https://doi.org/10.1016/j.epsl.2016.10.043

Lau, K.V., Maher, K., Altiner, D., Kelley, B.M., Kump, L.R., Lehrmann, D.J., Silva-Tamayo, J.C., Weaver, K.L., Yu, M., Payne, J.L., 2016. Marine anoxia and delayed Earth system recovery after the end-Permian extinction. Proceedings of the National Academy of Sciences 113, 2360–2365. https://doi.org/10.1073/pnas.1515080113

Laurent, O., 2012. Les changements géodynamiques à la transition Archéen-Protérozoïque : étude des granitoïdes de la marge Nord du craton du

Kaapvaal (Afrique du Sud) (PhD Thesis). Université Blaise Pascal - Clermont-Ferrand II.

Laurent, O., Björnsen, J., Wotzlaw, J.-F., Bretscher, S., Pimenta Silva, M., Moyen, J.-F., Ulmer, P., Bachmann, O., 2020. Earth's earliest granitoids are crystal-rich magma reservoirs tapped by silicic eruptions. Nat. Geosci. 13, 163–169. https://doi.org/10.1038/s41561-019-0520-6

Laurent, O., Doucelance, R., Martin, H., Moyen, J.-F., 2013. Differentiation of the late-Archaean sanukitoid series and some implications for crustal growth: Insights from geochemical modelling on the Bulai pluton, Central Limpopo Belt, South Africa. Precambrian Research, Precambrian Accretionary Orogens 227, 186–203. https://doi.org/10.1016/j.precamres.2012.07.004

Laurent, O., Martin, H., Doucelance, R., Moyen, J.-F., Paquette, J.-L., 2011. Geochemistry and petrogenesis of high-K "sanukitoids" from the Bulai pluton, Central Limpopo Belt, South Africa: Implications for geodynamic changes at the Archaean–Proterozoic boundary. Lithos, Secular variations in magmatism and tectonic implications 123, 73–91. https://doi.org/10.1016/j.lithos.2010.12.009

Laurent, O., Martin, H., Moyen, J.F., Doucelance, R., 2014a. The diversity and evolution of late-Archean granitoids: Evidence for the onset of "modern-style" plate tectonics between 3.0 and 2.5Ga. Lithos 205, 208–235. https://doi.org/10.1016/j.lithos.2014.06.012

Laurent, O., Rapopo, M., Stevens, G., Moyen, J.F., Martin, H., Doucelance, R., Bosq, C., 2014b. Contrasting petrogenesis of Mg–K and Fe–K granitoids and implications for post-collisional magmatism: Case study from the Late-Archean Matok pluton (Pietersburg block, South Africa). Lithos 196–197, 131–149. https://doi.org/10.1016/j.lithos.2014.03.006

Laurent, O., Vander Auwera, J., Bingen, B., Bolle, O., Gerdes, A., 2019. Building up the first continents: Mesoarchean to Paleoproterozoic crustal evolution in West Troms, Norway, inferred from granitoid petrology, geochemistry and zircon U-Pb/Lu-Hf isotopes. Precambrian Research 321, 303–327. https://doi.org/10.1016/j.precamres.2018.12.020

Laurie, A., Stevens, G., 2012. Water-present eclogite melting to produce Earth's early felsic crust. Chemical Geology 314–317, 83–95. https://doi.org/10.1016/j.chemgeo.2012.05.001

Laurie, A., Stevens, G., van Hunen, J., 2013. The end of continental growth by TTG magmatism. Terra Nova 25, 130–136. https://doi.org/10.1111/ter.12015

Lee, C.-T.A., Yeung, L.Y., McKenzie, N.R., Yokoyama, Y., Ozaki, K., Lenardic, A., 2016. Two-step rise of atmospheric oxygen linked to the growth of continents. Nature Geosci 9, 417–424. https://doi.org/10.1038/ngeo2707

Lefebvre, P., Gourgiotis, A., Mangeret, A., Sabatier, P., Le Pape, P., Diez, O., Louvat, P., Menguy, N., Merrot, P., Baya, C., Zebracki, M., Blanchart, P., Malet, E., Jézéquel, D., Reyss, J.-L., Bargar, J.R., Gaillardet, J., Cazala, C., Morin, G., 2021. Diagenetic formation of uranium-silica polymers in lake sediments over 3,300 years. Proceedings of the National Academy of Sciences 118, e2021844118. https://doi.org/10.1073/pnas.2021844118

Lefebvre, P., Noël, V., Lau, K.V., Jemison, N.E., Weaver, K.L., Williams, K.H., Bargar, J.R., Maher, K., 2019. Isotopic Fingerprint of Uranium Accumulation and Redox Cycling in Floodplains of the Upper Colorado River Basin. Environ. Sci. Technol. 53, 3399–3409. https://doi.org/10.1021/acs.est.8b05593

Lei, K., Zhang, Q., Liu, Y., Lu, K., Wu, L.-G., He, S., Li, X.-H., 2023. Heavy silicon and oxygen isotope signatures of TTGs formed in distinct tectonic settings. Precambrian Research 397, 107202. https://doi.org/10.1016/j.precamres.2023.107202

Leitzke, F.P., Fonseca, R.O.C., Göttlicher, J., Steininger, R., Jahn, S., Prescher, C., Lagos, M., 2018. Ti K-edge XANES study on the coordination number and oxidation state of Titanium in pyroxene, olivine, armalcolite, ilmenite, and silicate glass during mare basalt petrogenesis. Contrib Mineral Petrol 173, 103. https://doi.org/10.1007/s00410-018-1533-7

Lenardic, A., 2018. The diversity of tectonic modes and thoughts about transitions between them. Philosophical Transactions of the Royal Society A: Mathematical, Physical and Engineering Sciences 376, 20170416. https://doi.org/10.1098/rsta.2017.0416

Leong, J.A.M., Ely, T., Shock, E.L., 2021. Decreasing extents of Archean serpentinization contributed to the rise of an oxidized atmosphere. Nat Commun 12, 7341. https://doi.org/10.1038/s41467-021-27589-7

Li, C.-H., 2022. Late veneer and the origins of volatiles of Earth. Acta Geochim 41, 650–664. https://doi.org/10.1007/s11631-021-00517-8

Li, H., Tissot, F.L.H., 2023. UID: The uranium isotope database. Chemical Geology 618, 121221. https://doi.org/10.1016/j.chemgeo.2022.121221

Li, J., Liu, S.-A., Ma, H., Wu, C., Zhu, D.-C., Liu, J., 2024. Pervasive Neoarchean melting of subducted sediments generating sanukitoid and associated magmatism in the North China Craton, with implications for the operation of plate tectonics. GSA Bulletin 136, 3121–3136. https://doi.org/10.1130/B37279.1

Li, J., Tang, S., Zhu, X., Ma, J., Zhao, X., 2022. Titanium Isotope Analysis of Igneous Reference Materials using a Double-spike MC-ICP-MS Method. Acta Geologica Sinica - English Edition 96, 517–524. https://doi.org/10.1111/1755-6724.14728

Li, R.-Y., Ke, S., Li, S., Song, S., Wang, C., Liu, C., 2020. Origins of two types of Archean potassic granite constrained by Mg isotopes and statistical geochemistry: Implications for continental crustal evolution. Lithos 368–369, 105570. https://doi.org/10.1016/j.lithos.2020.105570

Li, Z.-X., Zhang, S.-B., Zheng, Y.-F., Hanchar, J.M., Gao, P., Lu, Y.-M., Su, K., Sun, F.-Y., Liang, T., 2021. Crustal thickening and continental formation in the Neoarchean: Geochemical records by granitoids from the Taihua Complex in the North China Craton. Precambrian Research 367, 106446. https://doi.org/10.1016/j.precamres.2021.106446

Liou, P., Guo, J., 2019. Generation of Archaean TTG Gneisses Through Amphibole-Dominated Fractionation. Journal of Geophysical Research: Solid Earth 124, 3605–3619. https://doi.org/10.1029/2018JB017024

Liou, P., Wang, Z., Mitchell, R.N., Doucet, L.S., Li, M., Guo, J., Zhai, M., 2022. Fe isotopic evidence that "high pressure" TTGs formed at low pressure. Earth and Planetary Science Letters 592, 117645. https://doi.org/10.1016/j.epsl.2022.117645

Liu, C.-Y.-H., Wu, Y.-B., Zhang, W.-X., Zhou, G.-Y., Chang, H., Hu, P., 2022. Petrogenesis of Paleozoic high BaSr granitoids from the Qinling orogen, Central China: Implications to the formation of Archean sanukitoids and TTGs. Lithos 428–429, 106814. https://doi.org/10.1016/j.lithos.2022.106814

Liu, H., Wang, W., Cawood, P.A., Mu, Y., Yao, J., Li, J., Guo, L., 2020. Synchronous late Neoarchean Na- and K-rich granitoid magmatism at an active continental

margin in the Eastern Liaoning Province of North China Craton. Lithos 376–377, 105770. https://doi.org/10.1016/j.lithos.2020.105770

Liu, H., Zartman, R.E., Ireland, T.R., Sun, W., 2019. Global atmospheric oxygen variations recorded by Th/U systematics of igneous rocks. Proceedings of the National Academy of Sciences 116, 18854–18859. https://doi.org/10.1073/pnas.1902833116

Liu, J., Touboul, M., Ishikawa, A., Walker, R.J., Graham Pearson, D., 2016. Widespread tungsten isotope anomalies and W mobility in crustal and mantle rocks of the Eoarchean Saglek Block, northern Labrador, Canada: Implications for early Earth processes and W recycling. Earth and Planetary Science Letters 448, 13–23. https://doi.org/10.1016/j.epsl.2016.05.001

Liu, S., Bao, H., Sun, G., Wang, W., Fu, J., Gao, L., Guo, R., Hu, Y., 2022. Archean crust-mantle geodynamic regimes: A review. Geosystems and Geoenvironment 1, 100063. https://doi.org/10.1016/j.geogeo.2022.100063

Livermore, B.D., Connelly, J.N., Moynier, F., Bizzarro, M., 2018. Evaluating the robustness of a consensus 238U/235U value for U-Pb geochronology. Geochimica et Cosmochimica Acta 237, 171–183. https://doi.org/10.1016/j.gca.2018.06.014

Lobach-Zhuchenko, S.B., Rollinson, H., Chekulaev, V.P., Savatenkov, V.M., Kovalenko, A.V., Martin, H., Guseva, N.S., Arestova, N.A., 2008. Petrology of a Late Archaean, Highly Potassic, Sanukitoid Pluton from the Baltic Shield: Insights into Late Archaean Mantle Metasomatism. Journal of Petrology 49, 393–420. https://doi.org/10.1093/petrology/egm084

Lobach-Zhuchenko, S.B., Rollinson, H.R., Chekulaev, V.P., Arestova, N.A., Kovalenko, A.V., Ivanikov, V.V., Guseva, N.S., Sergeev, S.A., Matukov, D.I., Jarvis, K.E., 2005. The Archaean sanukitoid series of the Baltic Shield: geological setting, geochemical characteristics and implications for their origin. Lithos 79, 107–128. https://doi.org/10.1016/j.lithos.2004.04.052

Longstaffe, F.J., McNutt, R.H., Schwarcz, H.P., 1980. Geochemistry of Archean meta-igneous rocks, Lake Despair area, Wabigoon Subprovince, northwestern Ontario. Can. J. Earth Sci. 17, 1046–1063. https://doi.org/10.1139/e80-104

Lourenço, D.L., Rozel, A.B., Ballmer, M.D., Tackley, P.J., 2020. Plutonic-Squishy Lid: A New Global Tectonic Regime Generated by Intrusive Magmatism on

Earth-Like Planets. Geochemistry, Geophysics, Geosystems 21, e2019GC008756. https://doi.org/10.1029/2019GC008756

Lowrey, J.R., Smithies, R.H., Champion, D.C., Cassidy, K.F., 2023. Systematic classification of Yilgarn Craton granitic rocks (Record 2023/12). Geological Survey of Western Australia, Perth, Australia.

Luo, G., Ono, S., Beukes, N.J., Wang, D.T., Xie, S., Summons, R.E., 2016. Rapid oxygenation of Earth's atmosphere 2.33 billion years ago. Science Advances 2, e1600134. https://doi.org/10.1126/sciadv.1600134

Luo, Y., Hughes, J.M., Rakovan, J., Pan, Y., 2009. Site preference of U and Th in Cl, F, and Sr apatites. American Mineralogist 94, 345–351. https://doi.org/10.2138/am.2009.3026

Lyons, T.W., Gill, B.C., 2010. Ancient Sulfur Cycling and Oxygenation of the Early Biosphere. Elements 6, 93–99. https://doi.org/10.2113/gselements.6.2.93

Lyons, T.W., Reinhard, C.T., Planavsky, N.J., 2014. The rise of oxygen in Earth's early ocean and atmosphere. Nature 506, 307–315. https://doi.org/10.1038/nature13068

Ma, X., Guo, J., Liu, F., Qian, Q., Fan, H., 2013. Zircon U–Pb ages, trace elements and Nd–Hf isotopic geochemistry of Guyang sanukitoids and related rocks: Implications for the Archean crustal evolution of the Yinshan Block, North China Craton. Precambrian Research 230, 61–78. https://doi.org/10.1016/j.precamres.2013.02.001

Mahbubul Ameen, S.M., Wilde, S.A., 2018. Multiple sources for Archean granitoids in the Yalgoo area, Yilgarn Craton, Western Australia: Geochemical and isotopic evidence. Precambrian Research 314, 76–110. https://doi.org/10.1016/j.precamres.2018.05.027

Makino, K., Tomita, K., 1989. Cation distribution in the octahedral sites of hornblendes. American Mineralogist 74, 1097–1105.

Mandl, M.B., 2019. Titanium isotope fractionation on the Earth and Moon: Constraints on magmatic processes and Moon formation (PhD Thesis). ETH Zurich. https://doi.org/10.3929/ETHZ-B-000351171

Maréchal, C.N., Télouk, P., Albarède, F., 1999. Precise analysis of copper and zinc isotopic compositions by plasma-source mass spectrometry. Chemical Geology 156, 251–273. https://doi.org/10.1016/S0009-2541(98)00191-0

Marenco, P.J., Martin, K.R., Marenco, K.N., Barber, D.C., 2016. Increasing global ocean oxygenation and the Ordovician Radiation: Insights from Th/U of carbonates from the Ordovician of western Utah. Palaeogeography, Palaeoclimatology, Palaeoecology, The Ordovician Revolution: Co-Evolution of Climate and the Biosphere 458, 77–84. https://doi.org/10.1016/j.palaeo.2016.05.014

Marimon, R.S., Hawkesworth, C.J., Dantas, E.L., Trouw, R.A.J., Teixeira, W., Hackspacher, P.C., Fetter, A., Ávila, C.A., Volante, S., Corrêa Neto, A.V., Bongiolo, E.M., Vinagre, R., Simon, M., 2022. The generation and evolution of the Archean continental crust: The granitoid story in southeastern Brazil. Geoscience Frontiers 13, 101402. https://doi.org/10.1016/j.gsf.2022.101402

Martin, E., Sigmarsson, O., 2005. Trondhjemitic and granitic melts formed by fractional crystallization of an olivine tholeiite from Reykjanes Peninsula, Iceland. Geol. Mag. 142, 651–658. https://doi.org/10.1017/S0016756805001160

Martin, H., 1987. Petrogenesis of Archaean Trondhjemites, Tonalites, and Granodiorites from Eastern Finland: Major and Trace Element Geochemistry. Journal of Petrology 28, 921–953. https://doi.org/10.1093/petrology/28.5.921

Martin, H., 1986. Effect of steeper Archean geothermal gradient on geochemistry of subduction-zone magmas. Geology 14, 753–756. https://doi.org/10.1130/0091-7613(1986)14<753:EOSAGG>2.0.CO;2

Martin, H., Chauvel, C., Jahn, B.-M., 1983. Major and trace element geochemistry and crustal evolution of Archaean granodioritic rocks from eastern Finland. Precambrian Research 21, 159–180. https://doi.org/10.1016/0301-9268(83)90039-6

Martin, H., Moyen, J.-F., 2002. Secular changes in tonalite-trondhjemite-granodiorite composition as markers of the progressive cooling of Earth. Geology 30, 319–322. https://doi.org/10.1130/00917613(2002)030<0319:SCITTG>2.0.CO;2

Martin, H., Moyen, J.-F., Rapp, R., 2009. The sanukitoid series: magmatism at the Archaean–Proterozoic transition. Earth and Environmental Science Transactions of The Royal Society of Edinburgh 100, 15–33. https://doi.org/10.1017/S1755691009016120

Martin, H., Smithies, R.H., Rapp, R., Moyen, J.-F., Champion, D., 2005. An overview of adakite, tonalite–trondhjemite–granodiorite (TTG), and sanukitoid: relationships and some implications for crustal evolution. Lithos, Geodynamic Controls on Adakite, TTG and Sanukitoid Genesis: Implications for Models of Crust Formation 79, 1–24. https://doi.org/10.1016/j.lithos.2004.04.048

Martin, L.A.J., Hermann, J., 2018. Experimental Phase Relations in Altered Oceanic Crust: Implications for Carbon Recycling at Subduction Zones. Journal of Petrology 59, 299–320. https://doi.org/10.1093/petrology/egy031

Massonne, H.-J., Fockenberg, T., 2022. Melting of phengite-bearing eclogite at pressures of 4 and 9 GPa relevant to deep regions of a subduction zone. Earth and Planetary Science Letters 584, 117475. https://doi.org/10.1016/j.epsl.2022.117475

Masurel, Q., Thébaud, N., Sapkota, J., De Paoli, M.C., Drummond, M., Smithies, R.H., 2022. Stratigraphy of the Agnew-Wiluna Greenstone Belt: review, synopsis and implications for the late Mesoarchean to Neoarchean geological evolution of the Yilgarn Craton. Australian Journal of Earth Sciences 69, 1149–1176. https://doi.org/10.1080/08120099.2022.2102076

Mathieu, L., 2022. Modeling the chemical heterogeneity of tonalite-trondhjemite-granodiorite intrusive suites. Lithos 422–423, 106744. https://doi.org/10.1016/j.lithos.2022.106744

Mauri, S., Heilbron, M., Bruno, H., Marques, R. de A., Neto, C., Valeriano, C. de M., Bersan, S., Romero, L.F., Geraldes, M.C., 2023. Rhyacian magmatic arc rocks with sanukitoid geochemical signature from the Juiz de Fora Complex, Minas-Bahia Orogenic System (SE-Brazil). Braz. J. Geol. 52, e20220038. https://doi.org/10.1590/2317-4889202220220038

Meng, X., Simon, A.C., Kleinsasser, J.M., Mole, D.R., Kontak, D.J., Jugo, P.J., Mao, J., Richards, J.P., 2022. Formation of oxidized sulfur-rich magmas in Neoarchaean subduction zones. Nat. Geosci. 15, 1064–1070. https://doi.org/10.1038/s41561-022-01071-5

Mengel, K., Green, D.H., 1989. Stability of amphibole and phlogopite in metasomatized peridotite under water-saturated and water-undersaturated conditions. Geological Society of Australia Special Publication No. 14 - Proceedings of the Fourth International Kimberlite Conference 1, 571–581.

Millet, M.-A., Dauphas, N., 2014. Ultra-precise titanium stable isotope measurements by double-spike high resolution MC-ICP-MS. Journal of Analytical Atomic Spectrometry 29, 1444–1458. https://doi.org/10.1039/C4JA00096J

Millet, M.-A., Dauphas, N., Greber, N.D., Burton, K.W., Dale, C.W., Debret, B., Macpherson, C.G., Nowell, G.M., Williams, H.M., 2016. Titanium stable isotope investigation of magmatic processes on the Earth and Moon. Earth and Planetary Science Letters 449, 197–205. https://doi.org/10.1016/j.epsl.2016.05.039

Miranda, D.A., Chaves, A.O., Oliveira, V.P., 2018. Petrologia e geoquímica dos litotipos neoarqueanos da região da Serra da Babilônia (Bom Sucesso-Minas Gerais): implicações geotectónicas. Comunicaçõe Geológicas 105.

Mole, D.R., Thurston, P.C., Marsh, J.H., Stern, R.A., Ayer, J.A., Martin, L.A.J., Lu, Y.J., 2021. The formation of Neoarchean continental crust in the south-east Superior Craton by two distinct geodynamic processes. Precambrian Research 356, 106104. https://doi.org/10.1016/j.precamres.2021.106104

Mondal, M.E.A., Raza, A., 2013. Geochemistry of sanukitoid series granitoids from the Neoarchaen Berach granitoid batholiths, Aravalli craton, northwestern Indian shield. Current Science 105, 102–108.

Moreira, H., Seixas, L., Storey, C., Fowler, M., Lasalle, S., Stevenson, R., Lana, C., 2018. Evolution of Siderian juvenile crust to Rhyacian high Ba-Sr magmatism in the Mineiro Belt, southern São Francisco Craton. Geoscience Frontiers 9, 977–995. https://doi.org/10.1016/j.gsf.2018.01.009

Moreira, H., Storey, C., Bruand, E., Darling, J., Fowler, M., Cotte, M., Villalobos-Portillo, E.E., Parat, F., Seixas, L., Philippot, P., Dhuime, B., 2023. Sub-arc mantle fugacity shifted by sediment recycling across the Great Oxidation Event. Nat. Geosci. 16, 922–927. https://doi.org/10.1038/s41561-023-01258-4

Moreira, H., Storey, C., Fowler, M., Seixas, L., Dunlop, J., 2020. Petrogenetic processes at the tipping point of plate tectonics: Hf-O isotope ternary modelling of Earth's last TTG to sanukitoid transition. Earth and Planetary Science Letters 551, 116558. https://doi.org/10.1016/j.epsl.2020.116558

Moyen, J.-F., 2020. Archean granitoids: classification, petrology, geochemistry and origin. Geological Society, London, Special Publications 489, 15–49. https://doi.org/10.1144/SP489-2018-34

Moyen, J.-F., 2011. The composite Archaean grey gneisses: Petrological significance, and evidence for a non-unique tectonic setting for Archaean crustal growth. Lithos, Secular variations in magmatism and tectonic implications 123, 21–36. https://doi.org/10.1016/j.lithos.2010.09.015

Moyen, J.-F., Laurent, O., 2018. Archaean tectonic systems: A view from igneous rocks. Lithos 302–303, 99–125. https://doi.org/10.1016/j.lithos.2017.11.038

Moyen, J.-F., Martin, H., 2012. Forty years of TTG research. Lithos 148, 312–336. https://doi.org/10.1016/j.lithos.2012.06.010

Moyen, J.-F., Martin, H., Jayananda, M., 2001. Multi-element geochemical modelling of crust–mantle interactions during late-Archaean crustal growth: the Closepet granite (South India). Precambrian Research 112, 87–105. https://doi.org/10.1016/S0301-9268(01)00171-1

Moyen, J.-F., Martin, H., Jayananda, M., Auvray, B., 2003. Late Archaean granites: a typology based on the Dharwar Craton (India). Precambrian Research, Archaean Tectonics, Volume 1 127, 103–123. https://doi.org/10.1016/S0301-9268(03)00183-9

Moyen, J.-F., Stevens, G., 2006. Experimental constraints on TTG petrogenesis: Implications for Archean geodynamics, in: Benn, K., Mareschal, J.-C., Condie, K.C. (Eds.), Geophysical Monograph Series. American Geophysical Union, Washington, D. C., pp. 149–175. https://doi.org/10.1029/164GM11

Moyen, J.-F., van Hunen, J., 2012. Short-term episodicity of Archaean plate tectonics. Geology 40, 451–454. https://doi.org/10.1130/G322894.1

Murphy, M.E., Macdonald, J.E., Fischer, S., Gardiner, N.J., White, R.W., Savage, P.S., 2024. Silicon isotopes in an Archaean migmatite confirm seawater silicification of TTG sources. Geochimica et Cosmochimica Acta 368, 34–49. https://doi.org/10.1016/j.gca.2024.01.018

Murphy, M.J., Stirling, C.H., Kaltenbach, A., Turner, S.P., Schaefer, B.F., 2014. Fractionation of 238U/235U by reduction during low temperature uranium mineralisation processes. Earth and Planetary Science Letters 388, 306–317. https://doi.org/10.1016/j.epsl.2013.11.034

Næraa, T., Kemp, A.I.S., Scherstén, A., Rehnström, E.F., Rosing, M.T., Whitehouse, M.J., 2014. A lower crustal mafic source for the ca. 2550 Ma Qôrqut Granite Complex in southern West Greenland. Lithos 192–195, 291–304. https://doi.org/10.1016/j.lithos.2014.02.013

Nandedkar, R.H., Hürlimann, N., Ulmer, P., Müntener, O., 2016. Amphibole–melt trace element partitioning of fractionating calc-alkaline magmas in the lower crust: an experimental study. Contrib Mineral Petrol 171, 71. https://doi.org/10.1007/s00410-016-1278-0

Nebel, O., Capitanio, F.A., Moyen, J.-F., Weinberg, R.F., Clos, F., Nebel-Jacobsen, Y.J., Cawood, P.A., 2018. When crust comes of age: on the chemical evolution of Archaean, felsic continental crust by crustal drip tectonics. Philosophical Transactions of the Royal Society A: Mathematical, Physical and Engineering Sciences 376, 20180103. https://doi.org/10.1098/rsta.2018.0103

Nebel, O., Vandenburg, E.D., Capitanio, F.A., Smithies, R.H., Mulder, J., Cawood, P.A., 2024. Early Earth "subduction": short-lived, off-craton, shuffle tectonics, and no plate boundaries. Precambrian Research 408, 107431. https://doi.org/10.1016/j.precamres.2024.107431

Nesbitt, H.W., Young, G.M., 1982. Early Proterozoic climates and plate motions inferred from major element chemistry of lutites. Nature 299, 715–717. https://doi.org/10.1038/299715a0

Nesbitt, R.W., Jahn, B.-M., Purvis, A.C., 1982. Komatiites: An early precambrian phenomenon. Journal of Volcanology and Geothermal Research 14, 31–45. https://doi.org/10.1016/0377-0273(82)90041-5

Nie, N.X., Dauphas, N., Alp, E.E., Zeng, H., Sio, C.K., Hu, J.Y., Chen, X., Aarons, S.M., Zhang, Z., Tian, H.-C., Wang, D., Prissel, K.B., Greer, J., Bi, W., Hu, M.Y., Zhao, J., Shahar, A., Roskosz, M., Teng, F.-Z., Krawczynski, M.J., Heck, P.R., Spear, F.S., 2021. Iron, magnesium, and titanium isotopic fractionations between garnet, ilmenite, fayalite, biotite, and tourmaline: Results from NRIXS, ab initio, and study of mineral separates from the Moosilauke metapelite. Geochimica et Cosmochimica Acta 302, 18–45. https://doi.org/10.1016/j.gca.2021.03.014

Nielsen, S.G., Shu, Y., Auro, M., Yogodzinski, G., Shinjo, R., Plank, T., Kay, S.M., Horner, T.J., 2020. Barium isotope systematics of subduction zones. Geochimica et Cosmochimica Acta 275, 1–18. https://doi.org/10.1016/j.gca.2020.02.006

Noce, C.M., 1995. Geocronologia dos eventos magmáticos, sedimentares e metamórficos na região do Quadrilátero Ferrífero, Minas Gerais (PhD Thesis).

Universidade de São Paulo. https://doi.org/10.11606/T.44.2016.tde-05012016-154125

Noordmann, J., Weyer, S., Georg, R.B., Jöns, S., Sharma, M., 2016. 238U/235U isotope ratios of crustal material, rivers and products of hydrothermal alteration: new insights on the oceanic U isotope mass balance. Isotopes in Environmental and Health Studies 52, 141–163. https://doi.org/10.1080/10256016.2015.1047449

Nutman, A.P., Bennett, V.C., Friend, C.R.L., Norman, M.D., 1999. Meta-igneous (non-gneissic) tonalites and quartz-diorites from an extensive ca. 3800 Ma terrain south of the Isua supracrustal belt, southern West Greenland: constraints on early crust formation. Contrib Mineral Petrol 137, 364–388. https://doi.org/10.1007/s004100050556

Och, L.M., Shields-Zhou, G.A., 2012. The Neoproterozoic oxygenation event: Environmental perturbations and biogeochemical cycling. Earth-Science Reviews 110, 26–57. https://doi.org/10.1016/j.earscirev.2011.09.004

Olejarz, J., Iwasa, Y., Knoll, A.H., Nowak, M.A., 2021. The Great Oxygenation Event as a consequence of ecological dynamics modulated by planetary change. Nat Commun 12, 3985. https://doi.org/10.1038/s41467-021-23286-7

Olierook, H.K.H., Kirkland, C.L., Hollis, J.A., Gardiner, N.J., Yakymchuk, C., Szilas, K., Hartnady, M.I.H., Barham, M., McDonald, B.J., Evans, N.J., Steenfelt, A., Waterton, P., 2021. Regional zircon U-Pb geochronology for the Maniitsoq region, southwest Greenland. Sci Data 8, 139. https://doi.org/10.1038/s41597-021-00922-x

O'Neill, C., Lenardic, A., Moresi, L., Torsvik, T.H., Lee, C.-T.A., 2007. Episodic Precambrian subduction. Earth and Planetary Science Letters 262, 552–562. https://doi.org/10.1016/j.epsl.2007.04.056

O'Neill, H.St.C., 2016. The Smoothness and Shapes of Chondrite-normalized Rare Earth Element Patterns in Basalts. Journal of Petrology 57, 1463–1508. https://doi.org/10.1093/petrology/egw047

O'Nions, R.K., Pankhurst, R.J., 1974. Rare-earth element distribution in Archaean gneisses and anorthosites, Godthåb area, West Greenland. Earth and Planetary Science Letters 22, 328–338. https://doi.org/10.1016/0012-821X(74)90142-3

Osmond, J.K., Cowart, J.B., 1976. The theory and uses of natural uranium isotopic variations in hydrology. Atomic Energy Review 14, 621–679.

Padrón-Navarta, J.A., López Sánchez-Vizcaíno, V., Menzel, M.D., Gómez-Pugnaire, M.T., Garrido, C.J., 2023. Mantle wedge oxidation from deserpentinization modulated by sediment-derived fluids. Nat. Geosci. 16, 268–275. https://doi.org/10.1038/s41561-023-01127-0

Palin, R.M., White, R.W., Green, E.C.R., 2016. Partial melting of metabasic rocks and the generation of tonalitic–trondhjemitic–granodioritic (TTG) crust in the Archaean: Constraints from phase equilibrium modelling. Precambrian Research 287, 73–90. https://doi.org/10.1016/j.precamres.2016.11.001

Palme, H., O'Neill, H.St.C., 2014. 3.1 - Cosmochemical Estimates of Mantle Composition, in: Holland, H.D., Turekian, K.K. (Eds.), Treatise on Geochemistry (Second Edition). Elsevier, Oxford, pp. 1–39. https://doi.org/10.1016/B978-0-08-095975-7.00201-1

Partin, C.A., Lalonde, S.V., Planavsky, N.J., Bekker, A., Rouxel, O.J., Lyons, T.W., Konhauser, K.O., 2013. Uranium in iron formations and the rise of atmospheric oxygen. Chemical Geology, Special Issue dedicated to H.D. Holland: Evolution of the atmosphere and ocean through time 362, 82–90. https://doi.org/10.1016/j.chemgeo.2013.09.005

Pavia, F.J., Cooperdock, E.H.G., de Obeso, J.C., Sims, K.W.W., Tissot, F.L.H., Klein, F., 2023. Uranium isotopes as tracers of serpentinite weathering. Earth and Planetary Science Letters 623, 118434. https://doi.org/10.1016/j.epsl.2023.118434

Pavlov, A.A., Kasting, J.F., 2002. Mass-Independent Fractionation of Sulfur Isotopes in Archean Sediments: Strong Evidence for an Anoxic Archean Atmosphere. Astrobiology 2, 27–41. https://doi.org/10.1089/153110702753621321

Pedreira Pérez, R., Tremblay, A., Stevenson, R.K., 2024. Archean crustal growth and reworking in the Superior Province, Canada: Insights from whole-rock geochemistry and Nd isotopic data of the La Grande, Nemiscau and Opatica subprovinces. Gondwana Research 135, 151-179. https://doi.org/10.1016/j.gr.2024.04.006

Penniston-Dorland, S.C., Kohn, M.J., Manning, C.E., 2015. The global range of subduction zone thermal structures from exhumed blueschists and eclogites:

Rocks are hotter than models. Earth and Planetary Science Letters 428, 243–254. https://doi.org/10.1016/j.epsl.2015.07.031

Perchuk, A.L., Zakharov, V.S., Gerya, T.V., Brown, M., 2019. Hotter mantle but colder subduction in the Precambrian: What are the implications? Precambrian Research 330, 20–34. https://doi.org/10.1016/j.precamres.2019.04.023

Perchuk, A.L., Zakharov, V.S., Gerya, T.V., Stern, R.J., 2025. Shallow vs. Deep subduction in Earth history: Contrasting regimes of water recycling into the mantle. Precambrian Research 418, 107690. https://doi.org/10.1016/j.precamres.2025.107690

Perring, C.S., Rock, N.M.S., 1991. Relationships between calc-alkaline acidic and basic (mantle-derived) magmas in Late Archaean composite dykes, Kambalda Goldfield, Western Australia. Precambrian Research 52, 245–273. https://doi.org/10.1016/0301-9268(91)90083-M

Pertermann, M., Hirschmann, M.M., 2003. Anhydrous Partial Melting Experiments on MORB-like Eclogite: Phase Relations, Phase Compositions and Mineral–Melt Partitioning of Major Elements at 2–3 GPa. Journal of Petrology 44, 2173–2201. https://doi.org/10.1093/petrology/egg074

Piccoli, F., Hermann, J., Pettke, T., Connolly, J. a. D., Kempf, E.D., Vieira Duarte, J.F., 2019. Subducting serpentinites release reduced, not oxidized, aqueous fluids. Sci Rep 9, 19573. https://doi.org/10.1038/s41598-019-55944-8

Planavsky, N.J., Asael, D., Hofmann, A., Reinhard, C.T., Lalonde, S.V., Knudsen, A., Wang, X., Ossa Ossa, F., Pecoits, E., Smith, A.J.B., Beukes, N.J., Bekker, A., Johnson, T.M., Konhauser, K.O., Lyons, T.W., Rouxel, O.J., 2014. Evidence for oxygenic photosynthesis half a billion years before the Great Oxidation Event. Nature Geosci 7, 283–286. https://doi.org/10.1038/ngeo2122

Plank, T., Langmuir, C.H., 1998. The chemical composition of subducting sediment and its consequences for the crust and mantle. Chemical Geology 145, 325–394. https://doi.org/10.1016/S0009-2541(97)00150-2

Pons, M.-L., Debret, B., Bouilhol, P., Delacour, A., Williams, H., 2016. Zinc isotope evidence for sulfate-rich fluid transfer across subduction zones. Nat Commun 7, 13794. https://doi.org/10.1038/ncomms13794

Poulton, S.W., Bekker, A., Cumming, V.M., Zerkle, A.L., Canfield, D.E., Johnston, D.T., 2021. A 200-million-year delay in permanent atmospheric oxygenation. Nature 592, 232–236. https://doi.org/10.1038/s41586-021-03393-7

Pourteau, A., Doucet, L.S., Blereau, E.R., Volante, S., Johnson, T.E., Collins, W.J., Li, Z.-X., Champion, D.C., 2020. TTG generation by fluid-fluxed crustal melting: Direct evidence from the Proterozoic Georgetown Inlier, NE Australia. Earth and Planetary Science Letters 550, 116548. https://doi.org/10.1016/j.epsl.2020.116548

Prissel, K.B., Krawczynski, M.J., Nie, N.X., Dauphas, N., Aarons, S.M., Heard, A.W., Hu, M.Y., Ercan Alp, E., Zhao, J., 2024. Fractionation of iron and titanium isotopes by ilmenite and the isotopic compositions of lunar magma ocean cumulates. Geochimica et Cosmochimica Acta 372, 154-170. https://doi.org/10.1016/j.gca.2024.01.006

Prouteau, G., Scaillet, B., Pichavant, M., Maury, R., 2001. Evidence for mantle metasomatism by hydrous silicic melts derived from subducted oceanic crust. Nature 410, 197–200. https://doi.org/10.1038/35065583

Ptáček, M.P., Dauphas, N., Greber, N.D., 2020. Chemical evolution of the continental crust from a data-driven inversion of terrigenous sediment compositions. Earth and Planetary Science Letters 539, 116090. https://doi.org/10.1016/j.epsl.2020.116090

Pufahl, P.K., Hiatt, E.E., 2012. Oxygenation of the Earth's atmosphere–ocean system: A review of physical and chemical sedimentologic responses. Marine and Petroleum Geology 32, 1–20. https://doi.org/10.1016/j.marpetgeo.2011.12.002

Qian, Q., Hermann, J., 2010. Formation of High-Mg Diorites through Assimilation of Peridotite by Monzodiorite Magma at Crustal Depths. Journal of Petrology 51, 1381–1416. https://doi.org/10.1093/petrology/egq023

Rahaman, M.S., Mondal, M.E.A., 2015. Evolution of continental crust of the Aravalli craton, NW India, during the Neoarchaean–Palaeoproterozoic: evidence from geochemistry of granitoids. International Geology Review 57, 1510–1525. https://doi.org/10.1080/00206814.2014.950607

Ranjan, S., Upadhyay, D., Abhinay, K., Srikantappa, C., 2020. Paleoarchean and Neoarchean Tonalite–Trondhjemite–Granodiorite (TTG) and granite magmatism in the Western Dharwar Craton, southern India: Implications for

Archean continental growth and geodynamics. Precambrian Research 340, 105630. https://doi.org/10.1016/j.precamres.2020.105630

Rapp, R.P., Norman, M.D., Laporte, D., Yaxley, G.M., Martin, H., Foley, S.F., 2010. Continent Formation in the Archean and Chemical Evolution of the Cratonic Lithosphere: Melt-Rock Reaction Experiments at 3-4 GPa and Petrogenesis of Archean Mg-Diorites (Sanukitoids). Journal of Petrology 51, 1237–1266. https://doi.org/10.1093/petrology/egq017

Rapp, R.P., Shimizu, N., Norman, M.D., Applegate, G.S., 1999. Reaction between slab-derived melts and peridotite in the mantle wedge: experimental constraints at 3.8 GPa. Chemical Geology 160, 335–356. https://doi.org/10.1016/S0009-2541(99)00106-0

Rapp, R.P., Watson, E.B., Miller, C.F., 1991. Partial melting of amphibolite/eclogite and the origin of Archean trondhjemites and tonalites. Precambrian Research, Precambrian Granitoids Petrogenesis, Geochemistry and Metallogeny 51, 1–25. https://doi.org/10.1016/0301-9268(91)90092-O

Raza, A., Gahlot, S.K., Garkhal, P., Jalutharia, H.K., 2022. Geochemistry of late Archaean Jhiri Granite in the North Delhi Fold Belt: Petrogenesis and implications for crustal growth in Aravalli Craton of the Indian shield. J Earth Syst Sci 131, 166. https://doi.org/10.1007/s12040-022-01905-1

Raza, A., Guha, D.B., Neogi, S., 2021. Geochemistry of late paleoproterozoic Anjana and Amet granites of the Aravalli craton with affinities to sanukitoid series granitoids: Implications for petrogenetic and geodynamic processes. Geochemistry 81, 125758. https://doi.org/10.1016/j.chemer.2021.125758

Reimink, J.R., Smye, A.J., 2024. Subaerial weathering drove stabilization of continents. Nature 629, 609–615. https://doi.org/10.1038/s41586-024-07307-1

Reinhard, C.T., Planavsky, N.J., 2022. The History of Ocean Oxygenation. Annual Review of Marine Science 14, 331–353. https://doi.org/10.1146/annurev-marine-031721-104005

Richter, S., Alonso-Munoz, A., Eykens, R., Jacobsson, U., Kuehn, H., Verbruggen, A., Aregbe, Y., Wellum, R., Keegan, E., 2008. The isotopic composition of natural uranium samples—Measurements using the new n(233U)/n(236U) double spike IRMM-3636. International Journal of Mass Spectrometry 269, 145–148. https://doi.org/10.1016/j.ijms.2007.09.012

Rock, N.M.S., 1991. Nature, Origin and Evolution of Lamprophyre Melts, in: Rock, N.M.S. (Ed.), Lamprophyres. Springer US, Boston, MA, pp. 125–149. https://doi.org/10.1007/978-1-4757-0929-2_8

Rodney, J., Andersen, M., Stubbs, D., Lissenberg, C.J., Gianola, O., Willbold, M., Elliott, T., 2024. Assessing the timing of deep ocean oxygenation from uranium elemental and isotopic compositions of ophiolites. [Preprint] Available at: https://eartharxiv.org/repository/view/7756/ (Accessed: November 2024)

Rogers, G., Dunning, G.R., 1991. Geochronology of appinitic and related granitic magmatism in the W Highlands of Scotland: constraints on the timing of transcurrent fault movement. Journal of the Geological Society 148, 17–27. https://doi.org/10.1144/gsjgs.148.1.0017

Rollinson, H., 2021. Do all Archaean TTG rock compositions represent former melts? Precambrian Research 367, 106448. https://doi.org/10.1016/j.precamres.2021.106448

Rollinson, H., Pease, V., 2021. Using Geochemical Data: To Understand Geological Processes, 2nd ed. Cambridge University Press, Cambridge. https://doi.org/10.1017/9781108777834

Roman, A., Arndt, N., 2020. Differentiated Archean oceanic crust: Its thermal structure, mechanical stability and a test of the sagduction hypothesis. Geochimica et Cosmochimica Acta, The continents: Origin, evolution and interactions with other reservoirs 278, 65–77. https://doi.org/10.1016/j.gca.2019.07.009

Roskosz, M., Amet, Q., Fitoussi, C., Dauphas, N., Bourdon, B., Tissandier, L., Hu, M.Y., Said, A., Alatas, A., Alp, E.E., 2020. Redox and structural controls on tin isotopic fractionations among magmas. Geochimica et Cosmochimica Acta 268, 42–55. https://doi.org/10.1016/j.gca.2019.09.036

Rozel, A.B., Golabek, G.J., Jain, C., Tackley, P.J., Gerya, T., 2017. Continental crust formation on early Earth controlled by intrusive magmatism. Nature 545, 332–335. https://doi.org/10.1038/nature22042

Rudge, J.F., Reynolds, B.C., Bourdon, B., 2009. The double spike toolbox. Chemical Geology 265, 420–431. https://doi.org/10.1016/j.chemgeo.2009.05.010

Rudnick, R.L., Gao, S., 2014. 4.1 - Composition of the Continental Crust, in: Holland, H.D., Turekian, K.K. (Eds.), Treatise on Geochemistry (Second Edition).

Elsevier, Oxford, pp. 1–51. https://doi.org/10.1016/B978-0-08-095975-7.00301-6

Rustioni, G., Audetat, A., Keppler, H., 2021. The composition of subduction zone fluids and the origin of the trace element enrichment in arc magmas. Contrib Mineral Petrol 176, 51. https://doi.org/10.1007/s00410-021-01810-8

Rzehak, L.J.A., Kommescher, S., Hoare, L., Kurzweil, F., Sprung, P., Leitzke, F.P., Fonseca, R.O.C., 2022. Redox-dependent Ti stable isotope fractionation on the Moon: implications for current lunar magma ocean models. Contrib Mineral Petrol 177, 81. https://doi.org/10.1007/s00410-022-01947-0

Rzehak, L.J.A., Kommescher, S., Kurzweil, F., Sprung, P., Leitzke, F.P., Fonseca, R.O.C., 2021. The redox dependence of titanium isotope fractionation in synthetic Ti-rich lunar melts. Contrib Mineral Petrol 176, 19. https://doi.org/10.1007/s00410-020-01769-y

Sahoo, S.K., Planavsky, N.J., Kendall, B., Wang, X., Shi, X., Scott, C., Anbar, A.D., Lyons, T.W., Jiang, G., 2012. Ocean oxygenation in the wake of the Marinoan glaciation. Nature 489, 546–549. https://doi.org/10.1038/nature11445

Saji, N.S., Rudnick, R.L., Gaschnig, R.M., Millet, M.-A., 2023. Titanium isotope evidence for the high topography of Nuna and Gondwana - Implications for Earth's redox and biological evolution. Earth and Planetary Science Letters 615, 118214. https://doi.org/10.1016/j.epsl.2023.118214

Savage, P.S., Georg, R.B., Williams, H.M., Burton, K.W., Halliday, A.N., 2011. Silicon isotope fractionation during magmatic differentiation. Geochimica et Cosmochimica Acta 75, 6124–6139. https://doi.org/10.1016/j.gca.2011.07.043

Scandolara, J.E., Saboia, A.M., Fuck, R.A., Corrêa, R.T., Rodrigues, J.B., Alves, C.L., 2024. Insights into the late Archean evolution of the Carajás Province: Geochemical and geochronological constraints from the Santana do Araguaia complex, Amazonian craton, Brazil. Journal of South American Earth Sciences 143, 104978. https://doi.org/10.1016/j.jsames.2024.104978

Schauble, E.A., 2007. Role of nuclear volume in driving equilibrium stable isotope fractionation of mercury, thallium, and other very heavy elements. Geochimica et Cosmochimica Acta 71, 2170–2189. https://doi.org/10.1016/j.gca.2007.02.004

Schauble, E.A., 2004. Applying Stable Isotope Fractionation Theory to New Systems. Reviews in Mineralogy and Geochemistry 55, 65–111. https://doi.org/10.2138/gsrmg.55.1.65

Schirrmeister, B.E., Gugger, M., Donoghue, P.C.J., 2015. Cyanobacteria and the Great Oxidation Event: evidence from genes and fossils. Palaeontology 58, 769–785. https://doi.org/10.1111/pala.12178

Schmidt, M.W., Vielzeuf, D., Auzanneau, E., 2004. Melting and dissolution of subducting crust at high pressures: the key role of white mica. Earth and Planetary Science Letters 228, 65–84. https://doi.org/10.1016/j.epsl.2004.09.020

Schoene, B., de Wit, M.J., Bowring, S.A., 2008. Mesoarchean assembly and stabilization of the eastern Kaapvaal craton: A structural-thermochronological perspective. Tectonics 27. https://doi.org/10.1029/2008TC002267

Schofield, D.I., Thomas, R.J., Goodenough, K.M., De Waele, B., Pitfield, P.E.J., Key, R.M., Bauer, W., Walsh, G.J., Lidke, D.J., Ralison, A.V., Rabarimanana, M., Rafahatelo, J.M., Randriamananjara, T., 2010. Geological evolution of the Antongil Craton, NE Madagascar. Precambrian Research 182, 187–203. https://doi.org/10.1016/j.precamres.2010.07.006

Scott, C.T., Bekker, A., Reinhard, C.T., Schnetger, B., Krapež, B., Rumble, D., III, Lyons, T.W., 2011. Late Archean euxinic conditions before the rise of atmospheric oxygen. Geology 39, 119–122. https://doi.org/10.1130/G31571.1

Scott, C.T., Lyons, T.W., Bekker, A., Shen, Y., Poulton, S.W., Chu, X., Anbar, A.D., 2008. Tracing the stepwise oxygenation of the Proterozoic ocean. Nature 452, 456–459. https://doi.org/10.1038/nature06811

Seixas, L.A.R., Bardintzeff, J.-M., Stevenson, R., Bonin, B., 2013. Petrology of the high-Mg tonalites and dioritic enclaves of the ca. 2130Ma Alto Maranhão suite: Evidence for a major juvenile crustal addition event during the Rhyacian orogenesis, Mineiro Belt, southeast Brazil. Precambrian Research 238, 18–41. https://doi.org/10.1016/j.precamres.2013.09.015

Semprich, J., Moreno, J.A., Oliveira, E.P., 2015. Phase equilibria and trace element modeling of Archean sanukitoid melts. Precambrian Research 269, 122–138. https://doi.org/10.1016/j.precamres.2015.08.004

Sen, C., Dunn, T., 1994. Dehydration melting of a basaltic composition amphibolite at 1.5 and 2.0 GPa: implications for the origin of adakites. Contr. Mineral. and Petrol. 117, 394–409. https://doi.org/10.1007/BF00307273

Shang, C.K., Liégeois, J.P., Satir, M., Frisch, W., Nsifa, E.N., 2010. Late Archaean high-K granite geochronology of the northern metacratonic margin of the Archaean Congo craton, Southern Cameroon: Evidence for Pb-loss due to non-metamorphic causes. Gondwana Research 18, 337–355. https://doi.org/10.1016/j.gr.2010.02.008

Shang, C.K., Siebel, W., Satir, M., Chen, F., Mvondo, J.O., 2004. Zircon Pb-Pb and U-Pb systematics of TTG rocks in the Congo Craton: Constraints on crust formation, magmatism, and Pan-African lead loss. Bulletin of Geosciences 79, 205–219.

Sheng, J., Quan, Y., Jiang, D., Deng, G., Li, G., Xu, Z., Huang, F., 2025. Uranium isotope fractionation during magmatic-hydrothermal interactions in pegmatites. Chemical Geology 677, 122632. https://doi.org/10.1016/j.chemgeo.2025.122632

Shields-Zhou, G., Och, L., 2011. The case for a Neoproterozoic Oxygenation Event: Geochemical evidence and biological consequences. GSAT 21, 4–11. https://doi.org/10.1130/GSATG102A.1

Shirey, S.B., Hanson, G.N., 1984. Mantle-derived Archaean monozodiorites and trachyandesites. Nature 310, 222–224. https://doi.org/10.1038/310222a0

Shu, Y., Nielsen, S.G., Le Roux, V., Ramos, D.S., Blusztajn, J., Auro, M., Leat, P.T., Horner, T.J., 2025. Mélange dehydration and melting beneath South Sandwich Islands arc. Nat Commun 16, 1440. https://doi.org/10.1038/s41467-025-56554-x

Silva-Silva, L.C., Oliveira, D.C., Barbosa de Souza, D., 2020. Geology and geochemical constraints on the origin of the Mesoarchean granitoids from Carajás province, Amazonian craton. Journal of South American Earth Sciences 100, 102568. https://doi.org/10.1016/j.jsames.2020.102568

Simon, M.B., Bongiolo, E.M., Ávila, C.A., Teixeira, W., Marimon, R.S., Oliveira, E.P., 2021. Archean sodic metagranitoids from the Southern São Francisco Craton: Review, petrogenesis, and tectonic implications. Lithos 398–399, 106246. https://doi.org/10.1016/j.lithos.2021.106246

Sisson, T.W., Grove, T.L., 1993. Experimental investigations of the role of H2O in calc-alkaline differentiation and subduction zone magmatism. Contr. Mineral. and Petrol. 113, 143–166. https://doi.org/10.1007/BF00283225

Sisson, T.W., Kelemen, P.B., 2018. Near-solidus melts of MORB + 4 wt% H2O at 0.8–2.8 GPa applied to issues of subduction magmatism and continent formation. Contrib Mineral Petrol 173, 70. https://doi.org/10.1007/s00410-018-1494-x

Sizova, E., Gerya, T., Brown, M., Perchuk, L.L., 2010. Subduction styles in the Precambrian: Insight from numerical experiments. Lithos, On high-grade metamorphism, crustal melting, migmatites and granites 116, 209–229. https://doi.org/10.1016/j.lithos.2009.05.028

Sizova, E., Gerya, T., Stüwe, K., Brown, M., 2015. Generation of felsic crust in the Archean: A geodynamic modeling perspective. Precambrian Research 271, 198–224. https://doi.org/10.1016/j.precamres.2015.10.005

Skjerlie, K.P., Johnston, A.D., 1993. Fluid-Absent Melting Behavior of an F-Rich Tonalitic Gneiss at Mid-Crustal Pressures: Implications for the Generation of Anorogenic Granites. Journal of Petrology 34, 785–815. https://doi.org/10.1093/petrology/34.4.785

Skjerlie, K.P., Patiño Douce, A.E., 2002. The Fluid-absent Partial Melting of a Zoisite-bearing Quartz Eclogite from 1·0 to 3·2 GPa; Implications for Melting in Thickened Continental Crust and for Subduction-zone Processes. Journal of Petrology 43, 291–314. https://doi.org/10.1093/petrology/43.2.291

Smit, M.A., Mezger, K., 2017. Earth's early O2 cycle suppressed by primitive continents. Nature Geosci 10, 788–792. https://doi.org/10.1038/ngeo3030

Smith, T.E., Choudhry, A.G., Huang, C.H., 1983. The geochemistry and petrogenesis of the Archean Gamitagama Lake igneous complex, southern Superior Province. Precambrian Research 22, 219–244. https://doi.org/10.1016/0301-9268(83)90050-5

Smithies, R.H., Champion, D.C., 2000. The Archaean High-Mg Diorite Suite: Links to Tonalite–Trondhjemite–Granodiorite Magmatism and Implications for Early Archaean Crustal Growth. Journal of Petrology 41, 1653–1671. https://doi.org/10.1093/petrology/41.12.1653

Smithies, R.H., Champion, D.C., Sun, S.-. S., 2004. Evidence for Early LREE-enriched Mantle Source Regions: Diverse Magmas from the c. 3·0 Ga Mallina

Basin, Pilbara Craton, NW Australia. Journal of Petrology 45, 1515–1537.
https://doi.org/10.1093/petrology/egh014

Smithies, R.H., Champion, D.C., Van Kranendonk, M.J., 2009. Formation of
Paleoarchean continental crust through infracrustal melting of enriched basalt.
Earth and Planetary Science Letters 281, 298–306.
https://doi.org/10.1016/j.epsl.2009.03.003

Smithies, R.H., Gessner, K., Lu, Y., Kirkland, C.L., Ivanic, T., Lowrey, J.R.,
Champion, D.C., Sapkota, J., Masurel, Q., Thébaud, N., Quentin de Gromard,
R., 2023. Geochemical mapping of lithospheric architecture disproves
Archean terrane accretion in the Yilgarn craton. Geology 52, 141-146.
https://doi.org/10.1130/G51707.1

Smithies, R.H., Lowrey, J.R., Sapkota, J., De Paoli, M.C., Hayman, P., Barnes, S.J.,
Champion, D.C., Masurel, Q., Thébaud, N., Grech, L.L., Drummond, M.,
Maas, R., 2022. Geochemical characterisation of the magmatic stratigraphy of
the Kalgoorlie and Black Flag Groups - Ora Banda to Kambalda region (No.
226). Geological Survey of Western Australia, Perth, Australia.

Smithies, R.H., Lu, Y., Johnson, T.E., Kirkland, C.L., Cassidy, K.F., Champion, D.C.,
Mole, D.R., Zibra, I., Gessner, K., Sapkota, J., De Paoli, M.C., Poujol, M.,
2019. No evidence for high-pressure melting of Earth's crust in the Archean.
Nat Commun 10, 5559. https://doi.org/10.1038/s41467-019-13547-x

Smithies, R.H., Lu, Y., Kirkland, C., Cassidy, K., Champion, D., Sapkota, J., De
Paoli, M., Burley, L., 2018. A new look at lamprophyres and sanukitoids, and
their relationship to the Black Flag Group and gold prospectivity (Record
2018/15). Geological Survey of Western Australia, Perth, Australia.

Smithies, R.H., Lu, Y., Kirkland, C.L., Johnson, T.E., Mole, D.R., Champion, D.C.,
Martin, L., Jeon, H., Wingate, M.T.D., Johnson, S.P., 2021. Oxygen isotopes
trace the origins of Earth's earliest continental crust. Nature 592, 70–75.
https://doi.org/10.1038/s41586-021-03337-1

Sossi, P.A., Debret, B., 2021. The Role of Redox Processes in Determining the Iron
Isotope Compositions of Minerals, Melts, and Fluids, in: Magma Redox
Geochemistry. American Geophysical Union (AGU), pp. 303–330.
https://doi.org/10.1002/9781119473206.ch15

Spandler, C., Yaxley, G., Green, D.H., Rosenthal, A., 2008. Phase Relations and
Melting of Anhydrous K-bearing Eclogite from 1200 to 1600°C and 3 to 5

GPa. Journal of Petrology 49, 771–795.
https://doi.org/10.1093/petrology/egm039

Sperling, E.A., Wolock, C.J., Morgan, A.S., Gill, B.C., Kunzmann, M., Halverson, G.P., Macdonald, F.A., Knoll, A.H., Johnston, D.T., 2015. Statistical analysis of iron geochemical data suggests limited late Proterozoic oxygenation. Nature 523, 451–454. https://doi.org/10.1038/nature14589

Squire, R.J., Allen, C.M., Cas, R.A.F., Campbell, I.H., Blewett, R.S., Nemchin, A.A., 2010. Two cycles of voluminous pyroclastic volcanism and sedimentation related to episodic granite emplacement during the late Archean: Eastern Yilgarn Craton, Western Australia. Precambrian Research, Geodynamics and architecture of a world class mineral province: the Archean eastern Yilgarn Craton, Western Australia 183, 251–274. https://doi.org/10.1016/j.precamres.2010.08.009

Steenfelt, A., Garde, A.A., Moyen, J.-F., 2005. Mantle wedge involvement in the petrogenesis of Archaean grey gneisses in West Greenland. Lithos, Geodynamic Controls on Adakite, TTG and Sanukitoid Genesis: Implications for Models of Crust Formation 79, 207–228. https://doi.org/10.1016/j.lithos.2004.04.054

Stern, R.A., Hanson, G.N., 1991. Archean High-Mg Granodiorite: A Derivative of Light Rare Earth Element-enriched Monzodiorite of Mantle Origin. Journal of Petrology 32, 201–238. https://doi.org/10.1093/petrology/32.1.201

Stern, R.A., Hanson, G.N., Shirey, S.B., 1989. Petrogenesis of mantle-derived, LILE-enriched Archean monzodiorites and trachyandesites (sanukitoids) in southwestern Superior Province. Canadian Journal of Earth Sciences 26, 1688–1712. https://doi.org/10.1139/e89-145

Stirling, C.H., Andersen, M.B., Potter, E.-K., Halliday, A.N., 2007. Low-temperature isotopic fractionation of uranium. Earth and Planetary Science Letters 264, 208–225. https://doi.org/10.1016/j.epsl.2007.09.019

Stirling, C.H., Halliday, A.N., Porcelli, D., 2005. In search of live 247Cm in the early solar system. Geochimica et Cosmochimica Acta 69, 1059–1071. https://doi.org/10.1016/j.gca.2004.06.034

Stolper, D.A., Bucholz, C.E., 2019. Neoproterozoic to early Phanerozoic rise in island arc redox state due to deep ocean oxygenation and increased marine

sulfate levels. Proc. Natl. Acad. Sci. U.S.A. 116, 8746–8755. https://doi.org/10.1073/pnas.1821847116

Stolper, D.A., Keller, C.B., 2018. A record of deep-ocean dissolved O2 from the oxidation state of iron in submarine basalts. Nature 553, 323–327. https://doi.org/10.1038/nature25009

Storck, J.-C., Greber, N.D., Duarte, J.F.V., Lanari, P., Tiepolo, M., Pettke, T., 2023. Molybdenum and titanium isotopic signatures of arc-derived cumulates. Chemical Geology 617, 121260. https://doi.org/10.1016/j.chemgeo.2022.121260

Sun, C., Graff, M., Liang, Y., 2017. Trace element partitioning between plagioclase and silicate melt: The importance of temperature and plagioclase composition, with implications for terrestrial and lunar magmatism. Geochimica et Cosmochimica Acta 206, 273–295. https://doi.org/10.1016/j.gca.2017.03.003

Sun, G., Liu, S., Gao, L., Hu, Y., Guo, R., Fu, J., Wang, M., Ma, C., Hu, F., 2019. Neoarchean sanukitoids and associated rocks from the Tengzhou-Pingyi intrusive complex, North China Craton: Insights into petrogenesis and crust-mantle interactions. Gondwana Research 68, 50–68. https://doi.org/10.1016/j.gr.2018.11.005

Sun, G., Liu, S., Wang, M., Bao, H., Teng, G., 2020. Complex Neoarchean mantle metasomatism: Evidence from sanukitoid diorites-monzodiorites-granodiorites in the northeastern North China Craton. Precambrian Research 342, 105692. https://doi.org/10.1016/j.precamres.2020.105692

Sutcliffe, R.H., Smith, A.R., Doherty, W., Barnett, R.L., 1990. Mantle derivation of Archean amphibole-bearing granitoid and associated mafic rocks: evidence from the southern Superior Province, Canada. Contr. Mineral. and Petrol. 105, 255–274. https://doi.org/10.1007/BF00306538

Syracuse, E.M., van Keken, P.E., Abers, G.A., 2010. The global range of subduction zone thermal models. Physics of the Earth and Planetary Interiors, Special Issue on Deep Slab and Mantle Dynamics 183, 73–90. https://doi.org/10.1016/j.pepi.2010.02.004

Szymanowski, D., Ellis, B.S., Wotzlaw, J.-F., Bachmann, O., 2019. Maturation and rejuvenation of a silicic magma reservoir: High-resolution chronology of the Kneeling Nun Tuff. Earth and Planetary Science Letters 510, 103–115. https://doi.org/10.1016/j.epsl.2019.01.007

Szymanowski, D., Wotzlaw, J.-F., Ellis, B.S., Bachmann, O., Guillong, M., von Quadt, A., 2017. Protracted near-solidus storage and pre-eruptive rejuvenation of large magma reservoirs. Nature Geosci 10, 777–782. https://doi.org/10.1038/ngeo3020

Tamblyn, R., Hermann, J., Hasterok, D., Sossi, P., Pettke, T., Chatterjee, S., 2023. Hydrated komatiites as a source of water for TTG formation in the Archean. Earth and Planetary Science Letters 603, 117982. https://doi.org/10.1016/j.epsl.2022.117982

Tang, M., Chen, H., Song, S., Sun, G., Wang, C., 2024. Zircon Eu/Eu* in Archean TTGs with implications for the role of endogenic oxidation in Archean crustal differentiation. Geochimica et Cosmochimica Acta 378, 259–269. https://doi.org/10.1016/j.gca.2024.06.031

Tang, M., Chen, K., Rudnick, R.L., 2016. Archean upper crust transition from mafic to felsic marks the onset of plate tectonics. Science 351, 372–375. https://doi.org/10.1126/science.aad5513

Tang, M., Erdman, M., Eldridge, G., Lee, C.-T.A., 2018. The redox "filter" beneath magmatic orogens and the formation of continental crust. Sci. Adv. 4, eaar4444. https://doi.org/10.1126/sciadv.aar4444

Tang, M., Lee, C.-T.A., Costin, G., Höfer, H.E., 2019. Recycling reduced iron at the base of magmatic orogens. Earth and Planetary Science Letters 528, 115827. https://doi.org/10.1016/j.epsl.2019.115827

Tatsumi, Y., 2006. High-Mg Andesites in the Setouchi Volcanic Belt, Southwestern Japan: Analogy to Archean Magmatism and Continental Crust Formation? Annual Review of Earth and Planetary Sciences 34, 467–499. https://doi.org/10.1146/annurev.earth.34.031405.125014

Tatsumi, Y., Ishizaka, K., 1982. Origin of high-magnesian andesites in the Setouchi volcanic belt, southwest Japan, I. Petrographical and chemical characteristics. Earth and Planetary Science Letters 60, 293–304. https://doi.org/10.1016/0012-821X(82)90008-5

Taylor, S.R., McLennan, S.M., 1995. The geochemical evolution of the continental crust. Reviews of Geophysics 33, 241–265. https://doi.org/10.1029/95RG00262

Tchameni, R., Mezger, K., Nsifa, N.E., Pouclet, A., 2000. Neoarchæan crustal evolution in the Congo Craton: evidence from K rich granitoids of the Ntem

Complex, southern Cameroon. Journal of African Earth Sciences 30, 133–147. https://doi.org/10.1016/S0899-5362(00)00012-9

Telus, M., Dauphas, N., Moynier, F., Tissot, F.L.H., Teng, F.-Z., Nabelek, P.I., Craddock, P.R., Groat, L.A., 2012. Iron, zinc, magnesium and uranium isotopic fractionation during continental crust differentiation: The tale from migmatites, granitoids, and pegmatites. Geochimica et Cosmochimica Acta 97, 247–265. https://doi.org/10.1016/j.gca.2012.08.024

Terentiev, R.A., Santosh, M., 2018. High magnesian granitoids in the Precambrian continental crust: Implication for the continuum between ferro–potassic and magnesio–potassic rock suites. Lithos 314–315, 669–682. https://doi.org/10.1016/j.lithos.2018.07.002

Terentiev, R.A., Santosh, M., 2017. Post-collisional high-Mg granitoids from the Paleoproterozoic East Sarmatian Orogen (East European Craton): Evidence for crust–mantle interaction. Lithos 274–275, 271–290. https://doi.org/10.1016/j.lithos.2017.01.004

Tian, S., Ding, X., Qi, Y., Wu, F., Cai, Y., Gaschnig, R.M., Xiao, Z., Lv, W., Rudnick, R.L., Huang, F., 2023. Dominance of felsic continental crust on Earth after 3 billion years ago is recorded by vanadium isotopes. Proceedings of the National Academy of Sciences 120, e2220563120. https://doi.org/10.1073/pnas.2220563120

Tiepolo, M., Oberti, R., Vannucci, R., 2002. Trace-element incorporation in titanite: constraints from experimentally determined solid/liquid partition coefficients. Chemical Geology, Chemistry and Physics of Accessory Minerals: Crystallisation, Transformation and Geochronoligical Applications 191, 105–119. https://doi.org/10.1016/S0009-2541(02)00151-1

Tiepolo, M., Oberti, R., Zanetti, A., Vannucci, R., Foley, S.F., 2007. Trace-Element Partitioning Between Amphibole and Silicate Melt. Reviews in Mineralogy and Geochemistry 67, 417–452. https://doi.org/10.2138/rmg.2007.67.11

Till, C.B., Grove, T.L., Withers, A.C., 2012. The beginnings of hydrous mantle wedge melting. Contrib Mineral Petrol 163, 669–688. https://doi.org/10.1007/s00410-011-0692-6

Tilley, D.B., Eggleton, R.A., 2005. Titanite Low-Temperature Alteration and Ti Mobility. Clays and Clay Minerals 53, 100–107. https://doi.org/10.1346/CCMN.2005.0530110

Tissot, F.L.H., Dauphas, N., 2015. Uranium isotopic compositions of the crust and ocean: Age corrections, U budget and global extent of modern anoxia. Geochimica et Cosmochimica Acta 167, 113–143. https://doi.org/10.1016/j.gca.2015.06.034

Tissot, F.L.H., Dauphas, N., Grossman, L., 2016. Origin of uranium isotope variations in early solar nebula condensates. Science Advances 2, e1501400. https://doi.org/10.1126/sciadv.1501400

Tissot, F.L.H., Dauphas, N., Grove, T.L., 2017. Distinct 238U/235U ratios and REE patterns in plutonic and volcanic angrites: Geochronologic implications and evidence for U isotope fractionation during magmatic processes. Geochimica et Cosmochimica Acta 213, 593–617. https://doi.org/10.1016/j.gca.2017.06.045

Tissot, F.L.H., Ibanez-Mejia, M., Boehnke, P., Dauphas, N., McGee, D., L. Grove, T., Mark Harrison, T., 2019. 238 U/ 235 U measurement in single-zircon crystals: implications for the Hadean environment, magmatic differentiation and geochronology. Journal of Analytical Atomic Spectrometry 34, 2035–2052. https://doi.org/10.1039/C9JA00205G

Tollan, P., Hermann, J., 2019. Arc magmas oxidized by water dissociation and hydrogen incorporation in orthopyroxene. Nat. Geosci. 12, 667–671. https://doi.org/10.1038/s41561-019-0411-x

Tripp, G.I., 2013. Stratigraphy and structure in the Neoarchaean of the Kalgoorlie district, Australia: critical controls on greenstone-hosted gold deposits (PhD Thesis). James Cook University. https://doi.org/10.25903/s5tq-hp18

Turnbull, R.E., Allibone, A.H., Matheys, F., Fanning, C.M., Kasereka, E., Kabete, J., McNaughton, N.J., Mwandale, E., Holliday, J., 2021. Geology and geochronology of the Archean plutonic rocks in the northeast Democratic Republic of Congo. Precambrian Research 358, 106133. https://doi.org/10.1016/j.precamres.2021.106133

Urey, H.C., 1947. The Thermodynamic Properties of Isotopic Substances. Journal of the Chemical Society 562–581.

Valley, J.W., 2003. Oxygen Isotopes in Zircon. Reviews in Mineralogy and Geochemistry 53, 343–385. https://doi.org/10.2113/0530343

Valley, J.W., Kinny, P.D., Schulze, D.J., Spicuzza, M.J., 1998. Zircon megacrysts from kimberlite: oxygen isotope variability among mantle melts. Contrib Mineral Petrol 133, 1–11. https://doi.org/10.1007/s004100050432

Valley, J.W., Lackey, J.S., Cavosie, A.J., Clechenko, C.C., Spicuzza, M.J., Basei, M.A.S., Bindeman, I.N., Ferreira, V.P., Sial, A.N., King, E.M., Peck, W.H., Sinha, A.K., Wei, C.S., 2005. 4.4 billion years of crustal maturation: oxygen isotope ratios of magmatic zircon. Contrib Mineral Petrol 150, 561–580. https://doi.org/10.1007/s00410-005-0025-8

van Hunen, J., Moyen, J.-F., 2012. Archean Subduction: Fact or Fiction? Annual Review of Earth and Planetary Sciences 40, 195–219. https://doi.org/10.1146/annurev-earth-042711-105255

van Hunen, J., van den Berg, A.P., 2008. Plate tectonics on the early Earth: Limitations imposed by strength and buoyancy of subducted lithosphere. Lithos, Rocks Generated under Extreme Pressure and Temperature Conditions: Mechanisms, Concepts, Models 103, 217–235. https://doi.org/10.1016/j.lithos.2007.09.016

van Keken, P.E., Hacker, B.R., Syracuse, E.M., Abers, G.A., 2011. Subduction factory: 4. Depth-dependent flux of H2O from subducting slabs worldwide. Journal of Geophysical Research: Solid Earth 116. https://doi.org/10.1029/2010JB007922

Van Kranendonk, M.J., 2010. Two types of Archean continental crust: Plume and plate tectonics on early Earth. American Journal of Science 310, 1187–1209. https://doi.org/10.2475/10.2010.01

Van Kranendonk, M.J., Collins, W.J., Hickman, A., Pawley, M.J., 2004. Critical tests of vertical vs. horizontal tectonic models for the Archaean East Pilbara Granite–Greenstone Terrane, Pilbara Craton, Western Australia. Precambrian Research, Archaean Tectonics, Volume 2 131, 173–211. https://doi.org/10.1016/j.precamres.2003.12.015

Van Kranendonk, M.J., Hugh Smithies, R., Hickman, A.H., Wingate, M.T.D., Bodorkos, S., 2010. Evidence for Mesoarchean (~3.2 Ga) rifting of the Pilbara Craton: The missing link in an early Precambrian Wilson cycle. Precambrian Research 177, 145–161. https://doi.org/10.1016/j.precamres.2009.11.007

Vandenburg, E.D., Nebel, O., Smithies, R.H., Capitanio, F.A., Miller, L., Cawood, P.A., Millet, M.-A., Bruand, E., Moyen, J.-F., Wang, X., Nebel-Jacobsen, Y., 2023. Spatial and temporal control of Archean tectonomagmatic regimes. Earth-Science Reviews 241, 104417. https://doi.org/10.1016/j.earscirev.2023.104417

Veizer, J., Mackenzie, F.T., 2014. 9.15 - Evolution of Sedimentary Rocks, in: Holland, H.D., Turekian, K.K. (Eds.), Treatise on Geochemistry (Second Edition). Elsevier, Oxford, pp. 399–435. https://doi.org/10.1016/B978-0-08-095975-7.00715-4

Vidal, P., Blais, S., Jahn, B.M., Capdevila, R., Tilton, G.R., 1980. U-Pb and Rb-Sr systematics of the Suomussalmi Archean greenstone belt (Eastern Finland). Geochimica et Cosmochimica Acta 44, 2033–2044. https://doi.org/10.1016/0016-7037(80)90201-X

Villa, I.M., Bonardi, M.L., De Bièvre, P., Holden, N.E., Renne, P.R., 2016. IUPAC-IUGS status report on the half-lives of 238U, 235U and 234U. Geochimica et Cosmochimica Acta 172, 387–392. https://doi.org/10.1016/j.gca.2015.10.011

Walder, A.J., Platzner, I., Freedman, P.A., 1993. Isotope ratio measurement of lead, neodymium and neodymium–samarium mixtures, Hafnium and Hafnium–Lutetium mixtures with a double focusing multiple collector inductively coupled plasma mass spectrometer. J. Anal. At. Spectrom. 8, 19–23. https://doi.org/10.1039/JA9930800019

Wang, D., Guo, J.-H., Qian, Q., Fu, B., 2018. Formation of Late Archean High-δ18O Diorites through Partial Melting of Hydrated Metabasalts. Journal of Petrology 59, 419–446. https://doi.org/10.1093/petrology/egy033

Wang, J., Long, X., 2024. Early Paleoproterozoic TTG gneisses and potassic granitoids in the southern Trans-North China Orogen: Key constraints on the tectonic setting during the tectono-magmatic lull and the initiation of plate tectonics. Earth-Science Reviews 250, 104713. https://doi.org/10.1016/j.earscirev.2024.104713

Wang, K., Liu, S., Wang, M., Yan, M., 2017. Geochemistry and zircon U-Pb-Hf isotopes of the late Neoarchean granodiorite-monzogranite-quartz syenite intrusions in the Northern Liaoning Block, North China Craton: Petrogenesis and implications for geodynamic processes. Precambrian Research 295, 151–171. https://doi.org/10.1016/j.precamres.2017.04.021

Wang, W., Huang, S., Huang, F., Zhao, X., Wu, Z., 2020. Equilibrium inter-mineral titanium isotope fractionation: Implication for high-temperature titanium isotope geochemistry. Geochimica et Cosmochimica Acta 269, 540–553. https://doi.org/10.1016/j.gca.2019.11.008

Wang, W., Lu, Y., Gao, L., Sun, G., Zhou, X., Yao, J., Yang, W., Liang, X., 2024. Late Archean K-rich intermediate magmatism driven by deep supracrustal recycling. Chemical Geology 662, 122215. https://doi.org/10.1016/j.chemgeo.2024.122215

Wang, W., Zeng, L., Gao, L.-E., Wang, Q., Guo, C., Hou, K., Liu-Zeng, J., 2018. Eocene-Oligocene potassic high Ba-Sr granitoids in the Southeastern Tibet: Petrogenesis and tectonic implications. Lithos 322, 38–51. https://doi.org/10.1016/j.lithos.2018.10.008

Wang, X., Johnson, T.M., Lundstrom, C.C., 2015. Low temperature equilibrium isotope fractionation and isotope exchange kinetics between U(IV) and U(VI). Geochimica et Cosmochimica Acta 158, 262–275. https://doi.org/10.1016/j.gca.2015.03.006

Wang, X., Ossa Ossa, F., Hofmann, A., Agangi, A., Paprika, D., Planavsky, N.J., 2020. Uranium isotope evidence for Mesoarchean biological oxygen production in shallow marine and continental settings. Earth and Planetary Science Letters 551, 116583. https://doi.org/10.1016/j.epsl.2020.116583

Wang, X., Planavsky, N.J., Hofmann, A., Saupe, E.E., De Corte, B.P., Philippot, P., LaLonde, S.V., Jemison, N.E., Zou, H., Ossa, F.O., Rybacki, K., Alfimova, N., Larson, M.J., Tsikos, H., Fralick, P.W., Johnson, T.M., Knudsen, A.C., Reinhard, C.T., Konhauser, K.O., 2018. A Mesoarchean shift in uranium isotope systematics. Geochimica et Cosmochimica Acta 238, 438–452. https://doi.org/10.1016/j.gca.2018.07.024

Wang, X., Zhu, W.-B., Zheng, Y.-F., 2022. Geochemical constraints on the nature of Late Archean basaltic-andesitic magmatism in the North China Craton. Earth-Science Reviews 230, 104065. https://doi.org/10.1016/j.earscirev.2022.104065

Watanabe, Y., Tajika, E., Ozaki, K., 2023. Evolution of iron and oxygen biogeochemical cycles during the Precambrian. Geobiology 21, 689–707. https://doi.org/10.1111/gbi.12571

Watkins, J.M., Clemens, J.D., Treloar, P.J., 2007. Archaean TTGs as sources of younger granitic magmas: melting of sodic metatonalites at 0.6–1.2 GPa. Contrib Mineral Petrol 154, 91–110. https://doi.org/10.1007/s00410-007-0181-0

Watkins, J.M., DePaolo, D.J., Watson, E.B., 2017. Kinetic Fractionation of Non-Traditional Stable Isotopes by Diffusion and Crystal Growth Reactions. Reviews in Mineralogy and Geochemistry 82, 85–125. https://doi.org/10.2138/rmg.2017.82.4

Webster, J.D., Piccoli, P.M., 2015. Magmatic Apatite: A Powerful, Yet Deceptive, Mineral. Elements 11, 177–182. https://doi.org/10.2113/gselements.11.3.177

Wei, G.-Y., Planavsky, N.J., He, T., Zhang, F., Stockey, R.G., Cole, D.B., Lin, Y.-B., Ling, H.-F., 2021. Global marine redox evolution from the late Neoproterozoic to the early Paleozoic constrained by the integration of Mo and U isotope records. Earth-Science Reviews 214, 103506. https://doi.org/10.1016/j.earscirev.2021.103506

Weller, O.M., Copley, A., Miller, W.G.R., Palin, R.M., Dyck, B., 2019. The relationship between mantle potential temperature and oceanic lithosphere buoyancy. Earth and Planetary Science Letters 518, 86–99. https://doi.org/10.1016/j.epsl.2019.05.005

Westall, F., Xiao, S., 2024. Precambrian Earth: Co-evolution of life and geodynamics. Precambrian Research 414, 107589. https://doi.org/10.1016/j.precamres.2024.107589

Weyer, S., Anbar, A.D., Gerdes, A., Gordon, G.W., Algeo, T.J., Boyle, E.A., 2008a. Natural fractionation of 238U/235U. Geochimica et Cosmochimica Acta 72, 345–359. https://doi.org/10.1016/j.gca.2007.11.012

Whalen, Joseph.B., Percival, J.A., McNicoll, V.J., Longstaffe, F.J., 2004. Geochemical and isotopic (Nd–O) evidence bearing on the origin of late- to post-orogenic high-K granitoid rocks in the Western Superior Province: implications for late Archean tectonomagmatic processes. Precambrian Research, Insights on Archean Continent - Ocean Assembly, Western Superior Province: Insights on Archean Continent 132, 303–326. https://doi.org/10.1016/j.precamres.2003.11.007

Wheeler, K.T., Walker, D., Fei, Y., Minarik, W.G., McDonough, W.F., 2006. Experimental partitioning of uranium between liquid iron sulfide and liquid

silicate: Implications for radioactivity in the Earth's core. Geochimica et Cosmochimica Acta 70, 1537–1547. https://doi.org/10.1016/j.gca.2005.11.023

Wiemer, D., Schrank, C.E., Murphy, D.T., Wenham, L., Allen, C.M., 2018. Earth's oldest stable crust in the Pilbara Craton formed by cyclic gravitational overturns. Nature Geoscience 11, 357–361. https://doi.org/10.1038/s41561-018-0105-9

Willbold, M., Elliott, T., Moorbath, S., 2011. The tungsten isotopic composition of the Earth's mantle before the terminal bombardment. Nature 477, 195–198. https://doi.org/10.1038/nature10399

Williams, H.M., Nielsen, S.G., Renac, C., Griffin, W.L., O'Reilly, S.Y., McCammon, C.A., Pearson, N., Viljoen, F., Alt, J.C., Halliday, A.N., 2009. Fractionation of oxygen and iron isotopes by partial melting processes: Implications for the interpretation of stable isotope signatures in mafic rocks. Earth and Planetary Science Letters 283, 156–166. https://doi.org/10.1016/j.epsl.2009.04.011

Williams, N.H., 2015. Titanium Isotope Cosmochemistry (PhD Thesis). The University of Manchester (United Kingdom).

Williams, N.H., Fehr, M.A., Parkinson, I.J., Mandl, M.B., Schönbächler, M., 2021. Titanium isotope fractionation in solar system materials. Chemical Geology 568, 120009. https://doi.org/10.1016/j.chemgeo.2020.120009

Winther, K.T., 1996. An experimentally based model for the origin of tonalitic and trondhjemitic melts. Chemical Geology 127, 43–59. https://doi.org/10.1016/0009-2541(95)00087-9

Wipperfurth, S.A., Guo, M., Šrámek, O., McDonough, W.F., 2018. Earth's chondritic Th/U: Negligible fractionation during accretion, core formation, and crust–mantle differentiation. Earth and Planetary Science Letters 498, 196–202. https://doi.org/10.1016/j.epsl.2018.06.029

Witt, W.K., Ford, A., Hanrahan, B., Mamuse, A., 2013. Regional-scale targeting for gold in the Yilgarn Craton: Part 1 of the Yilgarn Gold Exploration Targeting Atlas (No. 125). Geological Survey of Western Australia, Perth, Australia.

Wolf, M.B., Wyllie, P.J., 1994. Dehydration-melting of amphibolite at 10 kbar: the effects of temperature and time. Contr. Mineral. and Petrol. 115, 369–383. https://doi.org/10.1007/BF00320972

Wu, F., Turner, S., Schaefer, B.F., 2020. Mélange versus fluid and melt enrichment of subarc mantle: A novel test using barium isotopes in the Tonga-Kermadec arc. Geology 48, 1053–1057. https://doi.org/10.1130/G47549.1

Wu, Z., Wang, C., Allen, M.B., Tang, M., Chen, Y., Jia, L., Song, S., 2024. Rise of mantle oxidation by Neoarchean subduction in the North China Craton. Earth and Planetary Science Letters 646, 119006. https://doi.org/10.1016/j.epsl.2024.119006

Xu, Y., Polat, A., Meng, X.-J., Meng, Y.-K., Deng, X., Liu, Y., Yang, K.-G., 2019. The late Neoarchean transition from low- to high-K granitoids in western Liaoning Province, NE China: Clues from geochemistry and zircon U–Pb–Hf–O isotopes. Gondwana Research 76, 224–245. https://doi.org/10.1016/j.gr.2019.06.013

Xu, Y., Szilas, K., Zhang, L., Zhu, J.-M., Wu, G., Zhang, J., Qin, B., Sun, Y., Pearson, D.G., Liu, J., 2023. Ni isotopes provide a glimpse of Earth's pre-late-veneer mantle. Science Advances 9, eadj2170. https://doi.org/10.1126/sciadv.adj2170

Yao, J., Wang, W., Gao, L., Hu, F., Lu, D., He, X., Guo, L., 2023. Initiation of Mesoarchean nascent subduction zone in the North China Craton. GSA Bulletin 136, 949–963. https://doi.org/10.1130/B36877.1

Yaxley, G., Green, D., 1998. Reactions between eclogite and peridotite: Mantle refertilisation by subduction of oceanic crust. Schweizerische Mineralogische Und Petrographische Mitteilungen 78, 243–255.

Yearron, L.M., 2003. Archaean granite petrogenesis and implications for the evolution of the Barberton mountain land, South Africa (PhD Thesis). Kingston University.

Yogodzinski, G.M., Kelemen, P.B., Hoernle, K., Brown, S.T., Bindeman, I., Vervoort, J.D., Sims, K.W.W., Portnyagin, M., Werner, R., 2017. Sr and O isotopes in western Aleutian seafloor lavas: Implications for the source of fluids and trace element character of arc volcanic rocks. Earth and Planetary Science Letters 475, 169–180. https://doi.org/10.1016/j.epsl.2017.07.007

Young, E.D., Manning, C.E., Schauble, E.A., Shahar, A., Macris, C.A., Lazar, C., Jordan, M., 2015. High-temperature equilibrium isotope fractionation of non-traditional stable isotopes: Experiments, theory, and applications. Chemical Geology 395, 176–195. https://doi.org/10.1016/j.chemgeo.2014.12.013

Yu, Y., Li, D., Chen, Y., Kang, H., Geng, J., Xu, S., Wang, Y., Sun, M., 2021. Mantle cooling and cratonization of Archean lithosphere by continuous plate subduction: Constraints from TTGs, sanukitoids, and high-K granites, eastern North China Craton. Precambrian Research 353, 106042. https://doi.org/10.1016/j.precamres.2020.106042

Zhang, C., Holtz, F., Koepke, J., Wolff, P.E., Ma, C., Bédard, J.H., 2013. Constraints from experimental melting of amphibolite on the depth of formation of garnet-rich restites, and implications for models of Early Archean crustal growth. Precambrian Research 231, 206–217. https://doi.org/10.1016/j.precamres.2013.03.004

Zhang, J., Dauphas, N., Davis, A.M., Pourmand, A., 2011. A new method for MC-ICPMS measurement of titanium isotopic composition: Identification of correlated isotope anomalies in meteorites. Journal of Analytical Atomic Spectrometry 26, 2197–2205. https://doi.org/10.1039/C1JA10181A

Zhang, J., Wang, D., Guo, J., Ren, Y., Tian, H., Wang, H., Tong, X., Zhang, Y., Shi, J., Chang, Q., Xiang, Z., 2023. Petrogenesis of the ca. 2.5 Ga dioritic-TTG and granitic gneisses from the Huai'an Complex and its implications for crustal evolution and tectonic settings of the North China Craton. Lithos 444–445, 107104. https://doi.org/10.1016/j.lithos.2023.107104

Zhang, L., Zhang, H., Hawkesworth, C., Luo, B., Yang, H., Xu, W., Guo, L., Pan, F., Gao, Z., Tao, L., 2019. Sediment contribution in post-collisional high Ba-Sr magmatism: Evidence from the Xijing pluton in the Alxa block, NW China. Gondwana Research 69, 177–192. https://doi.org/10.1016/j.gr.2018.12.010

Zhang, Y., Gazel, E., Gaetani, G.A., Klein, F., 2021. Serpentinite-derived slab fluids control the oxidation state of the subarc mantle. Science Advances 7, eabj2515. https://doi.org/10.1126/sciadv.abj2515

Zhang, Y., Liu, H., Wang, Y., Chen, Q., Chen, C., Zhang, J., Fang, J., Zhang, L., Sun, W., 2025. A thickening event of the continental lithosphere ca. 2.2 billion years ago revealed by Nb/Ta-Dy/Yb systematics in basaltic rocks. Geoscience Frontiers 16, 101993. https://doi.org/10.1016/j.gsf.2024.101993

Zhang, Z.J., Dauphas, N., Johnson, A.C., Aarons, S.M., Bennett, V.C., Nutman, A.P., MacLennan, S., Schoene, B., 2023. Titanium and iron isotopic records of granitoid crust production in diverse Archean cratons. Earth and Planetary Science Letters 620, 118342. https://doi.org/10.1016/j.epsl.2023.118342

Zhao, X., Tang, S., Li, J., Wang, H., Helz, R., Marsh, B., Zhu, X., Zhang, H., 2020. Titanium isotopic fractionation during magmatic differentiation. Contrib Mineral Petrol 175, 67. https://doi.org/10.1007/s00410-020-01704-1

Zhao, X., Wang, X.-J., Jia, X., Evans, N., Yi, C., Chen, L.-H., Hanyu, T., Li, J., Wan, B., Zhu, X., Zhang, H., 2024. Titanium isotopic fractionation during alkaline magma differentiation at St. Helena Island. Contributions to Mineralogy and Petrology 179, 6. https://doi.org/10.1007/s00410-023-02085-x

Zhou, Y., Zhai, M., Mitchell, R.N., Cawood, P.A., Huang, G., Spencer, C.J., Chen, M., Li, Y., Zhao, T., Wu, T., 2024. Low δ18O and δ30Si TTG at ca. 2.3 Ga Hints at an Intraplate Rifting Onset of the Paleoproterozoic Supercontinent Cycle. Journal of Geophysical Research: Solid Earth 129, e2023JB027306. https://doi.org/10.1029/2023JB027306

Zhu, R.-Z., Fowler, M., Huang, F., Bruand, E., Wang, X.-J., Chen, L.-H., Storey, C., Yin, J., Lai, S., 2024. Barium-Mg isotopes in high Ba-Sr granites record a melt-metasomatized mantle source and crustal growth. Geochimica et Cosmochimica Acta 379, 124–133. https://doi.org/10.1016/j.gca.2024.07.004

Zimmer, M.M., Plank, T., Hauri, E.H., Yogodzinski, G.M., Stelling, P., Larsen, J., Singer, B., Jicha, B., Mandeville, C., Nye, C.J., 2010. The Role of Water in Generating the Calc-alkaline Trend: New Volatile Data for Aleutian Magmas and a New Tholeiitic Index. Journal of Petrology 51, 2411–2444. https://doi.org/10.1093/petrology/egq062

Appendix A – Measured δ⁴⁹Ti, δ²³⁸U and δ²³⁴U of geological reference materials

Table A1: Measured δ⁴⁹Ti (‰) of geological reference materials. 95% ci = 95% confidence interval. 2sd = 2 standard deviations. n = number of measurements.

Reference Material	δ⁴⁹Ti ‰	95% ci ‰	2sd ‰	n
JB-2	-0.023	0.024		
	-0.027	0.021		
	-0.028	0.020		
	-0.013	0.026		
	-0.033	0.021		
	-0.019	0.023		
	-0.031	0.021		
Weighted mean	*-0.026*		*0.021*	*7*
RGM-2	0.553	0.019		
	0.595	0.021		
	0.548	0.022		
	0.592	0.027		
	0.604	0.021		
	0.589	0.021		
	0.577	0.021		
	0.564	0.026		
	0.548	0.021		
Weighted mean	*0.574*		*0.021*	*9*
BCR-2	-0.005	0.021		
	-0.019	0.024		
Weighted mean	*-0.012*		*0.021*	*2*

Table A2: Measured δ²³⁸U (‰) and δ²³⁴U (‰) of geological reference materials. 2se = 2 standard errors. 2sd = 2 standard deviations. n = number of measurements.

Reference Material	δ²³⁸U ‰	2se ‰	2sd ‰	δ²³⁴U ‰	2se ‰	2sd ‰	n
BCR-2	-0.26	0.03		4	1		
	-0.26	0.04		3	1		
	-0.27	0.04		2	2		
	-0.25	0.03		1	2		
Weighted mean	*-0.26*		*0.03*	*3*		*1*	*4*
HU-1	-0.54	0.03		6	1		1
CZ-1	-0.02	0.03		4	1		
	-0.08	0.03		5	1		
	-0.03	0.03		-1	1		
	-0.08	0.03		3	1		
	-0.05	0.04		0	1		
	-0.09	0.05		-2	1		
	-0.01	0.06		3	1		
	-0.06	0.03		6	1		
	0.00	0.06		1	1		
	-0.11	0.04		0	1		
	-0.02	0.04		-7	2		
	-0.05	0.05		4	2		
	-0.03	0.03		9	2		
	-0.04	0.04		0	2		
	-0.02	0.05		-3	2		
	-0.02	0.04		4	2		
Weighted mean	*-0.05*		*0.04*	*2*		*1*	*16*

Appendix B – Table of all new titanium and uranium isotope data presented in this thesis

Table B1: All new titanium (δ⁴⁹Ti) and uranium (δ²³⁸U, δ²³⁴U) isotope data presented in this thesis. 95% ci = 95% confidence interval on $\delta^{49}Ti$, calculated via the method described in Chapter 2. 2se = 2 standard errors on $\delta^{238}U$ and $\delta^{234}U$, calculated via the method described in Chapter 2. n = number of measurements made. Lithological descriptions are taken from the references listed in Appendix C. Bt = biotite, Hbl = hornblende, Amp = amphibole, Qz = quartz, Fsp = feldspar, Pl = plagioclase, Kfs = K-feldspar.

Sample	Lithological Description	Age	Suite	Location	$\delta^{49}Ti$	95% ci	n	$\delta^{238}U$	2se	$\delta^{234}U$	2se	n
		Ma			‰	‰		‰	‰	‰	‰	
Sanukitoids and analogues												
235921 Enclaves	Mafic microgranular enclaves	~3421	Sanukitoid-like rocks	Pilbara	0.227	0.021	1	-0.35	0.05	-2	5	1
235921	Bt-Hbl granite	~3421	Sanukitoid-like rocks	Pilbara	0.299	0.023	1	-0.35	0.05	-10	5	1
142170	Bt granite	~3421	Sanukitoid-like rocks	Pilbara	0.292	0.021	1					
235917	Bt-Hbl quartz diorite	2948	High-Mg diorite suite	Pilbara	0.211	0.032	2	-0.14	0.05	-60	5	1
142945	Metafelsic volcanic rock	~2950	High-Mg diorite suite	Pilbara	0.232	0.015	1					
142260	Melanodiorite	~2950	High-Mg diorite suite	Pilbara	0.177	0.016	1					
142347	Melanodiorite	2498 ± 5	High-Mg diorite suite	Pilbara	0.133	0.016	1	-0.31	0.05	1	5	1
142257	Tonalite-granodiorite	~2950	High-Mg diorite suite	Pilbara	0.161	0.018	1					
227869	Fsp-porphyritic basalt	~2660	High La/Th (high Ni) BFG	Yilgarn	0.197	0.020	1	-0.33	0.03	-1	9	2
227873	Pl-porphyritic basalt	~2660	High La/Th (high Ni) BFG	Yilgarn	0.176	0.026	1	-0.24	0.03	-3	9	2
223149	Metabasalt	~2660	High La/Th (high Ni) BFG	Yilgarn	0.137	0.020	1	-0.31	0.03	0	9	2
505567	Amp-porphyritic lamprophyre	~2660	High La/Th (high Ni) BFG	Yilgarn	0.164	0.019	1	-0.25	0.03	3	9	2
505652	Lamprophyre	~2660	High La/Th (high Ni) BFG	Yilgarn	0.146	0.021	1	-0.25	0.03	2	9	2
227863	Metabasalt	~2660	High La/Th (high Ni) BFG	Yilgarn				-0.30	0.03	-3	9	2
211213	Metabasalt	~2660	High La/Th (high Ni) BFG	Yilgarn				-0.23	0.04	5	9	2
229900	Hbl-diorite	~2660	High La/Th (high Ni) BFG	Yilgarn	0.157	0.022	1	-0.29	0.05	2	5	1

Sample	Lithological Description	Age Ma	Suite	Location	δ⁴⁹Ti ‰	95% ci ‰	n	δ²³⁸U ‰	2se ‰	δ²³⁴U ‰	2se ‰	n
Sanukitoids and analogues												
228046	Granitic rock	~2660	High La/Th (high Ni) BFG	Yilgarn	0.208	0.024	1					
223100	Fsp-porphyritic dacite	~2660	High La/Th (high Ni) BFG	Yilgarn	0.221	0.024	1					
229913	Diorite	2666 ± 7	High La/Th (high Ni) BFG	Yilgarn	0.236	0.020	1					
223123	Pl-porphyritic dacite	~2660	High La/Th (high Ni) BFG	Yilgarn	0.213	0.025	1					
223112	Fsp-porphyritic dacite	~2660	High La/Th (high Ni) BFG	Yilgarn	0.210	0.026	1					
223146	Pl-porphyritic dacite	~2660	High La/Th (high Ni) BFG	Yilgarn	0.280	0.028	1					
223143	Pl-porphyritic dacite	~2660	High La/Th (high Ni) BFG	Yilgarn	0.286	0.025	1					
223157	Metabasalt	~2660	High La/Th (low Ni) BFG	Yilgarn	0.157	0.024	1	-0.24	0.03	5	9	2
229901	Hbl-porphyritic andesite	~2660	High La/Th (low Ni) BFG	Yilgarn	0.126	0.020	1	-0.28	0.03	2	9	2
227885	Felsic volcaniclastic sandstone	~2660	High La/Th (low Ni) BFG	Yilgarn	0.123	0.020	1					
211545	Meta-andesite	~2660	High La/Th (low Ni) BFG	Yilgarn	0.233	0.018	1					
230891	Hbl-Bt granitic rock	~2660	High La/Th (low Ni) BFG	Yilgarn	0.207	0.020	1	-0.26	0.05	1	5	1
211545	Meta-andesite	~2660	High La/Th (low Ni) BFG	Yilgarn	0.233	0.020	1					
223070	Felsic volcaniclastic rock	~2660	High La/Th (low Ni) BFG	Yilgarn	0.268	0.020	1					
227874	Pl-porphyritic basalt	~2690	Low La/Th BFG	Yilgarn	0.182	0.025	1	-0.30	0.05	0	9	2
501922	Porphyry	~2690	Low La/Th BFG	Yilgarn	0.180	0.021	1	-0.28	0.03	1	9	2
505465	Quartz diorite	~2690	Low La/Th BFG	Yilgarn	0.108	0.023	1	-0.31	0.04	7	9	2
230733	Felsic volcaniclastic rock	~2690	Low La/Th BFG	Yilgarn	0.139	0.021	1	-0.27	0.05	-13	5	1
224582	Meta-andesite	~2690	Low La/Th BFG	Yilgarn	0.170	0.020	1					
224513	Felsic volcaniclastic sandstone	~2690	Low La/Th BFG	Yilgarn	0.199	0.022	1					
230774	Felsic volcaniclastic rock	~2690	Low La/Th BFG	Yilgarn	0.186	0.020	1					
230787	Pl-porphyritic dacite	~2690	Low La/Th BFG	Yilgarn	0.202	0.023	1					
233603	Hbl-Bt metagranodiorite	~2690	Low La/Th BFG	Yilgarn	0.259	0.021	1					
223185	Metagranodiorite	~2690	Low La/Th BFG	Yilgarn	0.291	0.021	1					
AMT 03	Bt-Hbl tonalite	2130 ± 2	Alto Maranhão suite	São Francisco	0.224	0.023	1	-0.23	0.03	-3	9	2

Table B1 continued:

Sample	Lithological Description	Age Ma	Suite	Location	δ⁴⁹Ti ‰	95% ci ‰	n	δ²³⁸U ‰	2se ‰	δ²³⁴U ‰	2se ‰	n
Sanukitoids and analogues												
AMT 02	Bt-Hbl tonalite	2130 ± 2	Alto Maranhão suite	São Francisco	0.231	0.023	1	-0.35	0.05	-27	5	1
AMT 01a	Bt-Hbl tonalite	2130 ± 2	Alto Maranhão suite	São Francisco	0.229	0.023	1					
AMT 01b	Bt-Hbl tonalite	2130 ± 2	Alto Maranhão suite	São Francisco	0.223	0.024	1					
MAJF 51b	Hbl-Bt granodioritic banded gneiss	2117 ± 24		São Francisco	0.144	0.018	1	-0.31	0.05	-13	5	1
MAJF 42	Hbl-Bt granodioritic gneiss	2114 ± 10		São Francisco	0.133	0.045	2					
RA1	Appinite	425 ± 1.5	Rogart pluton	Scotland	0.143	0.023	1					
RA2	Appinite	425 ± 1.5	Rogart pluton	Scotland	0.214	0.022	1	-0.20	0.03	2	9	2
RT1	Bt-Hbl tonalite	425 ± 1.5	Rogart pluton	Scotland	0.260	0.023	1	-0.21	0.05	3	5	1
RHG2	Bt-Hbl granodiorite	425 ± 1.5	Rogart pluton	Scotland	0.300	0.023	1					
SR2	Appinite	425 ± 3	Strontian pluton	Scotland	0.150	0.004	2					
SR3	Hbl-Bt granodiorite	425 ± 3	Strontian pluton	Scotland	0.165	0.015	2	-0.29	0.05	4	5	1
SR4	Hbl-Bt granodiorite	425 ± 3	Strontian pluton	Scotland	0.176	0.023	1	-0.26	0.05	1	5	1
TTGs												
235965	Mesosome	~3425		Pilbara				-0.34	0.05	149	5	1
142870	Tonalite	~3500		Pilbara				-0.24	0.05	3	5	1
235913	Granodiorite	~3270		Pilbara				-0.25	0.05	-59	5	1
235945	Granodiorite	~3303		Pilbara				-0.39	0.05	11	5	1
178102	Granodiorite	~2787		Yilgarn				-0.24	0.06	-85	5	1
232744	Tonalite	~2696		Yilgarn				-0.21	0.05	6	5	1
227968	Granitic rock	~2675	High-Sr HP TTG	Yilgarn	0.329	0.015	2					
502247	Amp-Qz-Fsp porphyry	~2675	High-Sr HP TTG	Yilgarn	0.446	0.022	1	-0.31	0.03	19	9	2
505481	Qz-Amp-Pl porphyry	~2675	High-Sr HP TTG	Yilgarn	0.371	0.022	1	-0.25	0.04	-4	9	2
230558	Granitic rock	~2675	MP-like HP TTG	Yilgarn	0.227	0.014	2	-0.26	0.03	-4	9	2
501894	Porphyry	~2675	MP-like HP TTG	Yilgarn	0.252	0.013	2					

Table B1 continued:

Sample	Lithological Description	Age	Suite	Location	δ^{49}Ti	95% ci	n	δ^{238}U	2se	δ^{234}U	2se	n
		Ma			‰	‰		‰	‰	‰	‰	
TTGs												
504718	Bt monzogranite	~2675	MP-like HP TTG	Yilgarn	0.292	0.022	1	-0.30	0.03	-31	9	2
233734	Metadacite	~2675	MP-like HP TTG	Yilgarn	0.206	0.022	1					
222660	Granitic gneiss	~2675	MP TTG	Yilgarn	0.482	0.023	1					
240405	Metagranitic rock	~2675	MP TTG	Yilgarn	0.296	0.023	1	-0.32	0.03	0	9	2
502533	Tonalite	~2675	MP TTG	Yilgarn	0.292	0.023	1	-0.31	0.04	2	9	2
234000	Metagranitic rock	~2675	MP TTG	Yilgarn	0.236	0.023	1					
500854	Kfs-Pl porphyry	~2675	LP TTG	Yilgarn	0.513	0.016	2	-0.37	0.03	4	9	2
240623	Metagranitic rock	~2675	LP TTG	Yilgarn	1.385	0.020	1					
501345	Granite	~2675	LP TTG	Yilgarn	0.586	0.016	2					
504940	Felsic tuff	~2675	LP TTG	Yilgarn	0.463	0.016	2					
501356	Granite	~2675	LP TTG	Yilgarn	0.401	0.015	2	-0.36	0.04	-70	9	2
233699	Metagranitic rock	~2675	LP TTG	Yilgarn	1.077	0.016	2					

Appendix C – Table of spatial data and literature geochemical data references for samples analysed in this thesis

Table C1: Spatial data and literature whole rock elemental and isotopic data references for the samples analysed in this thesis. The full list of references[a] is provided at the end of the table. CPTZ = Central Pilbara Tectonic Zone. EGST = Eastern Goldfields Superterrane.

Sample	Location	Latitude, decimal degrees	Longitude, decimal degrees	Core Name	Depth in core m	References for elemental and isotopic data[a]
Sanukitoids and analogues						
235921 Enclaves	East Pilbara Terrane, Pilbara Craton	-21.08991	118.51366			[1]
235921	East Pilbara Terrane, Pilbara Craton	-21.08991	118.51366			[1]
142170	East Pilbara Terrane, Pilbara Craton	-21.0900	118.5131			[1]
235917	Mallina Basin, CPTZ, Pilbara Craton	-21.04373	117.94143			[1]
142945	Mallina Basin, CPTZ, Pilbara Craton	-21.46535	117.93473			[2]
142260	Mallina Basin, CPTZ, Pilbara Craton	-21.097003	118.020236			[3]
142347	Mallina Basin, CPTZ, Pilbara Craton	-20.998694	118.097773			[3]
142257	Mallina Basin, CPTZ, Pilbara Craton	-21.073670	118.034958			[3]
227869	Kalgoorlie Terrane, EGST, Yilgarn Craton	-30.823624	121.557757	12GMSD001	107.33 – 107.46	[2]
227873	Kalgoorlie Terrane, EGST, Yilgarn Craton	-30.823624	121.557757	12GMSD001	154.59 – 154.68	[2]
223149	Kalgoorlie Terrane, EGST, Yilgarn Craton	-31.3263371	121.7902486	CD16056A	1284.52 – 1284.63	[4]
505567	Kalgoorlie Terrane, EGST, Yilgarn Craton	-31.254380	121.695163			[2]
505652	Kalgoorlie Terrane, EGST, Yilgarn Craton	-31.254438	121.717520			[2]
227863	Kalgoorlie Terrane, EGST, Yilgarn Craton	-30.926391	121.574102	FED362	113.40 – 113.62	[5]
211213	Kalgoorlie Terrane, EGST, Yilgarn Craton	-31.225722	121.674641	KD330	204.30 – 204.44	[5]

Table C1 continued:

Sample	Location	Latitude, decimal degrees	Longitude, decimal degrees	Core Name	Depth in core m	References for elemental and isotopic data[a]
Sanukitoids and analogues						
229900	Kalgoorlie Terrane, EGST, Yilgarn Craton	-31.2978	121.7589	LD 7454	924.09 – 924.34	[5]
228046	Kalgoorlie Terrane, EGST, Yilgarn Craton	-31.326337	121.790249	CD16056A	1283.25 – 1283.41	[5]
223100	Kalgoorlie Terrane, EGST, Yilgarn Craton	-31.326337	121.790249	CD16056	801.63 – 801.89	[5]
229913	Kalgoorlie Terrane, EGST, Yilgarn Craton	-31.2978	121.7557	LD 7006	828.47 – 828.71	[5]
223123	Kalgoorlie Terrane, EGST, Yilgarn Craton	-31.326337	121.790249	CD16056A	1000.75 – 1000.86	[5]
223112	Kalgoorlie Terrane, EGST, Yilgarn Craton	-31.326337	121.790249	CD16056	943.66 – 944.00	[5]
223146	Kalgoorlie Terrane, EGST, Yilgarn Craton	-31.326337	121.790249	CD16056A	1258.23 – 1258.60	[5]
223143	Kalgoorlie Terrane, EGST, Yilgarn Craton	-31.326337	121.790249	CD16056A	1172.60 – 1172.83	[5]
223157	Kalgoorlie Terrane, EGST, Yilgarn Craton	-31.3263371	121.7902486	CD16056A	1455.38 – 1455.62	[4]
229901	Kalgoorlie Terrane, EGST, Yilgarn Craton	-31.2978	121.7557	LD 7006	949.75 – 949.87	[5]
227885	Kalgoorlie Terrane, EGST, Yilgarn Craton	-30.823624	121.557757	12GMSD001	305.17 – 305.50	[5]
211545	Kalgoorlie Terrane, EGST, Yilgarn Craton	-30.815452	121.536230	SE18	1046.16 – 1046.34	[5]
230891	Kalgoorlie Terrane, EGST, Yilgarn Craton	-31.027780	121.918243	18EISD001	1150.73 – 1151.05	[5]
211545	Kalgoorlie Terrane, EGST, Yilgarn Craton	-30.815452	121.536230	SE18	1042.23 – 1042.43	[5]
223070	Kalgoorlie Terrane, EGST, Yilgarn Craton	-31.326337	121.790249	CD16056	181.30 – 181.61	[5]
227874	Kalgoorlie Terrane, EGST, Yilgarn Craton	-30.823624	121.557757			[2]
501922	Kalgoorlie Terrane, EGST, Yilgarn Craton	-30.603092	121.594820			[2]
505465	Kalgoorlie Terrane, EGST, Yilgarn Craton	-31.262337	121.707811			[2]
230733	Kalgoorlie Terrane, EGST, Yilgarn Craton	-30.772866	121.279680	PDDD003	292.74 – 292.95	[5]
224582	Kalgoorlie Terrane, EGST, Yilgarn Craton	-30.736245	121.253266	PGDD15001	1178.17 – 1178.28	[5]
224513	Kalgoorlie Terrane, EGST, Yilgarn Craton	-30.761413	121.276641	MEDD144	253.00 – 253.15	[5]
230774	Kalgoorlie Terrane, EGST, Yilgarn Craton	-30.721911	121.216094	WKDD15004	213.69 – 214.06	[5]
230787	Kalgoorlie Terrane, EGST, Yilgarn Craton	-30.773491	121.291465	PDDD010	521.53 – 521.73	[5]
233603	Kalgoorlie Terrane, EGST, Yilgarn Craton	-30.40857	121.40003	PGCD0024	59.40 – 59.67	[5]

Table C1 continued:

Sample	Location	Latitude, decimal degrees	Longitude, decimal degrees	Core Name	Depth in core m	References for elemental and isotopic data[a]
Sanukitoids and analogues						
223185	Kalgoorlie Terrane, EGST, Yilgarn Craton	-30.549076	121.490884	RYDD14004	109.70 – 110.19	[5]
AMT 03	Mineiro Belt, São Francisco Craton	-20.6565431	-43.6716649			[6]
AMT 02	Mineiro Belt, São Francisco Craton	-20.6707198	-43.6429364			[6]
AMT 01a	Mineiro Belt, São Francisco Craton	-20.6516888	-43.7325297			[6]
AMT 01b	Mineiro Belt, São Francisco Craton	-20.6516888	-43.7325297			[6]
MAJF 51b	Mineiro Belt, São Francisco Paleocontinent	-21.5837280	-44.3833899			[7]
MAJF 42	Mineiro Belt, São Francisco Paleocontinent	-21.2869793	-44.1418248			[7]
RA1	Northern Highland Terrane, Scotland	57.993610	-4.197395			[8], [9]
RA2	Northern Highland Terrane, Scotland					[8], [9]
RT1	Northern Highland Terrane, Scotland	58.029737	-4.133558			[8], [9]
RHG2	Northern Highland Terrane, Scotland					[8], [9]
SR2	Northern Highland Terrane, Scotland	56.689017	-5.616935			[9], [10]
SR3	Northern Highland Terrane, Scotland	56.685100	-5.627994			[9], [10]
SR4	Northern Highland Terrane, Scotland	56.730766	-5.540805			[9], [10]
TTGs						
235965	East Pilbara Terrane, Pilbara Craton	-21.75661	119.23913			[1]
142870	East Pilbara Terrane, Pilbara Craton	-20.81288	120.56729			[1]
235913	Karratha Terrane, Pilbara Craton	-20.82914	116.85296			[1]
235945	East Pilbara Terrane, Pilbara Craton	-20.91388	120.55534			[1]
178102	Youanmi Terrane, Yilgarn Craton	-26.74518	118.30393			
232744	Youanmi Terrane, Yilgarn Craton	-28.14251	117.78442			
227968	Kalgoorlie Terrane, EGST, Yilgarn Craton	-31.21119	121.67346			[2]
502247	Kalgoorlie Terrane, EGST, Yilgarn Craton	-31.028103	121.600152			[2]

Table C1 continued:

Sample	Location	Latitude Decimal degrees	Longitude Decimal degrees	Core Name	Depth in core m	References for elemental and isotopic data[a]
TTGs						
505481	Kalgoorlie Terrane, EGST, Yilgarn Craton	-31.225697	121.669862			[2]
230558	Kalgoorlie Terrane, EGST, Yilgarn Craton	-30.33968	-120.79401			[2]
501894	Kalgoorlie Terrane, EGST, Yilgarn Craton	-30.595704	121.574202			[2]
504718	Kalgoorlie Terrane, EGST, Yilgarn Craton	-30.860039	121.157542			[2]
233734	Kalgoorlie Terrane, EGST, Yilgarn Craton	-31.02936	121.56274			[2]
222660	Kalgoorlie Terrane, EGST, Yilgarn Craton	-31.29826	121.30681			[2]
240405	Kalgoorlie Terrane, EGST, Yilgarn Craton	-30.17809	121.23090			[2]
502533	Kalgoorlie Terrane, EGST, Yilgarn Craton	-32.120730	121.936648			[2]
234000	Kalgoorlie Terrane, EGST, Yilgarn Craton	-30.38420	121.51736			[2]
500854	Kurnalpi Terrane, EGST, Yilgarn Craton	-29.357069	122.213874			[2]
240623	Kalgoorlie Terrane, EGST, Yilgarn Craton	-30.21838	120.95453			[2]
501345	Kalgoorlie Terrane, EGST, Yilgarn Craton	-27.081473	120.738437			[2]
504940	Kalgoorlie Terrane, EGST, Yilgarn Craton	-27.418373	120.939233			[2]
501356	Kalgoorlie Terrane, EGST, Yilgarn Craton	-27.272066	120.520228			[2]
233699	Kalgoorlie Terrane, EGST, Yilgarn Craton	-30.37482	121.08043			[2]

[a]*References: [1] Vandenberg et al. (2023); [2] Western Australia Geochemistry Database (WACHEM, Geological Survey of Western Australia, 2025); [3] Smithies and Champion (2000); [4] Smithies et al. (2019); [5] Smithies et al. (2022); [6] Moreira et al. (2018); [7] Bruno et al. (2021); [8] Fowler et al. (2001); [9] Zhu et al. (2024); [10] Fowler et al. (2008).*

Appendix D – Method for Rayleigh fractionation modelling of titanium isotopes during sanukitoid differentiation
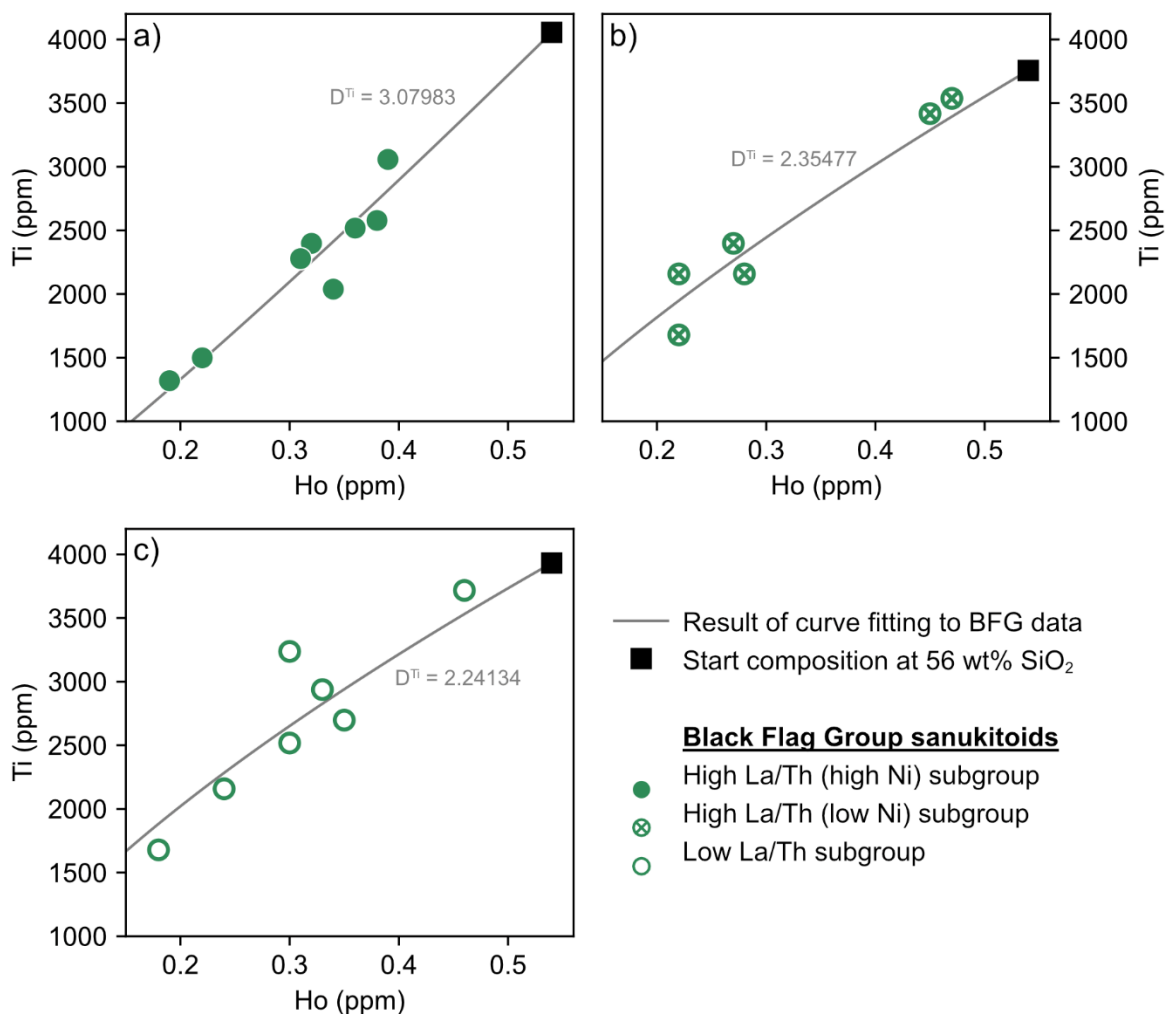
Figure D1: Ti (ppm) vs Ho (ppm) for the Black Flag Group subgroups – a) high La/Th (high Ni) BFG, b) high La/Th (low Ni) BFG), c) low La/Th BFG. The grey lines show the results of curve fitting equation D3 to the Ti and Ho concentration data.

I modelled the Ti isotope composition of the Black Flag Group (BFG) sanukitoids, Yilgarn Craton, during differentiation using Rayleigh fractionation. The three

subgroups of the BFG – high La/Th (high Ni), high La/Th (low Ni) and low La/Th – were each considered separately.

Rayleigh fractionation modelling requires calculation of the fraction of Ti remaining in the melt (F_{melt}^{Ti}) when each sample formed. To calculate F_{melt}^{Ti} I used the Rayleigh fractional crystallisation modelling for the BFG between 56 – 69 wt% SiO_2 of Smithies et al. (2019), which constrained the bulk partition coefficients (D_{bulk}^i) of various trace elements during differentiation. BFG Ti concentrations (C_{melt}^{Ti}) show strong positive correlation with Ho concentrations (C_{melt}^{Ho}, fig. D1). Melt Ti and Ho concentrations can be described as a function of their bulk partition coefficients by equations D1 and D2 respectively.

$$C_{melt}^{Ti} = C_0^{Ti} \left(F_{melt}^{\left(D_{bulk}^{Ti} - 1 \right)} \right) \quad (D1)$$

$$C_{melt}^{Ho} = C_0^{Ho} \left(F_{melt}^{\left(D_{bulk}^{Ho} - 1 \right)} \right) \quad (D2)$$

F_{melt} is the fraction of melt remaining in the system, while C_0^{Ti} and C_0^{Ho} are the initial concentrations of Ti and Ho in the melt respectively. Equations D1 and D2 are parametric equations that describe the trends in figure D1, and can be combined into a single equation (equation D3).

$$C_{melt}^{Ti} = C_0^{Ti} \left(\frac{C_{melt}^{Ho}}{C_0^{Ho}} \right)^{\left(\frac{D_{bulk}^{Ti} - 1}{D_{bulk}^{Ho} - 1} \right)} \quad (D3)$$

C_0^{Ti} was determined by linear regression of Ti (ppm) vs SiO_2, calculated at 56 wt% SiO_2 for each subgroup. C_0^{Ho} = 0.54 ppm and D_{bulk}^{Ho} are taken from Smithies et al. (2019) model 2. To determine the optimum value of D_{bulk}^{Ti} I did curve fitting of equation D3 to the BFG Ti and Ho concentration data using the curve_fit function from the SciPy optimize subpackage. The results of the curve fitting are shown by the grey lines in figure D1 and the optimum D_{bulk}^{Ti} values given in table D1.

I calculated F_{melt} for each sample with equation D4, using the previously determined optimum D_{bulk}^{Ti}.

$$F_{melt} = \left(\frac{C_{melt}^{Ti}}{C_0^{Ti}} \right)^{\left(\frac{1}{D_{bulk}^{Ti} - 1} \right)} \quad (D4)$$

F_{melt} values were then normalised to the F_{melt} value of the sample closest to the onset of the increase in δ⁴⁹Ti (F_{melt}^{prim}) to give $F_{melt\ (N)}$ (equation D5).

$$F_{melt\ (N)} = \frac{F_{melt}}{F_{melt}^{prim}} \quad (D5)$$

Finally, for each sample F_{melt}^{Ti} was calculated using equation D6, where C_{prim}^{Ti} is the Ti concentration of the sample closest to the onset of the increase in δ⁴⁹Ti.

$$F_{melt}^{Ti} = F_{melt\ (N)} \left(\frac{C_{melt}^{Ti}}{C_{prim}^{Ti}} \right) \quad (D6)$$

The solid-melt fractionation factor ($\alpha_{(solid-melt)}$) for each BFG subgroup was determined by weighted curve fitting of the Rayleigh fractionation equation (equation D7) to the measured δ⁴⁹Ti and calculated F_{melt}^{Ti} of the samples, again using the curve_fit function from the SciPy optimize subpackage.

$$\delta^{49}Ti = 10^3 \left(F_{melt}^{Ti}{}^{(\alpha_{(solid-melt)} - 1)} - 1 \right) + \delta^{49}Ti_0 \quad (D7)$$

$\delta^{49}Ti_0$ was taken as the δ⁴⁹Ti of the sample closest to the onset of the increase in δ⁴⁹Ti for each subgroup. The 2σ uncertainty in $\alpha_{(solid-melt)}$ was calculated from the variance returned by the curve_fit function. The values used for modelling and the optimum $\alpha_{(solid-melt)}$ for each BFG subgroup are shown in table D1, and figure D2 shows the final Rayleigh fractionation models.

Table D1: Values used and calculated by the Rayleigh fractionation modelling of Ti isotope compositions during differentiation of the Black Flag Group subgroups.

BFG Subgroup	C_0^{Ti} (ppm)	D_{bulk}^{Ti}	F_{melt}^{prim}	C_{prim}^{Ti} (ppm)	δ⁴⁹Ti$_0$ (‰)	$\alpha_{(solid-melt)}$	2σ
High La/Th (high Ni)	4055.54	3.07983	0.873	3057.45	0.157	0.99988	0.00003
High La/Th (low Ni)	3756.48	2.35477	0.957	3537.05	0.126	0.99988	0.00001
Low La/Th	3931.41	2.24134	0.956	3716.90	0.139	0.99989	0.00001
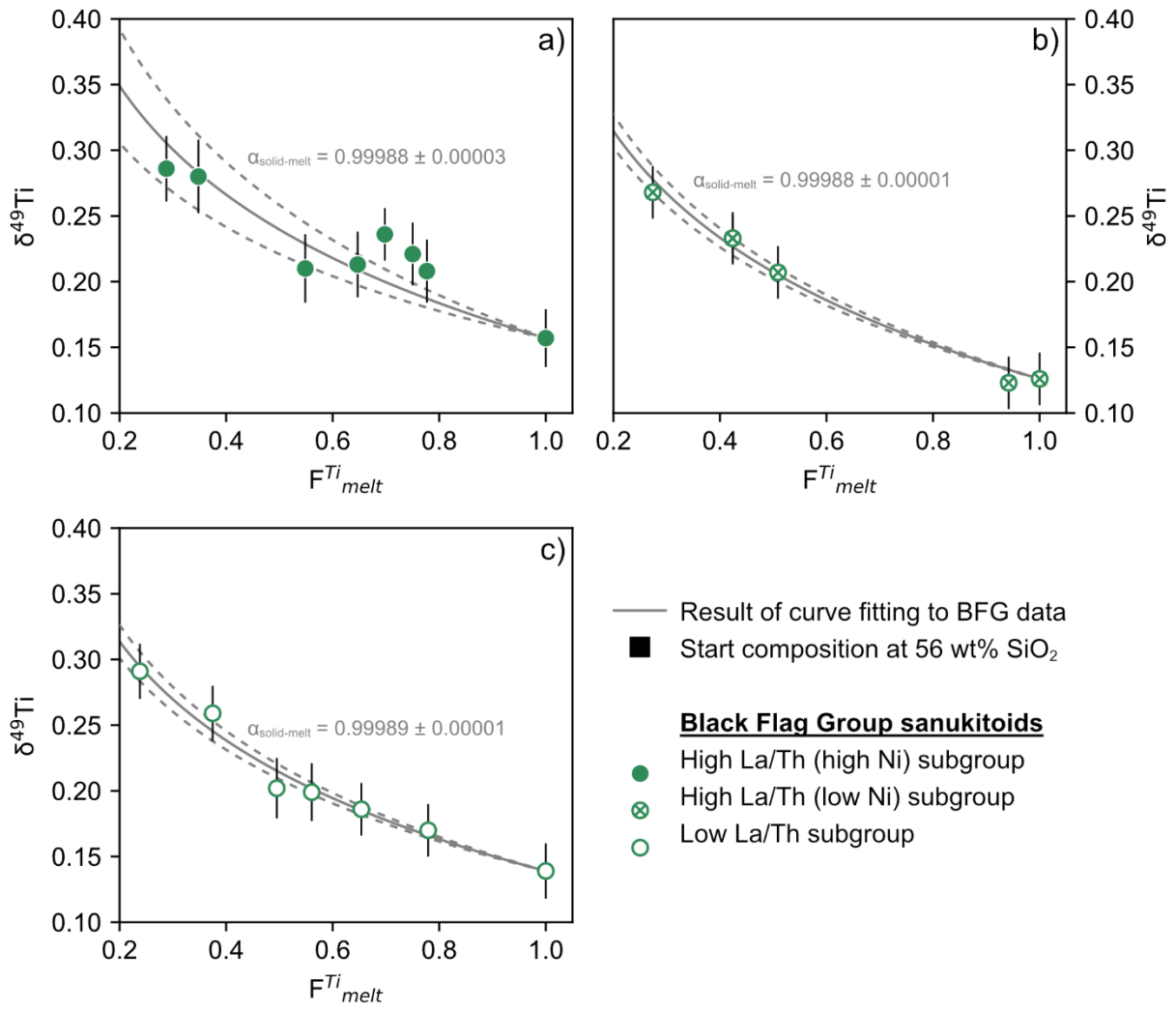
Figure D2: δ⁴⁹Ti vs calculated F^Ti_melt and Rayleigh fractionation models for the Black Flag Group subgroups – a) high La/Th (high Ni) BFG, b) high La/Th (low Ni) BFG), c) low La/Th BFG. The solid grey lines show the Rayleigh fractionation models, and the dashed grey lines show the 2σ uncertainty on those models. Uncertainty on sample δ⁴⁹Ti is shown as the 95% confidence interval.

Appendix E – Method for modelling of titanium isotope fractionation during partial melting

During partial melting, Ti isotope fractionation may arise due to the contrast in Ti coordination between the silicate melt (predominantly 5-fold coordination) and residual Ti-bearing minerals (either 6-fold coordination, 4-fold coordination or both). The magnitude of this mass-dependent Ti isotope fractionation ($\alpha_{mineral-melt}$) can be determined directly from measured natural and experimental mineral-melt pairs (Hoare et al., 2022; Mandl, 2019; Rzehak et al., 2022) or from *ab initio* calculations based on density functional theory (Aarons et al., 2021; Leitzke et al., 2018; W. Wang et al., 2020). When these fractionation factors are combined with melting temperatures, and phase proportions and Ti concentrations from partial melting experiments, I can model the Ti stable isotope fractionation during that partial melting.

I used direct measurements of mineral-melt pairs to constrain $\alpha_{mineral-melt}$ where available. Experimental rutile-melt pairs were analysed by Hoare et al. (2022) and Rzehak et al., (2022). The equation for $\alpha_{rutile-melt}$ was determined by weighted curve fitting of equation E1 to the measured $\alpha_{rutile-melt}$ values and temperatures (T) in kelvin using the curve_fit function from the SciPy optimize subpackage.

$$10^3 \ln \alpha_{rutile-melt} = A \frac{10^6}{T^2} \quad (E1)$$

A is a constant which was determined by the curve fitting, and the 2σ uncertainty in A was calculated from the variance returned by the curve_fit function. The resulting equation is shown in table E1. The same approach was done for $\alpha_{ilmenite-melt}$, using natural ilmenite-melt pairs from Hoare et al. (2022). Mandl (2019) measured only one amphibole-melt pair and one phlogopite- (biotite-) melt pair from the Kneeling Nun Tuff. These values, along with a crystallisation temperature of 775°C based on a combination of zircon, titanite, amphibole and plagioclase thermometers (Szymanowski et al., 2019, 2017), were used to constrain $\alpha_{amphibole-melt}$ and

$\alpha_{phlogopite-melt}$ (table E1). The same method was done for $\alpha_{orthopyroxene-melt}$ with the experimental orthopyroxene-melt pair from Rzehak et al. (2021) where all Ti present was tetravalent (fO₂ = air). The 2σ uncertainty on these $\alpha_{mineral-melt}$ values were propagated to determine the 2σ uncertainties on the equations in table E1.

Table E1: Ti isotope mineral-melt fractionation factors determined from natural and experimental mineral-melt pairs. T is the temperature in kelvin (K).

Mineral	Fractionation Factor (α)	References
Rutile	$10^3\ln\alpha = -0.4343\ (\pm\ 0.0693,\ 2\sigma)\ \times\ 10^6/T^2$	Hoare et al. (2022), Rzehak et al. (2022)
Ilmenite	$10^3\ln\alpha = -0.5997\ (\pm\ 0.0771,\ 2\sigma)\ \times\ 10^6/T^2$	Hoare et al. (2022)
Amphibole	$10^3\ln\alpha = -0.2296\ (\pm\ 0.0670,\ 2\sigma)\ \times\ 10^6/T^2$	Mandl (2019)
Phlogopite	$10^3\ln\alpha = -0.2571\ (\pm\ 0.0659,\ 2\sigma)\ \times\ 10^6/T^2$	Mandl (2019)
Orthopyroxene	$10^3\ln\alpha = -0.0056\ (\pm\ 0.0502,\ 2\sigma)\ \times\ 10^6/T^2$	Rzehak et al. (2021)

Direct measurements of mineral-melt pairs are not available for clinopyroxene, garnet, phengite, epidote or titanite, so I used the reduced partition function ratios (RPFRs, β) obtained by *ab initio* calculations to determine $\alpha_{mineral-melt}$. The fractionation factor between two phases i and j is given by the ratio of their RPFRs ($\alpha_{i-j} = \beta_i/\beta_j$, e.g. Young et al., 2015). As no β_{melt} has been calculated, I can instead use my $\alpha_{rutile-melt}$ determined directly from mineral-melt pairs (table E1) and β_{rutile} (table E2) to calculate α_{i-melt} (equation E2).

$$\alpha_{i-melt} = \frac{\beta_i}{\beta_{rutile}} \times \alpha_{rutile-melt} \quad (E2)$$

RPFRs for rutile and garnet (pyrope with Ti⁴⁺ in 6-fold coordination) are from W. Wang et al. (2020), for clinopyroxene (Ti⁴⁺ in 6-fold coordination) is from Leitzke et al. (2018), and for titanite is from Aarons et al. (2021). These are given in table E2. No *ab initio* constraints on Ti isotope fractionation factors are available for phengite or epidote. Both of these silicate minerals primarily host Ti in octahedral sites, so – like Klaver et al. (2024) did – I estimated their $\alpha_{mineral-melt}$ by assuming that their RPFRs are identical to garnet (W. Wang et al., 2020).

Table E2: Ti isotope reduced partition function ratios. T is the temperature in kelvin (K).

Mineral	Reduced Partition Function Ratio ($x = 10^6/T^2$)	References
Rutile	$10^3\ln\beta = 1.19767x - 0.00959x^2 + 0.000154x^3$	W. Wang et al. (2020)
Clinopyroxene	$10^3\ln\beta = 1.69903x - 0.00972x^2 + 0.000127x^3$	Leitzke et al. (2018)
Titanite	$10^3\ln\beta = 1.26x - 0.0115x^2 + 0.000254x^3$	Aarons et al. (2021)
Garnet	$10^3\ln\beta = 1.70195x - 0.01864x^2 + 0.000380x^3$	W. Wang et al. (2020)
Phengite	*estimated same as garnet*	
Epidote	*estimated same as garnet*	

To calculate the magnitude of Ti isotope fractionation occurring during partial melting ($\Delta^{49}Ti_{melt-protolith}$) I used a mass balance approach following Klaver et al. (2021, 2024). The bulk isotope ratio of a closed system during partial melting is that of the protolith ($R_{protolith}$) and is given by equation E3, where C is the Ti concentration, F is the proportion of the phase and R is the isotope ratio.

$$R_{protolith} \approx \frac{C_{melt}F_{melt}R_{melt} + C_iF_iR_i + C_jF_jR_j + \cdots}{C_{melt}F_{melt} + C_iF_i + C_jF_j + \cdots} \quad (E3)$$

As $\alpha_{i-melt} = R_i/R_{melt}$, equation E3 can be re-written as:

$$\frac{R_{melt}}{R_{protolith}} = \frac{\sum_i(C_iF_i)}{\sum_i(C_iF_i\alpha_{i-melt})} = \alpha_{melt-protolith} \quad (E4)$$

For a closed system $\Delta_{i-j} = (\alpha_{i-j} - 1) \times 1000$, meaning:

$$\Delta^{49}Ti_{melt-protolith} = \left(\frac{\sum_i(C_iF_i)}{\sum_i(C_iF_i\alpha_{i-melt})} - 1\right) \times 1000 \quad (E5)$$

Equation E5 was used to calculate $\Delta^{49}Ti_{melt-protolith}$, with C_i and F_i taken from partial melting experiments and α_{i-melt} determined from mineral-melt pairs or RPFRs as previously described. Table E3 lists the experimental studies used for modelling. As the melt is included as a phase in equation E5, the value $\alpha_{melt-melt} = 1$ is used. The Ti isotope composition of the protolith ($\delta^{49}Ti_{protolith}$) was taken to be the weighted mean $\delta^{49}Ti$ of Neoarchean komatiites (0.001 ± 0.003‰, 2se, n = 17), so melt $\delta^{49}Ti$ was calculated using equation E6.

$$\delta^{49}Ti_{melt} = \delta^{49}Ti_{protolith} + \Delta^{49}Ti_{melt-protolith} \quad (E6)$$

Uncertainty on α_{i-melt} calculated from mineral-melt pairs ($\alpha_{rutile-melt}$, $\alpha_{ilmenite-melt}$, $\alpha_{amphibole-melt}$, $\alpha_{phlogopite-melt}$ and $\alpha_{orthopyroxene-melt}$) were considered the only sources of uncertainty for $\Delta^{49}Ti_{melt-protolith}$ as the uncertainty cannot be determined

for RPFRs. 2σ uncertainty was propagated through the model to determine the 2σ uncertainty on $\Delta^{49}Ti_{melt-protolith}$. Where there were multiple sources of uncertainty present in a single model (e.g. both residual rutile and amphibole were present), the uncertainty on $\Delta^{49}Ti_{melt-protolith}$ was approximated using the variance formula (equation E7). σ_f is the standard deviation of the overall function, while σ_x and σ_y are the standard deviations of variables x and y respectively. Equation E7 was also used to calculate the 2σ uncertainty on $\delta^{49}Ti_{melt}$, taking into account the 2σ uncertainty on both $\delta^{49}Ti_{protolith}$ and $\Delta^{49}Ti_{melt-protolith}$.

$$\sigma_f = \sqrt{\left(\frac{\partial f}{\partial x}\right)^2 {\sigma_x}^2 + \left(\frac{\partial f}{\partial y}\right)^2 {\sigma_y}^2 + \cdots} \quad (E7)$$

Model results are presented in Chapter 3 and Appendix F.

Table E3: Experimental studies used to constrain melting temperatures, and phase proportions and Ti concentrations for modelling Ti isotope fractionation during partial melting.

Partial Melting Scenario	References
Anhydrous eclogite melting	Pertermann & Hirschmann (2003), Spandler et al. (2008), Yaxley & Green (1998)
Amphibolite dehydration melting	Sen & Dunn (1994), Wolf & Wyllie (1994), Zhang et al. (2013)
Eclogite dehydration melting	Massonne & Fockenberg (2022)
Fluid-fluxed eclogite melting	Carter et al. (2015), Kessel et al. (2005), Laurie & Stevens (2012), Martin & Hermann (2018), Schmidt et al. (2004), Sisson & Kelemen (2018)
Phlogopite-bearing peridotite melting	Condamine et al. (2016)

A limitation of this approach to modelling Ti isotope fractionation during metabasite partial melting is that the experimental studies used to constrain phase proportions and compositions all use slightly different starting materials. TiO_2 content is a particularly important variable as Hoare et al. (2023) found that more TiO_2-rich protoliths stabilise higher proportions of residual Ti-bearing oxides and hence generate melts with slightly higher $\delta^{49}Ti$ than TiO_2-poor protoliths. This effect can be seen in my model results. The amphibolite starting material used by Wolf & Wyllie (1994) has the

lowest TiO$_2$ content at 0.4 wt% and no residual oxides were identified during melting. In contrast, the eclogite starting material of Laurie & Stevens (2012) had the highest TiO$_2$ at 2.5 wt%, which stabilised higher proportions (weight fraction of 0.02 – 0.04) of Fe-Ti oxides than most other experiments and produced the heaviest melts with δ^{49}Ti of 0.32 – 0.37‰. However, TiO$_2$ content is not the sole compositional control on the stability and abundance of minerals driving Ti isotope fractionation. For example, the high FeO* content of Laurie & Stevens (2012)'s starting material (16.2 wt%) is likely an important reason why residual ilmenite is present in their lower pressure (2.2 GPa) experiment. As ilmenite fractionates Ti isotopes more strongly than rutile (Hoare et al., 2022), the presence of residual ilmenite leads to melts with higher δ^{49}Ti.

Ti isotope fractionation during metabasite partial melting has also been modelled by Zhang et al. (2023) and Hoare et al. (2023) using thermodynamic phase equilibria models to constrain phase proportions and compositions. Comparison with the models of Zhang et al. (2023) is difficult because they modelled polybaric metabasite melting along set geothermal gradients, whereas my models are of isobaric melting. The most direct comparison can be made between the Hoare et al. (2023) models of E-MORB (enriched mid-ocean ridge basalt) and picritic plateau basalt amphibolite dehydration melting at 1.3 GPa and my amphibolite dehydration melting models at 1 – 2 GPa. Modelled $\Delta^{49}Ti_{melt-protolith}$ for plateau basalt melting is ~0.10 – 0.17‰ and agrees with my models, whereas E-MORB melting generates slightly heavier melts (Δ^{49}Ti$_{melt-protolith} \approx 0.15 - 0.25$‰). This is likely because the E-MORB composition used by Hoare et al. (2023) has a higher TiO$_2$ content (1.53 wt%) than the starting materials in the amphibolite dehydration melting experiments used here (0.4 – 1.23 wt%). This results in higher proportions of residual rutile in the Hoare et al. (2023) E-MORB melting model and hence slightly higher $\Delta^{49}Ti_{melt-protolith}$. Conversely, the Hoare et al. (2023) plateau basalt model has similar TiO$_2$ content to my models and results in similar calculated melt δ^{49}Ti.

Appendix F – Results of titanium stable isotope partial melting models for eclogite, amphibolite, and phlogopite-bearing peridotite

The results of the titanium stable isotope modelling of experimental eclogite, amphibolite, and phlogopite-bearing peridotite partial melts, presented in Chapter 3, are available as a Microsoft Excel file at:

https://ars.els-cdn.com/content/image/1-s2.0-S0012821X24004990-mmc2.xlsx